MECHANICS OF THE MITRAL VALVE AFTER SURGICAL REPAIR – AN IN VITRO STUDY

A Dissertation
Presented to
The Academic Faculty

by

Sai Muralidhar Padala

In Partial Fulfillment
of the Requirements for the Degree
Doctor of Philosophy in the
School of Biomedical Engineering

Georgia Institute of Technology
May 2010

MECHANICS OF THE MITRAL VALVE AFTER SURGICAL REPAIR - AN IN VITRO STUDY

Approved by:

Dr. Ajit P. Yoganathan, Advisor
School of Biomedical Engineering
Georgia Institute of Technology

Dr. David H. Adams
Department of Cardiothoracic Surgery
Mt. Sinai School of Medicine

Dr. Pedro J. Del Nido
Department of Cardiothoracic Surgery
Children's Hospital Boston
Harvard University

Dr. Vinod H. Thourani
Department of Cardiothoracic Surgery
Emory University School of Medicine

Dr. John N.Oshinski
Department of Radiology
Emory University School of Medicine

Dr. Rudolph R. Gleason
Department of Mechanical Engineering
Georgia Institute of Technology

Date Approved: April 05, 2010

To Amma and Nannagaru for their love and sacrifices…

ACKNOWLEDGEMENTS

So much happened in 6 years, and so many people were part of it, that I find the task of acknowledging everyone, similar to making a guest list for an Indian wedding. For all those I mention here, a big thank you! And for all those I missed, pardon my memory; memory loss is the most common symptom reported in graduating PhDs.

Firstly, I thank my doctoral thesis advisor Dr. Ajit P. Yoganathan. You took a huge risk in providing me the opportunity to pursue graduate studies at Tech; and I am indebted to you for admitting me to the program and into your lab. It is under your tutelage that I stumbled, fell, dusted myself, learnt to climb the ropes, to patiently reach the summit and enjoy the view, and not be afraid to do it all over again. I am indebted to you for trusting me through this process, and teaching me that it's ok to listen to myself before what others have to say. I salute your passion and undying spirit, and thank you, Tripti, Anila and Anant for providing me a home so far away from home.

I am very thankful to my thesis committee members for guiding me through the last 5 years, and critically reviewing my experimental plans, abstracts and manuscripts. Specifically, I thank Dr. David H. Adams for providing the opportunity to present my work at the prestigious American Association of Thoracic Surgeons annual meeting in 2008 and 2009, and teaching me the difference between 'good' and 'perfect' presentations. I acknowledge Dr. Pedro Del Nido, for introducing me to the field of pediatric cardiac surgery and for being readily available to discuss my research ideas in spite of his busy clinical schedule. I am indebted to Dr. Vinod Thourani, for the energy he brings into the lab and for his immense optimism. Thank you for believing in me, and

I am excited to start my post-PhD career with you. Working with clinicians veered my focus at times to the big picture than the smaller details, and I thank Dr. John Oshinski and Dr. Rudy Gleason for grounding my feet in perfecting the engineering details to get a clearer vision of the bigger picture.

In the last 5 years this project evolved from basic engineering to clinical translation, and provided me the unique opportunity to work with several investigators across the world. Firstly, I thank my lucky stars for the opportunity to work with Dr. Nikolay Vasilyev, who I admire as someone with the hands of a surgeon but the brain of an engineer, someone I respect as my biggest critic and I thank you for getting me to think on my feet. Thank you Nick and I really mean it! Dr. Valavanur Subramanian in the last year for imparting your perspectives on mitral valve function, whether it is over a slice of pizza, or at a fancy Italian dinner in Boston. Thank you for your kind invitation to present a young investigator keynote at ISMICS, and for introducing me as an engineer who should be doing mitral valve surgery. Hopefully one day I will live up to your compliments! Dr. Joseph and Robert Gorman, I thank you for guiding me through writing several mitral valve grants, and for providing your immense expertise from the animal models. Joe, thank you for making it to my defense; I appreciate your interest in my work. Dr. Michael Sacks for lending me your biomechanics expertise and for writing recommendation letters in the short time frames I always give you. Thank you! As promised the chordal insertion paper was accepted before I got my last signature! There are several others who played an important role in shaping this project and me as a researcher, and I am thankful to each one of you.

Though the work in this thesis carries my name, it would not be possible without the excellent team of undergraduate researchers I had over the years. Subina Banerjee, Jim Owen, Sarah Hooson, Laura Croft, Moses Nyaribo, Scott Powell, Michael Sweet, Katie Bell, Ross Hutchison, Lazarina Gyoneva, Benedicte Cardinau, and Manuel Rausch; thank you for your curiosity, dedication and patience. I want to specially acknowledge Ross Hutchison and Lazarina Gyoneva, for patiently putting up with my unreasonable demands, for toiling with me over weekends because I dreamt of a new project the night before, and for never giving up on me even in the most frustrating times. I know it is surprising that I am graduating, but yes we made it! On the same note, a big thanks to the "Danish Connection" – Dr. Jensen, Jesper, Thomas, Morten, Soren, Rasmus, Tommy and Bjarne. You are some of the best engineers I have worked with, and I look forward to visiting infamous Aarhus in the near future. Skål!

It is tough to express in words how much I really owe the past and present members of the Cardiovascular Fluid Mechanics Laboratory! Leo, Jorge, Hiroumi, Anna, Chang, Zhaoming, Kerem, Prasad, Doni, Kartik S, Philippe, Diane, Helene, Kartik B, JP, Neela, Shiva, Dr. Kendoush, Resmi, Chris, Erin, Maria, David, Andrew, Brandon, Christina, Elaine, Swetha and Hubert, thank you for your friendship, support and advice. Back in 2004 when I was a 21 year old bright-eyed fresh graduate facing life outside India for the first time, you gave me a warm welcome and left an indelible imprint on my personality. Jorge, in ways that I cannot articulate you have taught me nuances of professional life that I will never forget. Thank You! A cheerful toast to all the members of the mitral [and tricuspid] valve group; we always ensured there was enough fun and drama in the otherwise arid life of the CFMLAB, and rest of the group couldn't be less

jealous! It is tough to get through the intense life of a PhD student, without help from the administrative support staff who always wore a smile and never turned down my requests and SOS messages. Michelle Mayberry, Colly Mitchell, Lakeisha Wheaton, Gail Spatt, Cosetta Williams, Chris Ruffin, Sally Gerrish, Shannon Sullivan, Floyd, Rudy Paratchek, Penelope Pollard, Sandra Wilson, and Tracie Dinkins, THANK YOU!

To all my friends, from kindergarten till now – you reflect the person I am, and I could not do it without you. Arun, Sai, Madhu, Ravi, Ajay, Ashwin, Rakshita, Anand, Avinash, Rajasekhar, Parikshit, Radhika, Zulfia, Archana and Deepti, thank you for standing by me in my up's and down's. Moving westward began a new chapter in my life and brought in new friendships. KB, Smitha, KS, Yash and Ayona, you made life in this alien land so easier to begin and I cherish all the time we spent cooking exotic creatures because KB found them 'interesting', arguing in public places that people around thought we were nuts, tasting fine wine and scotch [yes 'fine' is the right word], and just spending weekends discovering new restaurants. Srin, Mamta, Pritty, Rahul, Ramesh, Laveeta, Ryan and Andrea thank you for your friendship! I could have never asked for better roommates than Krishna, Vikram and Jaswanth, with whom I have explored Atlanta, and had some of the best times. JP and Neela, in the recent past you have got my back so many times that I admire your patience in putting up with me! I look forward to enjoying the 'ageing' Glenlivet with you on a forthcoming Friday. All's well that ends well, and I could not ask for a better friend than Diane, with whom in the last few months of this long PhD I went from "can't run beyond 100 meters" to "completing a 10K race". Thank you for inspiring me, keeping company for a morning coffee, lending me your ear and the

Buick when writing a 400 page document got too stressful, and for challenging me to talk without speaking, and hear the sound of silence.

I could write a whole chapter thanking my family for all that you have done for me, and I still wouldn't do justice. My parents Dr. P. S. N. Reddy and Dr. P. L. Prasunamba, you have sacrificed so much for yourselves so that I and Chakri could achieve bigger things. You taught me to pursue excellence over success, passion over fame, and to give more than I ask. Dr. Chakradhar Padala, you are a bad opponent but a great elder brother. You always set the standards very high for me to reach, but always helped me find the right path to reach the target, and I cherish being the pampered younger one. I could never ask for a better sister-in-law than Dr. Suchitra Konduri, for making my dream to attend a top 5 ranked graduate program a reality, and for all the affection you shower on me. Thank You Amma, Nannagaru, Anna and Vadina!

As I write the last few words of this infinitesimally long thesis, I look back at the bygone years and wonder if I am any less confused about career and life than 6 years ago. What have I learnt? What have I achieved? Soon did I realize that I learnt to persist even when things go awry, and to take responsibility without fearing the consequences. This career step built in me the courage to face the real world, and the capacity to achieve great things in the life to come…

TABLE OF CONTENTS

Page

LIST OF TABLES

LIST OF FIGURES

LIST OF ABBREVIATIONS

MV	Mitral Valve
LA	Left Atrium
LV	Left Ventricle
BS	Barlow's Syndrome
FED	Fibro Elastic Deficiency
MHV	Mechanical Heart Valve
BHV	Bioprosthetic Heart Valve
FMR	Functional Mitral Regurgitation
DLT	Direct Linear Transformation
ACGI	Adaptive Control Grid Interpolation

SUMMARY

Mitral valve disease is widely prevalent among pediatric and adult population across the world, and it encompasses a spectrum of lesions which include congenital valve defects, degenerative valve lesions, and valve dysfunction due to secondary pathologies. Though replacement of the diseased mitral valves with artificial heart valves has been the standard of care until early 1990's, current trends have veered towards complete surgical repair. These trends are encouraging, but current repair techniques are plagued with lack of durability and high rates of failure within 10 years after repair. With increasing number of patients receiving mitral valve repair, there is now an immediate need to understand the mechanisms of repair failure, and assess the role of several clinical risk factors on valve repair. In this thesis, an in vitro pulsatile left heart simulator was developed to mimic the congenital and adult mitral valve pathological morphologies in normal porcine valves, and simulate the pathological valve hemodynamics and mechanics. Different surgical repair techniques were used to correct the valve lesions, and the post repair valve hemodynamics, mechanics and geometry were assessed using quantitative measurement techniques. The extent to which each repair restores physiological valve function and mechanics was assessed, and the impact of different pathological risk factors on repair failure mechanisms was investigated. It is expected that the knowledge from this thesis would play an important role in the evolution of mitral valve surgical repair, and guide the development of more effective and long-lasting heart valve repair technologies.

CHAPTER 1

INTRODUCTION

1.1 THE MITRAL VALVE

The Mitral Valve [MV], which is the left atrioventricular valve in the human heart, maintains unidirectional blood flow from the left atrium [LA] into the left ventricle [LV]. The valve has a complex structure with multiple components, which work synchronously and maintain a delicate force balance to ensure proper valve function. During diastole, the valve opens to allow blood from the left atrium to fill the left ventricle; and during systole the valve closes to restrict back flow or regurgitation through the valve into the left atrium.

1.2 DISEASES OF THE MITRAL VALVE

Mitral valve disease is widely prevalent among pediatric and adult population across the world. The disease encompasses a spectrum of lesions which include congenital, degenerative, and functional pathologies. In the congenital population ($\leq$ 15 years of age), common pathologies include mitral annular stenosis [MS], common atrioventricular valve in complete atrioventricular canal defects [AVCD], mitral valve prolapse [MVP] in Marfan's Syndrome, and valve degeneration or bacterial endocarditis

in rheumatic heart disease. Among adults (≥ 15 years of age), mitral valve lesions can be primarily classified into degenerative and functional etiologies. The first kind, degenerative mitral valve disease is most prevalent in the western world, manifesting as Barlow's syndrome [BS] involving leaflet and chordal thickening, or Fibroelastic Deficiency [FED] involving leaflet and chordal thinning. The second type, functional mitral deficiencies are caused due to geometric distortion of the mitral valve structure due to underlying ventricular disease, either ischemic or idiopathic dilated cardiomyopathy.

1.3 MITRAL VALVE REPLACEMENT

Whether a diseased mitral valve should be replaced with a mechanical heart valve [MHV] or bio-prosthetic heart valve [BHV] has been a topic of controversy since early 1980's. Historically, surgical repair of mitral stenosis was attempted as early as 1942 but was associated with high rates of mortality due to the crude surgical techniques used, and dearth in techniques to arrest the heart during surgery[2]. With the advent of the heart-lung machine in early 1950's and the use of hypothermic cross clamping to completely arrest the heart [3], focus has shifted from improving the crude surgical techniques towards development of mechanical heart valves [4]. Several mechanical and bioprosthetic valves were used to replace the diseased mitral valves, with decent success [4-6]. However, the results from aortic valve replacement [AVR] could not be replicated on the mitral position due to complex valve hemodynamics, loss of annular-ventricular continuity after chordal excision, and the need chronic anticoagulation therapies.

1.4 BEGINNINGS OF MITRAL VALVE REPAIR

In an honorary lecture at the 63rd annual meeting of the American Association of Thoracic Surgeons in 1983, a French surgeon Dr. Alain Carpentier presented a landmark paper titled "The French Correction", on mitral valve repair [7]. In his talk and subsequent paper, he presented an armamentarium of surgical techniques to repair degenerative mitral valve pathologies that laid the cornerstone for the shift towards mitral valve repair [MVRe]. Though Dr. Carpentier was not the first one to propose the use of prosthetic rings for mitral valve repair[8], his talk encouraged the use of "remodeling annuloplasty rings" to "support the mitral valve repair". From a low repair rate of 5% in 1980's, the number of mitral valve repairs has consistently risen to 40.53% in 2000, and 59.78% in 2008 in patients with degenerative valve disease in the United States alone. Today, mitral valve repair is the standard of care over mitral valve replacement [MVR], with 99% of the patients offered valve repair at surgical centers experienced in valve repair and about 40% receiving valve repair at less experienced centers [9].

1.5 CURRENT TRENDS IN MITRAL VALVE THERAPY

In the current era of cardiac surgery, the benefits of mitral valve repair are well established, with increasing number of surgeons shifting towards complete repair over replacement. However, clinical data from retrospective trials indicates suboptimal outcomes with valve repair, with 15% to 80% of the patients presenting with recurrent mitral regurgitation [MR] due to repair failure within 10 years after the primary surgery [10-12]. The failure rates were largely dependent on the etiology of the diseased valve,

with higher repair success in degenerative lesions and lower repair success in congenital and functional lesions.

1.6 RISK FACTORS FOR REPAIR FAILURE

Mechanistic insights into the failure mechanisms for mitral valve repair are currently lacking. Though substantial clinical literature on outcomes of valve repair exists, the risk factors or a detailed knowledge of the mechanisms leading to repair failure are currently unknown. Results from most clinical studies are inconclusive, as the patients included in such studies have variable severities of the disease, different medical histories, and the institutional policies for repair techniques may vary. To overcome these shortcomings, animal models of mitral valve disease have been developed, but are limited to functional mitral regurgitation [FMR] [13-19]. Genetics behind congenital and degenerative mitral valve lesions are vague, thus impeding the development of animal models for these lesions.

1.7 OBJECTIVE OF THIS THESIS WORK

In this thesis, an in vitro pulsatile mitral valve model that can simulate congenital, degenerative and functional mitral valve lesions is developed. Echocardiographic and cadaveric data from human subjects is used to carefully mimic different mitral valve pathologies in this in vitro model, and different surgical techniques to correct these lesions are compared from hemodynamics and mechanics perspectives. The mechanisms of repair failure are understood by replicating different clinically identified risk factors on these surgically repaired valves, and their impact on valve function and mechanics is explained. It is expected that the knowledge attained from these studies would provide

the basis for improved repair techniques that have better acute and chronic outcomes, and also guide the development of optimal next generation mitral valve repair technologies.

1.8 EXPERIMENTAL DESIGN

This thesis is primarily classified into three specific aims focused on – [Aim 1] congenital mitral valve repair, [Aim 2] degenerative mitral valve repair, and [Aim 3] repair for functional mitral regurgitation. In the first aim, the hemodynamics of cleft mitral valve repair in atrioventricular canal defects was investigated. In the second aim, various studies focused on assessing the hemodynamics of current degenerative mitral valve repair techniques and engineering methods to improve the durability of repair were investigated. In the third aim, studies focused on understanding the role of pre operative mitral valve geometry in mitral valve repair for functional defects of the mitral valve as seen in ischemic and idiopathic dilated cardiomyopathy.

1.9 SUMMARY OF RESULTS

The results from this thesis provide mechanistic insights into the failure mechanisms of various surgical techniques practiced in current clinical setting. Impact of hemodynamic, structural and mechanical risks factors on the acute and extrapolated chronic outcomes of valve repair are reported. The data thus emphasizes on the need to shift focus from intra operative relief of mitral regurgitation, towards a structure-to-function approach to understand mitral valve pathologies and tailor repair techniques to the specific valve etiology.

CHAPTER 2

LITERATURE REVIEW

2.1 THE HUMAN CARDIOVASCULAR SYSTEM

The human body is a collection of organ systems, which have specific functions and work in tandem with one another. The cardiovascular (*Greek Etymology, Kardia = Heart; Vasculum = Small Vessel*) system is one such organ system that delivers nutrients, gases, hormones and cells to all the organ systems in the body, while maintaining their homeostasis. Every organ in the human body is perfused by the cardiovascular system through a complex vascular network that is designed to provide sufficient nutrients to every single cell in the human body, independent of its location in the human body.

The earliest known reference to the cardiovascular system is in the Ebers Papyrus in 16th Century BCE, where the connection between the heart and the arteries is acknowledged. By 6th century BCE, the knowledge of life sustaining fluids flowing through the body was known to Sushruta, an ayurvedic physician in ancient India [20]. In a recent review of his works, Dwivedi et al. reported reference to arteries as the channels carrying these vital fluids to distal organs[21]. Around 4th century BCE, valves in the human heart were discovered by a physician of the Hippocratic School, even though their

function was unknown. The Greek physician, Herophilus (335-280BC) distinguished arteries from veins but attributed the vascular pulse as an inherent property of the vessels. In 2nd century AD, the Greek physician Galen identified the dark red fluid flowing through the veins and the bright red fluid flowing through the arterial system, and proposed that the venous blood is created in the liver while the arterial blood was generated in the heart, with no blood coming back to either the liver or the heart. Later he corrected his findings, and proposed that blood is sucked into the heart from the venous system into the left ventricle, which ultimately passes through pores in the intra ventricular septum into the right ventricle. The pulsation of the arteries was thought to move the blood from the heart to the distal organs, but not the beating of the cardiac muscle. In 1025, Avicenna a Persian physician accepted Galen's view but developed accurate theories on cardiac cycles, contraction and relaxation of the myocardium, and valvular function. By 1242, Ibn al-Nafis an Arabic physician discovered the pulmonic circulation, and stated that the blood has to pass from the right ventricle into the lungs through the vena arteriosa, mingle with air in the lungs, and pass through the ateria venosa into the left ventricle. He also discovered that small communications or pores between the pulmonary artery and vein are necessary for transfer of blood and thus laid the foundation for the discovery of the capillary system. Few centuries later, William Harvey an English physician conducted a series of experiments and in 1628 reported that the beats produced by the heart provide continuous circulation of blood through minute connections between the arteries and veins, developing the closed system theory [22]. Though his ideas were a leap ahead of his predecessors, he did not discover the capillary system and it was unknown until Marcello Malpighi discovered it in 1661. These

physicians and keen scientific thinkers established the fundamental structure of the cardiovascular system shown in Figure 2-1, one organ at a time, and in this section a brief review of each organ as understood today is presented.

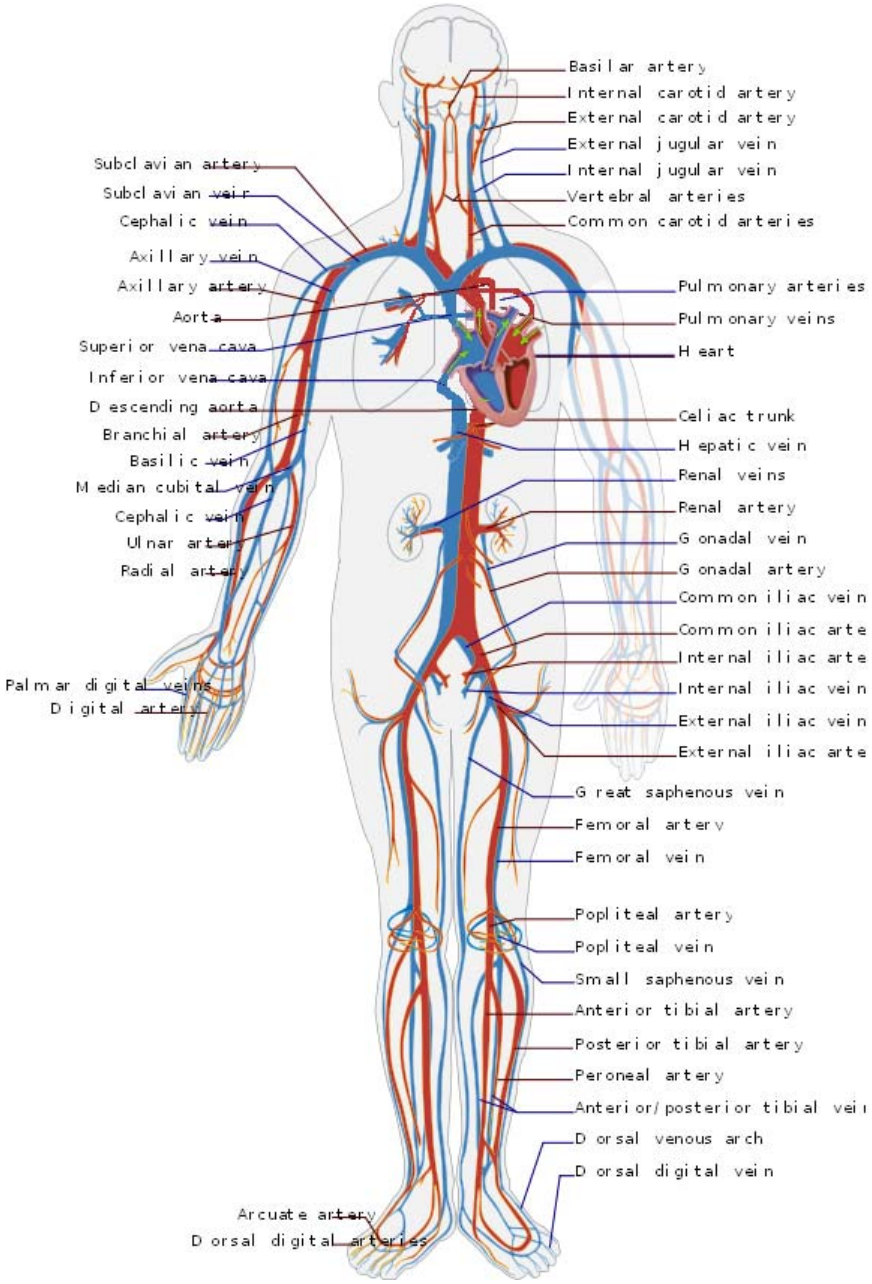

Figure 2-1 The Human Cardiovascular System
[Source - Wikipedia [22]]

The complex cardiovascular system primarily consists of three main components[23]:

- Heart
- Blood Vessels, and
- The Blood

2.1.1 THE HUMAN HEART

The human heart is an electro-mechanical pump with remarkable properties, but one whose failure is the leading non-accidental cause of death in developed countries. The primary function of the heart is to pump blood through the network of blood vessels to deliver nutrients and remove metabolic wastes from different organs. The heart has four chambers: two atria that are the low pressure reservoirs and two ventricles which are the high pressure pumping chambers as shown in Figure 2-2 [24]. The atrial walls are separated from the ventricular walls by a basal skeleton, which is a fibrous framework formed by the rings of the four heart valves and surrounding connective tissue. The two atrioventricular valves connect the atria to the ventricles and the two semilunar valves join the ventricles to the outflow tracts. These valves maintain unidirectional blood flow through the heart such that the mechanical work required to pump the blood is minimized.

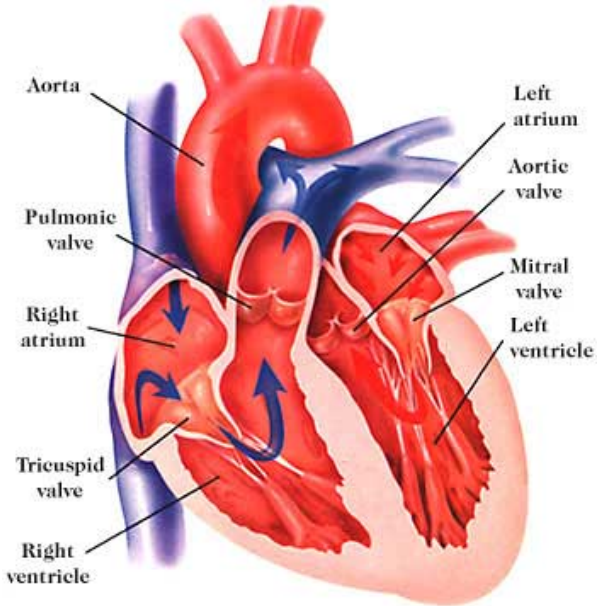

Figure 2-2 Illustration of the human heart
Source: www.usc.edu [23]

2.1.2 MYOCARDIAL ARCHITECTURE

2.1.2.1 Tissue Level Architecture

The mechanical function of the heart depends to a large extent on its material properties. The atria are thin walled compliant chambers that act as reservoirs for the blood flow to and from the lungs. The ventricular chambers, which are the pumps, are thick-walled muscular chambers. The right ventricle (max pressure: 2.5 kPa) which pumps blood to the lungs is much compliant and thinner than the left ventricle (max pressure: 15 kPa) that pumps blood to the distal organs of the body. The cardiac muscle is a composite of discrete layers of myocardial muscle fibers tightly bound by collagen, a protein that forms the connective network. The heart wall can be classified into three layers as shown in Figure 2-3 [25]: (a) ***Epicardium*** – the outermost layer of the heart that is reinforced with fibers that provide structural integrity, (b) ***Myocardium*** – the middle layers which is a synctium of contractile cardiac myocytes- the force generating

components, and (c) ***Endocardium*** – the innermost layer of endothelial cells that is in constant contact with blood. These layers have several lamineae that are loosely coupled and can slide relative to each other. The lamineae are four to six cells thick and branch in different directions throughout the ventricular walls.

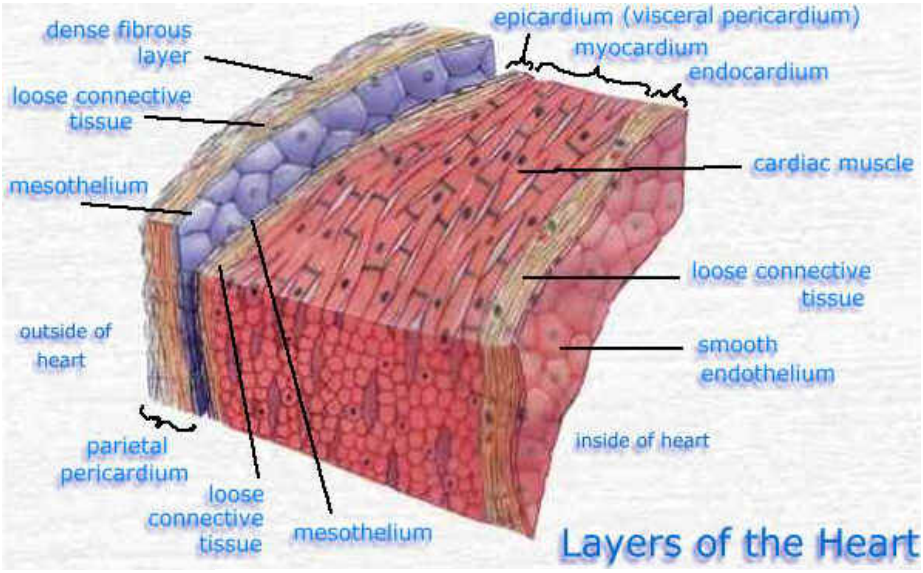

Figure 2-3 Layers of the Heart Wall
Source: http://www.jdaross.cwc.net [24]

2.1.2.2 Cellular Micro Architecture

Cardiac myocytes or muscle cells generate the active force in the myocardium, resulting in ejection of blood or the heart beat. Typically, myocytes are cylindrical with lengths ranging from 80 to 100µm and widths ranging from 10 to 20µm as shown in Figure 2-4 [26]. These myocytes are arranged in 3D patterns throughout the myocardium and are connected to one another through intercalated disks at their ends. These intercalated disks allow conduction of the voltage from one cell to another during electrical depolarization. Electrical impulses are generated by the pacemaker cells in the sino-atrial node, and these impulses propagate through the ventricular wall through a

specialized conduction system of Purkinje fibers. As the electrical impulses pass through the heart wall, the membrane potential of the Myocyte is altered. Multiple voltage gated ion channels are present in the cellular membrane that open due to the change in the voltage in the cell membrane. This result in influx and efflux of Ca^{2+}, K^{+} and Na^{+} ions from the cell.

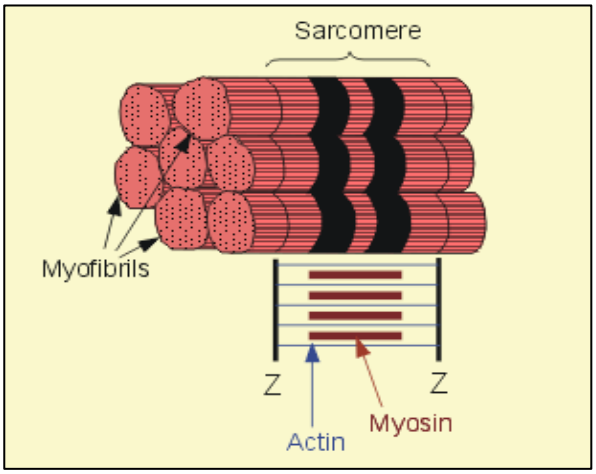

Figure 2-4 Sub-cellular structure of the cardiac myocyte depicting the myofibrils each of which contain myofilaments
Source: www.cvphysiology.org [25]

2.1.2.3 Sub-Cellular Contractive Biophysics

The rate of ionic flux across the cell membrane determines the magnitude of contractile force generated by the Myocytes. As the voltage gated channels on the cell membrane of the Myocyte open, the Ca^{2+} entering the cell combine with the contractile proteins in the cell and initiate contraction. The fundamental contractile or force generators of the Myocytes are the Sarcomeres, which are a network of the proteins Actin and Myosin. The Sarcomeres are typically 2µm in length and a chain of these Sarcomeres span between the two ends of the cardiac cell. Each cardiac Myocyte typically consists of

40-50 Sarcomeres in series and interconnected end-to-end through intercalated disks with an intricate network of a variety of proteins as shown in Figure 2-5. Myosin is the protein that makes up the thick filaments of the myofibril, and is related to the muscle's speed of contraction. Each Myosin molecule is composed of two heavy protein chains that intertwine to form a long coiled tail and a pair of tadpole like heads. Actin is the protein that makes up the thin filaments of the muscle fiber. One Actin molecule is a globular protein (G-Actin), represented by a round ball. Multiple globular proteins polymerize to form long chains or filaments (F-Actin). In three-dimensional array, the Actin and myosin molecules form a lattice of parallel, overlapping thin and thick filaments as shown in Figure 2-5[26]. As the muscle contracts, the thick and thin filaments slide past each other, moving the Z-disks of the sarcomere closer together. The force that pushes the Actin filament is the movement of the Myosin crossbridges that link Actin and Myosin. During muscular contraction, movement of the flexible Myosin crossbridges pushes Actin filaments towards the center of the sarcomere. At the end of the power stroke or contraction, the Myosin head releases its bound Actin, then swings back and binds to a new Actin molecule, ready to start another cycle.

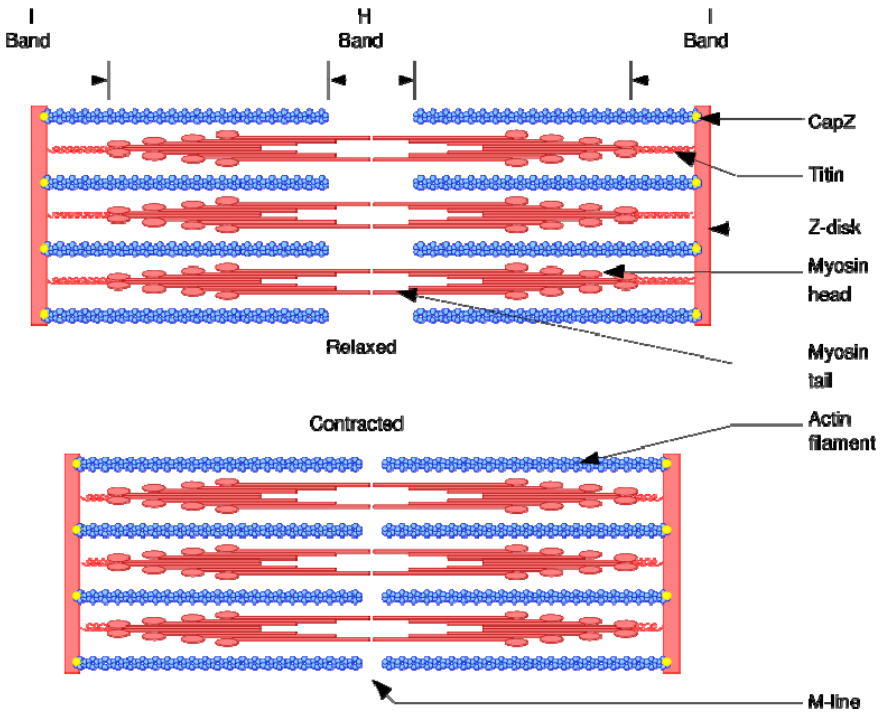

Figure 2-5 Schematic of the Actin-Myosin System
Source: www.cvphysiology.com [25]

2.1.2.4 Electro Mechanical Coupling

A key property of cardiac muscle is the ability of a single muscle fiber to execute graded contractions, in which the fiber varies the amount of force it generates. The force generated depends upon the number of active cross bridges in the Actin-Myosin system, which depends upon the cytosolic Ca^{2+} concentration. The flow of Ca^{2+} ions to the myocytes is determined by voltage gated Ca^{2+} channels on the membrane of the Myocyte. These voltage gated channels open when they receive an action potential generated by the auto rhythmic pacemaker cells via the electrical conduction system that spreads through the entire atrial and ventricular muscle. Electrical potential is generated by the pacemaker cells in the sinoatrial node (SA node), which spreads through adjacent myocytes via the gap junctions. As shown in Figure 2-6 [27], the depolarization wave starts in the SA

node, passes rapidly through the atrial muscle to the atrioventricular node (AV node). Ventricular depolarization subsequently starts when the depolarization wave spread towards the apex through the Purkinje fibers and then upwards from the apex along the outer walls, resulting in one complete contraction cycle.

(A)

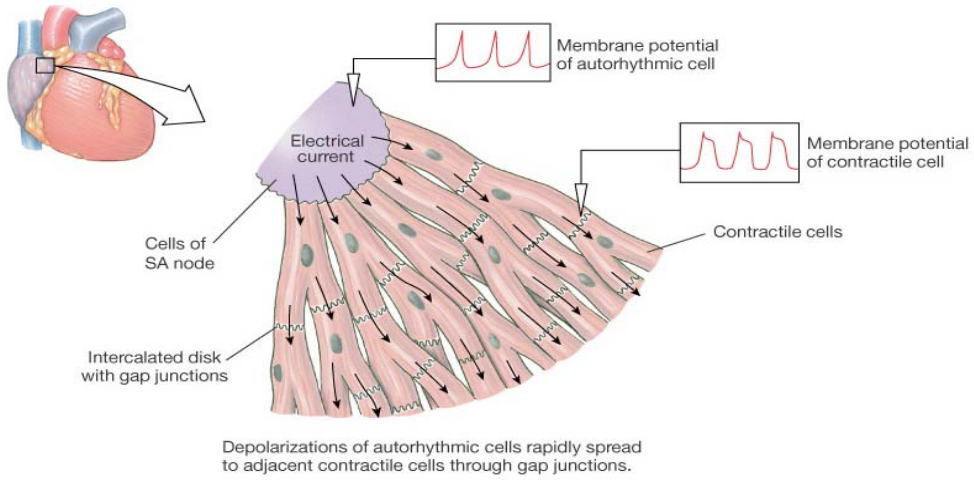

(B)

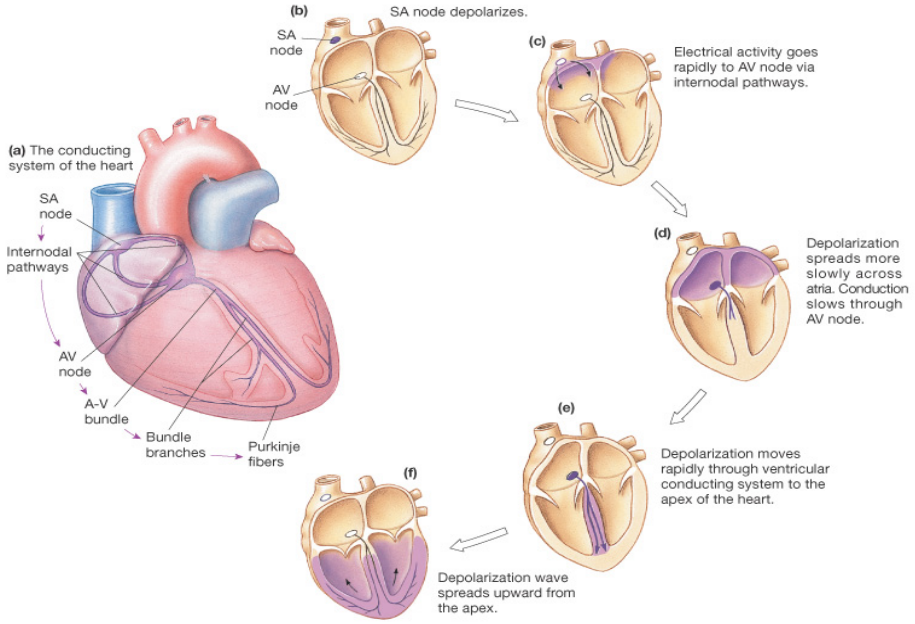

Figure 2-6 (A) The depolarization wave generated by the pacemaker cells spreading through adjacent myocytes via the gap junctions. (B) Path of the depolarization wave in a normal heart that induces sequential mechanical events in a cardiac cycle.

Source: Human Physiology – an Integrated Approach, by Dee Unglaub Silverthorn, III Edition[26]]

2.1.3 THE CARDIAC CYCLE

A cardiac cycle is defined as the duration from the beginning of one heart beat to the beginning of the next one. It is primarily divided into two phases: systole, the time when the muscle is contracted; and diastole, the time when the muscle is relaxed. In normal humans with an average heart rate of 70 beats per minute, the systolic duration is between 290-350 msec and diastole around 550-600msec, with the rest associated with isovolumic contraction and relaxation. Figure 2-7[27] schematically illustrates the events in one complete cardiac cycle, with the associated pressure and flow waveforms measured in the different chambers of the heart.

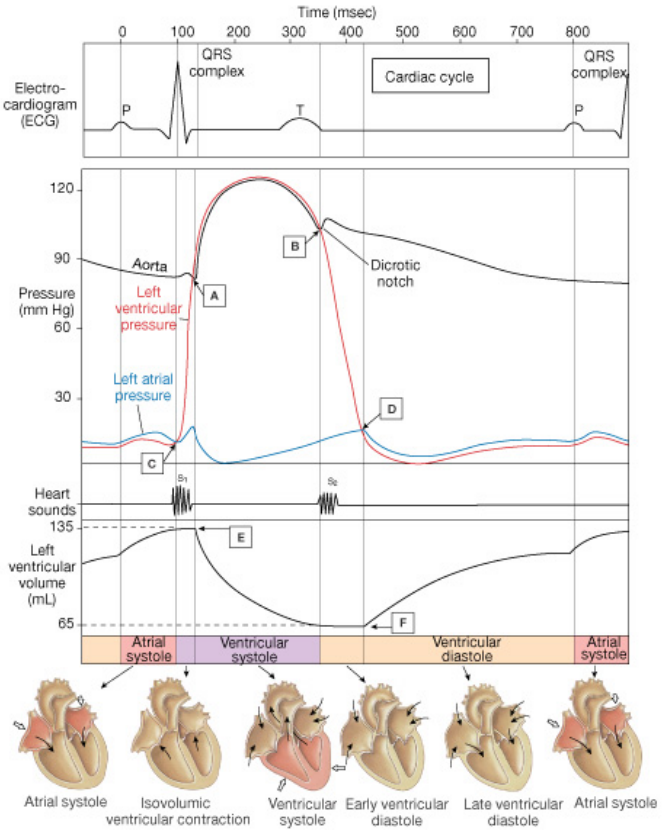

Figure 2-7 Wiggers diagram showing the relationship between the electrocardiogram, heart sounds, and pressure and volume changes in the human heart during the cardiac cycle. [26]

2.1.4 BLOOD VESSELS

Blood vessels are the channels through which oxygenated blood is transported to the distal organs, allows exchange of nutrients in the organs, and then carries waste away from the organs. Based on their function, blood vessels can be classified into arteries, which carry blood away from the heart; capillaries, which allow exchange of nutrients from the blood to the organs; and veins, which carry blood from the capillaries back to the heart. Both arteries and veins have a three layered structure – [Innermost] called the Tunica Intima, consists of endothelial cells that are form a synctium through the Glycocalyx, a polysaccharide intracellular network; [Middle] called the Tunica Media, consists of smooth muscle cells, circularly arranged elastic fibers, connective tissue and other polysaccharide substances; and [Outermost] called the Tunica Adventitia, entirely made of connective tissue and is vascularized. A schematic of the gross laminar cross section of the blood vessels is shown in Figure 2-8[27], though the thickness and composition of each layer differs between the arterial and the venous system.

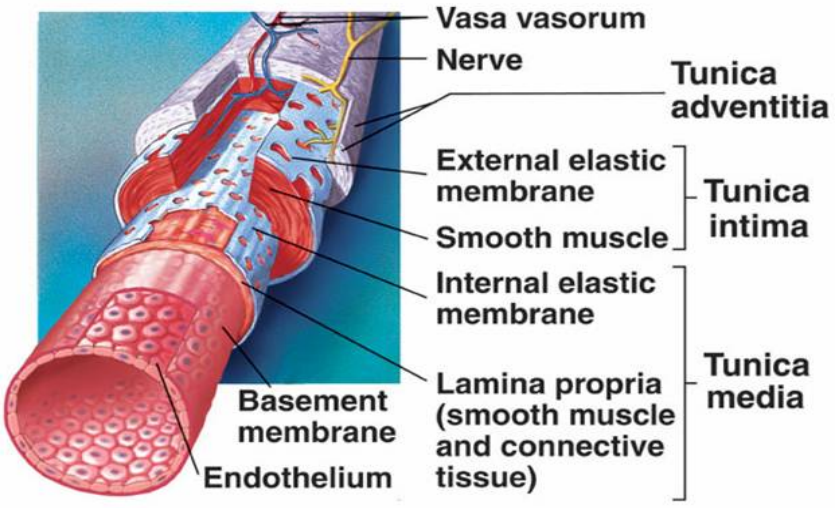

Figure 2-8 Cross sectional schematic of a blood vessel depicting the laminar structure and the respective constituents of each layer. Figure copyrighted by Tata McGraw Hill. [26]

2.1.5 BLOOD

Blood is a life sustaining bodily fluid that delivers necessary nutrients, gases and hormones to cells and transports away their waste. It is a multi phase emulsion that consists of: (A) Red Blood Cells, (B) White Blood Cells, and (C) Platelets. Plasma is the fluid portion of the blood, within which cellular elements are suspended. Waster is the main component of plasma, accounting for about 92% of its weight. Proteins account for another 7%, with the remaining 1% consisting of dissolved organic molecules, ions,

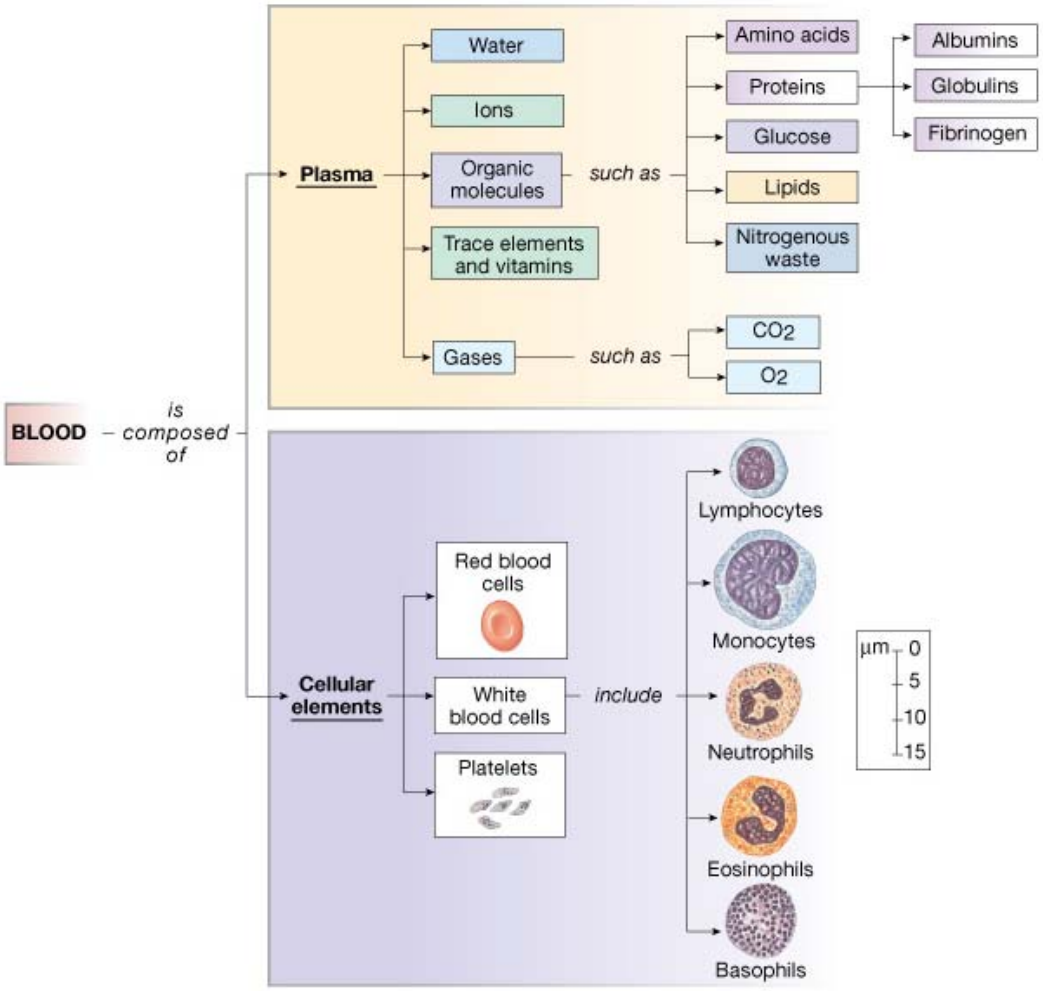

Figure 2-9 Plasma and cellular elements of human blood. [Figure reproduced from Human Physiology – an Integrated Approach, by Dee Unglaub Silverthorn, III Edition[26]]

vitamins, and dissolved oxygen and carbon dioxide. The liver makes most plasma proteins, Albumins, and releases them into the blood stream. The presence of proteins in blood increases its osmotic pressure compared to the interstitial fluid, and thus creates a gradient to pull water from the interstitial fluid into the capillaries. The plasma proteins serve several purposes including blood clotting, immune response, and carriers for steroid hormones, cholesterol, ions, and drugs. Figure 2-9 summarizes the composition of blood, separating the plasma and the cellular elements[27].

2.1.6 THE HEART VALVES

Valves in the heart ensure unidirectional blood flow through the heart, with one set of valves between the atria and the ventricles, and another between the ventricles and the great arteries as shown in Figure 2-10 [27]. Though both sets of valves serve the same purpose of preventing backward flow of blood, they are structurally distinct. The valves between the atria and the ventricles are called the atrioventricular valves, which includes the mitral valve between the left atrium and the left ventricle, and the tricuspid valve [TV] between the right atrium [RA] and the right ventricle [RV]. These valves are thin flaps of tissue that are attached at their base to the atrioventricular ring, and on the ventricular side the collagenous chordae tendineae [CT] attach the flaps to the papillary muscles [PM] in the myocardium. The second set of valves between the ventricles and the outflow tracts are called the semi lunar valves, which includes the aortic valve [AV] between the left ventricle and the aorta, and the pulmonary valve [PV] between the right ventricle and the pulmonary artery. These valves have three cuplike leaflets that fill with

blood and close under reverse pressure gradient. Because of their shape, these valves do not need chordae tendineae as the atrioventricular valves.

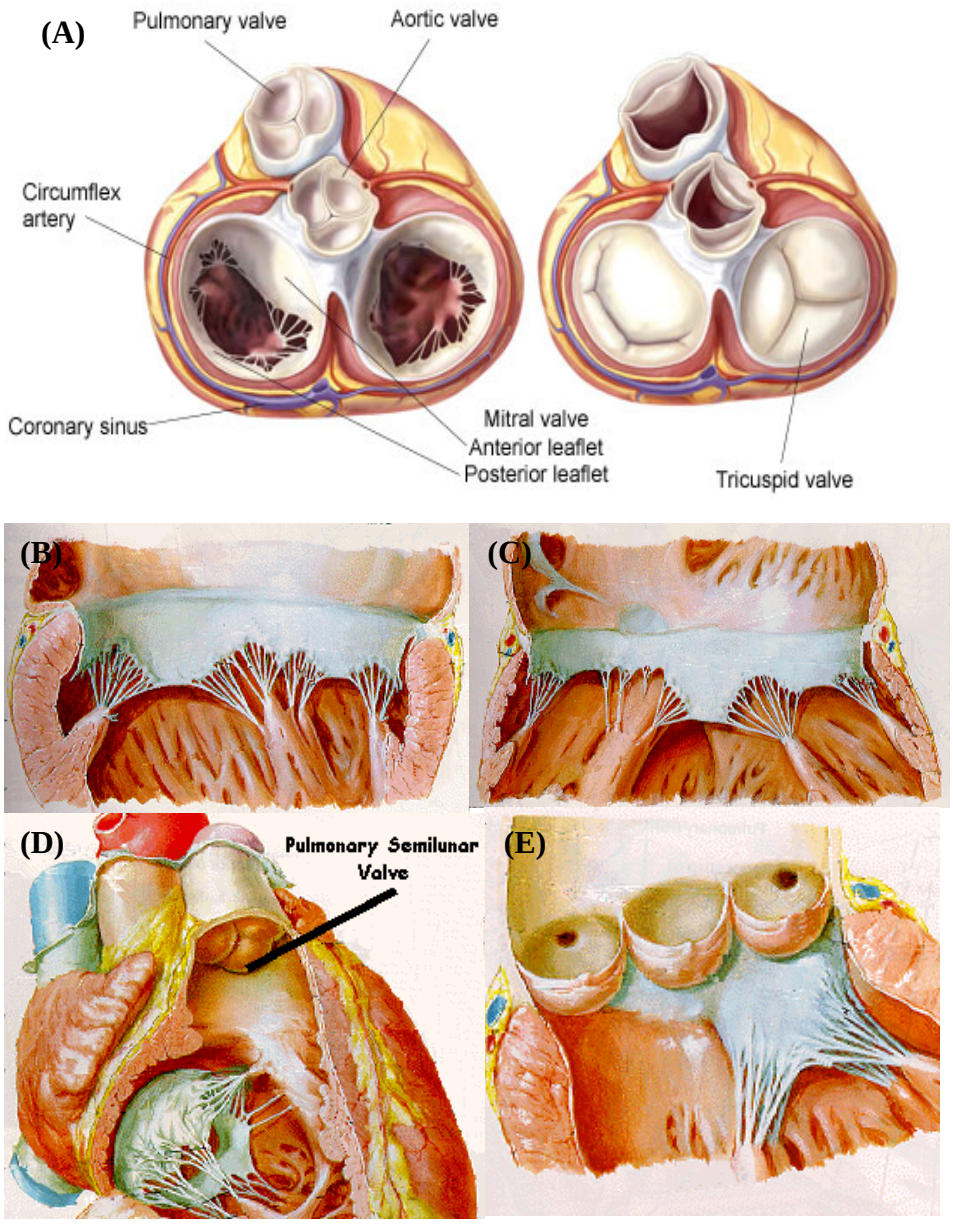

Figure 2-10(A) Schematic of the human heart depicting the four heart valves, (B) The mitral valve with the two leaflets, chordae and the two papillary muscles; (C) The tricuspid valve with the three leaflets and three papillary muscles; (D) The pulmonary valve with its three semi lunar leaflets; (E) The aortic valve with its two coronary and one non coronary semi lunar leaflet. [26]

2.1.7 THE MITRAL VALVE

The focus of the current study, the Mitral Valve or the left atrio-ventricular valve, is located between the left atrium and the left ventricle. The function of the mitral valve is to control the flow of oxygenated blood from the pulmonary veins to the left ventricle. The normal mitral valve opens during diastole, when the left atrium is filled and at a higher pressure than the left ventricle, which is relaxed in this cardiac phase. During systole the left ventricle contracts, and the increase in the pressure in the ventricle causes the MV to close, preventing blood from leaking into the left atrium and ensuring all the blood in the ventricle flows through the aortic valve to the distal organs.

2.1.7.1 Mitral Valve Anatomy

Physiological function of the MV requires interplay between the valve's four main components: the mitral annulus, valve leaflets, chordae tendineae and papillary muscles, shown in Figure 2-11 [28, 29]. A fibro muscular atrioventricular ring forms the base of the mitral valve at the junction of the left atrium and the left ventricle, with a veil of tissue attached to it all along its circumference, which form the mitral leaflets. Fibrous chordae tendineae extend from the ventricular surface of the two leaflets, and extent apically towards the papillary muscles in the left ventricle. These chordae follow a pattern of insertion, such that the leaflets assume an optimal systolic configuration that ensures complete valve competence. The two papillary muscles, antero-lateral and postero-medial, are myocardial structures that extend into the left ventricular cavity. Vasculature from the ventricular muscle richly perfuses the papillary muscles, and ensures their contractility during systole.

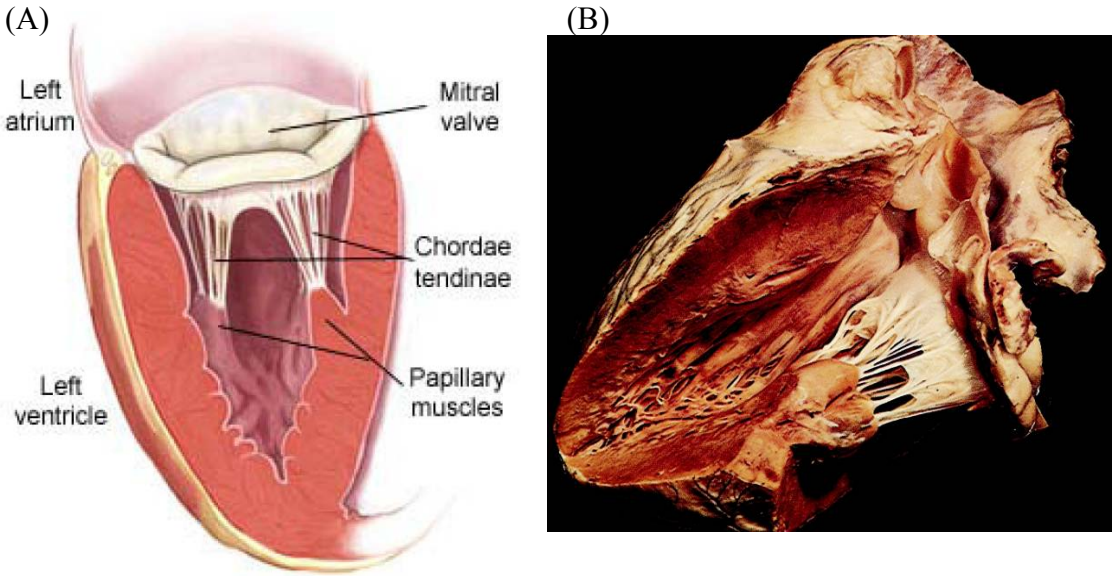

Figure 2-11 (A) Schematic of the mitral valve depicting its individual components; [Figure adapted from www.mitralvalverepair.org] (B) Actual human mitral valve from a cadaver heart [Figure adapted from Anderson R.H, Becker A.E. Thieme; Stuttgart, NY: 1982. Anatomy of the heart] [27, 28]

2.1.7.1.1 The Mitral Annulus

The mitral annulus is the anatomical junction between the left atrium and the left ventricle, and serves as the basal insertion site for the mitral valve leaflets. The anterior portion of the annulus is continuous with the base of the aortic non coronary and right coronary leaflets. The extremities of this anterior annular section are clearly demarcated by two fibrous trigones, which are dense fibrous protrusions. However, histological studies demonstrate a lack of fibrous ring in the anterior section but demonstrate tendon like structures that extend dorsally from the trigones along one-half of the mitral ring. In this region, the region where the mitral tissue inserts is attached directly to the left atrial and left ventricular endocardium. The posterior part of the annulus is a nebulous fibrous ring that is not visually distinct as the anterior annulus, but can be felt upon touch.

Though the entire mitral annulus has historically been defined as an incomplete and diaphanous structure, several studies have established the importance of the mitral annulus in the hemodynamic function of the mitral valve. Figure 2-12A shows the mitral annulus in an explanted heart, and Figure 2-12B[29] shows a histological cross section of the posterior leaflet insertion into the mitral annulus.

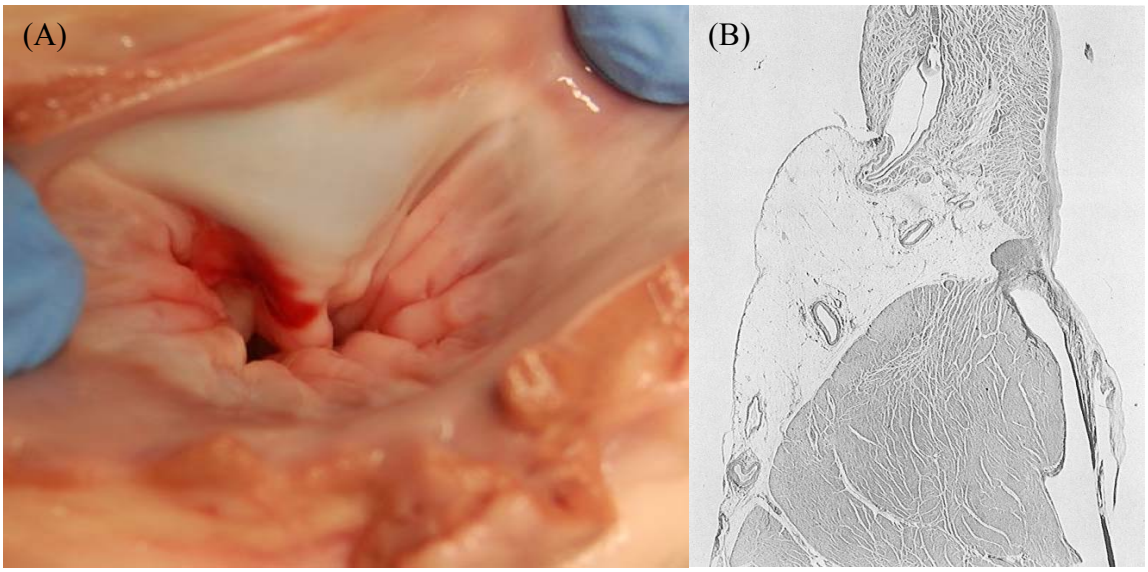

Figure 2-12 (A) An atrial view of a porcine mitral valve depicting the D-shaped mitral annulus, where the distinction of the annulus is easier along the anterior than the posterior segment; (B) A histological cross section of the region where the posterior mitral leaflet inserts into the mitral annulus. Figure adapted from Anderson R.H, Becker A.E. Thieme; Stuttgart, NY: 1982. Anatomy of the heart [28].

The mitral annulus is a dynamic structure, which changes in its shape and size during the cardiac cycle, as demonstrated in animal and human studies. Tsakiris et al. in 1971 demonstrated the dynamic contraction of the mitral annulus in anesthetized dogs using biplane roentgenograms, and deduced that the annulus is not a rigid structure as previously assumed[30]. The size of the annulus increased in late diastole until it reached its maximum area, which was coincident with the P wave of the electrocardiogram. Then

a rapid narrowing of the ring was observed during the atrial and ventricular contractions, followed by a rapid increase in size during ventricular iso-volumetric relaxation. Under control conditions in these dogs, a decrease of 19% to 34% was observed from the diastolic ring size. The most striking observation was that nearly two thirds of the annular size reduction occurred during atrial contraction, and the valve annulus was significantly reduced before the onset of ventricular systole as shown in Figure 2-13[30]. Mitral annular narrowing is also eccentric, with the largest shortening occurring due to the posterior segments extending from the commissures. This reduction in size is hypothesized to aid in the apposition of the posterior leaflet with the anterior.

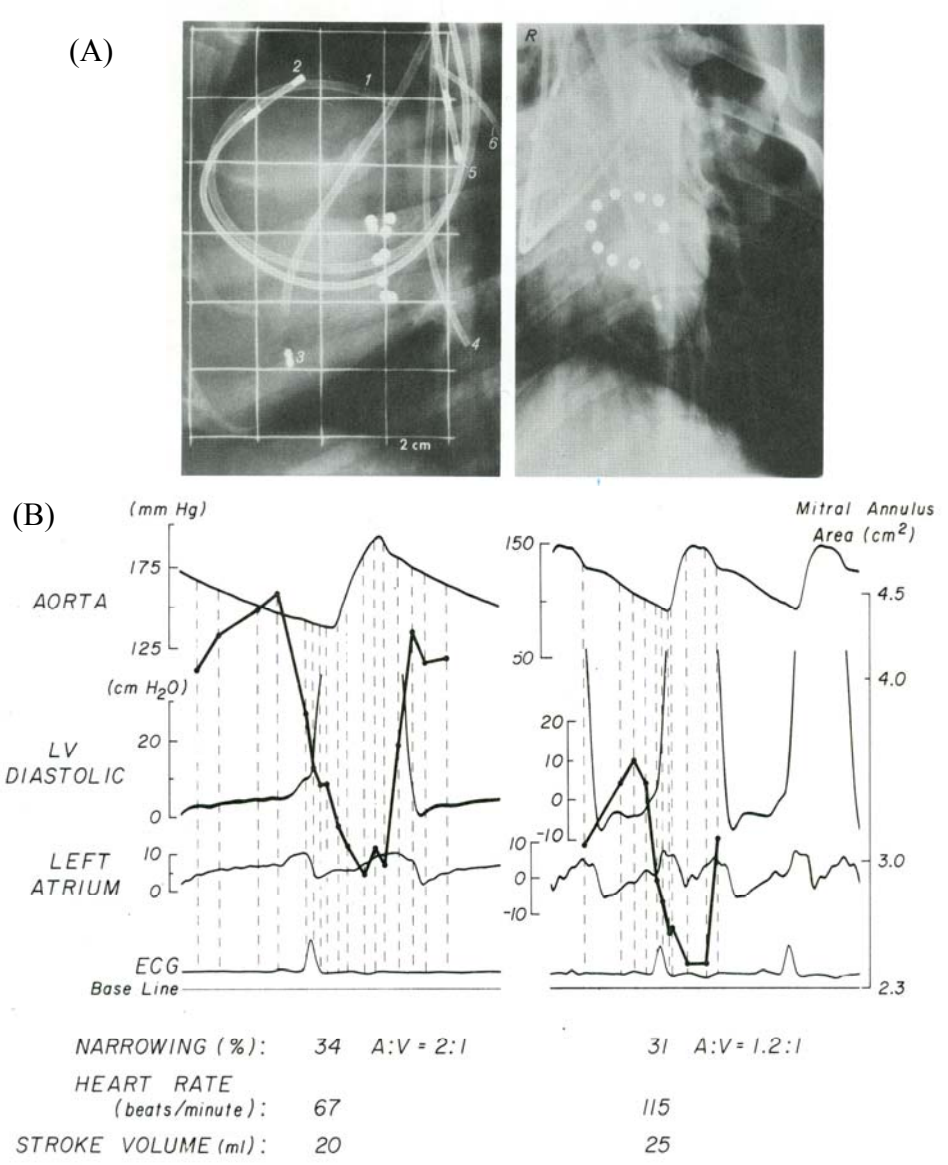

Figure 2-13(A) Roentgenograms of beads implanted around the mitral annulus in anesthetized dogs; (B) Changes in mitral annular area (bold solid line) under different hemodynamic conditions. [Figure reproduced from Tsakiris AG, J Appl Physiol, 30: 611 1971][29]

The mitral annulus in addition to change in its planar area also undergoes an apical-basal flexing, imparting it a saddle shape during systole from its flat diastolic configuration. Levine et al. were the first to discover this three dimensional shape of the mitral annulus when defining an optimal echocardiographic assessment technique for mitral valve prolapse as shown in Figure 2-14[31].

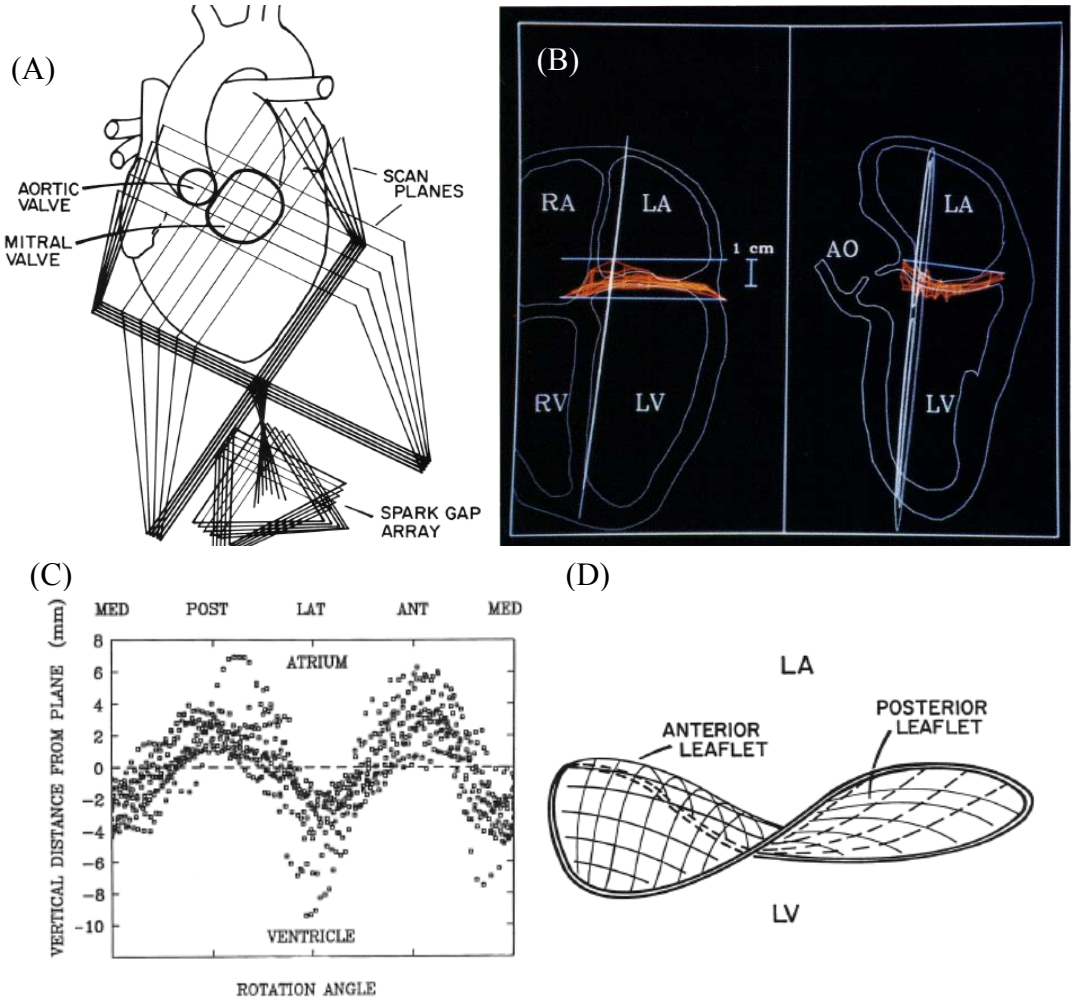

Figure 2-14 (A) Echocardiographic planes used in this study; (B) Manual tracings of the plane of leaflet coaptation in the 4 and 2 chamber views; (C) Tracings of the vertical distance from the least square fit of the annulus; (D) The reconstructed 3D shape of the mitral annulus demonstrating the saddle shape.[Figure reproduced from Levine RA, Circulation,1989, 80(3):589-93] [30]

2.1.7.1.2 Valve Leaflets

The mitral valve consists of a continuous veil of tissue inserted around the entire circumference of the mitral orifice, which is distinguished into [i] the anterior leaflet, and [ii] the posterior leaflet. The anterior leaflet that has a triangular structure and attaches to the mitral annulus between the trigones, with the greatest leaflet height at the free edge as shown in Figure 2-15. The basal portion of the leaflet is continuous with the aorto mitral curtain along the non coronary and left coronary aortic leaflets, while the apical portion of leaflet forms the free edge of the leaflet that aids coaptation. The posterior leaflet on the other hands covers the entire circumference from one commissure to another commissure, covering three fifths of the entire mitral annulus. The leaflet is divided into three individual scallops identified as the P1 (anterior or medial scallop), P2 (the middle scallop), and P3 (posterior or lateral scallop). The height of the posterior leaflet varies from the P1 cusp to the P3 cusp, with P2 cusp having the greatest height from the base to the free edge.

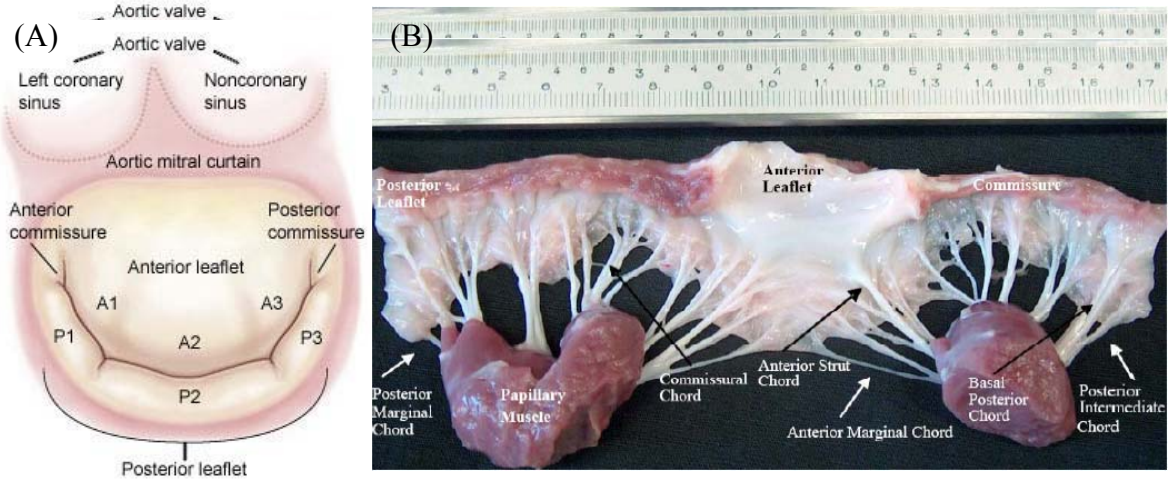

Figure 2-15 (A) Illustration of the systolic closed configuration of the mitral valve leaflets; (B) An excised spread out view of a porcine mitral valve depicting the smooth and rough zones of the valve, with the different chordal insertions into the ventricular surface of the leaflets.

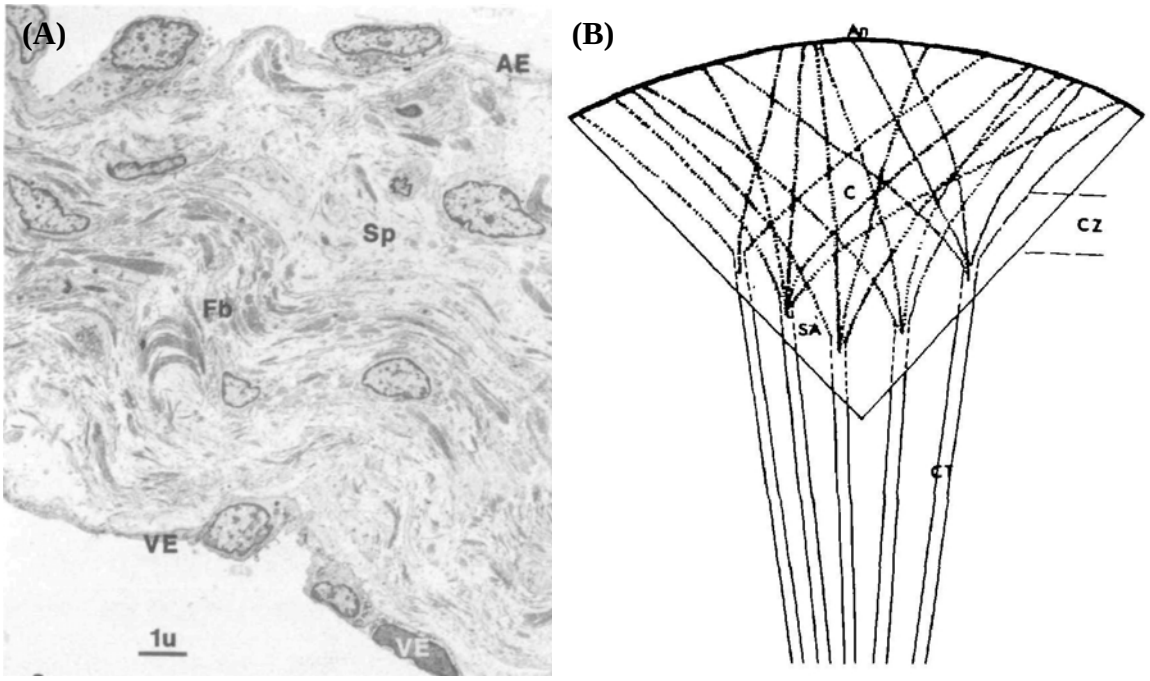

Figure 2-16 (A) Histological cross section of the anterior leaflet of the mitral valve composed of two distinct zones, the fibrosa(Fb) and the spongiosa(Sp) with loose collagen and scattered interstitial cells. The atrial endocardial surface (AE) has plump endothelial cells, while the cells on the ventricular surface are more flattened. (B) A depiction of the collagen orientation in the anterior leaflet of the mitral valve depicting the fan like structures emanating from the chordae tendineae and fanning to the mitral annulus. Figure reproduced from Fenoglio, Circulation Research, 1972, 31, 417-430[31].

Fenoglio and colleagues, in 1972 reported the laminar structure of the mitral valve leaflets with zonal distinction of the leaflet cross section into fibrosa and spongiosa as shown in Figure 2-16A [32]. Using histological examination they observed that the Fibrosa had dense collagen fibrils, while the Spongiosa had loose collagen with interstitial cells sparsely distributed in this zone. The atrial and ventricular surfaces of the leaflets are lined with endothelial cells, though of a different morphology on both sides. These authors also hypothesized a fan like distribution of the collagen fibrils in the leaflets that emerge from the region of chordal insertion and fan out to the base of the mitral valve leaflet as shown in Figure 2-16B [32].

2.1.7.1.3 Chordae Tendineae

The mitral chordae are tendinous structure that arise from the papillary muscle tips and insert into the ventricular surface of the anterior and posterior leaflets. They differ in number between each valve, but can be broadly classified into three classes based on the region of their insertion into the leaflet shown in Figure 2-17:

[1] Primary chordae tendineae (also called Marginal)

[2] Secondary chordae tendineae (also called Secondary/Strut)

[3] Tertiary chordae tendineae (also called Basal/Commissural)

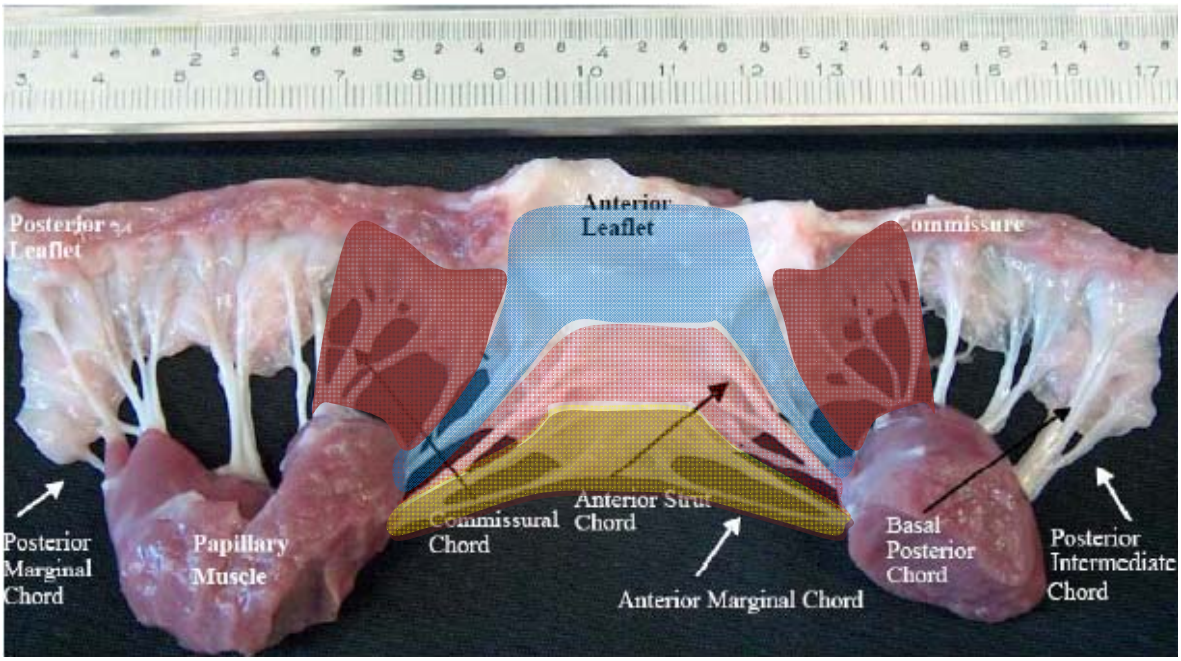

Figure 2-17 The anterior leaflet of the mitral valve divided into regions based on the site of chordal insertions. (Green Region) Free edge of leaflet with marginal chordal insertion, (Red Region) Belly of the leaflet with strut chordal insertion, (Blue Region) Basal region of the leaflet with basal chordae insertion, (Brown Region) Commissures with chordal insertions that fall within the tertiary group as well

The mitral valve typically consists of 8-12 chordae tendineae, 15-20mm long, and approximately 0.45mm in diameter before branching, either at the tip of the papillary muscle or their insertion into the leaflet. The chordae inserting into the anterior leaflet are

obliquely aligned along their longitudinal axis, while the ones on the posterior leaflet insert parallel to each other. Table 2-1 summarizes the chordal types, their average lengths and thickness as measured by Lam et al[33].

Table 2-1 Classification of length and thickness of chordae tendineae based on their site of insertion [Data reproduced from Lam et al][14]

Site of insertion	Types of chordae	Length (cm)	Thickness (mm)
Anterior leaflet	Rough zone chordae	1.75 ± 0.25	0.84 ± 0.28
	Strut chordae	1.86 ± 0.43	1.24 ± 0.51
Posterior leaflet	Rough zone chordae	1.40 ± 0.08	0.65 ± 0.24
	Basal chordae	0.84 ± 0.21	0.40 ± 0.29
	Cleft chordae	1.30 ± 0.18	0.78 ± 0.15
Commissural areas	Anterior lateral commissural chordae	1.2 ± 0.31	0.70 ± 0.20
	Posterior medial commissural chordae	1.4 ± 0.40	1.0 ± 0.30

The anterior leaflet has three types of chordae, the marginal chordae that insert into the free edge, the secondary that insert into the belly of the leaflet, and the basal that insert closer to the mitral annulus. The marginal chordae soon after their origin from the papillary muscle split into three branches, one inserting into the free margin of the leaflet, one into the intermediate area in the rough zone, and one slightly beyond the line of coaptation. The secondary chordae which are the thickest chordae originate from the tips of the anterior lateral and posterior medial papillary muscles and insert at the transition from the rough to the smooth zones. They are the thickest and carry the most load during systolic loading on the valve, and are also speculate to maintain annular-ventricular continuity. The third chordal type, the basal chordae, insert into the anterior leaflet close to the annulus and towards the commissural sections. Their exact function in the global mitral valve hemodynamic or mechanical function is currently unknown.

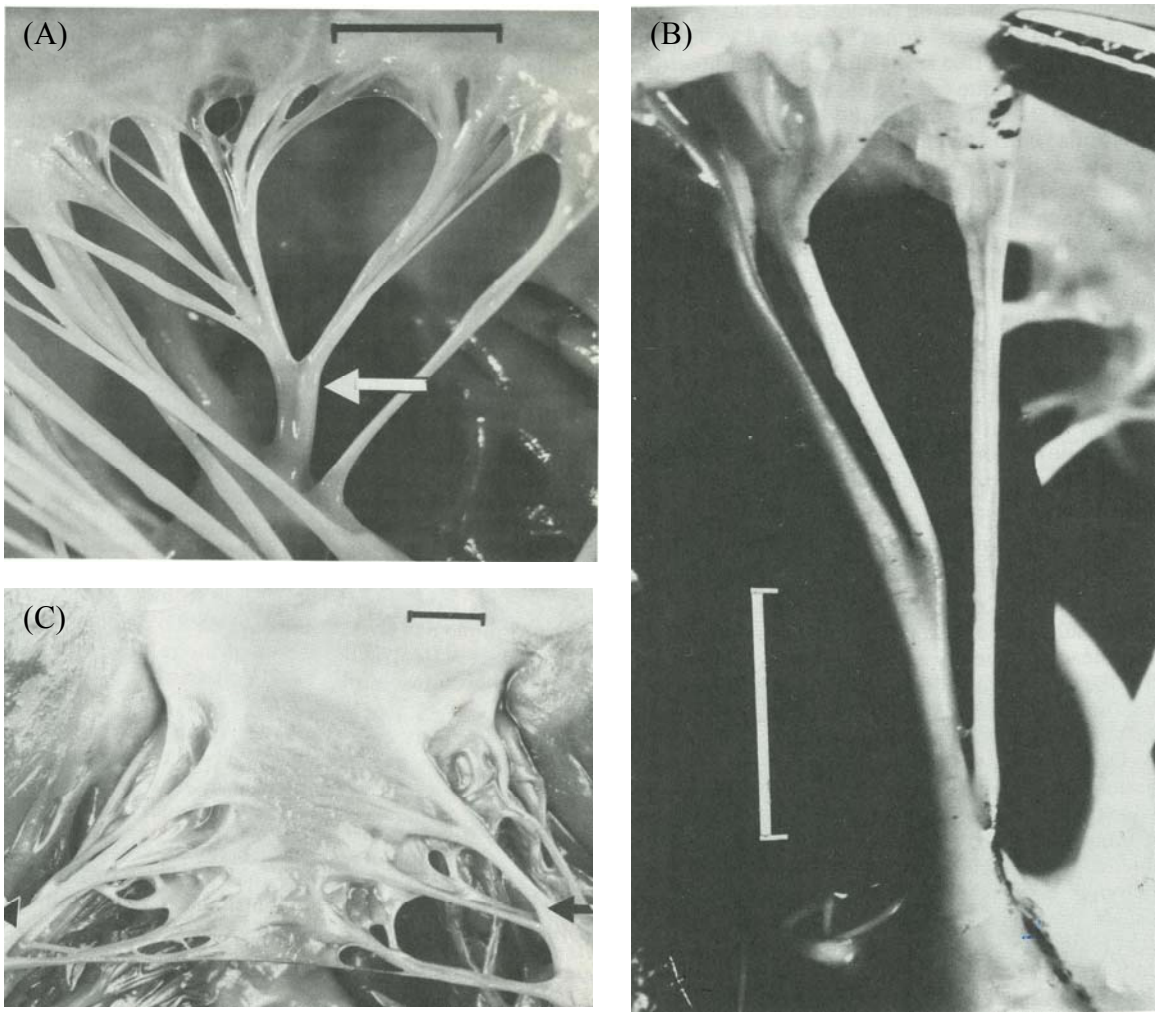

Figure 2-18 (A) The cleft chordae on the posterior commissures that show the fan like structures; (B) The marginal chordae emerging from the papillary muscle and splitting into three web of chordae; (C) Chordal distribution on the anterior leaflet of a human mitral valve. Figures reproduced from The Mitral Valve by Daniel Kalmanson, MD [33]

On the posterior leaflet, the chordal distribution is similar to the anterior but with a few exceptions. Posterior basal chordae, that are unique to this leaflet, are a set of chordae that extend directly from the papillary muscle to the insertion of the leaflet and do not divide along their entire stem. Additionally, cleft chordae are also seen at the regions dividing the posterior cusp into P1-P2 and P2-P3, where then fan out at the cleft to restrict it from prolapsing into the atrium during systole. Two sets of cleft chordae are

observed in humans, which divide the entire posterior leaflet into three scallops as shown in Figure 2-18[34].

Mechanical properties of chordae tendineae vary with their type and size. Liao and colleagues reported in 2003 that chordal grouping based on cross sectional area, there is a stark correlation between the chordal size, type and mechanical properties [35-38]. In this study, they reported that the thicker strut chordae are more extensible and less stiff than the thinner marginal chordae as shown by the data in Table 2-2 and Table 2-3. With increase in chordal diameter, the average crimp period of the collagen core that forms the chordae decreased. The marginal chordae that are the thinnest had smaller fibril diameters and a greater average fibril density than the other chordae. On the other hand the extensibility of the chordae seems to increase with increasing chordal diameter, but with a reduction in the tensile modulus. In the thicker chordae, the collagen fibrils are extensively crimped and thus allow better elongation than their thinner counterparts. These finds by Liao et al. [35-38] corroborate with other data reported in literature by Lam et al.[33] and Kunzelman et al[39].

Table 2-2 Comparison of mechanical properties of chordae according to their cross sectional area [Data reproduced from Liao et al][34-37]

Range of chordal area (mm^2)	0.1-0.5	0.5-1.0	1.0-2.0	2.0-3.0	Significance
Extensibility (% strain)	4.2±1.5	8.1±2.5	15.7±3.9	18.4±2.8	$p < 0.001$
Tensile modulus (MPa)	90.1±22.3	83.7±18.5	66.3±13.5	61.7±13.3	$p = 0.001$

Note: Values given as Mean ± S.D. Comparisons were made using one-way ANOVA. *p*-Values denote significant differences between groups.

Table 2-3 Comparison of mechanical properties of chordae according to chordal type [Data reproduced from Liao et al][34-37]

Chordal type	Marginal	Basal	Strut	Significance
Extensibility (% strain)	4.3±1.6	8.5±2.0	17.5±3.3	$p < 0.001$
Tensile modulus (MPa)	84.4±21.2	86.1±20.9	64.2±13.5	$p = 0.002$
Average chordal size (mm^2)	0.38±0.18	0.71±0.25	2.05±0.40	$p < 0.001$

Note: Values given as Mean ± S.D. Comparisons were made using one-way ANOVA. *p*-Values denote significant differences between groups.

Lim et al. reported a non-linear quasi static elastic response of the mitral valve chordae using uni-axial testing [40-44]. Once the outer elastic sheath of the chordae was removed, there was no change in the non linearity indicating that the mechanical properties of the chordae are determined primarily by the inner collagen core. In their study they also reported that with increased stretch, a greater force was required to strain the tissue indicating the non linearity. When the collagen fibrils are completely un-crimped, the bonds between each fibril start to stretch and this stretching requires a much higher force. Sedransk et al in 2002 investigated the failure mechanics of the chordae tendineae, and reported that the marginal chordae and the posterior leaflet chordae are thinner and failed at lower loads that the anterior chordae[45]. These findings are in agreement with the data from Lim et al., which reports that the marginal chordae have decreased extensibility in comparison to thicker strut and basal chordae. It was also concluded that the failure strength of the chordae was dependent primarily on the insertion position and not on the leaflet of insertion[44].

Ritchie et al. compared the mechanical properties of the chordae to their structural constituents using histological methods and confirmed that chordal loading correlated well with the variations in collagen and elastic content [46, 47]. Subsequently in 2006,

Jimenez et al. reported dynamic measurements of the chordal forces in an in vitro left heart simulator. In this study, the authors reported that under dynamic conditions the strut chordae bore the maximum load when compared to the marginal or basal chordae [48-50]. Table 2-4 summarizes the forces measured on the different chordae in this study.

Table 2-4 Force distribution on the chordae tendineae as measured by Jimenez et al. [29-31]

Chord	Number of Specimens	Tension Flat (N)	Tension Saddle (N)	Percentual Difference (%)	Statistical Significance
Anterior Strut	6	1.22±0.52	0.95±0.35	18.5±16.1	0.018
Posterior Intermediate	5	0.25±0.14	0.30±0.18	-22.3±17.1	0.022
Posterior Marginal	4	0.03±0.04	0.06±0.05	-137.8±188.6	0.12
Basal Posterior	6	0.19±0.10	0.31±0.25	48.5±89.9	0.122
Anterior Marginal	6	0.31±0.17	0.35±0.16	-58.5±111.4	0.145
Commissural	5	0.17±0.18	0.11±0.20	59.0±32.3	0.008

2.1.7.1.4 Papillary Muscles

The mitral valve function is integrally related to the ventricle, with the annulus residing in the left atrio-ventricular groove and the chordae tendineae connecting the ventricle via the papillary muscles. There are two papillary muscles arising from the left ventricular myocardium: the antero-lateral papillary muscle and the postero-medial papillary muscle. The antero-lateral papillary muscle often consists of one body or tip and obtains its blood supply from the left anterior descending and the diagonal or a marginal branch of the circumflex artery. Whereas, the postero-medial papillary muscle consists of two tips and gets its blood supply from the left circumflex or right coronary artery. Because of its single system of blood supply it is prone to injury from myocardial infarction. The attachment of the papillary muscles to the lateral wall of the left ventricle makes the ventricular wall an integral part of the mitral valve complex. Chronic or acute

left ventricular dilatation can lead to papillary muscle displacement with increased leaflet tethering due to tension on the chordae tendineae. The papillary muscles are active components that contract during systole and maintain a constant distance between the annulus and the papillary muscle tip, restricting the prolapse of the mitral leaflets into the atria during systolic closure. Their contraction is possible through the extensive vascular network in these muscle fibers as shown in Figure 2-19[34].

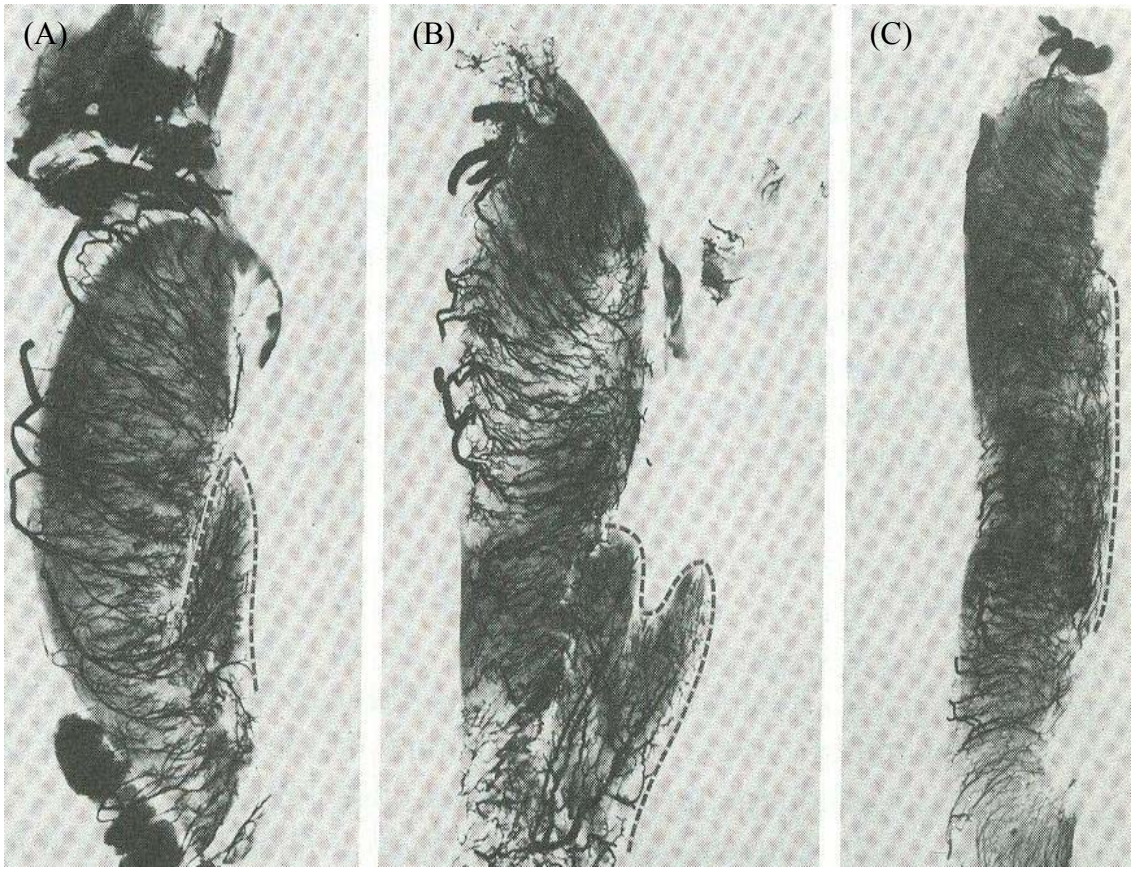

Figure 2-19 Arterial vasculature of the human left ventricular papillary muscles (A) finger like papillary muscle with a central artery distributing blood, (B) mixed type of papillary muscle with segmental distribution of vasculature, and (C) tethered type of papillary muscle with long penetrating intra myocardial vessels [Figure reproduced from The Mitral Valve by Daniel Kalmanson. [33]

2.1.8 PHYSIOLOGICAL MITRAL VALVE FUNCTION

The primary function of the mitral valve is to allow blood flow from the left atrium to the left ventricle during diastole, and prevent the backflow of blood from the left ventricle to the atrium during systole. To perform this physiological function synchronously with the cardiac phase, the mitral valve components works in tandem with one another to ensure proper closure of the leaflets. At the beginning of systole, higher pressure in the left ventricle and lower pressure in the left atrium accelerates the valve leaflets basally towards the mitral annulus. As the leaflets move closer to the mitral annulus, the limited extensibility of the chordae tendineae restricts the leaflets from prolapsing into the atrium. The chordae tendineae are inserted along the leaflet surface such that, they not only restrict leaflet prolapse but also impart a curvature to the leaflets that results in good anterior and posterior leaflet overlap and good coaptation. Typically, in humans the coaptation height measured along the A2-P2 ranges between 5mm to 8mm and varies with the valve size and body surface area of the subject [51, 52]. At peak systole, the papillary muscles also contract and transfer a force on the annulus that is apically directed. This force can be speculated to change the shape of the mitral annulus for a flat diastolic configuration to a three dimensional systolic saddle shape. Though the exact dynamics and interaction between each mitral valve component is currently unknown, it is demonstrated to some extent in this thesis that the transfer of forces from the sub annular to the annular planes plays a critical role in optimizing leaflet coaptation. As the ventricular pressure is rapidly falling during late systole, rapid left atrial filling increases the chamber pressure until an inflection point is reached when the mitral valve opens. The positive pressure gradient between the left atrium and the ventricle displaces

the mitral leaflets apically to their complete open position. The strut chordae on the anterior leaflet ensure that the open mitral leaflets do not obstruct the left ventricular outflow tract, and unobstructed left ventricular filling occurs. Figure 2-20 depicts the different forces acting on the mitral valve during the systolic and diastolic phase of the cardiac cycle, and illustrate the structure to function relationship between the chamber pressures and the kinematics of the mitral valve components.

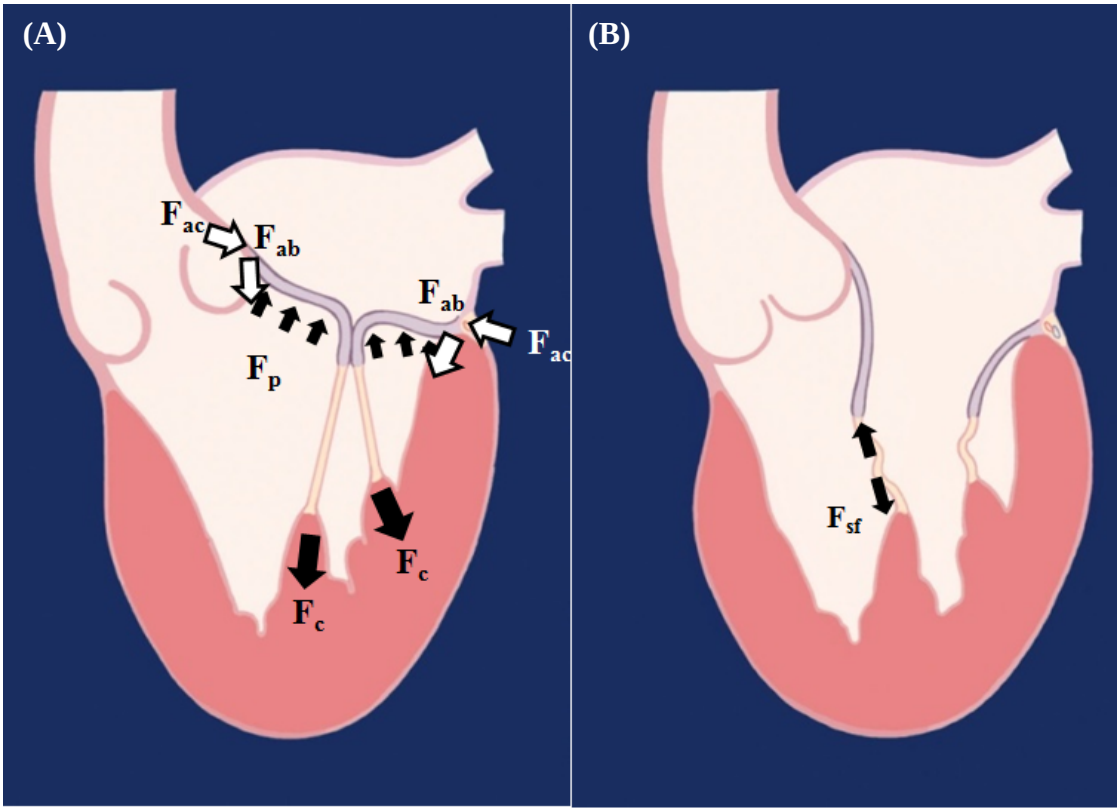

Figure 2-20 (A) Forces acting on the mitral valve structure during systolic closure. Fp is the pressure force acting on the leaflets due to elevated left ventricular pressure, Fc is the papillary muscle contraction force during systole, Fac is the annular contraction force, and Fab is the annular bending component. (B) Fsf is the tension in the anterior strut chordae during diastole when the chord prevents systolic anterior motion of the leaflet.

2.1.8.1 Valve Hemodynamics

Figure 2-21 presents the synchronous recording of the mitral valve flow, and ventricular and atrial chamber pressures in a calf [53, 54]. The duration of the total cardiac cycle is divided into six cardiac phases, and the events in each cardiac phase are discussed. Phase I is the time period of low flow rate and volume at pre diastole, when the mitral valve is just about to open. Phase II begins at the time point when the atrioventricular pressure gradient is positive and during this period the flow from the left atrium rapidly accelerates into the left ventricle and slowly declines. Phase III commences at atrial systole, when the left atrium contracts and pushes the fluid volume left in the chamber into the left ventricle, which is synchronous with the second bump on the flow. Though reversal of pressure gradient occurs at this stage, the flow decelerated yet persisted to fill the ventricle for an additional 15 msec. Phase IV is the only period of flow reversal, occurring during the isovolumic contraction. This volume could either be slight regurgitation or can be the volume of the fluid displaced by the valve leaflets into the left atrium, termed as the closing volume. Phase V varied between 15-40 msec and consisted of a small volume and low rate of flow following the atrial “c” wave. Phase VI extended throughout systole when no mitral valve flow was detectable.

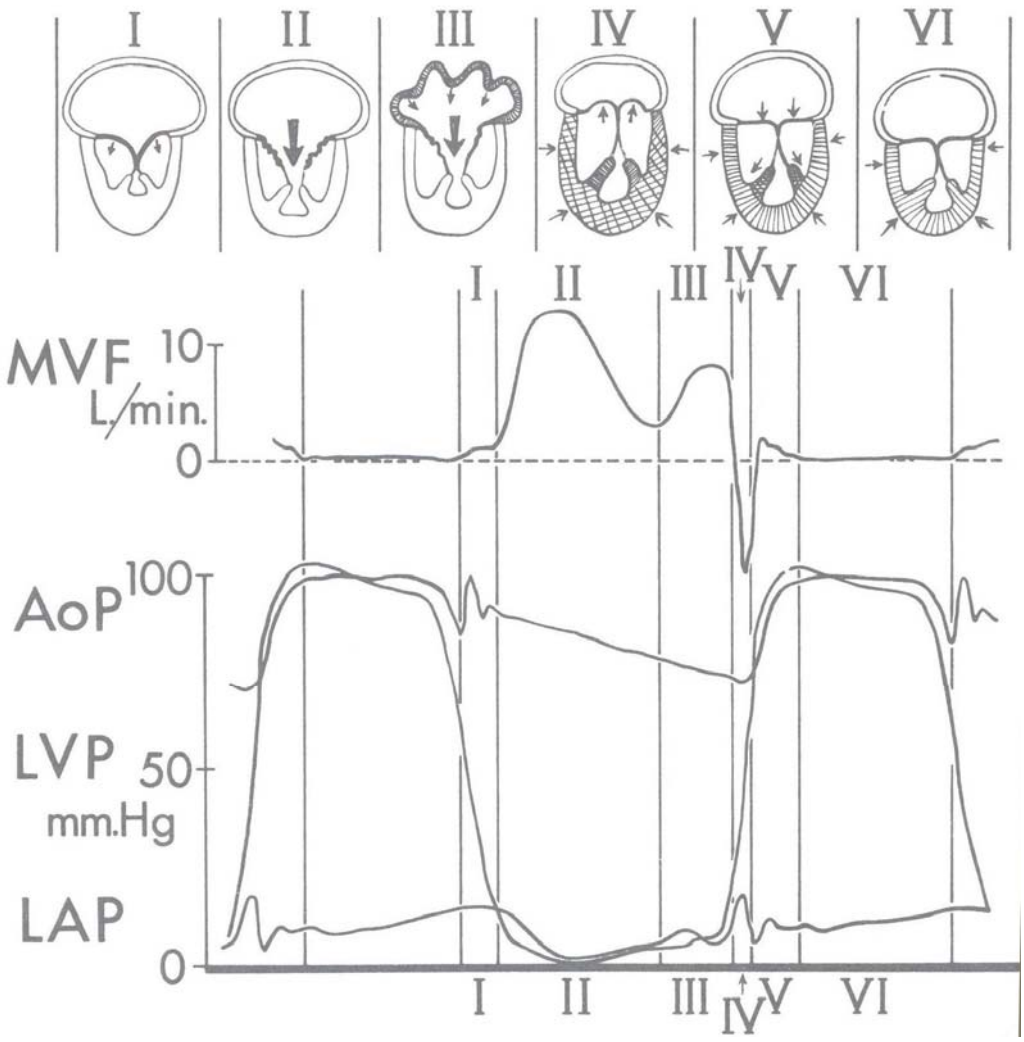

Figure 2-21 Mitral valve flow recorded during different phases on the cardiac cycle in calves. Figure reproduced from Nolan SP, Am Heart Journal, 77:784-791, 1969. [52,53]

Tsakiris et al. also studied the motion of the mitral valve leaflets during the cardiac cycle, by placing beads on the free edges of the anterior and posterior mitral cusps in anesthetized dogs [55]. The time series in Figure 2-22 shows the motion of the bead from systole to diastole, wherein the systolic closed position is considered the baseline. At the onset of diastole, both the mitral leaflets rapidly opened to their fully open position, surprisingly started to reclose immediately, and had a short period of rapid

reopening and then systolic closure. The initial diastolic closing following the full open position coincided with the formation of a left ventricular vortex behind the valve leaflet when the ventricle still has a smaller volume. As the flow through the mitral valve continued and was directed towards the apex and gained volume, leaflet closure was decelerated. Finally as the flow diverged and ran parallel to the ventricular walls, leaflet closure resumed and continued until the blood flow into the ventricle diminished.

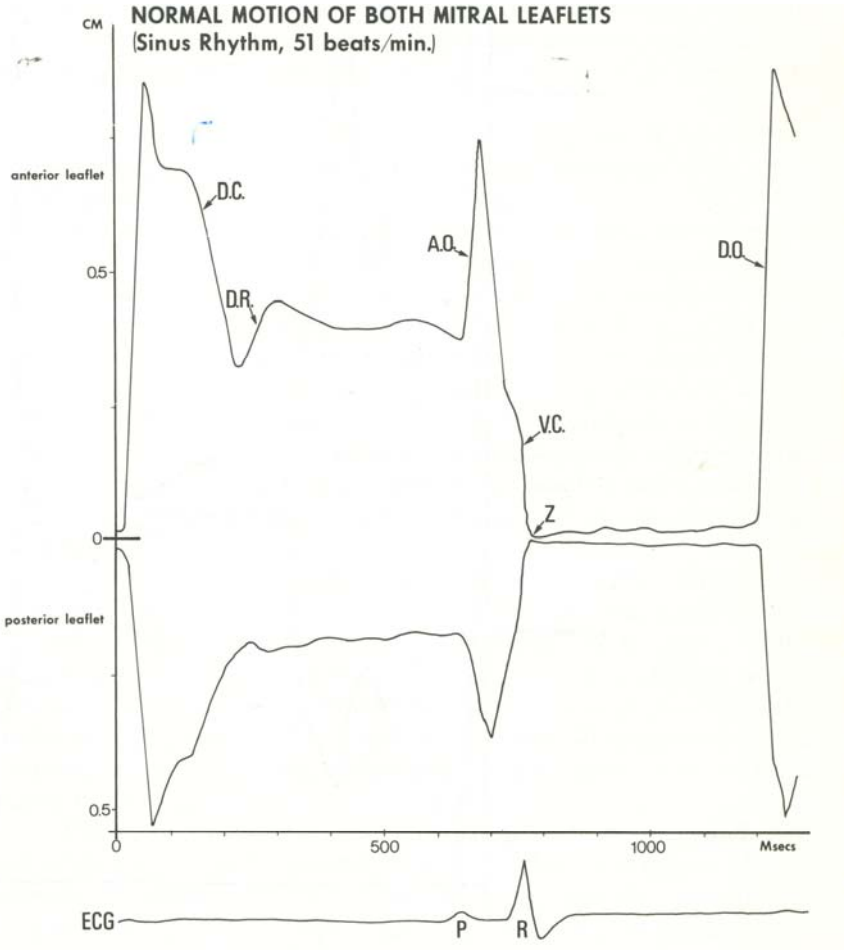

Figure 2-22 Motion of the free edges of the anterior and posterior leaflet in an anesthetized dog. Figure reproduced from Tsakiris et al. K Appl Physiology 39: 359, 1975[54]

2.1.8.2 Valve Mechanics

2.1.8.3 In Vivo Annular Strain Measurements

In 2009, Eckert et al. reported mitral annular kinematics in normal sheep using sonomicrometry crystals placed around the annular circumference [56]. From the measured displacement of the sonomicrometry crystals, they reported the annular axial strain, strain rate, bending and twist around the annulus. Axial strain showed spatial and temporal heterogeneity, the peaks ranging from -10% to 4%. Largest strain was measured around the commissures and along the posterior annular segment, but neither bending nor twist was observed in this study. Figure 2-23 summarizes the time series of the axial strain of the annulus at each marker position depicted in the central schematic.

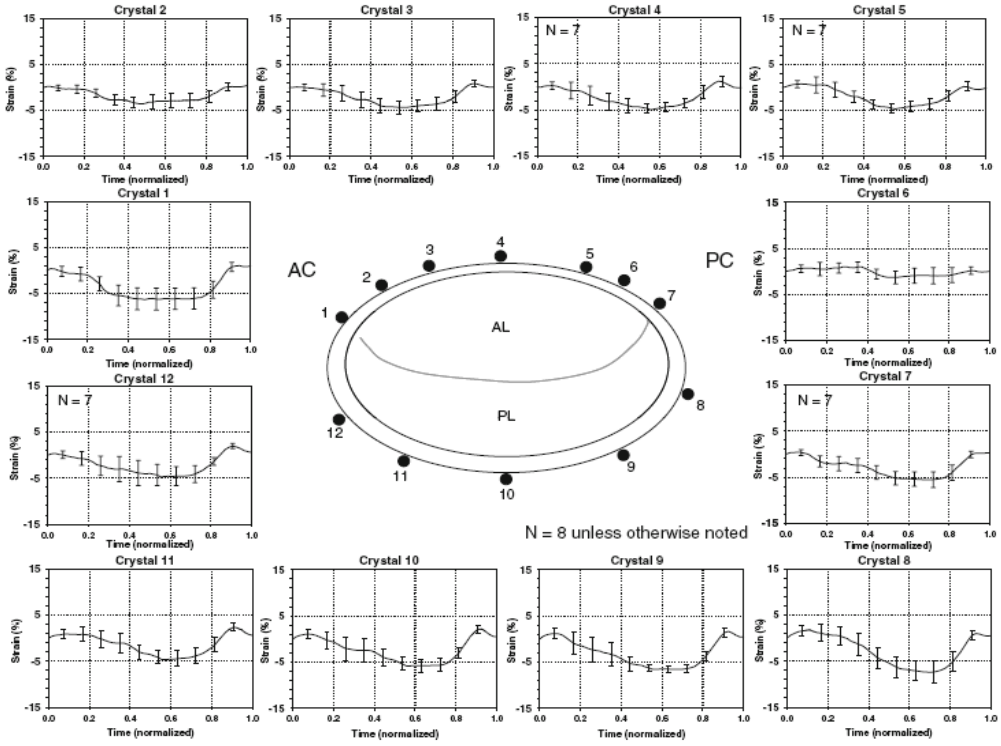

Figure 2-23 Axial strain at individual crystals placed along the circumference of the mitral annulus in a sheep. Data depicts the heterogeneity in the spatial strain pattern along the annulus. Figure reproduced from Eckert et al, Ann Biomed Eng, 2009[55]

2.1.8.3.1 In Vivo Leaflet Strain Measurements

In 2006, Sacks et al measured the dynamic deformation of the anterior leaflet of the mitral valve in sheep using sonomicrometry [57]. The anterior leaflet of nine Dorsett sheep was instrumented with nine 1-mm crystals, and the regional deformation was assessed. Data from their study, shown in Figure 2-24, demonstrated large anisotropic strains and peak strain rates of 400%/second, with a deformation plateau during systole. They also reported that with increased left ventricular pressure or annular geometry, the leaflet stiffness significantly increased and proposed this as a mechanism for leaflet adaptation to changing mechanical environment.

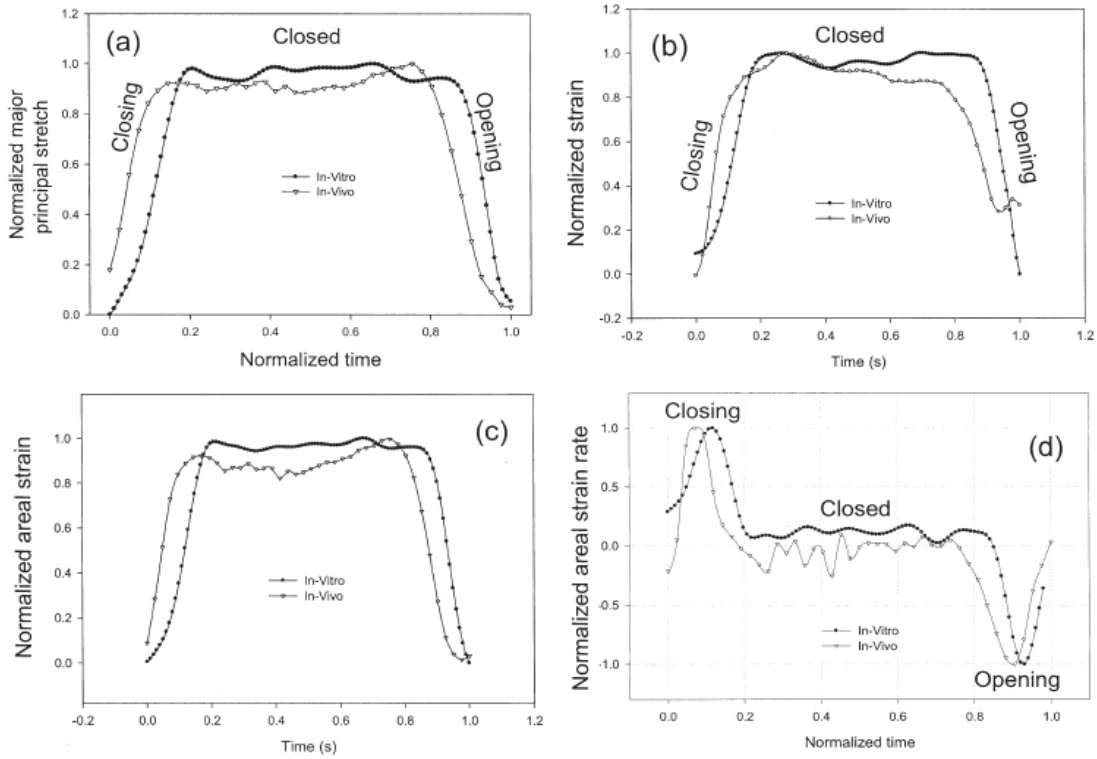

Figure 2-24 Time series of anterior leaflet deformation. (A) Depicts the temporal changes in the major principal strain that coincides with the circumferential axis of the leaflet; (B) Temporal changes in the minor principal strain along the radial axis of the leaflet; (C) Changes in the areal strain throughout the cardiac cycle; (D) Temporal changes in strain rate during the cardiac cycle. Figure reproduced from Sacks et al, 2006, Ann of Thoracic Surgery [56]

2.1.8.3.2 In Vitro Leaflet Strain Measurements

He and colleagues in 2002 and 2005 reported dynamic leaflet deformation of the anterior and posterior leaflets in an in vitro pulsatile left heart simulator[58, 59]. Results on the anterior leaflet shown in Figure 2-25 demonstrated that during valve closure the leaflet experienced large, anisotropic strains with peak stretch rates of 500%-1,000%/s. This rapid stretching was followed by a plateau phase characterized by relatively constant strain state. On the posterior leaflet, their findings shown in Figure 2-25 indicated a rapid rise in leaflet strain during valve closure followed by a plateau where no additional strain (i.e., no creep) occurred. The strain field was highly anisotropic with larger stretches and stretch rates in the radial direction. There were negligible stretches, or even compression (stretch < 1) in the circumferential direction at the beginning of valve closure.

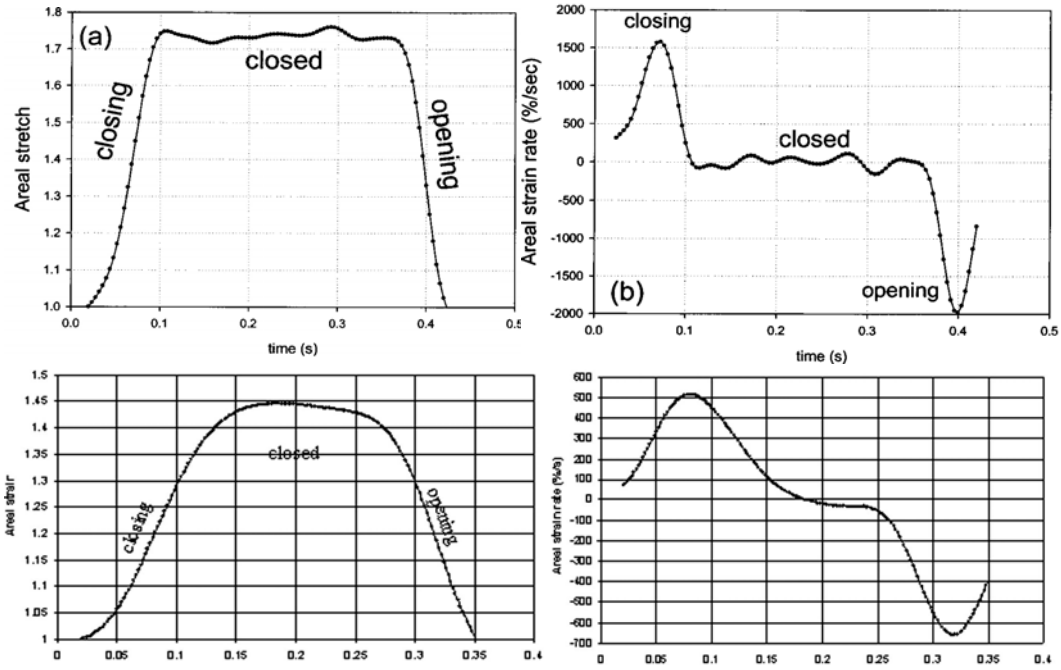

Figure 2-25 (Top Row) Dynamic areal stretch and areal stretch rate on the anterior leaflet; (Bottom Row) Dynamic areal stretch and stretch rate on the posterior leaflet [57,58]

2.1.8.3.3 In Vivo Chordal Force Measurements

Salisbury and colleagues in 1962 measured the forces on the strut chord of the anterior leaflet of the mitral valve under different hemodynamic and pathological conditions, and reported a dynamic change in the chordal force with changes in the hemodynamics and left ventricular shape and health [60]. Figure 2-26 shows the transducer that was used to measure these forces and the force measurements under physiological hemodynamic conditions.

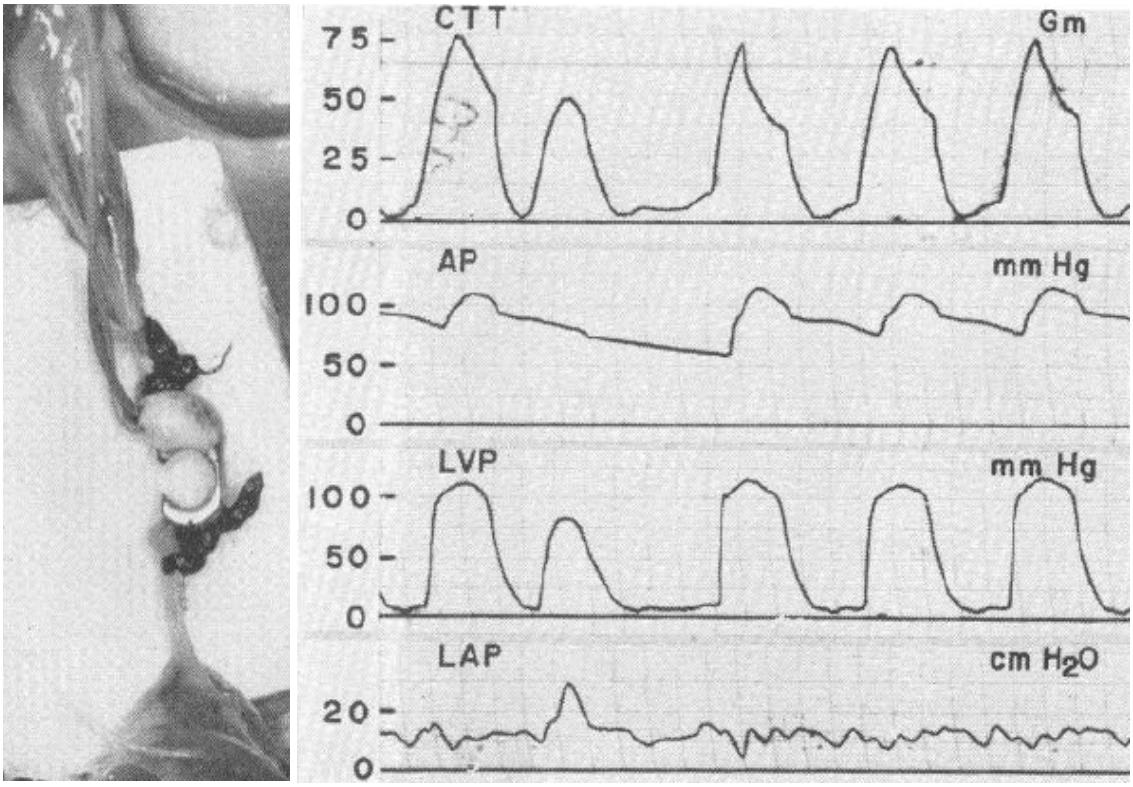

Figure 2-26 (A) The force transducer used to measure the chordal force in the mongrel dogs; (B) The graphs depict the measured forces on the chord at physiological left ventricular and aortic pressures. Figure reproduced from Salisbury et al. Am J Physiol, 205(2):385-392, 1962[59]

Jimenez et al, in 2006 reported measurements on six chordae tendineae on a porcine mitral valve conducted in an in vitro heart simulator, under normal and

pathological conditions where the papillary muscles were displaced in different spatial directions [48-50].

2.1.8.3.4 Computational Mechanics of the Mitral Valve

Kunzelman and colleagues in 2007 summarized their computational model of a mitral valve in which they sought to study the contribution of individual components of the valve to its observed mechanics [61-64]. A 3D model of the mitral valve, with fluid structure interaction was developed that includes the mitral leaflets and the chordae tendineae. Figure 2-27 shows their model with results obtained under different loading conditions on the valve. Peak strain was measured at the central A2 and P2 cusps, along both the circumferential and radial directions.

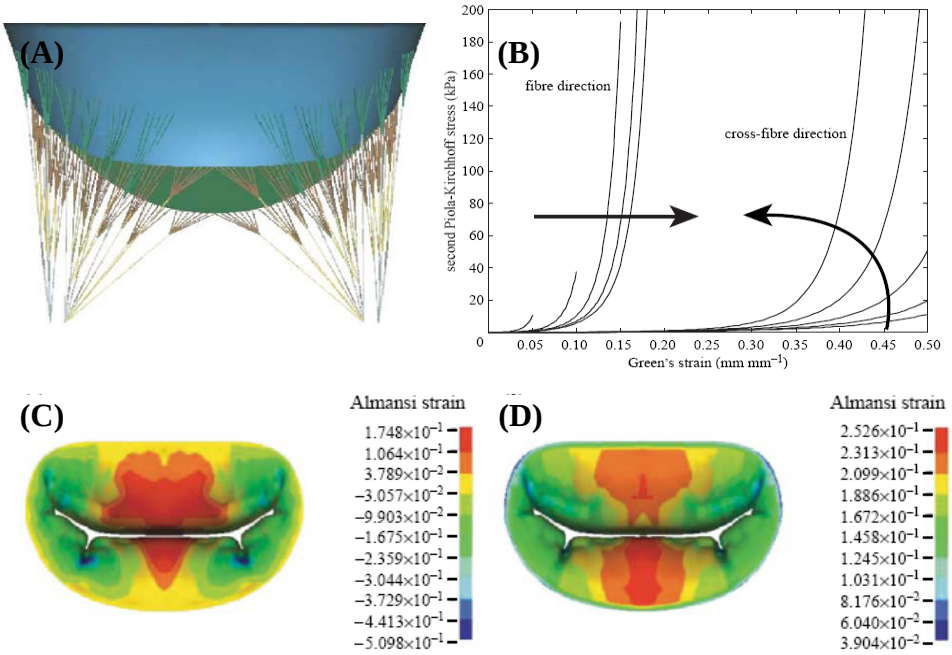

Figure 2-27 (A) The computer generated 3D model of the mitral valve; (B) The stress strain characteristics that were used in the computational model to calculate the leaflet stress; (C) Circumferential Almansi strain in the leaflet under normal geometry and loading conditions; (D) Radial Almansi strain the leaflet under normal geometry and loading conditions.[60-63]

2.2 MITRAL VALVE PATHOLOGIES

Mitral valve pathologies encompass a spectrum of lesions which include congenital defects, degeneration of valve tissue, and geometric distortions to the valve due to secondary reasons. Congenital lesions of the mitral valve include annular calcification leading to mitral stenosis, leaflet prolapse due to Marfan's syndrome, isolated cleft valve, undivided atrioventricular valve in ostium primum or septum secondum defects, and mitral regurgitation due to congestive heart failure caused by severe stenosis of the left main coronary artery. Though the underlying etiology of each congenital lesion is different, the common manifestations between all the lesions are leaflet and sub annular malformations that reduce valve competence. Degenerative mitral valve lesions occur in both children and adults, due to either genetic mutations such as Marfan's syndrome (lack of Fibrillin-1 gene), or acquired secondary diseases such as Rheumatic heart disease in developing countries, Fibroelastic deficiency in adult life due to collagen deficiencies, and Barlow's syndrome speculated to be caused due to genetic and mechanical factors. The last classification of mitral valve lesions, termed as the functional mitral valve defects, are caused due to perturbations to the mitral valve geometry secondary to other lesions such as ischemic dilated cardiomyopathy or hypertrophic dilated cardiomyopathy.

Irrespective of the lesion, surgical repair is currently the accepted standard of care over valve replacement, due to risks associated with anti coagulation therapy, growth of cardiac structure in pediatric patients, and lack of durability of the artificial valves. Surgical therapy for valvular heart disease has seen tremendous progress in the last two

decades. In the current era of cardiothoracic surgery, valve surgery to repair a diseased mitral valve has become a routine procedure that is associated with low mortality rates and excellent acute outcomes. With better understanding of pathological anatomy of mitral valve lesions and increasing surgical experience, several innovative methods for mitral valve repair are now established. However, long term durability and chronic outcomes using these techniques are concerning, with failure rates ranging from 5% to 40% for different mitral valve lesions. These disconcerting statistics indicate that, mitral valve repair for acute correction of regurgitation or stenosis are achieved, but chronic failure of these repair is inevitable and poorly understood. In the subsequent sections, a historical perspective of each mitral valve lesion studied in this thesis is presented, current patient outcomes are discussed, and a case for carefully investigating the hemodynamics and function of each surgical procedure is presented.

2.2.1 PEDIATRIC MITRAL PATHOLOGIES

In infants and children with complex congenital heart defects involving the left atrioventricular valve, surgical repair is the standard of care over valve replacement. Lack of an ideal mechanical or bio-prosthetic substitute for the mitral position is the primary reason. Secondly, valve replacement is not a definitive procedure for the underlying congenital lesion as the patient will inevitably outgrow the valve while being exposed to the risk of anti coagulation therapy. Repair of the mitral valve is thus attempted in all pediatric patients, by adopting a creative and carefully thought out approach to repair in the setting of a complex valve anatomy.

2.2.1.1 Atrio Ventricular Valve Repair in Canal Defects

Atrioventricular canal defects encompass a spectrum of lesions that are caused due to regressed growth of endocardial cushions, resulting in abnormalities of the atrioventricular valve form and function, and also presenting with atrial and ventricular communication [65]. In these patients, proliferative deficiencies in the endocardial cushions restrict the development of the canal septum posteriorly towards the actual atrial septum, and anteriorly towards the actual ventricular septum, thus resulting in a common atrioventricular valve without distinction between the mitral and tricuspid valves shown in Figure 2-28. Each morphological abnormality can occur to different degrees of severity, resulting in varying levels of exercise tolerance and congestive heart failure.

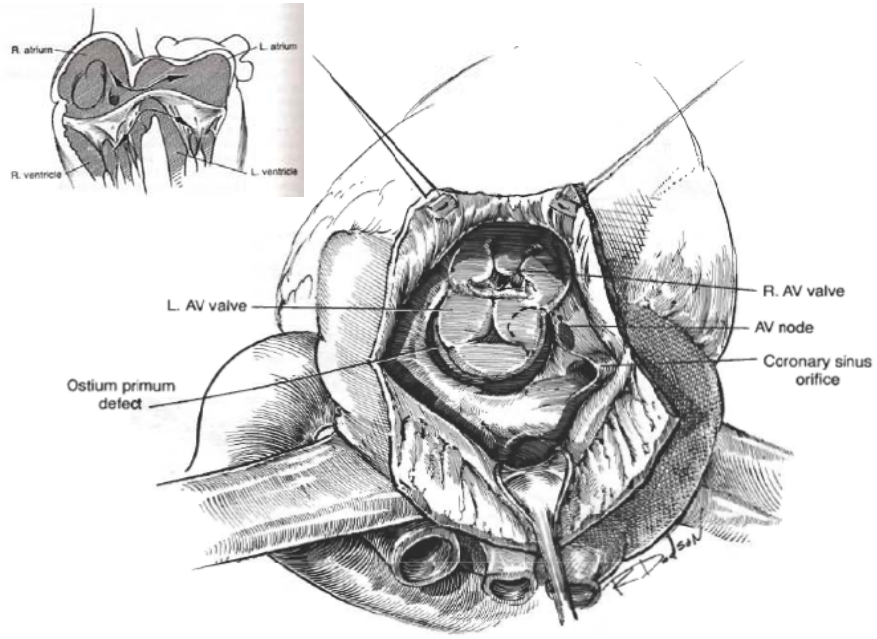

Figure 2-28 Surgical perspective of the common atrioventricular valve as seen through the right atrial access and through the atrial septal defect (Inset) Schematic of a heart with an ostium primum and septal secundum defects resulting in a common atrionventricular valve without separation of the annuli of the mitral and tricuspid valves; [Figure reproduced from Castaneda, Cardiac Surgery of the Neonate and Infant, Chapter 10][64]

Indications for surgery depend upon the form of the atrioventricular defect, and symptoms of congestive heart failure, at which point surgical correction is attempted. For the most severe of the cases, surgery may be in the first few weeks of life and in the asymptomatic patients within 6 months of birth as it is associated with lower mortality. Lillehi and associates were the first to attempt surgical correction of such defects in 1954 using cross circulation, but subsequent surgical management of this lesion carried a high mortality rate due to insufficient understanding of the anatomy of the atrioventricular canal [3]. In 1958, Lev described the conduction system in canal defect patients thereby allowing avoidance of complete heart block induced by surgery and thus reducing mortality rates [66]. Bharati et al. [67-69] and Rastelli et al. [70-77] contributed significantly towards understanding the anatomy of this lesion, leading to the development of various surgical techniques for reconstruction.

The natural focus of surgical repair in the initial years emphasized the management of atrioventricular valve tissue, and several surgical centers attempted these repairs. Rastelli and associates reported their experience with complete repair of the atrial ostium primum defect, the ventricular foramen closure and atrioventricular valve construction in infants in 1968 [74, 76], while Barratt-Boyes reported surgical repair under deep hypothermic circulatory arrest in 1973 [78]. At best, a 10% morality rate was reported in all these studies. This practice is now standardized, and in patients with inter-atrial or inter-ventricular communication, patch closure of the ventricular defect is performed first, followed by atrioventricular valve reconstruction and finally patch closure of the left atrium. Over the last 30 years, significant progress has been made in

septal closure procedures and excellent acute and chronic outcomes are reported in these patients.

Historically, atrioventricular valve reconstruction is performed in a staged approach with continuous saline testing for valve competence as shown in Figure 2-29. A pledgeted polypropylene suture is placed at the base of the cleft near the annulus, and the apposition of the cleft edges is tested by filling the ventricle with saline. Regurgitation is often observed through the cleft, and further closure of the cleft is attempted with repeated saline testing until complete valve competence is achieved. Commissurotomy is then performed to reduce the annular size and increase the length of central coaptation of the two apposing leaflets. In 1978, Carpentier proposed that the left atrioventricular valve can be constructed as a trifoliate valve without closing the anterior leaflet cleft[79]. He proposed that the open cleft may act as a commissure and enable apposition of the edges of the cleft, which was later proven to be inefficient due to the development of severe valvular regurgitation in the post operative period. Though this concept is still in practice at few centers, partial or complete closure of the cleft is prevalent as open clefts have been shown to be unpredictable and regurgitation is shown to cause thickening of the edges. Disagreement prevails in this aspect, as both success and failure have been reported using both approaches.

In the current era of surgical repair for congenital atrioventricular canal defects, the measure of operative success has shifted from early mortality to freedom from reoperation for residual valve lesions. In these patients, repair of the septal defects has been highly successful, but progressive post repair regurgitation across the left

atrioventricular valve still remains a challenging problem. More than 15% of the patients surviving repair have hemodynamically significant regurgitation, the causes of which may be multi factorial [12].

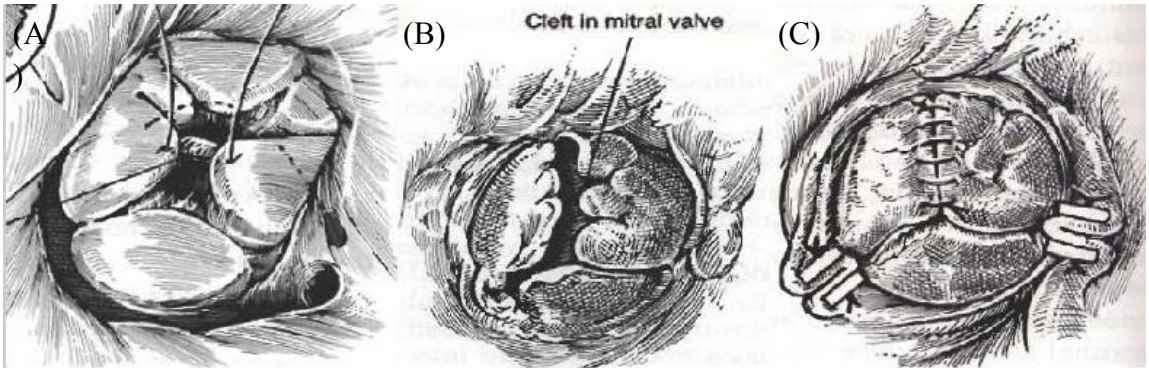

Figure 2-29 (A) The common atrioventricular valve with the bridging leaflets; (B) Cleft mitral valve formed after surgical separation of the annuli and septal defect closure; (C) Completely closed cleft with commissurometry to reduce annular size. Figures reproduced from Castaneda, Cardiac Surgery of the Neonate and Infant, Chapter 10. [64]

2.2.1.2 Risk Factors for Recurrent Regurgitation in Canal Defects

2.2.1.2.1 Procedural Risk Factors

Murashita and associates in 2004 reported their experience with left atrioventricular valve regurgitation after repair of ostium primum defect in a 61 patient series [12]. In their series ranging in age from 1 month to 62 years old patients (median age of 5.3 years old), 7 patients had a completely open cleft, 41 patients had partial cleft closure and 9 patients had complete cleft closure. Preoperative and postoperative regurgitation at hospital discharge, and late follow up was performed to assess the severity of regurgitation. In their series, left atrioventricular valve regurgitation was diagnosed pre operatively in all the patients; 25 patients with NYHA grade I regurgitation, 31 patients with grade II, 4 with grade III, and 1 with grade IV

regurgitation. After surgical correction and at hospital discharge, 18 patients had grade II regurgitation and 2 had grade III regurgitation. At long term follow up, nearly 20% of the patients had regurgitation of severity grade III or more, and they report that age at time of surgery, pre operative severity of regurgitation, and acute post operative severity of regurgitation, seemed to have dominant risk factors for late occurrence of regurgitation after surgical repair. Patients who are less than 2 years of age at surgery seemed to have poor outcomes over their older counterparts, as the recurrence of late regurgitation was higher in the younger population. This can be attributed to the early growth in the cardiac structures, which happens during the first year of life. Patients that presented with higher severity of regurgitation before surgery seemed to be more prone to recurrence of post operative regurgitation. Though the underlying reasons are not discussed in this publication, it can be speculated that the patients who present with severe grades of pre operative regurgitation may have abnormal annular or sub annular geometries, smaller leaflets and abnormal chordal insertions from the ventricular trough. Additionally, this report also indicates that even after rigorous surgical correction, acute remnant regurgitation is seen in some patients that worsen with time. However, the authors reported that the length of cleft closure did not seem to have any correlation with the late outcomes based on their statistical analysis, but the graphs clearly demonstrated that with a complete cleft closure at 15 years follow up nearly 80% of the patients had regurgitation. Figure 2-30 depicts the actuarial freedom from late regurgitation at acute and chronic follow up time points, in comparison with different risk factors assessed in this study.

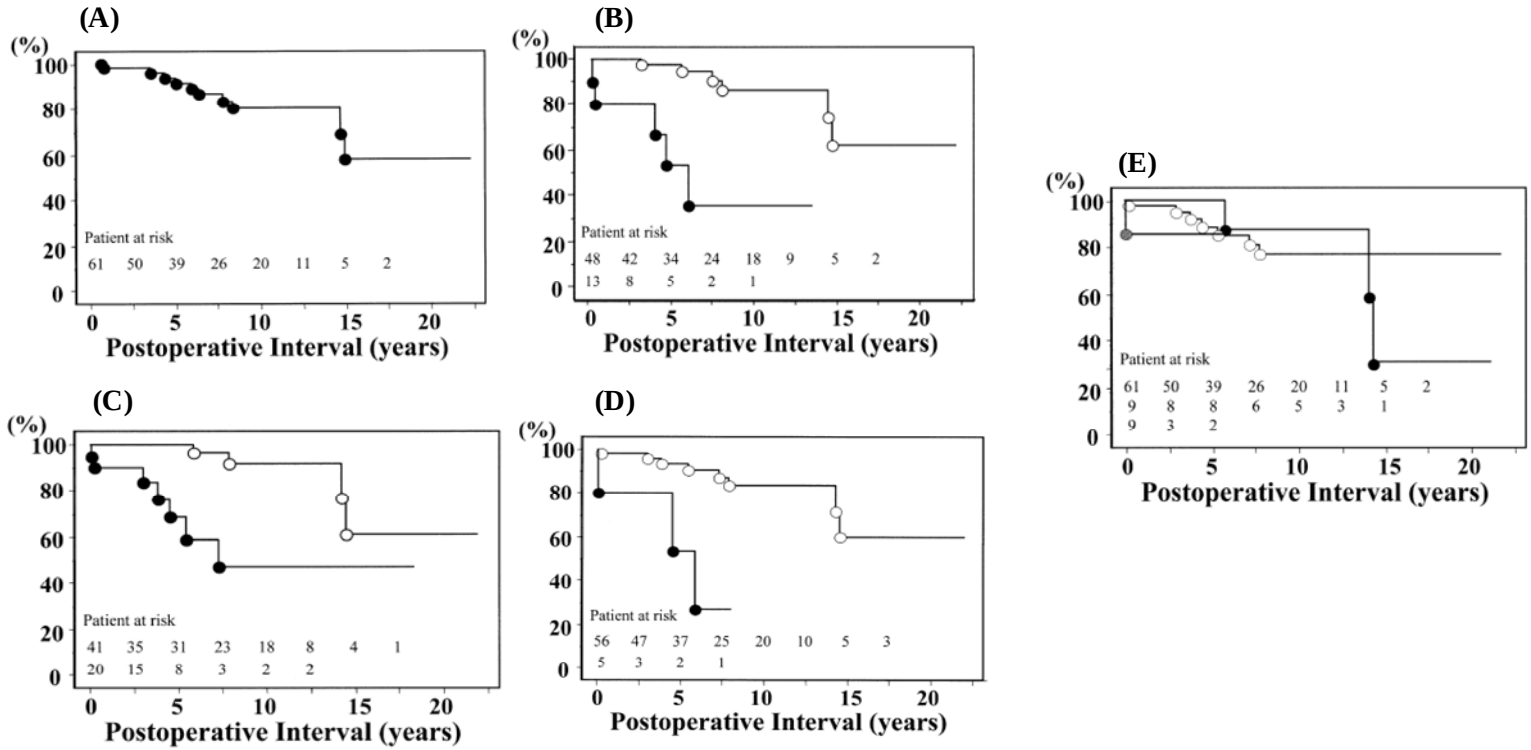

Figure 2-30 (A) Actuarial freedom from late atrioventricular valve regurgitation (LAVR) of Grade III or more after repair of cleft mitral valve with ostium primum defect; (B) Actuarial freedom from LAVR grade III or more in patients aged less than 2 years old (●) and equal to or greater than 2 years old (○) depicting poor outcomes in infants; (C) Actuarial freedom from LAVR grade III or more in patients with post operative LAVR grade II or more (●) and with LAVR less than grade II (○); (D) Actuarial freedom from LAVR grade III or more in patients with preoperative LAVR more than grade III or more (●) and with LAVR less than grade II (○); (E) Actuarial freedom from LAVR grade III or more in patients without cleft repair (●), partial cleft closure (◍), and with complete cleft closure (○).

Graphs reproduced from Murashita T et al. Ann Thorac Surg 2004; 77:2157-62. [11]

2.2.1.2.2 Morphological Risk Factors

In a more recent report by Kanani and colleagues in 2006, the authors report a morphological perspective on late incompetence of the left atrioventricular valve after repair of atrioventricular septal defects [1]. The authors compared the mitral valves from 92 normal hearts to those with atrioventricular septal defect with common atrioventricular junction, determining the shape of the leaflets and the arrangement of the sub annular apparatus in these hearts. The anterior leaflet of the mitral valve constructed after closure of the ostium primum defect and the ventricular foramen, was rectangular in shape with a triangular cleft at its center, compared to a triangular anterior leaflet in normal hearts as shown in Figure 2-31. In normal hearts the anterior leaflet is continuous with the left and non coronary aortic leaflets through the anterior annulus and the fibrous trigones, and in spite of its broad base covers only a third of the valve perimeter. On the

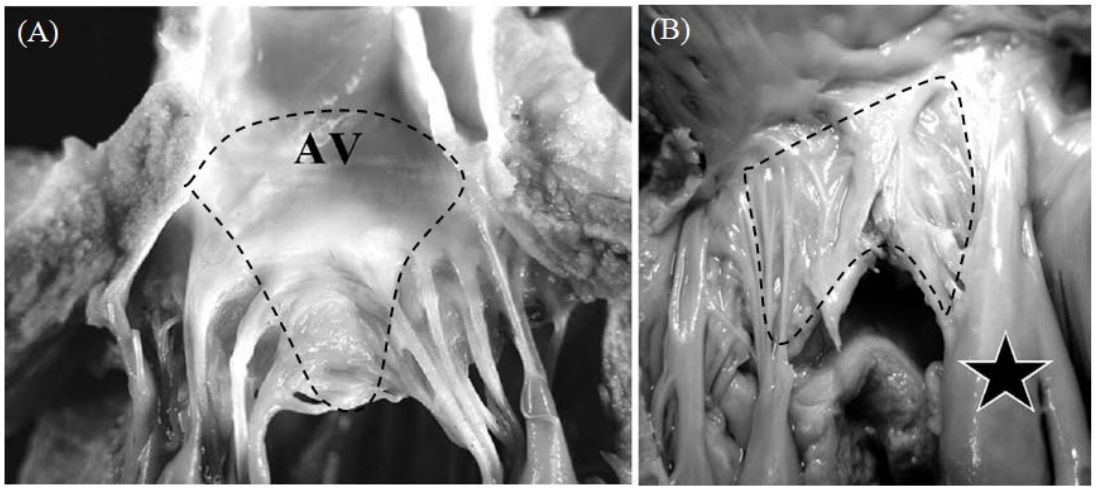

Figure 2-31 (A) Photograph of the anterior leaflet of the mitral valve from cadaver's depicting the triangular shape of the leaflet with an orderly radial arrangement of the chordae tendineae; (B) Photograph of the surgically constructed anterior leaflet of the cleft mitral valve shaped as a rectangle with a triangular cleft in the middle. In this case the cleft is closed partially using unpledgeted sutures. Figures reproduced from Kanani et al. JTCVS, 2006, 132(3): 640-646e3.[79]

other hand, the surgically constructed rectangular cleft anterior leaflet covers less than one third of the total circumference of the annulus.

The papillary muscles in the normal heart are located beneath the two commissures of the mitral valve leaflets, with chordae tendineae emerging from the tip of each papillary muscle and inserting into the ventricular surface of the anterior and posterior leaflets. As the chordae emerge from the papillary muscle, the stem of the chord splits into multiple branched webs, one of which inserts into the free edge of the leaflets, second into the base of the ventricle forming the strut chordae, and the third inserting near the base of the leaflet close to the mitral annulus. This type of chordal arrangement ensures a consistent and optimized configuration of the leaflet at peak systole for increased leaflet coaptation. Compared with such a physiological chordal distribution, in surgically created anterior leaflet in atrioventricular canal defects the chordae run along the longitudinal axis of the leaflet, reduced in number than the normal valve and manifesting with significant chordal fusion or thickening as shown in Figure 2-32.

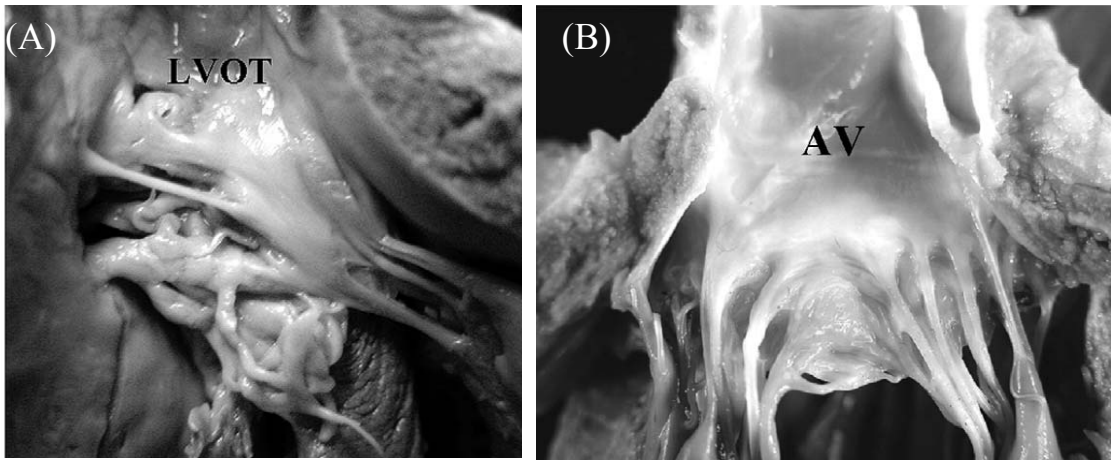

Figure 2-32 (A) Fused chordae running along the longitudinal axis of the leaflet in a surgically created anterior leaflet in canal defects; (B) Chordal distribution in a normal mitral valve leaflet depicting the distinction between the primary, secondary and tertiary chordae tendineae.[79]

Kohl and Silverman, using echocardiography techniques compared the position of the anterior leaflet cleft with papillary muscle position to differentiate between isolated cleft mitral valve and atrioventricular canal defect patients [80]. The authors report that in patients with canal defects, both papillary muscles originated closer to each other and were more posteriorly displaced towards the mural leaflet as shown in Figure 2-33.

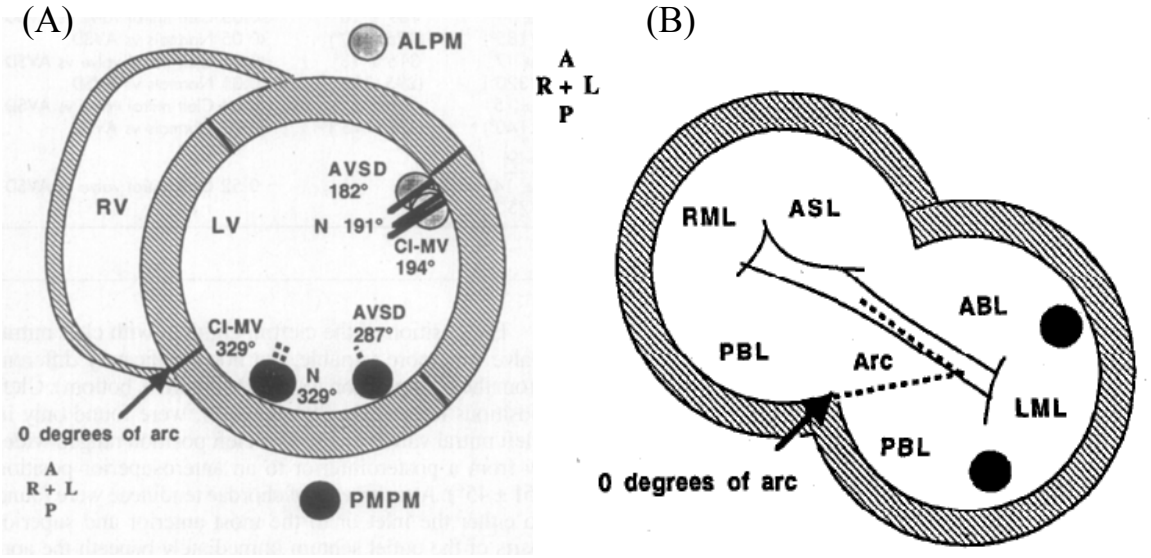

Figure 2-33 (A) Schematic depicting the papillary muscle positions in subjects with normal mitral valves (N), with isolated cleft mitral valve(CI-MV), and with complete atrioventricular canal defect (AVSD). In AVSD hearts, the papillary muscles are posteriorly and laterally displaced towards each other potentially due to the scooped ventricular geometry; (B) An atrial view of the common atrioventricular leaflet with the relative position of the papillary muscle with respect to the anterior leaflet cleft before surgical construction. [80]

2.2.1.2.3 Cardiac Structural Growth with Ageing

The congenital nature of canal defects requires surgical correction in the early weeks of life and current surgical techniques to not take into consideration the growth of cardiac structure with age. Figure 2-34 show nomograms that illustrate the changes in body surface area, and mitral valve structures with age in congenital heart defect patients.

From birth to 15 years of age body surface area increases from 0.2 m^2 to 1.4m^2, a 700% increase. With increasing body surface area, the mitral annular width along anterior and posterior axis also increased from 12mm to 30mm. Annular growth following surgical repair in conjunction with the smaller mural leaflet and rectangular anterior leaflet may induce recurrent regurgitation several weeks after surgery.

(A)

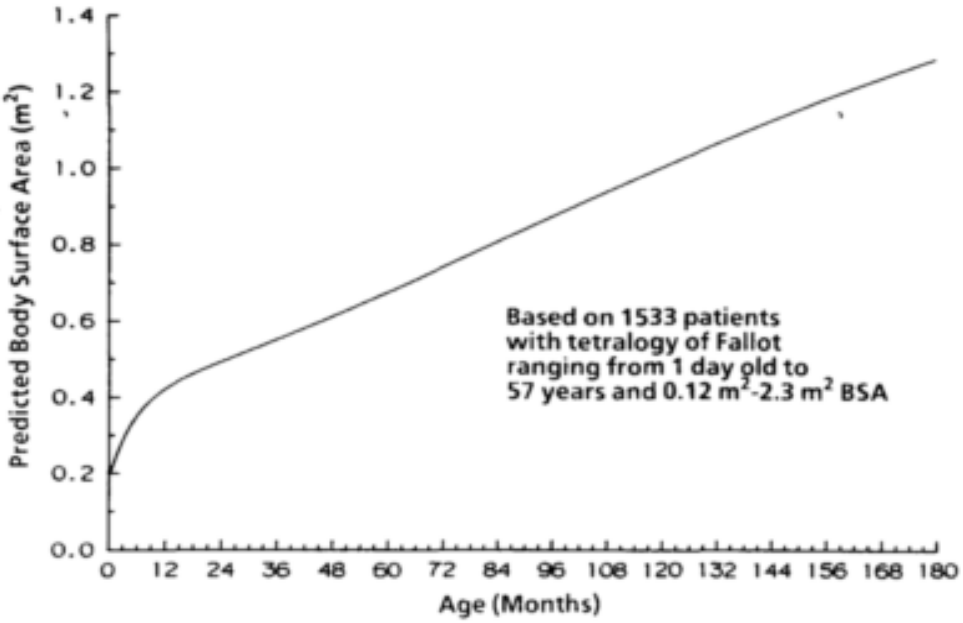

(B)

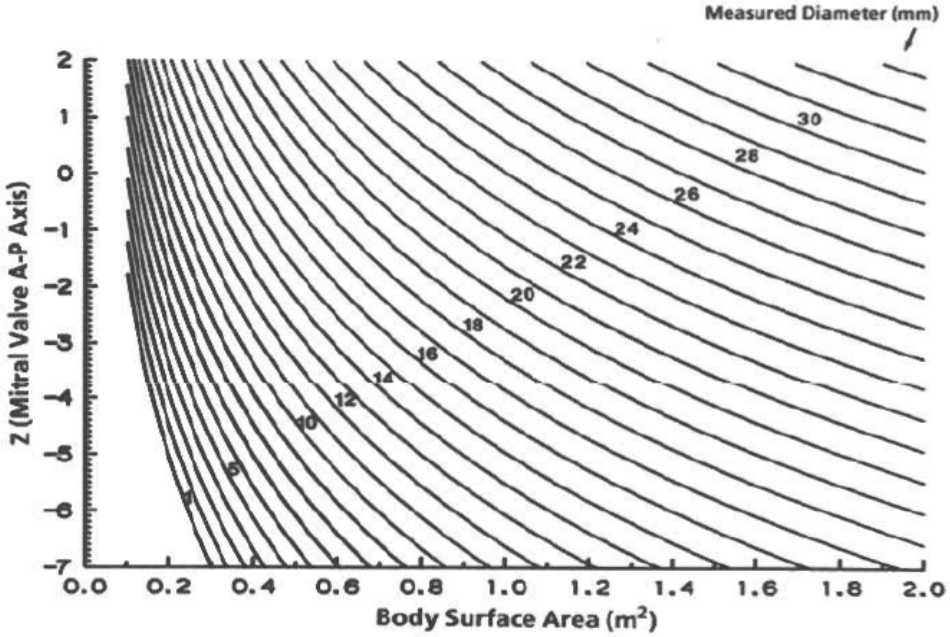

(C)

	Mitral Valve			
	Minor Axis (A-P)		Major Axis (Lat)	
BSA	Mean (mm)	±SD	Mean (mm)	±SD
0.25	12.0	10.2–13.8	15.0	11.8–18.2
0.30	13.6	11.8–15.4	17.3	14.1–20.5
0.35	14.9	13.1–16.7	19.2	16.0–22.4
0.40	16.1	14.3–17.9	20.9	17.7–24.1
0.45	17.1	15.3–18.9	22.3	19.1–25.5
0.50	18.0	16.2–19.8	23.7	20.5–26.9
0.60	19.5	17.7–21.3	25.9	22.7–29.1
0.70	20.8	19.0–22.6	27.9	24.7–31.1
0.80	22.0	20.2–23.8	29.5	26.3–32.7
0.90	23.0	21.2–24.8	31.0	27.8–34.2
1.00	23.9	22.1–25.7	32.3	29.1–35.5
1.20	25.5	23.7–27.3	34.6	31.4–37.8
1.40	26.8	25.0–28.6	36.5	33.3–39.7
1.60	27.9	26.1–29.7	38.2	35.0–41.4
1.80	28.9	27.1–30.7	39.6	36.4–42.8
2.00	29.8	28.0–31.6	40.9	37.7–44.1

Key: A-P, anteroposterior; BSA, body surface area; Lat, lateral; SD, standard

Figure 2-34 (A) Predicted growth in body surface area from birth to 15 years of age in patients with congenital heart defects; (B) Measured increase in mitral annular antero lateral dimension with increasing body surface area; (C) Numerical values for changes in the major and minor axes of the mitral annulus assuming an elliptical shape

Retrospective clinical studies identified several risk factors in these patients that induce regurgitation, and ultimately require reoperation or valve replacement. However, the biggest drawback of these clinical studies is that they are confined to speculation or statistical inference, but cannot provide a structure-to-function relationship between the risk factors and the outcomes. Controlled experimental models are thus required to simulate different levels of the pathological lesion, and investigate the independent and combined impact of each of the risk factors on valve competence. Large animal models would provide an ideal setting to conduct such experiments, but creating congenital lesions in large animal models is challenging and is associated with very limited success. These limitations call for the development of ex vivo or in vitro systems wherein the pathological valve geometry can be simulated and different risk factors and surgical techniques can be assessed for their hemodynamic efficacy and long term function.

2.2.2 DEGENERATIVE MITRAL PATHOLOGIES

Degenerative mitral valve disease is the most prevalent pathology among all mitral valve lesions, and afflicts 2.4% to 5% of men and women in most industrialized nations [81]. Even though the exact pathogenesis of the disease is currently unknown, degenerative mitral valve lesions can be primarily classified based on their etiology into – [a] Rheumatic valve degeneration, [b] Myxomatous valve degeneration, and [c] Fibro elastic deficient valve degeneration.

2.2.2.1 Rheumatic Valve Disease

Rheumatic fever is widely prevalent in the developing countries, and is the leading contributor to the increasing burden of heart valve disease in these nations. World Health Organization (WHO) estimated that 5-to-20 million children and young adults across the world suffer from chronic rheumatic heart fever, with a projected mortality rate of 90,000 per year [82]. Caused due to group A-beta hemolytic Streptococcus bacteria that infiltrate the epithelial cells of the upper respiratory tract, release of enzymes into the connective tissue results in a sequel of events such as endocarditis and pericarditis that ultimately lead to complete heart failure[83]. The bacteria also infiltrate the mitral valve leaflet tissue, increasing the leaflet thickness and stiffness, and resulting in fusion of the commissures and chordae tendineae as shown in Figure 2-35. These manifestations result in mitral stenosis and mitral regurgitation, and depending on the severity of degeneration the lesions are corrected either by surgical valve reconstruction/repair or by complete replacement of the valve with artificial heart valves. Patient outcomes to date have been

unsatisfactory, due to problems associated with anti coagulation therapy and durability of surgical repairs.

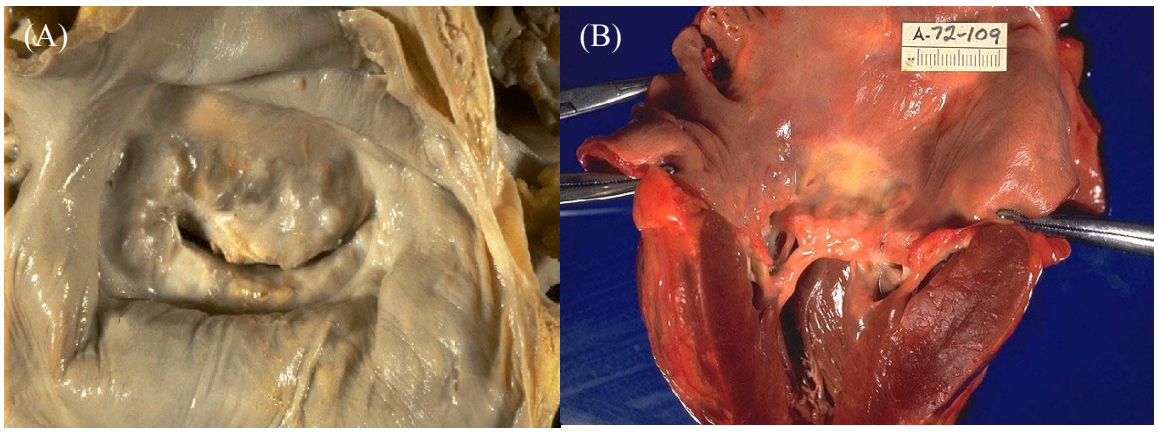

Figure 2-35 (A) Endocardial vegetations on the mitral valve leaflets in a patient with rheumatic heart disease;(B) Leaflet thickening and chordal fusion caused due to rheumatic degeneration. [Figures reproduced from www.wikimedia.org]

2.2.2.2 Barlow's Disease

Barlow's disease is the most prevalent degenerative mitral valve lesion in the Western world. Though the syndrome of mid-systolic click with a late systolic murmur was described in late 1800s, it was only in early 1960's was it associated with mitral regurgitation due to leaflet billowing as demonstrated by Barlow and colleagues using cine ventriculography[84-87]. Criley et al. identified the mechanism of regurgitation as posterior leaflet prolapse and coined the term mitral valve prolapse to explain this pathology[88]. Carpentier and colleagues later characterized the surgical lesions resulting from the myxoid changes in this pathology, reporting extensive leaflet thickening, leaflet distention and redundancy, chordal elongation and rupture, and annular dilatation[89]. Researchers have attributed both genetic mutations, and mechno-biological factors to play a role in the onset of tissue degeneration. Grau JB and colleagues in a recent review

point to three different loci on chromosomes 16,11 and 13, but no specific gene has been described yet[90]. They also reported that mitral valve prolapse due to degeneration is typically found in patients with connective tissue disorders such as Marfan's syndrome, Ehlers-Danlos, and Osteogenesis Imperfecta. Pedersen et al stretched explanted porcine tissue to different levels of strain and demonstrated the over expression of endothelin-1 receptors, which is typically seen in prolapsing valves[91, 92]. Irrespective of the disease mechanisms, myxoid degeneration process affects the entire valve and patients with this disease generally have complex valve pathology and dysfunction, which is often multi segmental as shown in Figure 2-36.

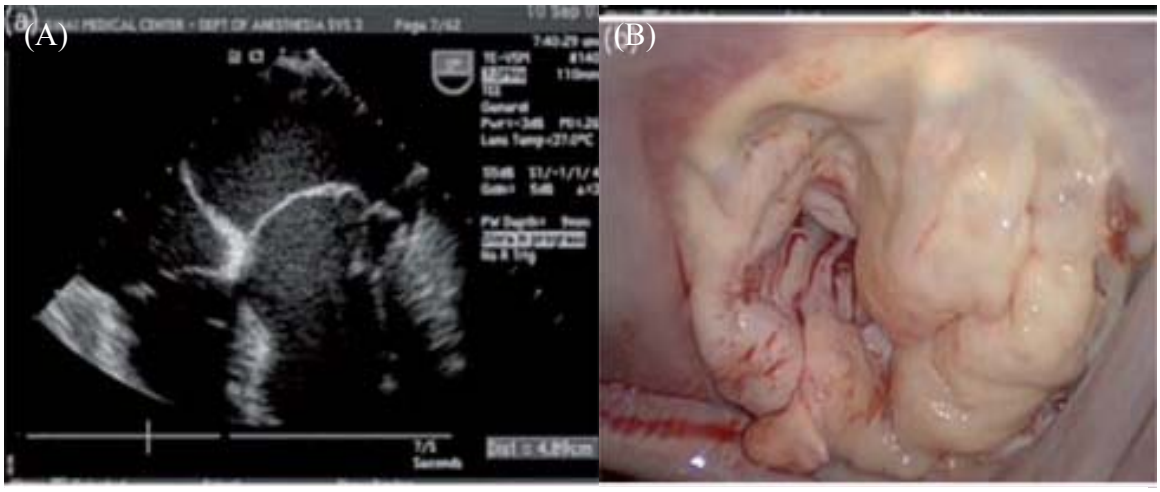

Figure 2-36 (A) Echocardiographic image of the mitral valve billowing into the left atrium; (B) Surgical view of a Barlow's mitral valve showing the multi segmental degeneration process and leaflet distension. [Figure reproduced from www.mitralvalverepair.org]

Patients presenting with Barlow's disease are generally old and aged 50 years or higher, who were aware for decades that they had a heart murmur. These patients are referred to the cardiologist only upon manifestation of symptoms such as atrial fibrillation, shortness of breath and fatigue, or ventricular or atrial enlargement as

observed on echo, and in some cases pulmonary hypertension. Based on the severity of regurgitation, the patients are subsequently referred to a cardiac surgeon for valve repair or replacement. With increased surgical expertise and robotic surgery, mitral valve repair has become the standard of care in these patients.

The most common surgical techniques to repair degenerative valves include resection of redundant leaflet tissue, with concomitant annuloplasty to stabilize the repair, though the scientific evidence behind the need for annuloplasty is not clearly understood. The choice of leaflet resection techniques is typically based upon the cardiac surgeon, the leaflet requiring repair, and the extent of leaflet billowing. Quadrangular resection is the most commonly used procedure on the posterior leaflet[7], which involves resecting a quadrilateral shape of the P2 cusp, followed by leaflet reconstruction and plication of the

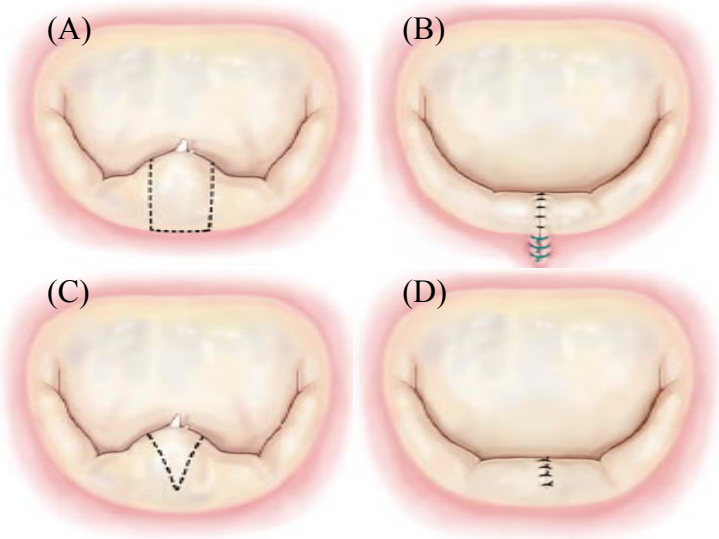

Figure 2-37 (A) Dotted line depicting the quadrangular section of the P2 that is resected; (B) Valve after complete leaflet reconstruction; (C) Dotted line depicting the triangular part of the free edge that is resected; (D) Valve after leaflet reconstruction

annulus as shown in Figure 2-37. This procedure not only reduces the leaflet area but also the height of the leaflet at the P2 cusp. However, the procedure is technically challenging and requires modification on an individual patient basis. Limited triangular resection is another procedure that is increasingly used [93], which involves resection of a smaller triangular segment at the free edge of the posterior leaflet as shown in Figure 2-37, but does not require annular plication. A folding plasty procedure was also recently proposed, but its clinical efficacy or technical feasibility is yet to be published [94, 95].

In the last decade, few non resective surgical techniques have also been developed shown in Figure 2-38, such as Neochordoplasty which involves replacement of the elongated or ruptured chordae with ePTFE chordae[96, 97], Edge-to-Edge repair which involves placement of a stitch between the edges of the anterior and posterior leaflets thus forming a double orifice mitral valve[98], and chordal translocation which involves translocation of the secondary chordae to the ruptured marginal positions[99-101]. Data on the efficacy of Neochordoplasty is abundant in recent literature, and Falk et al recently demonstrated the improved valve function and outcomes with this procedure over other resective techniques [96].

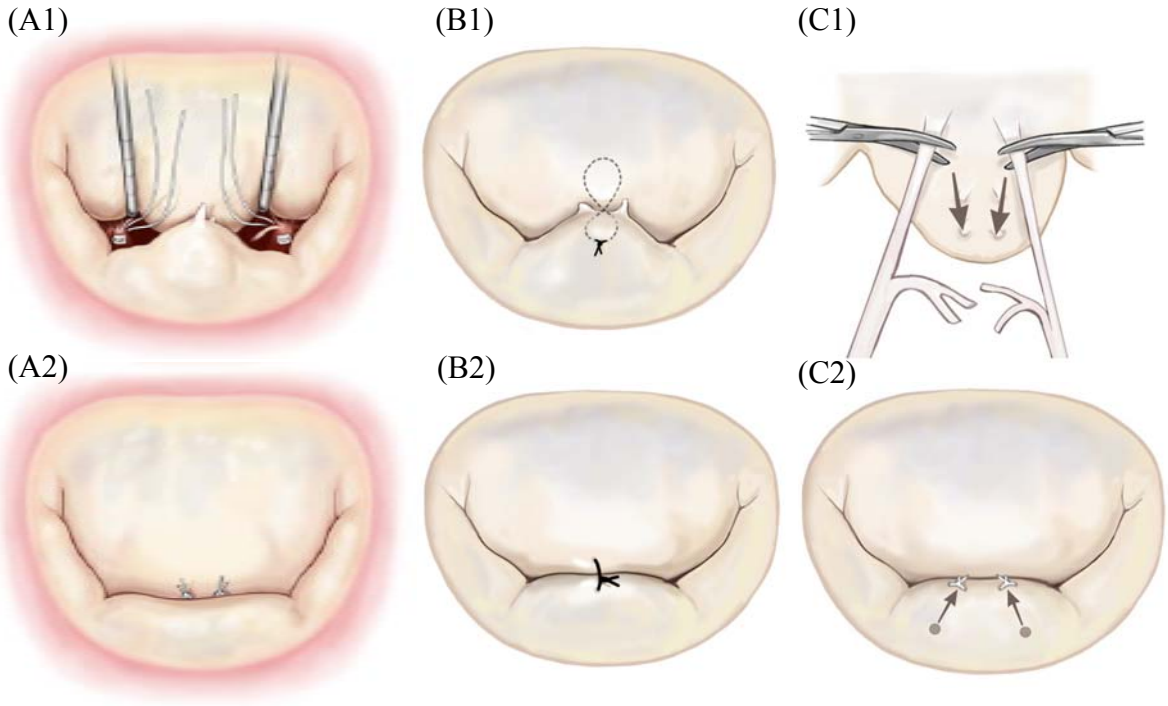

Figure 2-38 (A1) ePTFE suture with pledgeted ends placed on the tips of the papillary muscles; (A2) The ePTFE sutures passed through the free edges of the prolapsing posterior leaflet and knotted on the atrial surface after adjusting the chordal length; (B1) An "8" shaped stitch placed between the anterior and posterior free edges to provide structural support to the prolapsing segment; (B2) The double orifice valve formed after the edge to edge repair; (C1) Translocation of the secondary chordae on the prolapsing leaflet to the marginal position to restrict the free edge prolapse; (C2) Schematic depicting the change in chordal positions after the translocation procedure.

2.2.2.3 Fibro Elastic Deficiency

Fibroelastic deficiency is a common degenerative lesion of the mitral valve, specifically in younger patients [102]. In contrast to Barlow's disease, fibroelastic deficiency manifests with reduced leaflet tissue resulting from deficiencies in the production of collagen, elastin and proteoglycans [102]. Regressed ability of the cells to produce connective tissue, results in leaflet and chordal thinning and leaflet prolapse under chronic conditions. Histological analysis of these valves demonstrates alterations in the elastic fibers, even though the tri layered structure of the valve is completely preserved. Myxoid changes or thickening of the prolapsing segment is commonly seen in these patients, but are isolated to this segment. Figure 2-39 shows a fibroelastic deficient mitral valve with no visible distension of the mitral leaflets, isolated prolapse of the P2 segment with some myxoid changes.

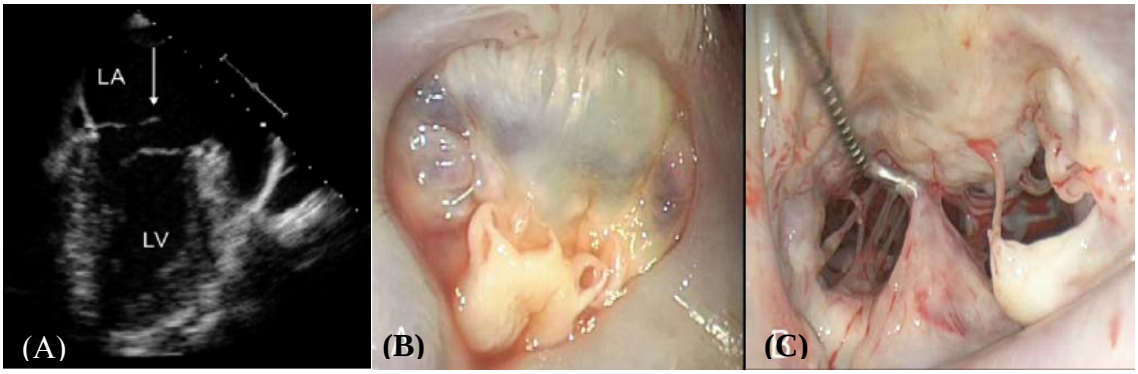

Figure 2-39 (A) Echocardiograph of the prolapsing mitral valve in a patient with fibroelastic deficiency. Unlike Barlow's disease that presents with significant leaflet billowing, chordal rupture in this case results in complete movement of the prolapsing leaflet into the left atrium, developing a large regurgitant orifice; (B) Myxoid changes to the prolapsing posterior mitral leaflet after chronic regurgitation, though the myxoid changes and leaflet thickening were isolated to the prolapsing segment; (C) Surgical view of the ruptured marginal chordae that caused the prolapse [Images courtesy of Dr. David Adams, Mt Sinai School of Medicine, NY]

Even though the etiology of Barlow's disease and Fibroelastic deficiency are quite different, most surgeons typically use the same resective techniques as used for the distended leaflets. Neochordoplasty is increasingly gaining popularity to repair valves with this lesion, and a very recent study by Falk V et al. demonstrated the improved outcomes with this procedure [96]. Edge to edge repair and chordal translocation are also used at times, but there is no published data reporting the clinical outcomes of these procedures in this particular disease setting.

2.2.2.4 Clinical Outcomes of Degenerative Mitral Repair

Patients with degenerative mitral valve disease are the most suitable for reconstructive surgery. Filsoufi F et al. reported in their clinical series that the operative mortality in these patients is as low as 0.5% at experienced centers with good ventricular function[103]. Long term survival in these patients is comparable to age-matched, gender adjusted series that did not undergo cardiac surgery. Carpentier in a recent report followed 162 patients for >20 years, who received reconstructive surgery for degenerative mitral valve lesions [104]. Mitral annuloplasty was performed in all the patients, with 126 patients receiving leaflet resection, and the rest receiving shortening or transposition of the chordae tendineae. The linearized rate of reoperation in these patients was 0.4% per year, and the freedom from reoperation was 97% for posterior leaflet repair, 86% for anterior leaflet repair and 83% for bi-leaflet repair. Figure 2-40 shows an estimate of reoperation rate based on the data reported by Carpentier, demonstrating the excellent long term outcomes of valve repair.

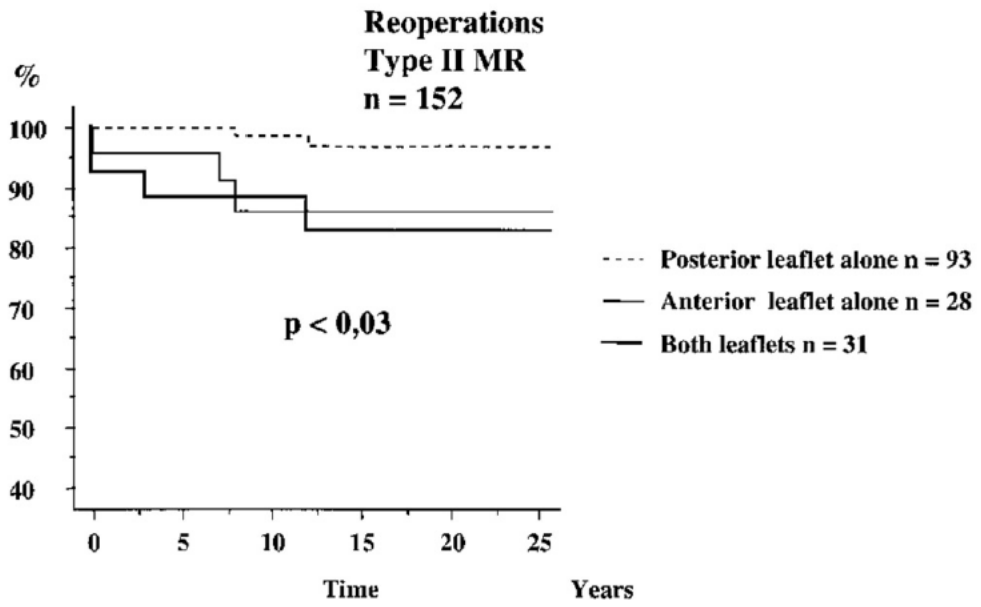

Figure 2-40 Reoperation rates at 20 years after mitral valve reconstruction using Carpentier techniques. Figure reproduced from Filsoufi F et al. Seminars in Thoracic and Cardiovascular Surgery, 2007, 19:103-110[104]

Flameng and coworkers in 2008 compared the durability of mitral valve repair in Barlow's patients with those with fibroelastic deficiency [10]. In 348 patients, survival was at 80.1% at 10 years after surgery and reoperation rates were at an acceptable 94.4%. However, the rate of recurrence of mitral regurgitation (>2/3 grade) was significantly higher at 98.7% at 1 month, 82.2% at 5 years and 64.9% at 10 years. The linearized recurrence rate was 3.2% per year in all the patients, but was higher at 6% in the Barlow's repairs than the 2.6% observed in fibroelastic deficiency. This data clearly indicates that reoperation rates are poor indicators of the actual outcomes of surgery, and since significant experience with degenerative mitral valve repair is now available the focus should veer towards optimizing repair techniques that restrict recurrence of mitral regurgitation after surgery. Figure 2-41shows the calculated reoperation and recurrence of mitral regurgitation rates as presented in this study.

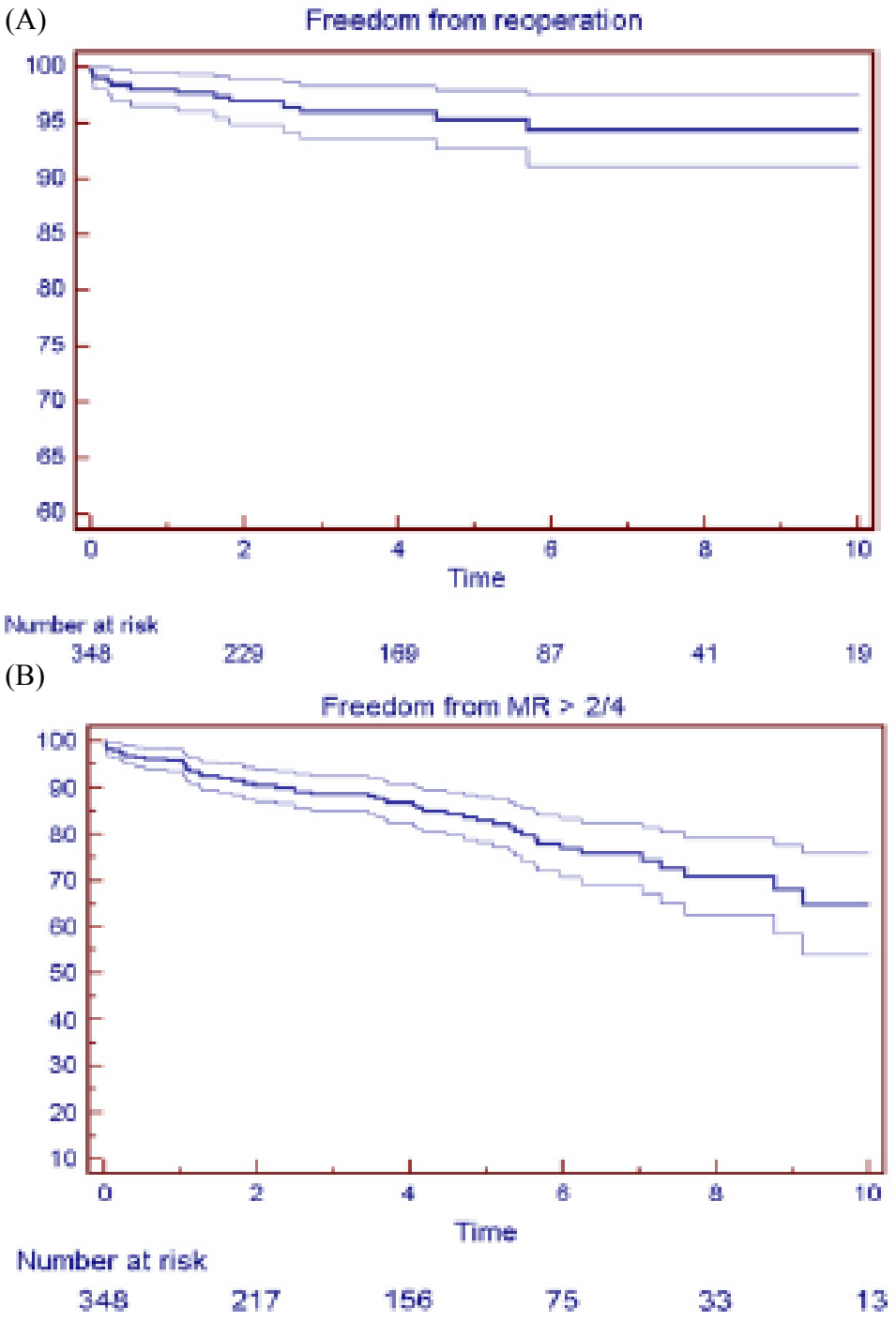

Figure 2-41(A) Reoperation rates after degenerative mitral valve surgery with a distinction between the Barlow's and Fibroelastic deficient valves; (B) Recurrence of mitral regurgitation within 10 years of the primary surgery between Barlow's and Fibroelastic Deficient Valves. Figures reproduced from Flameng et al. JTCVS 2008, 135: 274-82. [9]

Falk et al. in 2008 presented an excellent study comparing the use of neochordae loops to resection techniques to correct posterior leaflet prolapse due to fibroelastic deficiency [96]. Mitral valve repair was accomplished in 129 patients by randomizing them either to neochordoplasty group or to the resection group. Echocardiographic comparison of leaflet parameters was done in both the groups, and Figure 2-42 summarizes the results in these groups. Significant reduction in leaflet coaptation length in the resective group was observed in comparison to those who received neochordae. Restricted mobility of the leaflet after resection was also reported, but no quantitative data on leaflet mobility was provided.

MR	Baseline	After surgery	*P* value
Loops	3.4 ± 0.6	0.2 ± 0.5	*P* < .001
Resection	3.3 ± 0.5	0.1 ± 0.3	*P* < .001
P value	.74	.41	
LVEF (%)	**Baseline**	**After surgery**	***P* value**
Loops	65.2 ± 7.4	60.3 ± 8.6	*P* < .001
Resection	64.8 ± 8.3	56.9 ± 9.0	*P* < .001
P value	.14	.06	
***P* mean (mm Hg)**	**Baseline**	**After surgery**	***P* value**
Loops	1.98 ± 0.92	2.54 ± 1.11	*P* < .01
Resection	1.82 ± 0.83	3.03 ± 1.57	*P* < .001
P value	.38	.10	
LA width (mm)	**Baseline**	**After surgery**	***P* value**
Loops	51.2 ± 8.6	44.2 ± 8.3	*P* < .001
Resection	52.8 ± 9.1	44.0 ± 5.5	*P* < .0001
P value	.91	.36	
V mean (m/s)	**Baseline**	**After surgery**	***P* value**
Loops	0.66 ± 0.15	0.75 ± 0.15	*P* < .01
Resection	0.64 ± 0.13	0.8 ± 0.21	*P* < .001
P value	.40	.12	
LVVd (cm^2)	**Baseline**	**After surgery**	***P* value**
Loops	125 ± 39	104 ± 41	*P* < .01
Resection	135 ± 41	100 ± 37	*P* < .001
P value	.16	.53	
MOA (cm^2)	**Baseline**	**After surgery**	***P* value**
Loops	4.08 ± 1.21	3.54 ± 0.96	*P* < .01
Resection	4.23 ± 1.92	3.72 ± 1.1	*P* < .001
P value	.38	.34	
Line of coaptation (mm)	**Loops**	**Resection**	
After surgery	7.6 ± 3.6 mm	5.9 ± 2.6 mm	*P* = .03

LVEF, Left ventricular ejection fraction; *LA*, left atrium; *V mean*, mean transvalvular velocity; *LVVd*, left ventricular diastolic volume; *MOA*, mitral orifice area; *MR*, mitral regurgitation; *P mean*, mean pressure gradient. All data are presented as mean ± standard deviation.

Figure 2-42 Echocardiographic indices measured at baseline conditions and after surgery with either neochordoplasty or leaflet resection. Data reproduced from Falk et al. JTCVS 2008, 136: 1200-6 [96]

Though mitral valve repair for degenerative valve disease is considered a routine procedure with excellent outcomes, data fails to support the long term durability of the repairs. The risk factors leading to repair failure seem to be multi factorial, including timing of surgery, surgeon experience with valve repair, etiology of the valve, extent of degeneration, type of surgical procedure, technical details of the surgical procedure, presence of annular dilatation, and progression of disease after the repair. It is impossible to design clinical studies that can isolate the impact of each of these factors, and thus emphasizing the need for either ex vivo or in vitro hemodynamic and mechanics studies. While an optimal mitral valve repair technique may not exist, correlating the type of surgical repair to the etiology may provide the right direction towards improving surgical outcomes not only acutely after surgery but also at chronic follow up.

2.2.3 FUNCTIONAL MITRAL REGURGITATION

Regurgitation due to pure geometric perturbations to the mitral valve is the least understood and the most challenging pathology to manage clinically. Often diagnosed in patients with ischemic or hypertrophic cardiomyopathy, this mitral valve pathology is associated with changes in the annular and ventricular geometry due to other events. In cardiomyopathic patients, ventricular remodeling following a myocardial infarction or myocardial hypertrophy results in global dilatation of the left ventricle with outward displacement of the ventricular free wall. These changes to the ventricular geometry induce dilatation and flattening of the mitral annulus, and displacement of the papillary muscle tips away from the mitral annular plane as shown in Figure 2-43.

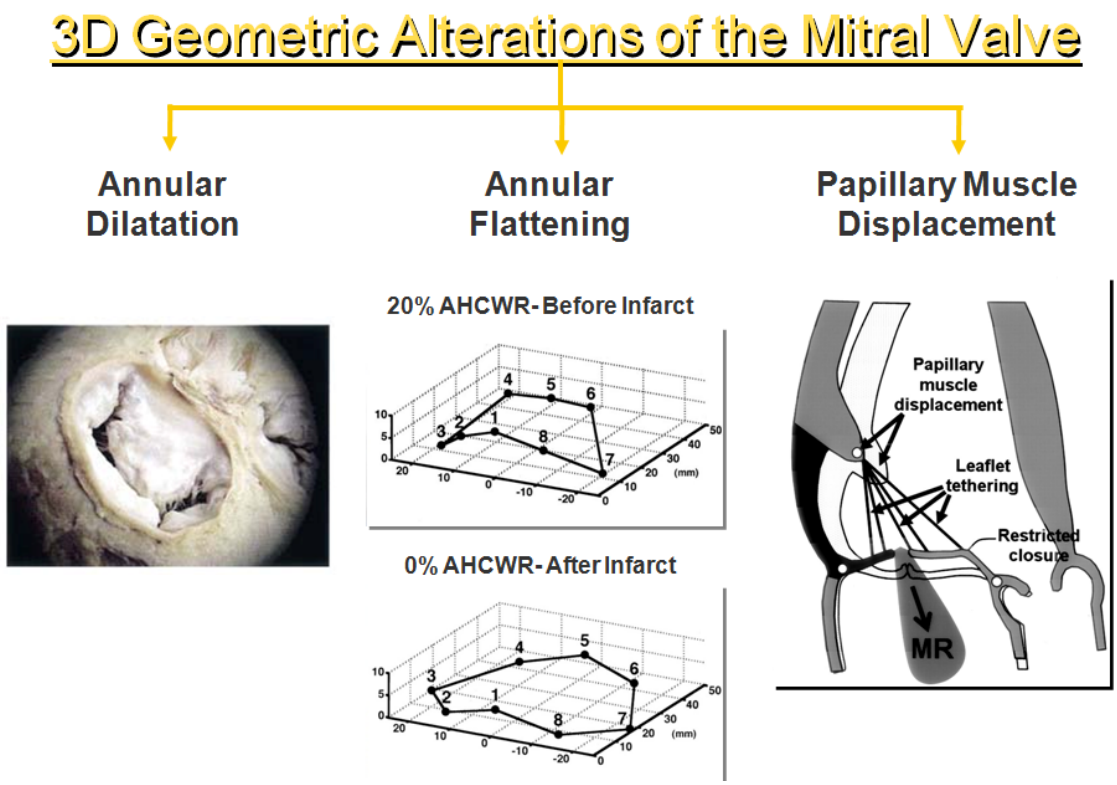

Figure 2-43 Summary of the geometric distortions to the mitral valve induced by ischemic or non ischemic dilated cardiomyopathy. The distinct changes to annular geometry include dilatation and flattening of the mitral annulus. Sub annular distortions to the valve were caused due to displacement of the papillary muscles apically, laterally or posteriorly from the mitral annular plane resulting in leaflet tenting as shown in the right most schematic. Figures adapted from Hueb et al. JTCVS 2002, 124:1216; Kaji S et al. Circulation 2005, 112: I4-9-414; Levine RA, Circulation 2005, 112: 745-748. [105-107]

Hueb and colleagues, and Ahmed et al had reported detailed studies on the dimensional changes in the mitral annulus in cardiomyopathic patients and animal models[105]. Hueb et al separated the annulus into fibrous portion (the anterior segment) and muscular portion (the posterior segment) and quantified the changes in their dimensions in ischemic and idiopathic cardiomyopathy patients and compared them to normal's. As shown in Figure 2-44A, significant changes in annular dimensions was observed on both segments, though changes were higher in the muscular section than the

fibrous section of the annulus [106, 107]. Ahmed et al additionally measured other relevant geometric parameters of the annulus, and reported the asymmetry in mitral annular dilatation as shown in Figure 2-44B[108].

(A)

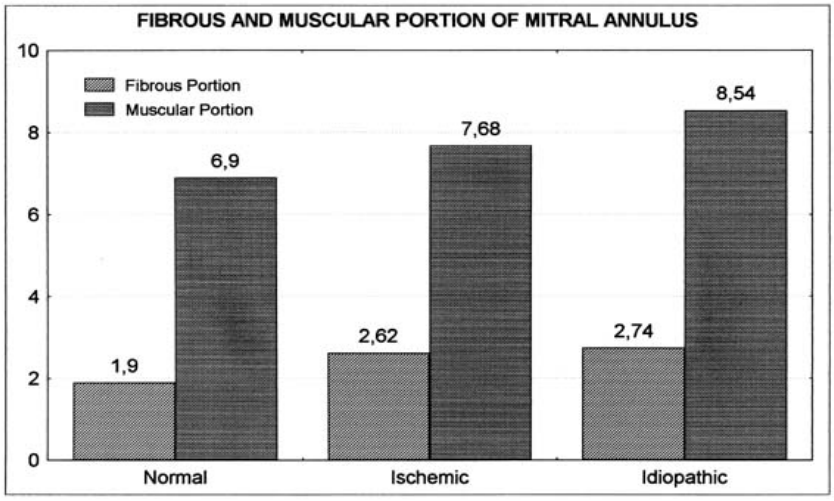

(B)

Variable	Controls	IMR	*p* Value
Annular perimeter (cm)	8.6 ± 0.2	10.7 ± 0.7	0.03
Anterior annular perimeter (cm)	4.1 ± 0.2	5.0 ± 0.4	0.08
Posterior annular perimeter (cm)	4.5 ± 0.2	5.6 ± 0.5	0.06
Intertrigonal distance (cm)	2.1 ± 0.1	2.8 ± 0.3	0.06
Annular area (cm^2)	5.7 ± 0.3	9.1 ± 1.2	0.03
Anterior annular area (cm^2)	2.5 ± 0.2	4.0 ± 0.7	0.08
Posterior annular area (cm^2)	3.2 ± 0.3	5.1 ± 0.9	0.08

Figure 2-44 (A) Changes in the mitral annular dimension as reported by Hueb et al, distinguishing between the anterior fibrous section and the posterior muscular section. (B) Changes in the annular perimeter, area and intertrigonal distance measured by Ahmed et al depicting the significant increases in annular perimeter and annular area between normal and ischemic heart disease patients, but showing no significant changes in the inter trigonal distances. Data adapted from Hueb et al. JTCVS 2002; and Ahmad et al. Ann Thorac Surg, 2004, 78:2063-8. [104,108]

In 2005, Watanabe et al. also described the differences in annular geometry with the extent and location of the myocardial infarction [109-111]. As shown in Figure 2-45, three dimensional images of the mitral annulus were obtained using 3D echocardiography and the annulus was reconstructed. Normal subjects had an elliptical D-shaped annulus with the saddle configuration during systole, but in patients with inferior myocardial infarction dilatation of the posterior annulus was observed, localized predominantly to the free wall region with significant flattening of the saddle shape. Similarly, in patients with anterior myocardial infarction, the increase in annular area was the highest, with dilatation of the annulus both at the trigones and the free edge as well.

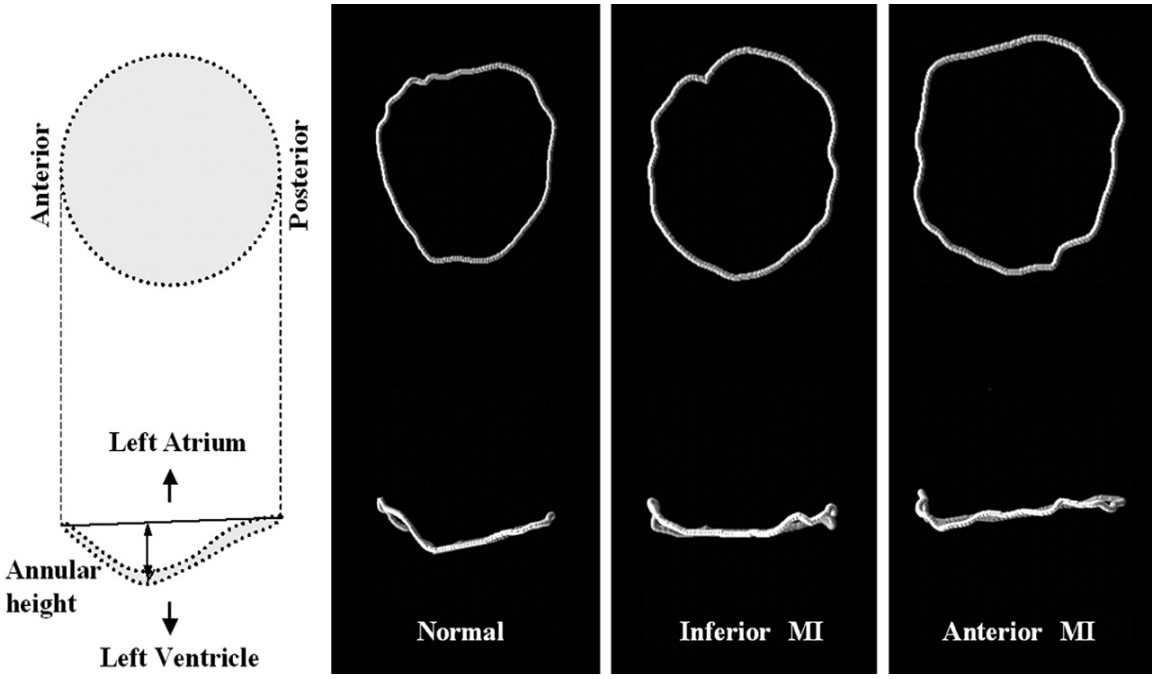

Figure 2-45 Three dimensional changes in the mitral annular size and shape with different infarct locations as measured from echocardiography. The saddle shaped D configuration of the normal annulus is clearly evident, that is lost with both anterior and inferior myocardial infarction. Maximum dilatation was observed in the anterior infarction case. Figure reproduced from Watanabe et al, Circulation 2005, 112, I-458 – 462. [109-111]

Using 3D echocardiography, Kaji S et al. quantified the changes in the three dimensional saddle shape of the mitral annulus in normal subjects and patients with chronic ischemic mitral regurgitation [106]. In patients with chronic ischemic mitral regurgitation, clear loss of the saddle shape was evident with associated annular dilatation. Whether the loss of saddle occurred due to changes in the left ventricular geometry, or if the changes occurred to altered force balance in the valve is unknown and needs further investigation. Figure 2-46 shows the points along the mitral annulus where the annular perimeter was traced and the three dimensional changes in the annular geometry with and without chronic ischemic mitral regurgitation are presented.

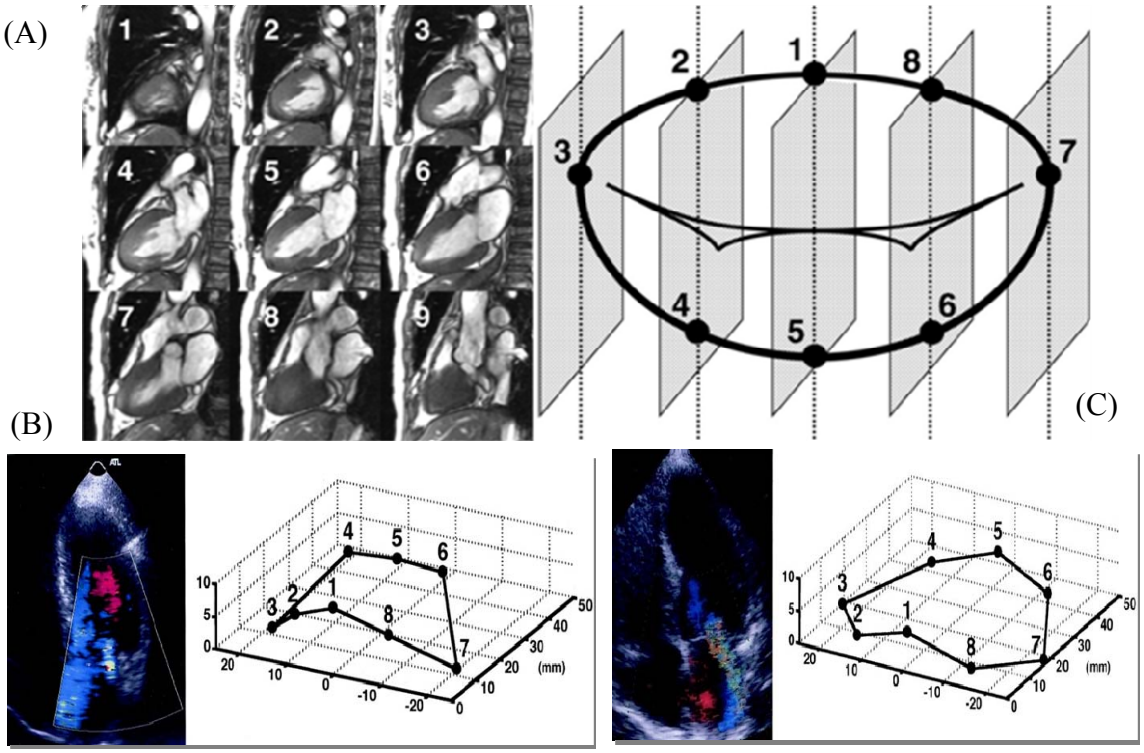

Figure 2-46 Mitral annular non planarity in normal and chronic ischemic mitral regurgitation patients was assessed using multi plane echocardiography at different points on the mitral annulus shown in (A). (B) Normal subjects without ischemic mitral regurgitation had a significant saddle shape of the mitral annulus; (C) Chronic ischemic mitral regurgitation subjects had a flattened annulus. Figure reproduced from Kaji, S. et al. Circ 2005; 112:I-409 -414I.[106]

Tibayan and colleagues [17-19], and the Gorman laboratory [13-16] were the first to quantify the changes at the sub annular level in animal models of ventricular ischemia. Tibayan et al using a chronic ischemic mitral regurgitation model in sheep reported the changes in the papillary muscle tip positions in 3-dimensional space. Figure 2-47 summarizes the changes observed in the dimensions measured between the papillary muscle tips and the mitral annular plane using rapid sonomicrometry crystals.

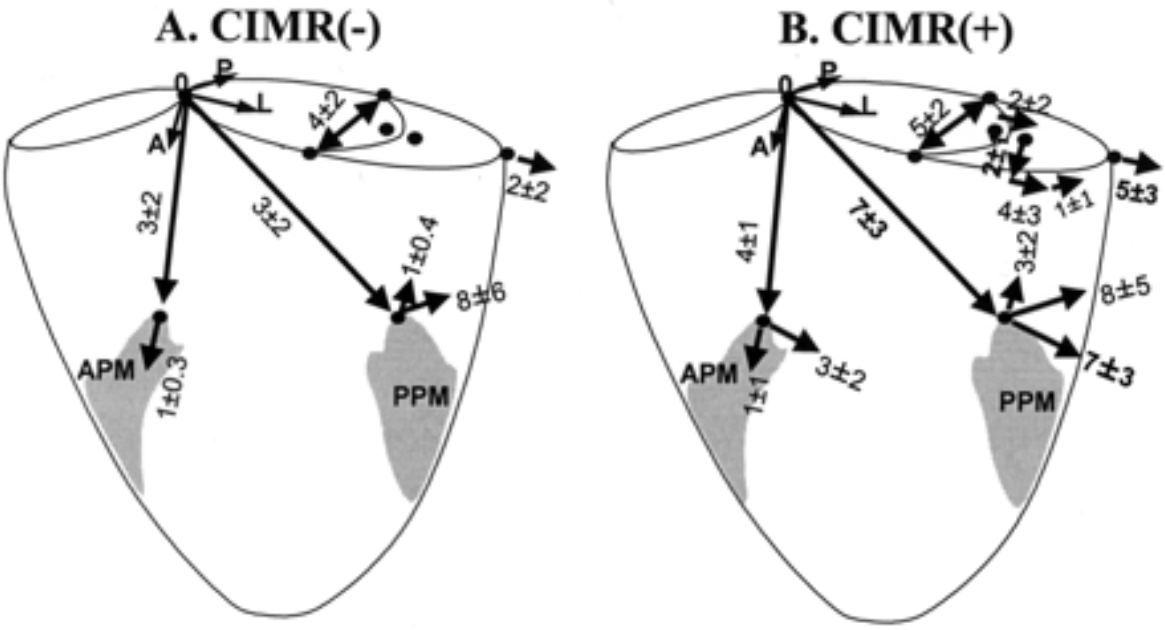

Figure 2-47 Changes in the papillary muscle tip positions in animals without chronic ischemic mitral regurgitation and with chronic ischemic mitral regurgitation. A significant increase in the distance of the trigones to the tips of the posterior papillary muscle were observed with outward movement of the posterior free wall. Figure reproduced from Tibayan et al. Circulation 2003, 108: II-116. [16-18]

Several animal and human studies quantified these changes in the valve geometry, their relevance to pathological valve function or mechanics are poorly understood. He et al. in 1997 demonstrated using an in vitro left ventricular simulator that the mitral valve leaflets have an area that is large enough to compensate for annular dilatation upto 80% of the normal size [112, 113]. However, as the papillary muscles were displaced

outwardly from the mitral annulus, the compensatory mechanism was lost and significant regurgitation occurred at even small magnitudes of dilatation as shown in Figure 2-48.

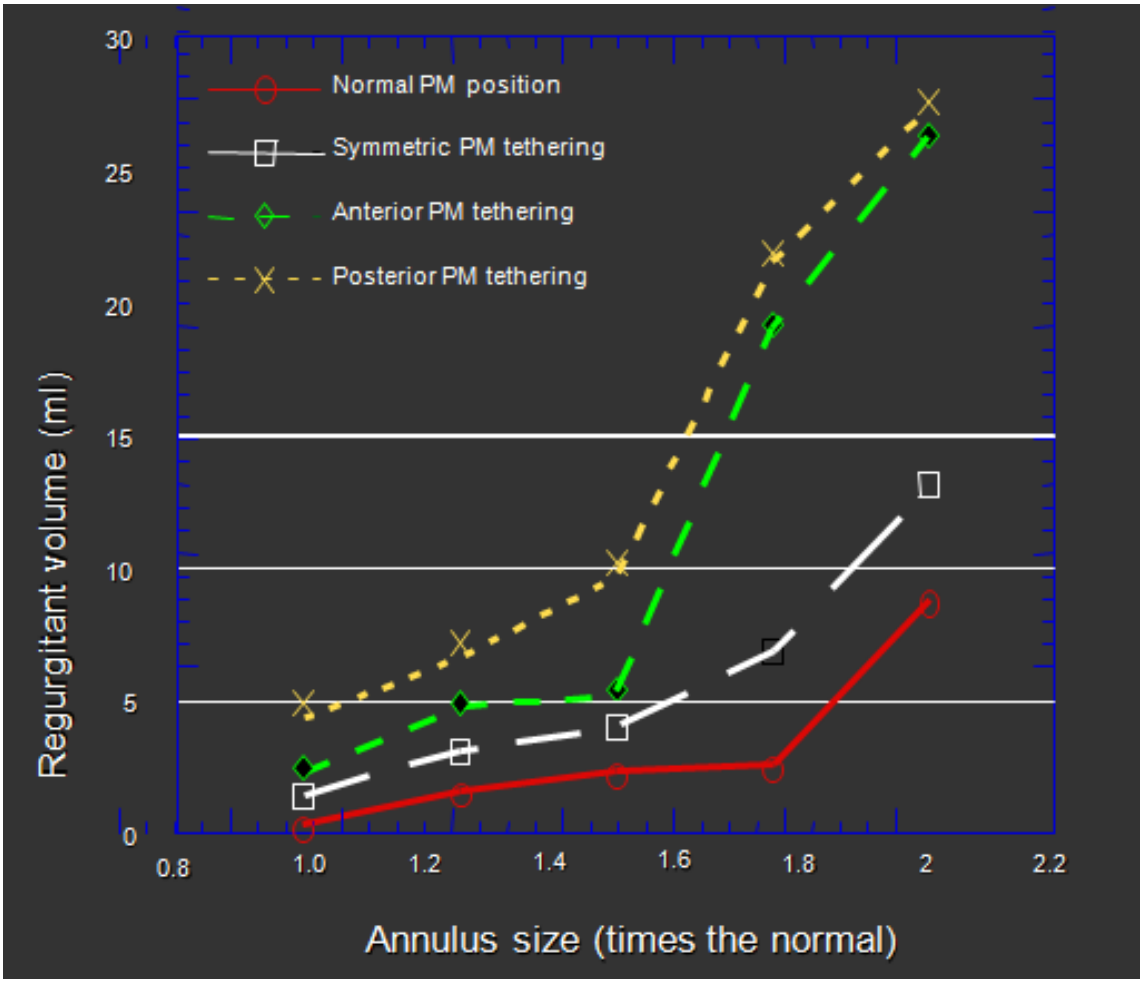

Figure 2-48 Schematic summarizing the in vitro experimental data from He et al. Isolated annular dilatation did not induce significant regurgitation until it was 80% of the normal annular size. Symmetric papillary muscle displacement along with a dilated annulus offset the regurgitation to higher magnitudes, but asymmetric papillary muscle displacement resulted in significant increases in the regurgitation volume even at 40% dilatation. [112, 113]

Mitral annuloplasty is the current standard of care for surgical repair of functional mitral regurgitation, which involves undersizing the dilated mitral annulus to improve leaflet coaptation and reduce regurgitation. Several commercial annuloplasty rings that are either rigid, semi rigid or completely flexible are in use today in clinical practice, but

the improvements of using one type of ring over another still remains vague. Some of the annuloplasty ring types are shown in Figure 2-49, with their different shapes, sizes and mechanical properties that address reduction in the septal lateral dimension.

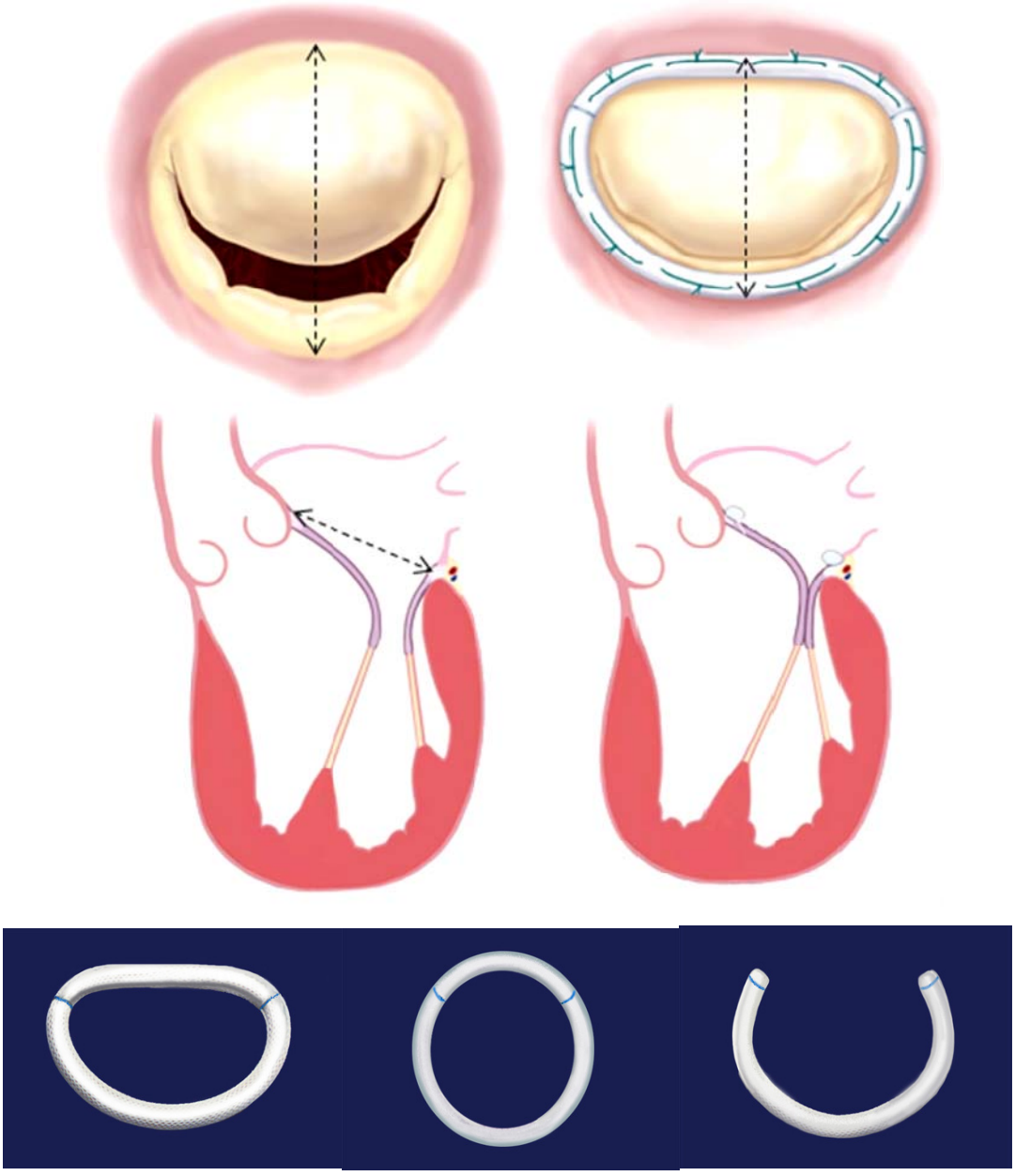

Figure 2-49 (A) Schematic depicting the annular undersizing concept used to reduce regurgitation and improve coaptation in the tethered mitral valve; (B) The three most common annuloplasty ring types used clinically with different material properties, sizes and shapes. Figure's courtesy - Dr. David H. Adams MD, Mt Sinai School of Medicine, NY.

2.2.3.1 Clinical Outcomes and Repair Durability

Overall clinical outcomes with annuloplasty for functional mitral regurgitation have been suboptimal, with high rates of persistent or recurrent mitral regurgitation even after rigorous surgical repair. Tahta et al used echocardiography to follow patients who have received mitral annuloplasty and measured the acute changes in mitral regurgitation immediately after mitral annuloplasty, and at 3 years after surgical repair[114]. Figure 2-50 summarizes the results from this study based on the grades of regurgitation acutely and at 3 years after mitral annuloplasty. Though clinically the poor outcomes of mitral annuloplasty are attributed to the annuloplasty ring type, but most recent data from Magne et al. clearly demonstrated that recurrence of regurgitation is seen irrespective of the annuloplasty ring type as presented in Figure 2-51[11].

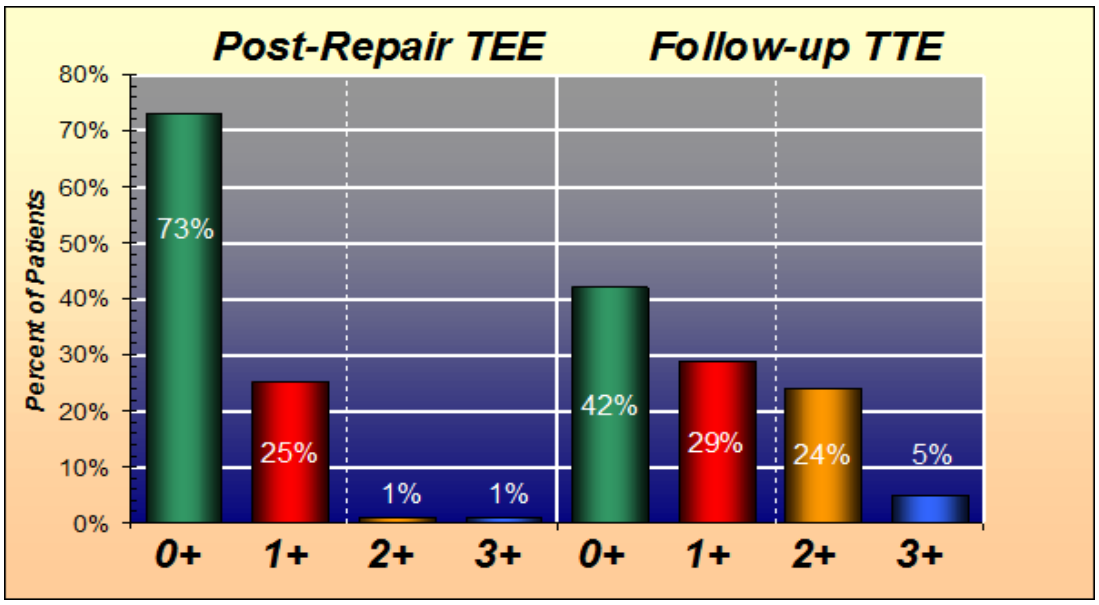

Figure 2-50 Percentage of patients in different regurgitation grades immediately after mitral annuloplasty and at 3 year follow up after mitral annuloplasty for functional mitral regurgitation. Acutely after surgery, a significant number of patients were either with absolutely no or trace regurgitation. However at a chronic 3 year follow up, significant number of patients developed upto 2-3+ regurgitation. Data reproduced from Tahta et al. Journal of Heart Valve Disease, 2002, 11:11. [114]

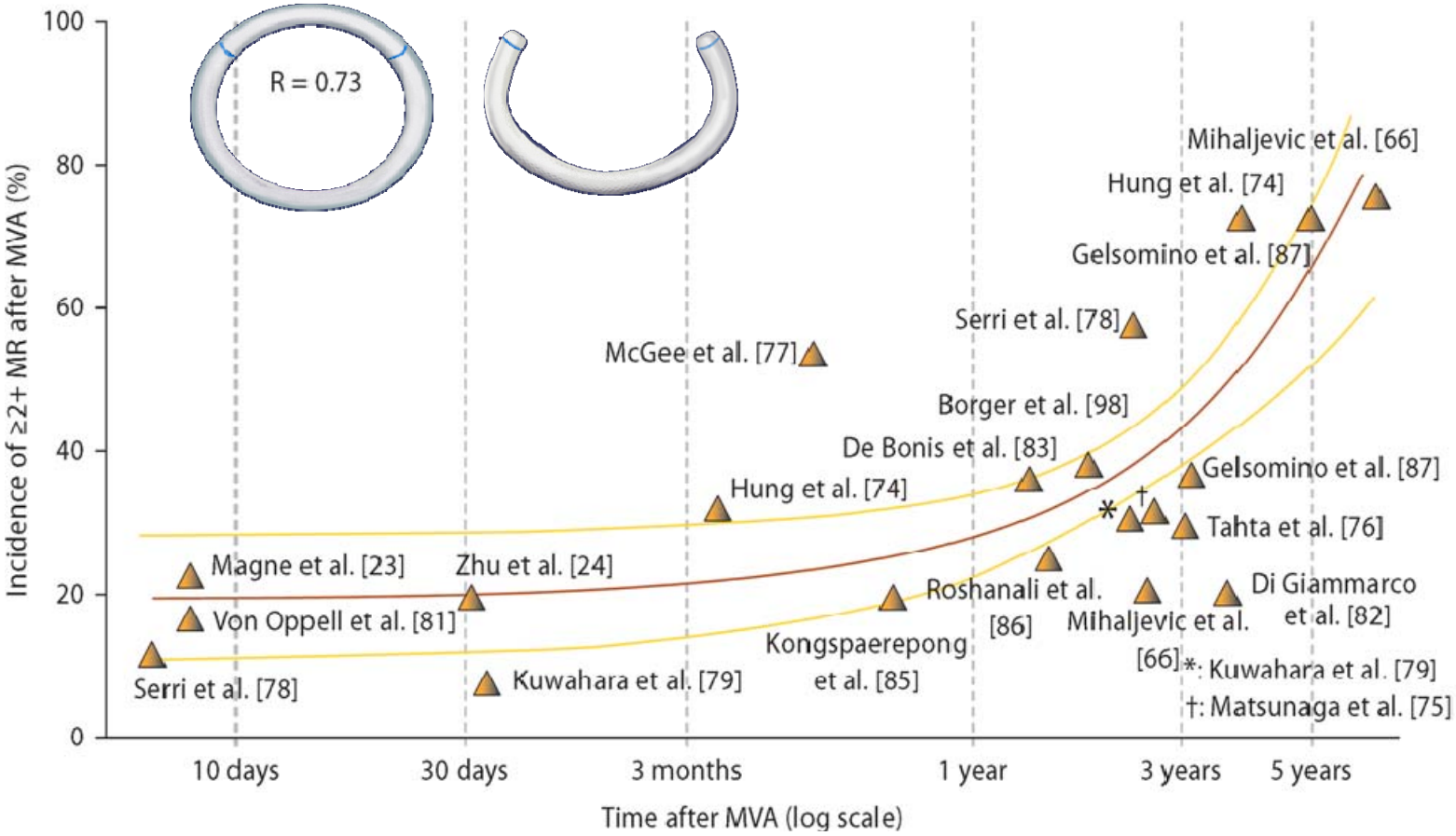

Figure 2-51 Data reproduced from Magne et al. on the efficacy of complete and semi complete annuloplasty rings that demonstrated the same outcomes with nearly 80% of the patients showing recurrent regurgitation within 5 years after mitral annuloplasty. Figure reproduced from Magne et al. Cardiology, 2009, 112: 244 – 259.[10]

2.2.3.2 Risk Factors of Failure of Mitral Annuloplasty in Functional Mitral Regurgitation

Failure of mitral annuloplasty for ischemic mitral regurgitation is a multi factorial problem. One of the primary causes of repair failure is that the ventricular aspect of the disease is rarely addressed and thus progressive left ventricular remodeling after annuloplasty, impedes leaflet coaptation and results in regurgitation. An important aspect of this problem that is clinically ignored is the variability in the ventricular and valve geometry between individual patients. Agricola et al. reported in 2004 the differences in the leaflet tethering patterns between anterior and inferior myocardial infarction and demonstrated that the geometry of the valve is significantly different between the two groups as shown in Figure 2-52 [115]. Srichai et al. also reported that the extent of scarring of the infarcted myocardium had a significant impact on the grade of regurgitation, in addition to the changes observed between the infarct locations. Figure 2-53summarizes these findings, and shows the clear differences in regurgitation between individual patients [116]. They also reported that even though in both the cases, there is statistically no difference in the mitral annular diameter, the extent of leaflet tethering measured as leaflet tenting area was significantly different. On these lines, Watanabe et al reported in 2006 that the pattern of leaflet tethering is significantly different between the two groups, with localized central tethering for an anterior infarct location and a diffused pattern of leaflet tethering for a posterior infarct location as shown in Figure 2-54[110]. Though this data exists, there is a absolute need for controlled experimental studies to understand the relevance of these geometric changes on surgical decision making and

potentially develop methods that allow pre surgical planning on an individualized patient basis.

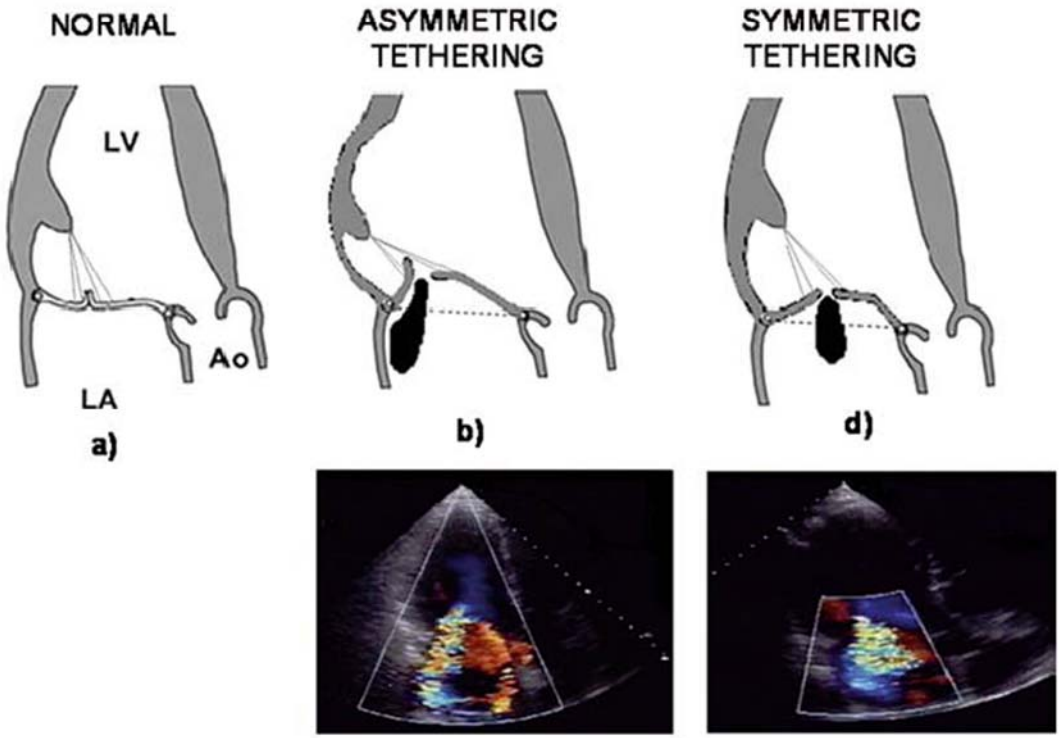

Figure 2-52 Differences in the tethering patterns between an anterior and posterior myocardial infarction, demonstrating the differences in the regurgitation grade between the two cases. Figure reproduced from Agricola et al. Eur J Echocardio, 2004, 5(5): 326-34. [115]

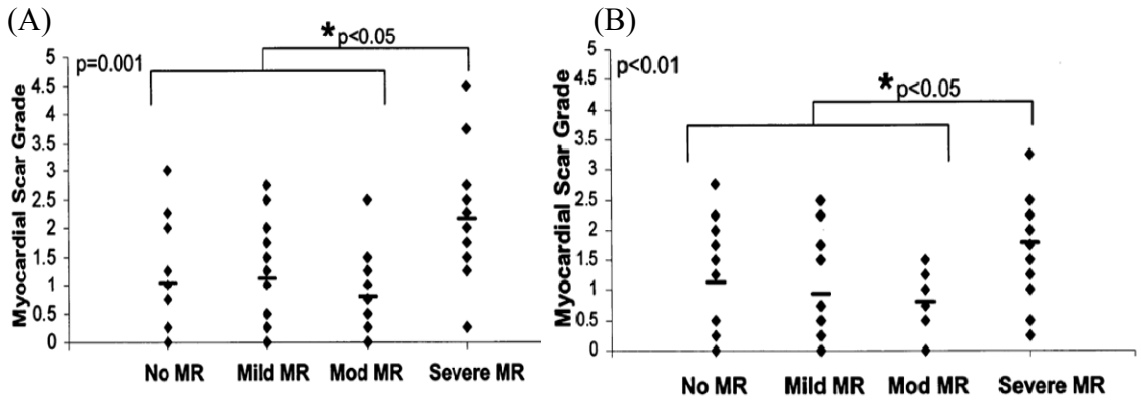

Figure 2-53 (A) Relationship between anterior myocardial scarring grade and the severity of mitral regurgitation, with higher levels of regurgitation with increased scarring; (B) Similar trends in severity of regurgitation were seen with posterior myocardial scarring. Figure reproduced from Srichai et al. Annals of Thorac Surg, 2005, 80(1): 170-8.[116]

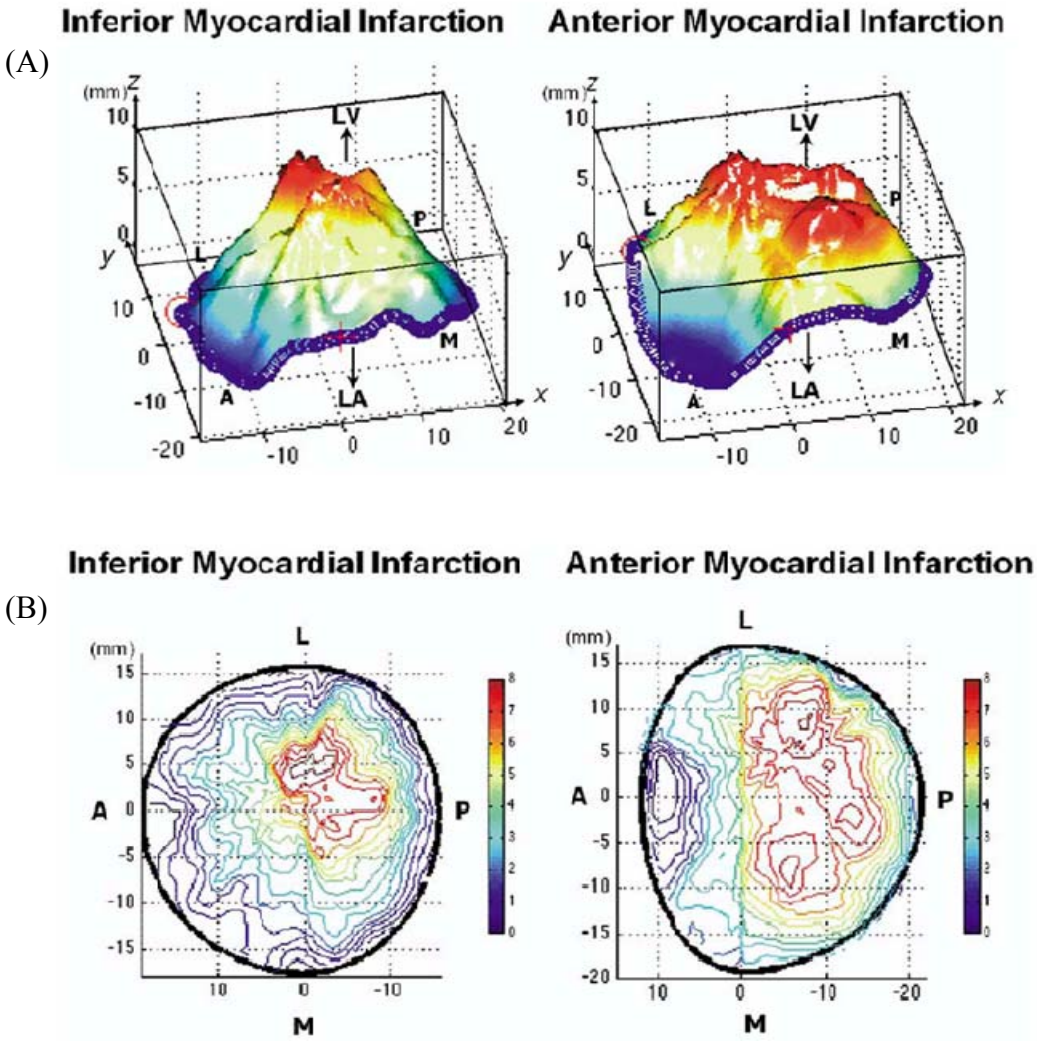

Figure 2-54 (A) 3D reconstruction of the leaflet tenting geometry with inferior and anterior myocardial infarction, showing the differences in tethering between the two geometries. In the inferior infarction case, the tethering was more localized than the diffused pattern observed with anterior myocardial infarction; (B) Projection of the tenting pattern onto the plane of the mitral annulus, where the differences in tenting are clearly evident. Figures reproduced from Watanabe et al. J Am Soc Echocardiograph 2006, 19(1): 71-5 [110]

2.2.4 ENGINEERING STUDY OF MITRAL VALVE REPAIR

2.2.4.1 Computational Study on the Impact of Mitral Annular Saddle on Leaflet Stress

Salgo et al. in 2002 demonstrated using a simplified model of the mitral valve that a 3-dimensional mitral annular saddle shape significantly improves systolic leaflet curvature and reduces stress in the leaflets[117]. Two types of fundamental shapes were first generated, an elliptic paraboloid to mimic leaflet billowing with a flat annulus and a hyperbolic paraboloid to model annular non-planarity without leaflet billowing. A linear, static, orthotropic material model was selected to mimic the collagen orientation in the leaflets, a constant thickness was maintained across the entire leaflet, and a 16kPa load was uniformly applied over the entire geometry. Their results shown in Figure 2-55 demonstrated a significant reduction in the peak leaflet stress between flat and curved leaflets, and with a flat versus saddle shaped annulus. A significant reduction in leaflet stress was observed at 15% saddle (defined as the ratio of the annular height to commissural width), which conformed well to the degree of saddle measured in healthy humans and animals. Additionally, lower leaflet stress was computed in curved leaflets over flat leaflets indicating that the mitral annular saddle may optimize the curvature of the leaflets, which in turn reduces the systolic stress acting on them. Based on this data, they conclude that nature conserves the saddle shape of the mitral annulus to provide a mechanical benefit to the valve. Though a very insightful study, the computational geometry used by these authors was simplified and lacked the sub-annular apparatus which has been shown to play an important role in the valve function.

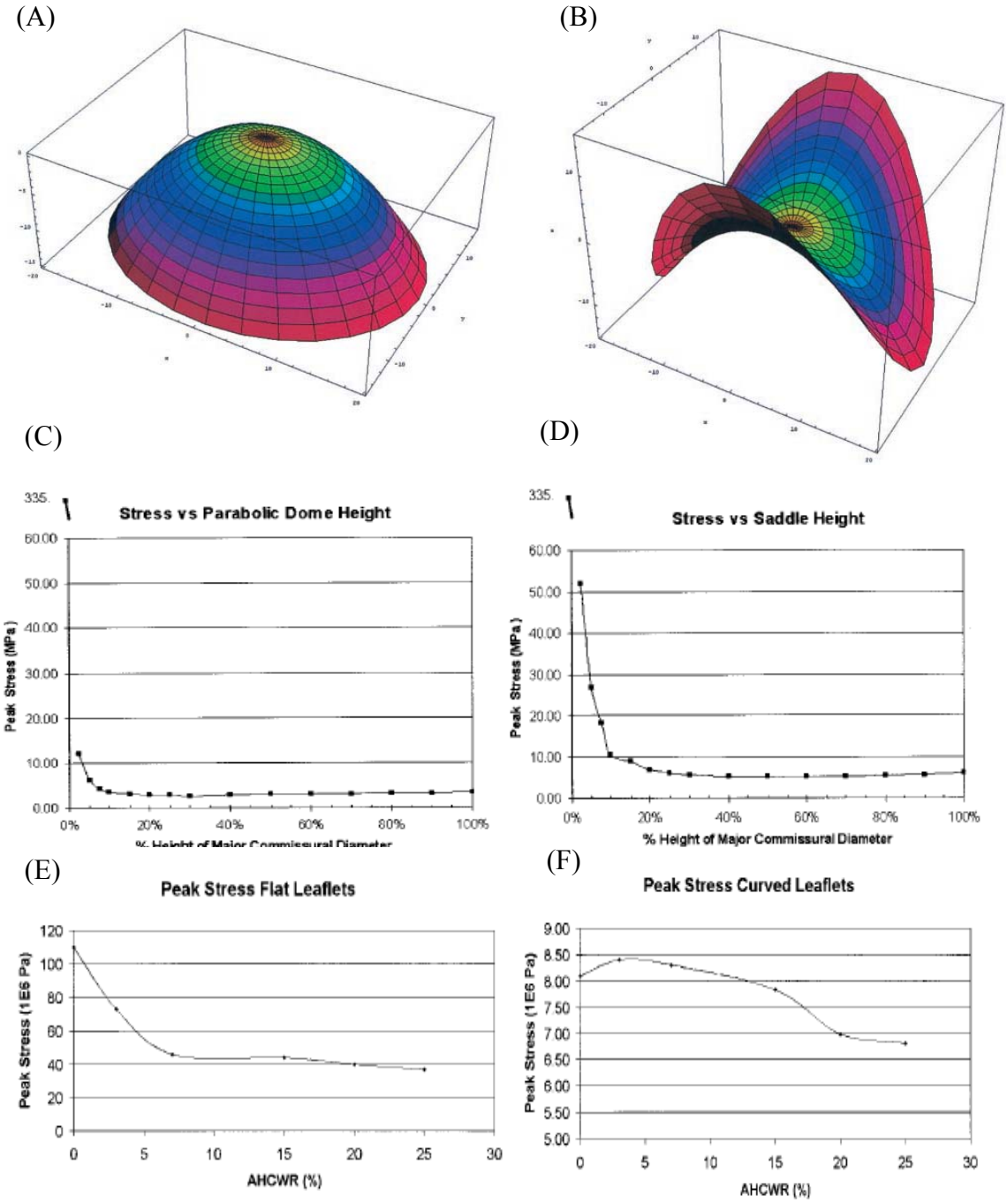

Figure 2-55 (A) A paraboloid shape used to mimic leaflet billowing, (B) A hyperboloid shape used to mimic annular saddle shape. (C) Significant reduction in peak leaflet stress with increasing height of the major commissural diameter, (D) Reductioin in leaflet stress with increasing degree of saddle, (E) Higher stress with flat leaflets and (F) Lower stress with curved leaflets. Reproduced from Salgo et al. Circulation, 2002. [117]

2.2.4.2 Finite Element Analysis of the Geoform Mitral Annuloplasty Ring

Votta et al. in 2007 reported a computational study on the impact of ring shape on the mitral valve function and mechanics [118]. In this finite element study, the authors compared the leaflet stresses between a simulated pathological functional mitral regurgitation case, a flat Physio® annuloplasty ring and a hump shaped Geoform® annuloplasty ring (Edwards Lifesciences, Irvine, CA). From their finite element study, they report that a Geoform ring has enhanced performance in the correction of regurgitation over a flat shaped ring. Leaflet coaptation length was significantly higher with a Geoform ring over a Physio ring, without the need for excessive annular undersizing as shown in Figure 2-56. . They also report that both the rings significantly altered the leaflet stress from the pathological state, even though there was minimal difference between the two ring types as shown in Figure 2-57.

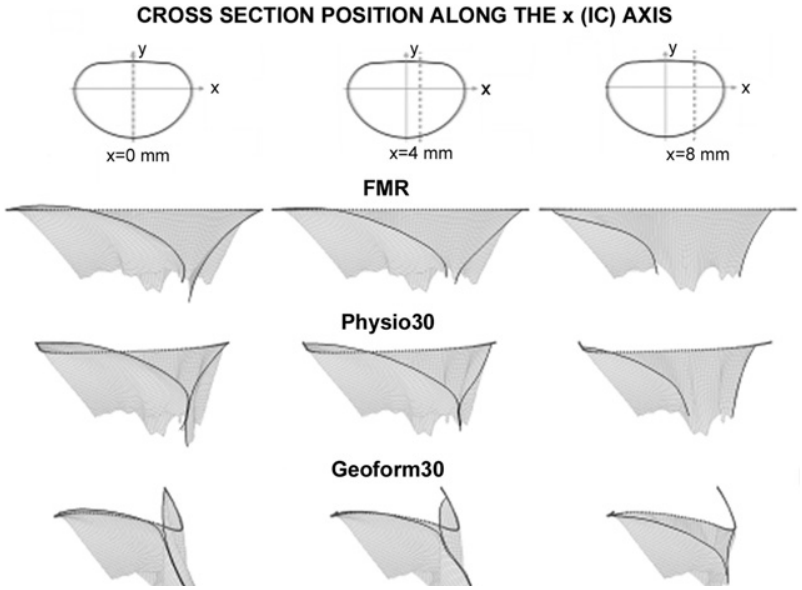

Figure 2-56 Cross sections of the mitral valve along the septal lateral plane at three different regions before ring implantation, after flat ring annuloplasty and with Geoform ring.

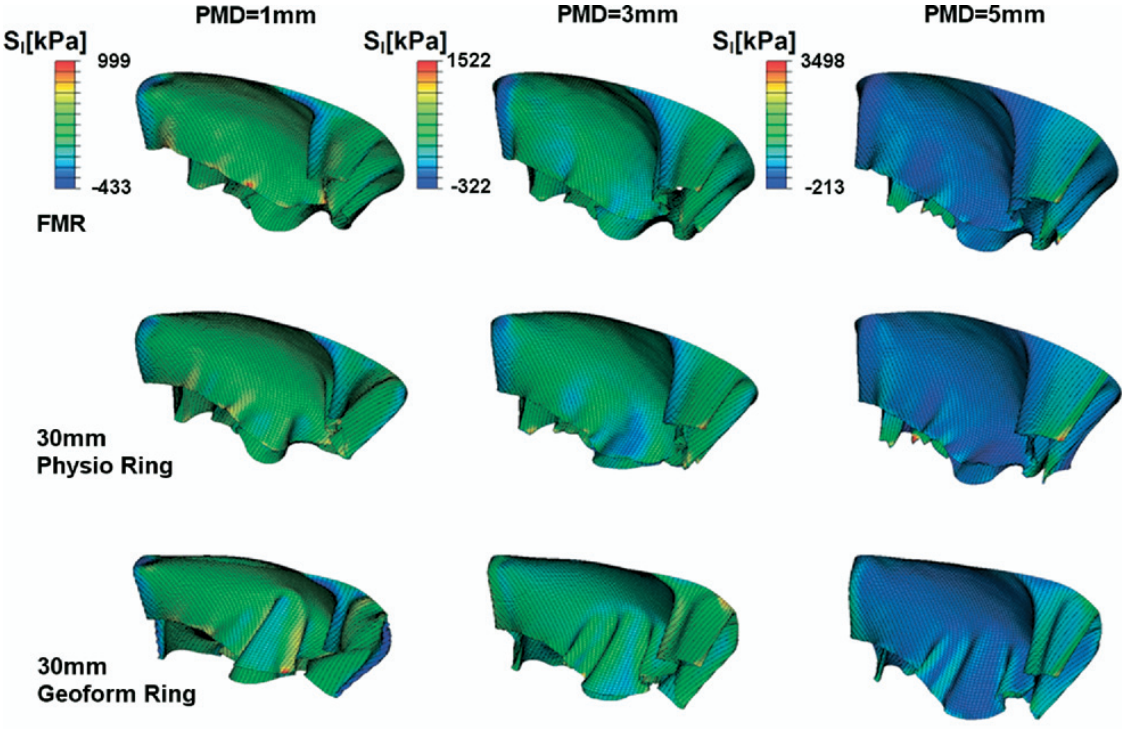

Figure 2-57 The maximum principal stress on the mitral valve under pathological conditions, after flat ring annuloplasty and Geoform annuloplasty. Three different positions of the papillary muscle were studied, by simulating apical displacements of 1mm, 3mm and 5mm

2.2.4.3 Role of Annular Tension on Dilatation of the Mitral Annulus in Leaflet Prolapse

He et al. recently reported a unique study on the role of mitral annular tension in dilatation of the annular size[119]. The authors hypothesize that during systolic valve closure, the radially outward forces imposed by the mitral leaflets resize the mitral annulus and increase the overall dimension. To test this hypothesis, the authors explanted porcine mitral valves and instrumented the annular circumference with multiple load cells, and pressurized the valve to systolic closure as shown in Figure 2-58. Under static loading conditions, they measured the forces along the annular circumference and report lower forces at the commissural sections and higher at the septal lateral sections.

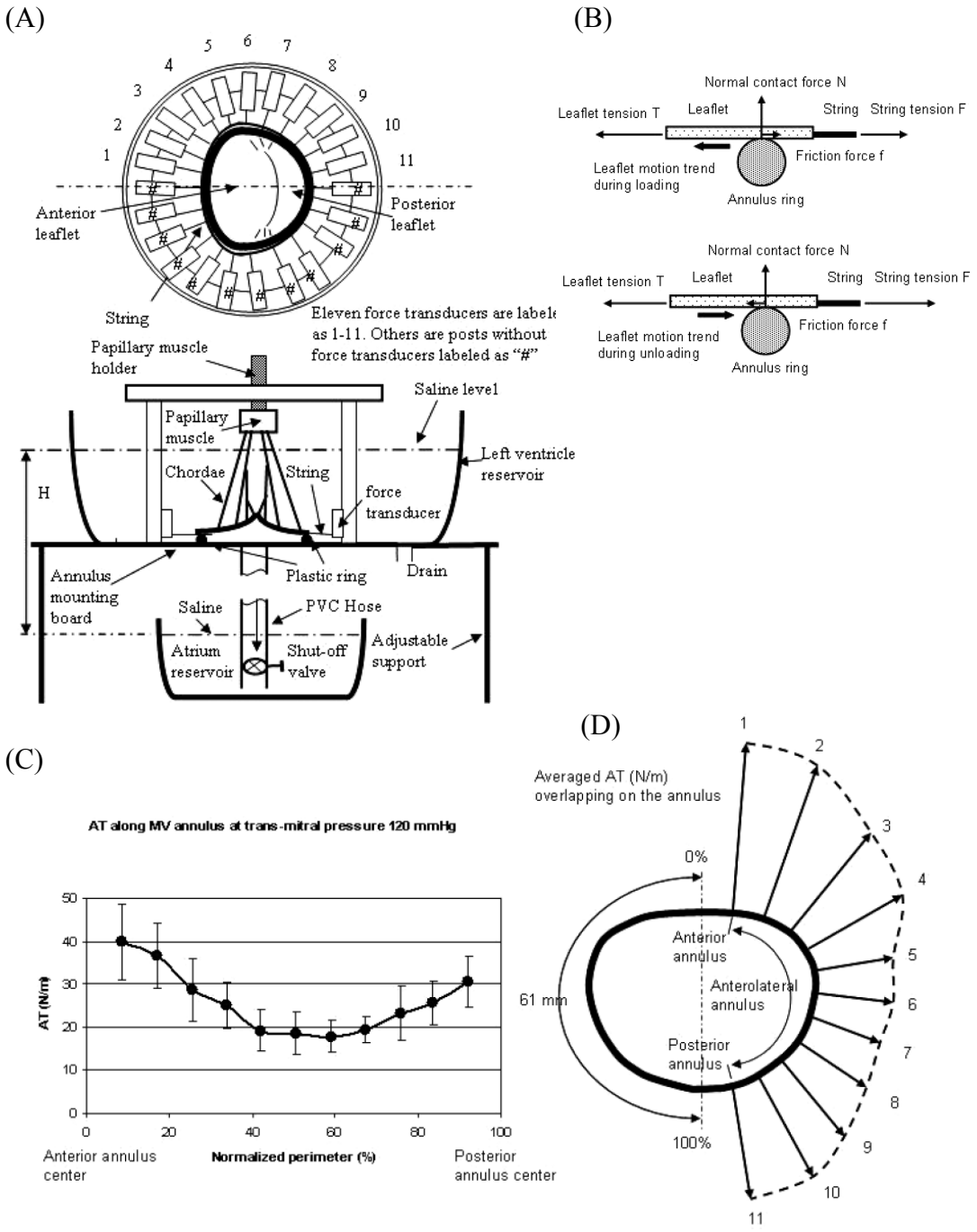

Figure 2-58 (A) Experimental setup used in this study depicting the 16 load cells that were mounted along the circumference of the mitral annulus, (B) Schematic of the hypothesized force distribution on the mitral annulus during systolic closure of the valve, (C) Force distribution along the different annular points at static pressure of 16 kPa, and (D) Schematic demonstrating higher forces at the septal-and-lateral sections of the annulus, and low forces at the commissural sections of the annulus. [119]

2.2.4.4 Hemodynamics of the Mitral Valve after Edge-to-Edge Repair

Li S et al. reported the impact of edge-to-edge repair on blood flow through the mitral valve under steady flow conditions using digital particle image velocimetry. They investigated the impact of length of the suture loop and position of the suture on valve fluid dynamics. Figure 2-59 depicts the Reynolds shear stress measured using particle image velocimetry at the three stitch locations. With a central stitch, diastolic flow was split into two symmetric jets on either sides of the suture. With lateral displacement of the stitch towards the commissure, the jets became asymmetric and when the stitch was placed at the commissural sections, physiological fluid dynamics were restored.

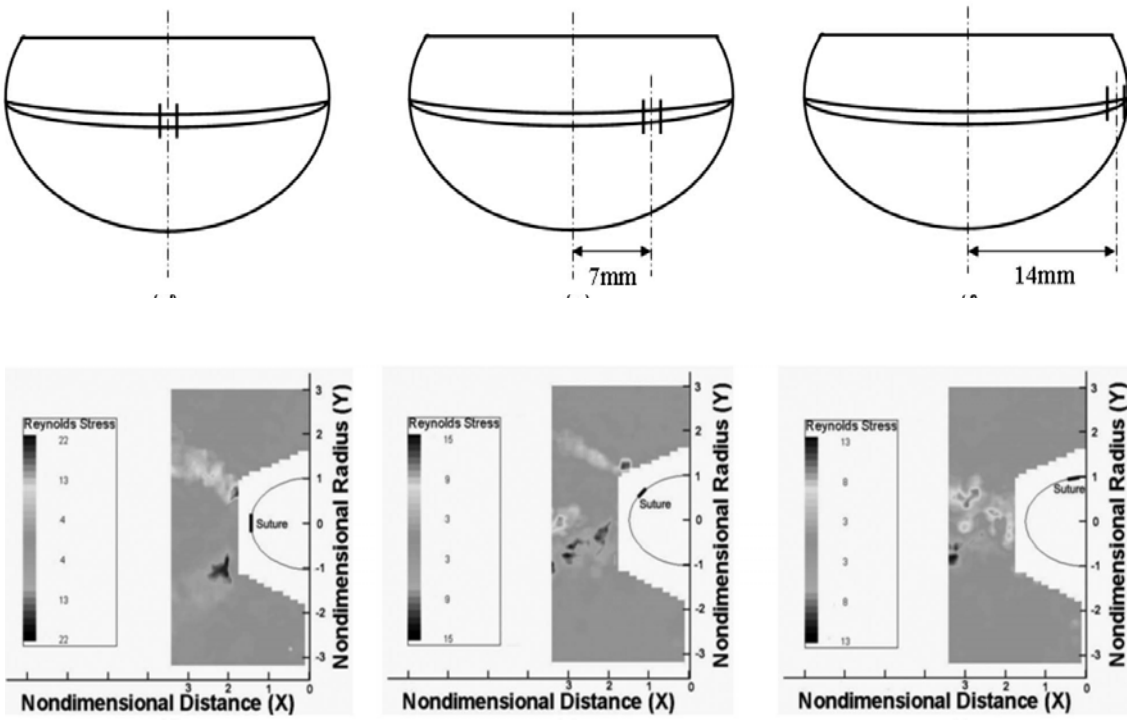

Figure 2-59 (Top) Three different locations of the edge-to-edge stitch that were investigated in this study; (Bottom) Reynolds shear stress calculated from particle image velocimetry, depicting the changes in the jet with stitch location

2.2.4.5 Single vs. Double Balloon Valvuloplasty to Relieve Mitral Stenosis

Schievano et al. in 2009 reported a finite element study comparing single to double balloon catheter systems to relieve mitral stenosis in patients with rheumatic heart disease[120]. The authors reported a finite element analysis in which they compared the impact of using one single large balloon, over two smaller balloons to relieve stenosis and improve valve hemodynamics. A fluid structure interaction model of the mitral valve was developed as shown in Figure 2-60, and the single and double balloon designs were incorporated into the computational model. Principal stress in the balloon and the mitral valve leaflets was calculated, and the authors reported that a double balloon was more effective in separating the fused commissures than a single balloon approach.

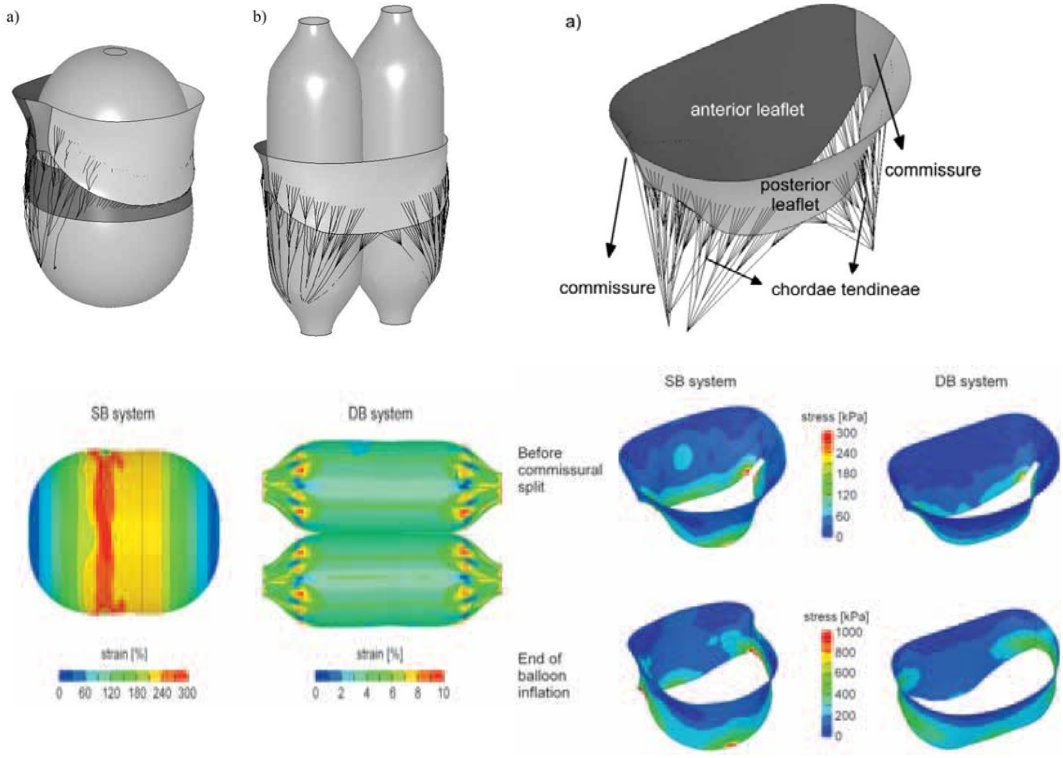

Figure 2-60 (A) Geometric models of the single and double balloons, (B) The virtual mitral valve model used in this study, (C) Strain calculated in the single and double balloons during valvuloplasty, (D) Stresses in the mitral valve with the two types of catheters [120]

CHAPTER 3

HYPOTHESIS AND SPECIFIC AIMS

3.1 HYPOTHESIS AND OBJECTIVES

Clinical data on mitral valve repair indicates that irrespective of the pathology, whether congenital, degenerative or functional, recurrence of mitral regurgitation is seen in 10% - 80% of the patients. At 10 years after primary surgery, recurrence of mitral regurgitation remains at ~15% in congenital mitral valve repairs [12], ~40% in degenerative mitral valve repairs [10], and ~80% in repairs for functional mitral regurgitation [11]. This data reveals a disheartening fact that even though experience with mitral valve repairs has increased significantly in the last two decades and excellent acute patient outcomes are reported, the long term durability and chronic outcomes remains very poor. In the current era of cardiac surgery, where the focus has shifted from valve replacement towards valve repair, such a scenario is unacceptable.

The reasons for failure of mitral valve repairs are multifactorial, and are poorly understood due to several reasons. Firstly, abundant clinical literature on mitral valve repair outcomes is available today, but the data are muddied by the usage of confusing nomenclature by different institutions, variability in the surgeon's expertise and the finer technical aspects of the surgery, extreme variability in valve surgery practices between

institutions, and to a large extent an increased focus on the annuloplasty ring type than the valve pathology. Secondly, industry impetus is focused towards establishing annuloplasty as the standard of care for all mitral valve lesions and further introducing percutaneous repair procedures, even though clinical outcomes and basic science studies clearly do not support these opinions and emphasize the need to better understand the valve pathological function, hemodynamics and mechanics.

The objective of this doctoral thesis was thus to develop an experimental framework that allows controlled investigation of the mechanisms leading to failure of mitral valve repair techniques. To achieve this goal, the thesis is structured into three focus areas: [a] design in vitro models of mitral valve pathologies that mimic the human pathology; [b] design techniques to measure and quantify the function, kinematics and mechanics of the valve; and [c] provide mechanistic insights into failure of mitral valve repairs using the hemodynamic and mechanics measurements.

Thus the central hypothesis of this thesis is that, ***an ideal mitral valve repair should aim to restore physiological function and mechanics of the valve, from its pathological state. Controlled experimental studies to understand the hemodynamics and mechanics of various mitral valve repairs will aid in identifying the efficacy of current repair techniques, understand their drawbacks, and open avenues for future improvements.***

To test this central hypothesis, an *in-vitro* experimental methodology was developed wherein congenital, degenerative and structural abnormalities of the mitral valve can be simulated. Obtaining human mitral valves with intact annular and sub

annular geometries is literally impossible and is not practical in the scope of this thesis. Thus native porcine mitral valves of different sizes were used in this thesis, which were structurally altered to mimic different valve pathologies. Precise control over the three dimensional mitral valve geometry, and the sub annular function in this in vitro system allowed mimicking different mitral lesions; which is challenging to create in animal models. A unique advantage of this system is that the efficacy of various surgical techniques can be simultaneously assessed on the same valve specimen, which is impossible to perform in an animal model. Additionally, the *in-vitro* system provides visual access and real-time measurement of valve regurgitation volume, leaflet and chordal kinematics and mechanics, which provides a complete understanding of valve function.

With this overall goal, in this thesis three specific mitral valve lesions were studied and the efficacy of surgical repair techniques applicable to each lesion was assessed. The three mitral valve lesions studied are:

[**Specific Aim 1**]: Congenital Cleft Mitral Valve in Atrioventricular Canal Defects

[**Specific Aim 2**]: Degenerative Mitral Prolapse due to Acute Chordal Rupture

- Isolated Posterior Leaflet Prolapse
- Isolated Anterior Leaflet Prolapse

[**Specific Aim 3**]: Functional Mitral Regurgitation in Cardiomyopathies

The specific aims represent the spectrum of mitral valve lesions for which surgical repair is the recommended option, and in which post-surgical repair failure is often reported.

3.2 SPECIFIC AIMS

3.2.1 SPECIFIC AIM 1 – PEDIATRIC MITRAL VALVE REPAIR

Atrioventricular canal defects encompass a spectrum of lesions of which the cleft mitral valve is very common. Correcting the ostium primum and septum secondum defects with separation of the common atrioventricular valve annuli into mitral and tricuspid valves, resulting in a mitral valve anatomy with a cleft in the anterior leaflet. Surgical closure of the cleft is currently recommended, but as the patient grows the repair fails resulting in recurrent regurgitation. Based on these clinical observations, ***it is hypothesized that dilatation of the mitral annulus due to increase in overall cardiac chamber size induces regurgitation at chronic follow up after primary surgery. Balanced use of annuloplasty with partial cleft closure may be a beneficial strategy to avoid late recurrence of regurgitation in these patients.***

To test this hypothesis, the following objectives are proposed-

(A) Develop an *in vitro* model of cleft mitral valve in canal defects

(B) Understand the hemodynamic function of the cleft mitral valve

(C) Delineate the impact of length of cleft closure, post-procedural changes in annular size on valve hemodynamics, and

(D) Investigate the role of undersizing annuloplasty as an adjunct procedure to improve long term post-operative hemodynamic outcomes

To develop an *in vitro* cleft mitral valve model, echocardiographs of patients with cleft mitral valves are analyzed and specific anatomical characteristics of the valve will be identified. Normal porcine mitral valves are anatomically altered to mimic the pathological cleft valve, and studied in the pulsatile simulator to understand the

hemodynamic function of the valve. Firstly, the impact of the length of cleft closure on the regurgitant volume will be assessed, as it still remains controversial in the surgical community. Though complete closure of the cleft is the most intuitive option to restrict regurgitation, it restricts mobility of the anterior leaflet and induces mitral stenosis in the long term. Thus, the first objective of this aim is to investigate an optimal cleft closure length at which mitral regurgitation can be eliminated without inducing stenosis in the valve. Secondly, the impact of growth in cardiac structure on the impact of the repaired cleft mitral valve will be assessed to understand if increase in mitral annular size in the post-operative period induces recurrent regurgitation. Thus, a mitral annular model whose annular area can be changed to desired dimensions will be built and the cleft mitral valve will be studied in this setup. Thirdly, the significance of mitral annuloplasty in restricting annular growth and avoiding recurrence of regurgitation in the long term will be studied. Mitral annuloplasty is rarely performed in pediatric patients currently because of the rigidity of the rings and the potential to induce stenosis. Thus, in this study not only will the impact of annuloplasty on reducing regurgitation will be assessed, but also the potential to induce mitral stenosis will be quantified. It is expected that an optimal level of combining annular undersizing with incomplete cleft closure may have the best hemodynamic outcomes compared to the current procedures.

3.2.2 SPECIFIC AIM 2 – DEGENERATIVE MITRAL VALVE REPAIR

Myxomatous degeneration or fibro-elastic deficiency of the mitral valve is the most common mitral valve lesion and accounts for the largest proportion of mitral valve repairs. Though leaflet prolapse and regurgitation are the diagnosed end points in both

types of degeneration, the etiology underlying the disease varies and calls for different surgical procedures for optimal outcomes. Today, Myxomatous mitral valve repair procedures have become the "standard of care" and used indiscriminately for fibroelastic deficient valves as well, without diligent examination of the underlying etiology, resulting in higher rates of late recurrence of regurgitation. ***The hypothesis of this aim is that etiologic classification of degenerative mitral valve repairs is important to tailor surgical techniques to the lesion. In fibroelastic deficient valves, the use of routine leaflet resection techniques should be opposed and leaflet preservation should be practiced.***

To test this hypothesis, the following objectives are proposed.

(A) Develop an *in vitro* model of posterior and anterior prolapse due to acute chordal rupture.

(B) Compare resective vs. non- resective techniques for posterior leaflet prolapse

(C) Compare neochordoplasty to chordal translocation for posterior prolapse

(D) Compare resective vs. non-resective techniques for anterior leaflet prolapse

(E) Understand the efficacy of percutaneous edge-to-edge repair in correcting posterior and anterior prolapse

(F) Investigate the role of saddle annuloplasty compared to flat annuloplasty in improving mechanics of the mitral valve leaflets

In this thesis, the studies will be confined to fibro-elastic degeneration of the mitral valve due to lack of information on myxomatous degeneration and the complexity in simulating the biological changes in normal mitral valves. Fibro-elastic degeneration presents with leaflet prolapse due to marginal chordal rupture either on the posterior

leaflet, or anterior leaflet, with minimal leaflet distension or myxoid changes. In vitro models of uni-leaflet prolapse will be developed using normal porcine valves in which chordal rupture is mimicked. Hemodynamic valve function, and leaflet kinematics can be measured in this *in vitro* system using various measurement techniques. The *in vitro* pathological valve will then be repaired using standard surgical techniques, and the efficacy of the repairs in restoring physiological valve function and mechanics is quantified. Specifically for posterior leaflet prolapse, five surgical techniques will be studied – quadrangular resection of prolapsing cusp with plication of the mitral annulus, limited triangular resection of the prolapsing cusp, replacement of the ruptured marginal chordae with poly-tetrafluoro ethylene (ePTFE) suture loops, translocation of posterior strut chordae to the marginal positions and percutaneous edge-to-edge repair procedure. On the anterior leaflet, triangular resection of the prolapsing segment, replacement of the ruptured marginal chordae with neochordae and edge-to-edge repair will be assessed. Quadrangular resection with annular plication and chordal translocation will not be performed on the anterior leaflet due to limited tissue on the anterior leaflet and the importance of strut chordae in governing leaflet mobility and ventricular function respectively. In the final sub-aim, the impact of flat vs. saddle annuloplasty on the mechanics of the posterior leaflet will be studied, to investigate if the use of 3D commercial annuloplasty rings may reduce the suture line stresses in degenerative valve repair and improve long term outcomes.

3.2.3 SPECIFIC AIM 3 – SURGICAL REPAIR FOR FUNCTIONAL MITRAL REGURGITATION

Functional mitral regurgitation, either due to ischemic or non-ischemic dilated cardiomyopathy remains a surgical challenge. Persistent or recurrent mitral regurgitation is diagnosed in most patients after mitral annuloplasty, and is attributed to progressive ventricular disease, and variability in valve geometry between individual patients. Though widely accepted as a risk factor for repair failure, the impact of mitral valve geometry on annuloplasty and sub annular repair techniques is currently unknown and may be a significant risk factor to consider. ***The hypothesis of this aim is that the three dimensional geometry of the mitral valve impacts the hemodynamic outcomes of annular and sub annular repairs for functional mitral regurgitation. A patient specific approach to quantify valve geometry is required to tailor surgical techniques to individual subjects.***

To test this hypothesis, the following objectives are proposed.

[A] To develop an in-vitro model of functional mitral regurgitation in which the 3D mitral valve can be precisely altered

[B] Investigate the failure mechanisms of annuloplasty under different mitral valve geometric configurations

[C] Investigate the role of 3D mitral valve geometry on the efficacy of secondary chordal cutting procedure, and

[D] Quantify the impact of chordal cutting on the chordal force redistribution

An in-vitro simulator that allows precise control over the 3D annular and sub-valvular geometry of the mitral valve will be used in this thesis to replicate the clinical

setting of functional mitral regurgitation. Two mitral valve geometries will be studied, annular dilatation + 10mm apical displacement of the papillary muscles, and secondly annular dilatation + 10mm apical-posterior-lateral papillary muscle displacement. Hemodynamic function of the valve will be assessed under physiological and pathological settings, and parameters that describe systolic coaptation geometry and leaflet mobility will be quantified. Upon establishing the disease models, mitral annuloplasty will be performed using an adjustable annulus model in which the septal lateral dimension of the mitral valve can be changed to desired levels in the range of 24-40 mm. The hemodynamic function and mechanics of the mitral valve will be carefully assessed after mitral annuloplasty and compared to those obtained under physiological and pathological conditions, to assess the degree to which annuloplasty improved valve function and the underlying reasons for failure to restore complete valve competence. Secondary chordal cutting is the sub-valvular technique that will be studied concomitantly with annuloplasty, wherein the secondary "strut" chordae on the anterior leaflet are transected to improve anterior leaflet mobility and leaflet coaptation. The impact of secondary chordal cutting in restoring physiological valve function and mechanics will be studied, and the potential redistribution of chordal forces due to transection of the anterior strut chordae will be assessed.

3.3 EXPECTED OUTCOMES AND CLINICAL RELEVANCE

The overall impact of these studies is expected to be two-fold:

3.3.1 SCIENTIFIC APPROACH TO MITRAL VALVE REPAIR

Data from this thesis will provide mechanistic insights into the failure mechanisms of surgical techniques that are currently in clinical practice. Etiologic classification of the pathology, and the impact of relevant risk factors on chronic outcomes would guide the surgeon towards a scientific decision making approach rather than an experience/intuition based approach to valve repair. Cultivating such an approach may be useful in improving the long term outcomes of mitral valve repair, and also pave the path towards an "individualized, patient specific" approach compared to a "one for all" approach to mitral valve repair.

3.3.2 GUIDE THE DEVELOPMENT OF VALVE REPAIR TECHNOLOGIES

The data from this thesis may also provide impetus to develop valve repair technologies that not just focused on the mitral annulus. Several sub annular and percutaneous techniques are currently in development, with the primary focus to translate sub optimal surgical techniques to percutaneous delivery approaches. However, this thesis would provide the data and literature required to push device development in the appropriate direction.

CHAPTER 4

MATERIALS

In this chapter the design and operating principles of the major equipment used in this thesis are described. Specifically, the hardware and functional capabilities of the in vitro pulsatile left heart simulator, C-ring force transducers, high speed image acquisition system and 2D/3D ultrasound system are described in detail.

4.1 PULSATILE LEFT HEART SIMULATOR

All the experiments were conducted in the *in vitro* left heart simulator developed in the Cardiovascular Fluid Mechanics Laboratory at Georgia Institute of Technology. The simulator is a pulsatile, pump-driven system, in which physiological and pathological hemodynamic function of mitral valves can be studied. As shown in Figure 4-1, the simulator consists of nine main components: (a) Reservoir; (b) Left Atrial Chamber; (c) Mitral Annular Plate; (d) Left Ventricular Chamber; (e) Papillary Muscle Positioning System; (f) Pulsatile Prime Mover; (g) Programmable Solenoid System; (h) Compliance and Resistances; and (i) Data Acquisition Hardware and Software.

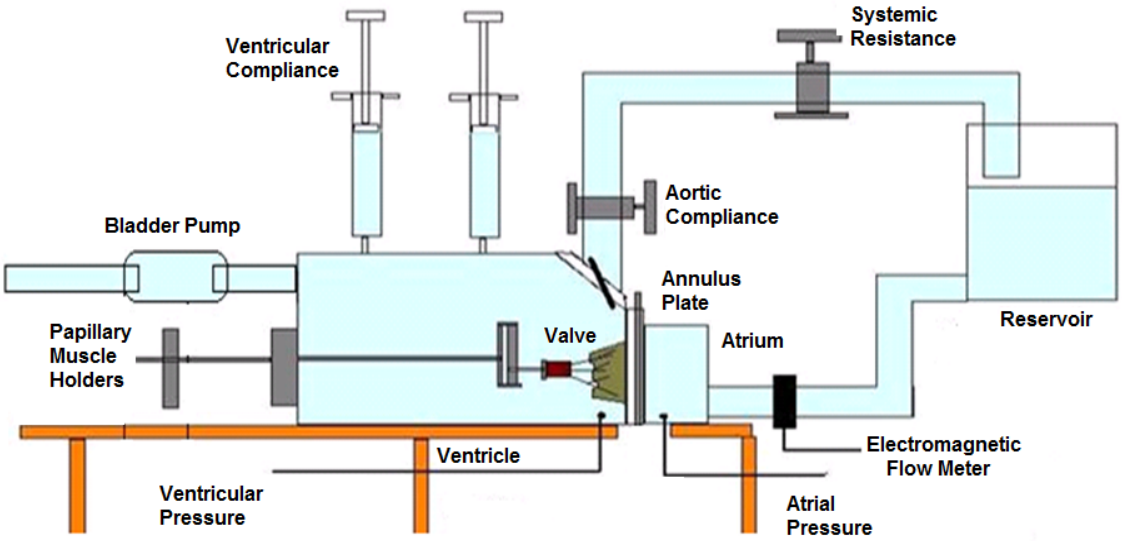

Figure 4-1 Schematic of the Georgia Tech Left Heart Simulator developed and used in this study

4.1.1 DESCRIPTION OF THE LEFT HEART SIMULATOR

4.1.1.1 Lung Reservoir

A reservoir of saline maintained at a static pressure of 12mm Hg is connected to the left atrial chamber using polyvinyl chloride pipes of 1" Ø ID, to simulate the atrial pressure head. An in-line electromagnetic flow probe (6-Series - 28mm, Carolina Medical Instruments, NC) is placed between the reservoir and the atrium to measure the mitral inflow and regurgitant volume.

4.1.1.2 Left Atrial Chamber

The left atrium is a cuboid shaped chamber with a length of 89 mm, width of 70.17 mm and a height of 45.31mm as shown in Figure 4-2. The total cavity volume of the atrial chamber is 283 cm^3, which is equivalent to the largest physiological volume of

the left atrium in normal adults. The chamber has an inlet on its anterior face that is connected to the lung reservoir and allows fluid flow from the reservoir into the atrial chamber. The chamber's posterior face chamber consists of an open flange that attaches to the mitral annular plate. The superior and the medial faces of the left atrium have two ports with leur lock valves that allow air bleeding from the simulator and a connection port for a pressure transducer.

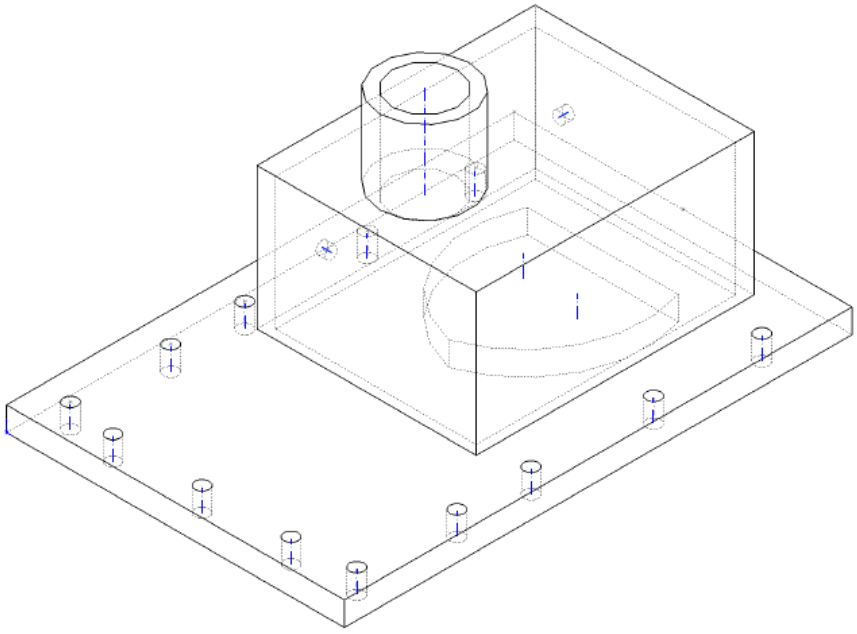

Figure 4-2 Computer model of the left atrial chamber used in the Georgia Tech left heart simulator

4.1.1.3 Mitral Annular Plate Model

The mitral annular plate is a metal frame that houses the silicone mitral annulus onto which the porcine mitral valve is sutured. The silicone annulus consists of a tension spring embedded in silicone and enclosed by a water proof cloth forming a D-shaped annulus depicted in Figure 4-3. The annulus is then sutured onto a thicker membrane

(Darlexx, Shawnut Mills, MA), which is then fastened onto the aluminum frame of the annular plate. In this thesis, two types of silicone annulus models were designed and used: (A) Variable Annular Size Model and (B) Variable Annular Shape Model.

Figure 4-3 Photograph of the adjustable size mitral annular plate with a spring loaded silicone annulus (Striped Cloth) and the blue colored water proofing polyester

4.1.1.3.1 Variable Annular Size Model

This model was designed to allow precisely controlled adjustment of the mitral annular area, either to simulate pathological mitral annular dilatation or a reduction in annular size consistent with an annuloplasty procedure. A spring-rope mechanism was used to adjust the annular area to several levels ranging between 6 cm^2 to 14 cm^2. A stainless steel wire rope was passed through the spring core of the silicone annulus, and the two ends of the wire were pulled from the open ends of the annulus. The ends of the

wire were then crossed and the two ends passed through the aluminum frame and connected to an aluminum shaft as shown in Figure 4-4. By rotating the shaft, the septal-lateral dimension of the mitral annulus was adjusted to the desired lengths, ranging from 20 mm-44 mm.

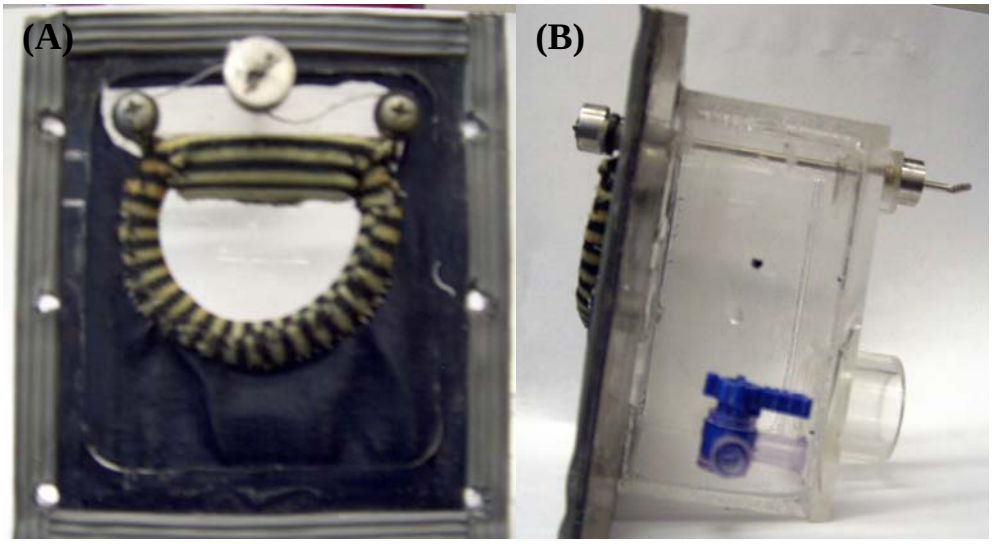

Figure 4-4 (A) En face view of the adjustable mitral annulus model; (B) Side view of the left atrial chamber with the annulus

4.1.1.3.2 Variable Annular Shape Model

This model was used to alter the 3-dimensional shape of the mitral annulus; from a flat shape to different degrees of saddle. The internal core of this annulus consists of a flexible linked chain that can flex in the out-of-plane direction as shown in Figure 4-5A. The chain is then embedded in silicone and formed into a D-shape such that the curved part of the D represents the posterior annulus and the straight part represents the anterior annulus. A sliding element that can move along its axis was connected at the posterior end of the annulus, such that the septal-lateral dimension of the annulus is self-adjusted when the degree of non-planarity of the annulus increases. Two push-rods are connected

at the two commissures of the mitral annulus so as to impose an apical force on the annulus and induce non-planarity in the annulus as shown in Figure 4-5 B-E.

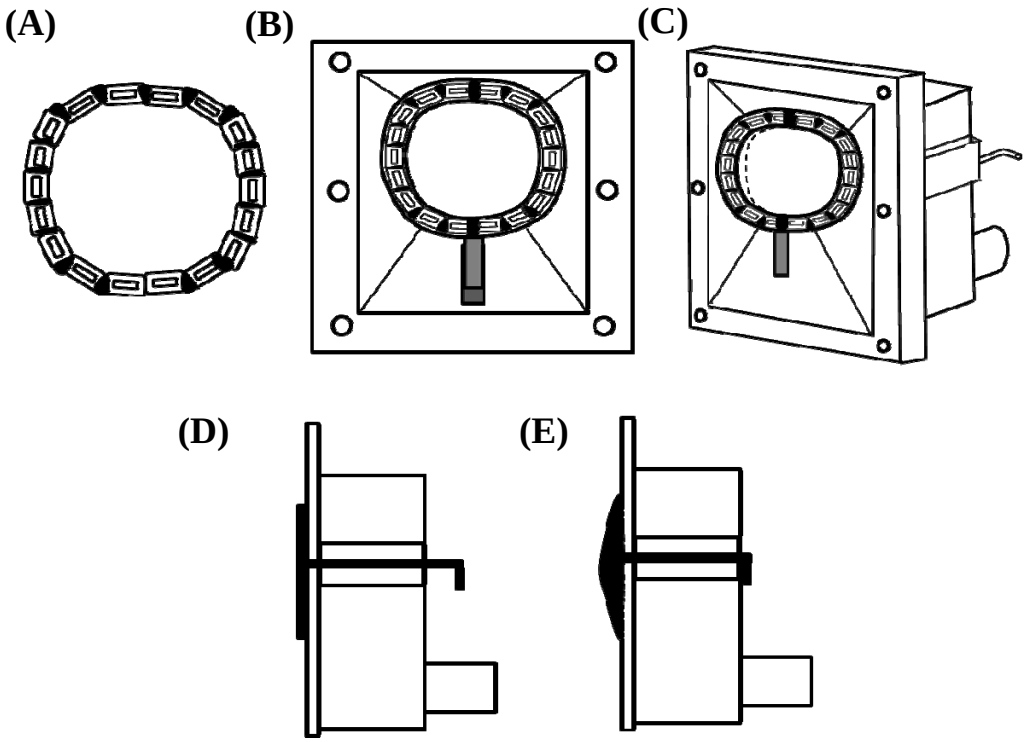

Figure 4-5 (A) Flexible link chain used in the saddle annulus model; (B) The link chain mounted onto the atrial chamber and sutured to a sliding element at the bottom; (C) Push rods built into the atrial chamber at the two commissural points to deform the annulus in the out-of-plane direction; (D) Side view of the annulus in the flat configuration; (E) Side view of the annulus in the saddle configuration

4.1.1.4 Left Ventricular Chamber

The left ventricular chamber is a rigid acrylic chamber with a flow inlet, a flow outlet, and a connection to a bladder pump that generates the physiological pressure and flow conditions. Inside, the mitral valve sutured onto the annular plate is positioned at the flow inlet using papillary muscle positioners as shown in Figure 4-6A, such that the valve

controls the flow of saline from the atrium into the ventricle. A mechanical tilting disc aortic valve (Medtronic Hall Valve, MN) shown in Figure 4-6B was used in the flow outlet position to maintain uni-directional flow from the ventricle into the outflow tract. The medial face of the chamber has a pressure port located at the same height as the atrial pressure port as shown in Figure 4-7 , and the top face of the chamber has two ports to which plastic syringes are connected. These syringes are used to inject air into the ventricular chamber which provides the required compliance to the otherwise rigid ventricular chamber.

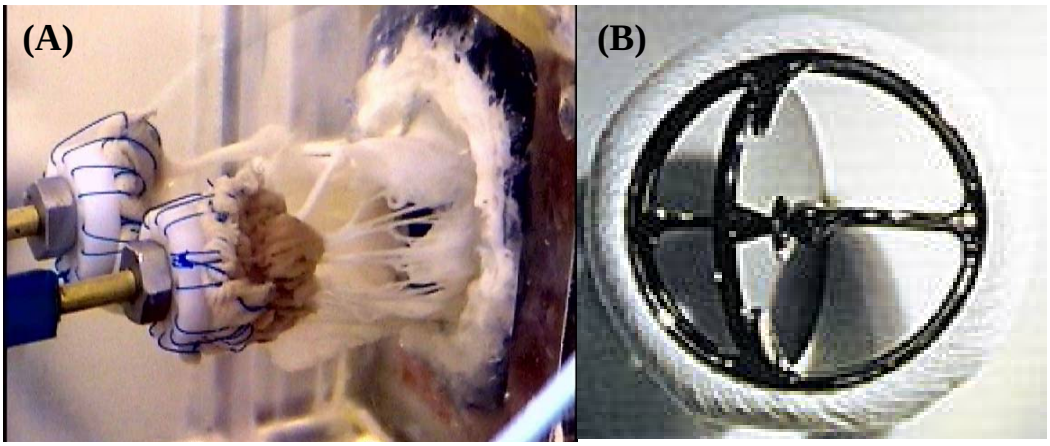

Figure 4-6 (A) Porcine mitral valve sutured onto the silicone annulus and the two papillary muscle positioners in the left heart simulator; (B) The tilting disc artificial heart valve used in the aortic position

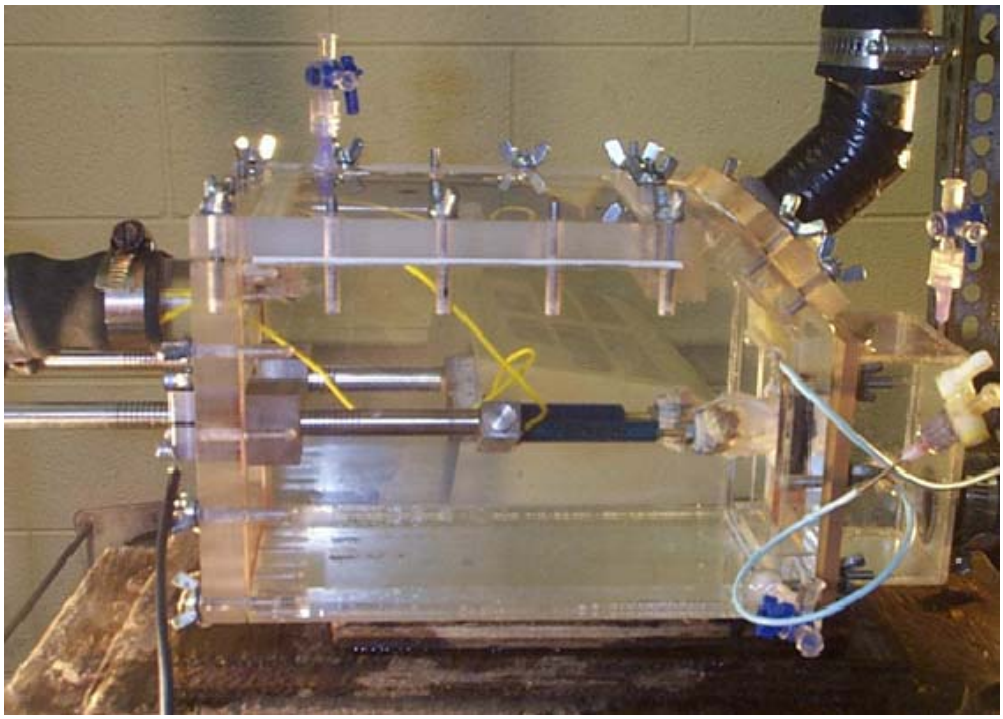

Figure 4-7 The acrylic left ventricular chamber used in the study with the bladder pump on the left (not shown), the left ventricular outflow(black tape) at the right top part of the image and the left atrial chamber on the extreme right

4.1.1.5 Papillary Muscle Positioning System

Two geared fixtures were designed to hold the mitral valve papillary muscles in the left ventricular chamber, pictured in Figure 4-8A. They consist of five components: (a) stainless steel frame, (b) Teflon connectors, (c) linear adjustment screw with bevel gears, (d) external positioning system, and (e) water-proof flanges. The stainless steel frames are inserted into the left ventricular chamber through water proof flanges on the apical plate of the ventricle, and the linear adjustment screw with the bevel gears (Part #A1X4MY06020, SDP-SI Inc, NY) are mounted onto this frame as shown in Figure

4-8B . The long stainless steel shaft connected to the driving bevel gear allows rotation of the linear screw and thus anterior-posterior motion of the papillary muscles. The stainless steel frame can also be slid and rotated to simulate apical-basal and lateral displacement of the papillary muscles respectively. The Teflon connectors are sutured onto the base of the papillary muscles and mounted onto the linear adjustment screw using a male threaded stud. This setup allows for precise displacement of the papillary muscles in the apical-basal, anterior-posterior and lateral planes upto a resolution of 0.9 mm.

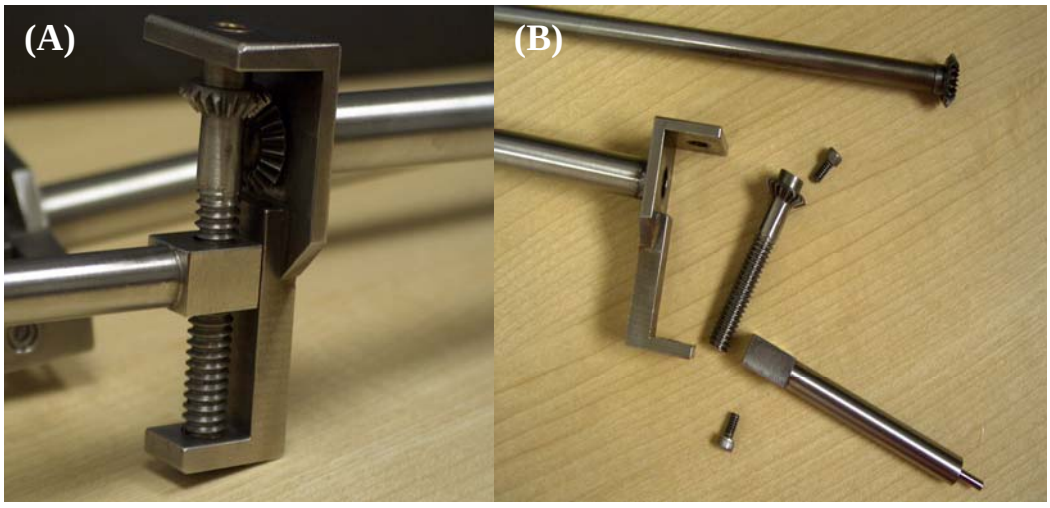

Figure 4-8 (A) Close up view of the bevel gears that drive the linear motion of the threaded stud and thus the shaft on which the papillary muscles are sutured onto; (B) A blown up view of the papillary muscles showing independent components

A simple calculation system based on trigonometric ratios was developed that enables conversion of angle rotations into linear projections, as shown in Figure 4-9 to simulate linear displacement upto 12 mm in the three directional planes.

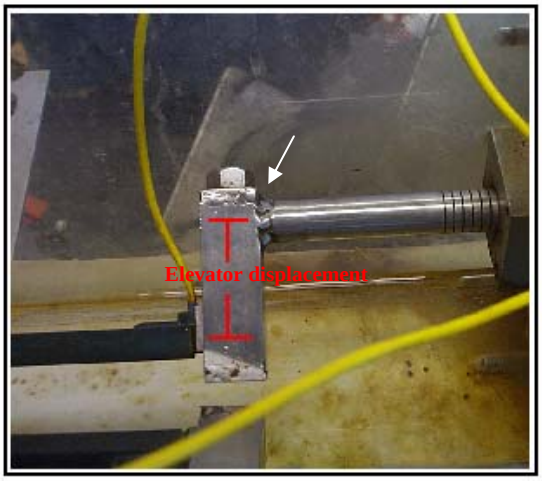

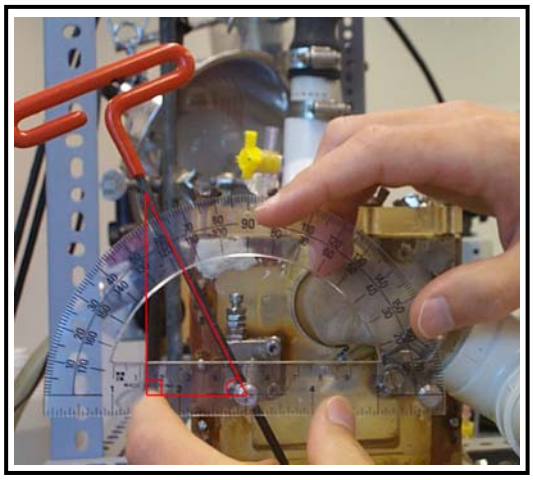

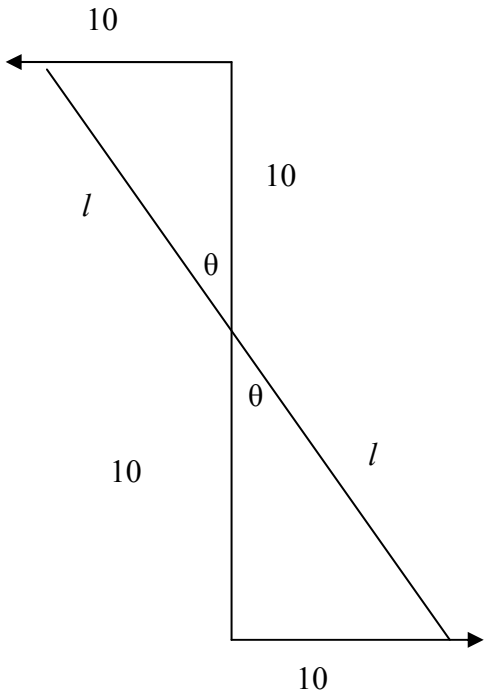

l = (10mm)/(cos θ)

θ : measured angle

# of rotations = l / 0.91

where 0.91 is the pitch of the screw stud of the papillary muscle system

Figure 4-9 Schematic depicting the trigonometric ratio's used to calculate the angles required to displace the papillary muscles in the posterior and lateral directions

4.1.1.6 Pulsatile Bladder Pump

The prime mover to generate the pulsatile pressure and flow conditions was a compressible bladder pump that was built in the laboratory. It consists of a silicone bladder (Clear Silicone Shore 30- Cured at 400 F for 2 hours, Hi-Tech Elastomers Co Ltd, CA) that is enclosed in an air-tight cylindrical acrylic chamber (Part # 8486K593, McMaster-Carr, GA) and metallic plates (Part # 9057K13, McMaster-Carr, GA) as shown in Figure 4-10. The chamber is provided with one inlet and two outlet ports that allow filling and draining of the chamber with compressed air. The ports are connected using clear silicone tubing to a series of solenoid valves and an air compressor. When compressed air is let into the chamber, the positive pressure gradient between the chamber and the silicone bladder make the bladder collapse. Since the bladder is directly connected to the ventricle through polyvinyl pipes, the collapsing action increases the left ventricular pressure and thus simulating systolic ventricular contraction. When the compressed air is rapidly drained from the chamber, the bladder expands back to its original state of ventricular diastolic relaxation.

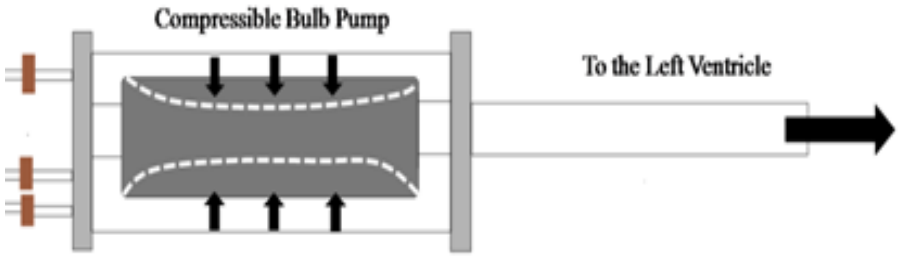

Figure 4-10 Schematic of the compressible bladder pump depicting its operation principle

4.1.1.7 Programmable Solenoid Valve System

The contraction and relaxation of the bladder pump is controlled via a series of programmable solenoid valves (Model 6213, Burkert Fluid Control Systems, Irvine, CA) which govern the flow of compressed air into the compressible bulb pump chamber. These valves are controlled via a DC signal such that a positive voltage opens the valves while a zero voltage would close them. Three solenoid valves were used in the pulsatile left heart simulator. Two valves were dedicated to rapidly drain the compressed air from the pump chamber and one valve to fill the chamber. The valves were connected in a parallel fashion as shown in Figure 4-11 using copper tubing (Part # 8967K893, McMaster Carr, GA) and end-connectors (Part # 5520K815, McMaster Carr, GA), and the entire system was then connected to a air compressor (Part # T-35HD-1 HP Ultra Oil-Less Air Compressor, Thomas Air-Pac, WI) that maintained a constant air flow at a pressure of 20 psi. Each valve was controlled using a timed relay circuit that could be interfaced via a DOS program (Trigger.exe) with an internal clock. The relay circuit consists of several analog switches that can be independently timed, so as to allow current to the solenoid valves in a controlled fashion. Using this program desired heart rates, systolic and diastolic duration and any time delays can be programmed into the relay circuit.

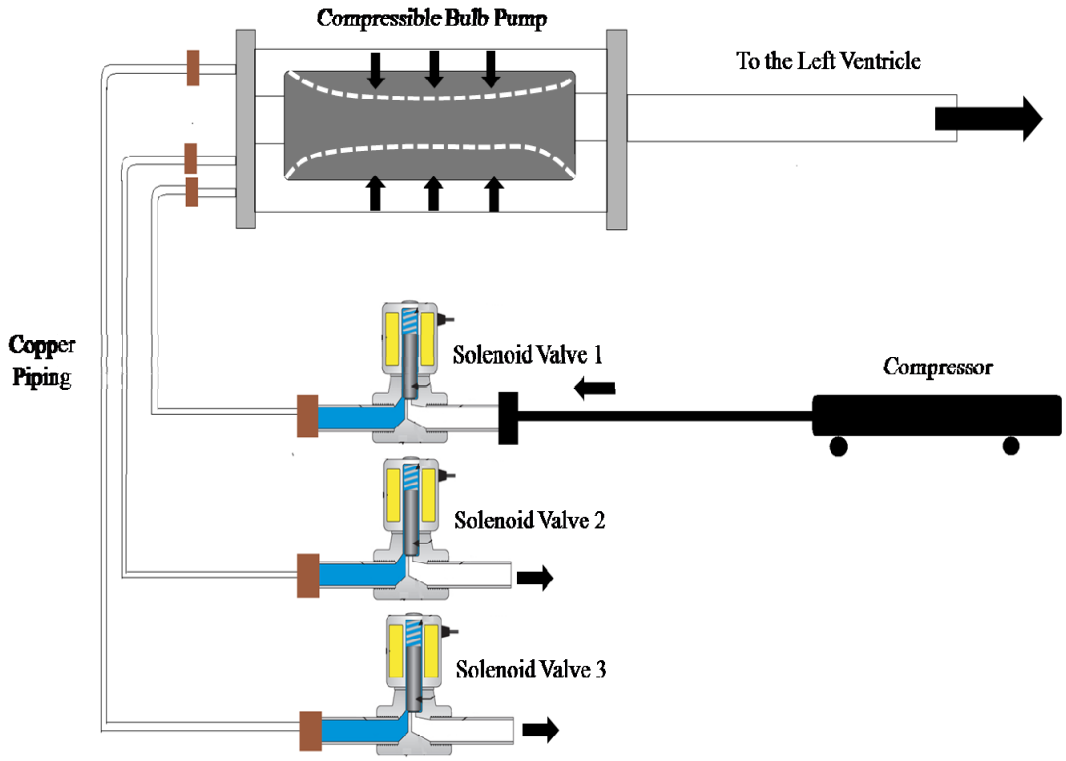

Figure 4-11 The bladder pump system connected to a parallel series of solenoid valves. The valve # 1 is the systolic valve connected to an air compressor providing air at 20psi, while the other two solenoid valves emptied air from the pump to relax the bubble pump

4.1.1.8 Flow Loop Plumbing

A combination of polyvinyl pipes and rubber tubing were used to complete the flow loop plumbing. The same silicone bladder used to make the pump was used downstream of the aortic valve to simulate compliance of the aorta, and adjustable hose clamps (Part # 05-846Q, Castaloy Jumbo Hosecock Clamp,Fisher Scientific, Pittsburgh, PA) were used to induce systemic resistance into the flow loop.

4.1.2 DATA ACQUISITION HARDWARE AND SOFTWARE

To continuously monitor the hemodynamic conditions in the left heart simulator, a data acquisition system was built using components from different vendors that suit the specifications of the system. The main hardware components used in the data monitoring and recording system are: (a) differential pressure transducer with signal conditioner; (b) electromagnetic flow probe with signal conditioner; (c) portable data acquisition card with signal connector; and (d) custom data acquisition software.

4.1.2.1 Differential Pressure Transducer

A variable reluctance differential pressure transducer (DP-09, Northridge, CA, USA) was used to measure the pressures in the left heart simulator. The DP-09 model is a low cavity volume stainless steel pressure transducer that can measure differential pressures ranging from ±0.5 psi to ±500 psi, while maintaining ± 0.5% linearity at high natural frequencies. This model was best suited to measure transvalvular pressure gradients up to 200 mm Hg at a highest heart rate of 2.6 Hz, without any drift or non-linearity in the measured signal. The transducer as shown below in Figure 4-12 consists of a magnetic permeable stainless steel diaphragm clamped between two blocks of stainless steel embedded with an inductance coil with an E-shaped frame.

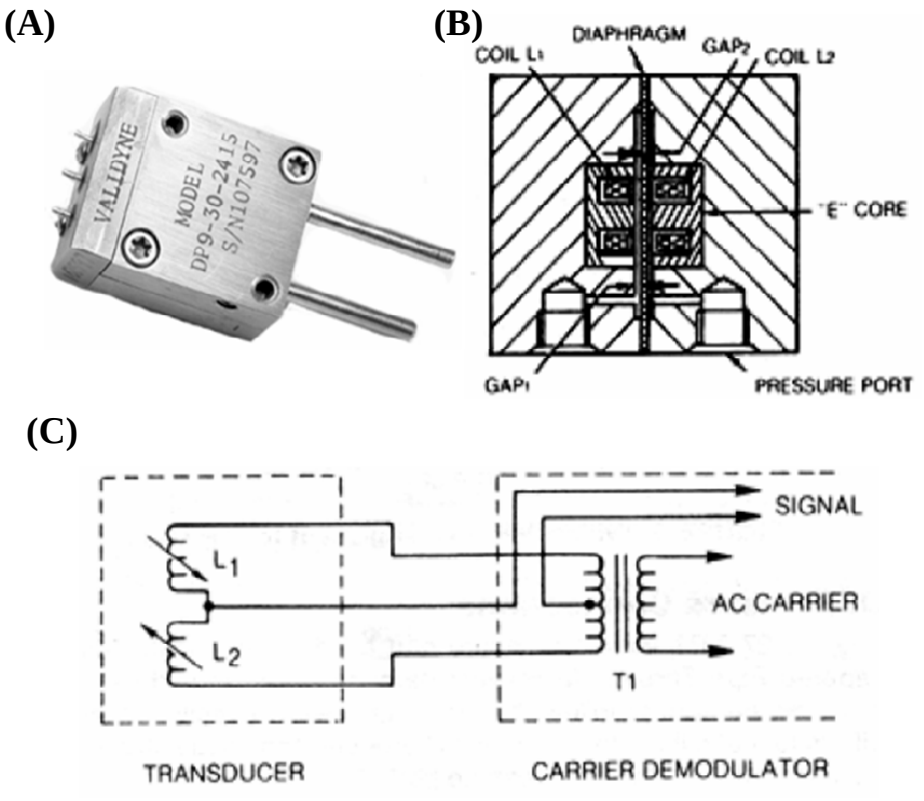

Figure 4-12 (A) Validyne differential pressure transducer; (B) Cross sectional view of the transducer depicting the inductance coils and the pressure cavities; (C) Circuitry diagram of the transducer and the signal conditioner

In the un-deflected state, the diaphragm is centered between the two blocks maintaining an equal distance of 0.005" between the diaphragm and the legs of the E-shaped core. As a differential pressure is applied on the two sides of the diaphragm, it deflects into the lower pressure cavity thus reducing the cavity volume on the deflected side. Thus the reluctance of the cavity into which the diaphragm has deflected into, is reduced and that on the higher pressure side is increased. The transducer is connected into an AC bridge circuit forming one half of a four arm bridge, and the center tapped secondary of the carrier transformer in the signal demodulator forming the other half. The

output of the transducer is thus an AC signal whose peak-to-peak amplitude is dependent upon the deflection of the diaphragm and whose phase is determined by the direction of deflection. A CD23 digital signal conditioner (Validyne Engineering, Northridge, CA) was used with the differential pressure transducer. The CD23 provides a 5-V_{rms}, 5 KHz carrier excitation voltage to the transducer and has the solid state circuitry to amplify, demodulate and filter the transducer signals and also to output a ± 10 VDC signal. Before using the DP-09 transducer with the CD23 conditioner in the left heart simulator, it was calibrated against ten different barometric differential pressures using a protocol described in section 5.3.1.

4.1.2.2 Electro Magnetic Flow Meter

An in-line electromagnetic flow meter (EFP) (26mm, 600 Series, Carolina Medical Electronics, East Bend, NC) was used to measure the diastolic flow and systolic regurgitant flow in the left heart simulator. The 600 series EFP works on the principle of Hall effect, wherein charge carries of a current carrying conductor when placed in a transverse magnetic field experience a sideways Lorentz force resulting in a charge separation in the direction perpendicular to the magnetic and the current. The resultant voltage difference obtained due to charge separation is proportional to the applied magnetic field, and is famously known as the Hall Effect. The flow measurement system consists of three main components: (a) Flow Probe, (b) Ground and (c) Signal Conditioner. The flow probe as shown in Figure 4-13 is a donut shaped device consisting of a copper coil that generates a magnetic field when current is passed through it. This flow probe and the ground are connected to a signal conditioner (Model FM501, Square

Wave Digital Flow Conditioner, Carolina Medical Electronics, East Bend, NC) that can measure low noise, high resolution pulsatile data with a frequency response selectable up to 100 Hz. The signal conditioner sends a 500 Hz square wave, 0.5 A, up to ± 15 V signal to the flow probe, and measures the voltage difference due to charge separation using two polarizer's on the flow probe. The voltage difference measured from the flow probe is amplified using a solid state circuitry in the signal conditioner, and flow rates in the range of 5 ml/min to 19.99 L/min can be measured. The flow probe and the signal conditioner were calibrated at measured flow rates using a protocol described in section 5.3.2.

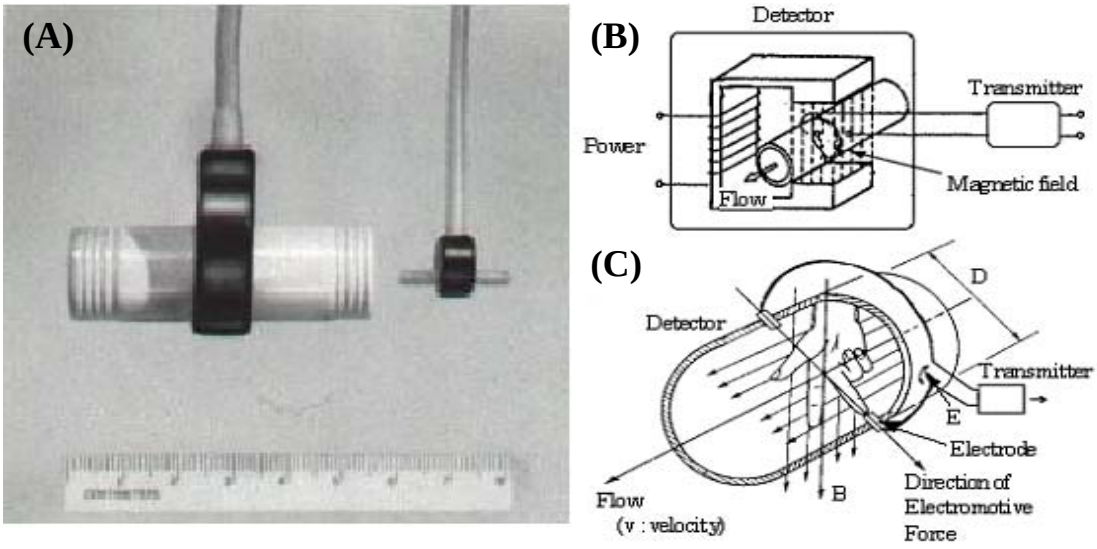

Figure 4-13 (A) Carolina medical electromagnetic flow probe; (B) The transmitted and flow probe configuration that generates the charge separation proportional to the flow rate; (C) Schematic depicting the Hall Effect.

4.1.2.3 Portable Data Acquisition Card and Signal Conditioning System

Pressure and flow data were synchronously monitored and recorded using a data acquisition system (DAQ) that was custom built in the laboratory. The DAQ system consists of three components: (a) BNC-2110 Isolated Signal Connector, (b) PCMCIA

1200 Signal Acquisition Card, and (c) a PCMCIA port accessible laptop with the hardware to run LABVIEW software. All the above components including the software were obtained from National Instruments, Austin, Texas, USA. The BNC 2110 series signal connector blocks with signal-labeled BNC connectors as shown in Figure 4-14 are used for easy connectivity of analog I/O, digital I/O and counter/trigger signals to the multifunction PCMCIA card. The NI-DAQ 1200 is a legacy, low cost, multifunction I/O card for PCMCIA that provides eight single ended or four differential analog inputs at 100kS per second, 12-bit performance. It also allows digital triggering from an external source, and has three built in 16-bit, 8 MHz counters; two 12-bit analog outputs; and 24 digital I/O lines. The DAQ card is inserted into the PCMCIA slot in the laptop (F-Series VAIO, Sony Corporation, USA) and the data was monitored and recorded using custom software (DAQANAL) built in LABVIEW 5.1. The software was designed such that the sampling frequency, trigger timing and delay, and signal filters can be prescribed as desired by the user. Graphical interfaces to monitor the measured data were provided, and the flow and pressure data over multiple cardiac cycles can be synchronously recorded, averaged and exported into excel spreadsheets.

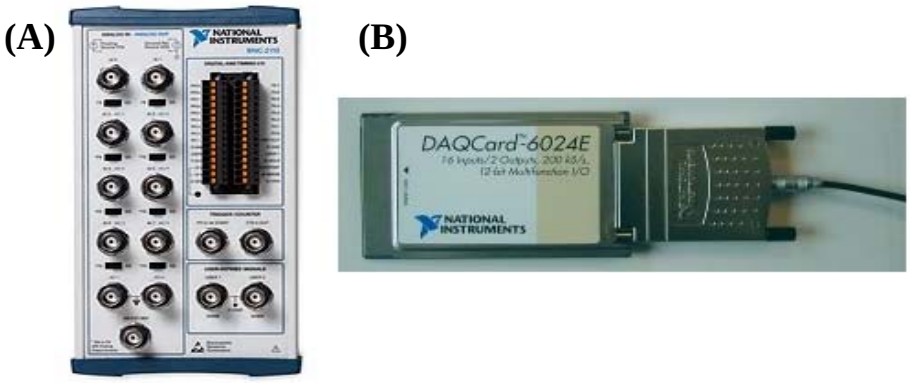

Figure 4-14 (A) BNC-2110 Connector Block; (B) DAQCARD 6024-E portable data acquisition system used in the left heart flow simulator

4.1.3 C-RING FORCE TRANSDUCERS

To measure the forces on individual mitral valve chordae tendineae, force transducers were designed and manufactured in the laboratory. The design specifications of the force transducers are:

- Small size such that physiological function of the chordae tendineae or the valve is not disturbed
- Deformation that matches the elongation of the chordae tendineae
- Measure high frequency forces in saline without baseline drift while maintaining linearity
- Ability to sustain function for atleast 48 hours when submerged in saline

Based on these design specifications, a C-ring force transducer with a maximum dimension of 4mm, and a thickness of 1mm was developed using 2 strain gauges as shown in Figure 4-15. Also, the total mass of the C-ring transducers is low which allows multiple transducers to be instrumented on the same valve. The operating principles and manufacturing methods of the transducer are described below.

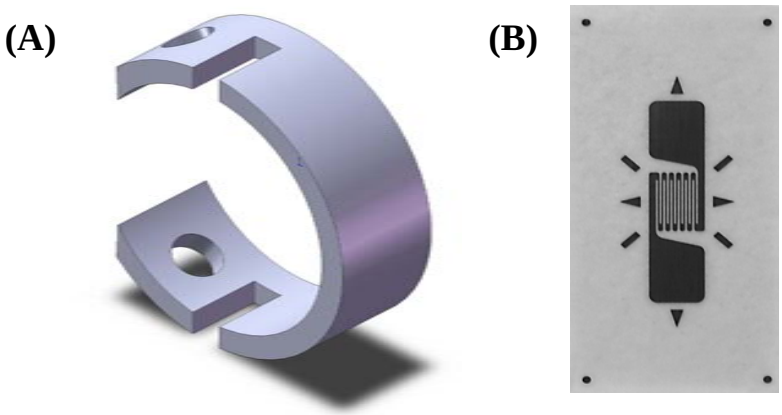

Figure 4-15 (A) Isometric view of the brass C-ring design used in the force transducer; (B) Strain gauges used in manufacturing the force transducers

The C-ring transducer is based on strain gauge (SG) technology that detects the slightest deformation of the chordae tendineae to measure the corresponding force governing the deformation. The miniature size allowed easy implantation of the transducers onto the chordae without intervening with the physiological function of the valve.

4.1.3.1 Operating Principles

The C-ring force transducer is based on the simple principle that the linear deformation of a material can be detected using precision strain gauges that can be translated into a force with prior calibration. Strain gauges measure deformation through a proportional change in their resistance, resulting in a change in voltage difference in a constant current circuit. However, the change in resistance is very small and thus a Wheatstone bridge configuration is typically used to detect the relative changes in resistance. In this study, a half bridge Wheatstone circuit was used as shown in Figure 4-16, where one gauge is mounted along the longitudinal centerline of the convex surface of the C-ring, with a mating gauge on the corresponding concave surface. These two gauges form the adjacent arms in the bridge circuit, and assuming uniform temperature throughout the thickness of the C-ring, the bridge output is doubled.

By providing an excitation voltage V_{EX} to the bridge, it is possible to generate a voltage drop across the bridge and thus determine the resistance of the strain gauge. The generated voltage differences are normally very small, and thus the signal is amplified with dedicated instrumentation. Elaborating on the operating principles from a mathematical perspective, the C-ring setup can be explained as below:

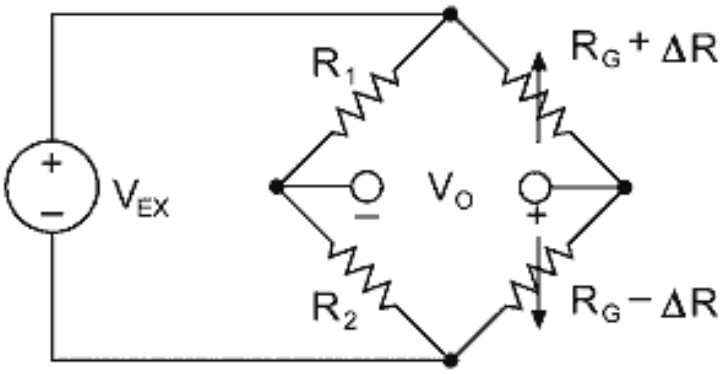

Figure 4-16 A half bridge Wheatstone circuit

The resistance R_0 of a metal, i.e. a SG, is given by Equation 4-1:

$$R_0 = \rho \frac{l_0}{A_0} \qquad \text{Equation 4-1}$$

where:

R_0: resistance [Ω]

ρ: resistivity [Ωm]

l_0: length [m]

A_0: area [m^2]

When a force F stresses the brass ring, it is elongated by some amount ∂l so that the new length is l + ∂l. It is also true that in such a stress-strain- condition, although the C-ring lengthens, its volume will remain nearly constant. Because the volume V unstressed is $V = l_0A_0$, it follows that if the volume remains constant and

the length increases, then the area must decrease by some amount ∂A defined by Equation 4-2:

$$V = l_0 \cdot A_0 = (l_o + \partial l) \cdot (A_0 - \partial A) \qquad \text{Equation 4-2}$$

The change in length and area are related to the measured resistance as described by Equation 4-3:

$$R_0 = \rho \frac{(l_0 + \Delta l)}{A_0 - \Delta A} \qquad \text{Equation 4-3}$$

Combining Equation 4-1 and Equation 4-3, the new resistance can be calculated as defined in Equation 4-4:

$$R \cong \rho \cdot \frac{l_0}{A_0}(1 + 2\frac{\Delta l}{l_0}) \qquad \text{Equation 4-4}$$

Therefore the change in resistance can be defined by Equation 4-5 as:

$$\Delta R \cong 2R_0 \frac{\Delta l}{l_o} \qquad \text{Equation 4-5}$$

Equation 4-5 clearly shows that the strain ∂l/l converts directly into a resistance change. Thus, the gauge factor G, describes the relationship between the change in resistance and the measured strain given by Equation 4-6:

$$G = \frac{\Delta R / R}{\Delta L / L} \qquad \text{Equation 4-6}$$

4.1.3.2 Signal Amplification

To amplify the small voltage differences generated by the half bridge circuit, a signal amplifier was built using OEM components. Figure 4-17 outlines the flow of data through the various components of the signal conditioning system which amplifies, filters and smoothens the signal for recording using the data acquisition system.

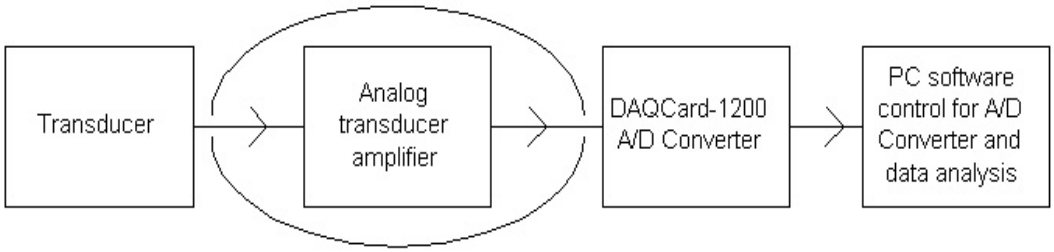

Figure 4-17 Flow chart demonstrating the analog amplifier introduced into the data acquisition system

The design specifications for the signal amplifier are:

- 6 channel input/output
- 350 Ω bridge resistors for the Wheatstone half bridge that act as passive resistors to complete the half-bridge circuit
- Potentiometers of the required ratings for offset adjustment to balance the Wheatstone bridge
- 120V power supply with galvanic separation from the Wheatstone bridge circuit
- Signal filtering that decreases aliasing and improves signal to noise ratio for optimal force measurements

4.1.3.3 Manufacturing Methods

The detailed protocol for manufacturing the C-ring force transducers and the signal amplifier are now presented. The C-ring made of Brass is 6mm in Ø and has a thickness of 0.8mm, with a notch and two holes at either ends that allow suturing the ring onto the mitral valve chordae tendineae. The C-rings are designed and custom manufactured at a local machine shop (J. M. Machining, Lawrenceville) and the strain gauges were purchased from a strain gage vendor (Part # 031-DE Vishay Micro measurements, NC).After acquiring these materials, the C-ring force transducers were then manufactured using 15 sequential steps as described below:

Step 1 – Positioning the C-ring: The manufactured brass C-rings were clamped in a miniature vice to position the C-ring for ease of handling, optimal visual access and to avoid contamination due to contact with other objects.

Step 2: Degreasing the C-ring: To remove the surface contamination and particulate matter on the C-rings a degreaser (CSM-1A, Measurement Group, Raleigh, NC) was applied on the surface using a sterilized cotton swab. An even coat of the degreaser was first applied on the ring and another sterilized swab was used to remove the degreaser from the surface. Evaporation of the degreaser to dry the C-ring surface is not an optimal choice as it does not remove the particular matter present on the C-ring as physical scraping using a cotton swab. To avoid recontamination of the surface, the cotton swabs should scrape the surface in one direction and in only one pass. During this process, surface contamination due to contact with human fingers must be avoided by wearing sterile gloves.

Step 3: Surface Conditioning: The surface conditioner is a water based solution that allows better adhesion of chemical bonding agents to the metal surface of the C-ring. Using a new cotton swab, step 2 was repeated with a surface conditioner (M-Prep Conditioner, Measurement Group, Raleigh, NC, USA).

Step 4: Surface Neutralization: The surface neutralizer reduces any residual charge on the brass surface, and Step 2 was repeated with a surface neutralizing solution (M-Prep Neutralizer 5A, Measurement Group, Raleigh, NC, USA).

Step 5: Surface Bonding: After applying the surface conditioner and neutralizer, the C-ring surface is chemically clean and pH neutral. To manufacture the C-rings, a bonding material with optimal viscosity was selected (M-Bond 43B, Measurement Group, Raleigh, NC, USA) and stored at room temperature. At its optimal state, the bonding material was applied to the surface of the C-rings with due care to avoid covering the holes and notches in the C-ring to allow suturing the rings onto the chordae tendineae. After covering the C-rings in an even coat of bonding solution, the rings are baked in an oven for 1 hour at 257°F (125 °C). This step is repeated twice after which the C-ring is ready for mounting the strain gages.

Step 6: Preparing the Strain Gages: Two strain gauges (EA-06-031DE-350. Measurement Group, Raleigh, NC, USA) are selected and carefully removed from their package and stored in a sterile and dry container. The membrane onto which the strain gages are printed onto is typically larger than the width of the C-ring and thus using a fine scissors, the membrane is carefully trimmed as shown in Figure 4-18, to match the C-ring dimensions. Extensive care must be taken to avoid damage to the strain gages

from human contact by using forceps. The membrane can be trimmed very close to the circuit, but care should be taken to avoid any scratches or cuts into the actual circuitry. The terminals at the top and bottom of the C-rings can be trimmed to a desired length but care must be taken to allow enough length for soldering of wires.

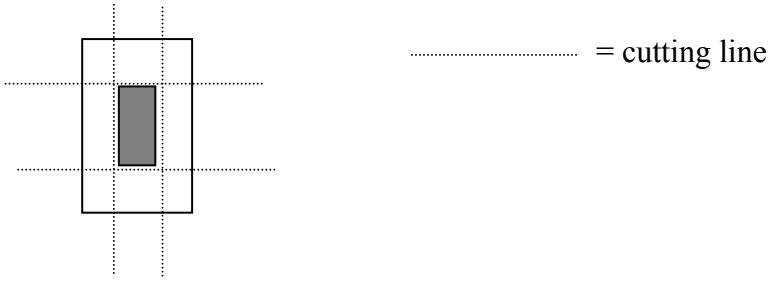

Figure 4-18 Schematic depicting the cutting lines around the strain gage

Step 7: Mounting the Strain Gages: Commercially available super glue was used to mount the strain gages onto the C-ring surface as shown in Figure 4-19. In this case, super glue instant bond adhesive (Cortec Spray Technologies Division, Spooner, WI, USA) was used to fix the inner and outer strain gages to the brass surface.

Inner Strain Gauge Mounting: The C-ring is positioned in the vice such that the two ends are facing upwards with direct visual access to the concave section of the ring. Appropriate quantity of super glue was applied onto the inner surface of the ring and evenly spread over the surface using a piece of paper. Using two forceps the trimmed strain gauge is positioned onto the glued surface (approximately at the middle of the C-ring) and carefully placed on the C-ring while applying minimal pressure. A thin thread (134-AWP Single Conductor, Measurement Group, Raleigh, NC, USA) is tightly held in the two hands of another person, and carefully the tightened string is rolled over the strain

gage to attach it to the underlying bonding surface. This procedure ensures that the entire strain gauge is firmly attached to the brass surface and any excessive glue is squeezed out from below the strain gage.

Outer Strain Gauge Mounting: The C-ring is now flipped around in the vice with the two ends of the C-ring facing downwards. The procedure explained above is repeated again with another strain gauge and extensive care is taken to avoid disturbing the position of the already glued inner strain gage. After both the stain gauges are mounted, three fine strings are used to firmly hold the gages to the surface until the glue cures and perfect adhesion is ensured.

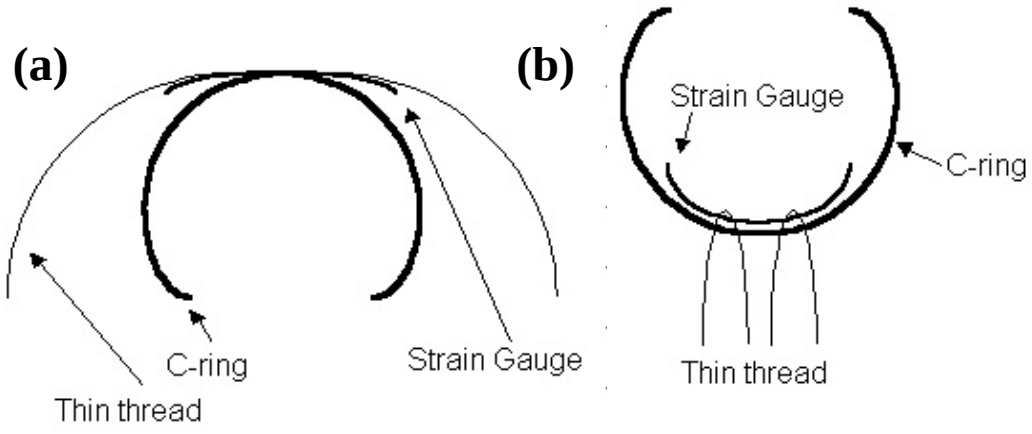

Figure 4-19 Schematic depicting the strain gage mounting method – (a) Outer gage mounting, (b) Inner gage mounting

Step 8: Protecting the C-ring: To avoid damage to the strain gages in the next steps of manufacturing, they were covered in drafting tape (PDT-1, Measurement Group, Raleigh, NC, USA).

Step 9: Pre-soldering the Terminals: To interconnect the strain gages and attach the wire conductors to the strain gages, the terminals are pre-soldered by placing a minute quantity

of tin solder on the strain gage terminal. The soldering should be done carefully and swiftly as the strain gages can be damaged by exposure to excessive heat from the solder for prolonged periods.

Step 10: Interconnecting Strain Gages: To put the two resistors in a Wheatstone circuit, the strain gages need to be interconnected to each other as described previously. Using a thin metal conductor with enamel coating (134-AWP Single Conductor, Measurement Group, Raleigh, NC, USA) one end of the inner strain gage is connected to another end on the outer strain gage. The C-ring is first braced in the vice and with the conductor in one hand and the soldering iron in another; the conductor is soldered into the pre-solder on the inner strain gage. The conductor is then bent around the ring and adjusted for appropriate length to avoid residual stress or bending, and the other end of the conductor is soldered to the outer strain gage terminal. The connection is then tested using an ohmmeter, ensuring that the resistance measured across each strain gage is 350±5Ω. If the resistance is less, probably the strain gage was damaged due to the solder connecting to the circuitry and if this happens, the strain gages should be removed and all the steps starting from Step 4 should be repeated. If the resistance is higher than desired, the strain gage may be under constant strain either due to poor bonding or shrinking of the plastic membrane of the strain gage under prolonged exposure to soldering iron.

Step 11: Soldering Conductors to Terminals: 3.3 feet of a 3-conductor cable (336-FTE, Measurement Group, Raleigh, NC, USA) was used to connect the strain gage terminals to the signal conditioner. The conductors were first tinned appropriately to ensure active surface wetting and good heat transfer, and their lengths adjusted to exactly match the

positions of the strain gage terminals without bending. The ends of the conductor cable are stripped to approximately 1.5mm using a flame lighter. The exposed ends of the connectors are then soldered onto the terminals longitudinally while holding the soldering iron in one hand and the conductor in the other. The conductor cable has three conductors, each with a different color (white, black and red). The black conductor connects to the outer gage, at the end where the inter-connect from the inner gage connects to the outer as shown in Figure 4-20. The red conductor attaches to the other end of the outer gage, and the white conductor to the non-interconnect end of the inner gage. The connections are then tested using an ohmmeter to ensure a resistance of 350Ω is measured across the circuit.

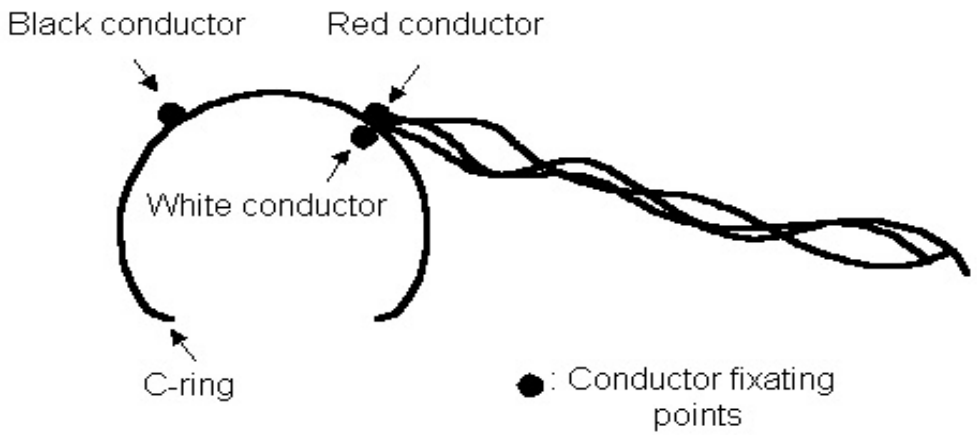

Figure 4-20 Schematic depicting the wire connections to the C-ring

Step 12: Fixing the Wire: The solder terminals on the strain gages are fragile, and may easily break due to bending of tethering of the wire. To avoid such damage, the wires are clamped onto the C-ring frame using a thin string as shown in Figure 4-21

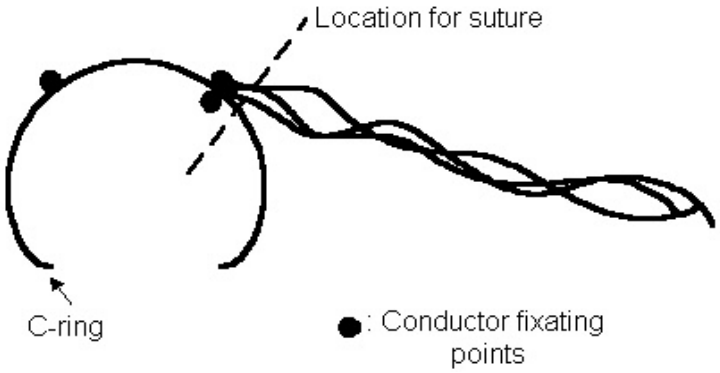

Figure 4-21 Schematic depicting the location where the conducting wire is fixed

Step 13: Second Bond to Cover Solder Terminals: Step 5 is repeated thrice on the C-ring to cover the solder terminals and the ends of the conductor with the adhesive bond.

Step 14: Rubber Coating for Use in Water: To use the force transducers in saline solution, the entire C-ring force transducer is covered in a Nitrile rubber coating (M-Coat B, Measurements Group, Raleigh, NC, USA). The M-Coat B should be applied when it is cold (atleast 1 hr in the fridge) as at lower temperatures it has lower viscosity and is therefore easier to apply on the C-ring. 3 hours after applying the first coat, a second coat should be applied and the C-rings must be allowed to cure for 24 hours at room temperature and to increase their chemical resistance, baked for 1 hour at +200°F (+95°C).

Step 15: Solder to connector*:* 3.3 feet of the 3 conductor cable (300-FTE, Measurement Group, Raleigh, NC, USA) is used to connect the C-ring to the signal amplifier. The end of the conductor cable is connected to a HR10A-7P-4S plug with four connectors (Hirose

Electric Inc, Simi Valley, CA, USA) with only three active terminals being used. When the plug is positioned into the female end in the amplifier, the red cable is connected to terminal 1, white to terminal 2 and black to terminal 4 on the plug.

4.1.3.4 Signal Amplifier Manufacturing Methods

The signal amplifier used in this work was developed in the laboratory using OEM parts and allows simultaneous measurement of signals from six C-rings. Since the six channels have identical circuits and are replicated using the same components, the manufacturing methods for a single channel are described here.

4.1.3.4.1 Wheatstone Bridge Specifications

The passive strain gages used in the amplifier complete the Wheatstone half-bridge and 350Ω resistors were chosen based on previous studies. To ensure stability of the strain gages, the power dissipation of the gages should be within limits that allow good dynamic range in measurements with good signal to noise ratio. Large dynamic ranges can be obtained using higher excitation voltages but that quadruples the power dissipation expressed mathematically by Equation 4-7:

$$P = \frac{V^2}{R} \qquad \text{Equation 4-7}$$

.

The manufacturer of the strain gages (Vishay Measurement Group, Raleigh, NC, USA) recommends a power dissipation of approximately 5mW, in the half-bridge configuration. To ensure stability and safety of the strain gages an additional resistor R_S was added in series with the bridge as shown in Figure 4-22.

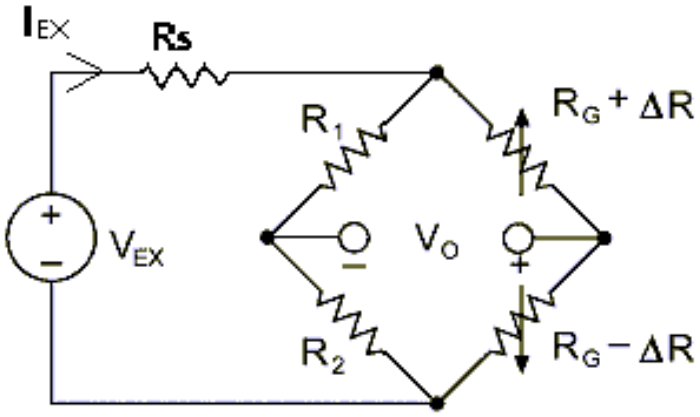

Figure 4-22 Schematic showing the half bridge configuration with a series resistor

The maximum current allowed through each bridge is given by Equation 4-8:

$$P = U \cdot I = I^2 \cdot R \Leftrightarrow I = \sqrt{\frac{P}{R}} = \sqrt{\frac{0.005W}{350\Omega}} = 3.78mA \qquad \text{Equation 4-8}$$

Since the current flows through both the bridge branches, the maximal excitation current required is calculated by Equation 4-9:

Equation 4-9

$$I_{EX} = 2 * 3.78mA = 7.56mA$$

The strain gage input modules used in the signal amplifier (Dataforth, Dallas, TX) provide a stable 3.333V supply voltage and thus the total resistance in the circuit should not be less than the value given in Equation 4-10:

$$V_{EX} = I_{EX} \cdot R_{Total} \Rightarrow R_{Total} \geq \frac{V_{EX}}{I_{EX}} = \frac{3.333V}{7.86mA} = 440\Omega \qquad \text{Equation 4-10}$$

Knowing this, R_S can easily be found from Equation 4-11:

$$R_{Total} = R_S + R_{Bro}$$
$$\Rightarrow R_S \geq R_{Total} - R_{Bro} = 440\Omega - 350\Omega = 90\Omega$$

Equation 4-11

4.1.3.4.2 Completing the Wheatstone Bridge

The miniature size of the C-ring transducers does not allow completion of the Wheatstone bridge on the ring, thus passive resistors were used in the signal conditioner to complete the bridge circuit.

4.1.3.4.3 Offset Balancing

Due to leakage currents from saline solution and other reasons, the strain gages can drift substantially from their zero ground. Therefore a provision to adjust the base zero of the circuit is required in the amplifier. This was achieved by balancing the Wheatstone bridge on the input size of the amplifier by shunting the strain gage. A potentiometer was connected in parallel to the strain gage allowing shunt calibration. The larger the potentiometer range, the better is the outcome as smaller resistances allow finer adjustments. The strain gage manufacturer specifications indicated that the resistance of the gage changes by ± 10 Ω, and thus if one strain gage is 340Ω the other would be 360Ω. Thus the smallest value of the shunt potentiometer is given by Equation 4-12:

$$R_{SG,\min} = \frac{R_{SG,\max} \cdot R_{Shunt,\min}}{R_{SG,\max} + R_{Shunt,\min}} \Leftrightarrow R_{Shunt,\min} =$$
$$-\frac{R_{SG,\max} \cdot R_{SG,\min}}{R_{SG,\min} - R_{SG,\max}} = -\frac{360\,\Omega \cdot 340\,\Omega}{340\,\Omega - 360\,\Omega} = 6.12\,k\Omega$$

Equation 4-12

When the two shunts are in their extreme positions with least resistances, the total resistance of the circuit will be $R_S + 2 \cdot R_{pot,min} = 235\ \Omega + 2 \cdot 2\ \Omega = 239\Omega$. The maximum current thus running through the circuit is given by Equation 4-13:

$$U = R \cdot I \Leftrightarrow I = \frac{U}{R} = \frac{3.333V}{239\Omega} = 13.9mA$$ Equation 4-13

Thus the power dissipation in the potentiometers at least resistance is thus given by Equation 4-14:

$$P = I^2 \cdot R = (13.9mA)^2 \cdot 2\Omega = 0.4mW$$ Equation 4-14

The power dissipation in R_S will thus be 45.4 mW which is within the specified range by the manufacturer. Thus all components were within the allowable power dissipation limits even in the worst case scenario. The diagram of the entire circuit on the input side of the strain gage is shown in Figure 4-23.

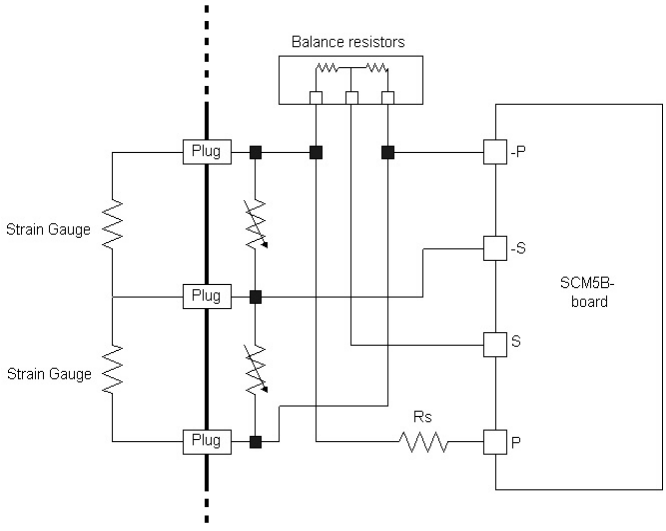

Figure 4-23 Input circuit of the entire strain gage – amplifier with shunt potentiometers and safety resistances. The four terminals to the right in the diagram are attached to the SCM5B board. The terminals –P,-S, S and P go directly to the Strain Gauge Input Modules. The three wires going into the amplifier box goes through the same plug (HR-10 connector).

The potentiometers were connected in parallel to the lead wire in series with the active strain gages. A TFE-336 low resistance wire was used as the lead (Measurements Group, Raleigh, NC, USA) as it has a thin diameter (0.127mm) resulting in a resistance of 1.414Ω/m @+24°C. The potentiometers are calibrated such that there is zero bridge output when no force is acting on the force transducer.

4.1.3.4.4 Strain Gauge Input Module Specifications

Special strain gage input modules (SCM5B38-03, Dataforth Inc, Dallas) were used that can acquire data from strain gages in a Wheatstone half bridge circuit as shown in Figure 4-24, and provide an output voltage of ±5V. This voltage output range is compatible with the data acquisition system and the input modules offer a 100dB CMRR at the critical mains frequency around 60Hz. A wide signal bandwidth of 10kHz is available and above 10 KHz they filter signals using a low pass filter with 120dB/decade. Good accuracy, linearity with minimal drift, and a stable excitation voltage of 3.333V when connected to bridge resistors in the range of 100Ω to 10kΩ made them the suitable modules.

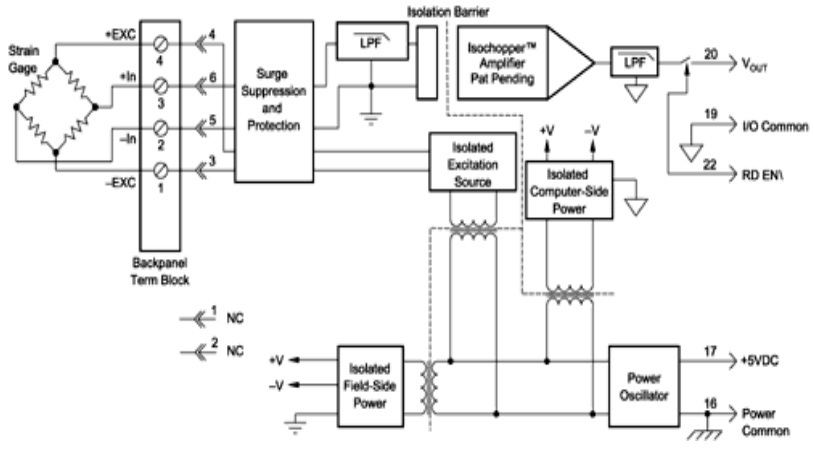

Figure 4-24 Circuit diagram of the strain gage input module

4.1.3.4.5 Galvanic Separation from Power Supply

The strain gage input modules provide galvanic separation of the C-rings from the power supply. Galvanic separation removes any disadvantages due to voltage differences between the input and output circuits. As mentioned previously, the fully isolated excitation voltage from the input modules is used in the Wheatstone half bridge. The power supply for the amplifier was chosen such that it had short circuit protection, over voltage protection, a stable 5V output and is of reasonable physical size. A power supply rated at 5V at 3 Amps (Condor D.C Power Supplies Inc) was used as it fit the requirements well.

4.1.3.4.6 Signal Amplifier

The amplifier box was made of metal with small holes drilled into the sides to minimize the interference originating from electromagnetic radiation. BNC connectors were used to connect the C-rings to the strain gage input modules and all the wires were insulated enough to avoid inference due to electromagnetic radiation. A small fan was fit into the box for convective heat transfer away from the circuit components.

The layout of the circuit for the entire amplifier box is shown in Figure 4-25

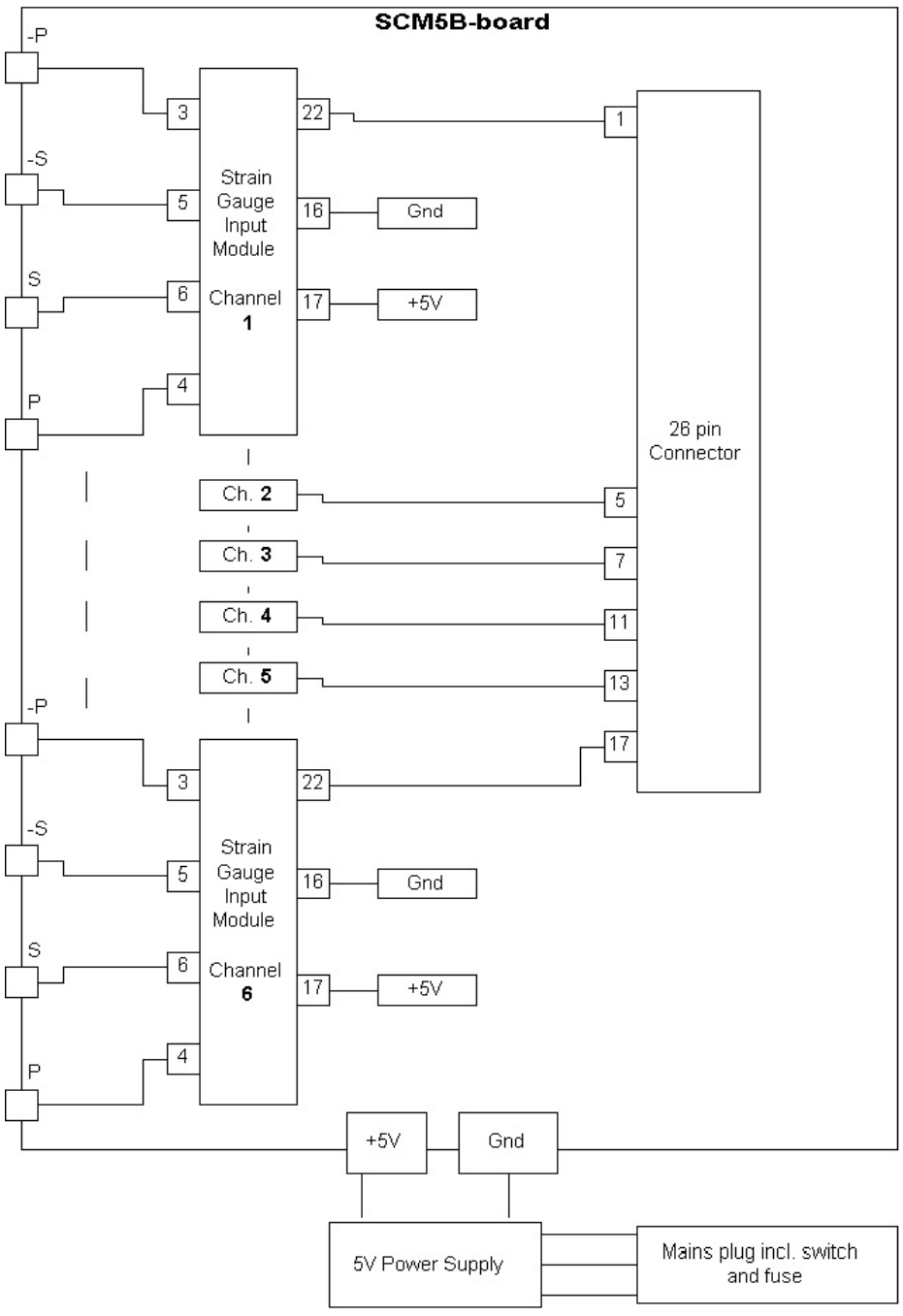

Figure 4-25 Outline of the amplifier box. The four inputs per channel seen on the left in the diagram are the same four as seen in the figure 17with the shunt calibrators. The six output BNC-plugs are connected to the 26-pin connector.

4.1.3.5 High Speed Imaging System

To compute the leaflet strains at high temporal and spatial resolution, a high speed camera system was used as described below.

4.1.3.5.1 Layout of the High Speed Imaging System

The instrument layout for the high speed imaging system used in this thesis is shown in Figure 4-26. It consists of a two high speed monochromatic frame grabbers equipped with a progressive scan CMOS sensor and macro lens with 105mm focal length which are connected to a camera link PCI bus interface with 4 GB buffer memory. The PCI bus provides an interface between the dual channel data acquisition system and the software drives on the computer hard drive. Detailed specifications and operating principles of each component are described in the following sections.

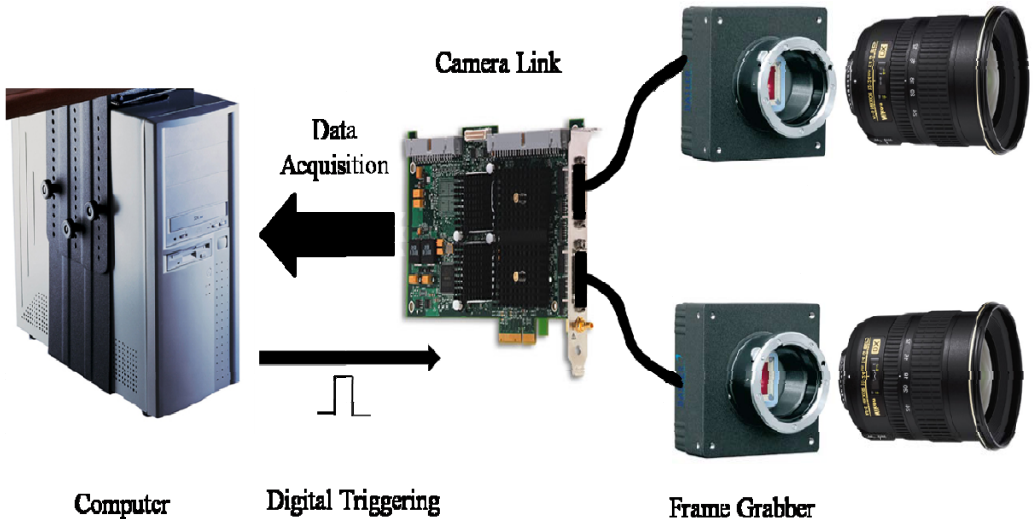

Figure 4-26 Layout of the high speed imaging system

4.1.3.5.2 Frame Grabbers

High performance digital cameras from Basler Corp, Germany (504 Series) shown in Figure 4-27, were used to image the valve leaflets in this study. The camera consists of a 1.3 megapixel (1280 X 1024 pixels) monochromatic progressive scan CMOS sensor, resulting in a pixel size of 12µ X 12µ. The progressive scanning capability of the imaging sensor enabled continuous image scanning, thus allowing acquisition of high resolution images of the mitral valve at 500 frames per second. The cameras were powered through a single source 12-VDC power supply. They communicated with the control unit through a Camera Link frame grabber system that allowed a maximum data transfer rate of 680 megabytes per second. The cameras have an F-type mount for lenses of required focal length.

Figure 4-27 Basler A510k frame grabber with a CMOS chip

4.1.3.5.3 Optical Lens

Two macro lenses from Nikon Corporation (Micro Nikkor 105mm f: 1-2.8) were used as they optimally fit the required focal length for imaging the valve leaflets. The optical components of the lens were made of glass and the design of the lens keeps the bore length constant at various magnifications. The aperture size could be manually adjusted to the desired size using an aperture ring on the lens, with the ability to adjust between f-stop values of 1 and 2.8. Due to the fixed focal length of the lenses, the cameras were mounted on two tripods whose location could be adjusted to obtain the desirable image clarity.

4.1.3.5.4 Data Acquisition System

A commercial package software (EPIX, EPIX imaging, Buffalo Grove, IL) was used to control the frame grabbers and to acquire and save the images to the computer. The software has the provision to adjust the exposure time, number of frames to acquire and the resolution at which to acquire them. To synchronize the image acquisition to the hemodynamics of the flow loop, an RS-232 cable was connected to the PCI bus port and a square wave corresponding to the beginning of systole was used as a trigger to acquire the high speed images. As the images are acquired they were stored in the temporary memory on the PCI card, and were later transferred as a series of TIFF files to the hard drive of the computer.

4.1.3.6 Ultrasound Imaging System

A real-time 3D ultrasound imaging system (Philips iE33 system, Philips Healthcare, Andover, MA) was used to acquire 3D and 2D tissue Doppler and color Doppler images of the valves in the left heart simulator. Two matrix array probes (X7-1 Pediatric Probe; X3-2 Adult Probe) were used that enable acquisition of 2D planes and of 3D volumes. The probes have a matrix of piezoelectric crystals that are sequentially timed to acquire multiple slices along the sagittal and longitudinal planes to reconstruct a 3D volume. The acquisition was timed with the hemodynamics of the left ventricular flow loop. A photograph of the imaging system with the two ultrasound probes is show in Figure 4-28 below.

Figure 4-28 (A) The Philips iE33 Ultrasound System; (B) The X7-2 and X3-1 probes used in this study

4.1.3.6.1 Ultrasound Probes

The ultrasound probes contain a 2D matrix of piezoelectric crystals that can be electrically excited to produce sound waves, which can be focused into the region of interest in the human body. In response to an applied excitation voltage, the piezoelectric crystals expand and generate sound waves of finite frequencies as shown in Figure 4-29A that are directed into the body. When the sound waves approach a tissue, they are reflected back and the pressure of the sound wave in turn makes the piezoelectric crystals generate a finite voltage as shown in Figure 4-29B.

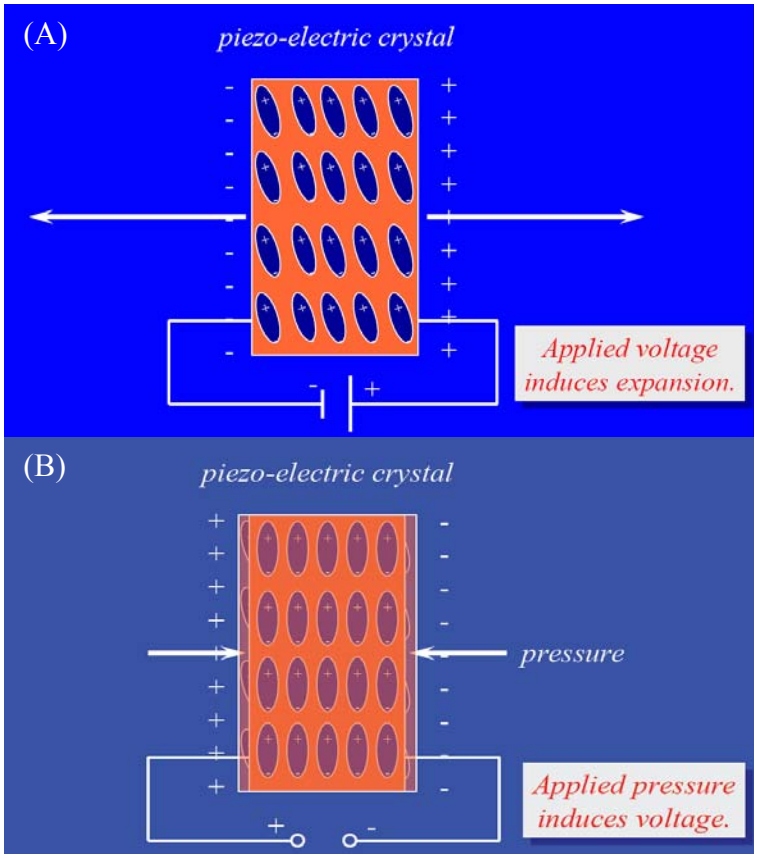

Figure 4-29 (A) The piezoelectric crystals in the ultrasound transducer generate sound waves upon expansion due to a finite electrical voltage applied to them; (B) The pressure wave generated due to reflection of sound waves from the human body induce vibrations in the crystals thus generating a voltage.

In this thesis, the X7-2 and X3-1 probes were used which could generate frequencies in the range of 7 to 2 MHz and 3 to 1 MHz respectively. Both probes have an array of 2400 crystals that can be sequentially excited to generate a live 3D rendering of the mitral valve, but at the same time generate 2D slices and color Doppler images as well. The X 3-1 probe was used mainly because the frequencies of the transducer matched the depth of imaging very well.

4.1.3.6.2 QLAB Software

The ultrasound images acquired using the matrix probes were transferred to a server, and analyzed using QLAB, licensed software from Philips Medical Systems (Andover, MA). The software allowed 3D viewing of the valve image, custom cropping along multiple planes, distance and angle measurement between structures, and also calculation of regurgitant volume by direct integration of flow through the traced regurgitant orifice. For all the experiments conducted in this thesis, both 2D and 3D echocardiographic images were recorded and images that are optimal for the required measurements were used.

CHAPTER 5

METHODS AND PROTOCOLS

In this chapter, the methods and protocols used to conduct the experiments in each of the specific aim are presented. Firstly, general protocols pertinent to valve selection, development of in vitro pathological valve models, and operation of the left heart simulator are presented. Secondly, technical details and protocols for surgical repair of each of the mitral valve lesions are discussed. Finally, the methods to acquire hemodynamic, echocardiographic and mechanics data are presented.

5.1 INTRODUCTION

The common objective of the experiments presented in this thesis is to understand the hemodynamics and mechanics of the mitral valve under pathological and post-procedural conditions. Firstly, models of different mitral valve lesions were mimicked by altering the anatomy of normal porcine mitral valves and thoroughly validated against clinical data. After rigorous validation of the disease model, various clinically relevant surgical techniques were used to repair the valves and post-repair valve hemodynamics and function were assessed and compared to the control conditions. On these lines, this chapter details the experimental design and protocols for each specific aim.

5.2 VALVE SELECTION AND PREPARATION

5.2.1 PORCINE MITRAL VALVE MODEL

In this thesis, mitral valves from fresh porcine hearts of varying sizes were used. The porcine heart is structurally and functionally very similar to the human heart, and with the limited availability of normal human hearts for research studies, we chose to use porcine hearts for these studies. The morphology of the porcine and human mitral valves depicted in Figure 5-1

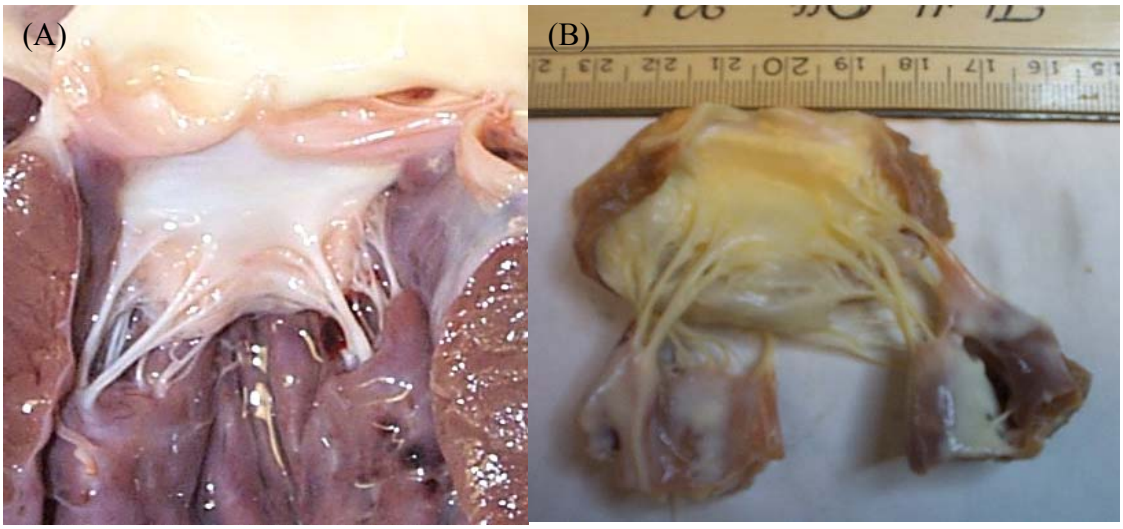

Figure 5-1 (A) Photograph of a porcine mitral valve demonstrating the anterior leaflet structure with the primary, secondary and tertiary chordae tendineae; (B) Photograph of a human mitral valve with similar leaflet structure and distribution of the chordae tendineae as that of the porcine mitral valve

Figure 5-1A shows the anterior leaflet of the mitral valve with the primary/ marginal chordae inserting into the free edge of the anterior leaflet and a set of secondary/basal/strut chordae originating from the same stem as the marginal chordae, but inserting into the base of the anterior leaflet. Another web of chordae insert into the commissural region of the anterior leaflet and directly into the mitral annulus closer to the commissures, called the tertiary/commissural chordae. In the human mitral valve shown

in Figure 5-1B, the overall distribution of chordae tendineae and the region of insertion into the anterior leaflet are identical. Previously, He et al. also compared the hemodynamic function of porcine and human mitral valves in a similar in vitro left heart simulator and obtained comparable leaflet kinematics, regurgitant volumes and leaflet coaptation lengths between the two species [112, 113]. Published data comparing the mechanical properties of human and porcine mitral valve chordae tendineae from Kunzelman et al. [39, 63] and Veseley et al. [35-38] also showed similarity between the valve material properties, further strengthening the choice of porcine mitral valves for this study.

5.2.2 VALVE SELECTION

Fresh porcine hearts were obtained from the local abattoir (Holifield Farms, Covington, GA) and transported to the laboratory within 2 hours of slaughter. In the laboratory, the hearts were cleaned under warm water to remove blood clots within the ventricular cavity and preserved in 0.9% vol/vol saline solution. The membranous pericardial sac surrounding the heart muscle was removed and the left atrium was carefully excised at its base, exposing the mitral valve as shown in Figure 5-2A. To maintain consistency between the size of the valves used and the gross anatomy of the valve, an annuloplasty ring sizer (Physio® Annuloplasty Ring, Edwards Lifesciences®, Irvine, CA) was used to measure the size of the anterior leaflet of the mitral valve as shown in Figure 5-2B. Upon identifying valves of similar sizes, a longitudinal incision was made through the aortic valve along the left anterior descending artery until the apex of the heart. This incision opens the left ventricular cavity as shown in Figure 5-2C,

exposing the entire mitral valve structure. The valve is carefully inspected so that there are no anatomical malformations, ruptured chordae tendineae or multiple diffused papillary muscle heads as shown in Figure 5-2D.

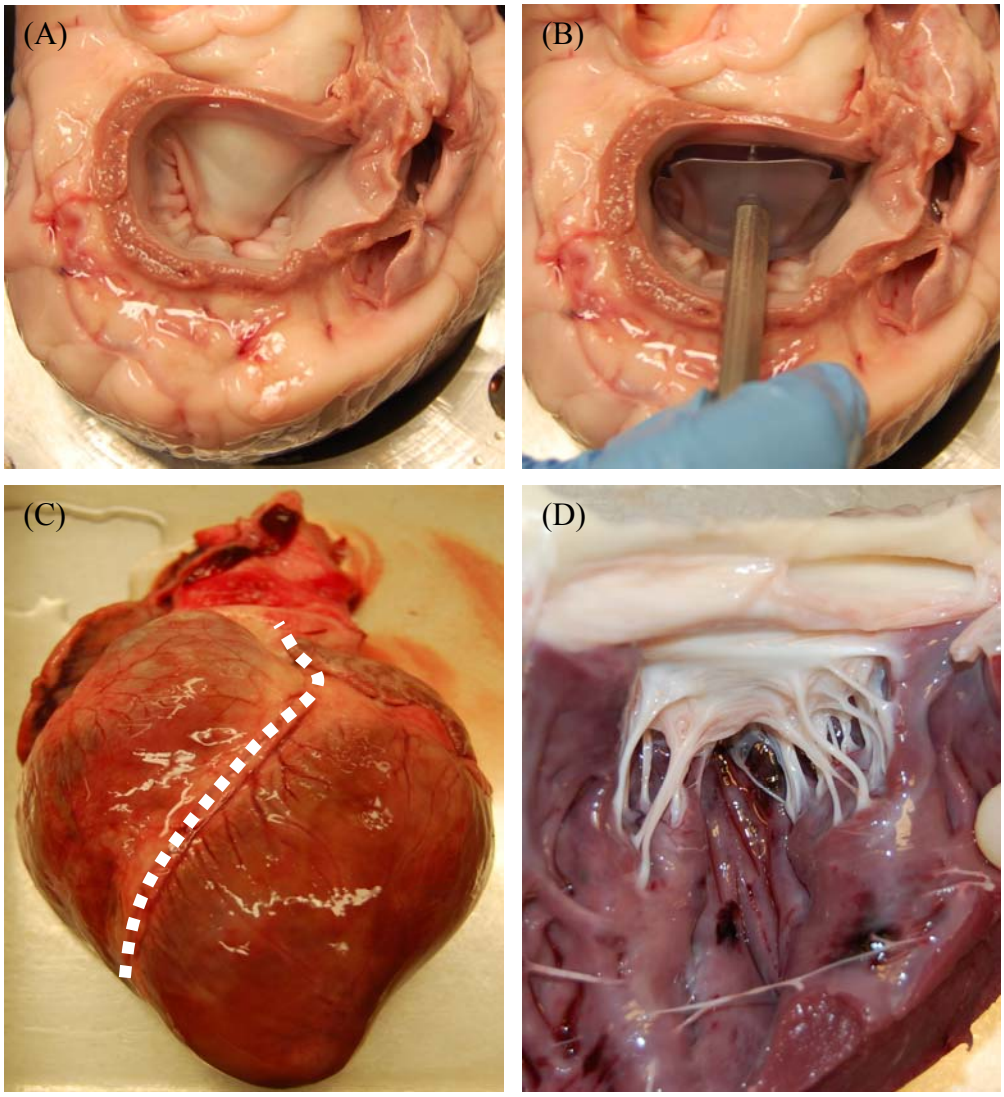

Figure 5-2 (A) Atrial face of the mitral valve exposed after excising the left atrium; (B) Sizing the mitral valve using the annuloplasty ring sizer; (C) Incision made along the left anterior descending artery of the heart until the apex to expose the mitral valve subvalvular apparatus; (D) Entire mitral valve structure exposed for examination for any malformations or ruptured chordae

5.2.3 VALVE EXTRACTION

After choosing the hearts with mitral valves of required sizes, they were carefully extracted from the heart while preserving the annular and sub-annular geometry intact. Using a scissors, the mitral valve was separated from the left atrium at the level of the annulus and using a scalpel the two papillary muscles were carefully separated from the left ventricular myocardium. After extracting the valve, the remaining myocardium surrounding the mitral annulus was trimmed to a thin layer with utmost care to avoid cutting through the mitral leaflets. 5mm of the left atrial tissue surrounding the mitral annulus was left behind, to enable suturing the mitral valve onto the silicone annulus shown in Figure 4-3. The anterior leaflet surface was also carefully cleaned by removing the non-coronary aortic leaflet and trimming the fibrous trigones until flush with the non-fibrous anterior annulus. The mitral valve at different stages of the extraction process is depicted in Figure 5-3.

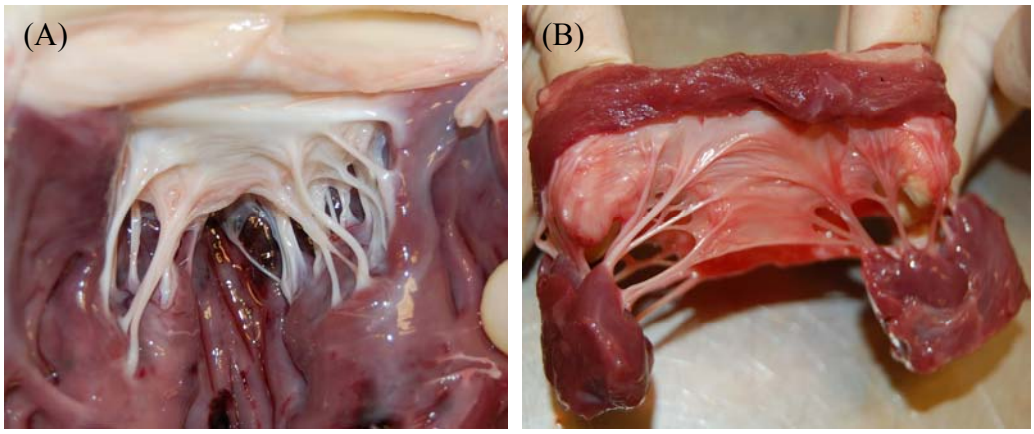

Figure 5-3 (A) Mitral valve exposed but before explantation from the heart; (B) Extracted mitral valve with the annular and sub-annular components intact

5.2.4 VALVE PREPARATION

Upon extraction, the mitral valve annulus loses its native D-shape and to ensure that the valve is appropriately sutured onto the silicone annulus, five positioning knots were placed at the two trigones, the two commissures and at the annulus along the central posterior cusp as shown in Figure 5-4A. Once the valve is positioned, a preliminary test for valve closure was conducted by pressing the anterior and posterior leaflets to coapt. If the valve was either too undersized or the leaflets were abnormal, they were excluded from the study. After selecting an appropriately sized valve, it was sutured onto the silicone annulus in a continuous loop fashion to ensure firm attachment of the mitral annulus to the silicone ring without kings or openings in the annular suture line as shown in Figure 5-4B. The papillary muscles are then enclosed in Dacron®, and two small Teflon® rings are sutured onto the base of the muscles to mount the valve onto the papillary muscle fixtures in the left heart simulator.

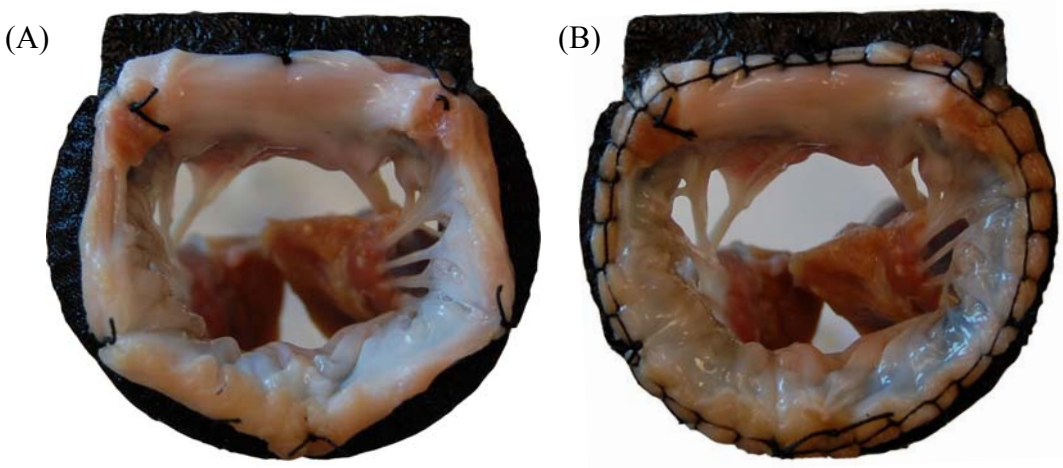

Figure 5-4 (A) Extracted mitral valve positioned onto the D-shaped silicone annulus using positioning sutures; (B) The mitral valve after suturing onto the annulus using a continuous suture method

5.3 IN VITRO LEFT HEART SIMULATION – OPERATION AND CALIBRATION

The left heart simulator was maintained regularly, with routine maintenance procedures involving replacement of the rubber gaskets between the walls of the ventricular and atrial chamber to reduce fluid leaks and pressure loss, replacing the screw studs and wing nuts as they tend to rust from contact with saline, and routinely clean the bevel gears in the papillary muscle system for smooth rotation. Specific protocols for calibrating the pressure transducer, flow transducer and the C-ring force transducer are presented in the following sections.

5.3.1 PRESSURE TRANSDUCER CALIBRATION

The Validyne® differential pressure transducer was calibrated at monthly intervals and tested for stability as well. Figure 5-5A shows a schematic of the pressure transducer, with the two inlet valves (yellow) and the two bleed valves (blue). The inlet valves are three-way leur lock valves, one end of which are connected to the inlet of the transducer, one end is connected to a manometer and one end to a syringe filled with saline. The bleed valves are three-way leur lock valves that remove air bubbles caught in the transducer and ensure that the inner chambers of the transducer are completely filled with saline. Electrical output from the transducer was connected to the signal conditioner and the value on the digital display was zeroed and the span was set at 50%. A voltmeter was then connected to the output of the signal conditioner, to measure the actual voltage output to the applied pressure head.

The input valves were then connected to the two arms of a U-tube manometer (‘positive’ arm and ‘negative’ arm) shown in Figure 5-5B and the two tubes were filled with saline upto 185mm of the column. Both the columns were equally filled with saline upto 190mm first, and to remove any air trapped in the chambers both the columns were bled to 185mm mark. After removing the air and ensuring both the columns of the manometer were stable at 185mm mark on the scale, the transducer was zeroed again. While keeping the positive arm at 185mm, the level of saline in the negative arm was adjusted to 163.1mm, 136.1mm, 108.8mm, 81.6mm, 54.4mm, 27.2mm and 0mm respectively. At each saline level, the voltage output from the signal conditioner was recorded. After reaching 0mm, the negative arm is filled back to 185mm Hg and the procedure was repeated with the positive column at 163.1mm and 136.1mm and the voltage output was recorded. The calibration was performed thrice, and the average voltage output for each pressure reading was plotted against each other. A linear regression fit was performed through the data and the slope of the line was used as the calibration value for the transducer.

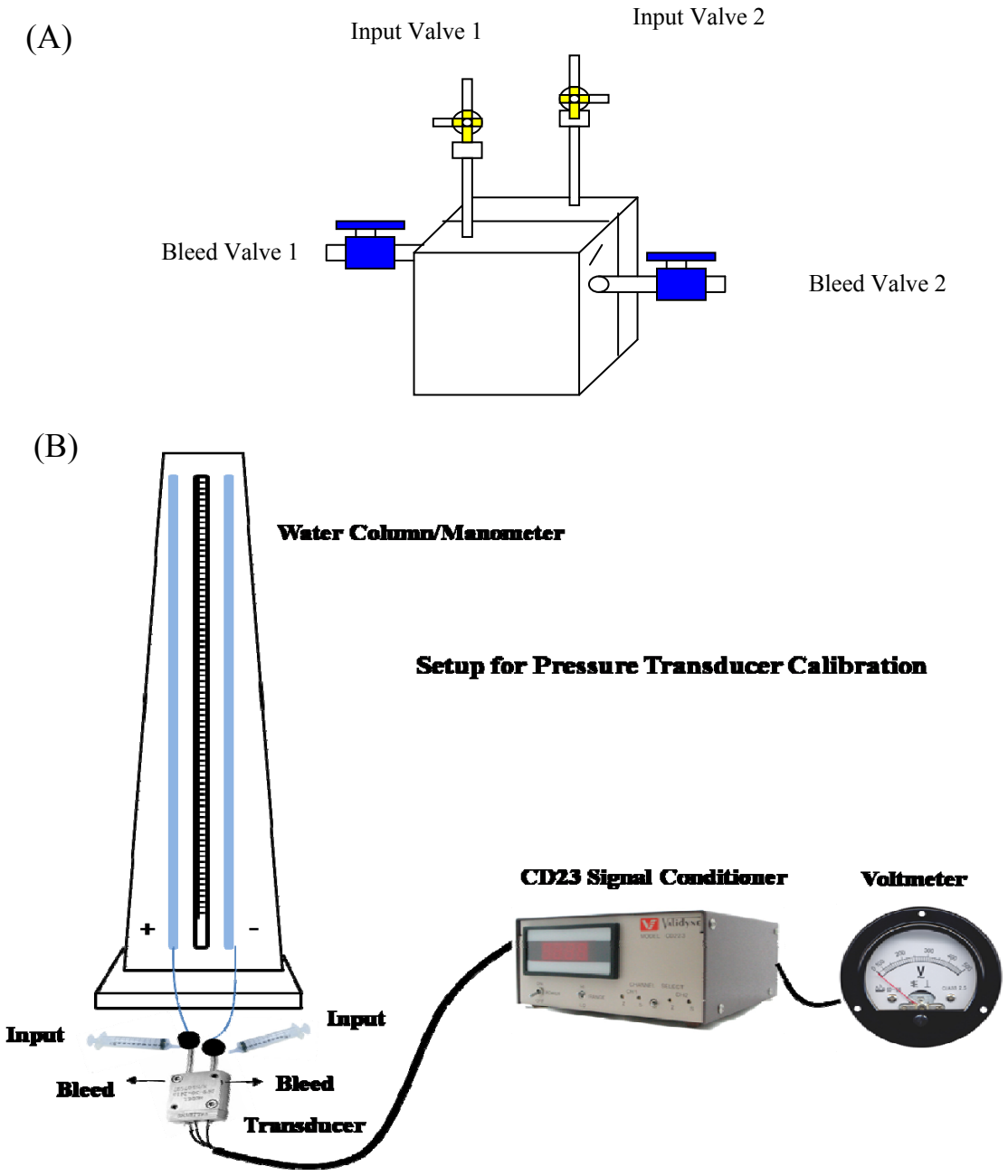

Figure 5-5 (A) Schematic of the pressure transducer depicting the inlet and bleed valves on both the chambers; (B) Setup for the pressure transducer calibration where the transducer is connected to a water column

Figure 5-6 shows an example calibration curve performed on the Validyne® pressure transducer. The data presented are the average of 3 trials at each pressure. Since the transducer is zeroed when the pressure is zero, the linear regression fit is forced to pass through the origin thus making the intercept zero.

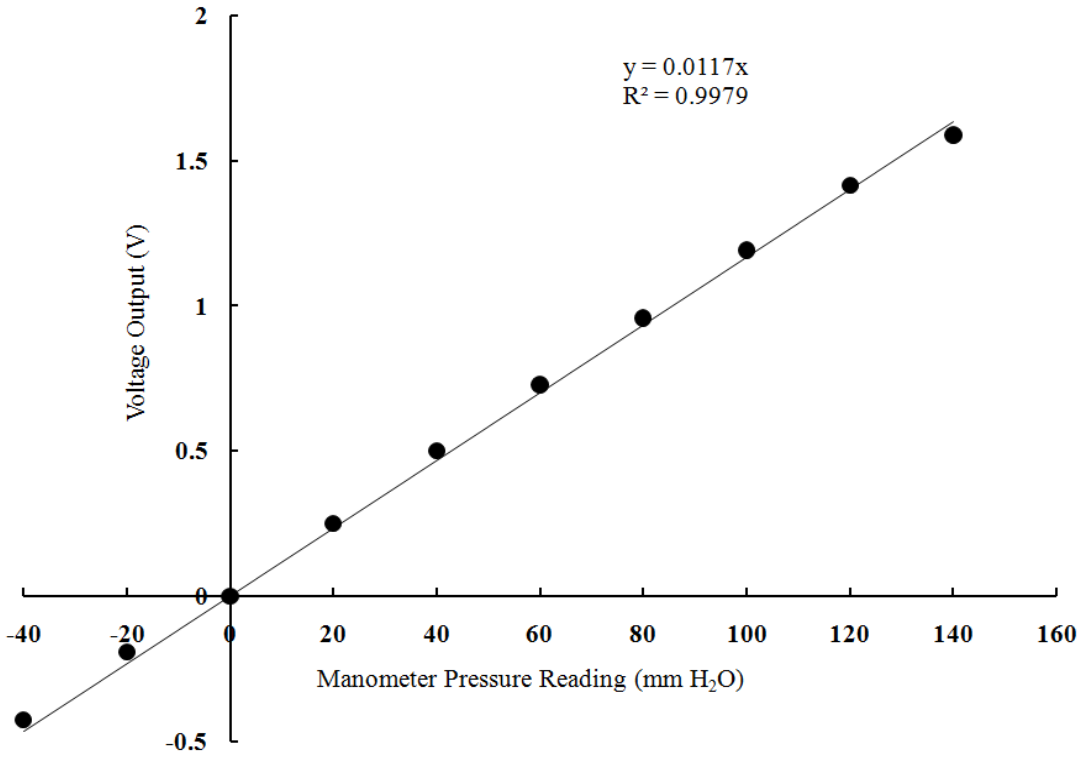

Figure 5-6 A representative calibration curve depicting the relationship between the imposed manometer pressure, and the measured voltage output on the multimeter

5.3.2 FLOW TRANSDUCER CALIBRATION

The flow probe and amplifier were calibrated at regular intervals to ensure accuracy and stability of the measurements. The square wave electromagnetic flow has high sensitivity and adequate frequency response, with a selectable frequency response upto 100Hz. The amplifier has separate recorder output that can provide mean and pulsatile data simultaneously, with protective circuits to detect large deviations from

normal operating parameters. The range of accuracy for the flow measurements is between ± 5% after a 30-minute warm up period.

The voltage output of the flow probe was calibrated against measured flow rates in a closed loop system, in which a calibrated rotameter was used. A schematic of the flow loop is shown in Figure 5-7, where the electromagnetic flow probe is connected in series with a centrifugal pump and a rotameter. Firstly, the rotameter was calibrated by pumping saline through it for 60 seconds and collecting the saline draining from the rotameter into a graduated flask, while recording the position of the rotameter float on the vertical scale. This bucket-and-stop watch method helped in validating the accuracy of the rotameter for the given fluid media. The rotameter calibration was performed at different flow rates, and a linear regression was performed between the "calculated" flow rates from the bucket-and-stop watch method, and the "measured" flow rates from the rotameter as shown in Table 5-1 and Figure 5-8. In the second step, the electromagnetic flow probe was connected to the square wave electromagnetic amplifier, and the power knob on the amplifier was positioned at null. Using the "null" knob, the digital readout on the amplifier was adjusted to "zero". The power knob is then positioned on "balance" and the digital readout is adjusted to "zero" again, as it typically shifts a little in this position. In the final step, the power knob on the amplifier is positioned to "+", and the frequency response to 10Hz and the digital readout is tuned to "zero" again. While performing the initial "zeroing", care is taken to ensure that the centrifugal pump is switched off, air bubbles are removed and there is no flow through the closed loop. A voltmeter was then connected to the "PULSE" channel on the back of the amplifier to record the exact voltage output from the amplifier after signal conditioning and filtering. The centrifugal

pump was then powered through a 120V wall power supply, and connected to a rheostat that allowed precise control over the rotational speeds of the pump impeller and thus control the flow rates in the loop. The voltage output of the flow probe was calibrated against 5 flow rates in the forward flow direction, and 5 flow rates in the backward flow direction as shown in Figure 5-10 . Each calibration was repeated twice and the measured voltage was averaged. After completing the calibration, the mean voltage measurements were plotted against the rotameter measurements and a linear regression analysis was performed, with the gradient of the linear regression fit considered as the "calibration" value.

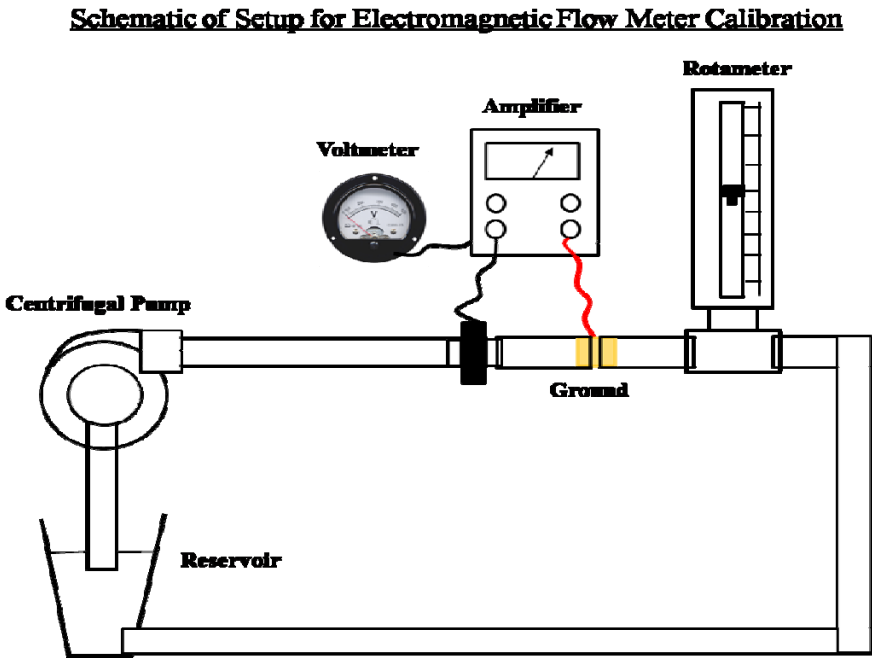

Figure 5-7 Schematic of the flow loop setup to calibrate the square wave electromagnetic flow probe and the amplifier against a standard measurement from a flow rotameter

Table 5-1 A illustrative example of the flow rate measurements from the bucket and stopwatch method and the rotameter

Rotameter calibration with Saline solution				5/31/2005
Volume	Time	Flow rate (L/s)	Flow rate (L/min)	Rotameter
2920	10.23	0.285434995	17.12609971	29.5
1860	17.24	0.107888631	6.473317865	10.5
2900	18.01	0.161021655	9.661299278	16
3060	14.75	0.207457627	12.44745763	21
3040	12.06	0.252072968	15.12437811	25.5
3340	10.79	0.309545876	18.57275255	31.5
2075	19.77	0.104957006	6.297420334	10.5
2700	17.38	0.155350978	9.321058688	15.5
2325	11.53	0.201647875	12.09887251	20
2562.5	9.98	0.256763527	15.40581162	25.5
2990	9.5	0.314736842	18.88421053	31.5
3480	6.76	0.514792899	30.88757396	52
3120	5.17	0.603481625	36.20889749	60
3080	5.17	0.595744681	35.74468085	59.5
2700	10.72	0.251865672	15.1119403	25
2325	11.52	0.201822917	12.109375	20
2200	14.79	0.148749155	8.92494929	15
2125	21.02	0.101094196	6.06565176	10

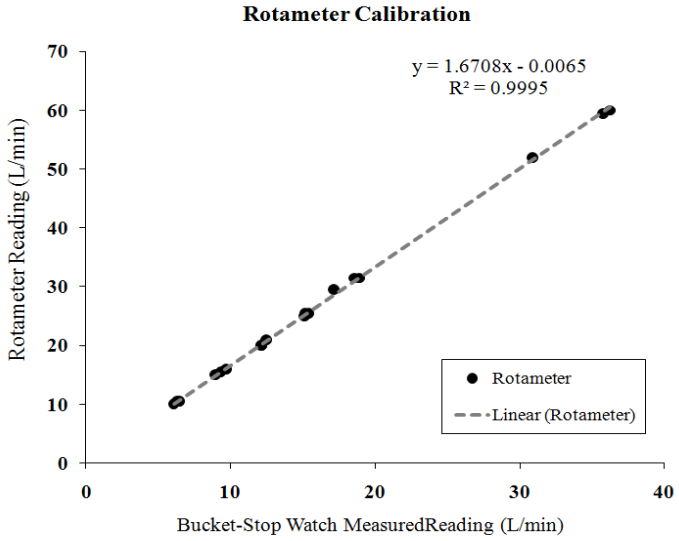

Figure 5-8 A typical rotameter calibration curve showing the correlation between the rotameter reading and the bucket-stopwatch measurement

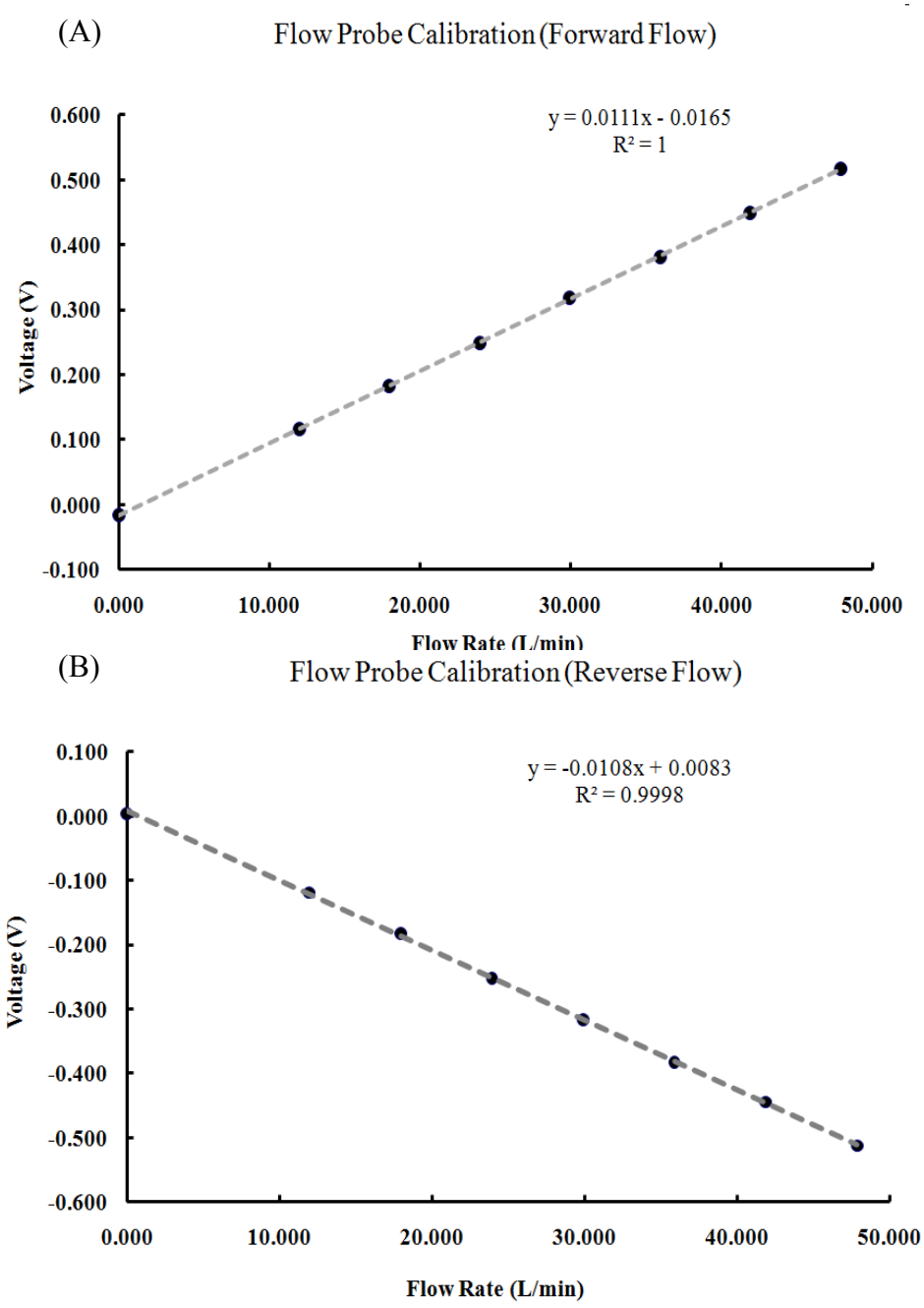

Figure 5-10 (A) Representative calibration plot for forward flow in the electromagnetic flow probe; (B) Representative calibration plot for backward flow in the flow probe

5.3.3 C-RING FORCE TRANSDUCER CALIBRATION

Due to the miniature size and fragility of the strain gauges used to construct the C-ring force transducer, they are regularly calibrated for stability and sensitivity. The C-ring transducer is part of a Wheatstone half bridge, thus if the strain gauge resistances are not within the prescribed range of 350 ± 10Ω, the bridge circuit becomes unstable. The deviation in the resistance should then be eliminated using a shunt potentiometer provided on each channel. After "zeroing" each transducer and the corresponding channel, the voltage output of the transducer is calibrated against standard weights. The C-ring transducer is suspended from a steady frame as shown in Figure 5-11, using thin 134 AWP wire (Measurements Group, NC). The thin 134 AWP wire is passed through the top hole of the C-ring and tied into a loop to suspend the ring from the frame. A second wire is similarly passed through the bottom hole of the C-ring and tied into a loop to suspend weights. Pre-measured weights were suspended in the lower loop using shortened polyester 2-0 suture (E-sutures, NY), with the tapered needle of the suture bent into a hook.

The sensitivity of the C-ring transducer is measured at various static weights, with the applied force on the transducer defined by Equation 5-1:

$$F = (m)\,(a) \qquad \text{Equation 5-1}$$

where F = force acting on the C-ring transducer

m = mass

a = acceleration due to gravity (9.8 m^2/sec)

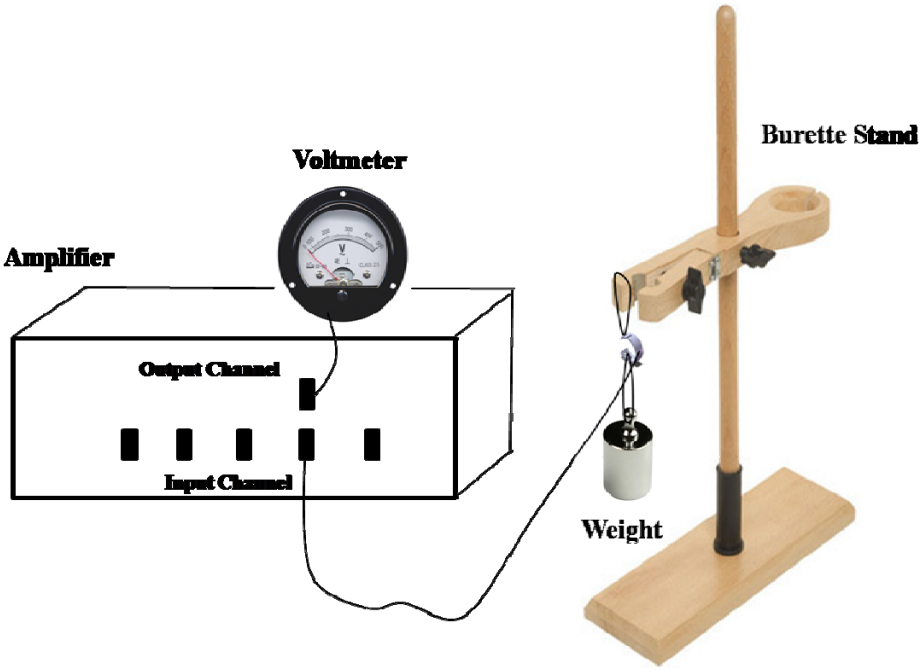

Figure 5-11 A schematic of the calibration setup for the C-ring force transducer

The transducer is connected to one of the 6 channels on the amplifier, and a voltmeter (Fluke, 27) is connected to the corresponding output channel. The C-ring is then positioned on the steady frame, and without suspending any loads the output voltage on those channels is slowly adjusted to zero by turning the potentiometer using a flat head screwdriver. After "zeroing" the transducers, four different weights are suspended from the transducer and the corresponding voltage output from the transducer for each weight is recorded. The measurements are conducted thrice for every weight and the voltage output measured for the three trials is averaged, and a calibration plot with the suspended weights on the abscissa and the voltage output on the ordinate was plotted. A linear regression fit was performed through the plotted data, and the slope of the line was considered as the "calibration" coefficient for that C-ring transducer for that particular

channel. Each transducer was thus calibrated for a corresponding channel, and was used for that channel alone as the sensitivity and stability of the potentiometers on each channel varied slightly. A representative chart of a C-ring calibration is shown in Table 5-2 and a calibration plot is shown in Figure 5-12.

Table 5-2 A representative tabulation of the weights used and the corresponding average voltage output measured from the C-ring transducer

Weight (gm)	Force (N)	Voltage (V)
0	0	0
133	1.31	0.3
146	1.44	0.36
267	2.62	0.66
294	2.89	0.73

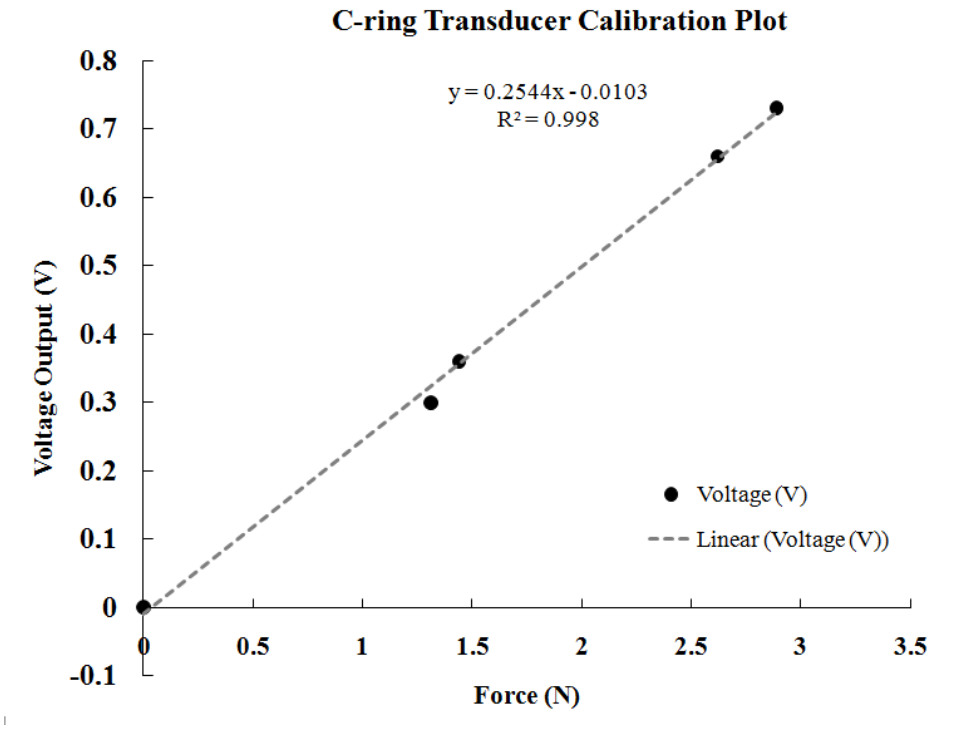

Figure 5-12 A representative calibration plot for the force transducer showing the correlation between voltage output and applied force

Though the strain gauges were sealed in a multi layer polymer coating and isolated from moisture, when completely immersed in saline they tend to drift due to leakage currents. The leakage currents offset the Wheatstone bridge, resulting in drifting of the C-ring from its baseline zero point. Thus, after suturing the C-rings onto the mitral valve chordae tendineae and mounting the valve into the left heart simulator, the transducers were "zeroed" again after complete immersion in the saline solution. Thus, the baseline for all the force measurements using C-ring transducers was with the mitral valve in the diastolic open position in the left heart simulator, with minimal to no forces acting on the chordae tendineae. Typically, the voltage output of the transducer was within a range of ± 200 mV, which falls sufficiently within the ± 5V range of the data acquisition system.

5.3.4 HEMODYNAMIC DATA ACQUISITION AND ANALYSIS

All the data acquisition was performed using the hardware described in Chapter 4. Custom software developed in the laboratory, DAQANAL (Labview 5.1, National Instruments, Austin, TX) was used as an interface between the data acquisition hardware and computer. DAQANAL is a multi-channel acquisition system in which data can be simultaneously recorded from 8 analog channels, either continuously or synchronized through a digital trigger. The software was equipped with frequency filters, signal smoothening modules and bandwidth adjustment to record the data appropriately. The data are stored in a temporary buffer by the software, which sequentially writes the data to the desired directory on the computer. Few screenshots of the software are shown in Figure 5-13.

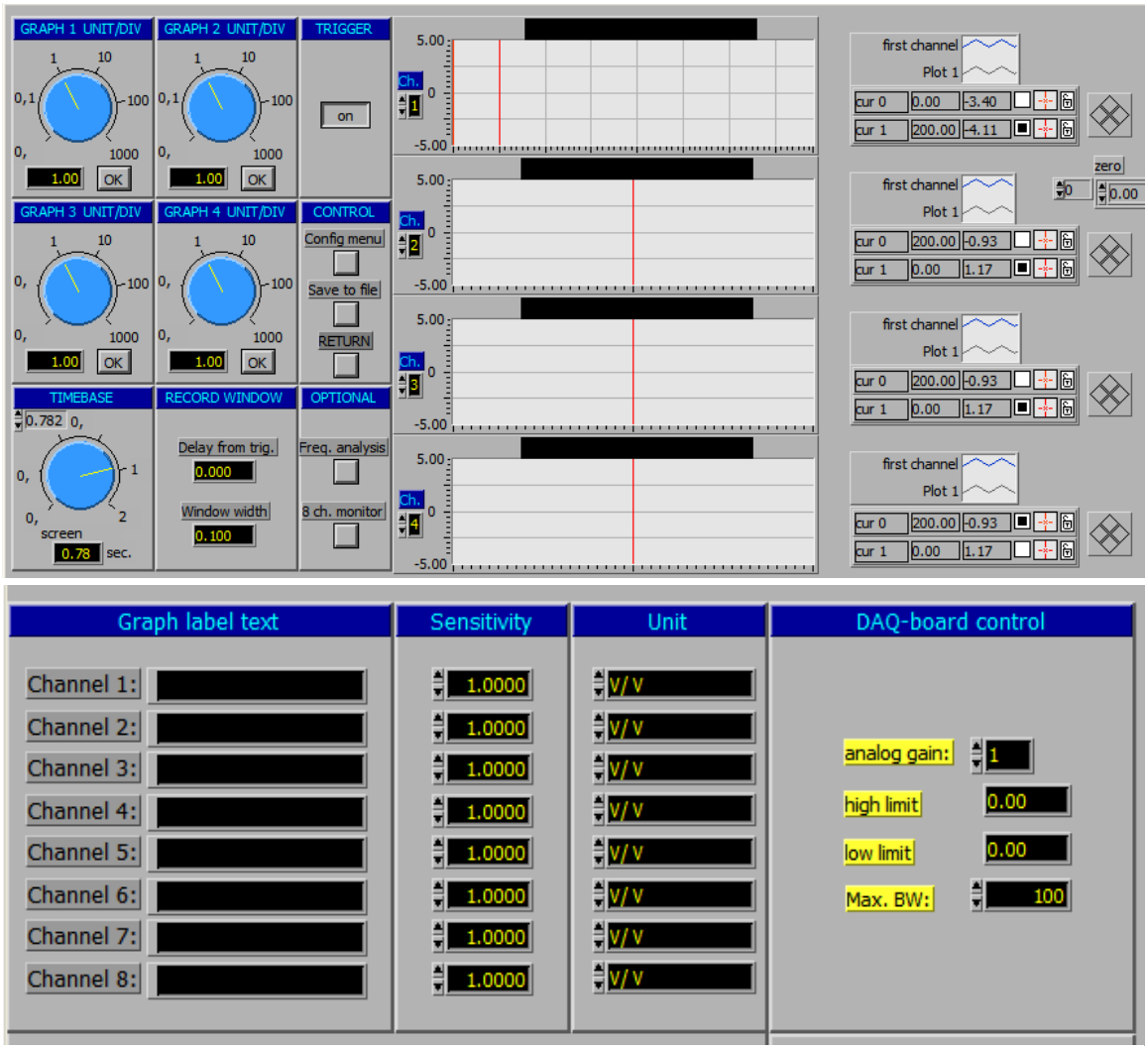

Figure 5-13 Screenshot of a window in DAQANAL software used to input signal conditioning parameters, calibration coefficients for each channel based on the hardware connected to the channel, with the ability adjust the maximum bandwidth of the signal.

In this program, a maximum of 2 channels can be simultaneously monitored in real time in a quantitative fashion, even though qualitatively all 8 channels can be visualized on the same window shown in Figure 5-14 .

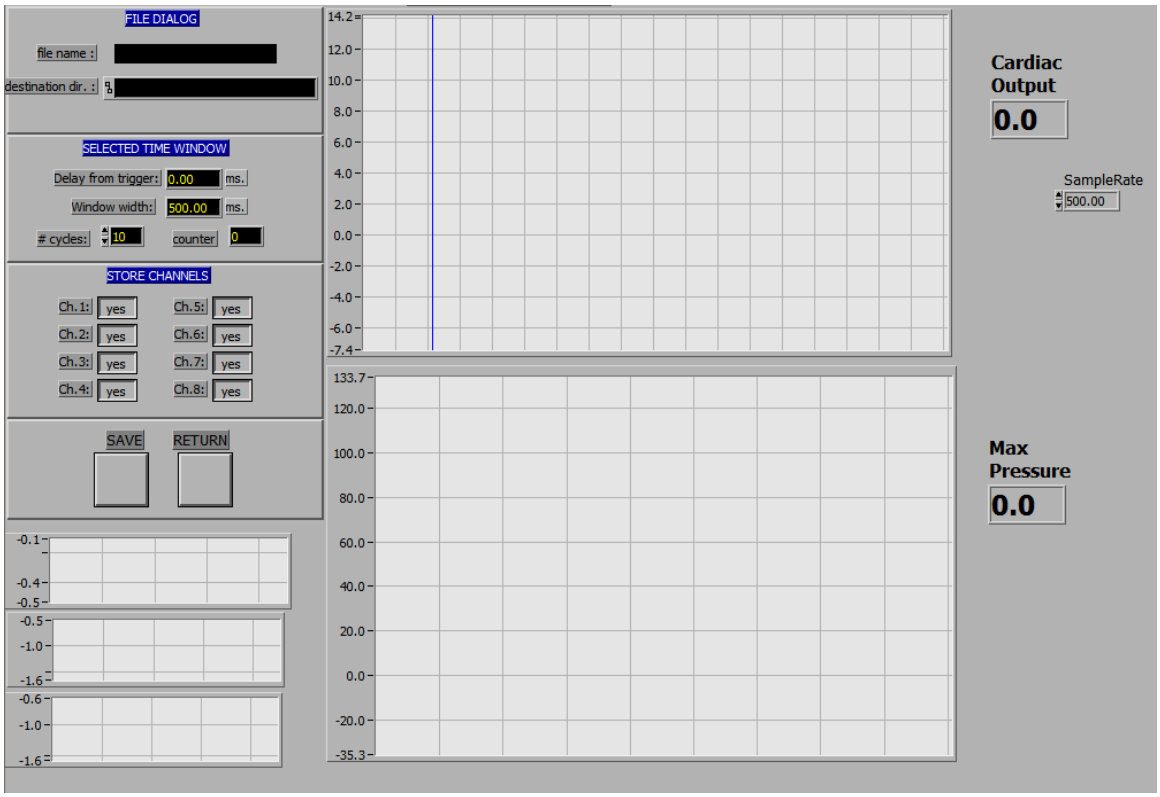

Figure 5-14 Screenshot of the window to monitor and store data in DAQANAL

Upon acquiring and storing the data to the hard drive, the analysis module of DAQANAL is used to average the data over multiple cardiac cycles, and perform numerical integration of the data to calculate the regurgitation volume, net stroke volume, gross stroke volume, regurgitation fraction and other derived parameters from the recorded data. Fourier analysis of the data can also be performed, and probability distributions plots for the data can be plotted as required. Figure 5-15 shows screen shots of the program to calculate the regurgitation volume and stroke volume using numerical integrating of the flow curve. The red and the green sliders allow traversing the curve and defining the bounds of the curve that need to be integrated.

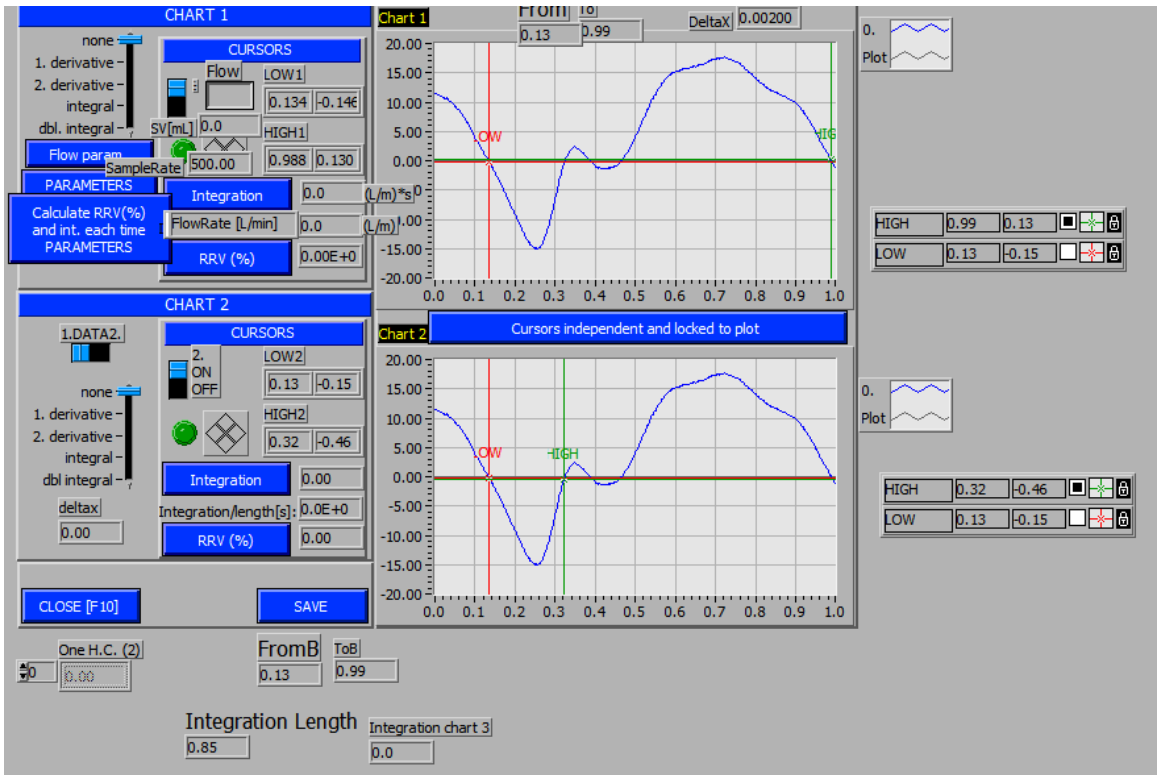

Figure 5-15 Screenshot of the analysis module to calculate the regurgitation volume and stroke volume from the flow curve

5.3.5 ECHOCARDIOGRAPHIC DATA ANALYSIS

Echocardiographic data analysis was performed using QLAB 5.1 (Philips Medical Systems, Andover, MA) under a licensed agreement, or using PMDSVIEW 2.1 (Philips Medical Systems, Andover, MA). For all echocardiographic analysis, a double-blinded multi user analysis was performed to consider the inter-user variability and avoid any bias in the data analysis. All the echocardiographic acquisitions were performed at the same depth and along identical planes, so that comparison of the data between different experimental conditions was possible.

5.4 PATHOLOGICAL MODELS OF MITRAL VALVE LESIONS

The crux of this thesis work weighted significantly on the development of bench top models of mitral valve defects/pathologies in congenital, degeneration and ischemic mitral valve lesions. As previously mentioned, porcine mitral valves with normal anatomy and material properties were selectively altered to mimic each pathological lesion. Upon altering the valve components or anatomy, it was mounted in the in-vitro left heart simulator and tested under pulsatile hemodynamic conditions so that videos and echocardiographic images of the valve could be obtained and compared to human data, to validate the accuracy of the model to clinical scenario. Each of the lesions developed in this study are explained in detail in the following sections.

5.4.1 CLEFT MITRAL VALVE IN CONGENITAL ATRIOVENTRICULAR CANAL DEFECT

The main anatomical features of a cleft mitral valve in humans with complete atrioventricular canal defects are:

[a] Leaflet Defects:

- wedge shaped cleft in the central part of the anterior leaflet
- smaller posterior leaflet with the commissures moved posteriorly

[b] Annular Defects:

- Oval shaped annulus, with a flat anterior and ovoid posterior annulus

[c] Sub-annular Defects:

- Scooped ventricular geometry with posterior and lateral displacement of the papillary muscles

- Both papillary muscle heads are closer to one another than in normals

To mimic these anatomical deficiencies, the native porcine mitral valve anatomy was altered in sequential steps:

Step 1 Reduction in Posterior Leaflet Size

To reduce the posterior leaflet area and create a triangular shaped leaflet, a quadrangular section of the leaflet was resected from the P2 cusp of the posterior leaflet as shown in Figure 5-16. Following resection, the annulus at this region was plicated outwards and sutured together using a compression stitch with 3-0 silk sutures. Once the opposite edges of the resected region moved closer after annular plication, a 4-0 prolene suture was used to carefully approximate the edges in an interrupted fashion. Several interrupted knots were used to approximate the edges, such that there were no crevices or openings between the knots that may lead to regurgitation.

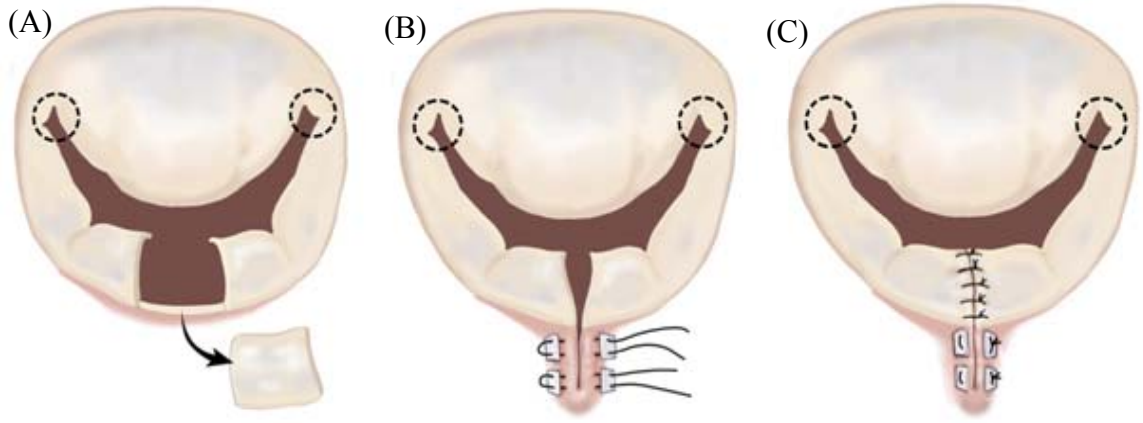

Figure 5-16 (A) Quadrangular resection of the posterior leaflet of the porcine mitral valve, with the dotted circles depicting the position of the papillary muscles; (B) Plication of the annulus at the region of resection and suturing, which brings the free edges closer; (C) Final leaflet shape after closing the free edges in an interrupted fashion

Step 2 Creating Wedge Shaped Anterior Leaflet Cleft

After reducing the size of the posterior leaflet and reconstructing it, a wedge shaped cleft was made in the anterior leaflet as shown in Figure 5-17. The cleft was made by first section the anterior leaflet along a straight line dividing the A2 cusp, and the A2 was divided into two leaflets. Then, two cuts were made by trimming the free edges starting from the annulus to the free edge, such that the base of the cleft at the free edge was $1/6^{th}$ the total height of the anterior leaflet. After creating the cleft, the papillary muscles were moved towards each other as described in Step 3.

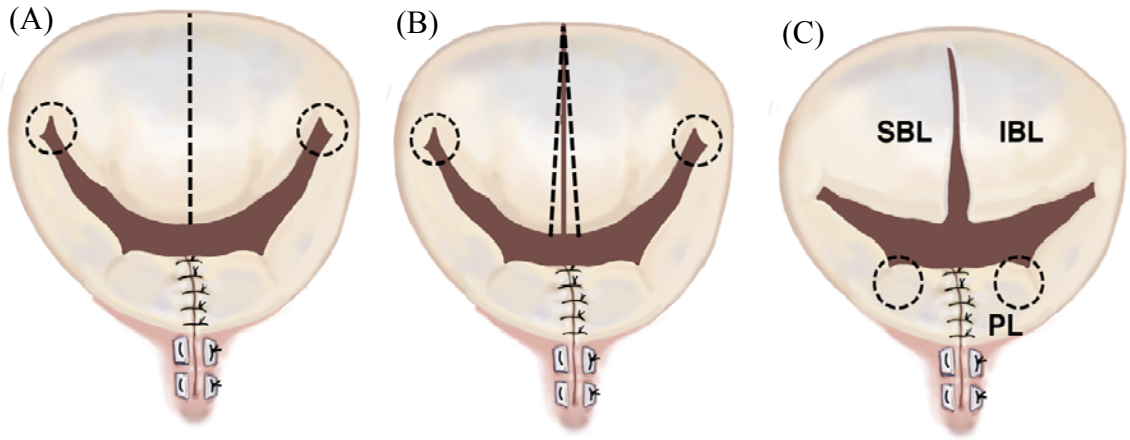

Figure 5-17 (A) A straight incision was first made along the dotted line at the center of the anterior leaflet from the free edge to the annulus; (B) Two more incisions were made along the free edges such that the base of the cleft is a sixth of the height of the cleft, which is equivalent to the height of the anterior leaflet; (C) Anterior cleft after trimming, with the papillary muscle positions moved towards the posterior leaflet from the commissures and laterally towards each other to depict the scooped geometry of the ventricle

Step 3 Simulating the Scooped Geometry of the Ventricle

To simulate the scooped geometry of the ventricle and pathological position of the papillary muscles, both the muscles were displaced posteriorly and laterally towards each other. From a short axis perspective of the left ventricle, Figure 5-18 shows the displacement of the papillary muscles in the ventricle to simulate the smaller and severely curved ventricular geometry in atrioventricular canal defect patients.

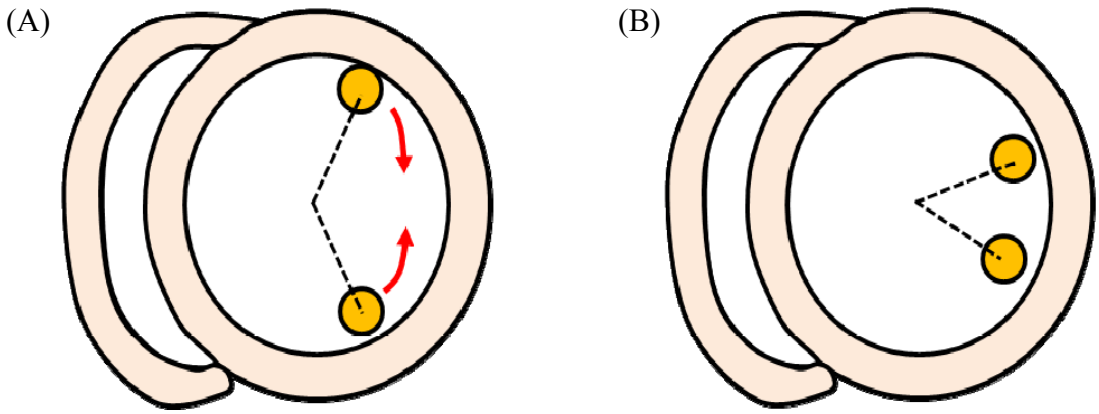

Figure 5-18 (a) Papillary muscles depicted as ● in their normal positions with the red arrows showing the direction of their displacement to mimic the canal defect conditions; (b) Pathological positions of the papillary muscles after posterior lateral displacement.

5.4.2 POSTERIOR LEAFLET PROLAPSE IN FIBROELASTIC DEFICIENCY

Posterior leaflet prolapse in fibroelastic deficient mitral valves typically occurs due to rupture of the marginal chordae tendineae inserting into the free edge of the P2 cusp. These chordae being the thinnest and most stretched due to motion of the free edge, are prone to rupture in this disease wherein absence of fibrillin-1 gene results in degeneration of the mechanical properties of the native mitral valve leaflet. Rupture of these chordae results in isolated prolapse of the P2 free edge into the left atrium, though the leaflet structure typically remains unchanged and comparable to normal subjects. In

this study, acute posterior leaflet was created by selectively transecting the marginal chordal web inserting into the free edge of the posterior leaflet from both the papillary muscle heads as shown in Figure 5-19A. This chordal transection resulted in prolapse of the P2 cusp into the atrium as shown in Figure 5-19 B-C.

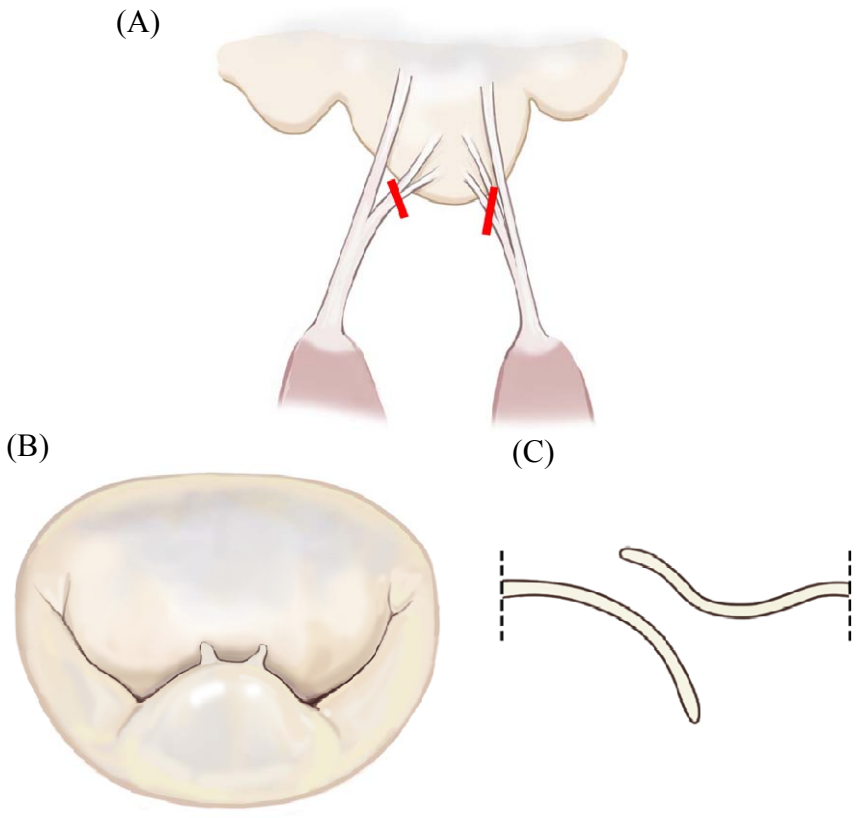

Figure 5-19 (A) The red lines depict the transection of the marginal chordal web inserting into the free edge of the posterior mitral leaflet; (B) Isolated P2 prolapse resulting from marginal chordal transection; (C) A side sectioned view of the valve leaflets showing prolapse of the posterior leaflet and its movement above the anterior leaflet resulting in an oblique regurgitation jet

5.4.3 ACUTE ANTERIOR LEAFLET PROLAPSE MODEL

Similar to posterior leaflet prolapse, rupture of the anterior marginal chordae tendineae is seen in patients with fibroelastic deficiency. Identical in mechanisms, rupture of the marginal chordae that insert into the A2 cusp of the anterior mitral leaflet result in isolated prolapse of the A2 segment. In this study, anterior marginal chordal rupture was induced by transecting those chordae, which in turn resulted in prolapsing of the A2 cusp into the left atrium as shown in Figure 5-20, and an oblique posteriorly directed regurgitation jet.

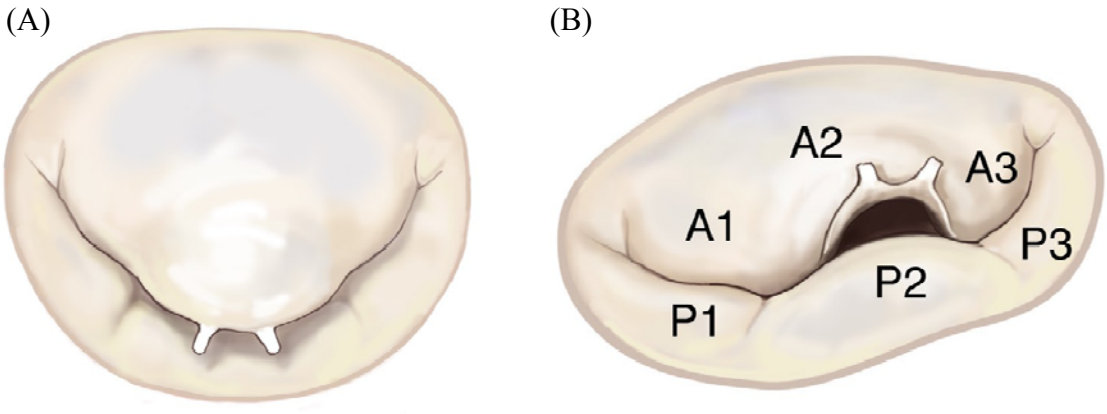

Figure 5-20 (a) Anterior leaflet prolapse resulting from transecting the marginal chordae tendineae inserting into the free edge of the A2 cusp; (b) An isometric view of the prolapsing anterior leaflet showing the movement of the A2 free edge into the atrium thus creating a regurgitation orifice

5.4.4 ANNULAR SHAPE CHANGES IN FUNCTIONAL MITRAL REGURGITATION

The mitral annulus assumes a physiological saddle shape in normal subjects, however flattening of the mitral annulus is commonly seen in pathologies such as ischemic and non-ischemic dilated cardiomyopathy or artificial flattening of the mitral

annulus in degenerative valve disease by surgically implanting a flat annuloplasty ring onto a native saddled annulus. To study the impact of mitral annular flattening on mitral valve mechanics, an adjustable shaped mitral annulus was developed as shown in Figure 4-5. The degree of the non-planarity of the mitral annulus was defined by Equation 5-2.

% Saddle = [Annular Height] *100/ [Commissural Width] Equation 5-2

5.4.5 3D GEOMETRIC PERTURBATIONS OF THE MITRAL VALVE TO MIMIC FUNCTIONAL MITRAL REGURGITATION

Functional mitral regurgitation, either due to ischemic or non-ischemic dilated cardiomyopathy occurs mainly due to geometric changes of the mitral valve at the annular and sub-annular levels. Typically, the three predominant geometric changes that are reported in this lesion are - (a) annular dilatation; (b) annular flattening; and (c) papillary muscle displacement. The three changes typically occur together in patients with this pathology, but the extent to which the annulus dilated, flattens or the papillary muscles are displaced varies largely between the patients. In this study, only few geometric variations that are significantly different between the patients were simulated, and typically the maximum extent to which they occur in patients was studied. The mitral annulus was dilated from a native 28mm to 36mm, the annulus was flattened completely and two settings of papillary muscle displacements were studied:

- 10mm apical displacement only
- 10mm apical + 10mm lateral + 10mm posterior displacement

In all the cases only symmetric displacement of both the papillary muscles was studied, though in practice both symmetric and asymmetric papillary muscle displacement may occur depending on the region and extent of infarction on the left ventricular wall. Figure 5-21 illustrates the geometric alterations imposed on the porcine mitral valve to mimic the pathological valve geometry.

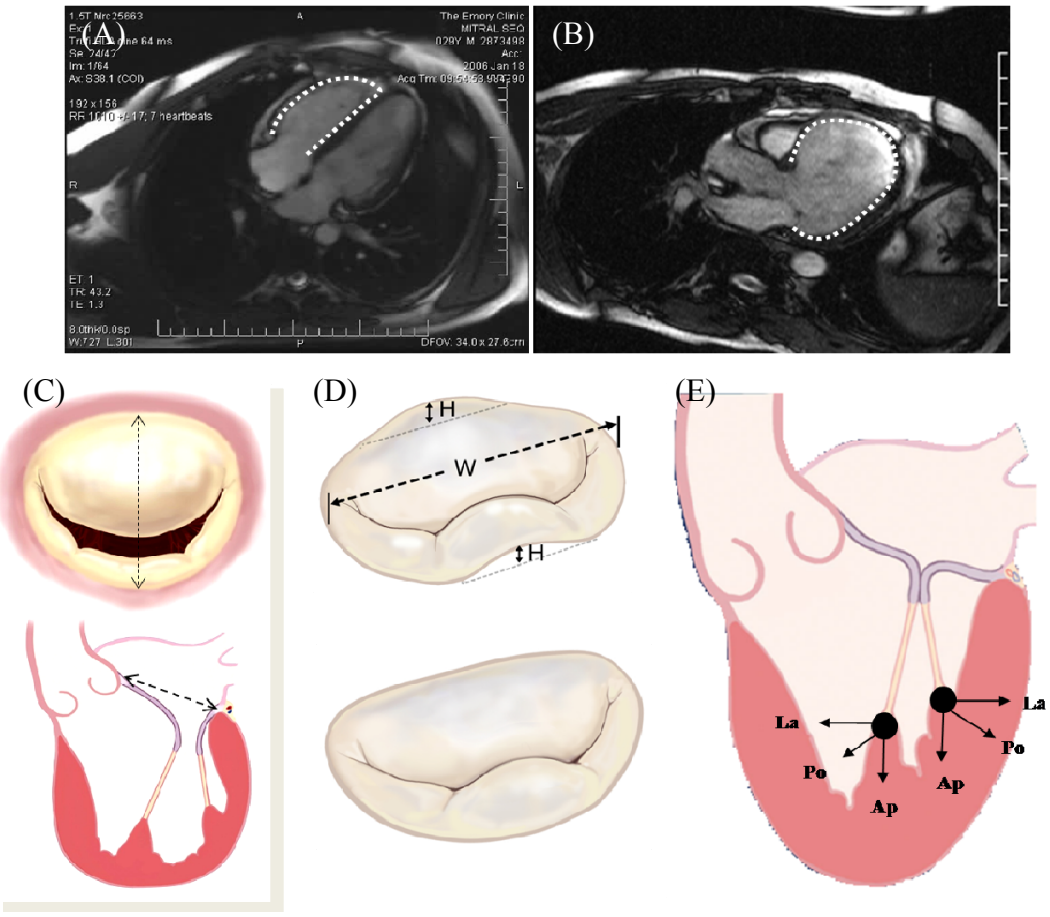

Figure 5-21 (A) Left ventricular shape depicted by the dotted line in a normal volunteer; (B) A dilated left ventricle in a patients with chronic ischemic cardiomyopathy; (C) Dilatation of the mitral annulus simulated by increasing the septal lateral dimension of the silicone annulus; (D) Annular flattening simulated by imposing a 0% saddle on the annulus; (E) Sub-annular papillary muscle displacement simulated by displacing the muscle tips in the apical, posterior and lateral directions, either independently or together.

5.5 PROTOCOLS TO PERFORM SURGICAL TECHNIQUES

5.5.1 SPECIFIC AIM 1 - CLEFT MITRAL VALVE REPAIR

The open cleft on the anterior mitral leaflet was closed using 4-0 Prolene sutures in an interrupted fashion as shown in Figure 5-22. Interrupted knots were used as they are most optimal in bringing the free edges of the leaflet together, without overlapping the edges and tethering the leaflet. The cleft was closed to three different levels starting from the mitral annulus – 1/3rd of the cleft length, 2/3rd of the cleft length and complete cleft length closed. At each level of cleft closure, five annular configurations were studied – Normal, Dilated – 20% and 40%, and Undersized – 20% and 40% respectively.

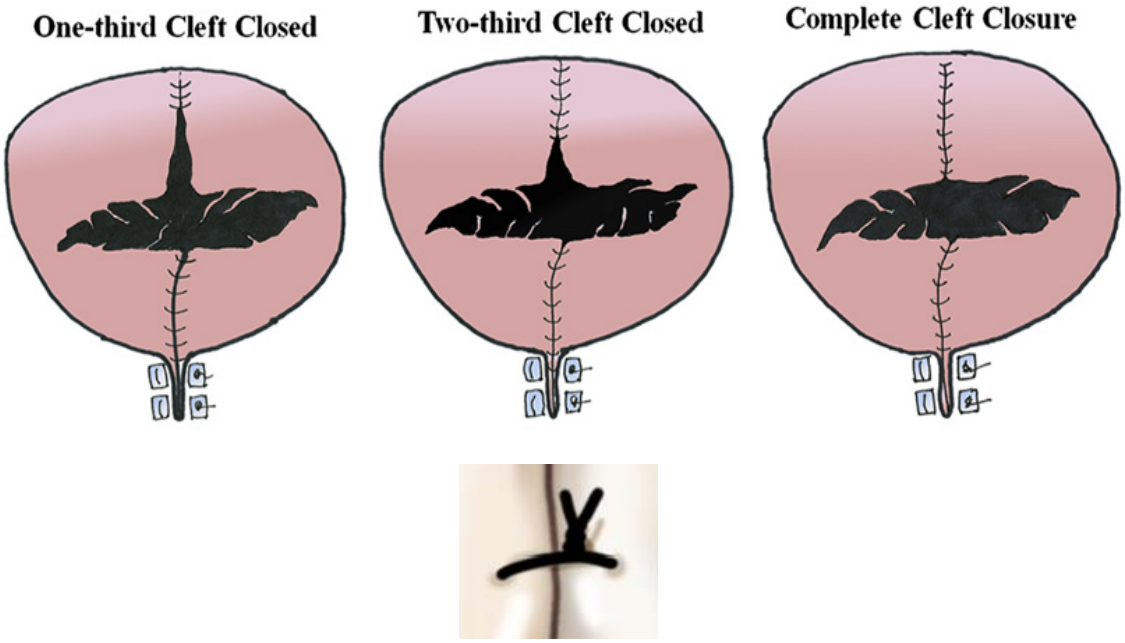

Figure 5-22 (Top) Different levels of cleft closure in the pathological model of the cleft mitral valve ; (Bottom) The interrupted knot technique used to close the cleft

5.5.1.1 Experimental Protocol

Eight (N=8) porcine mitral valves will be used for this study and each valve was studied under the following experimental conditions.

Baseline/Control Conditions

The freshly extracted porcine mitral valve (before altering the geometry) is mounted into the experimental setup and tested under pediatric hemodynamic conditions of: 120beats/min heart rate, 85mm Hg peak left ventricular pressure and an average cardiac output of 2.5L/min. For this test, the annular size is maintained at the normal size of the valve while in the intact heart, and the papillary muscles in their physiological positions. The normal position of the papillary muscles is determined such that the commissural chordae are in a single plane and the tips of the papillary muscles are in the plane passing through the leaflet coaptation. The flow rate and transmitral pressure gradient are measured and the regurgitation volume is calculated.

Disease Conditions

The geometry of the valve is then altered as described in the preceding sections and the experiments are repeated under the same pediatric hemodynamic conditions. This valve shall mimic the anatomy of the LAV valve in AVC defects, and is tested under two papillary muscle positions: (a) Normal position as the baseline condition and (b) Obliquely displaced position with 10 mm displacements in the posterior and lateral directions. The oblique position of the papillary muscles is typically found in patients with AVC defects due to abnormal ventricular growth. Relevant hemodynamic

measurements are then obtained. After this step, an anterior leaflet cleft is created by sectioning the skirt of the anterior leaflet from the free edge to the mitral annulus.

Repair/Risk Factor Conditions

Cleft Closure

To investigate the impact of cleft closure, the cleft is closed to four levels which are: (a) Fully open cleft (b) One-third cleft closed (c) Two-third cleft closed and (d) Cleft completely closed. The extent of cleft closure for individual valves is determined by measuring the total length of the cleft and dividing into three equal lengths. For each level of cleft closure, the cleft is closed using evenly spaced interrupted knots of 4-0 Prolene sutures (Ethicon Inc, Somerville, NJ, USA). The valves are studied under identical pediatric hemodynamic conditions used previously and relevant hemodynamic parameters are obtained.

Annular Dilatation

Annular dilatation is simulated on each of the four cleft closure conditions, by increasing the mitral annular area by 20% and 40% of its normal size. The annular area is calculated by measuring the septal-lateral and commissure-to-commissure dimensions of the mitral annulus and approximating the shape to an ellipse. The annulus is made to an area of 4.0 cm^2 initially, and then increased to 4.8 cm^2 for the 20% dilated size and to 5.6 cm^2 for the 40% dilated size. These two levels of dilatation are selected as they represent the mitral annular growth rate from infancy to 5 years after birth, assuming the repair is conducted during infancy. Dilatation of the annulus is simulated on the four cleft closure lengths and the regurgitation volumes for each annulus size are calculated.

Annular Undersizing

To investigate if reducing the annular size during primary repair could be of any benefit, the annulus is undersized from its normal size of 4.0 cm^2 to 3.2cm^2 simulating 20% undersizing and 2.4cm^2 simulating 40% undersizing. The effect of undersizing is studied on the open cleft, one-third closed cleft, two-third closed cleft and the fully closed cleft conditions.

5.5.1.2 Measured Endpoints

Regurgitation Volume

Regurgitant volume through the valve is calculated from the recorded transmitral flow curve. The flow curve is averaged over 15 cardiac cycles and the area under the negative part of the flow curve is integrated to obtain the regurgitation volume.

Effective Orifice Area

To measure the degree of stenosis after undersizing the annulus, the diastolic effective orifice area (EOAs) for each valve under all test conditions is calculated using the modified Bernoulli equation. The mean diastolic flow rate (Q_{rms}) and the root mean squared diastolic transmitral pressure gradient (ΔP_{mean}) are obtained from the recorded data and averaged over 15 cardiac cycles. The diastolic effective orifice area is calculated as:

$$EOA = Q_{rms} / [51.6(\sqrt{\Delta P_{mean}})] \qquad \text{Equation 5-3}$$

Echocardiographic Study

2D echocardiographic measurements were obtained at frequencies between 38-60 Hz, at an imaging depth of 12 cm and a transducer frequency of 3.7 MHz. Apical long-axis views cutting the leaflets across the anterior and posterior leaflets are acquired at different points on the mitral annulus. Three-dimensional (3D) echocardiographic measurements are obtained with a 3D matrix-array ultrasound sector transducer (X7-2 Matrix Probe, iE33 System, Philips Medical Systems, Andover, MA) at 3.75 MHz, adjusted to provide optimal imaging with the highest possible frame rate at a sampling depth of 12 cm. Color Doppler images were obtained at the same depth, at a baseline velocity of 61.7 mm/sec and a color gain of 25-35%, which is optimized to individual acquisitions. Echocardiographic and color Doppler images are obtained to assess the forward and the leakage flow through the cleft and the coaptation regions. The images are imported into QLAB software for quantification of various Doppler parameters, and into PMDSVIEW for length measurements.

5.5.1.3 Statistical Analysis

All the data are reported as mean ± 1 standard deviation. The data are tested for normality using an Anderson-Darling test (MINITAB 15). Different experimental groups are compared using paired t-tests considering statistical significance at a p value of < 0.05 with a 95% confidence interval.

5.5.2 SPECIFIC AIM 2 – SURGICAL REPAIR FOR POSTERIOR LEAFLET PROLAPSE

In this thesis, three commonly used surgical techniques were used to repair isolated posterior leaflet prolapse due to chordal rupture – (a) Quadrangular resection with annular plication; (b) Limited triangular resection; and (c) Artificial neochordoplasty. The protocols adopted to perform each of the surgical techniques are presented here.

5.5.2.1 Part A – Resective vs. Non-Resective Techniques for Repair of Posterior Leaflet Prolapse

Quadrangular Resection with Annular Plication

Quadrangular resection was performed on each valve by resecting a rectangular section of the P2 segment and compressing the annulus at this region as shown in Figure 5-23. The dimensions of the resected segment were chosen such that the breadth of the rectangle equaled the distance between the two ruptured marginal chordae, and the length extended from the free edge to the mitral annulus. The section of the annulus in the resected region was then plicated and approximated using 3-4 compression sutures. The free edges after resection were carefully approximated using interrupted knots with 3-0 silk sutures as shown in Figure 5-24.

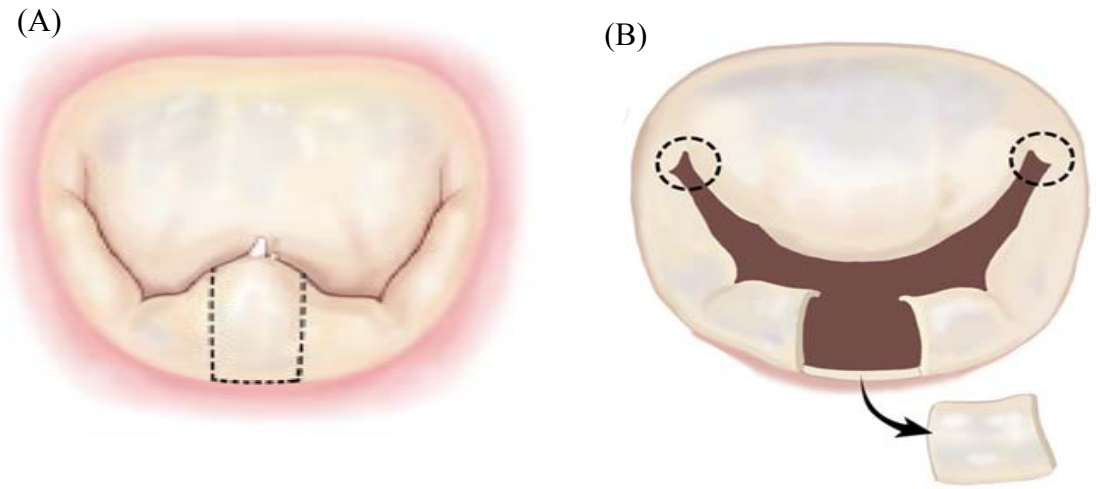

Figure 5-23 (A) Dotted line depicts the quadrangular section of the prolapsing leaflet that will be resected; (B) Quadrangular section resected from the leaflet

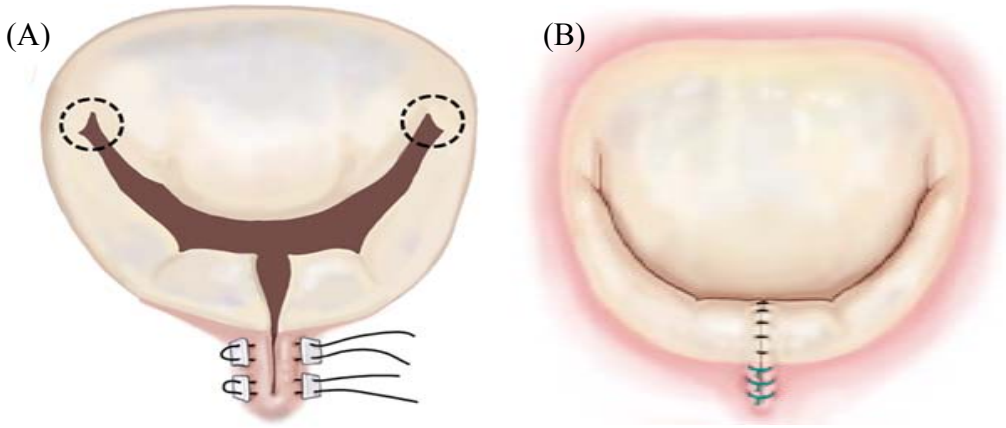

Figure 5-24 (A) Annular compression at the resected region; (B) The reconstructed posterior leaflet after quadrangular resection

Triangular Resection

Triangular resection was performed on the free edge of the P2 scallop as shown in Figure 5-25. The total height of the posterior leaflet from the free edge to the annulus was measured and a triangular segment that has a height of 1/3(total leaflet height) and a base width equal to the length between the two ruptured marginal chordae was resected as

reported in an earlier study by Gazoni et al. [93]. The posterior leaflet was reconstructed by carefully approximating the free edges of the triangular resection using interrupted 3-0 silk sutures (Ethicon Inc, NJ), such that minimal tension was induced on the residual leaflet segments. Upon reconstructing the leaflet the valve was again tested under pulsatile hemodynamics conditions that were previously used.

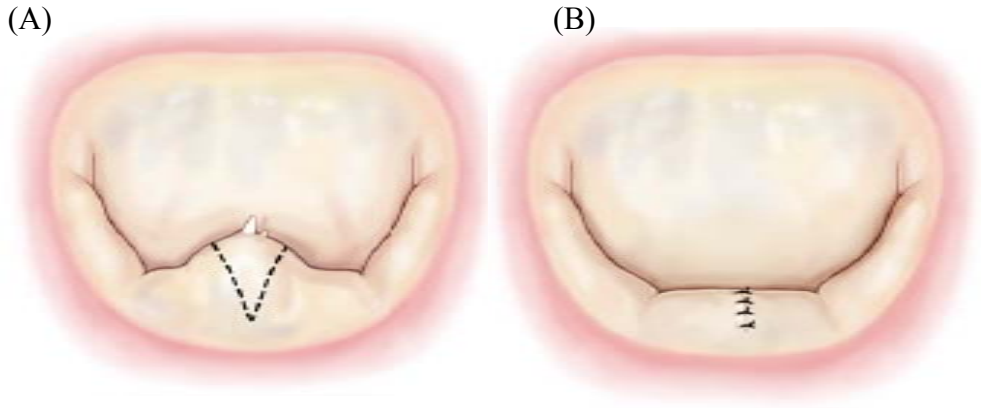

Figure 5-25 (A) Dotted line showing the section of the posterior leaflet that will be resected; (B) Reconstructed posterior leaflet after suturing the free edges after triangular resection

Neochordoplasty

In this procedure, the transected marginal chordae tendineae were replaced with loops of 5-0 ePTFE sutures as shown in Figure 5-26 . The ventricular chamber was filled with saline to close the mitral valve, and length of the neochordae was adjusted and tied onto a Teflon® pledget on the tip of the papillary muscle. The valve was then tested under pulsatile hemodynamic flow conditions as listed in the previous sections and relevant hemodynamic and echocardiographic endpoints were measured.

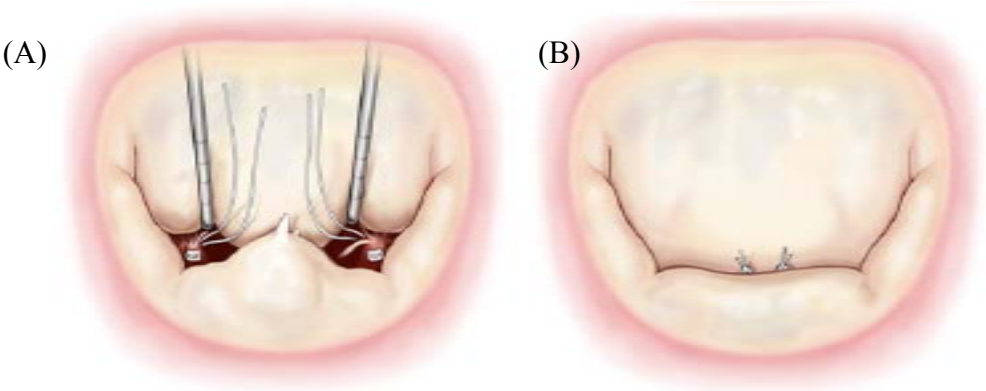

Figure 5-26 (Left) Inserting the neochordae into the tips of the papillary muscles; (Right) Competent mitral valve after neochordoplasty

5.5.2.1.1 Experimental Protocol

Each mitral valve is studied under the experimental conditions in the order listed below:

Baseline/Control Conditions

The annulus is maintained at its normal size, and the papillary muscles are fixed in their normal positions, i.e., with the papillary muscle tips perpendicular to the mitral annular plane and in the plane passing through leaflet coaptation, such that the commissural chordae from the same papillary muscle are parallel to each other. The valve is studied under adult hemodynamic conditions of 120 mm Hg peak transmitral pressure, 5L/min cardiac output at 70bpm. The regurgitant volume and stroke volume are volumetrically measured, and leaflet coaptation length, and indices that elucidate leaflet mobility are recorded using 3d echocardiography.

Disease Conditions

After acquiring the baseline data, the two marginal chordae on the free edge of the posterior leaflet are transected resulting in severe segmental prolapse of the P2 cusp. The simulator is again run under identical hemodynamic conditions, and the hemodynamic and echocardiographic measurements are obtained. P2 prolapse is validated by reconstructing the 3D geometry of the mitral valve from the echocardiographic images and superimposed with only the reverse color Doppler data, showing the regurgitation jet. The regurgitation and stroke volumes are also quantified using the flow probe.

Repair Conditions

Neochordoplasty

In this procedure, the transected marginal chordae tendineae are replaced with loops of 5-0 ePTFE sutures. The ventricular chamber is filled with saline to close the mitral valve, and length of the neochordae are adjusted and tied onto a Teflon® pledget on the tip of the papillary muscle. The valve is then tested under pulsatile hemodynamic flow conditions as listed in the previous sections and relevant hemodynamic and echocardiographic endpoints are measured.

Limited Triangular Resection

Upon acquiring data in step (c), the neochordae are removed and a triangular resection is performed on the free edge of the P2 scallop. The total height of the posterior leaflet from the free edge to the annulus is measured and a triangular segment that has a height of 1/3(total leaflet height) and a base width equal to the length between the two ruptured marginal chordae is resected as reported in an earlier study by Gazoni et al[93].

The posterior leaflet is reconstructed by carefully approximating the free edges of the triangular resection using interrupted 3-0 silk sutures (Ethicon Inc, NJ), such that minimal tension is induced on the residual leaflet segments. Upon reconstructing the leaflet the valve is again tested under pulsatile hemodynamics conditions.

Quadrangular Resection with Annular Compression

Quadrangular resection is performed on the same valve by resecting a rectangular section of the P2 segment and compressing the annulus at this region. The dimensions of the resected segment are chosen such that the breadth of the rectangle equaled the distance between the two ruptured marginal chordae, and the length extended from the free edge to the mitral annulus. The section of the annulus in the resected region is then plicated and approximated using three of four compression sutures. The free edges after resection are carefully approximated using interrupted knots with 3-0 silk sutures, in a similar fashion to the triangular resection group. The valve is then tested under pulsatile hemodynamic conditions.

5.5.2.1.2 Measured Endpoints

Regurgitation Volume

Regurgitant volume through the valve is calculated from the recorded transmitral flow curve. The flow curve is averaged over 15 cardiac cycles and the area under the negative part of the flow curve is integrated to obtain the net regurgitation volume.

Echocardiographic Measurements

2D echocardiographic measurements were obtained at frequencies between 38-60 Hz, at an imaging depth of 12 cm and a transducer frequency of 3.7 MHz. Apical long-axis views cutting the leaflets across the anterior and posterior leaflets are acquired at different points on the mitral annulus. Three-dimensional (3D) echocardiographic measurements are obtained with a 3D matrix-array ultrasound sector transducer (X7-2 Matrix Probe, iE33 System, Philips Medical Systems, Andover, MA) at 3.75 MHz, adjusted to provide optimal imaging with the highest possible frame rate at a sampling depth of 12 cm. Color Doppler images were obtained at the same depth, at a baseline velocity of 61.7 mm/sec and a color gain of 25-35%, which is optimized to individual acquisitions. Echocardiographic and color Doppler images are obtained to assess the forward and the leakage flow through the cleft and the coaptation regions. The images are imported into QLAB software for quantification of various Doppler parameters, and into PMDSVIEW for length measurements. Peak systolic leaflet coaptation length, posterior leaflet angle and distance of the coaptation plane from the posterior annulus are measured.

5.5.2.1.3 Statistical Analysis

All the data are reported as mean ± 1 standard deviation. The data are tested for normality using an Anderson-Darling test (MINITAB 15). Different experimental condition groups are compared using paired t-tests considering statistical significance at a p value of < 0.05 with a 95% confidence interval.

5.5.2.2 Part B – Neochordoplasty versus Chordal Translocation for Repair of Posterior Leaflet Prolapse

A novel surgical technique studied in this thesis to correct posterior leaflet prolapse is translocation of the posterior strut chordae to the marginal position. The underlying hypothesis of this procedure is that on the posterior leaflet, the marginal chordae control the motion of the free edge and the strut chordae even though important in determining the curvature of the leaflet, may not play a detrimental role. As shown in figure xx, the strut chordae were transected at their insertion points on the base of the posterior leaflet, and using 4-0 prolene sutures were relocated to the free edge of the leaflet. These translocated strut chordae now restrict prolapse of the free edge into the left atrium, and thus restore normal valve competence.

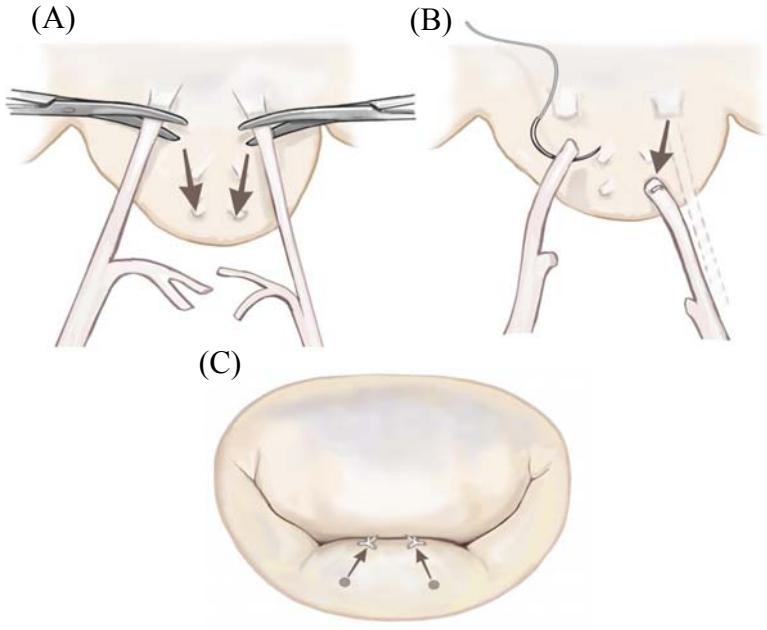

Figure 5-27 (A) Transection of the strut chordae tendineae; (B) Translocation fo the free edge of the P2 scallop; (C) An en face view of the valve showing the relocation of the chordae tendineae

5.5.2.2.1 Experimental Protocol

Each mitral valve is studied under the experimental conditions in the order listed below:

Control/Baseline Conditions

The annulus is maintained at its normal size, and the papillary muscles are fixed in their normal positions, i.e., with the papillary muscle tips perpendicular to the mitral annular plane and in the plane passing through leaflet coaptation, such that the commissural chordae from the same papillary muscle are parallel to each other. The valve is studied under adult hemodynamic conditions of 120 mm Hg peak transmitral pressure, 5L/min cardiac output at 70bpm. The regurgitant volume and stroke volume are volumetrically measured, and leaflet coaptation length, and indices that elucidate leaflet mobility are recorded using 3d echocardiography.

Posterior Leaflet Prolapse

After acquiring the baseline data, the two marginal chordae on the free edge of the posterior leaflet are transected resulting in severe segmental prolapse of the P2 cusp. The simulator is again run under identical hemodynamic conditions, and the hemodynamic and echocardiographic measurements are obtained. P2 prolapse is validated by reconstructing the 3D geometry of the mitral valve from the echocardiographic images and superimposed with only the reverse color Doppler data, showing the regurgitation jet. The regurgitation and stroke volumes are also quantified using the flow probe.

Repair Techniques

Neochordoplasty

In this procedure, the transected marginal chordae tendineae are replaced with loops of 5-0 ePTFE sutures. The ventricular chamber is filled with saline to close the mitral valve, and length of the neochordae are adjusted and tied onto a Teflon® pledget on the tip of the papillary muscle. The valve is then tested under pulsatile hemodynamic flow conditions as listed in the previous sections and relevant hemodynamic and echocardiographic endpoints are measured.

Chordal Translocation

The secondary chordae on the posterior leaflet were transected atleast 2mm from their insertion into the leaflet, and transferred to the marginal chordal position using Prolene sutures. The sutures are passed through the chord and then the leaflet, and are knotted on the atrial surface. After the procedure, the left ventricular chamber is filled with saline and the valve is tested for its static competence before studying it under pulsatile hemodynamic conditions.

5.5.2.2.2 Data Acquisition

Regurgitation Volume

Regurgitant volume through the valve is calculated from the recorded transmitral flow curve. The flow curve is averaged over 15 cardiac cycles and the area under the negative part of the flow curve is integrated to obtain the net regurgitation volume.

Echocardiographic Measurements

2D echocardiographic measurements were obtained at frequencies between 38-60 Hz, at an imaging depth of 12 cm and a transducer frequency of 3.7 MHz. Apical long-axis views cutting the leaflets across the anterior and posterior leaflets are acquired at different points on the mitral annulus. Three-dimensional (3D) echocardiographic measurements are obtained with a 3D matrix-array ultrasound sector transducer (X7-2 Matrix Probe, iE33 System, Philips Medical Systems, Andover, MA) at 3.75 MHz, adjusted to provide optimal imaging with the highest possible frame rate at a sampling depth of 12 cm. Color Doppler images were obtained at the same depth, at a baseline velocity of 61.7 mm/sec and a color gain of 25-35%, which is optimized to individual acquisitions. Echocardiographic and color Doppler images are obtained to assess the forward and the leakage flow through the cleft and the coaptation regions. The images are imported into QLAB software for quantification of various Doppler parameters, and into PMDSVIEW for length measurements. Peak systolic leaflet coaptation length, posterior leaflet angle and distance of the coaptation plane from the posterior annulus are measured.

5.5.2.2.3 Statistical Analysis

All the data are reported as mean ± 1 standard deviation. The data are tested for normality using an Anderson-Darling test (MINITAB 15). Different experimental condition groups are compared using paired t-tests considering statistical significance at a p value of < 0.05 with a 95% confidence interval.

5.5.2.3 Part C – Mechanics of Strut Chordae Insertion Region

In this section the techniques to measure surface strains on the transitional zone where the anterior strut chordae insert into the leaflet are described.

5.5.2.3.1 Experimental Setup

The region of interest on the ventricular surface of the anterior leaflet was marked with a uniform grid of tissue dye markers, and the motion of the markers throughout the cardiac cycle was imaged using a high frame rate imaging system described in 4.1.3.5. The two cameras were positioned on the ventricular chamber such that the insertion region can be imaged throughout the cardiac cycle. A frame rate of 250 frames/second was used with optimal aperture size to ensure adequate temporal resolution within the cardiac cycle. The acquired images were saved as a series of TIFF (Tagged Image File Format) images, and the coordinates of each marker were obtained using custom codes written in MATLAB provided in Appendix B.

5.5.2.3.2 Marker Tracking

The markers on the each image frame from camera A were first digitized using a custom MATLAB code, and the [x, y] coordinates of each marker for each frame were saved to a tab delimited text file. Since the images were acquired at a high frame rate of 250 frames/ sec, each cardiac cycle had approximately 200 images of the valve opening and closure. Manual digitization of each marker in every image would be extremely time consuming, thus an adaptive grid interpolation scheme (ACGI) previously developed in our laboratory was used to interpolate the marker positions between every 10 images [121]. This method reduced the total time required for marker digitization by $1/10^{th}$

compared to the manual method. Using the ACGI technique, the markers in all the frames for both the cameras was performed as representatively shown in Figure 5-28. The [x, y] coordinates from camera 1 were saved to a text file titled ‘acoord.txt’ and the coordinates from camera 2 to ‘bcoord.txt’.

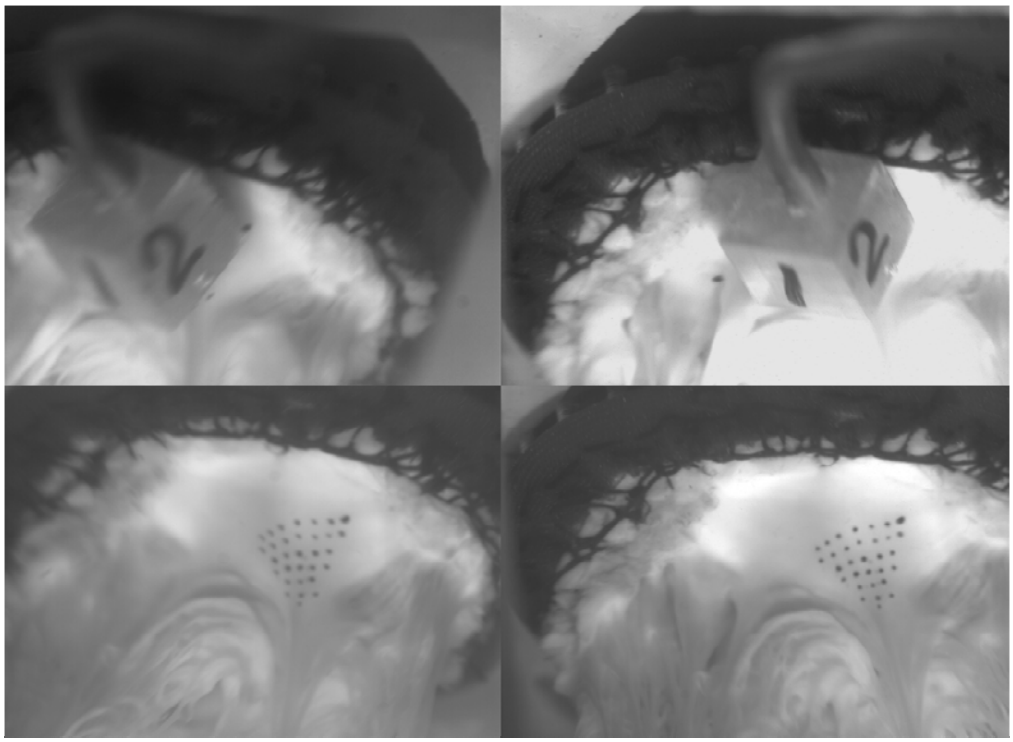

Figure 5-28 A representative image pair of the calibration cube and of the chordal insertion region marked with 31 tissue dye markers

5.5.2.3.3 Calibration for Direct Linear Transformation

To define a reference coordinate frame between the two cameras, a calibration cube of known dimensions is used. An aluminum cube of 10.6mm edge dimension was designed, and machined with a long end connector that allows insertion of the cube into the left heart simulator. After setting up the cameras in their required positions, the calibration cube is inserted into the left ventricle through the open top part of the

chamber, and positioned exactly in the mitral annular plane. The cube is inclined such that 6 common cube vertices are clearly visible in both the cameras. Once the cube positioned is finalized, still images of the two cubes are captured in both the cameras and saved to the hard drive in TIFF format.

The saved images are then exported into Sigma Scan Pro (Systat Software Inc, San Jose, CA) and a common coordinate system is defined that is consistent between the two cameras. The vertices are numbered in a clockwise direction, starting with the face closest to the camera lens, and by carrying the numbering to the face farthest from the camera lens. Once the vertices were digitized, the vertex coordinates from both cameras were saved to two separate tab delimited text files. Since the length of each edge of the cube is known as 10.6mm, a text file that defines the coordinate system starting with vertex # 1 as the origin [0,0,0], vertex # 2 as [10.6,0,0], vertex # 3 as [10.6,10.6,0], vertex # 4 as [0,10.6,0], vertex # 5 as [0,0,10.6], and vertex # 6 as [10.6,0,10.6].

5.5.2.3.4 Direct Linear Transformation

The individual 2D marker coordinates of image pairs are converted into a 3D coordinate system using a Direct Linear Transformation (DLT). This method is based on the simple fact that recording images using a camera, is a simple mapping of object O in the object space to image I' in the film plane. For digitizing this recorded image it is projected to image I in the projection plane as shown in Figure 5-29.

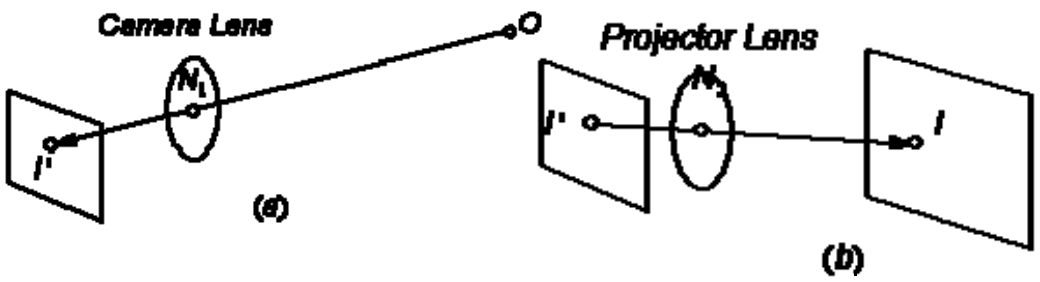

Figure 5-29 (A) Projection of an object O from object space to the film space I`; (B) Projection of the object from film space I' to projection space I to enable digitization of the markers. Figure reproduced from *www.kwon3d.com*

For simplicity, the projected image and the object can be directly related as shown in Figure 5-30, and a new point N which is the new node point or the projection center. Two reference frames are now defined, object-space reference frame (the XYZ system) and image-plane reference frame (the UV system). Points I, N & O thus form a straight line and this is the so-called collinearity condition. To make the image-plane reference frame 3-dimensional, an axis W from the nodal point N to the image plane reference frame is added as shown in Figure 5-30.

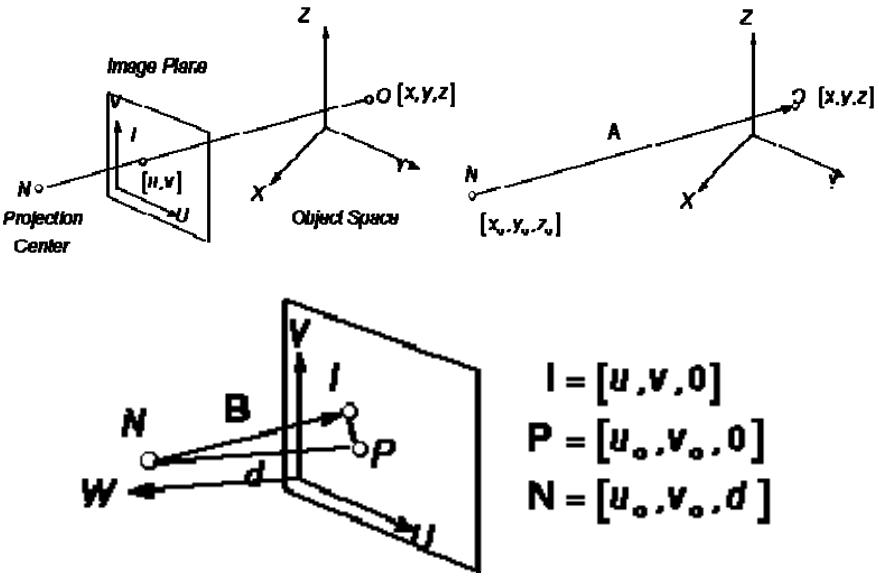

Figure 5-30 Direct projection of the object from object space into projection/image space, and the transformation of the image plane from 2D space into 3D space

5.5.2.3.5 Surface Fitting and Strain Computation

To compute the strain field, a custom MATHCAD program was used (PTC, Needham, MA) to transform the 3D coordinates into an in-plane coordinate system (*u-v-n*) based on a tangent plane. The u-v coordinates were then projected onto the deformed surface and thus formed a convective coordinate system that deforms with the surface. The origin of the *u-v-n* system was located at the center of the marker array, with corresponding unit vectors, e^u, e^v, and e^n. In this thesis, e^u was defined parallel to the markers 1 and 7, e^n the surface normal was computed using $e^n = e^u \, X \, e^{m4\text{-}m31}$, where $e^{m4\text{-}m31}$ is the unit vector parallel to markers 4 and 31 and $e^v = e^n \, X \, e^u$. Each marker *x-y-z* coordinate triplet for each frame was subsequently translated and rotated into the reference frame *u-v-n* coordinate system.

To compute the strain field within the insertion region delimited by the markers, a finite element-based C^2 surface interpolation is used. The position of any marker in the reference state is given by $R^0(u,v) = ue^u + ve^v + ne^n$, where n represents the normal component. To fit the marker array, a C^2 cubic hermite shape element was used for each displacement component. The reference surface fit yields the initial shape of the chordal insertion region defined by the 31 marker array. The metric tensor in the reference configuration, g^0 was computed from R^0 using formulae reported in literature [122]. To determine the strains for each frame f and component $i = (1, 3)$ the displacements for each marker d_i^f were first computed as the difference between the reference and deformed spatial marker positions. Thus the position vector for frame f of any point on the deformed surface is given by $R^f(u, v) = d_1^f e^u + d_2^f e^v + d_3^f e^n + R^0(u,v)$, where $d_i^f(u, v)$ is the fitted displacement field for the axial component i for the current frame f. From R^f, the components of the metric tensor g^f in the deformed configuration are computed and the resulting Almansi (i.e., Eulerian) finite strain tensor for each frame was determined using $e = 0.5(g^f - g^0)$. The principal values of e were expressed as principal stretches λ_1 and λ_2, with corresponding principal angle θ_p referred to the u-axis of the reference state. The areal stretch, representing the total change in the leaflet area, was computed using $\Delta = \lambda_1 * \lambda_2$. The corresponding stretch rates for each frame were computed using a three-point numerical derivate algorithm and expressed as percent per second.

5.5.2.3.6 Data Analysis and Statistical Methods

All the parameters computed at each marker position and averaged over the eight valves. The temporal and peak magnitudes of each parameter are reported, and compared using a paired t-test for statistical significance at 95% confidence interval.

5.5.2.4 Part D – Efficacy of Edge-to-Edge Repair for Posterior Leaflet Prolapse

Minimally invasive edge-to-edge repair is a technique gaining popularity to correct posterior leaflet prolapse due to its procedural ease and ability to perform the procedure through percutaneous technologies. In this study, a surgical version of edge-to-edge repair was studied wherein the prolapsing posterior leaflet was anchored onto the structurally stable anterior leaflet. An "8" shaped stitch was used to perform the edge-to-edge procedure as shown in Figure 5-31 , so that the overlap region between the leaflets was maximized and higher stability was ensured. After performing the edge-to-edge repair, the valve was tested at three annular configurations: normal, 15% dilatation and 30% dilatation.

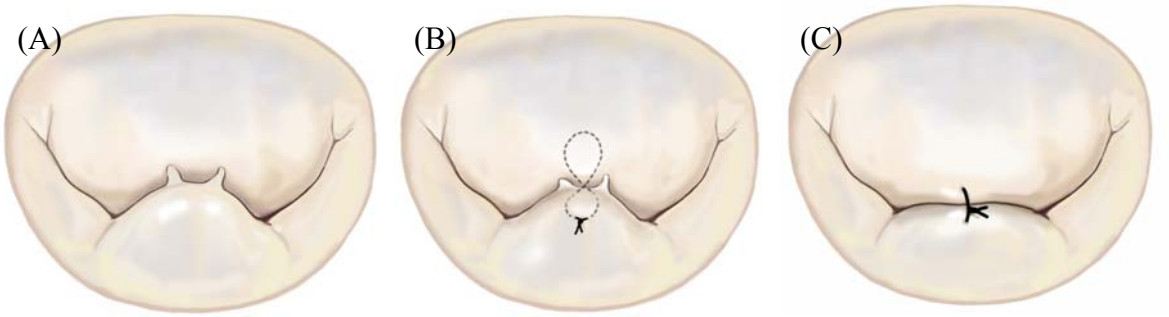

Figure 5-31 (A) Isolated posterior leaflet prolapse due to acute chordal rupture; (B) The"8" shaped stitch showing the suture passing through the posterior leaflet, followed by the anterior leaflet and then sutured onto the posterior leaflet so that atleast 5mm of contact is established between the anterior and posterior leaflet; (C) The mitral valve after edge to edge repair

5.5.2.4.1 Experimental Protocol

Each mitral valve is studied under the experimental conditions in the order listed below:

Control/Baseline Conditions

The annulus is maintained at its normal size, and the papillary muscles are fixed in their normal positions, i.e., with the papillary muscle tips perpendicular to the mitral annular plane and in the plane passing through leaflet coaptation, such that the commissural chordae from the same papillary muscle are parallel to each other. The valve is studied under adult hemodynamic conditions of 120 mm Hg peak transmitral pressure, 5L/min cardiac output at 70bpm. The regurgitant volume and stroke volume are volumetrically measured, and leaflet coaptation length, and indices that elucidate leaflet mobility are recorded using 3D echocardiography.

Posterior Leaflet Prolapse

After acquiring the baseline data, the two marginal chordae on the free edge of the posterior leaflet are transected resulting in severe segmental prolapse of the P2 cusp. The simulator is again run under identical hemodynamic conditions, and the hemodynamic and echocardiographic measurements are obtained. P2 prolapse is validated by reconstructing the 3D geometry of the mitral valve from the echocardiographic images and superimposed with only the reverse color Doppler data, showing the regurgitation jet. The regurgitation and stroke volumes are also quantified using the flow probe.

Repair Conditions

Edge to edge repair was performed by placing an "8" shaped stitch between the prolapsing free edge of the P2 cusp, and the structurally stable A2 cusp. The stitch is placed atleast 4mm above the leaflet margin, and a laterally overlap of ~1cm is ensure between the two leaflets at the location of the stitch. The repair is first tested with a normal annular size (32mm), and then dilated by 15% to 34mm and by 30% to 36mm respectively. At each level of annular dilatation, hemodynamic and echocardiographic data are acquired and quantified.

5.5.2.4.2 Measurement Techniques

Regurgitation Volume

Regurgitant volume through the valve is calculated from the recorded transmitral flow curve. The flow curve is averaged over 15 cardiac cycles and the area under the negative part of the flow curve is integrated to obtain the net regurgitation volume.

Echocardiographic Measurements

2D echocardiographic measurements were obtained at frequencies between 38-60 Hz, at an imaging depth of 12 cm and a transducer frequency of 3.7 MHz. Apical long-axis views cutting the leaflets across the anterior and posterior leaflets are acquired at different points on the mitral annulus. Three-dimensional (3D) echocardiographic measurements are obtained with a 3D matrix-array ultrasound sector transducer (X7-2 Matrix Probe, iE33 System, Philips Medical Systems, Andover, MA) at 3.75 MHz, adjusted to provide optimal imaging with the highest possible frame rate at a sampling depth of 12 cm. Color Doppler images were obtained at the same depth, at a baseline

velocity of 61.7 mm/sec and a color gain of 25-35%, which is optimized to individual acquisitions. Echocardiographic and color Doppler images are obtained to assess the forward and the leakage flow through the cleft and the coaptation regions. The images are imported into QLAB software for quantification of various Doppler parameters, and into PMDSVIEW for length measurements. Peak systolic leaflet coaptation length, posterior leaflet angle and distance of the coaptation plane from the posterior annulus are measured.

5.5.2.4.3 Statistical Analysis

All the data are reported as mean ± 1 standard deviation. The data are tested for normality using an Anderson-Darling test (MINITAB 15). Different experimental condition groups are compared using paired t-tests considering statistical significance at a p value of < 0.05 with a 95% confidence interval.

5.5.2.5 Part F – Impact of Mitral Annular Saddle Shape on the Deformation of the P2 Segment of the Posterior Mitral Leaflet

To understand the impact of annuloplasty ring shape on the mechanics of the posterior leaflet of the mitral valve, strain was measured on the central P2 cusp at 0%, 10% and 20% static annular saddle. The experimental setup, and methods used to quantify leaflet strain are identical to those previously reported and briefly described here.

5.5.2.5.1 Experimental Setup

A 4x4 array of markers (~200μ) are placed on the atrial surface of the P2 cusp and the valve is mounted into the left heart simulator and studied under pulsatile hemodynamic conditions. Two high speed cameras are placed facing the left atrial surface and separated by ~ 30^{o}, and the marker array is imaged throughout the cardiac cycle. Image acquisition through both cameras is triggered synchronously with the cardiac timing of the left heart simulator and the hemodynamic acquisition and the acquired images shown in Figure 5-32 from each camera are stored as a series of TIFF files onto the hard drive. A calibration cube of edge size 10.6mm is then inserted into the left heart simulator through the top face of the ventricle, and placed in the plane of the mitral annulus. The calibration cube is then imaged using both cameras and the static images are saved to the hard drive for later processing.

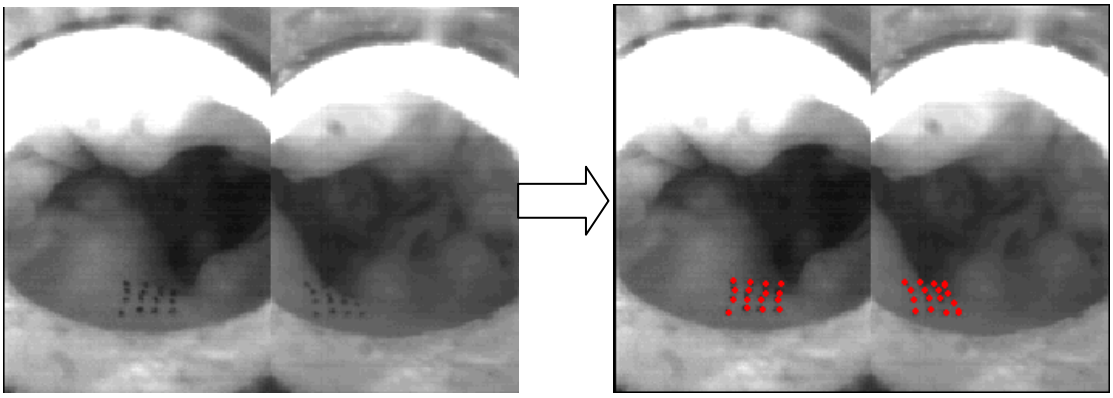

Figure 5-32 A representative image pair of leaflet markers obtained from the two high speed cameras. The red dots depict the markers after digitizing them on the high speed images.

5.5.2.5.2 Marker Digitization and Direct Linear Transformation

Detailed techniques to digitize the 2D marker coordinates from the sequence of images from each camera are explained in previous sections. Identical MATLAB codes reported in these sections are used to reconstruct the 2D marker coordinates from the camera images, and direct linear transformation is used to calculate the 3D marker coordinates. Once the 3D cloud of markers for each temporal point is obtained, a previously developed algorithm is used to compute the leaflet strains.

5.5.2.5.3 Surface Fitting and Strain Computations

A C^0 surface fitting algorithm was used to reconstruct the reference and deformed surfaces. The position of any marker in the reference state is given by $R^0(u,v) = ue^u + ve^v + ne^n$, where n represents the normal component. The reference surface fit yields the initial shape of the leaflet region defined by the 16 marker array. The metric tensor in the reference configuration, g^0 was computed from R^0 using formulae reported in literature [122]. To determine the strains for each frame f and component $i = (1, 3)$ the displacements for each marker d_i^f were first computed as the difference between the reference and deformed spatial marker positions. Thus the position vector for frame f of any point on the deformed surface is given by $R^f(u, v) = d_1^f e^u + d_2^f e^v + d_3^f e^n + R^0(u,v)$, where $d_i^f(u, v)$ is the fitted displacement field for the axial component i for the current frame f. From R^f, the components of the metric tensor g^f in the deformed configuration are computed and the resulting Almansi (i.e., Eulerian) finite strain tensor for each frame was determined using $e = 0.5(g^f - g^0)$. The principal values of e were expressed as principal stretches λ_1 and λ_2, with corresponding principal angle θ_p referred to the u-axis

of the reference state. The areal stretch, representing the total change in the leaflet area, was computed using $\Delta = \lambda_1 * \lambda_2$. The corresponding stretch rates for each frame were computed using a three-point numerical derivate algorithm and expressed as percent per second.

5.5.2.5.4 Data Analysis and Statistical Methods

All the parameters computed at each marker position and averaged over the eight valves. The temporal and peak magnitudes of each parameter are reported, and compared using a paired t-test for statistical significance at 95% confidence interval.

5.5.3 SPECIFIC AIM 3 - SURGICAL REPAIR FOR FUNCTIONAL MITRAL REGURGITATION

5.5.3.1 Impact of Pre-Operative Valve Geometry on the Outcomes of Annular and Sub-annular Repair for Functional Mitral Regurgitation

3D geometry of the mitral valve plays a key role in determining the efficacy and long term durability of repair for functional mitral regurgitation. In this aim, the impact of valve geometry on undersizing annuloplasty and anterior strut chordal cutting was investigated. Annuloplasty is the current standard of care in clinical practice, and was performed in this study by reducing the size of the mitral annulus to 28mm from its dilated size. Sub-annular repair was performed by resecting the two strut chordae inserting into the base of the anterior leaflet as shown in Figure 5-33.

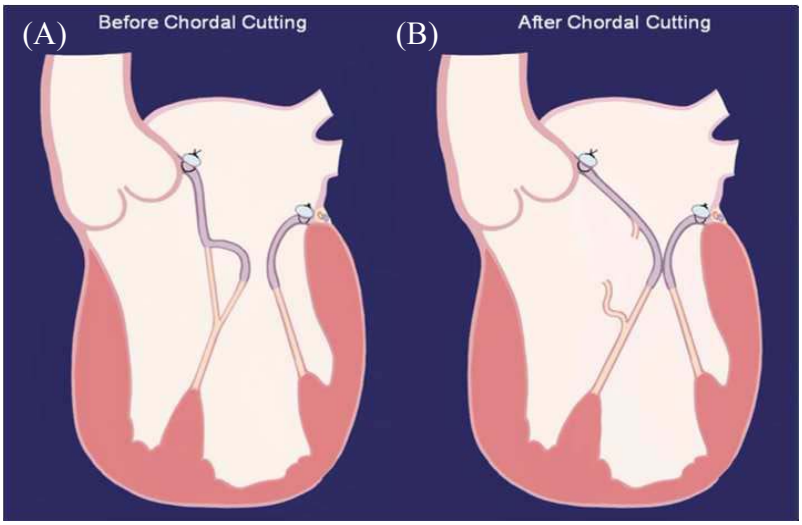

Figure 5-33 (Left) Tethering of the anterior leaflet after annuloplasty but no secondary chordal cutting; (B) Strut chordal transection performed on the anterior leaflet to relieve tethering

5.5.3.1.1 Experimental Protocol

Each mitral valve was studied under the following conditions:

Control/Baseline Conditions

The annulus is maintained at its normal size, and the papillary muscles are fixed in their normal positions, i.e., with the muscle tips perpendicular to the mitral annular plane and in the plane passing through leaflet coaptation, such that the commissural chordae from a papillary muscle are parallel to each other. The valve is studied under physiological hemodynamic conditions of 120 mmHg peak transmitral pressure, 5L/min cardiac output at 70 beats per minute (bpm). Mitral valve hemodynamics, regurgitation fraction and valve geometric endpoints are measured.

Disease Conditions

Mitral regurgitation is induced in the normal valve by simulating two different pathological conditions: (a) annular dilatation (36mm) + 10mm apical papillary muscle displacement; and (b) annular dilatation (36mm) + 10mm apical, 10mm lateral, 10mm posterior papillary muscle displacement. Resulting mitral valve geometry due to the imposed geometric changes is measured using 3D echocardiography and the hemodynamic endpoints are quantified.

Repair Conditions

Annular Repair Technique - True Sizing Annuloplasty

The first objective is to assess if ring annuloplasty would suffice in reducing mitral regurgitation in both pathological geometries. Ring annuloplasty procedure is simulated on the regurgitant valves by reducing the septal lateral dimension to 28mm, restoring it to its physiological levels. Commercial annuloplasty rings were not used to avoid any pre conceived bias. After true-sizing of the annulus, reduction in regurgitation volume is measured and the mitral valve geometry is carefully quantified from the echocardiographic images.

Sub-annular Repair Technique - Secondary Chordal Cutting

In this study, only anterior strut chordal cutting is performed and its benefits in increasing anterior leaflet mobility and improving valve competence are studied. Maintaining the annulus at the true dimension of 28mm, the two basal strut chordae tethering the anterior leaflet are carefully severed at the insertion region of the chordae

into the leaflet using a scalpel, without disturbing the annular dimensions or papillary muscle positions. The valves are again tested under identical hemodynamic conditions, and all the hemodynamic and geometric parameters are quantified.

5.5.3.1.2 Measurement Techniques

Regurgitation Fraction

The transmitral flow curve is averaged over 15 cardiac cycles and the negative part of the flow curve is integrated to obtain the regurgitation volume per beat, and normalized with the stroke volume to obtain the regurgitant fraction.

Echocardiographic Study

3D echo and color Doppler measurements were obtained with a X7-2 pediatric 3D matrix array probe (iE33 System, Phillips Medical Systems, Andover, MA) at 3.75 MHz, at the highest possible frame rate at the sampling depth of 12 cm. Echocardiographic images were acquired (1) along the apical long-axis view cutting across both the leaflets antero-posteriorly at the midpoint of the major axis of the annulus, (2) apical long-axis view to the left of center, capturing the P1- A1 coaptation and (3) to the right of center capturing P3-A3 coaptation. From views (1), (2), (3) the systolic leaflet coaptation length, and tenting height/area were quantified in a double blinded fashion using QLAB 6.3(Philips Medical Imaging, Andover, MA).

5.5.3.1.3 Statistical Analysis

All the measured endpoints are reported as mean ± standard deviation. The data are tested for normality using the Anderson-Darling Test in MINITAB 15. The experimental groups were compared using a paired t-test considering statistically significant difference at a $p < 0.05$ with a 95% confidence interval. A non-parametric Wilcoxon signed-rank test was conducted on the echo data, as some experimental conditions were not normally distributed. The same P value and confidence interval guidelines were applied.

CHAPTER 6

RESULTS

The results are organized into three primary sections based on the specific aims: [1] Congenital Mitral Valve Repair; [2] Degenerative Mitral Valve Repair; and [3] Surgical Repair for Functional Mitral Regurgitation. In each section, the results are organized in the following order:

[A] Validation of the in-vitro pathological valve model

[B] Pre-Surgical Hemodynamics, Kinematics and Function

[C] Post-Surgical Hemodynamics, Kinematics and Function

To validate the *in-vitro* pathological valve models, 3D echocardiographic images of the porcine valves were obtained in the pulsatile left heart simulator and compared to echocardiographic images from human subjects with that specific valve pathology. Relevant indices such as morphological features, hemodynamic outcomes and leaflet kinematics were quantified and compared to the data available in the literature. However in some valve pathologies, hemodynamic data from human subjects were not available in

the literature and thus validation of the model was limited to comparison of geometric features.

The surgical repairs used in this thesis were performed according to clinical guidelines and standards. If a surgical repair is currently practiced clinically, it was replicated as it is performed on human subjects to avoid deviation in results due to procedural differences between the laboratory setting and actual clinical practice. All the repairs were first practiced on porcine hearts under the guidance of an experienced cardiac surgeon, after which they were replicated on the valves in the pulsatile left heart simulator.

To study the impact of geometric factors on the valve function and mechanics after surgery, changes in annular or sub-annular features were simulated based on a thorough literature review. Though changes in cardiac geometries in human subjects depends largely on their individual physiology, valve geometry or the timing of their surgery, a general trend in annular dimensions or ventricular geometry could be outlined from literature. The studies were thus limited to these features, as simulating every geometric variation would be impractical within the scope of this thesis.

The end points measured in each specific aim are either currently used in clinical practice to diagnose mitral valve pathologies and quantify surgical repair outcomes, or are new with high potential for translation. In the latter case, realistic endpoints were developed using measurement techniques that are practical in the clinical setting and thus have potential for clinical translation. For leaflet mechanics studies, a direct marker

visualization method was used which cannot be implemented in-vivo, but can be used as a "truth method" to validate 3D echocardiography for mechanics measurements.

6.1 CONGENITAL MITRAL VALVE REPAIR

6.1.1 VALIDATION OF CLEFT MITRAL VALVE MODEL

To validate the isolated anterior leaflet cleft valve model used in this study, we acquired 3D echocardiographic images (Philips iE33 Echocardiography System, Andover, MA) of the porcine valve in the pulsatile left heart simulator. Figure 6-1A-F show the sequential alterations to the valve geometry to simulate the cleft mitral valve pathology, and Figure 6-1G-H show the systolic reconstructions from a human subject with a cleft mitral valve [1] and the in-vitro heart model, respectively. In Figure 6-1G, the dotted black line represents the mitral annular shape with a straight anterior portion and a curved posterior portion. The anterior leaflet is clearly divided into two bridging leaflets (Superior Bridging Leaflet (SBL) and Inferior Bridging Leaflet (IBL)) by the central cleft, while the posterior/mural leaflet is significantly smaller compared to a normal valve. The commissures are displaced posteriorly and thus tether on the anterior leaflet edges, potentially restricting the motion of the free edges of the anterior leaflet. During systole, a combination of restricted anterior leaflet and smaller posterior leaflet results in opening of the anterior cleft and loss of leaflet coaptation as seen in Figure 6-1G. Similar geometric characteristics were seen in the systolic echocardiographs obtained on the *in-vitro* valve model as well, thus validating the bench-top cleft mitral valve model. Valve

hemodynamics was not compared, as the pressure and flow recordings in pediatric patients with a cleft mitral valve were unavailable in the literature.

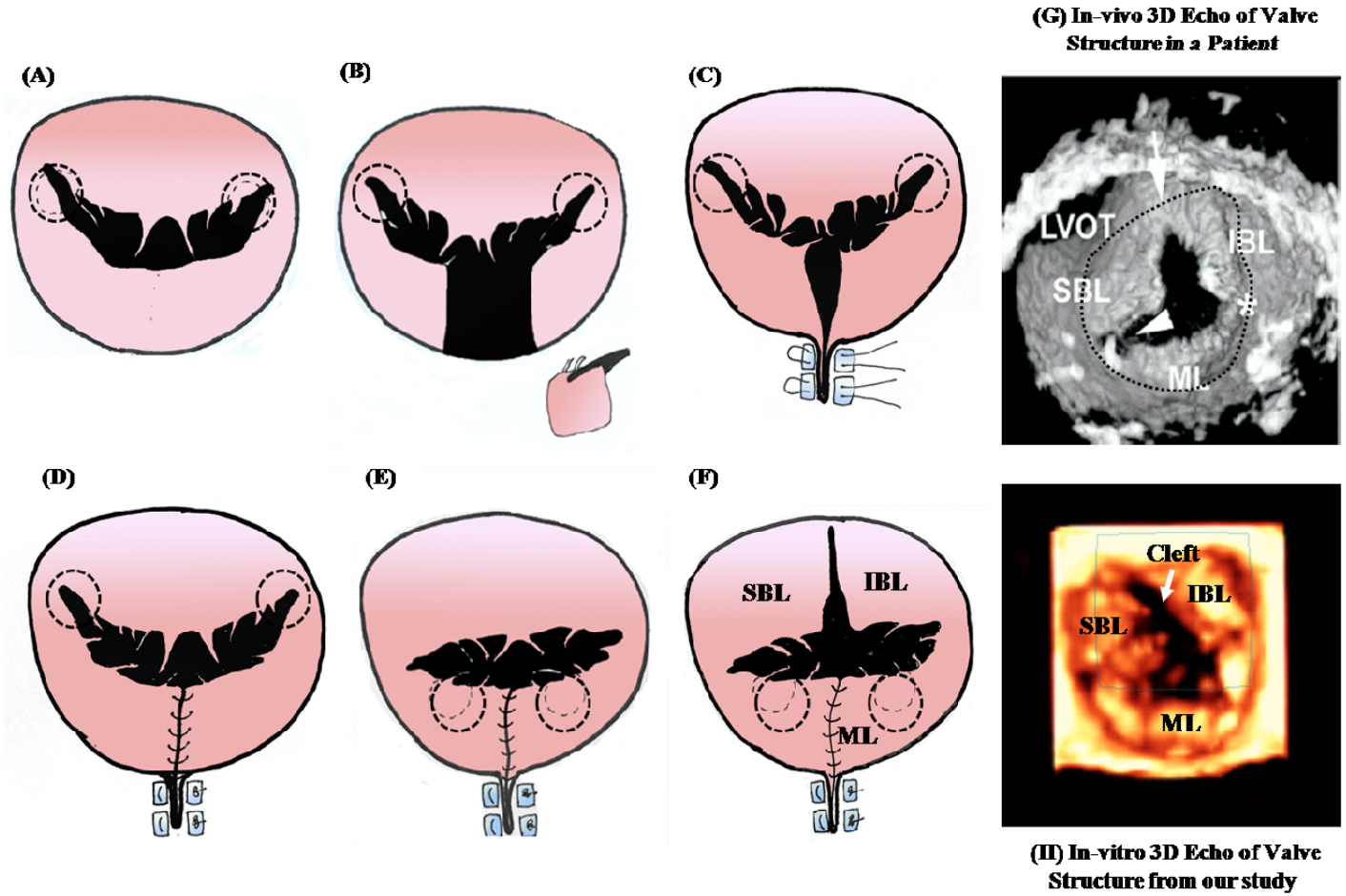

Figure 6-1 (A-F) Sequential steps to alter the native mitral valve geometry to mimic the left atrioventricular valve in the canal defects. The dotted circles indicate the position of the papillary muscles. The images on the right (G,H) compare the valve structure with cleft (arrow) obtained from our *in-vitro* setup under pulsatile hemodynamic conditions with one obtained from a patient, using 3D echocardiography. SBL: Superior Bridging Leaflet, IBL: Inferior Bridging Leaflet, ML: Mural/Posterior Leaflet

6.1.2 IMPACT OF SMALLER MURAL LEAFLET AND OBLIQUE PAPILLARY MUSCLE POSITION ON VALVE HEMODYNAMICS

To understand the impact of smaller posterior leaflet area, and the scooped ventricular geometry on the hemodynamic function of the cleft mitral valve, the regurgitation volumes of the normal mitral valve before creating the cleft defects and the valve after creating the pathological geometric features (still without the cleft) were measured. With the physiological valve geometry i.e., normal annular size and physiological papillary muscle positions, there was no regurgitation recorded across the valve. Reducing the area of the mural leaflet with posterior annular plication, (but with normal annular size and papillary muscle positions) induced 0.7±0.3 ml/beat of regurgitation that was statistically insignificant ($p=0.12$). Oblique displacement of the papillary muscles with posterior and lateral displacement of the muscles increased the regurgitation volume to 0.7±0.3 ml/beat with a normal annular size ($p=0.07$), though no statistical difference between the groups could be established. These results indicate that the smaller posterior leaflet or the pathological papillary muscle positions by themselves do not directly impact the hemodynamic function of the valve. However, when the mitral annulus was dilated by 20% and 40% respectively, a significant increase in the regurgitation volumes was measured as tabulated in Table 6-1. With the oblique papillary muscle position, the regurgitation volume increased to 4.2±1.1 ml/beat ($p< 0.0001$) at 20% annular dilatation and 9.3±2.4 ml/beat at 40% annular dilatation ($p < 0.0001$), in comparison to 0.7±0.3 ml/beat with the normal annular size.

Table 6-1 Comparison of the regurgitation volumes between the normal papillary muscle position and the obliquely positioned pathological papillary muscle position at different annular sizes

	Normal Annulus Size (ml/beat)	20% Dilated Annulus Size (ml/beat)	40% Dilated Annulus Size (ml/beat)
Valve with Smaller Posterior Leaflet and Normal Papillary Muscle Position	0 ± 0	3.5 ± 0.8	9.5 ± 2.3
Valve with Smaller Posterior Leaflet and Oblique Papillary Muscle Position	0.7 ± 0.3	4.2 ± 1.1	9.3 ± 2.4

6.1.3 IMPACT OF LENGTH OF CLEFT CLOSURE

Four levels of cleft closure were evaluated in this study with a normal size annulus: unclosed cleft, 1/3rd cleft closed, 2/3rd cleft closed and full cleft closure, as shown in Figure 6-2. For each length of cleft closure, the regurgitation volumes were measured by direct flow measurement. Figure 6-3 illustrates the comparison between regurgitation volumes for the four levels of cleft closure at a normal annular size. With the cleft fully open a regurgitant volume of 12.56±2.4 ml/beat was recorded, which is can be considered a moderate amount of regurgitation under pediatric hemodynamic conditions. Closure of the cleft to one-third of its total length reduced the regurgitant volume to 9.96±2.1 ml/beat and with statistically significant reduction from the fully open cleft case ($p = 0.001$). Two-thirds cleft closure further reduced the regurgitation to 4.9±1.9 ml/beat, which was significantly smaller than the fully open cleft ($p<0.001$) and

one-third cleft closure (p=0.001) respectively. With complete closure of the cleft, most of the regurgitation was reduced to mild levels of 1.4 ± 1.6 ml/beat, which was a significant reduction compared to rest of the three groups (p<0.001 for all the three groups).

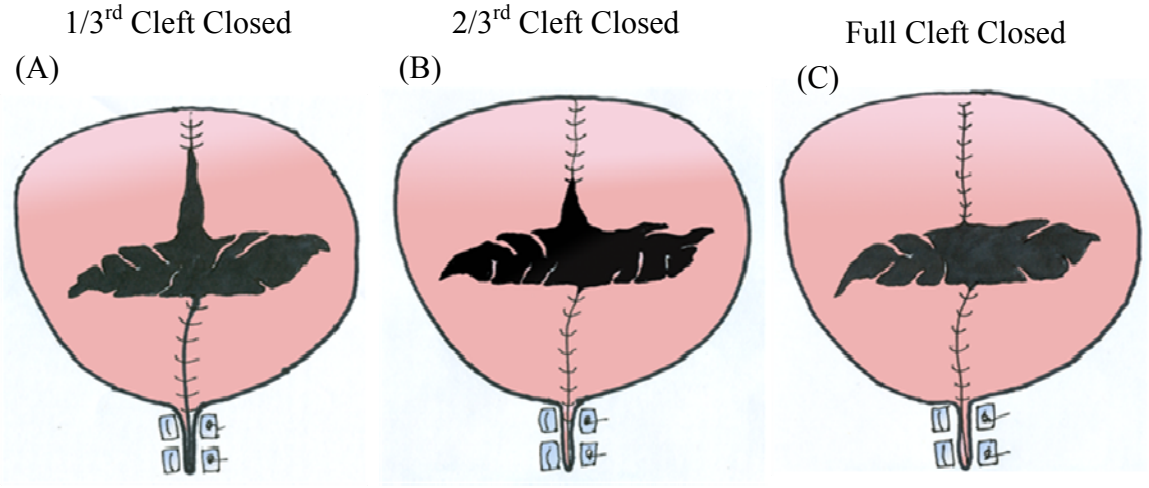

Figure 6-2 Schematic showing the three levels of cleft closure used in this study. (A) 1/3rd cleft closure wherein only the region closest to the annulus was closed, (B) 2/3rd cleft closure with most of the cleft closed except for the region near the free edge, (C) Cleft completely closed

To clearly illustrate the role of the length of cleft closure, the regurgitation volumes with different cleft lengths were normalized by the volume with the fully open cleft. A strong inverse correlation was observed between the length of cleft closure and the mitral regurgitation volume, as shown in Figure 6-4 and defined by Equation 6-1:

$$\text{Normalized Regurgitant Volume} = -0.956(\text{Cleft Closure Length}) + 1.012 \qquad \text{Equation 6-1}$$

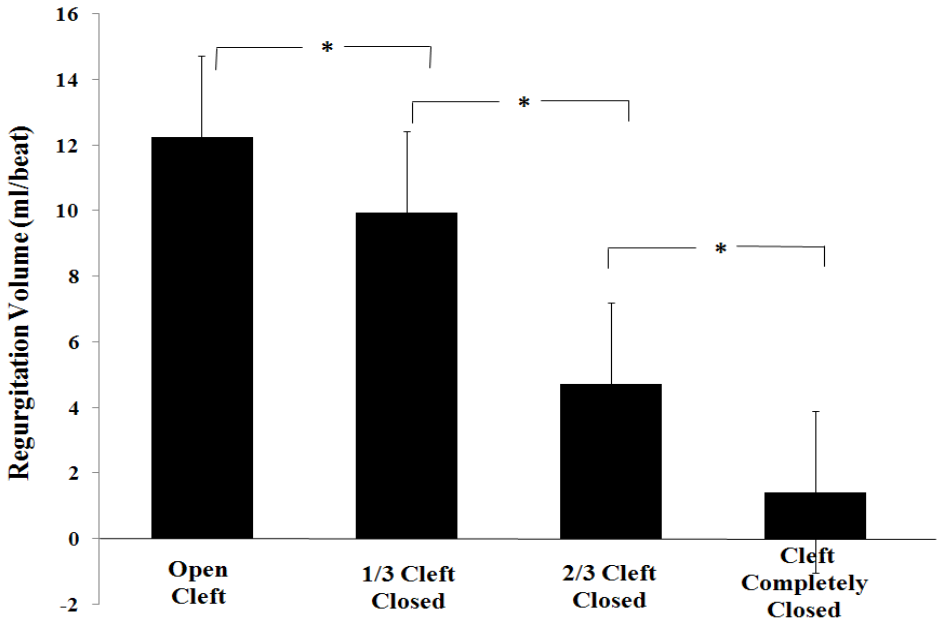

Figure 6-3 Regurgitation volumes obtained for an open, one-third closed, two-third closed and completely closed cleft lengths

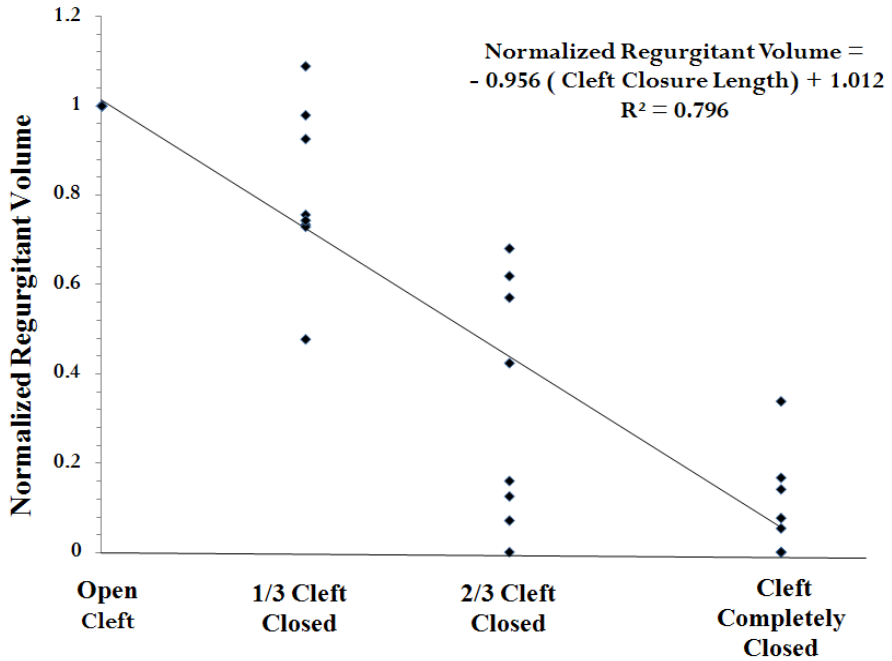

Figure 6-4 Normalized regurgitation volume plotted against the cleft closure length for each valve. Normalized regurgitation volume was obtained by dividing the regurgitation volume for the one-third, two-third and fully-closed conditions with the corresponding open cleft regurgitation volume. The equation clearly shows a negative correlation between the regurgitation volume and the cleft closure length.

6.1.4 IMPACT OF POST SURGICAL ANNULAR DILATATION

One of the challenges with pediatric mitral valve repair is the growth of cardiac structures in the post-operative period. As the body surface area of the patient increases with age, a 20-40% increase in mitral annular area has been reported in normograms from these patients. To understand the impact of such increase in annular size on the competence of the repaired cleft valve, for each level of cleft closure 20% and 40% annular dilatation was simulated and its impact on regurgitation volume was quantified. Results from these experiments demonstrated that annular dilatation induced significant increase in regurgitant volume irrespective of the length of cleft closure. For a fully open cleft the regurgitant volume increased from 12.2 ± 2.1 ml/beat at normal annulus size to 13.7 ± 1.1 ml/beat ($p = 0.001$) for 20% dilatation and 14.7 ± 0.8 ml/beat ($p=0.027$) for 40% dilatation respectively. When a third of the cleft was closed, a 20% increase in the annular size resulted in a significant change in the regurgitant volume from 9.9 ± 2.8 ml/beat at normal size to 12.1 ± 2.4 ml/beat ($p = 0.001$). With further dilatation of the annulus to 40%, the regurgitant volume increased to 14.0 ± 1.7 ml/beat, which was significantly different from both the normal annulus ($p =0.002$) and the 20% dilated annulus ($p =0.007$). For the two-third cleft closure, the regurgitant volume changed from 4.7 ± 3.3 ml/beat at normal annulus size to 8.5 ± 2.5 ml/beat ($p = 0.002$) and 11.4 ± 1.8 ml/beat ($p=0.0001$), for 20% and 40% increase in annular size respectively. When the cleft was completely closed these levels of annular dilatation resulted in a significant increase in the regurgitant volumes from 1.4 ± 2.8 ml/beat for normal annular size to 4.5 ± 2.3 ml/beat ($p = 0.0001$) for 20% increase in annular size and 8.7 $\pm$ 1.5 ml/beat ($p = 0.0001$) for 40% increase in annulus size as shown in Figure 6-5.

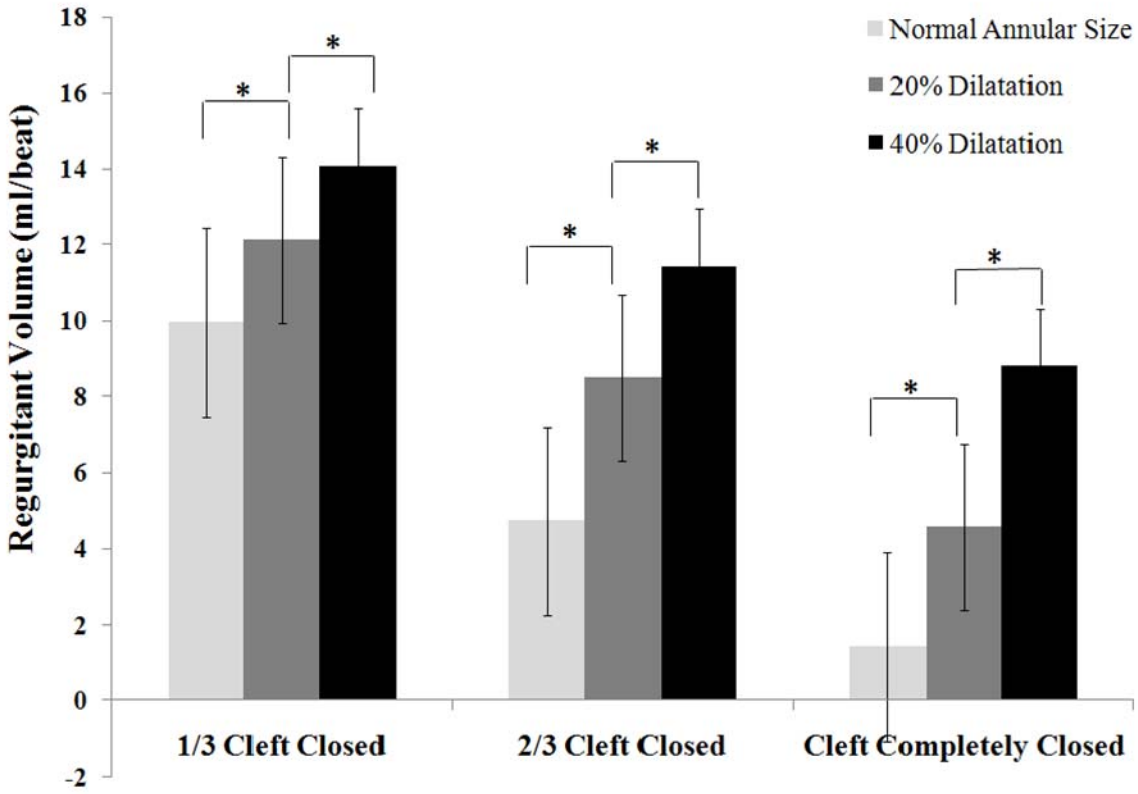

Figure 6-5 Increase in the systolic regurgitation volume due to annular dilatation for the three levels of cleft closure. (Left) At 1/3rd cleft closure, a 50% increase in regurgitation is visible from the normal to the most dilated state. (Center) With 2/3rd cleft closure a 60% increase in regurgitation was measured at the most dilated state, (Right) At complete cleft closure, the increase in regurgitation with annular dilatation was much higher at 400%

6.1.5 IMPACT OF ANNULAR UNDERSIZING ON REGURGITATION

The results from the previous section clearly demonstrate that with increase in annular area, regurgitation significantly increases. Thus to test if mitral annular undersizing has an impact in reducing regurgitation volume and if it renders the valve stenotic, valve competence with 20% and 40% annular undersizing were also studied. Figure 6-6 illustrates the effect of undersizing the annulus on the regurgitant volume for the four cleft closure lengths. For the fully open cleft, a 20% reduction in the annular area from the normal decreased the regurgitant volume from 12.56 ± 2.4 ml/beat to 10.83 ± 1.8 ml/beat and to 9.8 ± 1.9 ml/beat for 40% annular undersizing. Similarly, for the one-third cleft closure length, a 20% reduction in annular area decreased the regurgitant volume from 9.95 $\pm$ 3 ml/beat to 7.78 $\pm$ 2 ml/beat ($p = 0.007$). An additional 20% reduction in annular area (40% cumulative reduction in the annulus size), decreased the regurgitation volume significantly to 4.44 $\pm$ 1.9 ml/beat ($p = 0.001$). Similarly, for the two-third cleft closure length the regurgitation volume decreased from 4.73 $\pm$ 2.8 ml/beat at the normal annular size to 2.05 $\pm$ 2.1 ml/beat ($p = 0.518$)for 20% reduction in the annulus size and further undersizing by an additional 20% decreased the MR to 0.7 $\pm$ 1.2 ml/beat ($p = 0.533$). The p-values are in comparison to the regurgitation volume of the valve with a smaller posterior leaflet and obliquely placed papillary muscles, and without an anterior cleft.

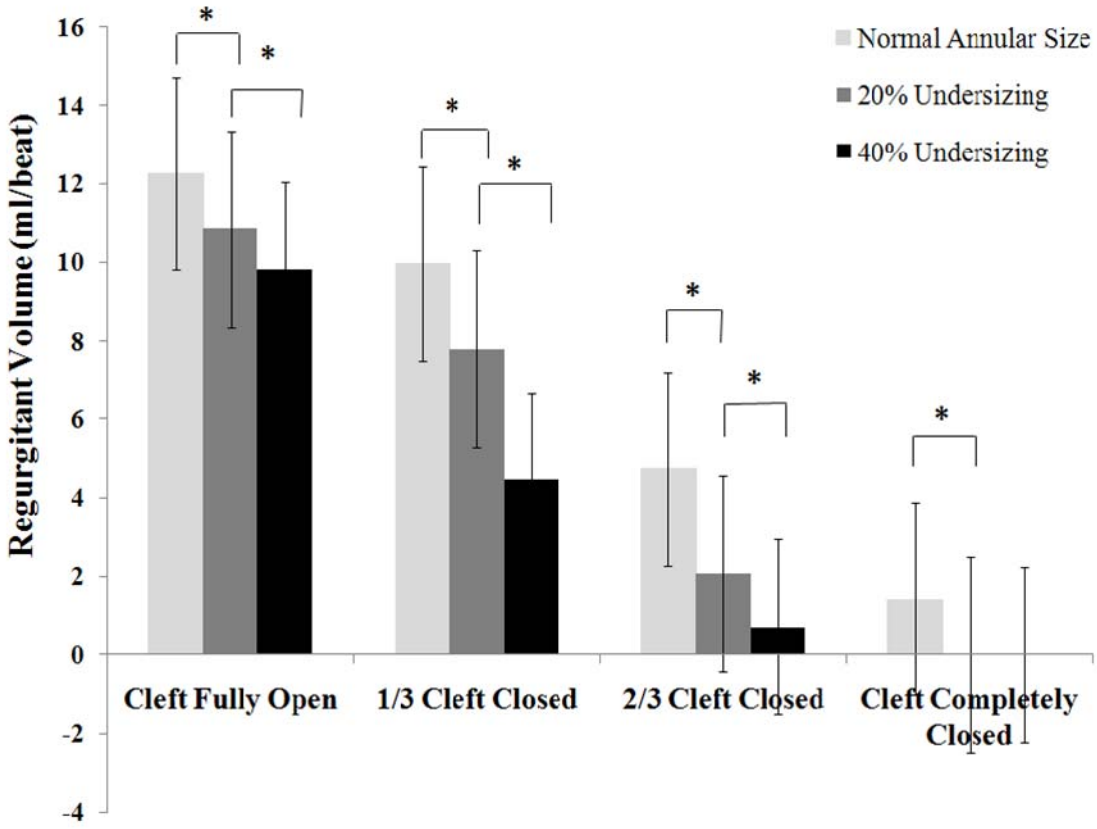

Figure 6-6 Decrease in the systolic regurgitation volume with 20% and 40% annular undersizing for the three levels of cleft closure.

6.1.6 DIASTOLIC EFFECTIVE ORIFICE AREA: PRE AND POST SURGERY

Mitral annular undersizing though beneficial in reducing regurgitation in the cleft mitral valve, it could potentially induce mitral stenosis due to restricted growth of the mitral annulus. Such mitral stenosis may potentially impede diastolic ventricular filling, which could have several deleterious effects on the ventricular function and also may lead to chronic pulmonary hypertension. For the eight valves studied, diastolic effective orifice area was calculated from the transvalvular flow and pressure gradient, both pre and post surgery. Figure 6-7 demonstrates the average effective orifice area for each experimental condition in comparison to the baseline (fully open cleft and normal annular size). At baseline conditions, the calculated effective orifice area was 3.23±0.49 cm^2. When $1/3^{rd}$ of the cleft was closed and the annular size was at its normal levels, the orifice area changed to 4.32±1.95 cm^2 and with 40% undersizing of the annulus reduced to 3.46±1.81cm^2. However the differences between these groups were not statistically significant (p =0.734). When the cleft was further closed to $2/3^{rd}$ of its total length and the annular size was normal, the calculated effective orifice area was 3.94±1.76 cm^2 and with 20% undersizing was 3.37±1.09, with no statistical difference between the groups. Complete cleft closure with normal sized annulus had an effective orifice area of 3.5±1.5cm^2. It should be noted that the effective orifice area was calculated for the groups that demonstrated reduction in regurgitation and thus have the potential for restoring valve competence, thus the $1/3^{rd}$ cleft closure with 20% undersizing and $2/3^{rd}$ cleft closure with 40% undersizing are not reported.

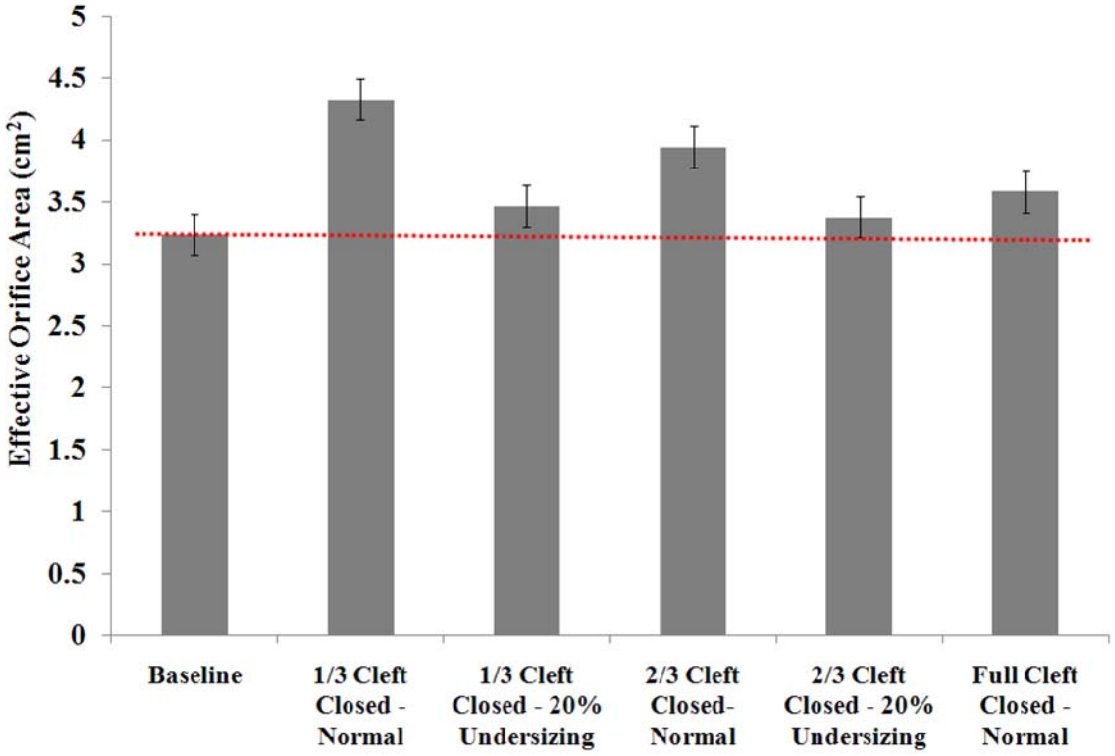

Figure 6-7 Pre and post surgical effective orifice areas measured from the transmitral pressure and flow curves

6.1.7 ECHOCARDIOGRAPHIC IMAGING OF REGURGITANT JETS

To validate the quantitative hemodynamic results, 3D echocardiographic images were obtained using an adult matrix probe array (X7-2, Philips Medical Systems, Andover, MA) for each experimental condition. Figure 6-8 shows the 3D color Doppler images showing the regurgitant jet and the valve leaflets during peak systole. The results demonstrate that when the anterior cleft is completely open, irrespective of manipulating the annular size, and significant regurgitation persisted. These findings corroborate with the quantitative hemodynamic results reported earlier in sections 6.1.3, 6.1.4, and 6.1.5.

Similar results were observed with 1/3rd cleft closure, however with a slightly reduced severity of regurgitation. The 3D color Doppler images show the overall regurgitation through the valve, but were not used to quantify the direction of the jet or the region of regurgitation specifically. With 2/3rd of the cleft closed, regurgitation was observed with the normal or dilated annulus configuration, but not when the annulus was undersized. With reduction in the septal-lateral dimension of the annulus, the open part of the cleft may be included into the coaptation and thus provide the required seal to stop regurgitation during systole. Full cleft closure eliminated regurgitation completely as expected, as during systole there would be no regurgitant orifice through which blood can flow back into the left atrium. However when the annulus was dilated, mild regurgitation persisted in these valves even after the cleft was completely closed.

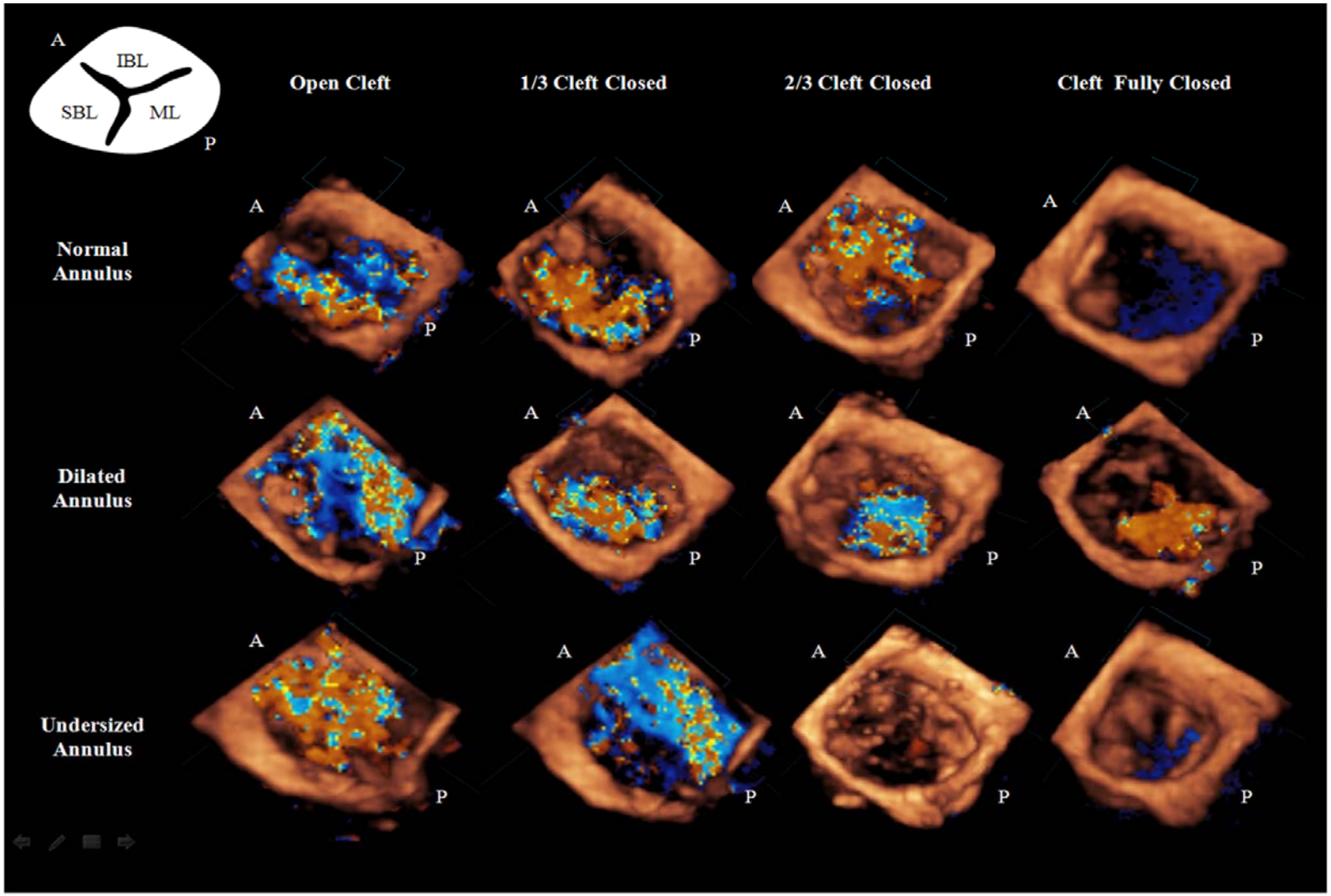

Figure 6-8 Color Doppler images of the cleft mitral valve at different cleft closure lengths and annular sizes, depicting the regurgitation jets through the valve.

6.2 DEGENERATIVE MITRAL VALVE REPAIR

Degenerative mitral valve disease encompasses a spectrum of lesions, with different etiologic basis and pathologic manifestations. In the western world the two most common adult degenerative mitral valve lesions are Barlow's disease and Fibroelastic deficiency. There is a large volume of work on surgical strategies for Barlow's disease, but knowledge of optimal techniques to repair fibroelastic deficient mitral valves has been minimal. In this study, an in vitro model of mitral valve prolapse due to acute chordal rupture was developed to simulate the clinical case of fibroelastic deficiency.

6.2.1 VALIDATION OF IN VITRO MODEL FOR ACUTE POSTERIOR LEAFLET PROLAPSE

Leaflet prolapse was simulated in normal porcine mitral valves by transecting the marginal chordae inserting into the free edge of the leaflet, either posterior or anterior based on the experiment. Typically, valves with fibroelastic deficiency are structurally normal without any distension or billowing which justifies the use of normal valves for this study. The prolapsing valves were studied in the pulsatile left heart simulator, and echocardiographic images were obtained to record the leaflet motion and regurgitation jets. The acquired data was then compared to intra-operative videos and echocardiographs provided by Dr. David H. Adams from the Mt. Sinai School of Medicine. Accuracy of the valve model was ensured with a qualitative comparison of the in vitro and in vivo images and the comparison is shown in Figure 6-9A-E.

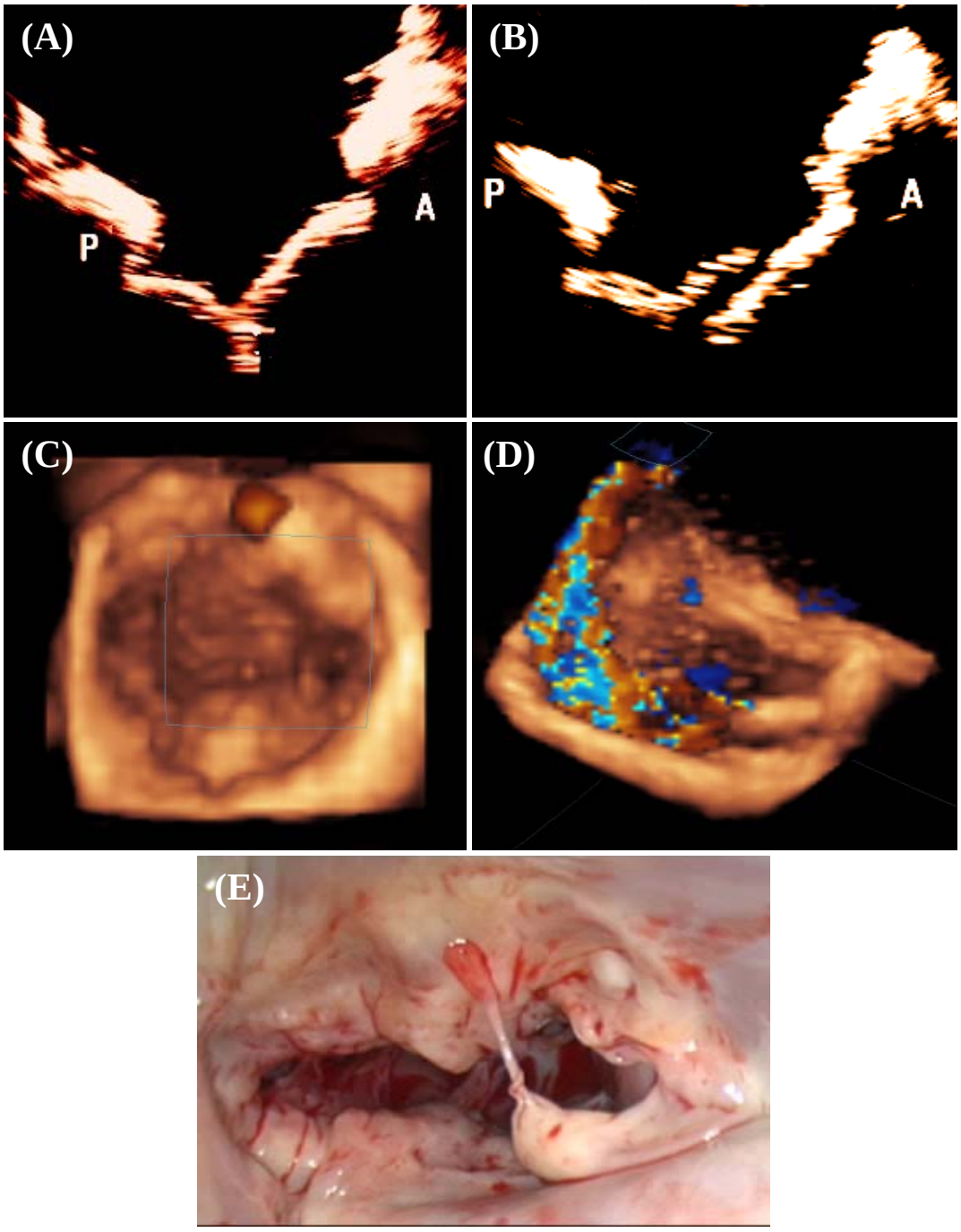

Figure 6-9 (A) 2D echo of a normal mitral valve with excellent coaptation, (B) Posterior leaflet prolapse after marginal chordal rupture, (c) 3D echocardiographic image of the normal valve with good coaptation, (d) An eccentric anteriorly directed regurgitation jet due to posterior leaflet prolapse, (e) An intra-operative image with an isolated ruptured chord on the posterior leaflet

Figure 6-9A shows the 2D-echocardiographic image along the septal lateral plane of the mitral valve, at the A2 and P2 valve cusps. Excellent leaflet coaptation is evident from the images, without any regurgitation evident on the valve. After marginal chordal transection, isolated prolapse of the P2 cusp is observed as shown in Figure 6-9B with the posterior leaflet overriding the anterior leaflet and resulting in a regurgitation orifice. En-face 3D echocardiographic image of the normal valve as shown in Figure 6-9C depicts good coaptation from the commissure-to-commissure of the valve. Figure 6-9D shows an eccentric regurgitant jet in a posterior leaflet prolapse valve, flowing along the anterior leaflet surface into the left atrium which is equivalent to the clinical setting. Figure 6-9E shows an intra operative image of the valve with the isolated posterior chordal rupture, which was the scenario simulated in the in vitro model.

6.2.1.1 Part A – Hemodynamic Comparison of Resective and Non- Resective Techniques to Correct Acute Posterior Leaflet Prolapse

Three types of surgical repair techniques were compared in this study to correct posterior leaflet prolapse in a fibro-elastic deficient valve, and the post-repair hemodynamics and valve kinematics are reported. The efficacy of each technique in restoring physiological valve function and mechanics is reported and discussed.

6.2.1.1.1 Impact of Leaflet Resection on Post-Repair Regurgitation

Mitral regurgitation volumes were measured pre and post surgery in the in-vitro acute posterior leaflet prolapse model. Under control/baseline conditions with normal porcine mitral valves, no regurgitation was recorded as shown in Figure 6-10. Transecting the marginal chordae inserting into the free edge of the P2 cusp induced

isolated P2 prolapse with severe regurgitation of 19.31±4.3ml/beat. Surgical correction of the valves was performed in three sequential steps, with neochordoplasty being performed first, followed by triangular resection and finally quadrangular resection with annular plication. Neochordoplasty significantly reduced mitral regurgitation compared to the prolapse group, with an average remnant regurgitation of 2.8±1.2ml/beat (p=0.007, compared to prolapse). Limited triangular resection also reduced regurgitation significantly to 2.5±1.0ml/beat (p=0.008), and was comparable to the neochordoplasty group. Remnant regurgitation after quadrangular resection was slightly higher than the other two repair groups at 4.3±1.5ml/beat, but the reduction was significant compared to the prolapse group (p=0.007).

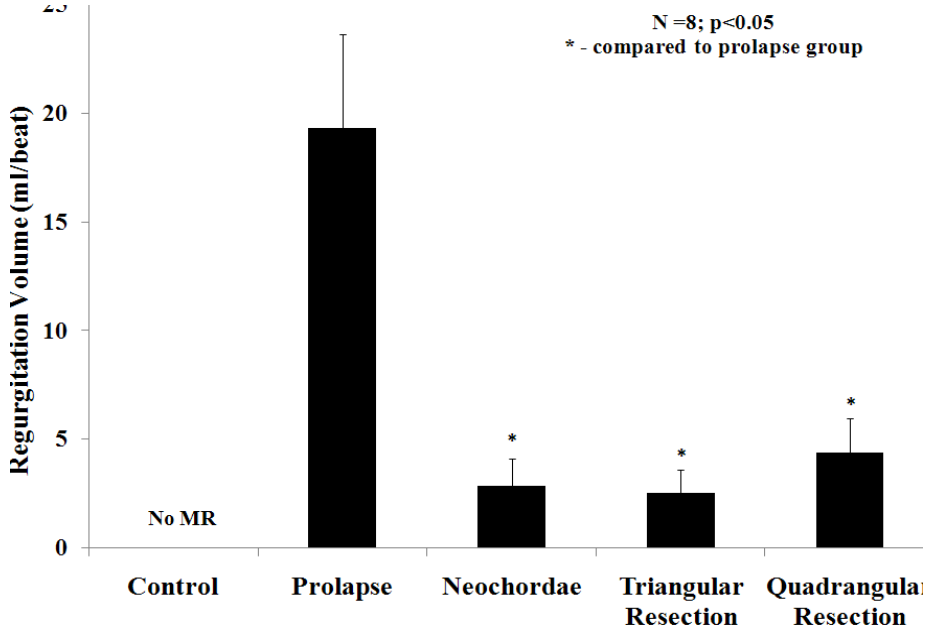

Figure 6-10 Pre and post repair regurgitation volumes for the three procedures demonstrating comparable reduction in regurgitation between the three surgical procedures

6.2.1.1.2 Impact of Leaflet Resection on Leaflet Coaptation Length

During systolic valve closure, the length or area of coaptation of the anterior and posterior leaflets plays a key role in determining the severity or lack of regurgitation. In this study, 2D leaflet coaptation length was measured along the septal-lateral plane of the mitral annulus under control and post-repair conditions. At baseline with native porcine mitral valves, an average coaptation length of 11.4±1.4mm was measured, which corroborates with previously published data on porcine mitral valves. With marginal chordal transection and isolated P2 prolapse, coaptation along the A2-P2 cusps was completely lost as shown in Figure 6-11. Neochordoplasty restored coaptation to physiological levels of 11.8±1.7mm, and was statistically comparable to the control group ($p=0.2$). Limited triangular resection at the P2 free edge restored coaptation length to 9.4±1.4mm, which was significantly smaller than the control group ($p=0.01$) and also compared to neochordoplasty group ($p= 0.05$). Quadrangular resection with annular plication was the last procedure, and the coaptation length with this surgical procedure was reduced to 7.2±0.8mm, which was significantly smaller than the control ($p=0.0001$), neochordoplasty ($p<0.001$) and triangular resection ($p=0.03$) groups.

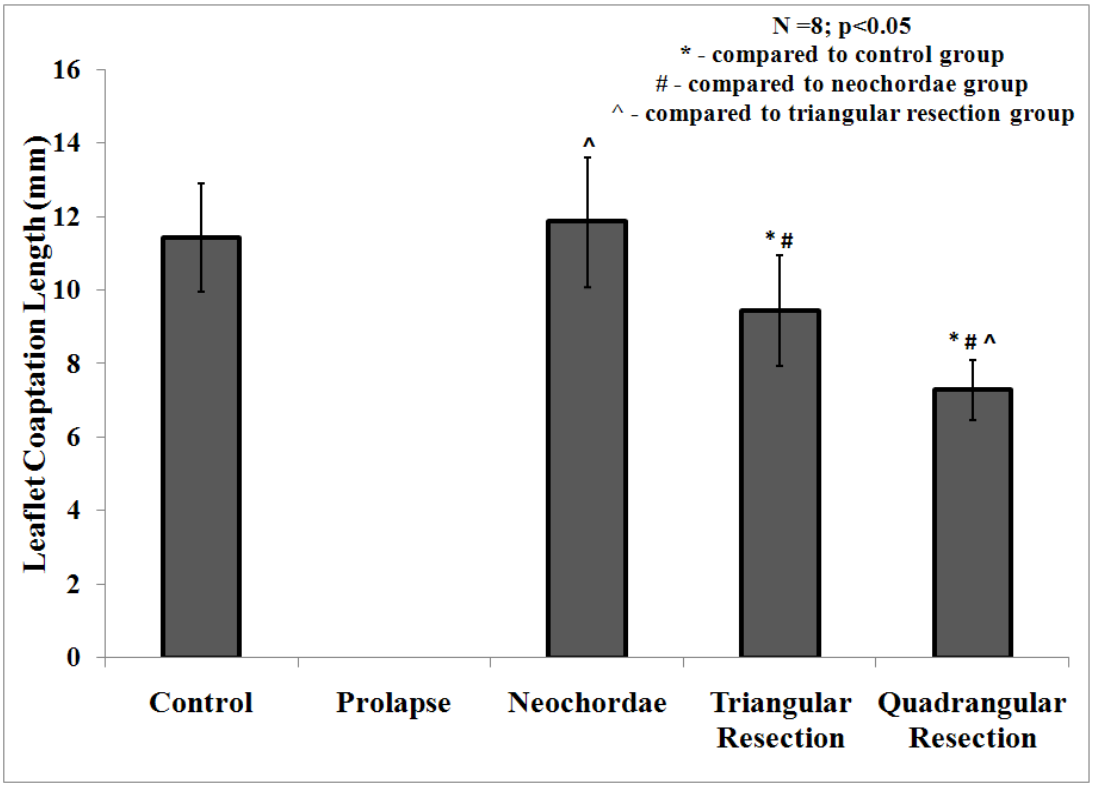

Figure 6-11 Pre and post operative leaflet coaptation lengths for the three procedures demonstrating higher coaptation lengths for non-resective neochordoplasty in comparison to resective procedures

6.2.1.1.3 Leaflet Mobility as an Index to Assess Repair Durability

Posterior leaflet mobility after each surgical repair was assessed using simple echocardiographic measurements:(a) Perpendicular distances from the leaflet coaptation zone to the posterior (Δp) and anterior (Δa) annulus in the septal-lateral plane; (b) Peak systolic excursion angles of the posterior (α) and anterior (β) leaflets; and (c) Depth of leaflet coaptation from the mitral annular plane as shown in Table 6-2. The distance of the coaptation zone from the anterior and posterior annulus were nearly equal in the control case (Δp=14.2±1.9mm, Δa=20.8±1.9mm), showing that the leaflet coaptation was centrally positioned from the anterior and posterior annulus in normal valves. A similar

coaptation geometry was observed after Neochordoplasty (Δp=15.4±1.2mm, p=0.09; Δa=20±2.1mm, p=0.35) as the control group. However, both limited triangular resection (Δp=13.1±1.4mm, p=0.03; Δa=22.2±2.6mm, p=0.04) and quadrangular resection (Δp=10.2±2.0mm, p=0.006; Δa=23.9±2.5mm, p=0.01) restricted posterior leaflet mobility, resulting in displacement of the coaptation zone posteriorly. Additionally, we quantified the peak systolic leaflet angles made by the posterior and anterior leaflets with the mitral annulus as a measure of systolic leaflet mobility. The posterior leaflet angles in the neochordoplasty group (α=34.2±3.6^o, p=0.77), and limited triangular resection (α=37.4±3.3^o,p=0.25) were comparable to the control (α=33.5±6.6^o), but were significantly higher in the quadrangular resection group (α=51.2±10.8^o, p=0.01), as shown in Table 6-2. The anterior leaflet angles were consistent between the four conditions, indicating that the anterior leaflet has a threshold beyond which it cannot move to coapt with the posterior leaflet due to the limited extension of the anterior chordae tendineae.

Table 6-2 Post-Surgical Leaflet Kinematics with Resective and Non-resective Surgical Repair Procedures

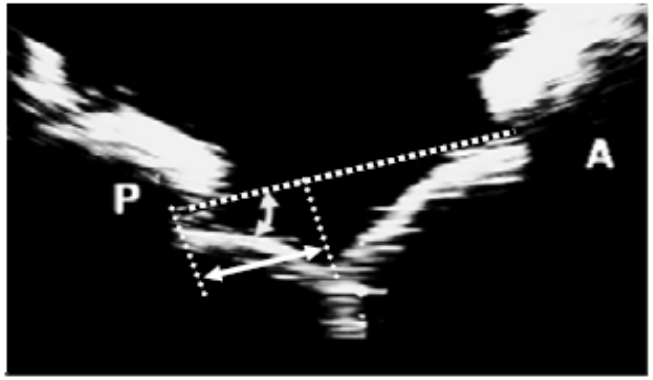

	Control	Neochordoplasty	Triangular Resection	Quadrangular Resection
Posterior Leaflet Angle (α) in degrees	33.5 ± 6.6	34.2 ± 3.6	37.4±3.3	51.5 ± 10.8#*
Anterior Leaflet Angle (β) in degrees	29.5 ± 3.6	28.4 ± 3.9	27.5 ± 5.4	27.4 ± 4.0

and * represents statistical difference compared to neochordoplasty ($p<0.05$) and control ($p<0.05$) respectively.

6.2.1.1.4 Analysis of Opening and Closing Leaflet Kinematics

2D echocardiographic images of the mitral valve leaflets along the septal-lateral plane were obtained to assess leaflet mobility and systolic coaptation geometry. As shown in Figure 6-12A-2, under physiological geometry the mitral valve had good coaptation with the line of coaptation nearly midway from the anterior and posterior mitral annulus. Transecting the marginal chordae induced isolated P2 prolapse as shown in Figure 6-12B-2 inducing an anteriorly directed regurgitation jet (not shown in the figure). Figure 6-13 shows the diastolic and systolic leaflet positions after the three surgical repair techniques. The most significant finding from these echocardiographic images was that with increased leaflet resection or plication of the annulus, the mobility of the posterior leaflet was significantly reduced. As seen with quadrangular resection with annular plication case in Figure 6-13 C-1 & C-2, the coaptation plane is moved posteriorly from the anterior annulus due to the restricted leaflet mobility.

Systolic coaptation geometry is significantly different between the three repair groups, with quadrangular resection and annular plication case significantly worse compared to the control case. Comparing the diastolic and systolic positions of the posterior leaflet after quadrangular resection indicates minimal leaflet movement even with raising transvalvular pressure gradient, implying that the leaflet is experiencing an opposing force that contributed to the leaflet immobility against the ventricular driving force. On the other hand, limited triangular resection of the prolapsing free edge did not seem to impact leaflet mobility and was comparable to neochordoplasty and the physiological systolic coaptation.

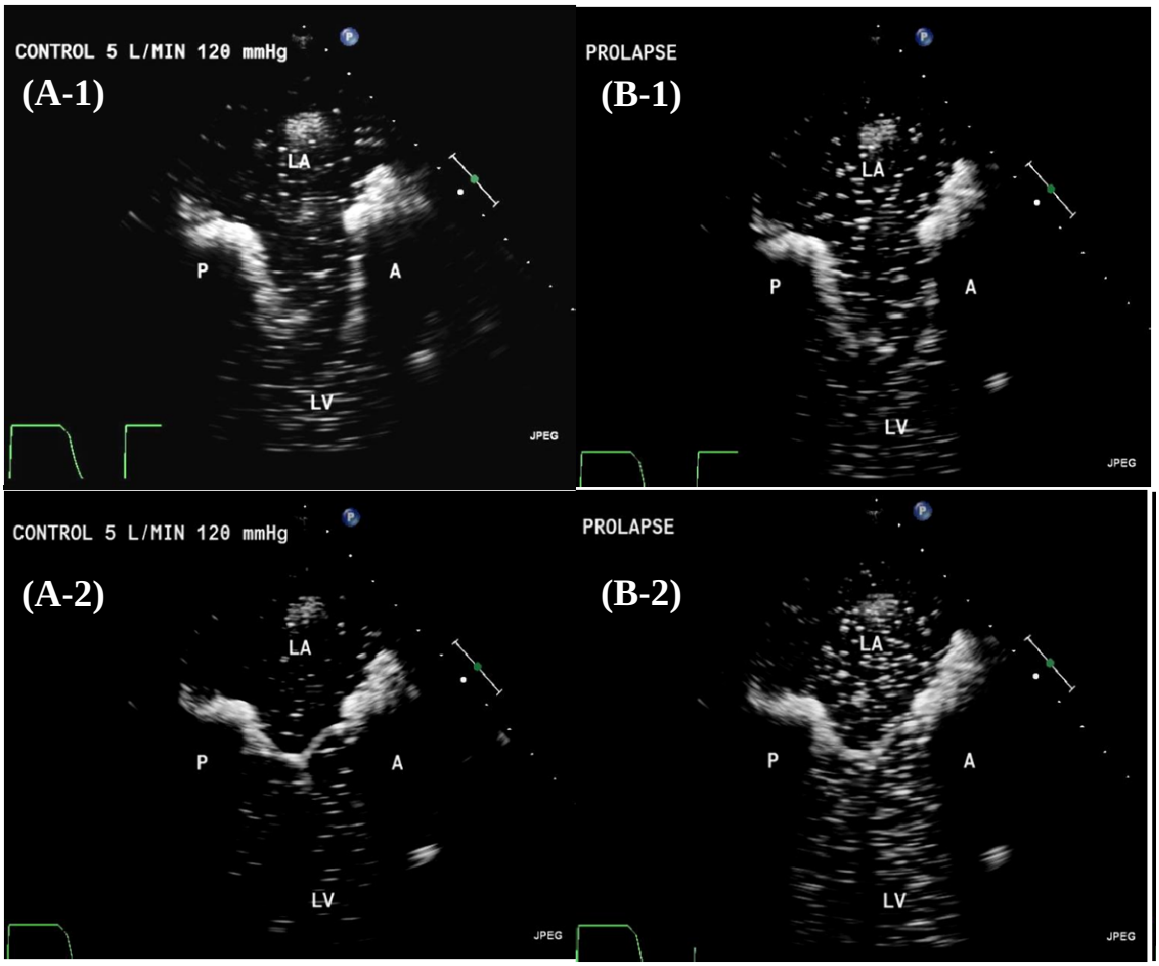

Figure 6-12 (A-1) Diastolic open position of the mitral valve leaflets under control conditions; (A-2) Systolic closed position of the valve leaflets under control conditions; (B-1) Diastolic open position after posterior marginal chordal transection; (B-2) Isolated P2 cusp prolapse after marginal chordal transection.

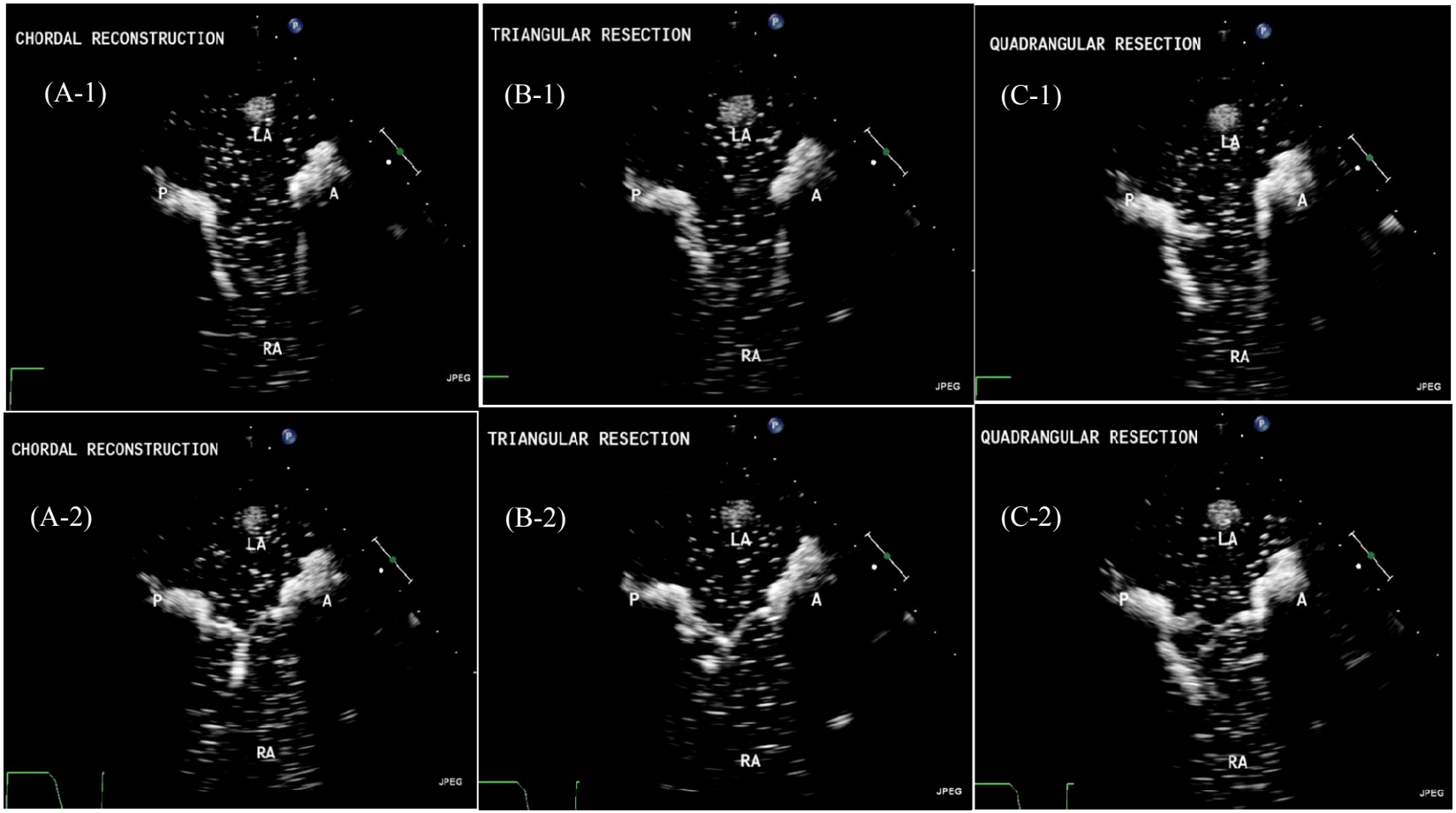

Figure 6-13 Diastolic fully open and peak systolic closed positions of the mitral valve after the resective and non-resective procedures. (A-1) Diastolic fully open position after chordal reconstruction using ePTFE neochordae; (A-2) Peak systolic coaptation after neochordoplasty demonstrating the excellent overlap between the anterior and posterior leaflets, midway from the anterior and posterior annuli; (B-1) Diastolic open position after triangular resection; (B-2) Systolic closed position after triangular resection; (C-1) Diastolic open position after quadrangular resection; (C-2) Systolic closed position after quadrangular resection depicting the immobile posterior leaflet and excessive posterior movement of the anterior leaflet.

6.2.1.2 Part B – Efficacy of Neochordoplasty and Chordal Translocation to Correct Acute Posterior Leaflet Prolapse

6.2.1.2.1 Comparison of Hemodynamic Efficacy

Under control/baseline conditions with normal porcine mitral valves, no regurgitation was recorded as shown in Figure 6-14. Transecting the marginal chordae inserting into the free edge of the P2 cusp induced isolated P2 prolapse and a regurgitation of 13.7 ± 12.7 ml/beat. Surgical correction of the valves was performed in two steps, with neochordoplasty being performed first, followed by translocation of the secondary chordae on the posterior leaflet to the ruptured marginal chordal position on the prolapsing posterior cusp. Neochordoplasty significantly reduced mitral regurgitation compared to the prolapse group, with an average remnant regurgitation of 3.2 ± 2.9 ml/beat ($p=0.007$ – compared to prolapse). Chordal translocation also reduced regurgitation to 2.3±2.6ml/beat ($p=0.008$), and was comparable to the neochordoplasty group. The results clearly indicate that from a hemodynamic perspective, both neochordoplasty and chordal translocation have similar efficacy in reducing regurgitation.

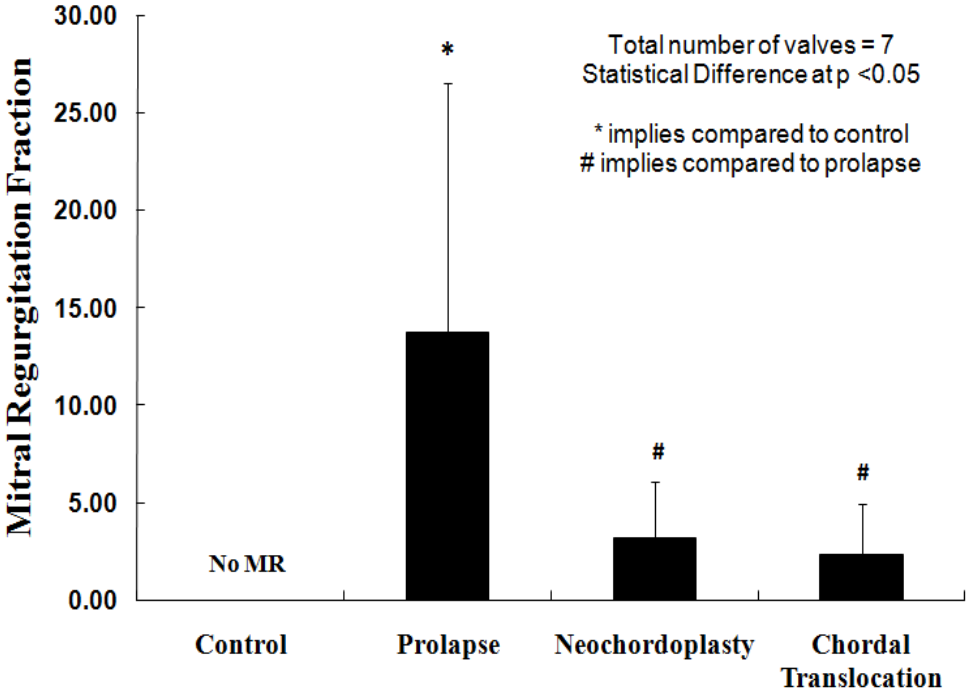

Figure 6-14 Comparison of pre-repair and post-repair regurgitation volumes with neochordoplasty and chordal translocation for acute posterior leaflet prolapse, demonstrating comparable results between the two surgical techniques

6.2.1.2.2 Comparing Leaflet Coaptation Length

2D leaflet coaptation length was measured along the septal-lateral plane of the mitral annulus under control and post-repair conditions. At baseline with native porcine mitral valves, an average coaptation length of 11.0±4.0 mm was measured, which is in the range of previously published data on porcine mitral valves. With marginal chordal transection and isolated P2 prolapse, coaptation along the A2-P2 cusps was completely lost as shown in Figure 6-15. Neochordoplasty restored coaptation to physiological levels of 14.0 ± 4.0 mm, and was statistically comparable to the control group (p=0.2). An average coaptation length of 12.5 ± 0.45 mm was measured after chordal translocation to

the marginal position, and was comparable to both the neochordae (p =0.7) and control (p=0.8).

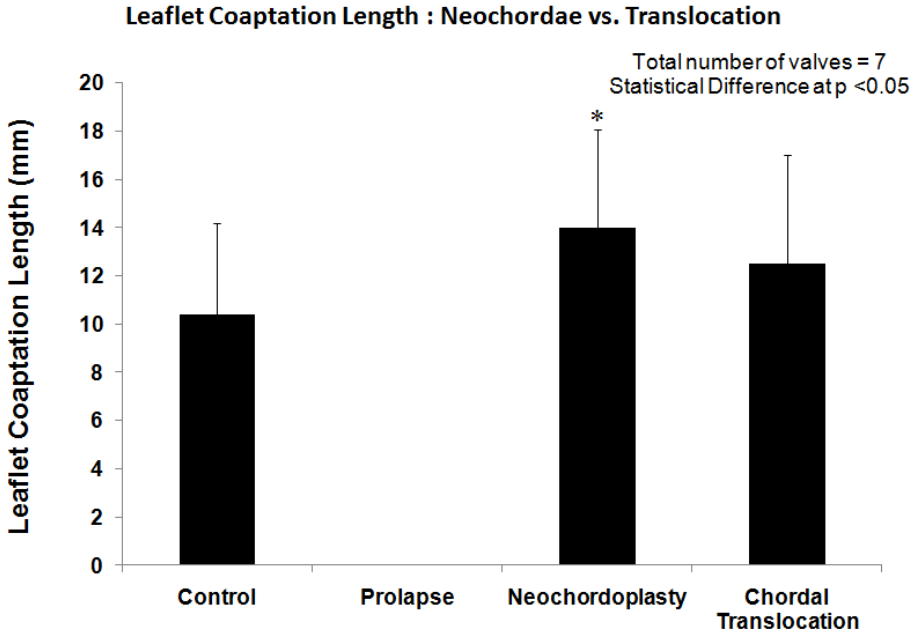

Figure 6-15 Leaflet coaptation length after neochordoplasty and chordal translocation showing comparable measurements between the two techniques.

6.2.1.2.3 Comparing Posterior Leaflet Mobility after Surgical Repair

Posterior leaflet mobility after each surgical repair was assessed using simple echocardiographic measurements: (a) Perpendicular distances from the leaflet coaptation zone to the posterior annulus in the septal-lateral plane, (b) Peak systolic posterior angle. The distance of the coaptation zone from posterior annulus were statistically equal in the control (19.8 ± 2.2mm), Neochordoplasty (19.8 ± 0.5 mm) and chordal translocation (20.5 ± 1.0 mm) cases. The results shown in Figure 6-16 demonstrate that the systolic posterior angle was comparable between neochordoplasty and chordal translocation,

which is an indicator that both repairs effectively restore posterior leaflet mobility to the control levels.

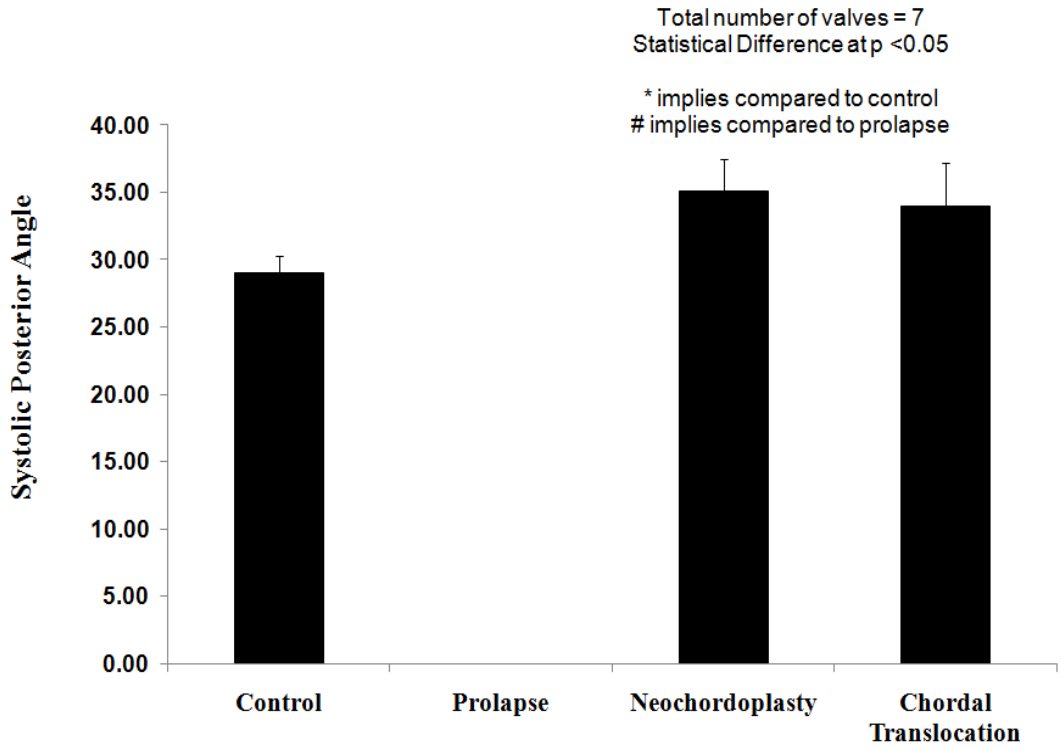

Figure 6-16 Comparison of pre-repair and post-repair posterior leaflet angle with neochordoplasty and chordal translocation for acute posterior leaflet prolapse

6.2.1.3 Part C – Mechanics of the Strut Chordae Insertion Region

6.2.1.3.1 Reference Surface Fitting and Marker Array Placement

The finite element surface fitting technique fit the spatial positions of the 31 marker array very well, with $R^2 \geq 0.98$ and a mean error of ±0.07 mm as shown in Figure 6-17. Figure 6-18 illustrates the deformation of the finite element mesh from late diastole, through systole, till early diastole, depicting the regions where the largest out of plane deformation is observed.

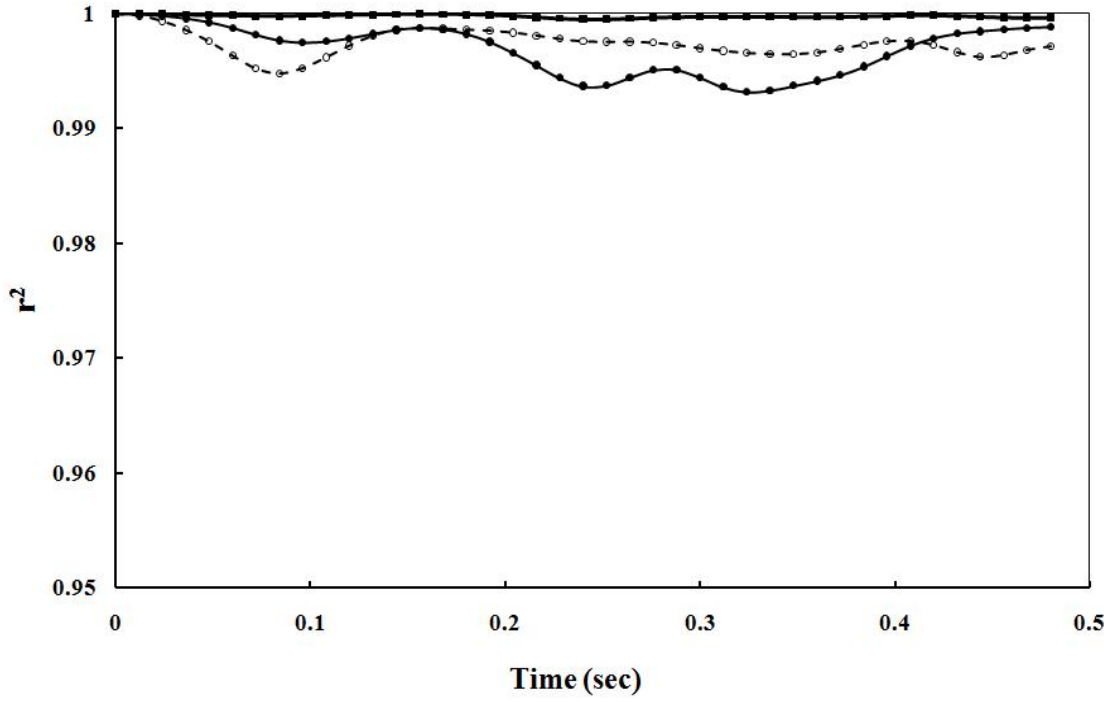

Figure 6-17 Averaged goodness of fit between the marker coordinates and the finite element surface at different time points in the cardiac cycle. Excellent fit was obtained throughout the cardiac cycle validating the use of appropriate shape functions to define the surface.

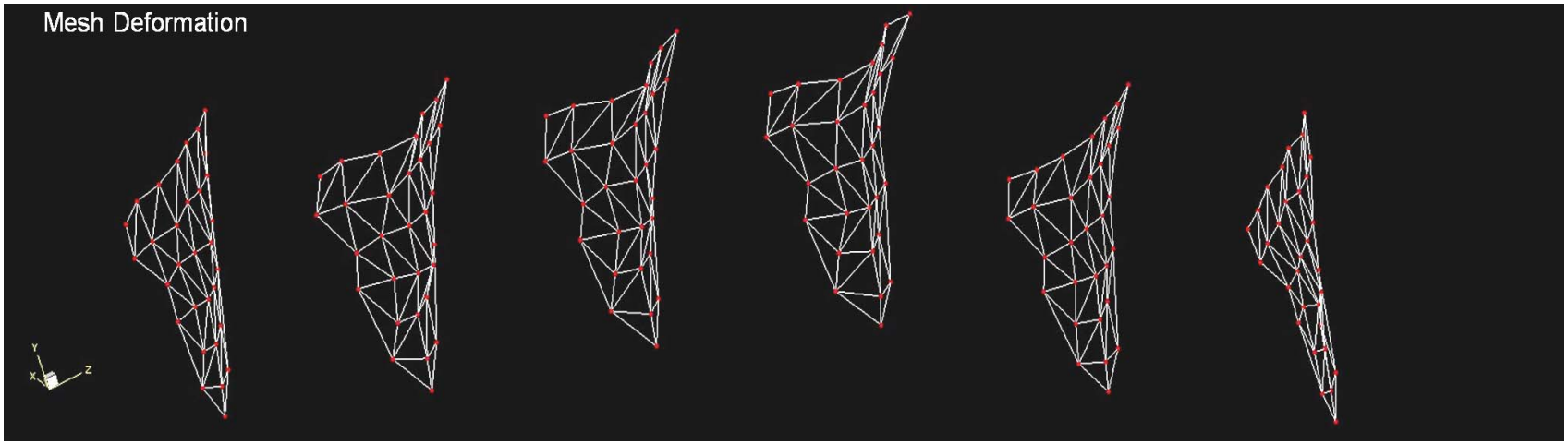

Figure 6-18 Deformation of the chordal insertion zone represented as a finite element mesh, with the red dots depicting the 31 markers used to reconstruct the zone and the while lines representing the elements that form the mesh. It can be clearly seen that during diastole when the valve is completely open, the finite element mesh is flat. But with increasing transmitral pressure, significantly out-of-plane deformation is observed with higher curvatures at the leaflet edges.

6.2.1.3.2 Areal Stretch Distribution

The strain field over the chordal insertion region is heterogeneous with higher stretch magnitudes concentrated at the edges of the insertion region than the central region. Figure 6-19A shows the chordal insertion region on the anterior leaflet marked with tissue dye, and Figure 6-19B depicts the sub-division of the chordal insertion zone into sub-divisions for data analysis. Figure 6-19C depicts the areal stretch magnitude mapped over the region delimited by the markers, and the heterogeneity in the stretch magnitude is clearly evident. A banded stretch pattern was observed with the focal point at the region of bifurcation of the cylindrical collagen core of the chord into a planar collagen structure of the leaflet. Bands of lower stretch magnitude were observed near the center, while those with significantly higher stretch magnitude were concentrated towards the edges of the insertion zone during systole. At diastolic loading, a homogenous distribution of stretch was recorded.

Figure 6-20 shows the temporal changes in areal stretch averaged over the eight valves at multiple markers. Highest stretch magnitudes were observed at markers 1 and 7 that are closer to the regions where the strut chordae has mostly fanned out into a planar leaflet structure. These markers are proximal to the leaflet regions that move basally towards the mitral annulus during systolic loading, thus higher stretches are expected at these markers. However, stretch at the central marker 4, which is along the same latitude as markers 1 and 7, was significantly smaller in magnitude. The peak areal stretch magnitude was different at each of these markers, 1.89±0.73 at marker 1, 1.22±0.33 at marker # 4($p=0.044$ compared to marker # 1); and 1.60±0.42 at marker # 7 ($p=0.05$

compared to marker # 4). However there was no significant difference between the measured stretch at markers 1 and 7 ($p=0.354$). Overall, the temporal changes in the areal stretch pattern are different between the three regions – the left edge (markers 1, 15, 25) has a gradual increase in stretch until it reaches a peak after which it gradually restores back to the reference state, the central region (markers 4,17,26,31) has minimal stretch throughout the cardiac cycle, whereas the right edge (markers 7,19,27) has a rapid increase in stretch followed by unloading within a very short period, as shown in Figure 6-20.

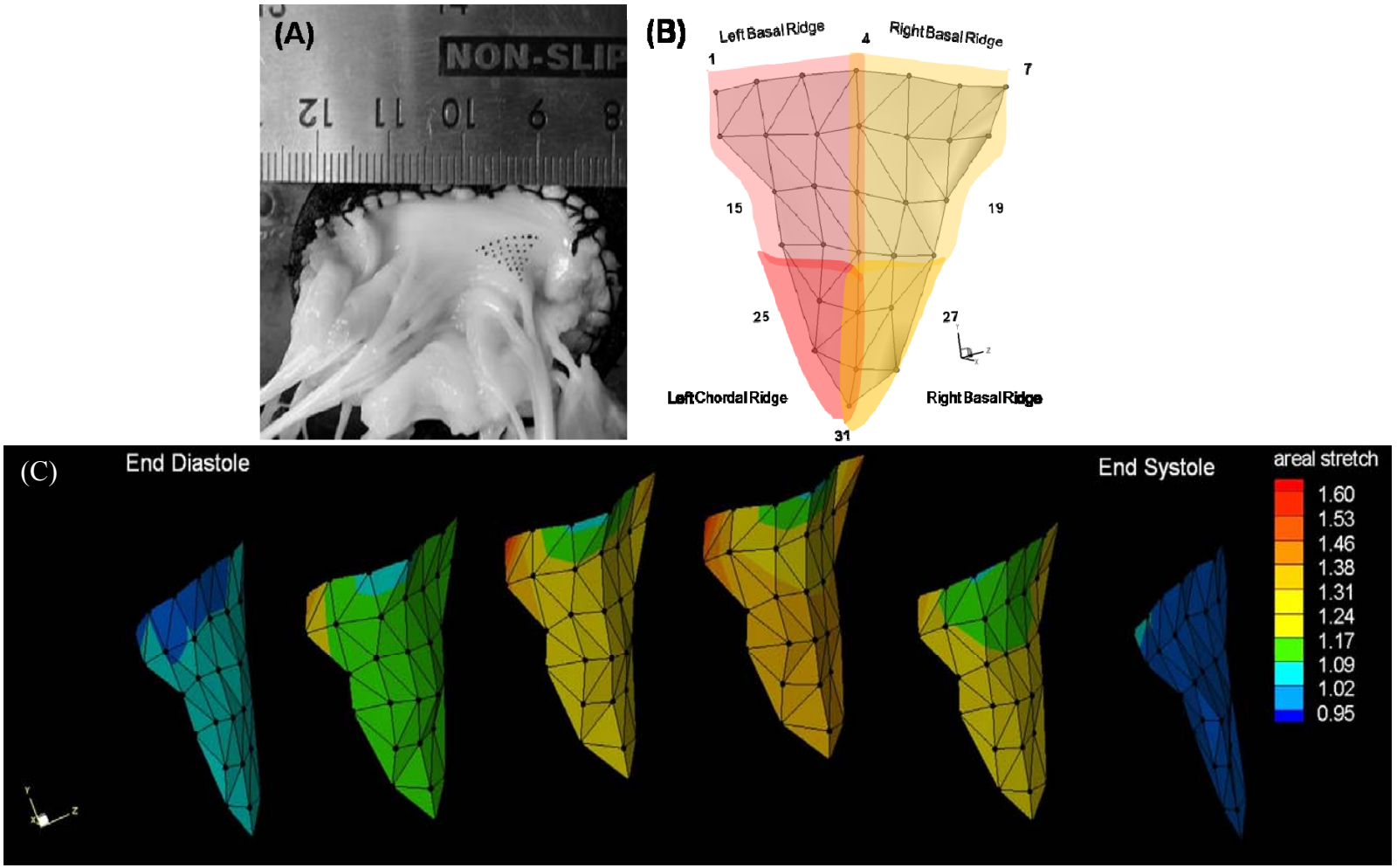

Figure 6-19 (A) Tissue marker array on one of the anterior strut chordae insertion zone; (B) The insertion zone sub divided into local regions for data analysis, considering the heterogeneity in the stretch distribution; (C) Temporal changes in the areal stretch over the entire chordal insertion zone from end diastole, through systole till end systole demonstrating the higher magnitudes at the edges of the insertion zone and lower magnitudes at the zone center

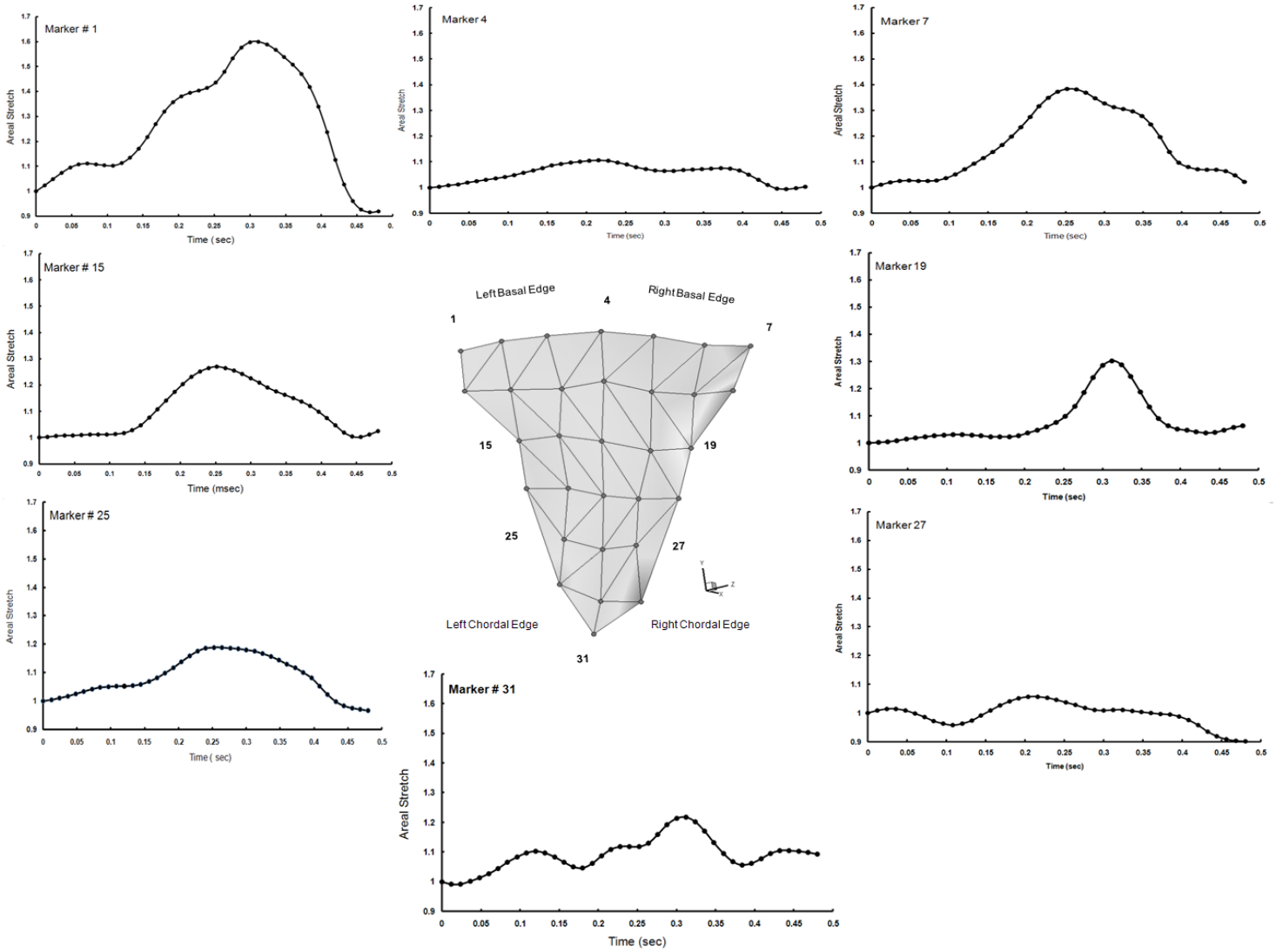

Figure 6-20 Temporal changes in the averaged areal stretch magnitude at selected markers in the chordal insertion region, demonstrating the spatial and temporal heterogeneity across the region

6.2.1.3.3 Major and Minor Principal Stretches

Figure 6-21(Top) shows a typical mapping of the major principal stretch magnitudes and vectors and Figure 6-21 (Bottom) shows the minor principal stretch on the entire region of the strut chordae insertion during systolic valve closure. Similar to trends in areal stretch, major principal stretch magnitude is significantly higher along the edges of the insertion region than the center. Regional stretch in the radial direction is significantly higher in the sub-regions along the left chordal edge and the right basal edge compared to rest of the insertion region. Direction of the major principal stretch is predominantly in the radial direction throughout systole, with the vectors pointing towards the annulus. Small changes in the principal vector direction were recorded indicating that cross-fiber shear stress is quite small. Minor principal stretch magnitude is significantly higher on the basal edges of the insertion zone than the center or towards the chord, with the minor principal stretch vector predominantly in the circumferential direction. Figure 6-22 shows the temporal changes in the major principal stretch at selected markers on different sub regions of the chordal insertion region, and Figure 6-23shows the changes in the minor principal stretch at the same locations. In the major principal direction, the maximum stretch was at marker 31 on the strut chord, followed by the right edge and the smallest being along the left edge of the chordal insertion zone. In the minor principal direction, the maximum stretch was at the left edge of the chordal insertion zone, followed by the right edge and then the central axis.

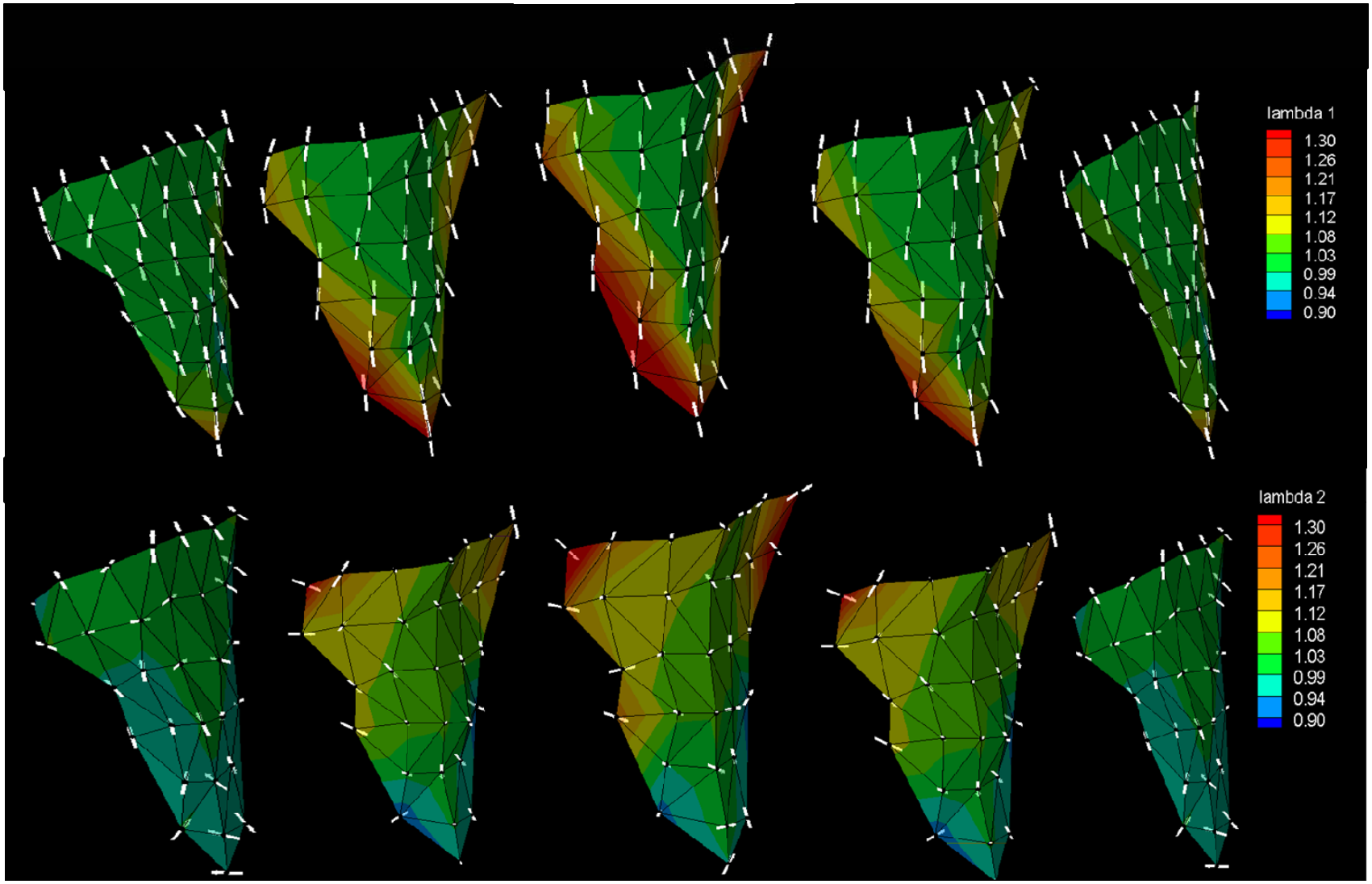

Figure 6-21(Top Gallery) The series of images demonstrate the change in major principal stretch magnitude and direction during systole, (Bottom Gallery) depicts the change in minor principal magnitude and direction during systolic loading of the valve.

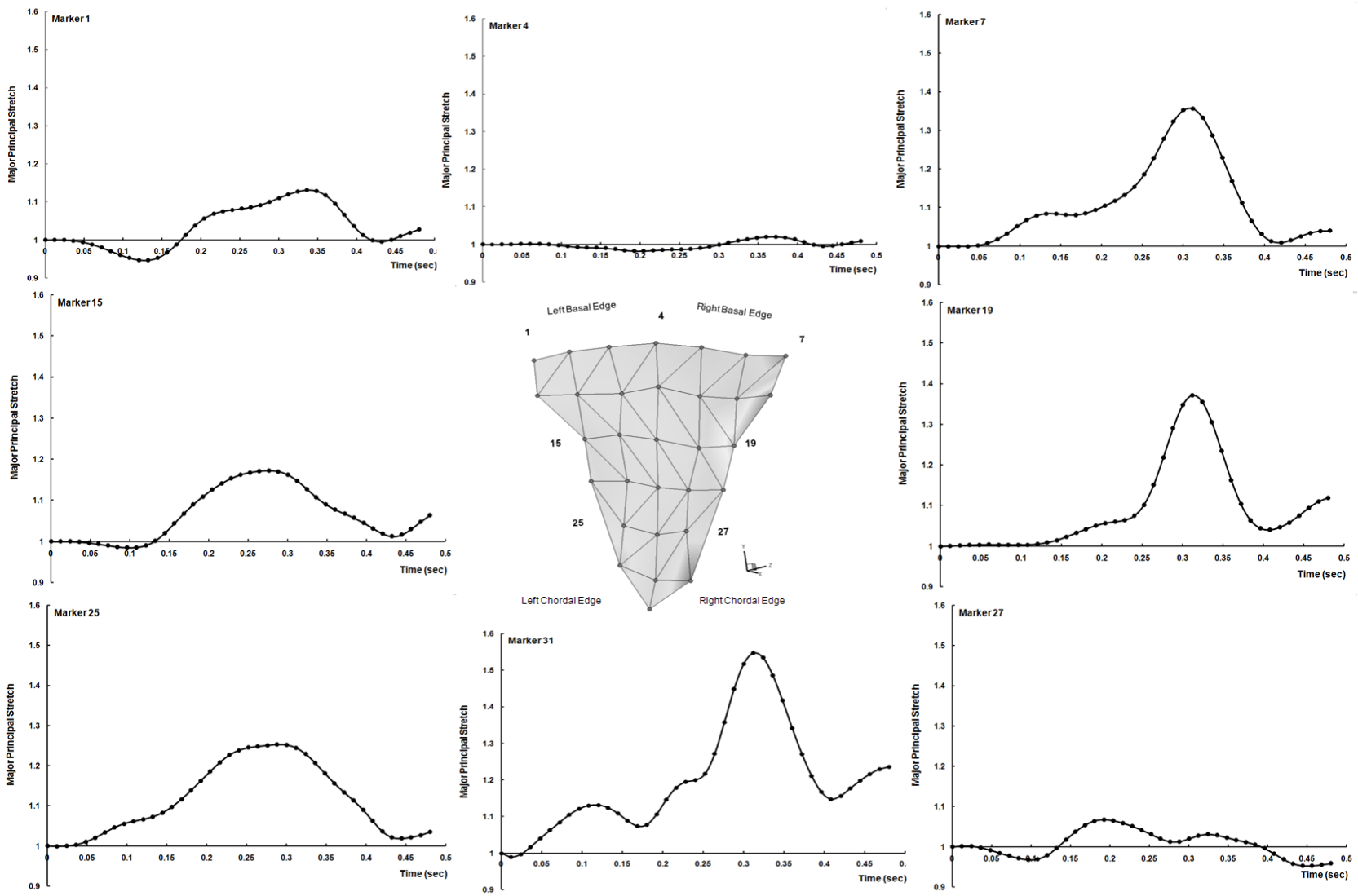

Figure 6-22 Temporal changes in the major principal stretch at different points in the chordal insertion zone demonstrating the heterogeneity in the surface strains

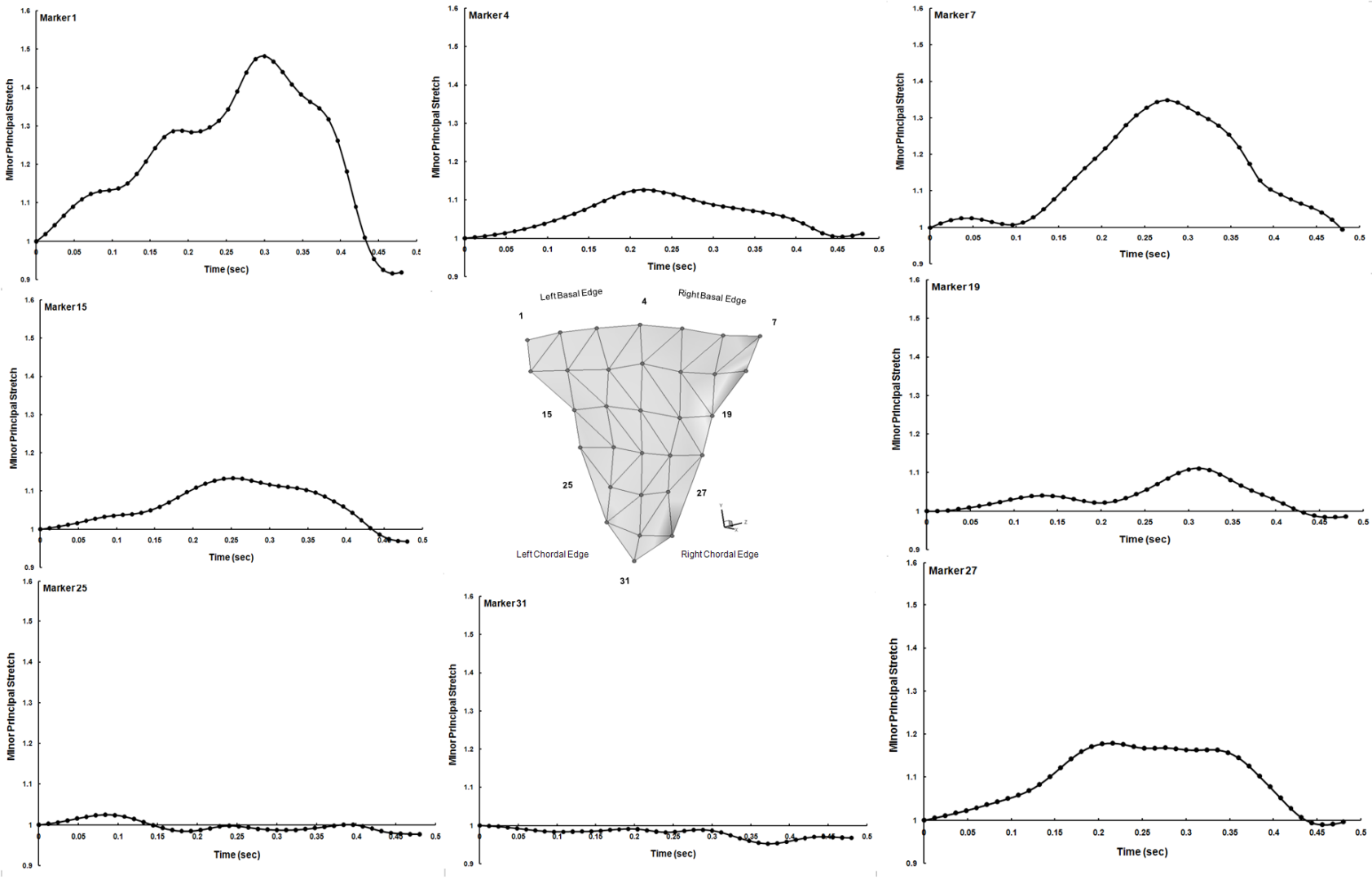

Figure 6-23 Temporal changes in the minor principal stretch at different points in the chordal insertion zone demonstrating the heterogeneity in the surface strains

6.2.1.3.4 Regional Stretch Rate

Stretch rates in the two principal directions are used to assess the regional variations in strains. In Table 6-3 report the stretch rate at 3 markers on the left edge, 3 on the central axis, 3 on the right edge of the insertion zone, and finally 1 marker on the strut chord. In the major principal direction, the stretch rates on the left edge were significantly higher than the right edge and the central axis where the stretch rate is smallest. Maximum stretch rates are recorded on the strut chordae (marker 31) that corroborated with previous findings from our laboratory[46]. In the minor principal direction, there are few localized regions of high stretch rate compared to the rest of the region of interest. These hot spots were mainly at the regions that are close to the A2 cusp that has the largest basal motion during systolic coaptation (markers 1, 15); and in the region close to the leaflet commissure, (markers 7 and 19).

6.2.1.3.5 Ultrastructural Examination

Small angle light scattering and histological data demonstrated a complex transition from the highly aligned chordae to the leaflet main body as shown in Figure 6-24. In particular, a drop in alignment (OI values changed from 25° to 45° within a few mm as observed on the collagen fibril distribution mapping, with substantial arching in the vicinity of the chordal insertion zone.

Table 6-3 Peak major and minor principal stretch and stretch rate at different markers on the left and right edges of the chordal insertion zone, and along the axis of the strut chordae that fans out into the planar leaflet

	Max Major Principal Stretch	Max Major Principal Stretch Rate (%/sec)	Max Minor Principal Stretch	Max Minor Principal Stretch Rate (%/sec)
Left Edge				
Marker 1	1.19 ± 0.13	207 ± 80	1.81 ± 0.74	719 ± 448
Marker 15	1.24 ± 0.27	197 ± 112	1.17 ± 0.23	170 ± 138
Marker 25	1.38 ± 0.24	197 ± 98	1.08 ± 0.11	64 ± 60
Center Line				
Marker 4	1.10 ± 0.09	45.6 ± 44.4	1.19 ± 0.24	98.7 ± 144
Marker 17	1.09 ± 0.09	39.4 ± 25	1.10 ± 0.14	103 ± 119
Marker 26	1.09 ± 0.10	64.3 ± 28.5	1.05 ± 0.06	53.2 ± 18.8
Right Edge				
Marker 7	1.58 ± 0.89	492 ± 558	1.62 ± 0.45	286 ± 111
Marker 19	1.53 ± 0.78	581 ± 507	1.18 ± 0.18	121 ± 84
Marker 27	1.21 ± 0.31	169.3 ± 162	1.06 ± 0.06	73 ± 59.2
Strut Chord				
Marker 31	1.72 ± 1.00	739 ± 784	1.05 ± 0.08	61 ± 62.1

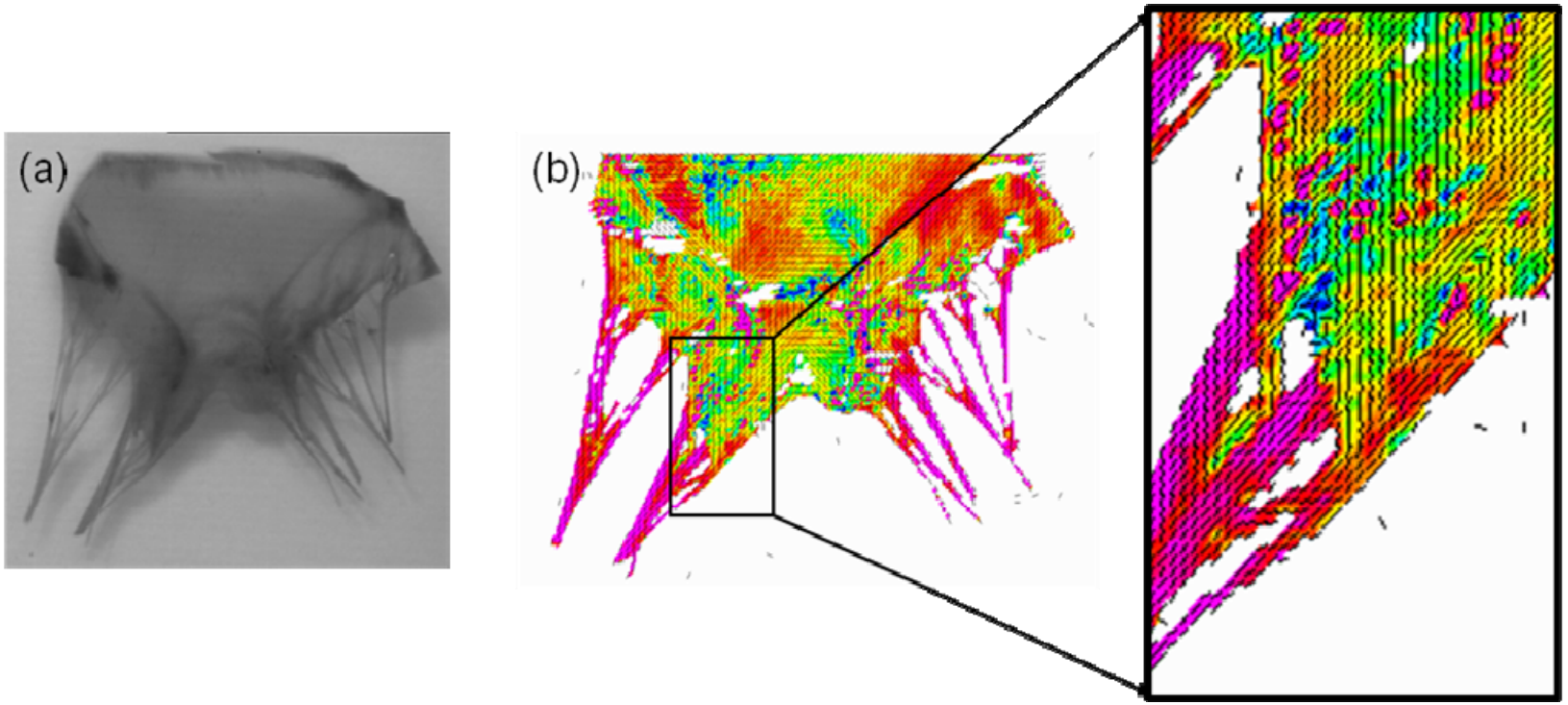

Figure 6-24 (A) Image of an ovine MVAL fixed at 5 mmHg showing the chordae, (B) corresponding SALS data showing detailed maps of the collagen fiber orientation. Inset- high resolution data of a chordal insertion region.

6.2.1.4 Part D – Hemodynamic and Kinematic Insights into the Efficacy of Edge-to-Edge Repair to Correct Posterior Leaflet Prolapse in a Normal and Dilated Annulus

6.2.1.4.1 Hemodynamic Efficacy of Edge-to-Edge Repair

Mitral regurgitation fraction (MRF = (MR/SV)*100) was calculated for the eight valves, and the averaged data are reported in Figure 6-25. Under control conditions, all valves had excellent competence without any regurgitation observed on the color Doppler images. Marginal chordal transection induced isolated P2 prolapse and an average regurgitant fraction of 10.2±5.0. Edge-to-edge stitch between the prolapsing P2 cusp and the A2 cusp significantly reduced regurgitation to 2.0±1.1 at normal annular size of 28mm. However, with annular dilatation recurrent regurgitation of 4.2±1.4 at 15% dilatation compared to normal annulus, and to 6.2±1.2 at 30% dilatation.

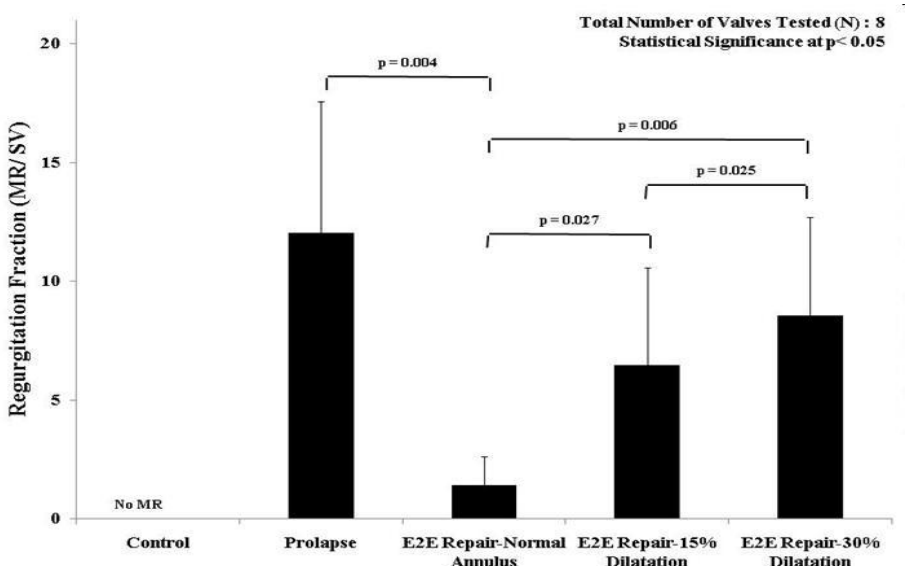

Figure 6-25 Mitral regurgitation volumes after Edge to Edge repair with a physiologic sized annulus and with annular dilatation

6.2.1.4.2 Impact of Annular Dilatation on Leaflet Coaptation Length Following Edge-to-Edge Repair

The leaflet coaptation length was measured across A1-P1, A2-P2 and A3-P3 planes and the measurements were averaged over the eight valves. Figure 6-26 shows the averaged coaptation length data measured under control conditions at 8.22±0.6mm at A1-P1 plane, 9.47±1.5mm at A2-P2 plane, and 8.37±0.7mm at A3-P3. The prolapse group did not have leaflet coaptation due to the prolapse induced by marginal chordal rupture. Edge-to-edge repair with a normal annulus corrected P2 prolapse, and restored coaptation length to 7.70±0.8mm at A1-P1, 8.83±0.9mm at A2-P2 and 7.70±1.14mm at A3-P3 planes. With 15% dilatation, the coaptation length along each of the planes reduced to 6.70±1.0mm at A1-P1, 7.86±0.6mm at A2-P2 and 6.88±1.35mm at A3-P3. With 30% dilatation, a further reduction in coaptation length to 5.90±0.8mm at A1-P1, 7.18±0.7mm at A2-P2 and 6.27±1.57mm at A3-P3 was measured.

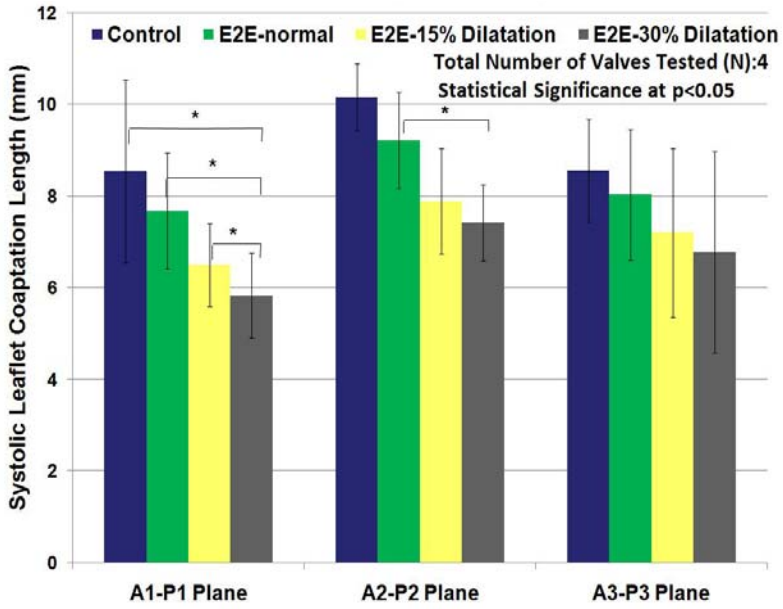

Figure 6-26 Changes in leaflet coaptation length with increase in annular size from a normal size to 15% and 30% dilatation

6.2.1.5 Part E – Impact of Mitral Annular Non-planarity on Mechanics of the Posterior Mitral Leaflet

6.2.1.5.1 Temporal Changes in Areal Strain with Different Degrees of Annular Saddle

Figure 6-27 illustrates the temporal changes in areal strain with a flat, 10% and 20% saddled annulus, during systole. All valves experienced rapid stretch rate during early systole with subsequent peaking of the stretch due to collagen locking at peak systole, and finally rapid unloading from late systole to early diastole. A similar trend was seen in both the major and minor principal strains respectively for all the valves as shown in Figure 6-28 and Figure 6-29. The total time of leaflet deformation, i.e. the duration during which the leaflet deformed from the reference state to a peak and then returned to the reference state, was significantly different between the three annular shapes. With a flat annulus (0% AHCWR), the total deformation time was significantly larger at 389±10ms compared to 360±9ms for 10% saddle and 273±11ms with 20% saddle.

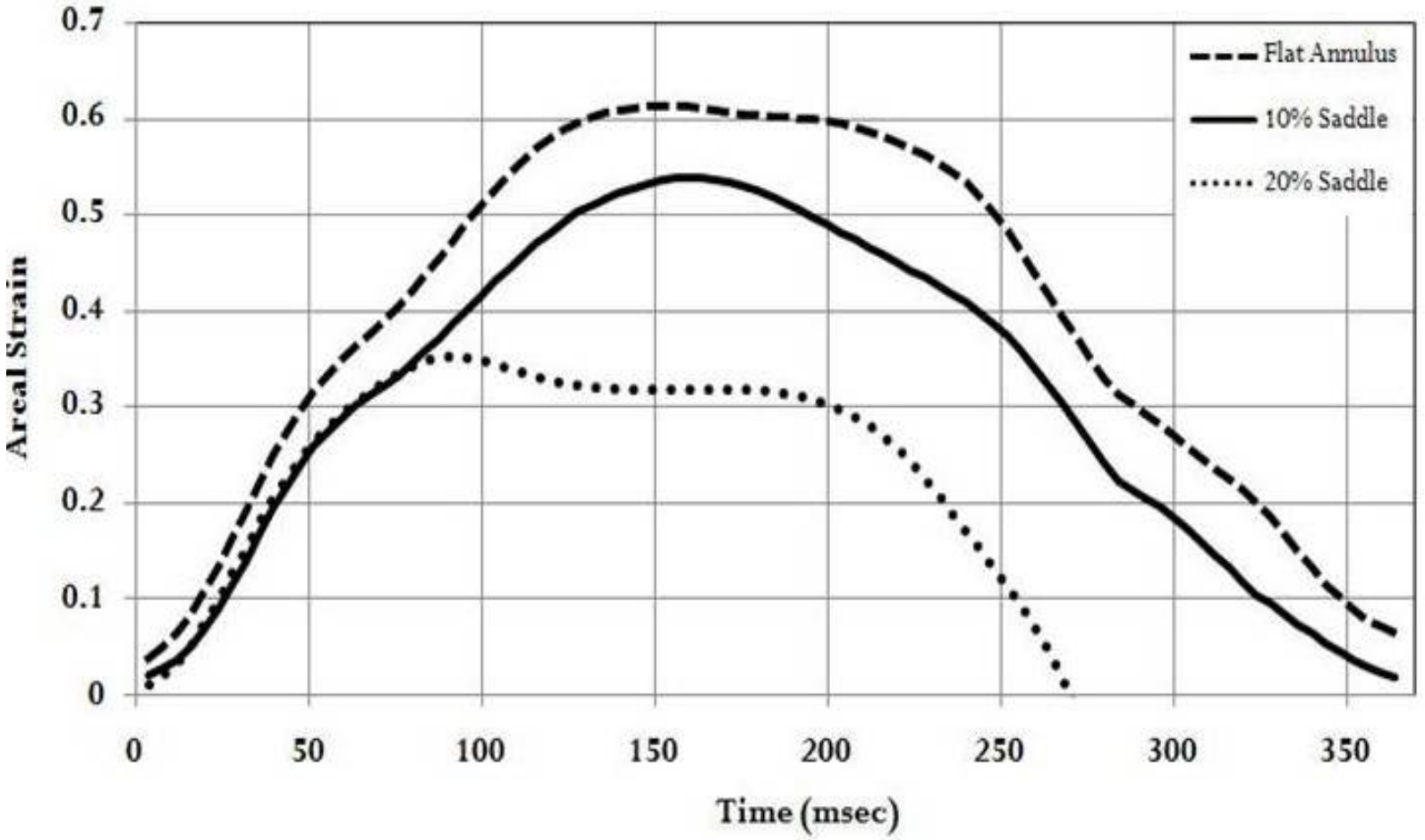

Figure 6-27 Temporal changes in the areal strain magnitude between the three degrees of annular saddle. Maximum areal strain is measured for a flat annulus, followed by 10% saddle and the least being 20% saddle.

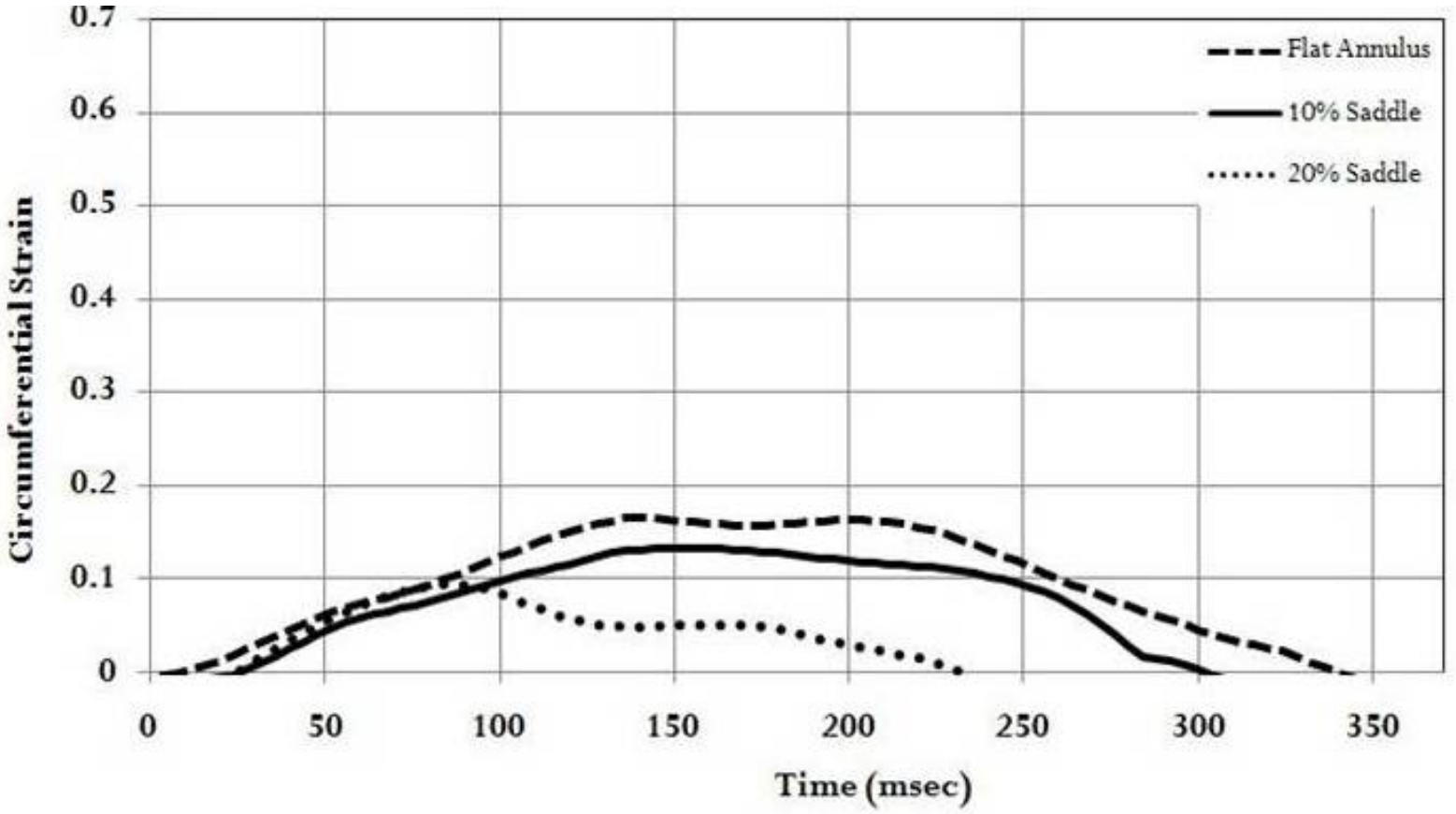

Figure 6-28 Temporal changes in the circumferential strain magnitude between the three degrees of annular saddle. Maximum circumferential strain was measured with a flat annulus and significantly reduced strain with 20% saddle

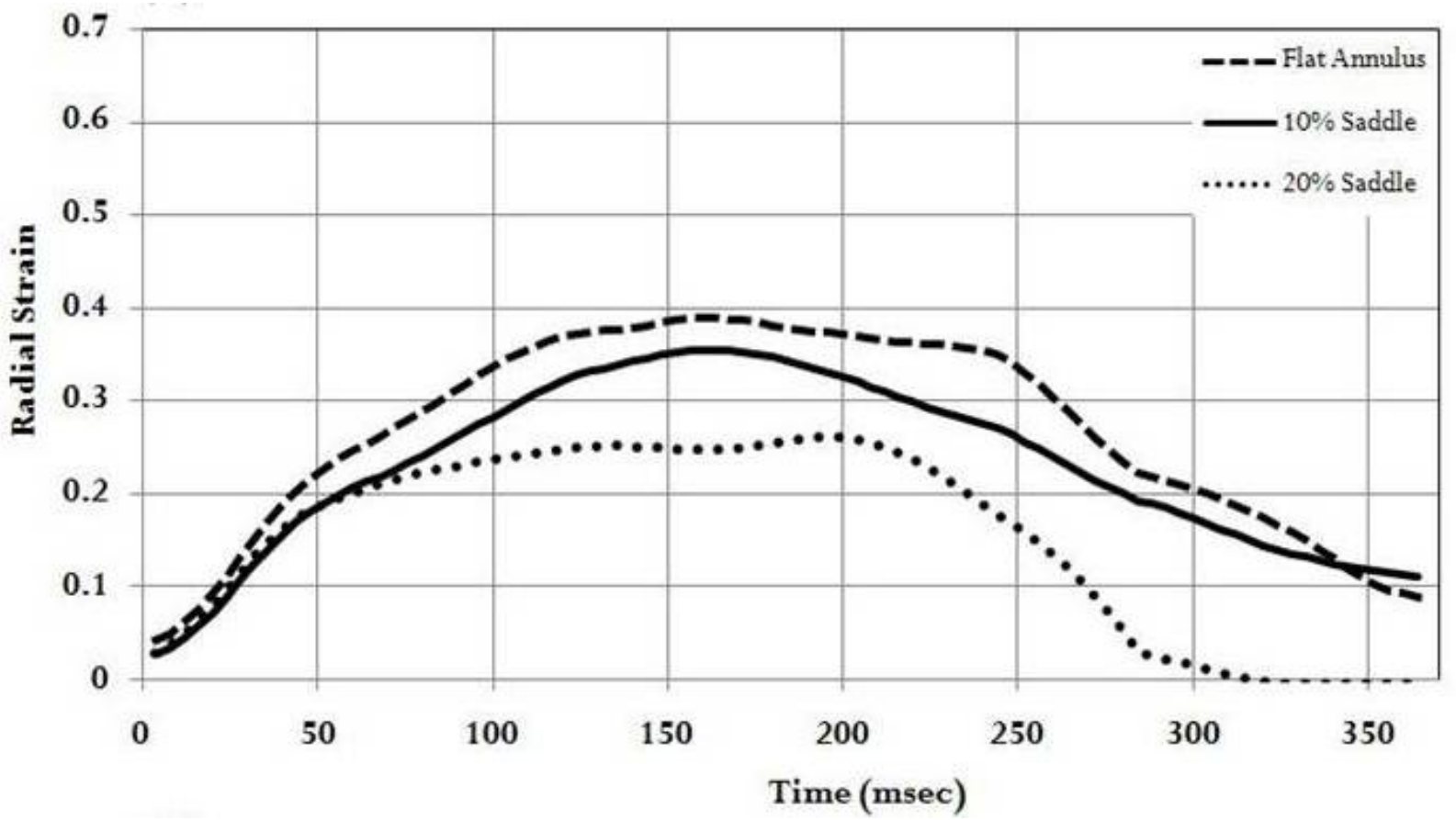

Figure 6-29 Temporal changes in the radial strain magnitude between the three degrees of annular saddle. Maximum radial strain was measured with a flat annulus, which reduced with increasing saddle.

6.2.1.5.2 Peak Areal Strain Magnitudes

The peak areal strain magnitude was computed for the eight valves tested in this study and the average magnitudes are reported in Figure 6-30. Areal strain magnitudes significantly decreased from 0.68±0.1 for a flat annulus, to 0.57±0.1 for a 10% AHCWR annular shape (p=0.03) and to 0.38±0.09 for 20% AHCWR annular shape (p=0.005), respectively.

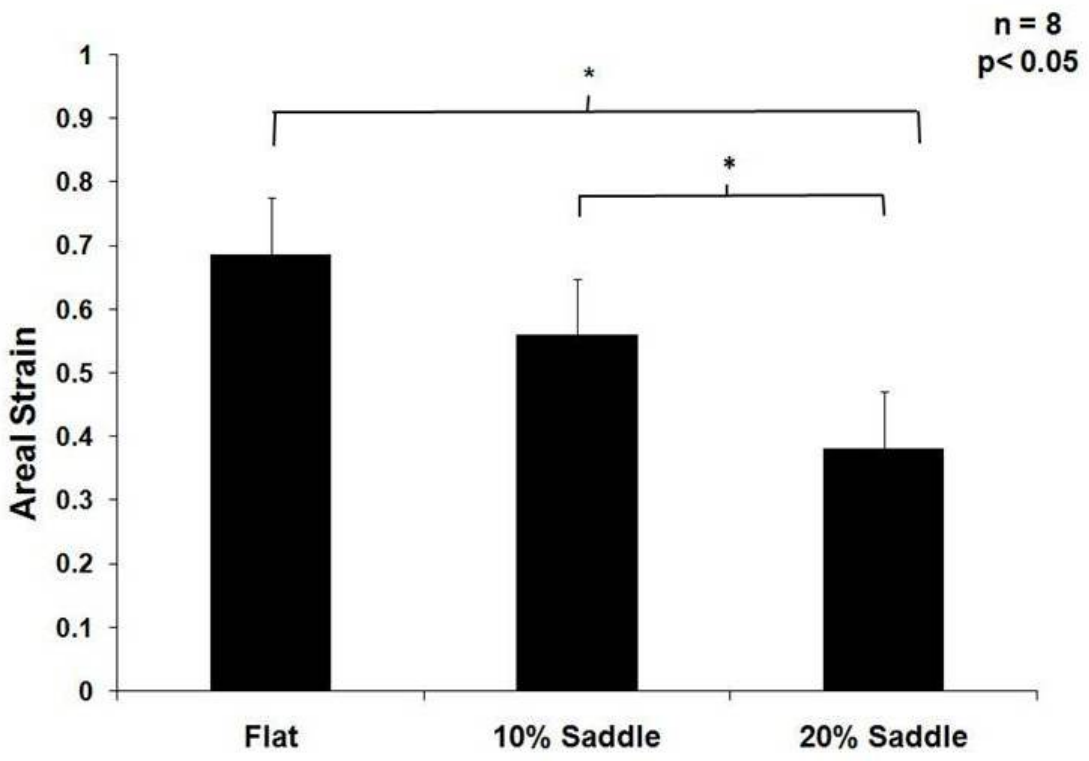

Figure 6-30 Average peak systolic areal strain magnitudes at different degrees of mitral annular saddle measured from the in vitro experimental setup. Significant reduction in the peak magnitudes from flat to 20% saddle were observed.

6.2.1.5.3 Peak Radial and Circumferential Strain Magnitudes

Similar reductions were observed in peak strains both in the circumferential (commissure-commissure direction) and radial (free edge to annulus) directions. In the circumferential direction, the peak systolic strain did not change from 0.18±0.07 at 0% AHCWR to 0.17±0.08 at 10%AHCWR (p=0.816), but significantly reduced to 0.1±0.08 at 20% AHCWR (p=0.01) as shown in Figure 6-31. Similarly, in the radial direction there was no significant change in the peak strain magnitude from 0.44±0.13 at 0% AHCWR to 0.35±0.12 for 10% saddle (p=0.196), but reduced significantly to 0.29±0.08 at 20% saddle (p=0.031) as shown in Figure 6-31 and Figure 6-32.

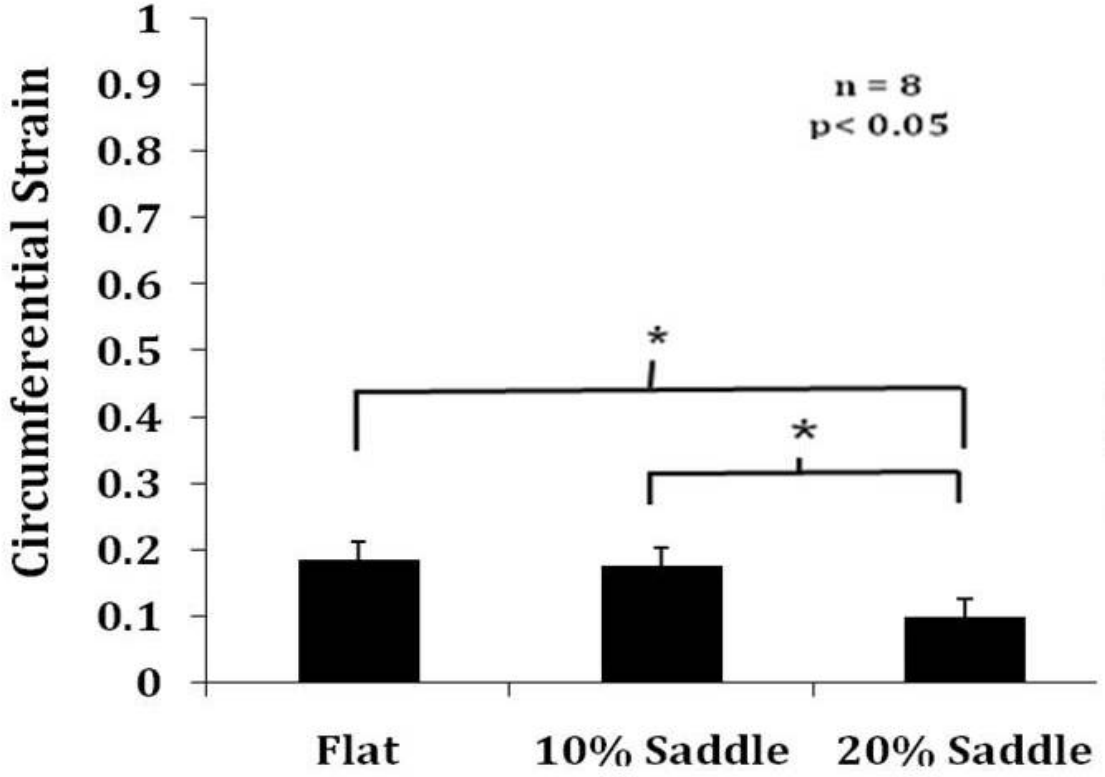

Figure 6-31 Reduction in circumferential strain with increasing degree of annular saddle

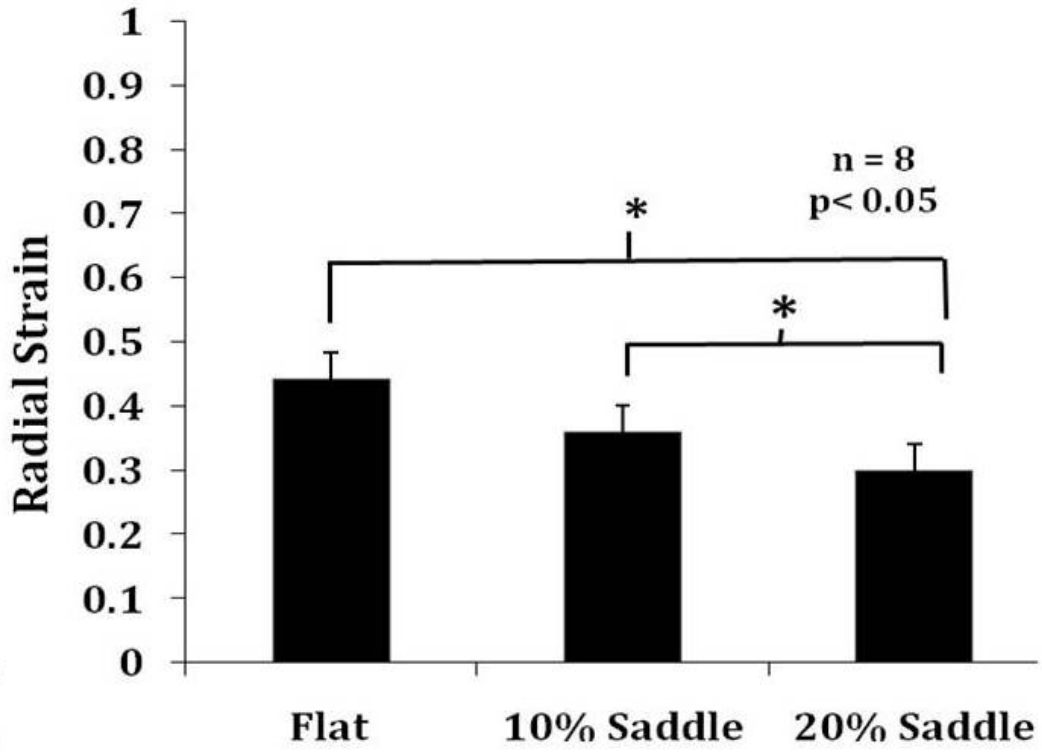

Figure 6-32 Reduction in areal strain with increasing annular saddle

6.2.1.5.4 Principal Angle

Principal angle measured as the angle between the geometric axis of the leaflet and the principal strain vectors, at each time point in the cardiac cycle. This parameter is a measure of the shear strain in the leaflets, because if the shear strain in leaflets is minimal the principle angle is low and vice versa. In this study, the peak principal angles over the entire cardiac cycle were nearly equal for the flat (0.91±0.60), 10% saddle (-0.38±0.56) and 20% saddle (0.02±1.11), indicating minimal shear strain in the leaflets during systolic valve closure.

6.3 REPAIR FOR FUNCTIONAL MITRAL REGURGITATION IN DILATED CARDIOMYOPATHY

Variability in the valve geometry between individual patients is hypothesized to impact the outcomes of mitral valve repair in treating functional mitral regurgitation. To test this hypothesis, in this thesis an *in vitro* model of functional mitral regurgitation was developed. The model was designed such that precise control over the annular size, annular shape and spatial position of the papillary muscles was possible, which allowed simulating different pathological valve geometries. Mitral annuloplasty was performed on each valve, followed by a sub-annular secondary chordal cutting procedure. In this section, detailed results on the impact of 3-dimensional valve geometry on the post-repair valve hemodynamics and mechanics are presented.

6.3.1 VALIDATION OF IN VITRO REGURGITATION MODEL

In this thesis, two mitral valve geometries were studied – [a] annular dilatation with 10mm isolated apical papillary muscle displacement; and [b] annular dilatation with 10mm apical+ 10mm posterior+ 10mm lateral displacements. Previous studies from our lab demonstrated that a significant change in valve function was seen when the papillary muscles were displaced only in one spatial direction versus in all the three directions. Thus we expect that the outcomes of the valve repair may also be significantly different between the two geometries, and thus may provide mechanistic insights into clinical annuloplasty failure.

2D echocardiographic images obtained along the septal lateral plane of the mitral annulus clearly demonstrate tethering of the anterior and posterior mitral leaflets,

resulting in restricted leaflet mobility. When the papillary muscles are displaced from their normal positions, the anterior leaflet assumes a sea-gull shape due to localized tethering at the strut chordal insertion regions. Figure 6-33A shows a normal mitral valve coaptation, Figure 6-33B shows a mitral valve with dilated annulus and apical papillary muscle displacement, and Figure 6-33C shows a mitral valve with a dilated annulus and apical, posterior and lateral papillary muscle displacement. With apical papillary muscle displacement, there was increase in tenting area as measured from echocardiographs and significant loss of coaptation. The leaflet curvature at peak systolic coaptation also changed significantly. With apical, posterior and lateral displacement, the changes in systolic coaptation geometry were more pronounced with significant tethering and bending of the anterior leaflet at the site of the strut chordae insertion. These observations corroborate with the clinical findings reported from patients with dilated cardiomyopathy, which are well recorded in the literature.

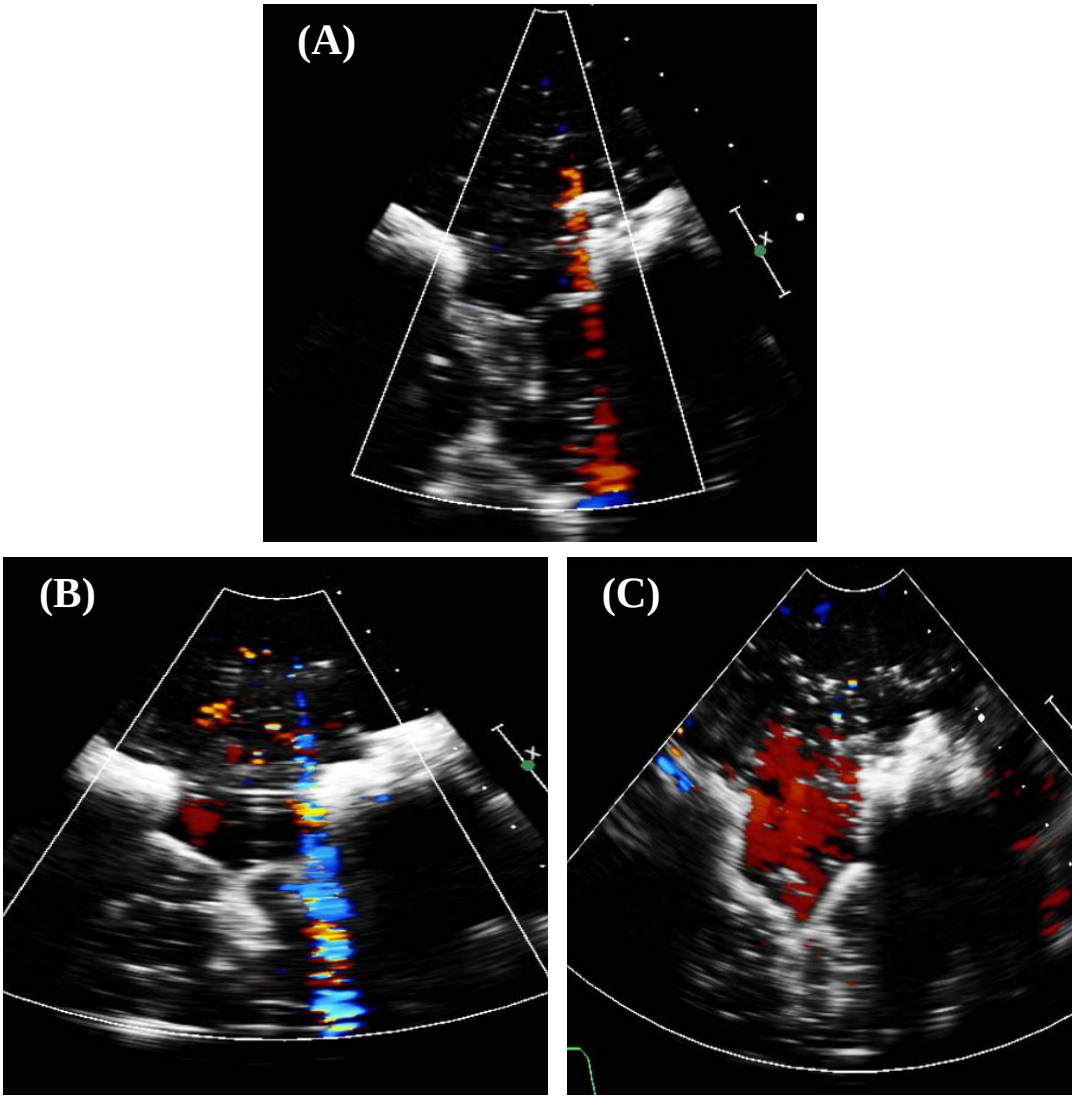

Figure 6-33 (A) Systolic coaptation of a normal mitral valve with excellent coaptation and minimal tenting area between the leaflets and the mitral annular plane, (B) Systolic coaptation geometry after annular dilatation and apical displacement of the papillary muscles, depicting increased tenting area and reduced leaflet coaptation, (C) Coaptation geometry after apical, posterior and lateral papillary muscle displacement with significantly high tenting area and slight bending of the anterior leaflet at the region of strut chordae insertion.

6.3.2 ROLE OF 3D MITRAL VALVE GEOMETRY ON THE OUTCOMES OF MITRAL ANNULOPLASTY

6.3.2.1 Impact of 3D Valve Geometry on the Hemodynamic and Kinematic Outcomes of True Sizing Mitral Annuloplasty for Functional Mitral Regurgitation

True-sized mitral annuloplasty to restore physiological septal-lateral dimension and reduce/eliminate functional mitral regurgitation is the current clinical standard of care. However, regurgitation persists or recurs within 5 years after mitral annuloplasty and in this study the mechanisms leading to persistence/recurrence of mitral regurgitation in this disease etiology are studied. To simulate the variability in mitral valve geometry between patients, two types of pathologic valve geometric scenarios were simulated: [a] annular dilatation with apical papillary muscle displacement; and [b] annular dilatation with apical-posterior-lateral papillary muscle displacement.

With physiological valve geometry (Control/Baseline), all the eight valves were competent with no mitral regurgitation. Annular dilatation with displacement of the papillary muscles by 10mm in the apical direction induced an average regurgitation fraction of 10.54±5.5, which is significantly higher compared to the baseline conditions ($p=0.001$). True-sizing the mitral annulus from its dilated size to its physiological size of 28mm reduced MRF to 4.78 ± 5.27, which was significantly smaller than the disease state ($p=0.032$) and was comparable to the regurgitation volume in the control group ($p=0.07$) as shown in Figure 6-34.

The experiment was repeated with the second pathological valve geometry, i.e. annular dilatation with apical-posterior-lateral papillary muscle displacement. With physiological valve geometry (Control/Baseline), all the eight valves were competent with no mitral regurgitation. Annular dilatation with displacement of the papillary muscles by 10mm in the apical direction, 10mm in the posterior direction and 10mm in the lateral direction induced an average regurgitation of 23.02±5.7, which is significantly higher compared to the baseline conditions ($p=0.001$). True-sizing the mitral annulus from its dilated size to its physiological size of 28mm reduced mitral regurgitation to 16.70 ± 7.8, which was reduced compared to the disease state ($p=0.01$) , but by clinical standards still considered to be moderate to severe. Remnant regurgitation was significantly higher than the control group or the post-annuloplasty group in the latter case, and thus was considered to be a failed procedure for this particular setting of the valve geometry.

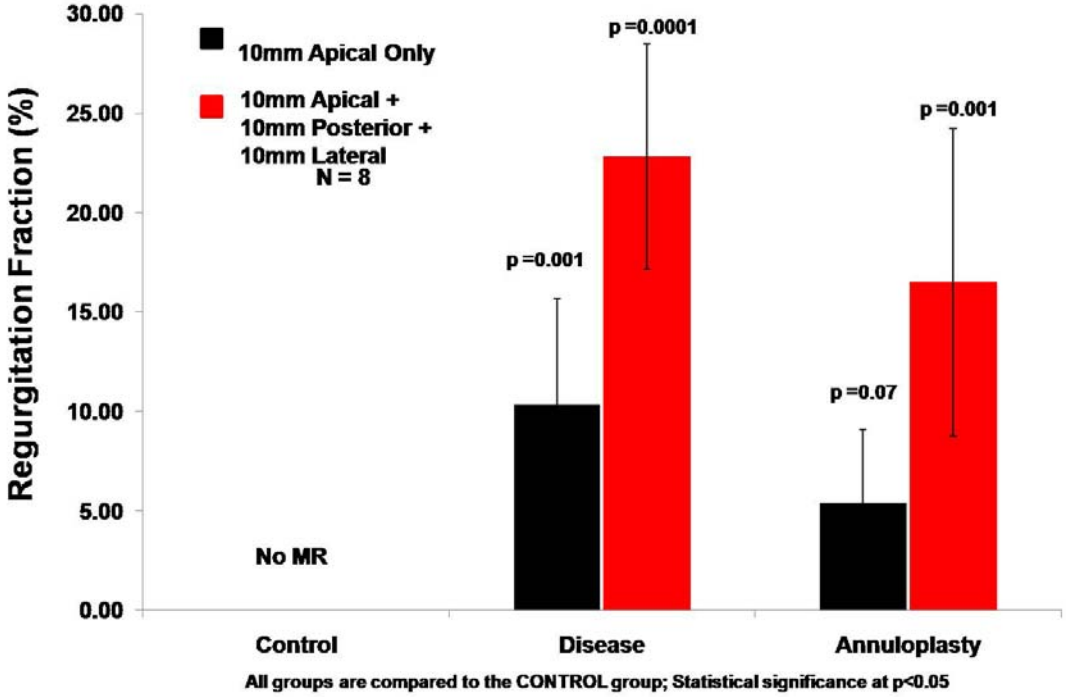

Figure 6-34 Mitral regurgitation volumes after true-sizing annuloplasty for functional mitral regurgitation due to two different pathological valve geometries

6.3.3 IMPACT OF ANNULOPLASTY ON REDUCTION IN TENTING HEIGHT

Mitral annuloplasty reduces the septal-lateral dimension of the mitral valve, but does not address the sub-valvular tethering induced by papillary muscle displacement. However the hemodynamic results demonstrated that isolated mitral annuloplasty could have a beneficial effect with apical papillary muscle displacement, but not when the muscles are displaced apically, posteriorly and laterally. To explain these results, the impact of mitral annuloplasty on the sub-valvular mechanics of the mitral valve was investigated on the two simulated pathological valve geometries. Both tenting height and tenting area were measured along A1-P1, A2-P2 and A3-P3 cusps on all the valves as

they are used as representative indices to assess sub-valvular tethering in the clinical setting.

Along the central A2-P2 cusps, the measured systolic tenting height was 7.3±1.7 mm under control/baseline conditions. Annular dilatation and 10mm apical displacement of both the papillary muscles tethered the mitral leaflets and increased the tenting height during systolic closure to 9.86± 2.0 mm, which was significantly higher than the baseline group (p=0.036). Annuloplasty reduced tenting height to 8.7±1.8 mm, which was not significantly different from the disease group (p=1.00). Along the left commissural cusps (A1-P1), a tenting height of 5.4 ± 1.8 mm was measured under control/baseline conditions. With annular dilatation and papillary muscle tethering, the tenting height increased to 7.68±1.95 mm (p=0.05) indicating leaflet tethering even at the commissural cusps. After annuloplasty, commissural tenting increased slightly to 8.14 ± 1.9 mm (p=0.312) compared to the diseased group. Similarly along the right commissural cusps (A3-P3) , annular dilatation and papillary muscle displacement increased tenting height to 8.11 ± 2.0mm from a baseline value of 5.02 ± 1.3mm (p = 0.018). Annuloplasty did not seem to have an impact on tenting height as a distance of 7.84 ± 2.0 mm (p=0.72) was measured even after the repair along the A3-P3 commissural cusps as shown in Figure 6-35, Figure 6-36 and Figure 6-37.

In the second pathological case with annular dilatation and 10mm apical-10mm lateral-10mm posterior displacement of the papillary muscles, a tenting height of 12.7 ± 1.7 mm was measured along the A2-P2 central cusps, which was significantly higher than the baseline value of 7.26 ± 1.7 mm (p <0.001). Annuloplasty slightly reduced

tenting height to 10.5 ± 3.0 mm (p=0.04). Along the left commissural cusps (A1-P1), a tenting height of 5.4 ± 1.8 mm was measured under control/baseline conditions. With annular dilatation and papillary muscle tethering, the tenting height increased to 11.45 ± 2.06 mm (p=0.001) indicating significant leaflet tethering even at the commissural cusps. After annuloplasty, commissural tenting reduced slightly to 9.68 ± 3.0 mm (p=0.038) compared to the diseased group. Similarly along the right commissural cusps (A3-P3) , annular dilatation and papillary muscle displacement increased tenting height to 11.94 ± 3.2 mm from a baseline value of 5.02 ± 1.3mm (p=0.002). Annuloplasty did not seem to have an impact on tenting height as a distance of 9.54 ± 4.0 mm (p=0.02) was measured even after the repair along the A3-P3 commissural cusps as shown in Figure 6-35, Figure 6-36 and Figure 6-37.

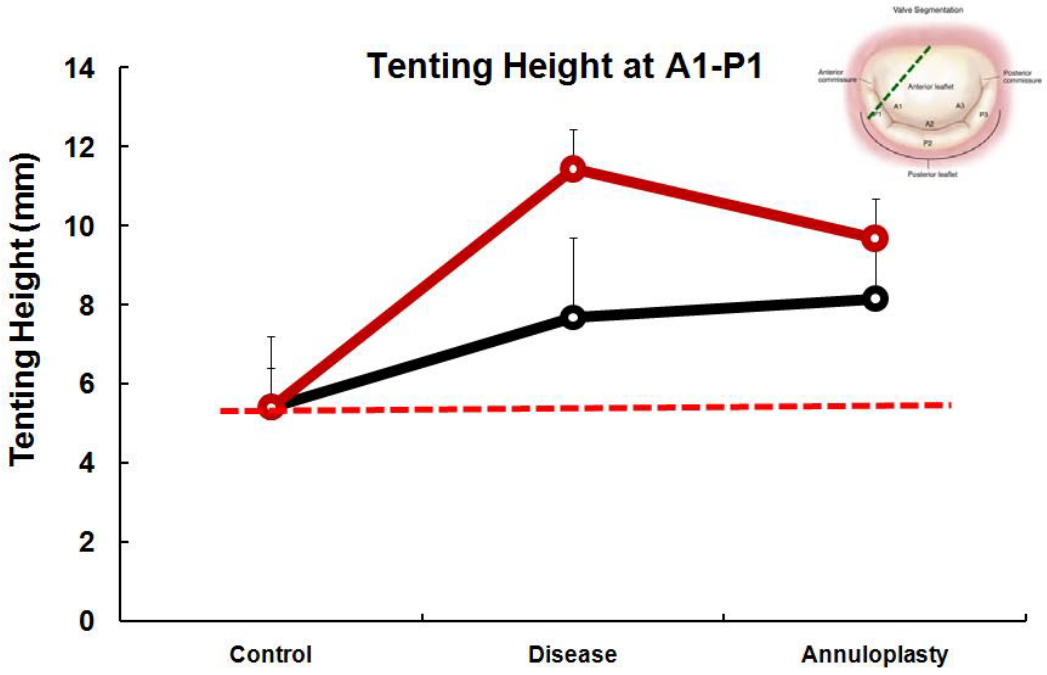

Figure 6-35 Tenting height measured at the commissural A1-P1 commissural section under different experimental conditions

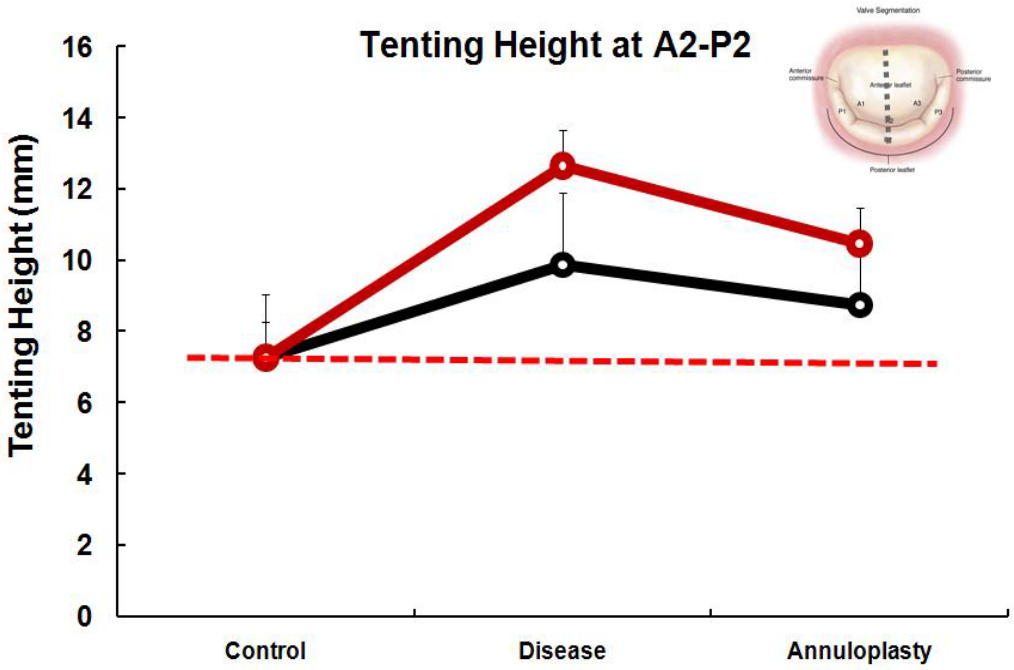

Figure 6-36 Tenting height measured at the central A2-P2 section under different experimental conditions

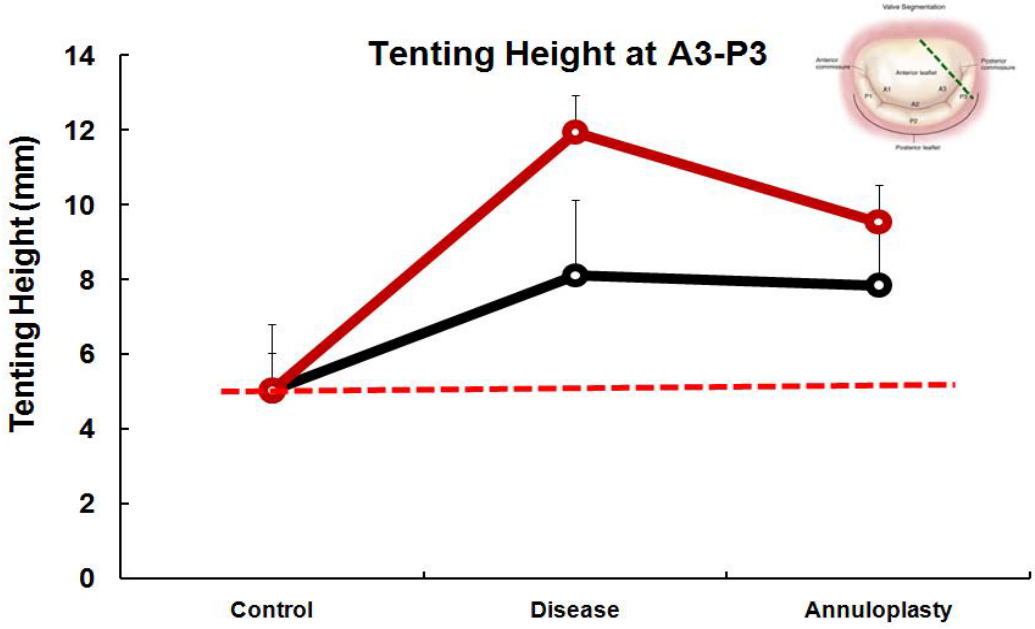

Figure 6-37 Tenting height measured at the commissural A3-P3 section under different experimental conditions

6.3.4 EFFICACY OF ANNULOPLASTY IN REDUCING TENTING AREA

Tenting height as measured in the previous section describes the perpendicular distance of the point of leaflet coaptation to the mitral annular plane. Obviously, as sub-valvular tethering increases the point of leaflet coaptation moves apically towards the ventricular apex and can thus be used as a measure of ventricular tethering. However, tenting height does not provide any information regarding the leaflet systolic geometry, because for the same tenting height different leaflet configurations can exist. To overcome this limitation, tenting area enclosed between the two mitral leaflets and the mitral annulus during peak systole was measured.

Along the central A2-P2 cusps, the measured systolic tenting area was 60.9 ± 31 mm^2 under control/baseline conditions. Annular dilatation and 10mm apical displacement of both the papillary muscles tethered the mitral leaflets and increased the tenting area at peak systolic closure to 129.7 ± 28.4 mm^2, which was significantly higher than the baseline group (p=0.01). Annuloplasty reduced tenting area to 87 ± 17.1 mm^2, which was significantly reduced from the disease group (p=0.021) but not comparable to the control (p= 0.021). Along the left commissural cusps (A1-P1), a tenting area of 58.7 ± 23.1 mm^2 was measured under control/baseline conditions. With annular dilatation and papillary muscle tethering, the tenting height increased to 100.5 ± 28 mm^2 (p=0.004) indicating leaflet tethering even at the commissural cusps. After annuloplasty, commissural tenting decreased slightly to 91.5 ± 26 mm^2 (p=0.47) compared to the diseased group. Similarly along the right commissural cusps (A3-P3) , annular dilatation and papillary muscle displacement increased tenting area to 103.4 ± 36.4 mm^2 from a

baseline value of 64.33 ± 27.74 mm^2 (p=0.049). Annuloplasty seemed to have some impact on tenting area as 66.07 ± 17.0 mm^2 (p=0.052) was measured even after the repair along the A3-P3 commissural cusps as shown in Figure 6-38, Figure 6-39, and Figure 6-40.

In the second pathological case with annular dilatation and 10mm apical-10mm lateral-10mm posterior displacement of the papillary muscles, a tenting area of 186.43 ± 36.4 mm^2 was measured along the A2-P2 central cusps, which was significantly higher than the baseline value of 60.89 ± 31 mm^2 (p<0.001). Annuloplasty slightly reduced tenting area to 128.66 ± 44 mm^2 (p=0.006). Along the left commissural cusps (A1-P1), a tenting area of 58.74 ± 23.17 mm^2 was measured under control/baseline conditions. With annular dilatation and papillary muscle tethering, the tenting area increased to 170.73 ± 40 mm^2 (p=0.001) indicating significant leaflet tethering even at the commissural cusps. After annuloplasty, commissural tenting reduced slightly to 116.09 ± 23.4 mm^2 (p=0.007) compared to the diseased group. Similarly along the right commissural cusps (A3-P3) , annular dilatation and papillary muscle displacement increased tenting area to 160.3 ± 52.7 mm^2 from a baseline value of 64.3 ± 27.7 mm^2 (p=0.003). Annuloplasty did not seem to have an impact on tenting area as an area of 106.61 ± 39.19 mm^2 (p=0.003) was measured even after the repair along the A3-P3 commissural cusps as shown in Figure 6-38, Figure 6-39, and Figure 6-40.

Tenting Area along A1-P1 cusps

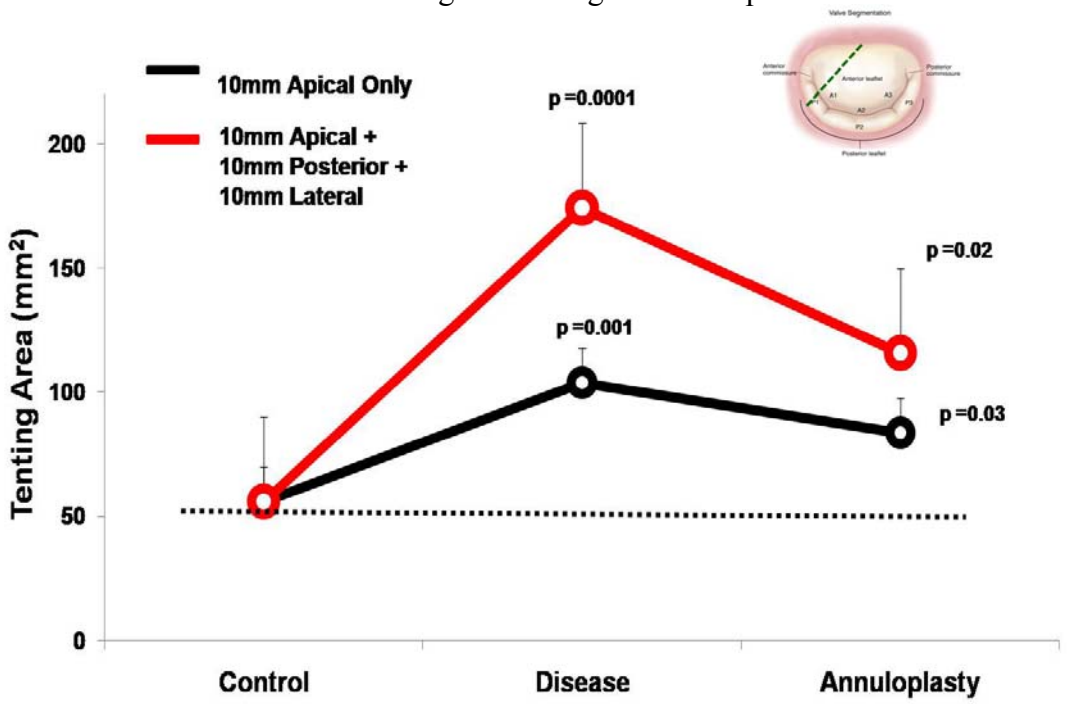

Figure 6-38 Changes in systolic tenting area under different experimental conditions, both before and after annuloplasty along the A1-P1 commissural cusps

Tenting Area along A2-P2 cusps

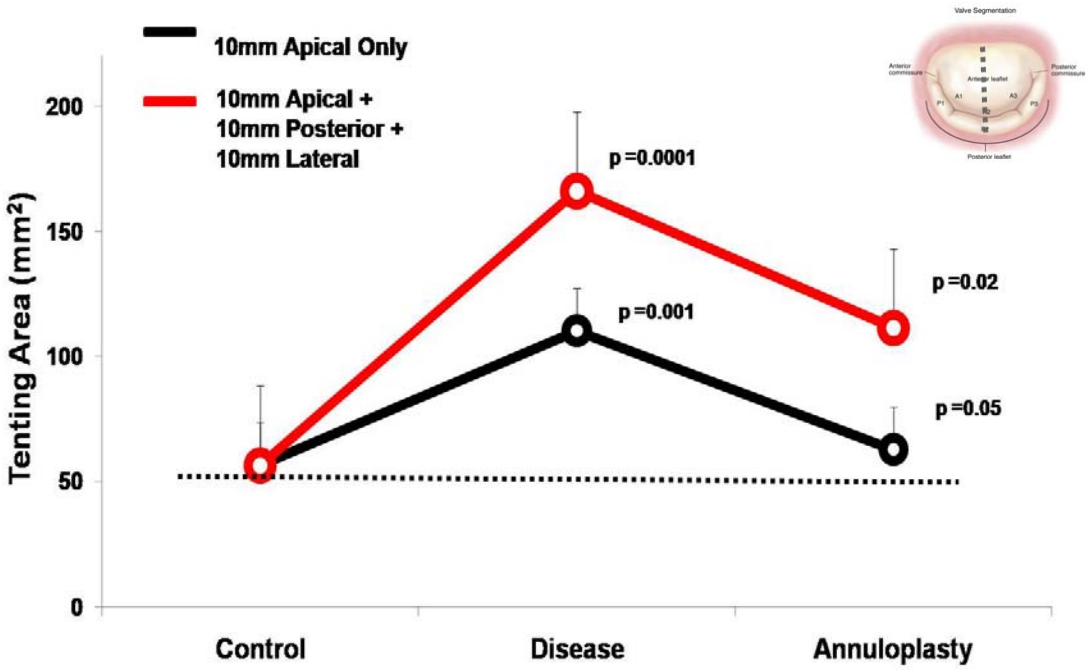

Figure 6-39 Changes in systolic tenting area before and after annuloplasty along the A2-P2 central cusps.

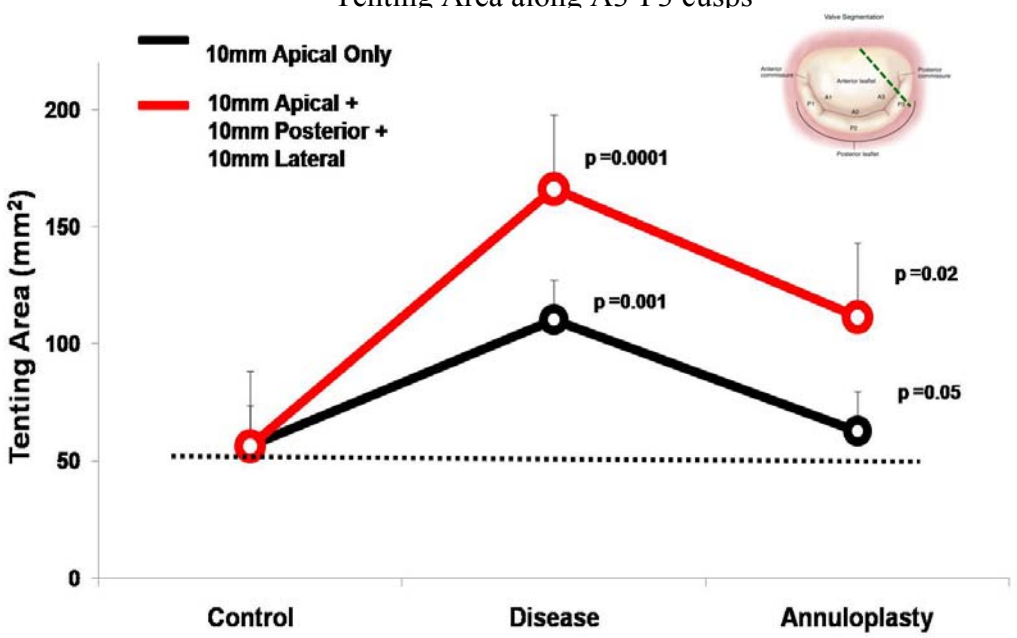

Figure 6-40 Changes in systolic tenting area before and after annuloplasty along the A3-P3 commissural cusps.

6.3.5 IMPACT OF ANNULOPLASTY ON SYSTOLIC LEAFLET COAPTATION LENGTH

Septal-lateral reduction of the mitral annulus is assumed to restore better leaflet coaptation compared to the pre-annuloplasty disease case. However, annuloplasty alone as shown by results in the earlier sections does not reduce sub-valvular tethering and thus may restrict leaflet mobility and may not improve leaflet coaptation as desired. To test this hypothesis, the leaflet coaptation length along A1-P1, A2-P2 and A3-P3 cusps of the mitral valve was measured using 2D echocardiography.

Along the central A2-P2 cusps, the measured leaflet coaptation length was 9.7±1.0 mm under control/baseline conditions. Annular dilatation and 10mm apical displacement of both the papillary muscles tethered the mitral leaflets and decreased the

leaflet coaptation length during systolic closure to 7.49± 0.9 mm, which was significantly lower than the baseline group (p=0.001). Annuloplasty increased leaflet coaptation length to 9.03 ± 0.7 mm, which was significantly higher than the disease group (p=0.002) and close to the baseline measurements (p=0.013). Along the left commissural cusps (A1-P1), a leaflet coaptation length of 7.47 ± 1.0 mm was measured under control/baseline conditions. With annular dilatation and papillary muscle tethering, the leaflet coaptation length decreased to 6.68 ± 0.85 mm (p=0.06). After annuloplasty, commissural leaflet coaptation length increased to 7.47 ± 0.93 mm (p=0.246) compared to the diseased group, but the change was insignificant. Similarly along the right commissural cusps (A3-P3) , annular dilatation and papillary muscle displacement changed leaflet coaptation length to 7.18 ± 0.6 mm from a baseline value of 8.09 ± 0.8 mm (p=0.01). Annuloplasty did not seem to have an impact on coaptation length, as a distance of 7.47 ± 0.9 mm (p=0.379) was measured even after the repair along the A3-P3 commissural cusps.

In the second pathological case with annular dilatation and 10mm apical-10mm lateral-10mm posterior displacement of the papillary muscles, a leaflet coaptation length of 6.97 ± 0.8 mm was measured along the A2-P2 central cusps, which was significantly lower than the baseline value of 9.77 ± 1.0 mm (p<0.001). Annuloplasty slightly increased leaflet coaptation length to 7.27 ± 1.5 mm, but the increase was not statistically significant (p=0.434). Along the left commissural cusps (A1-P1), a leaflet coaptation length of 7.47 ± 1.0 mm was measured under control/baseline conditions. With annular dilatation and papillary muscle tethering, the leaflet coaptation length decreased to 5.98 ± 0.63 mm (p<0.001) indicating significant leaflet tethering and loss of coaptation even at

the commissural cusps. After annuloplasty, commissural tenting coaptation length slightly increased to 6.75 ± 0.75 mm (p=0.014) compared to the diseased group. Similarly along the right commissural cusps (A3-P3) , annular dilatation and papillary muscle displacement decreased coaptation length to 6.17 ± 0.6 mm from a baseline value of 8.09 ± 0.8 mm (p=0.003). Annuloplasty did not seem to have an impact on coaptation length as a distance of 6.66 ± 0.5 mm (p=0.122) was measured even after the repair along the A3-P3 commissural cusps.

6.3.6 IMPACT OF 3D MITRAL VALVE GEOMETRY ON THE EFFICACY OF SUB-ANNULAR SECONDARY CHORDAL CUTTING TECHNIQUE

6.3.6.1 Impact of Mitral Valve Geometry on the Hemodynamic Efficacy of Secondary Chordal Cutting Procedure

2D echocardiographs of mitral valves in patients with ischemic mitral regurgitation due to dilated ventricles often demonstrate tethering of the anterior leaflet at the basal region and subsequent reduced mobility. Based on this observation transection of the two second order chordae that insert into the base of the anterior leaflet was proposed as a procedure to eliminate regurgitation in these valves. In this section, the results from investigating the efficacy of secondary chordal cutting in reducing mitral regurgitation in two pathologic valve geometries are presented. The two types of pathologic valve geometric scenarios are: [a] annular dilatation with apical papillary muscle displacement; and [b] annular dilatation with apical-posterior-lateral papillary muscle displacement.

With physiological valve geometry (Control/Baseline), all the eight valves were competent with no mitral regurgitation. Annular dilatation with displacement of the papillary muscles by 10mm in the apical direction induced an average regurgitation fraction of 10.54 ± 5.5, which is significantly higher compared to the baseline conditions (p=0.001). True-sizing the mitral annulus from its dilated size to its physiological size of 28mm reduced mitral regurgitation to 4.78 ± 5.27, which was significantly smaller than the disease state (p=0.032) and was comparable to the regurgitation volume in the control group (p=0.07). After secondary chordal cutting, regurgitation was reduced to trace levels of 3.61 ± 2.87, which was closer to the baseline conditions though statistically different (p=0.01).

The experiment was repeated with the second pathological valve geometry, i.e. annular dilatation with apical-posterior-lateral papillary muscle displacement. With physiological valve geometry (Control/Baseline), all the eight valves were competent with no mitral regurgitation. Annular dilatation with displacement of the papillary muscles by 10mm in the apical direction, 10mm in the posterior direction and 10mm in the lateral direction induced an average regurgitation fraction of 23.02±5.7, which is significantly higher compared to the baseline conditions (p=0.001). True-sizing the mitral annulus from its dilated size to its physiological size of 28mm reduced mitral regurgitation to 16.70 ± 7.8, which was smaller compared to the disease state (p=0.003) , but by clinical standards still high. These results summarized in Figure 6-41, clearly demonstrate that in the efficacy of annuloplasty and secondary chordal cutting depends to a large extent on the valve geometry. Secondary chordal cutting in this case left

significant remnant mitral regurgitation of 18.56 ± 4.19, which was not significantly different from the annuloplasty group (p=0.176) and significantly higher than the baseline conditions (p<0.0001). These results clearly indicate that in this pathological geometric setting of the mitral valve, cutting the secondary chordae on the anterior leaflet did not seem to have a positive impact in reducing residual regurgitation after mitral annuloplasty.

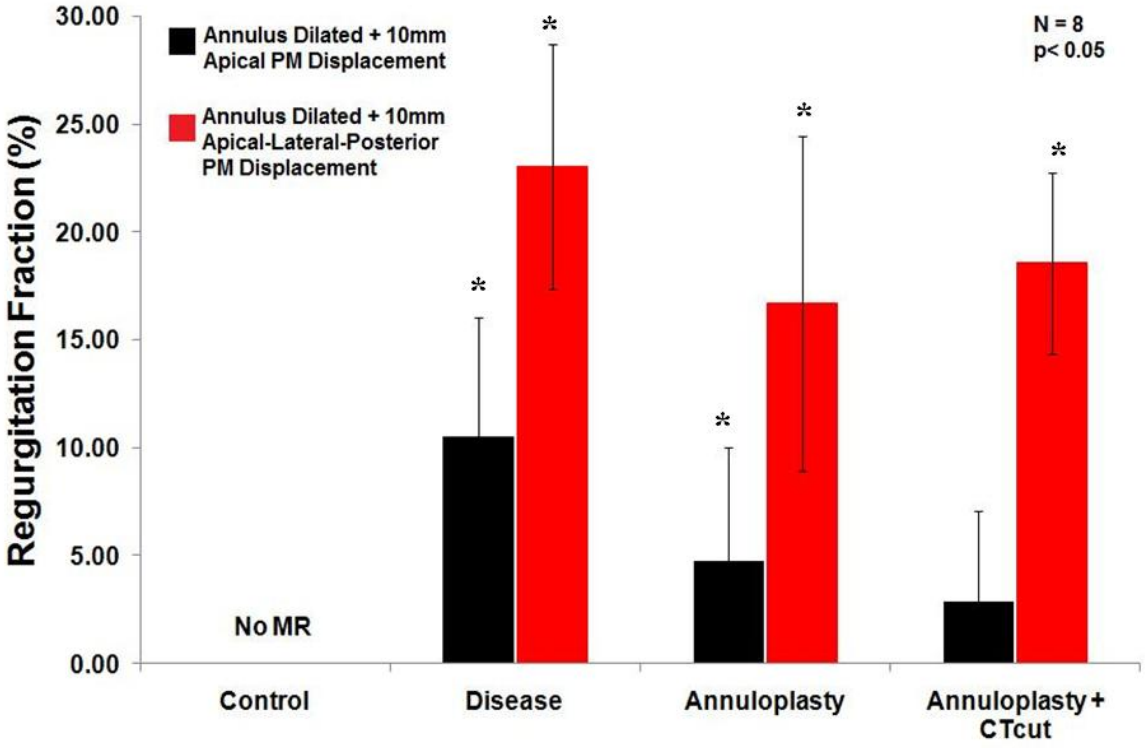

Figure 6-41 Changes in mitral regurgitation fraction under different experimental conditions. As expected under disease states, there was moderate to severe regurgitation that was dependent on the pathological geometry of the valve. Annuloplasty reduced regurgitation in both cases, but regurgitation was persistent in both cases. Chordal cutting reduced regurgitation only in the apical displacement case but not in the apical-posterior-lateral displacement case.

6.3.6.2 Impact of Secondary Chordal Cutting on Systolic Tenting Height

Results from previous sections clearly illustrate that isolated mitral annuloplasty may reduce mitral regurgitation, but does not eliminate the sub-valvular tethering caused due to papillary muscle displacement. Hypothetically, transecting the secondary chordae should relieve sub-annular tethering to some extent and aid movement of the systolic coaptation length towards the mitral annulus and reduce regurgitation. However, hemodynamic results from the previous section clearly indicate that secondary chordal cutting restored valve competence only when the papillary muscles were displaced apically but not when they were displaced apically, posteriorly and laterally. To understand the mechanisms underlying the difference in results, the tenting height after secondary chordal cutting at the A1-P1, A2-P2 and A3-P3 cusps was measured.

Along the central A2-P2 cusps, the measured systolic tenting height was 7.3±1.7 mm under control/baseline conditions. Annular dilatation and 10mm apical displacement of both the papillary muscles tethered the mitral leaflets and increased the tenting height during systolic closure to 9.86± 2.0 mm, which was significantly higher than the baseline group ($p=0.036$). Annuloplasty reduced tenting height to 8.7±1.8 mm, which was not significantly different from the disease group ($p=1.00$). Secondary chordal cutting reduced tenting height to 6.46 ± 1.26 mm, which was significantly smaller than the disease state ($p=0.006$) and also the annuloplasty group ($p=0.008$). Along the left commissural cusps (A1-P1), a tenting height of 5.4 ± 1.8 mm was measured under control/baseline conditions. With annular dilatation and papillary muscle tethering, the tenting height increased to 7.68±1.95 mm ($p=0.05$) indicating leaflet tethering even at the

commissural cusps. After annuloplasty, commissural tenting increased slightly to 8.14 ± 1.9 mm (p=0.312) compared to the diseased group. Secondary chordal cutting reduced tenting height to 6.32 ± 0.75 mm, which was smaller than the annuloplasty group (p=0.07) and approaching statistical significance. Similarly along the right commissural cusps (A3-P3) , annular dilatation and papillary muscle displacement increased tenting height to 8.11 ± 2.0mm from a baseline value of 5.02 ± 1.3mm (p=0.018). Annuloplasty did not seem to have an impact on tenting height as a distance of 7.84 ± 2.0 mm was measured (p=0.720 compared to disease) even after the repair along the A3-P3 commissural cusps. Secondary chordal cutting reduced tenting height to 6.49 ± 0.91mm, which was significantly smaller than the disease (p=0.219) but the change was statistically insignificant.

In the second pathological case with annular dilatation and 10mm apical-10mm lateral-10mm posterior displacement of the papillary muscles, a tenting height of 12.7 ± 1.7 mm was measured along the A2-P2 central cusps, which was significantly higher than the baseline value of 7.26 ± 1.7 mm (p<0.001). Annuloplasty slightly reduced tenting height to 10.5 ± 3.0 mm, but the reduction was not statistically significant (p=0.1). Secondary chordal cutting did not seem to have an impact on tenting height as a distance of 10.0 ± 3.32 mm was measured, which was not significantly different from the annuloplasty group (p=0.761). Along the left commissural cusps (A1-P1), a tenting height of 5.4 ± 1.8 mm was measured under control/baseline conditions. With annular dilatation and papillary muscle tethering, the tenting height increased to 11.45 ± 2.06 mm (p=0.001) indicating significant leaflet tethering even at the commissural cusps. After

annuloplasty, commissural tenting reduced slightly to 9.68 ± 3.0 mm (p=0.04) compared to the diseased group. Secondary chordal cutting did not change tenting height as a distance of 9.45 ± 2.96 mm persisted even after the procedure, which was not different from the annuloplasty (p=0.895) group. Similarly along the right commissural cusps (A3-P3) , annular dilatation and papillary muscle displacement increased tenting height to 11.94 ± 3.2 mm from a baseline value of 5.02 ± 1.3mm (p=0.002). Annuloplasty reduced tenting height to a distance of 9.54 ± 4.0 mm along the A3-P3 commissural cusps (p=0.02). After secondary chordal cutting a tenting height of 9.78 ± 2.79 mm was measured, which was statistically equivalent to the tenting height measured after annuloplasty (p=0.862). These results are summarized in Figure 6-42, Figure 6-43, and Figure 6-44.

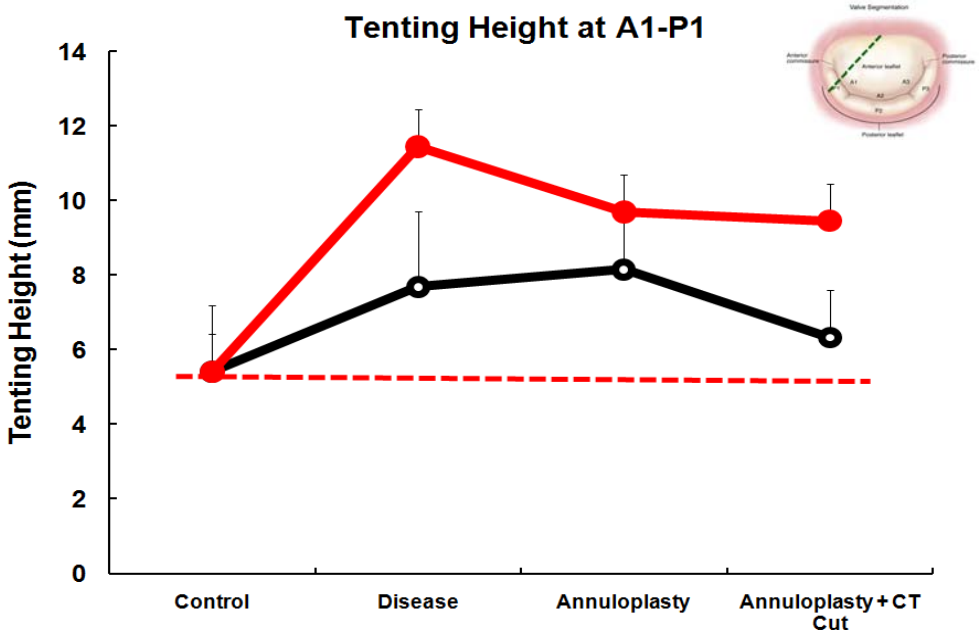

Figure 6-42 Changes in tenting height along the commissural A1-P1 cusps before surgical repair, after annuloplasty and after sub-annular chordal cutting

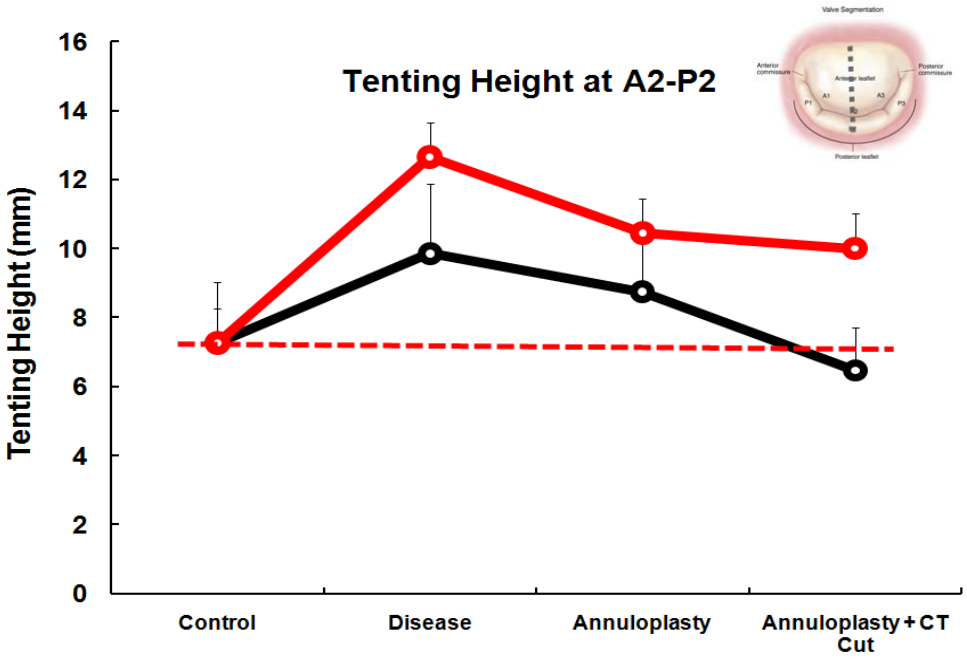

Figure 6-43 Changes in tenting height along the central A2-P2 cusps before surgical repair, after annuloplasty and after sub-annular chordal cutting

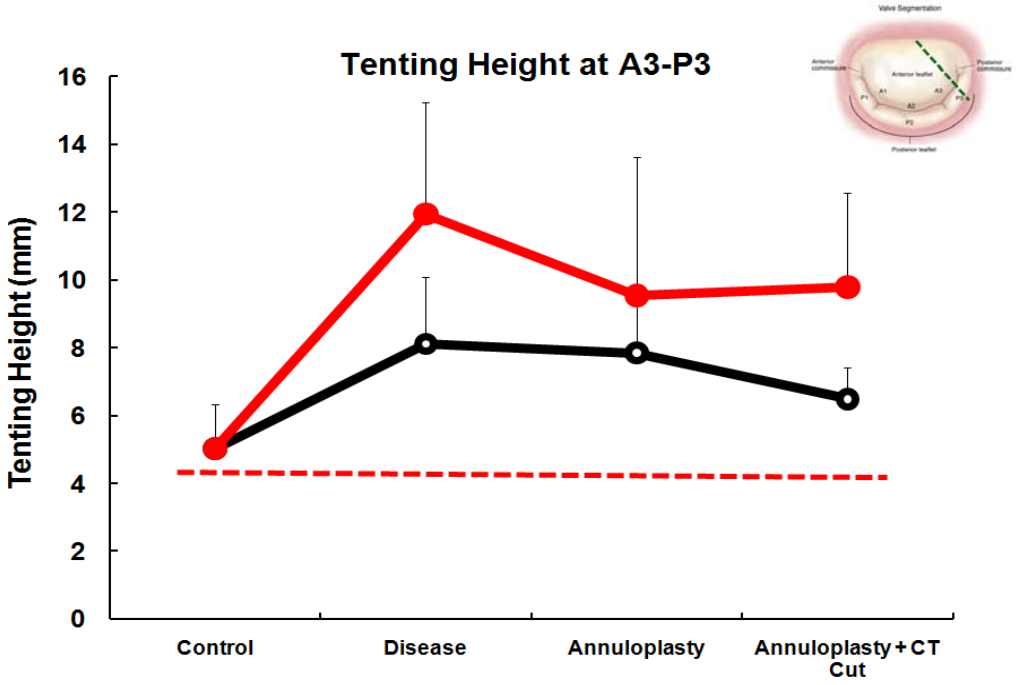

Figure 6-44 Changes in the tenting height along the commissural A3-P3 cusps before surgical repair, after annuloplasty and after chordal cutting

6.3.6.3 Impact of Secondary Chordal Cutting on Systolic Tenting Area

Tenting area, defined as the area enclosed by the two mitral leaflets and the mitral annulus is reported here as a quantifiable measure of sub-valvular tethering, pre and post surgical repair. Secondary chordal cutting should relieve local leaflet tethering of the anterior leaflet base, if not the entire leaflet and thus may restore the normal anterior leaflet curvature from the tethered sea-gull shaped leaflets.

Along the central A2-P2 cusps, the measured systolic tenting area was 60.9 ± 31 mm^2 under control/baseline conditions. Annular dilatation and 10mm apical displacement of both the papillary muscles tethered the mitral leaflets and increased the tenting area at peak systolic closure to 129.7 ± 28.4 mm^2, which was significantly higher than the baseline group ($p<0.001$) Annuloplasty reduced tenting area to 87 ± 17.1 mm^2, which was significantly reduced from the disease group ($p=0.02$) but was not completely relieved . Cutting the secondary chordae on the anterior leaflet reduced tenting area to 65.9 ± 8.5 mm^2 which is comparable to the baseline conditions ($p=0.68$). At the left commissural cusps (A1-P1), a tenting area of 58.7 ± 23.1 mm^2 was measured under control/baseline conditions. With annular dilatation and papillary muscle tethering, the tenting height increased to 100.5 ± 28 mm^2 ($p<0.001$) indicating leaflet tethering even at the commissural cusps. After annuloplasty, commissural tenting decreased slightly to 91.5 ± 26 mm^2 ($p=0.47$) compared to the diseased group. Additionally secondary chordal cutting further reduced tenting area to 57.07 ± 19.3 mm^2, which was comparable to the baseline ($p=0.007$). Similarly along the right commissural cusps (A3-P3) , annular dilatation and papillary muscle displacement increased tenting area to 103.4 ± 36.4 mm^2

from a baseline value of 64.33 ± 27.74 mm^2 ($p<0.001$). Annuloplasty reduced tenting area to 66.07 ± 17.0 mm^2 after the repair along the A3-P3 commissural cusps as shown in Figure 6-45. Chordal cutting further reduced tenting area to 56.06 ± 12.26 mm^2 , which was comparable to the baseline ($p=0.04$).

In the second pathological case with annular dilatation and 10mm apical-10mm lateral-10mm posterior displacement of the papillary muscles, a tenting area of 186.43 ± 36.4 mm^2 was measured along the A2-P2 central cusps, which was significantly higher than the baseline value of 60.89 ± 31 mm^2 ($p=0.001$). Annuloplasty slightly reduced tenting area to 128.66 ± 44 mm^2 ($p=0.006$), and secondary chordal cutting though reduced tenting area to 105.83 ± 35.75 mm^2 it was not comparable to the baseline ($p=0.07$) . Along the left commissural cusps (A1-P1), a tenting area of 58.74 ± 23.17 mm^2 was measured under control/baseline conditions. With annular dilatation and papillary muscle tethering, the tenting area increased to 170.73 ± 40 mm^2 ($p=0.001$) indicating significant leaflet tethering even at the commissural cusps. After annuloplasty, commissural tenting reduced slightly to 116.09 ± 23.4 mm^2 ($p=0.006$) compared to the diseased group, and secondary chordal cutting further reduced tenting area to 96.03 ± 35.24 mm^2 which was significantly higher than the baseline ($p=0.07$). Similarly along the right commissural cusps (A3-P3) , annular dilatation and papillary muscle displacement increased tenting area to 160.3 ± 52.7 mm^2 from a baseline value of 64.3 ± 27.7 mm^2 ($p<0.001$). Annuloplasty did not seem to have an impact on tenting area as an area of 106.61 ± 39.19 mm^2 was measured even after the repair along the A3-P3 commissural

cusps as shown in Figure 6-45. Chordal cutting failed to impact tenting area, which was measured at 102.36 ± 39.24 mm^2 and was significantly higher than the baseline.

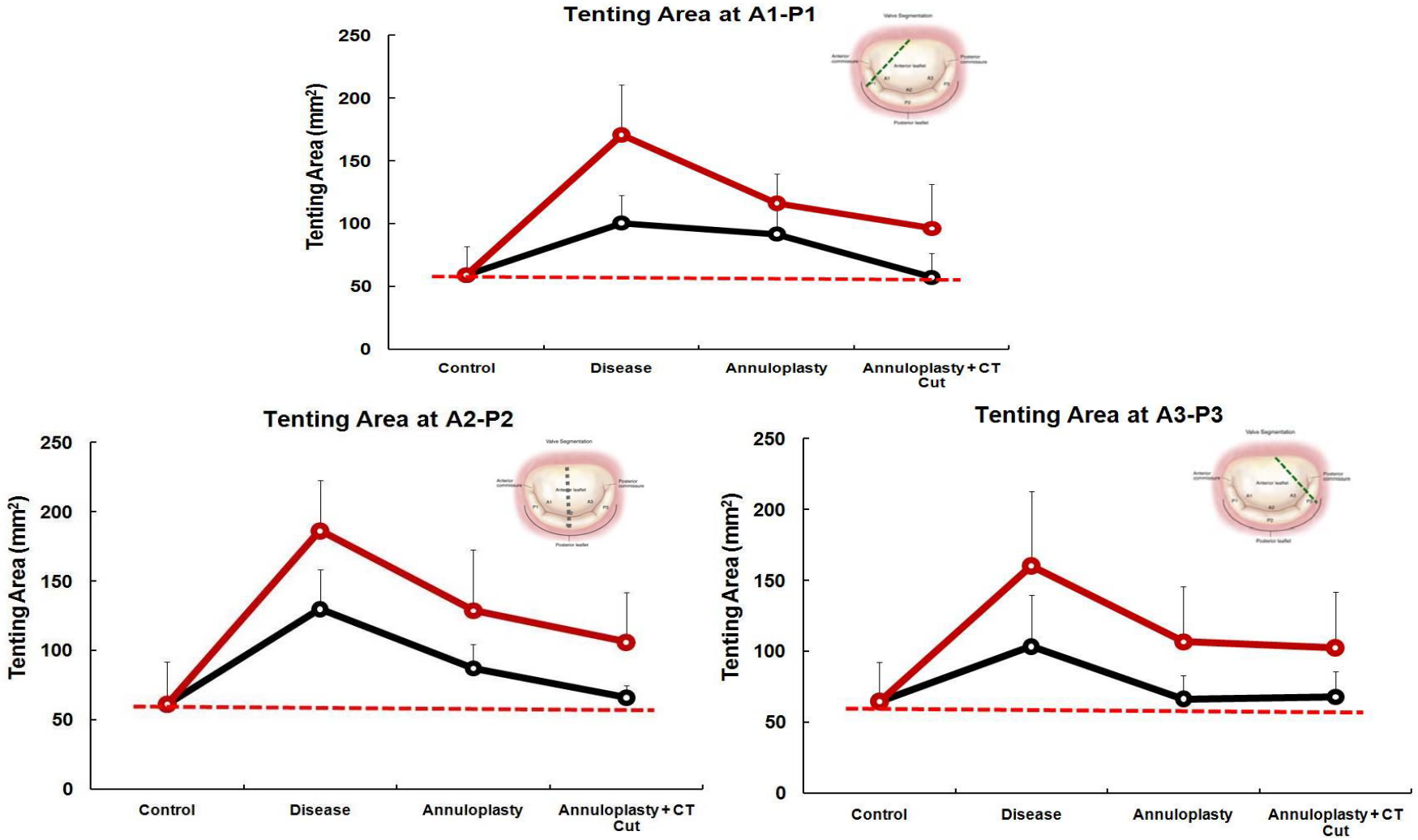

Figure 6-45 Tenting area measured along the central and commissural cusps of the mitral valve pre and post chordal cutting. Measurements along both the central and commissural cusps indicate a decrease in tenting area with ring and chordal cutting, but a larger decrease was seen with apical displacement compared to apical-posterior-lateral displacement.

6.3.6.4 Impact of Secondary Chordal Cutting on Systolic Leaflet Coaptation Length

Relieving sub-valvular tethering to some extent using secondary chordal cutting may allow better leaflet mobility and thus may aid in increasing systolic leaflet coaptation length. To investigate this hypothesis, the leaflet coaptation length along A1-P1, A2-P2 and A3-P3 cusps of the mitral valve was measured using 2D echocardiography before and after chordal cutting procedure.

Along the central A2-P2 cusps, the measured leaflet coaptation length was 9.7±1.0 mm under control/baseline conditions. Annular dilatation and 10mm apical displacement of both the papillary muscles tethered the mitral leaflets and decreased the leaflet coaptation length during systolic closure to 7.49± 0.9 mm, which was significantly lower than the baseline group ($p=0.001$). Annuloplasty increased leaflet coaptation length to 9.03 ± 0.7 mm, which was significantly higher than the disease group ($p=0.002$) and comparable to the baseline measurement.. Secondary chordal cutting further enhanced leaflet coaptation length to 10.36 ± 1.74 mm. Along the left commissural cusps (A1-P1), a leaflet coaptation length of 7.47 ± 1.0 mm was measured under control/baseline conditions. With annular dilatation and papillary muscle tethering, the leaflet coaptation length decreased to 6.68 ± 0.85 mm ($p=0.002$). After annuloplasty, commissural leaflet coaptation length increased to 7.47 ± 0.93 mm ($p=0.013$) compared to the diseased group and secondary chordal cutting further increased coaptation length to 8.97 ± 1.55 mm. Similarly along the right commissural cusps (A3-P3) , annular dilatation and papillary muscle displacement decreased leaflet coaptation length to 7.18 ± 0.6 mm from a baseline value of 8.09 ± 0.8 mm ($p<0.001$). Annuloplasty did not seem to have an impact

on coaptation length as a distance of 7.47 ± 0.9 mm was measured even after the repair along the A3-P3 commissural cusps as shown in Figure 6-46. However secondary chordal cutting increase coaptation length to 10.38 ± 0.67 mm, which was comparable to the baseline.

In the second pathological case with annular dilatation and 10mm apical-10mm lateral-10mm posterior displacement of the papillary muscles, a leaflet coaptation length of 6.97 ± 0.8 mm was measured along the A2-P2 central cusps, which was significantly lower than the baseline value of 9.77 ± 1.0 mm ($p<0.001$). Annuloplasty slightly increased leaflet coaptation length to 7.27 ± 1.5 mm, but the increase was not statistically significant ($p=0.4$). Chordal cutting increased the coaptation length to 8.77 ± 0.53 mm, which was comparable to the baseline. Along the left commissural cusps (A1-P1), a leaflet coaptation length of 7.47 ± 1.0 mm was measured under control/baseline conditions. With annular dilatation and papillary muscle tethering, the leaflet coaptation length decreased to 5.98 ± 0.63 mm ($p<0.001$) indicating significant leaflet tethering and loss of coaptation even at the commissural cusps. After annuloplasty, commissural tenting coaptation length slightly increased to 6.75 ± 0.75 mm compared to the diseased group. Chordal cutting did not impact leaflet coaptation at this commissural section, as a length of 6.89 ± 0.44 mm was measured. Similarly along the right commissural cusps (A3-P3) , annular dilatation and papillary muscle displacement decreased coaptation length to 6.17 ± 0.6 mm from a baseline value of 8.09 ± 0.8 mm . Annuloplasty did not seem to have an impact on coaptation length as a distance of 6.66 ± 0.5 mm was measured even after the repair along the A3-P3 commissural cusps as shown in Figure

6-46. Chordal cutting did not aid restoration of leaflet coaptation, evident from the measured value of 6.90 ± 0.48 mm.

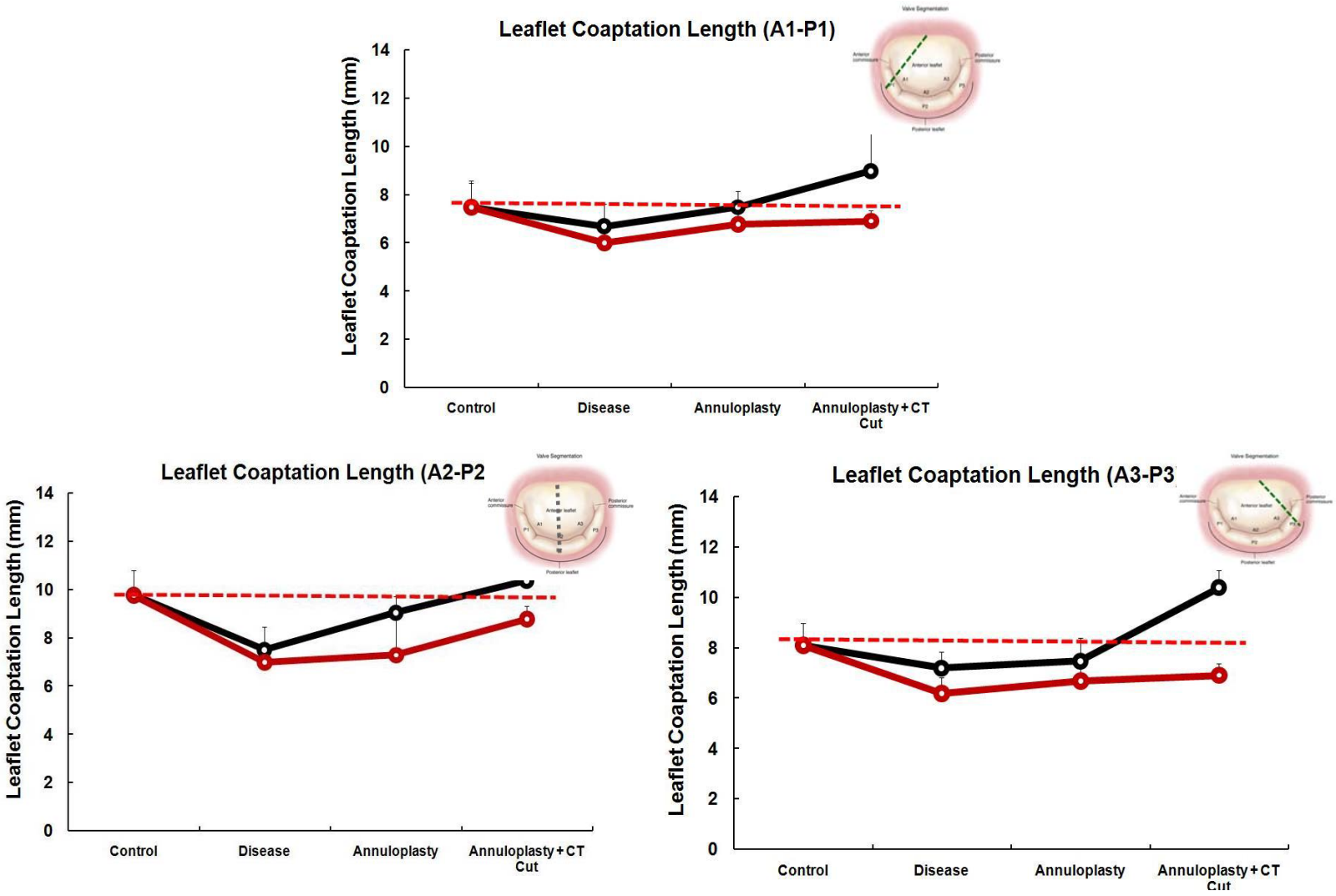

Figure 6-46 Variations in leaflet coaptation length with annular and sub-annular repair techniques at the central and commissural cusps. In the apical displacement case, secondary chordal cutting restored coaptation to physiological levels, but not in the apical posterior lateral displacement case.

6.3.6.5 Impact of Secondary Chordal Cutting on Anterior Marginal Chordal Tension

Secondary chordae on the anterior leaflet are the main load bearing elements in the mitral valve structure, and play a key role in determining leaflet kinematics during systole and diastole. Anatomically, the secondary chordae and the marginal chordae in the porcine hearts emerge from the same chordal stem, but at different locations on the stem. Thus, secondary chordal cutting may significantly redistribute the forces on the marginal chordae emerging from the same chordal stem and may be detrimental to their performance and failure. In this section, the forces on the marginal chordae before and after secondary chordal cutting with three papillary muscle positions – 10mm apical, 10mm apical+10mm lateral, 10mm apical+10mm posterior +10mm lateral are reported. In Figure 6-47, the changes in left and right anterior marginal chordal forces with normal valve geometry, with papillary muscle displacement and after secondary chordal cutting are presented. On the left anterior marginal chord, a peak force of 0.0302N at control, 0.045N with apical papillary muscle displacement, and a force of 0.060N after secondary chordal cutting. With apical and lateral displacement of the papillary muscles, the peak force increased to 0.084 N, and with subsequent chordal cutting increased to 0.180 N. With apical, lateral and posterior displacement, the force increased to 0.122 N and after chordal cutting increased to 0.230 N. Similarly, on the right anterior marginal chord, a peak force of 0.065N was measured at control, 0.072 N with apical papillary muscle displacement, and 0.079 N after chordal cutting in this case. With apical-lateral papillary muscle displacement a peak force of 0.102 N was measured, with a corresponding increase to 0.176N after chordal cutting. With apical-lateral-posterior papillary muscle

displacement, a peak force of 0.173N was measured, which increased to 0.3222N after chordal cutting.

Figure 6-48 depicts the temporal changes in the marginal chordal forces under different experimental conditions. In the top row, the temporal changes in the left marginal chordal force are shown wherein the force pattern changed with the experimental condition. Under control conditions, the peak marginal chordal force was measured immediately after the rapid rise in the systolic pressure, following which a flat plateau was observed until end-systole. A similar trend was observed with apical papillary muscle displacement as well, with a rapid rise in force followed by a plateau and gradual fall in the measured force. However, after chordal cutting, the maximum force on the marginal chordae seems to be slightly offset towards mid systole and a plateau in the forces was not observed. A similar trend was observed with apical and lateral displacement of the papillary muscles, but the magnitude of forces was significantly higher in this group compared to the apical papillary muscle displacement. However, with apical-posterior-lateral displacement, under disease condition itself the systolic plateau in forces was not observed, with a rapid rise and subsequent rapid fall in the force before and after secondary chordal cutting. A similar trend in forces was observed even in the right marginal chord, as shown in the bottom row of the Figure 6-48.

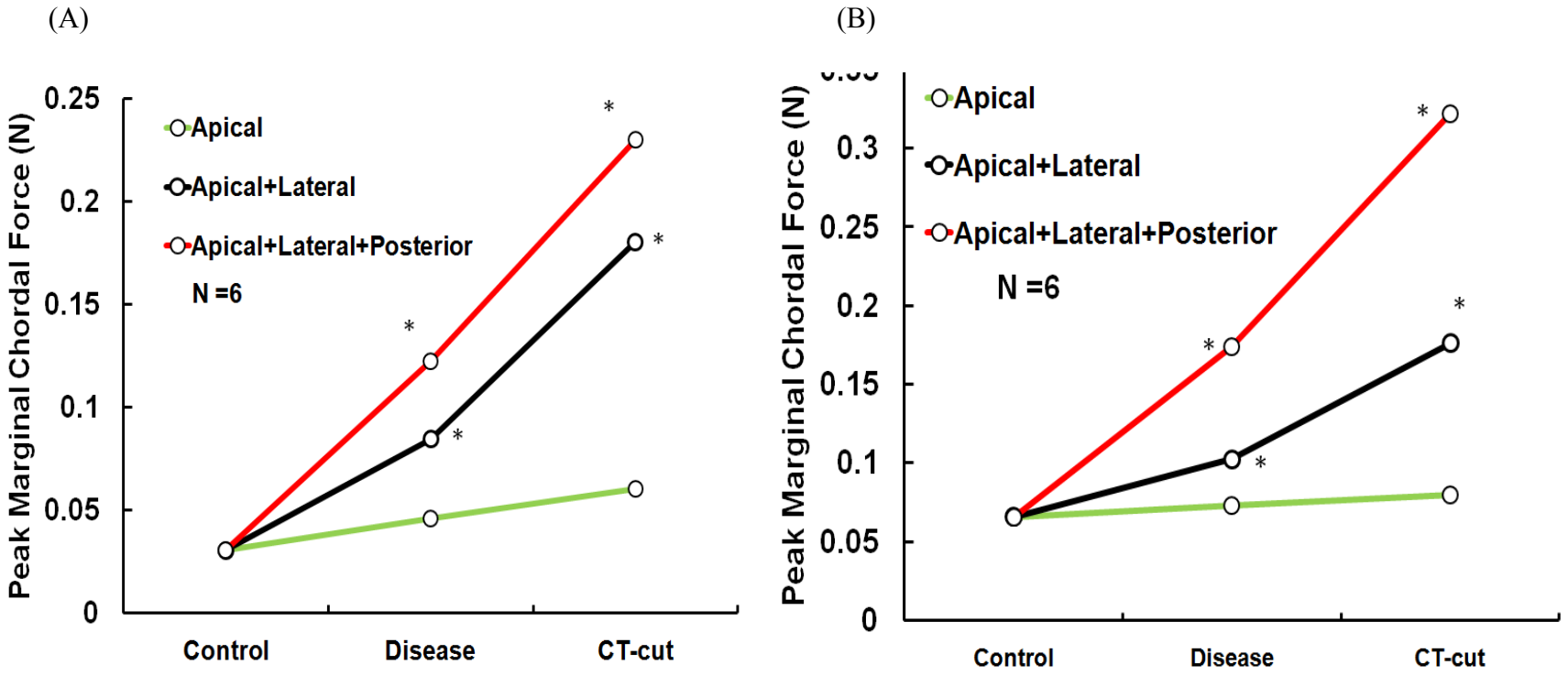

Figure 6-47 Changes in the marginal chordal force with different papillary muscle positions, before and after chordal cutting procedure, (A) Changes in the forces on the left marginal chord and (B) shows the changes on the right marginal chord

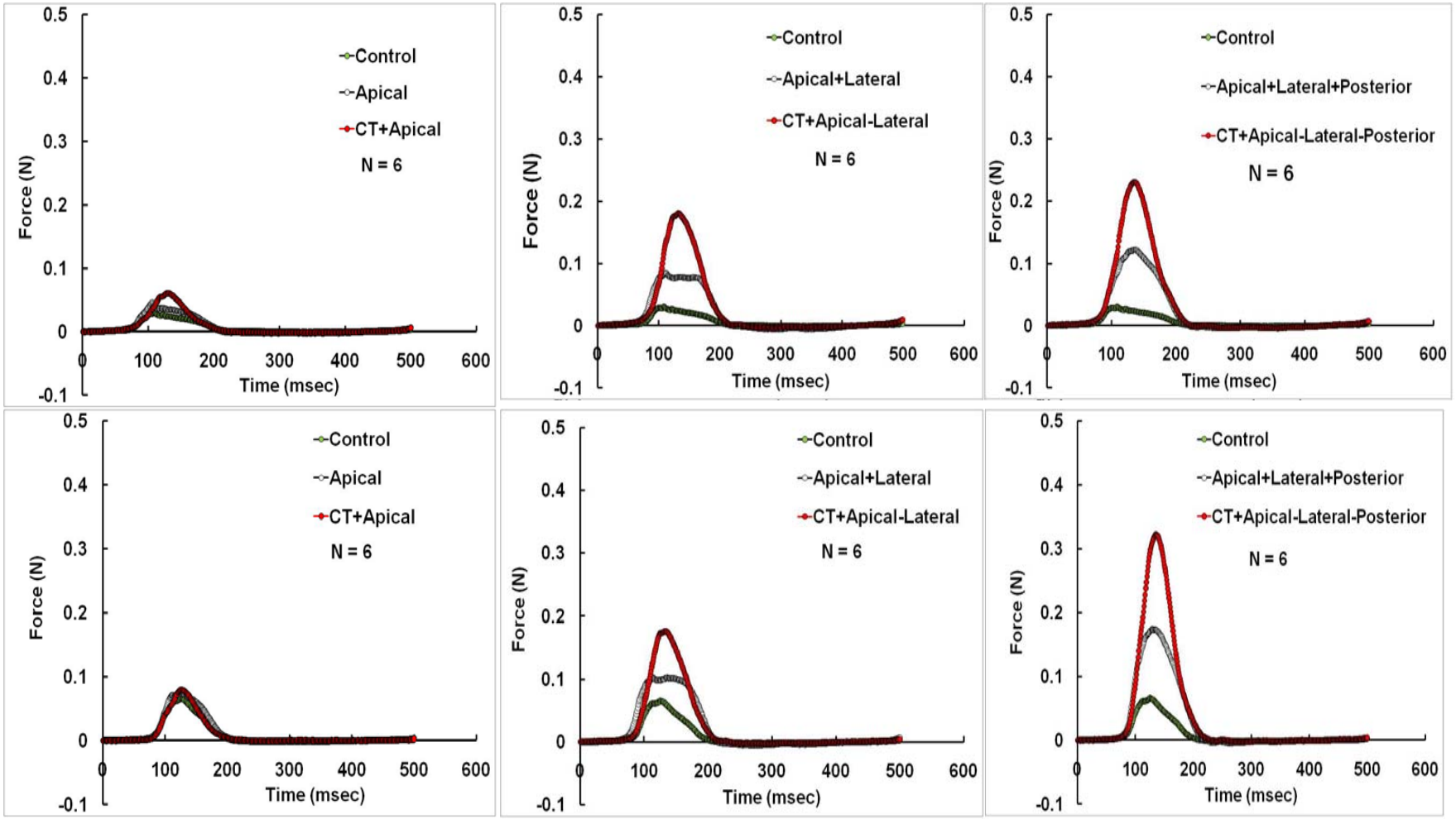

Figure 6-48 (Top Row) Temporal force measurements on marginal chordae tendineae under physiological, three different pathological mitral valve geometries, and after secondary chordal cutting in the three different conditions. The figures demonstrate a significant increase in marginal chordal force before after chordal cutting, in the apical+lateral and apical+lateral+posterior papillary muscle displacement cases.

CHAPTER 7

DISCUSSION

In this chapter, the results for each specific aim are presented from an analyzed and a morphological or hemodynamic basis to the results is presented. An engineering perspective on the acute outcomes observed in this thesis is presented, and a discussion on the relevance of these findings to clinical practice and outcomes are delineated. Finally, the limitations of the studies in each aim are outlined and improvements to current studies are recommended.

7.1 CONGENITAL CLEFT MITRAL VALVE REPAIR

Congenital heart defects are complex anatomical defects, which are surgically challenging to repair. Surgical procedures performed in the pre-natal stages or at early age lack long term durability due to several reasons. With increased surgical experience focus has veered from mortality as an index of operative success towards the long term quality of life subsequent to surgical repair[1]. Often the long term outcomes are sub optimal due to partial or complete failure of the repair, due to growth of the cardiac and valvular structures after surgery, changes in cardiac hemodynamics and to some extent the mechanical properties of the valve.

Atrio-Ventricular Canal (AVC) defect is one such congenital cardiac lesion for which surgical repair is challenging and is typically associated with poor long term durability. Surgical correction of this lesion involves a sequence of procedures that encompass separation of the atrioventricular valve from the muscular septum, closure of the atrial and ventricular septal defects, and reconstruction of the mitral and tricuspid valves. Though success with repair of septal defects has been excellent, late incompetence of the left atrioventricular valve remains a challenge and reoperation rates remain disconcertingly high. Pathological morphology of the valve, structural deficiencies at the annular and sub annular levels and disarray in the chordal structures are some of the risk factors, though the contribution of each is currently unclear.

7.1.1 IMPACT OF CLEFT VALVE MORPHOLOGY ON VALVE FUNCTION

Understanding the morphological deficiencies of the valve is the first step towards identifying risk factors for repair failure, or to develop new techniques for valve reconstruction. Kanani et al. reported an excellent study on the morphology of the left atrioventricular valve in these patients, clearly delineating the leaflet and chordal geometries[1]. They compared the mitral valve structures between normal hearts (N=92, Cardiac Registry, Children's Hospital, Boston, MA) and hearts with atrioventricular septal defect with a common atrioventricular junction (N=72; Cardiac Archive, Great Ormond Street Hospital, London (28), Children's Hospital of Pittsburgh, PA (30), Children's Hospital, Boston, MA (14)). They observed that the anterior leaflet of the mitral valve was uniformly triangular in normal mitral valves with the base of the leaflet continuous with the fibrous region at the base of left and non-coronary leaflets of the

aortic valve as shown in Figure 7-1A. The chordal structures were distributed across the entire leaflet, classified based on their insertion regions into primary chordae (free edge), secondary chordae (middle of leaflet), and tertiary chordae (at commissures or directly into the annulus). In comparison, the newly created neo-anterior leaflet in the repaired left atrioventricular valve was more rectangular, with a triangular recess at the distal end of the surgically closed cleft as shown in Figure 7-1B. The chordae inserted longitudinally into the leaflet, and were separate from each other than splitting from one chordal stem as seen in the normal mitral valve. In the in-vitro cleft valve model, the leaflet was forced to be rectangular by moving the commissures laterally, and a wedge shaped cleft was created to mimic the triangular recess at the distal end after cleft closure. However, deficiencies in the chordal insertion were simulated only to the extent to which the altered leaflet change forces change in their orientation, but no morphological changes to the tendinous chordae were attempted.

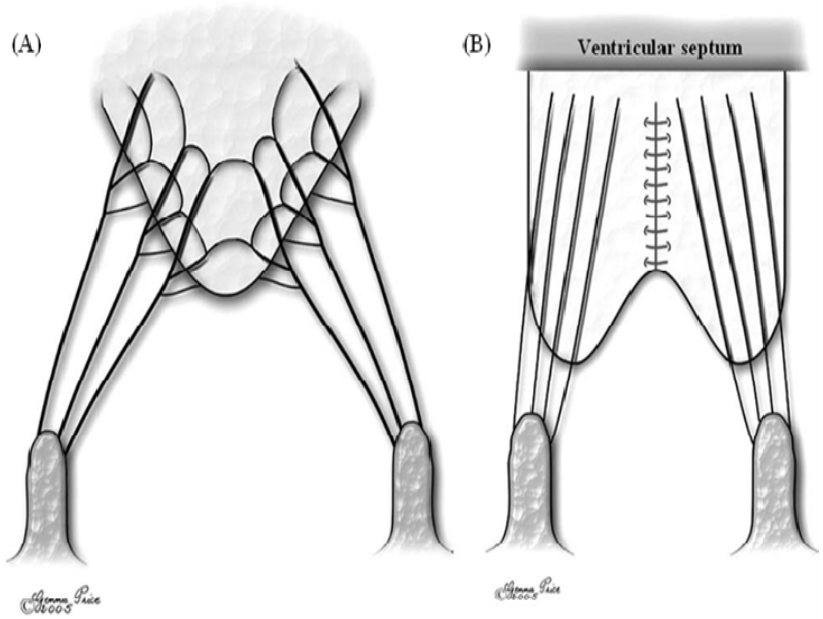

Figure 7-1 Schematic representation of the anterior leaflet of a normal mitral valve and the neo-anterior leaflet of the reconstructed mitral valve in an atrioventricular canal defect. (A) The triangular anterior leaflet with the base continuous with the aortic valve leaflets through the fibrous trigones. The chordae tendineae are systematically arranged into primary, secondary and tertiary chordae that insert from the free edge to the base of the leaflet. (B) The neoanterior leaflet on the other hand is more rectangular with a triangular recess in the center where the cleft was closed. The chordal structure is malformed as well with the chordae running into the longitudinal axis of the leaflets. Figure reproduced from Kanani et al.[1]

Additionally fusion of the chordae tendineae with chordal tags are reported in these pathological valves, with absence of the central chordae tendineae in the vicinity of the cleft as shown in Figure 7-2. By creating a wedge shaped cleft, all of the primary and some of the secondary chordae were removed in the in vitro model, and thus the strut chordae inserting longitudinally near the annulus and the tertiary chordae were the primary load bearing elements. Chordal fusion was not simulated in this model, as there are no data available on the structure, function or mechanics of these fused chordae in comparison to the normal chordae tendineae.

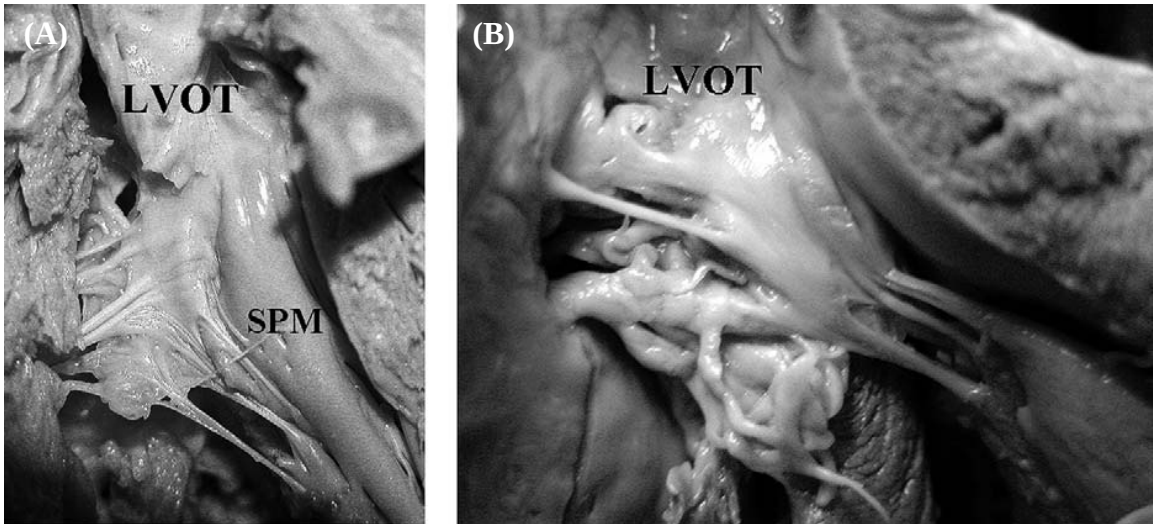

Figure 7-2 Sub annular apparatus from heart specimens with atrioventricular canal defects. (A) chordal fusion and leaflet straddling due to proximity of the papillary muscle head to the leaflet edge; (B) Abnormal chordal forms and tags inserting into the leaflet from the papillary muscles and the ventricular wall, but with absence of central chordae. Figure reproduced from [1]

Kohl et al. using echocardiographic analysis analyzed the video recordings of 11 children to study the nature of the cleft position, chordal attachments and associated pathology of both entities[80]. They found that in patients with atrioventricular canal defects, the cleft position was positioned centrally on the anterior leaflet, and was consistent between patients. However, the papillary muscles in these patients were posteriorly displaced towards one another, with reduced included angle between the two papillary muscles as shown in Figure 7-3A. In the in vitro simulator, this morphological feature was simulated by displacing the papillary muscles in the heart simulator laterally by 10mm and posteriorly by 10mm towards each other until the positions reported in Kohl et al. were achieved. Often this sub annular geometry is not corrected surgically, and thus assessing the impact of the scooped geometry of the ventricle on the valve function is important and was studied in this model. The posterior leaflet was also

reduced in size to mimic the triangular shape of the mural leaflet in these defects as shown in Figure 7-3B.

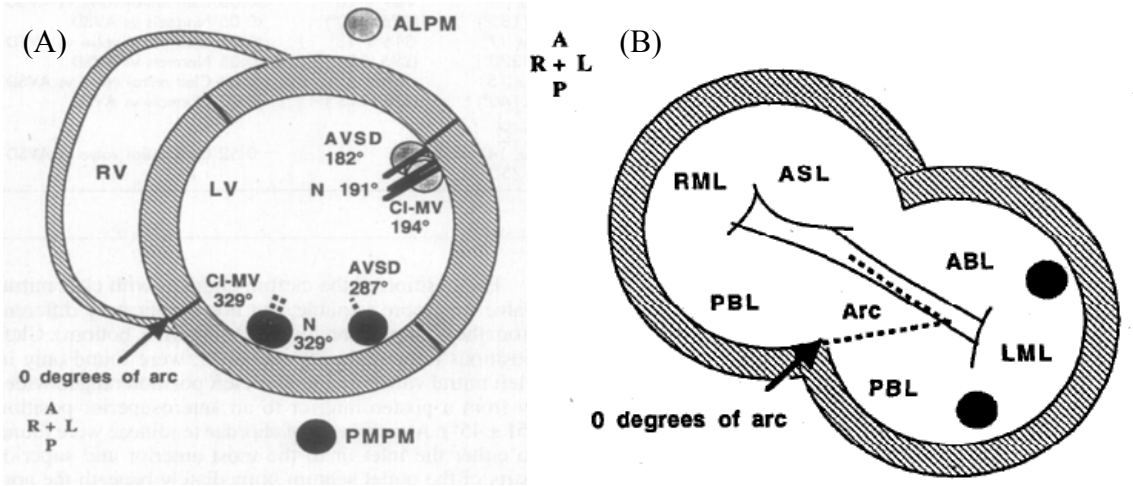

Figure 7-3 (A)Mean position of the papillary muscles in the atrioventricular cleft mitral valves in comparison to an isolated cleft mitral valve, demonstrating the posterior and lateral displacement of the two papillary muscle heads in the former case; (B) Schematic representation of the common atrioventricular orifice, with respect to the papillary muscle positions.

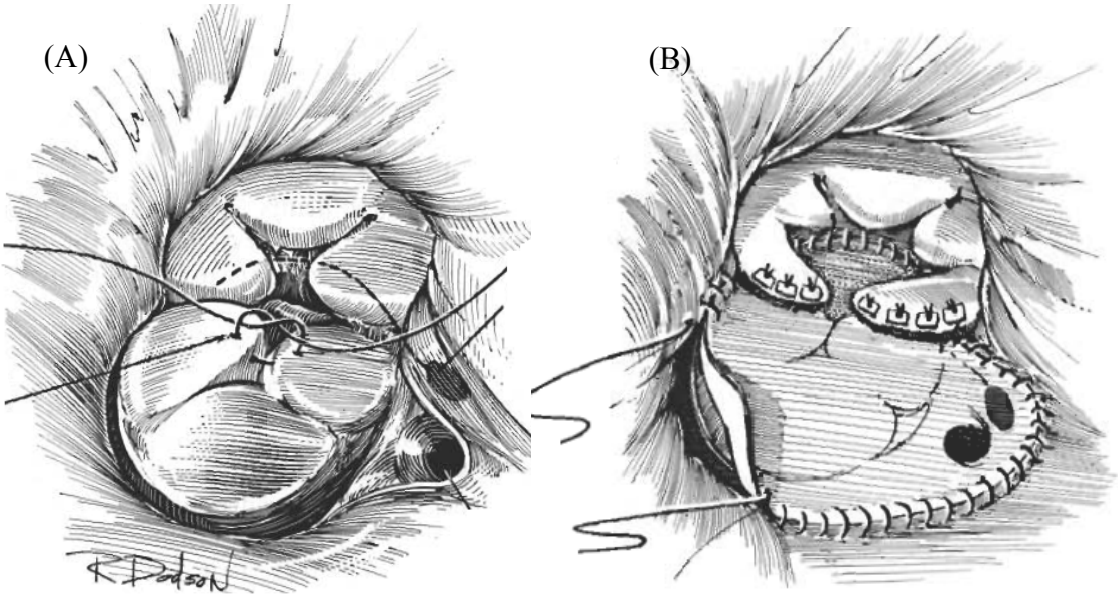

Figure 7-4 (A) Construction of the left and right atrioventricular valves from the common atrioventricular valve orifice using a suture knot at the annular-anterior leaflet junction; (B) The oval shaped annulus formed after patching the septal defects using pericardial patches at the base of the valve. Figure reproduced from Castaneda et al. Chapter 10, Atrioventricular Canal Defects, Congenital Heart Defects and Procedures.

Finally, the mitral annular shape in the in vitro model was shaped to mimic the pathological annular shape resulting from the pericardial patching of the septal defects at the atrial and ventricular levels. As shown in Figure 7-4 , a suture knot at the cleft-annulus junction and pericardial patching of the septum resulted in a “semi-oval” shaped annulus that was used in this study.

3D echocardiographic images from the in vitro cleft valve model and in vivo echocardiographs clearly demonstrated the similarity between the two models. Figure 7-5 depicts the in vitro vs. in vivo [123] comparison at systolic ejection, where the open cleft on the anterior leaflet is clearly visible with restricted motion of the posterior leaflet.

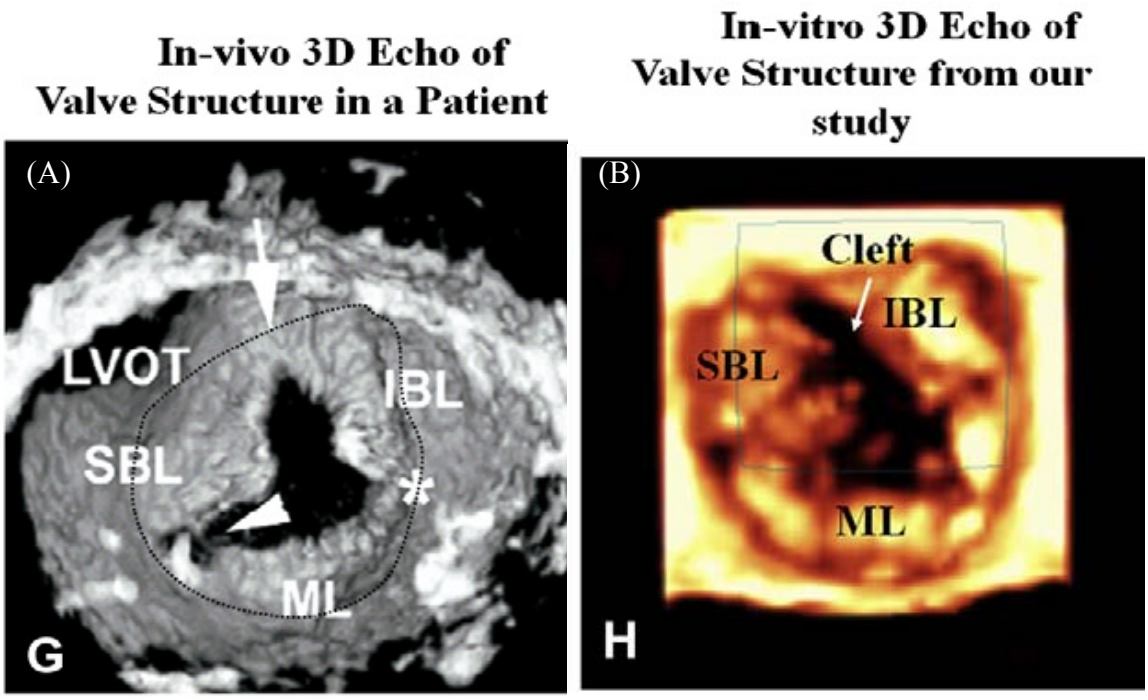

Figure 7-5 (A) In-vivo 3D echocardiograph of the mitral valve depicting the cleft in the anterior segment with the two bridging leaflets and a smaller posterior leaflet, (B) Shows an in vitro echocardiograph demonstrating the similarities between the two valves at systolic ejection with loss of coaptation between the opposing bridging leaflets and the mural leaflet. Image (A) reproduced from Takahashi et al. 2006. J Am Soc Echocardiography.

7.1.2 IMPACT OF CLEFT CLOSURE AND ANNULAR DILATATION ON VALVE HEMODYNAMICS

The in vitro methodology adopted in this study is thus functionally equivalent to the atrioventricular valve defect-like anatomy. This model overcomes the unavailability of large animal models, which are challenging to develop for congenital defects such as these, as the exact genetic exclusions or biological mechanisms underlying the defect are unknown. Though *in-vitro* methodology is limited by its rigid ventricular chamber, non-physiological ventricular shape and lack of annular dynamics, these limitations do not affect the variables that are investigated in this study. Additionally, the *in-vitro* approach provides precise control over the valve geometry, hemodynamic conditions and also provides the ability to study different repair procedures on the same valve.

Using this in vitro model, the risk factors for left atrioventricular valve regurgitation after complete cleft closure were investigated and some surgical measures to address this challenge are suggested. The first important conclusion of this study is that complete cleft closure reduces regurgitation completely in comparison to partial cleft closure, with a normal annulus. This result is intuitive, because closing the cleft completely will eliminate any crevices or holes in the anterior leaflet and thus avoid regurgitation. The regurgitation volume decreased from the open cleft case by 18% for one-third cleft closure, by 61% for two-third cleft closure, and by 90% when the cleft was completely closed. These data clearly demonstrate that the best hemodynamic outcomes are possible, only when the cleft is completely closed from the mitral annulus to the leaflet free edge. However, clinically it is thought that complete cleft closure may reduce mobility of the anterior leaflet and thus induce mitral stenosis. In this study we did

not measure any statistically significant increase in the stenosis, and mobility of the anterior leaflet was not compromised. However, if partial cleft closure is intended, at least two thirds of the cleft should be closed to achieve hemodynamic benefit. Closing the cleft only proximal to the mitral annulus leaves a majority of the cleft open, allowing regurgitation, and thus should be avoided. When more than two-thirds of the cleft is closed, regurgitation is reduced as the posterior leaflet may blanket the open part of the cleft at systolic coaptation. Often, mild regurgitation persists through this region as the edges of the cleft are thin and unstable at high systolic pressures. These results agree with the clinical findings of Wetter et al. who confirmed in 96 patients that larger the extent of cleft closure better are the hemodynamics [124].

Notwithstanding complete cleft closure, significant regurgitation can still occur in these valves. Acar et al. reported a nice echocardiographic analysis of valve anatomy after surgery for septal defects in the atrioventricular canal defect patients [125]. They observed that post operative regurgitation was typically observed at two locations

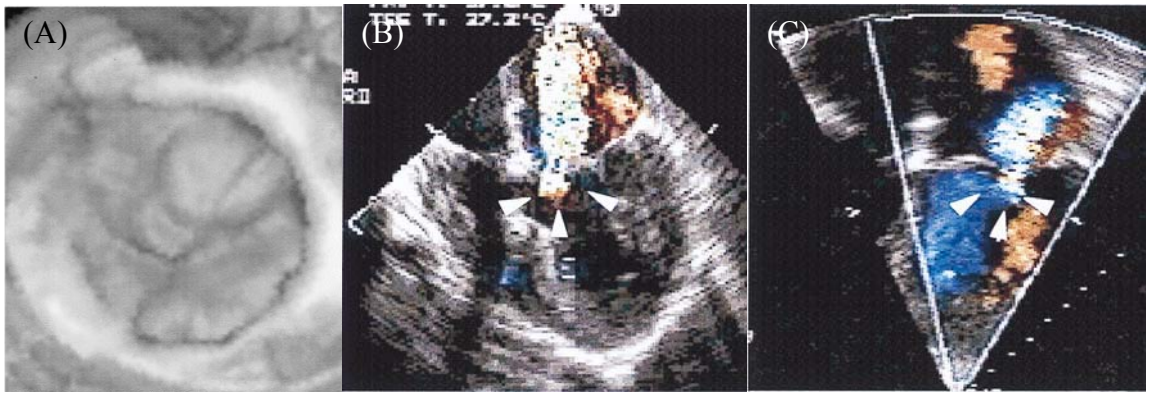

Figure 7-6 (A) A 3D echocardiograph of the surgically reconstructed mitral valve after cleft closure and septal defect patching; (B) A four chamber view depicting the regurgitation jet through the residual cleft that is medial to the annulus, (C) Another four chamber view depicting a regurgitation jet at the coaptation zone between the bridging leaflets and mural leaflets. Figures reproduced from Acar, P et al. Am J Cardiol, 1999; 83.

medially from the region of the coaptation of the superior and inferior components of the anterior leaflets (the residual cleft); and from the region of coaptation with the mural leaflet as shown in Figure 7-6. This study led to the hypothesis that even after complete cleft closure, loss of coaptation between the bridging and mural leaflets is possible which is typically not addressed surgically.

As the in vitro model already accounts for the reduced leaflet size, the impact of post surgical annular dilatation on the valve hemodynamics was studied. The nomograms in Figure 7-7 depict the expected changes in the mitral annular anterior-posterior diameter with increase in body surface area of the patient, and these projected annular dimensions were simulated in the in vitro model. Results from this study demonstrate that increase in the septal lateral dimension of the mitral annulus, induces clinically significant regurgitation, even if the cleft is completely closed. Figure 7-8 depicts the regurgitation through the valve with a dilated annulus at different cleft closure lengths. It is clearly evident from these echocardiograms that when the cleft is completely or partially open, regurgitation occurs through the residual opening. Figure 7-8_provides a key insight that even after complete cleft closure it is still possible to have central regurgitation due to loss of coaptation between the anterior and the posterior leaflets. With a 20% increase in annular size, regurgitation volumes increased up to 45% for a two-third cleft closure and by 69% for complete cleft closure. At 40% annular dilatation, regurgitation increased by 59% for the two-third cleft closure and by 84% for the complete cleft closure. An interesting inference from these results is the higher rate of increase in regurgitation due to annular dilatation, for a fully closed cleft compared to a partially closed cleft.

(A)

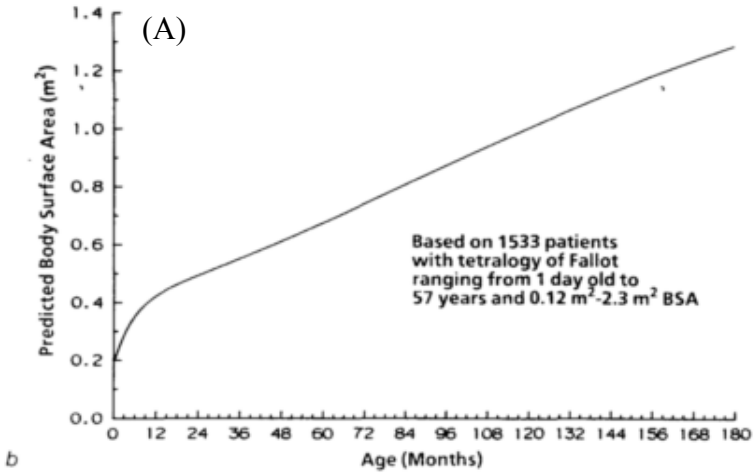

b

(B)

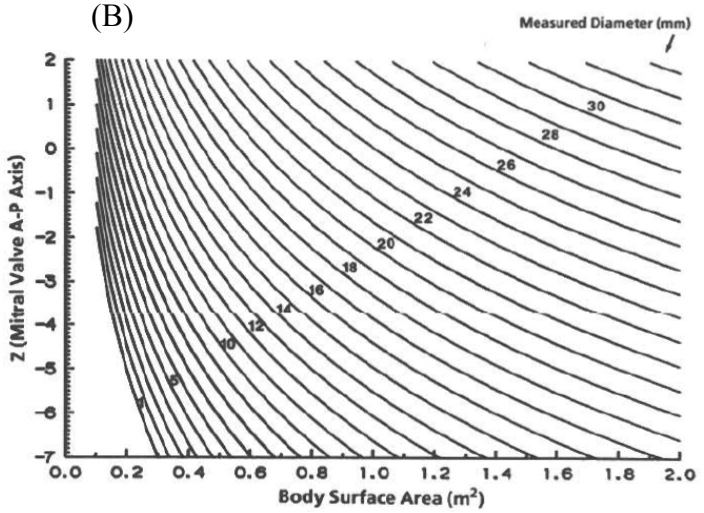

(C)

	Mitral Valve				Tricuspid Valve	
	Minor Axis (A-P)		Major Axis (Lat)		Major Axis (Lat)	
BSA	Mean (mm)	±SD	Mean (mm)	±SD	Mean (mm)	±SD
0.25	12.0	10.2–13.8	15.0	11.8–18.2	15.4	12.0–18.8
0.30	13.6	11.8–15.4	17.3	14.1–20.5	17.6	14.2–21.0
0.35	14.9	13.1–16.7	19.2	16.0–22.4	19.5	16.1–22.9
0.40	16.1	14.3–17.9	20.9	17.7–24.1	21.1	17.7–24.5
0.45	17.1	15.3–18.9	22.3	19.1–25.5	22.6	19.2–26.0
0.50	18.0	16.2–19.8	23.7	20.5–26.9	23.9	20.5–27.3
0.60	19.5	17.7–21.3	25.9	22.7–29.1	26.1	22.7–29.5
0.70	20.8	19.0–22.6	27.9	24.7–31.1	28.0	24.6–31.4
0.80	22.0	20.2–23.8	29.5	26.3–32.7	29.7	26.3–33.1
0.90	23.0	21.2–24.8	31.0	27.8–34.2	31.1	27.7–34.5
1.00	23.9	22.1–25.7	32.3	29.1–35.5	32.4	29.0–35.8
1.20	25.5	23.7–27.3	34.6	31.4–37.8	34.6	31.2–38.0
1.40	26.8	25.0–28.6	36.5	33.3–39.7	36.5	33.1–39.9
1.60	27.9	26.1–29.7	38.2	35.0–41.4	38.2	34.8–41.6
1.80	28.9	27.1–30.7	39.6	36.4–42.8	39.6	36.2–43.0
2.00	29.8	28.0–31.6	40.9	37.7–44.1	40.9	37.5–44.3

Key: A-P, anteroposterior; BSA, body surface area; Lat, lateral; SD, standard deviation.

Figure 7-7 (A) Nomogram of the relationship between age or patients with congenital heart defects and the predicted body surface area; (B) Nomogram depicting the expected mitral annular anterior-posterior dimension of the mitral valve with increase in body surface area; (C) A table depicting the change in the major and minor axis of the mitral valve dimensions with body surface area. Data provided by Dr.Nikolay Vasilyev, Children's Hospital, Boston, MA

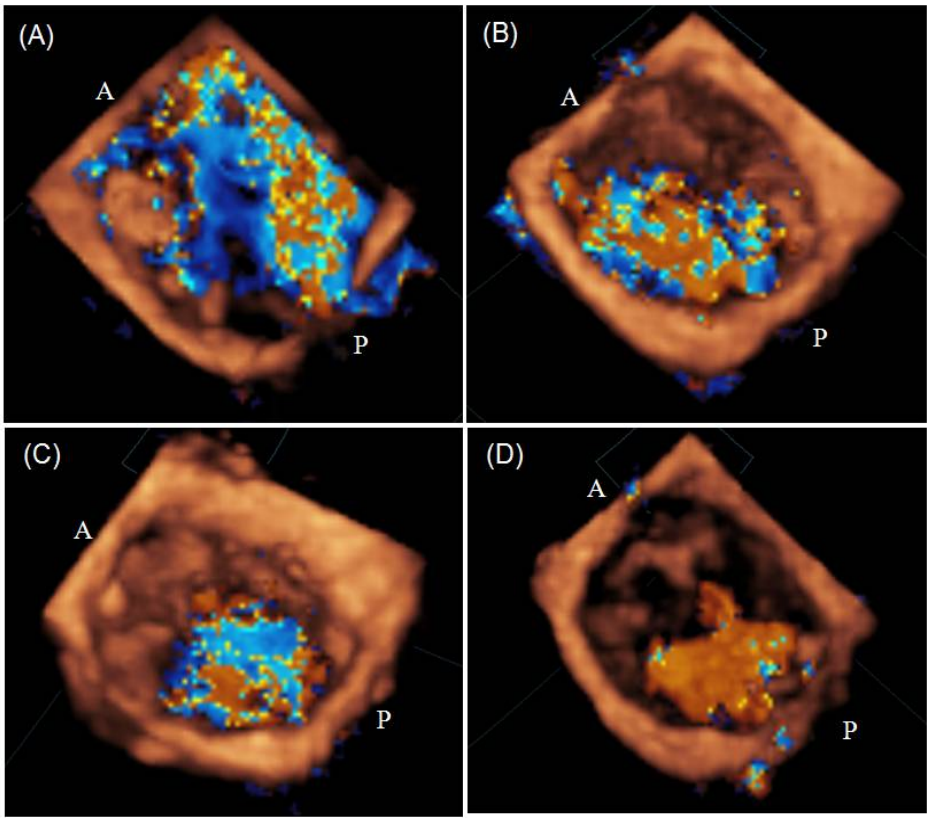

Figure 7-8 (A) Severe regurgitation through the valve with annular dilatation and a completely open cleft, (B) Moderate regurgitation with one third cleft closed, (C) Moderate regurgitation at the residual cleft after 2/3rd cleft closure but with annular dilatation, and (D) Regurgitation through the valve due to annular dilatation but with a completely closed cleft. [Obtained at Georgia Institute of Technology using Philips iE33 System, X 7-2 probe]

Annular dilatation, simulated as an increase in the septal lateral dimension of the annulus, may induce regurgitation via two mechanisms. He et al. in an in vitro study demonstrated that normal mitral valve leaflets can compensate up to 60% increase in annular size, with trivial regurgitation through the valve [113]. In these congenitally malformed valves, the leaflets are smaller in size and lose their ability to compensate for higher levels of annular dilatation. Thus even at low levels of annular dilatation, loss of central coaptation and ensuing regurgitation is possible. Secondly, interaction between the two malformed mitral leaflets and the annulus may restrict adequate leaflet motion for

proper systolic valve closure. Posterior displacement of the annulus moves the chordal insertion points on the posterior leaflet away from the tips of the papillary muscles. Tethering of the posterior leaflet is possible due to this chordal misalignment, and may restrict proper systolic valve closure as shown in Figure 7-9. Additionally, chordae inserting into the anterior leaflet edges tether on the leaflets which could be confounded by annular dilatation inducing regurgitation even after complete cleft closure.

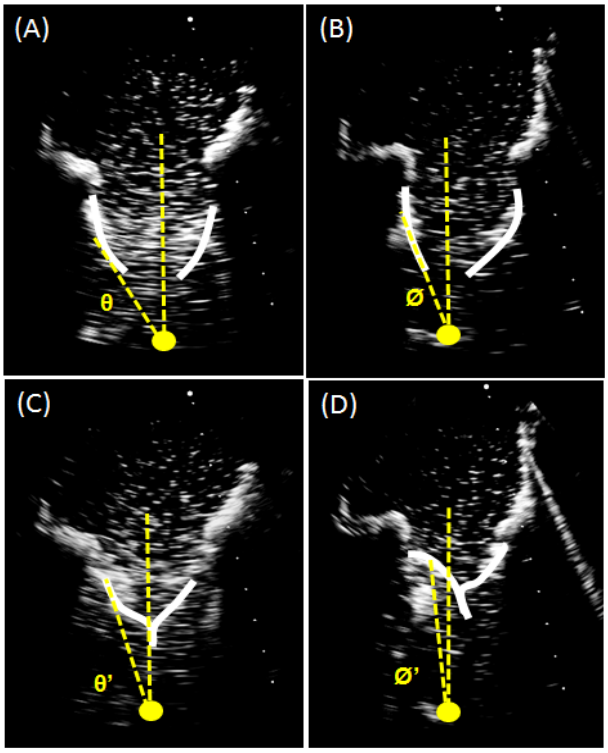

Figure 7-9 Schematic depicting the impact of annular dilatation on the leaflet-papillary muscle interaction. The yellow circle on each picture represents the tip of the papillary muscle, and the angle depicts the included angle between the leaflet tangent and a normal from the papillary muscle tip to the mitral annular plane. (A) Dilated annulus with a larger included angle than the normal annulus shown in (B). Similarly, (C) and (D) depict the leaflet position with respect to the vertical axis, where in the dilated state tethering of the leaflet is evident from the slight bend in the leaflet, which is absent in the normal state. [Obtained at Georgia Institute of Technology using Philips iE33 System, X 7-2 probe]

These important valve features have to be acknowledged when surgically repairing the valve in these defects. Often posterior leaflet augmentation techniques are adopted to extend the leaflets to compensate for annular dilatation, but such procedures are challenging to perform due to fragility of the leaflet tissue and the risk of severing the chordae inserting into the ventricular surface of the leaflets.

7.1.3 ANNULAR UNDERSIZING AND ITS ROLE IN IMPROVING POST REPAIR HEMODYNAMICS

Annular undersizing may be a promising alternative to patch augmentation in repairing these valve defects. In this study annular undersizing was simulated as reduction in the septal-lateral dimension, and its impact on different levels of cleft closure was assessed. With a completely open cleft, as expected regurgitation persisted through the cleft even after 40% annular undersizing and thus was considered a failed repair. At one-third cleft closure, significant reduction in regurgitation was measured at 40% annular undersizing. However, it may be risky to severely undersize the annulus in these young patients as in the long term they may develop mitral stenosis, which can have detrimental impact on left ventricular diastolic function. With two third cleft closure and 20% annular undersizing, regurgitation was reduced by 58% from the normal annular size at the same cleft length. This study supports the hypothesis that a partial cleft closure is sufficient when undersizing the annulus. Acknowledging this fact is useful when confronting difficult anatomies such as in valves with a single papillary muscle. Additionally, the open part of the cleft could provide better leaflet mobility benefitting diastolic ventricular filling.

7.1.4 CLINICAL IMPLICATIONS

Undersizing in these patients could serve three purposes: restrict annular dilatation, enhance leaflet coaptation and restore complete valve competence with only a partial cleft closure. Since canal defects are corrected at infancy, restricting annular dilatation during initial years after the repair could prevent late regurgitation. However, this procedure has to be considered cautiously, and adult mitral annuloplasty rings should not be used due to their rigidity and lack of growth potential in the long term. Using Polydioxanone or absorbable annuloplasty rings is recommended since they allow somatic growth of the annulus by gradual degradation with time. This strategy may attenuate early morbidity, and also allow for better long term valve growth and performance. Honjo et al. [126] in their retrospective report on infants who underwent mitral valve repair for congenital mitral regurgitation, reported a desirable growth of the mitral annulus following a mitral annular repair without artificial material, shown in Figure 7-10. Biodegradable rings may provide similar outcomes, and thus should be increasingly used in pediatric mitral valve repair. One such ring that is commercially available in Europe today is the BioRing® (Bioring SA, Lonay, Switzerland) and is being considered for clinical trials in the United States of America.

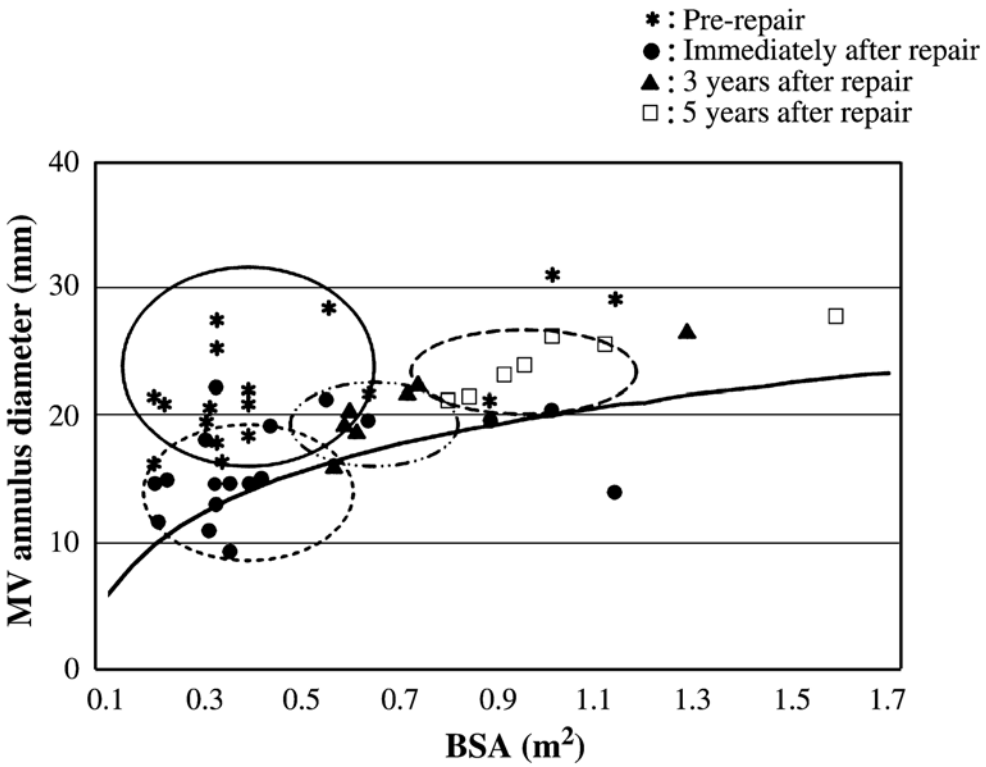

Figure 7-10 Annular growth curve reported by Honjo et al after mitral annular techniques that do not use artificial materials and thus allow growth of the annulus. Though initially the mitral annular diameter is reduced due to undersizing or commissurotomy, the annulus grows and tends to catch up with a physiological growth rate [Figure reproduced from Honjo et al, Interact Cardio Vasc Thorac Surg, 2006; 5:589-593]

7.1.5 LIMITATIONS OF THE IN VITRO STUDY

Although the in vitro model adopted in this study simulates human AVC-like valve anatomy and function to a good extent, it has some inherent limitations. In this model, chordal attachments in the cleft vicinity inserting from the ventricular septum (Rastelli type A) were not simulated. These chordal attachments could contribute to some extent to the postoperative regurgitation. The rigid ventricular chamber used in this study does not mimic the ventricular motion, whose effects on the valve function were not studied.

7.1.6 SUMMARY

In summary, this study provides novel mechanistic insights into a complex problem of LAV repair in AVC defects. Cleft closure and post-operative annular dilatation have a significant impact on repair outcome. To reduce reoperation rates and to maintain long-term valve competence, it is demonstrated that cleft closure with annular undersizing is proven to be beneficial.

7.2 DEGENERATIVE MITRAL VALVE REPAIR

7.2.1 SURGICAL REPAIR FOR FIBROELASTIC DEFICIENCY

Mitral valve prolapse is a common manifestation of a spectrum of degenerative lesions, which encompass chordal elongation, chordal rupture, leaflet distension and annular dilatation. Cuffer and Barbillon, first reported the midsystolic click and systolic murmur syndrome in 1887, but early studies attributed it to extracardiac disease until 1966, when Barlow et al using ventricular imaging demonstrated the aneurysmal protrusion of the valve leaflet into the left atrium. Since Criley first proposed the term "mitral valve prolapse"; focus has been on echocardiographic diagnosis of mitral valve prolapse and indicators for surgical referral [88, 127]. Carpentier in his seminal paper titled the "French Correction", reported the first series of patients in whom repair of anterior and posterior leaflet prolapse was performed [7]. In the subsequent decades, the Carpentier procedures became standardized techniques for mitral valve repair for degenerative lesions. Though prolapsing mitral valves are routinely corrected today using the 'standardized procedures', differentiation of the degenerative lesion and optimizing the surgical procedure for that lesion are generally less emphasized. Falk in a recent

clinical study compared the use of PTFE suture loops to leaflet resection for posterior leaflet prolapse in fibroelastic deficient lesion, and reported better outcomes with neochordoplasty than resection due to the absence of leaflet distension in these valves [96]. Data from this study clearly illustrates that even though leaflet resection may be the "standard" technique to correct leaflet prolapse, it should not be the procedure adopted in all patients with leaflet prolapse. Flameng et al. also reported a retrospective study on the durability of mitral valve repair for Barlow's disease and fibroelastic deficiency, and observed that 33.1% of the patients had recurrent mitral regurgitation at 10 years after surgery [10]. These studies strengthen the hypothesis that choice of surgical repair should be governed by the lesion, and thus emphasizing on the need for controlled experimental data comparing different surgical techniques for a given lesion.

7.2.2 VALIDATION OF THE IN VITRO POSTERIOR LEAFLET PROLAPSE MODEL

In this study, posterior leaflet prolapse due to acute rupture of the marginal chordae tendineae, as frequently reported in fibroelastic deficient mitral valves, was simulated. Transecting two pairs of posterior marginal chordae resulted in prolapse of the free edge of the P2 cusp, which is identical to the type of leaflet prolapse observed in fibroelastic deficient mitral valve patients. 3D echocardiographic images obtained from the in vitro simulator clearly demonstrate the prolapse, and the direct comparison to surgical photograph and echocardiograph are shown in Figure 7-11.

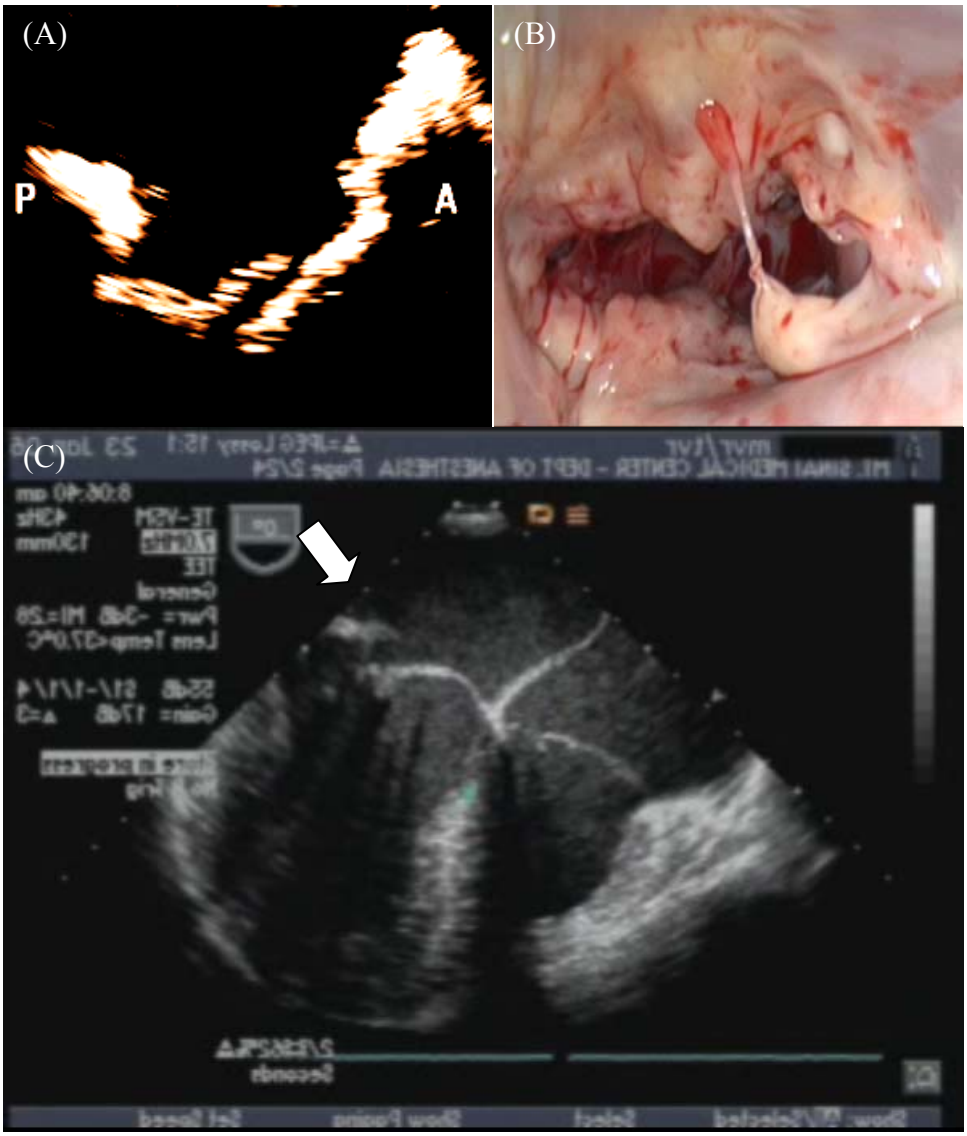

Figure 7-11 (A) A 2D long axis view of the prolapsing posterior leaflet from the in vitro left heart simulator; (B) An intra operative photograph of the mitral valve with the ruptured posterior leaflet chord (Courtesy – David H. Adams, MD, Mt Sinai School of Medicine); (C) An echocardiograph obtained from a patient with fibroelastic deficiency depicting prolapse of the P2 cusp (white arrow), with no billowing of the anterior leaflet of the valve (Courtesy - David H. Adams, MD, Mt Sinai School of Medicine)

An eccentric regurgitation jet going along the anterior leaflet into the left atrium, was recorded on the color Doppler as shown in Figure 7-12, which is identical to the regurgitation jets that are seen clinically in patients with isolated posterior leaflet prolapse, thus confirming the validity of this model.

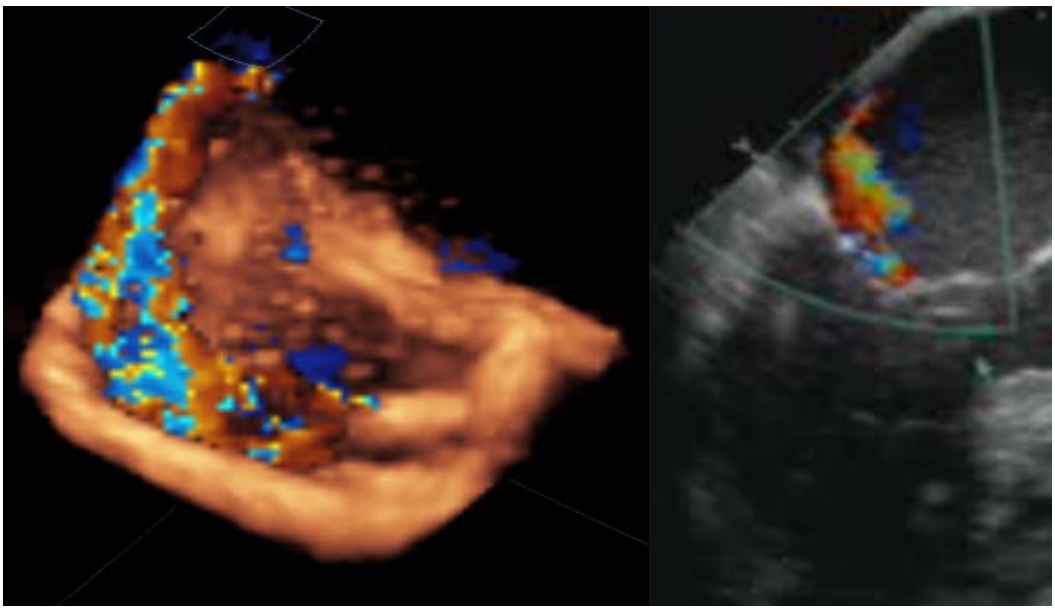

Figure 7-12 (A) 3D color Doppler acquisition of the in vitro valve model depicting the eccentric regurgitation jet riding along the anterior leaflet of the valve; (B) A color Doppler acquisition from a patient with isolated posterior leaflet prolapse, depicting the same eccentric jet as observed in vitro

The three surgical procedures to repair the prolapsing leaflet: neochordoplasty with PTFE sutures; limited triangular resection; and quadrangular resection with annular compression at the P2 cusp were chosen, as they are the most common procedures used in humans. Quadrangular resection with annular plication or compression was proposed by Carpentier for repair of distended valves in Barlow's syndrome[7], triangular resection by Kron for a spectrum of degenerative valve lesions[93] and neochordoplasty by Mohr for isolated chordal rupture[96]. Results from this study demonstrated that for fibroelastic deficient valves, with acute chordal rupture but no leaflet distension, both resective and

non-resective techniques had identical hemodynamic outcomes. However, significant differences in the leaflet motion and kinematics were recorded which may have a detrimental role to play in the durability of the repair.

7.2.3 IMPACT OF SURGICAL REPAIR TYPE ON POST REPAIR VALVE MORPHOLOGY AND FUNCTION

To understand the relevance of each surgical repair to acutely prolapsing valves, it is important to understand the changes that each surgical technique induces on the valve structure. Quadrangular resection with annular plication, is widely used for correction of posterior leaflet prolapse, but was initially proposed by Carpentier [7] for use on severely distended leaflets in which excess tissue needs to be resected to reconstruct a normal valve. Typically applicable for Barlow's valves, this procedure involves removal of the entire P2 cusp and plication of the annulus at this region as shown in Figure 7-13, thus removing the prolapsing segment and also preventing leaflet billowing. However, in fibroelastic deficient valves that do not have any leaflet tension, resecting the P2 cusp using quadrangular resection restricts the mobility of the reconstructed leaflet. This loss in mobility is supported by the data from this study, which can be explained using two mechanisms as depicted in Figure 7-13A-D. Firstly, lack of extra tissue requires forceful closure of the cleft resulting from the P2 resection and induces significant tethering on the suture line. During systolic valve closure, the suture line may tether the commissural cusps inwards towards the P2 cusp and this complex loading may restrict proper leaflet motion. Secondly, with removal of the P2 cusp the secondary chordae on the P2 cusp are relocated to the center of the leaflet to the edge of the suture line. These mechanically

superior strut chordae may restrict leaflet motion, and thus induce abnormal tethering on the center of the leaflet. Therefore, this study puts emphasis on the importance of selecting the appropriate subset of patients with prolapse and distended tissue to adopt this procedure.

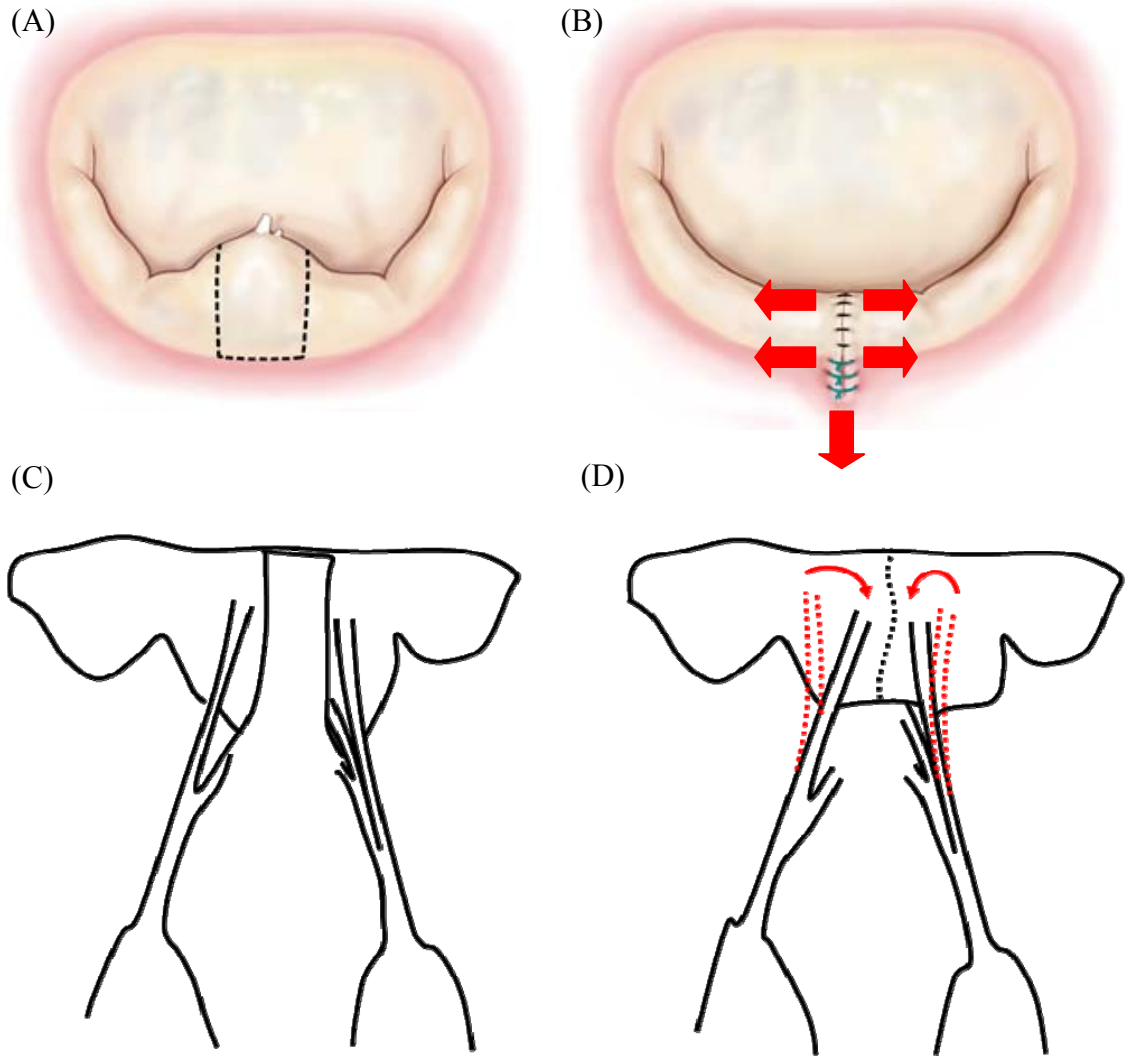

Figure 7-13 (A) Dotted line depicting the region resected from the posterior leaflet using the quadrangular resection procedure; (B) Red arrows depict the forces imposed on the suture line after leaflet reconstruction using sutures; (C) Ventricular view of the valve after removal of the quadrangular section of the leaflet from the P2 cusp, and (D) Relocation of the secondary chordal insertion points after posterior leaflet reconstruction, where the suture line is depicted as the dotted line

Additionally, the P2 segment has the largest area and leaflet height and thus contributes significantly towards achieving a good leaflet coaptation length. Removal of the P2 cusp thus reduces the leaflet area/height available for restoring physiological coaptation length in the fibroelastic deficient valves. In Barlow's syndrome valves, both the leaflet area and leaflet height are significantly increased and quadrangular resection is aimed at reducing redundant leaflet area and also reducing leaflet height to restrict systolic anterior motion of the valve. This aspect of the surgery is often ignored by surgeons, and thus adopted as a "generic prolapse repair" resulting in poor outcomes for the fibroelastic deficient valve lesions [10]. Often, quadrangular resection in non distended leaflets results in a mono-cusp valve with completely restricted posterior leaflet motion and abnormal valve closure.

Limited triangular resection is a conservative tissue resection approach, which may be a good alternative option that significantly reduces the size of resection and eliminates the need for annular plication. Findings from this study indicate that in non-distended leaflets, triangular resection restricts leaflet prolapse and preserves good leaflet coaptation and posterior leaflet mobility. While the outcomes of triangular resection were better than quadrangular, a 2.0 mm reduction in coaptation length and a 2.3mm posterior displacement of the leaflet coaptation were measured in comparison to the control group. Even though mobility in this case is better than that with the quadrangular resection case, this type of resection may induce tension in the free edge of the leaflet as depicted in Figure 7-14. Whether these minor differences between triangular resection and controls have long-term physiological importance should be verified through a randomized

clinical trial. However, this procedure overcomes the two major drawbacks of quadrangular resection and maybe a procedure that should be used more extensively.

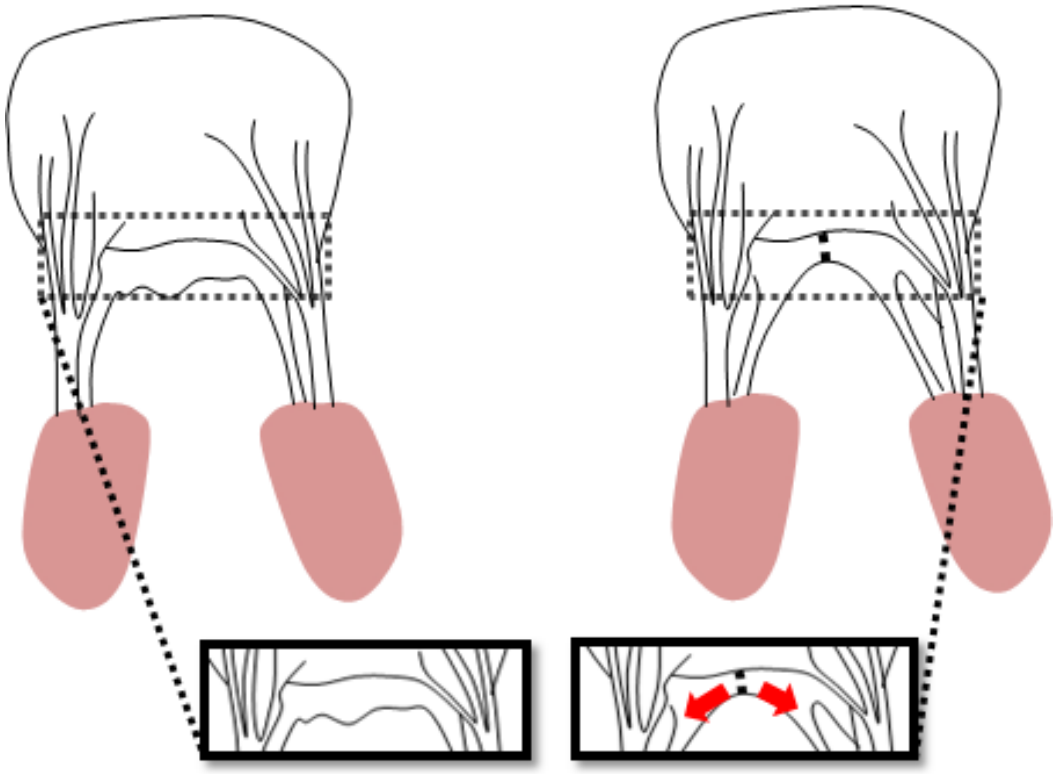

Figure 7-14 Schematic depicting the concept of free edge tethering after triangular resection that may restrict the motion of the posterior leaflet to some extent. The close up images represents schematically the potential mechanism for free edge tethering

In recent years, several surgical centers have reported the use of neochordoplasty for correction of prolapse, and emphasize on the importance of leaflet preservation for better hemodynamics and long term durability [96]. This study confirms that hypothesis, and demonstrates that posterior leaflet mobility and leaflet coaptation length can be restored to physiological levels using this procedure. By replacing the ruptured marginal chordae with PTFE chordae, the native leaflet structure of the chordal insertion regions are not disturbed and thus theoretically the valve function may be restored completely.

Neochordoplasty, as performed in this study seemed to have a benefit over leaflet resection in acute leaflet prolapse without leaflet distension. Replacing the ruptured chordae with a single ePTFE loop not only eliminated regurgitation as efficiently as the standard resection procedures but also restored leaflet coaptation length to physiological levels, with excellent mobility of the posterior leaflet. In this study, each papillary muscle head had two pairs of neochordae; one pair supporting the free edge of the prolapsing segment while the other supporting the segment 1cm laterally away from the free edge. Such a chordal distribution was chosen in this study so that the entire free edge is supported, and localized prolapse in the regions surrounding the neochordae can be eliminated. Though this arrangement resulted in excellent results in this study, it remains unclear if there is an "optimal" positioning of neochordae, other than to avoid crossing native chordae.

7.2.4 CLINICAL IMPLICATIONS

This study demonstrates the importance of tissue preservation over tissue resection to correct acute posterior leaflet prolapse with otherwise normal valve leaflets. The important message of this study is that etiologic classification of mitral valve prolapse is essential for appropriate surgical correction. Thus, the cardiologists when diagnosing mitral valve prolapse should quantify and appropriately describe the nature of prolapse (e.g. leaflet billowing or not, isolated prolapse or prolapse of entire leaflet etc) and provide information that the cardiac surgeon can use to pre-operatively plan the surgery.

7.2.5 LIMITATIONS

Any clinical implications of this study must be stated circumspectly. Firstly, this study represents an acute case of leaflet prolapse due to isolated chordal rupture without any annular or leaflet pathologic change(s). Clearly, mitral valves with normal function and tissue properties were utilized which do not take into account any preexisting patient pathologies (e.g, bacterial endocarditis), which may impact the choice of mitral valve repair. In the chronic state, myxoid changes in the leaflet tissue and distension are observed and complex resection procedures are required in repairing such valves[9]. In this study, the neochordal length was determined with the valve closed, but such an exact measurement is impossible in the clinical setting due to the flaccid heart conditions under which the length is adjusted. One other limitation is the use of the same valve preparation for all experimental groups, which dictated the order of the repair procedures.

7.2.6 SUMMARY

In summary, this study demonstrates that both resective and non-resective repair procedures are effective in eliminating mitral regurgitation due to acute posterior leaflet prolapse. However, conservatively resecting the leaflet without annular procedures or adopting procedures that completely avoid resection appear to improve post-repair valve function and geometry in this experimental model of acute chordal rupture. These findings corroborate recent clinical findings [10, 128, 129], emphasizing the importance of the leaflet preservation concept in mitral valve repair, and warrant caution in irrationally using quadrangular resection to correct non-distended fibroelastic deficient leaflets.

7.2.7 NEOCHORDOPLASTY VERSUS CHORDAL TRANSLOCATION FOR POSTERIOR LEAFLET PROLAPSE

In the previous study comparing resective and non-resective techniques for repair of posterior leaflet prolapse, focus was on comparing leaflet repair techniques to chordal replacement. The results clearly demonstrated that replacement of the ruptured chordae with artificial chordae improved hemodynamic and leaflet kinematic outcomes. Replacement of the chordae, however, is associated with two procedural challenges – [a] access to the papillary muscle tips to insert the neochordae; and [b] determining the length and orientation of the neochordae on a flaccid heart which is on cardiopulmonary bypass. Experienced surgeons have overcome these challenges, and few surgeons have also reported specialized calipers to pre-measure the loop length [130-132].

In this study, an easier method that can simulate the hemodynamic and kinematic outcomes of neochordoplasty was sought. Based on anatomical studies, translocation of the secondary chordae on the posterior leaflet to the prolapsing free edge was hypothesized to be a comparable technique and thus its efficacy was assessed. In the systolic closed position of a normal valve, the offset between the plane of secondary chordal insertion and marginal chordal insertion is small (~3mm). In this study it was hypothesized that translocation of the secondary posterior chordae to the marginal position would restore coaptation as shown in Figure 7-15.

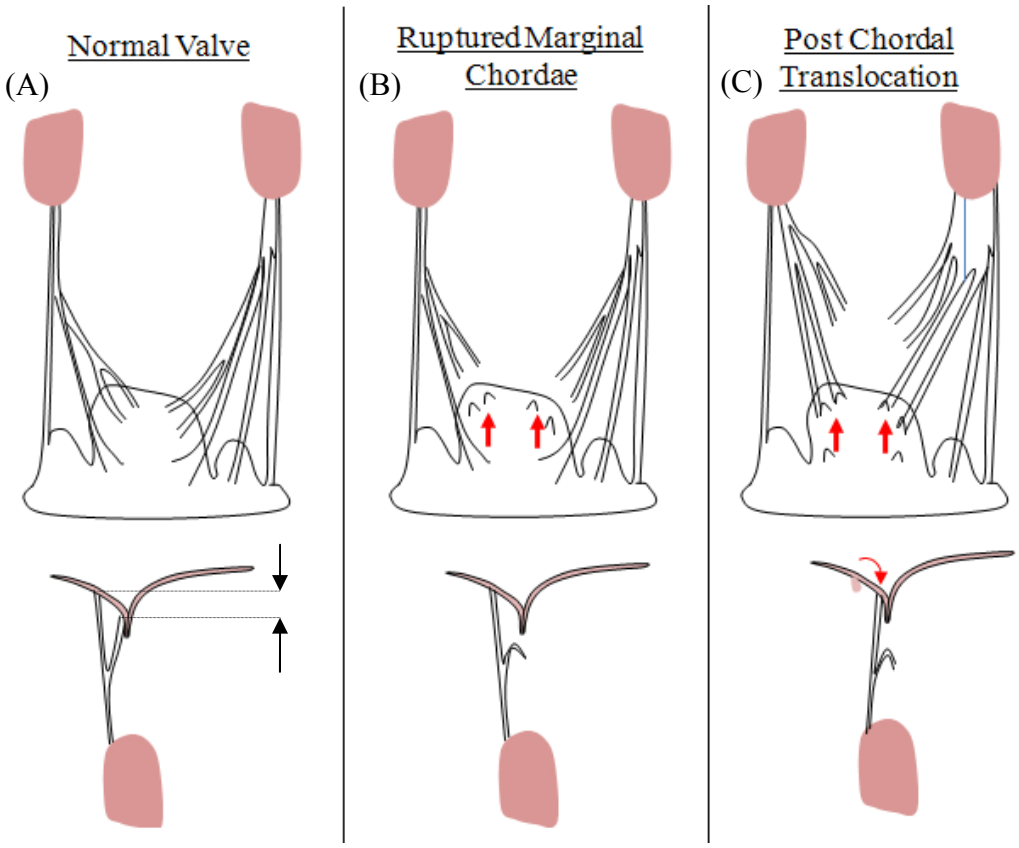

Figure 7-15 (A) Schematic of a normal posterior leaflet with chordal insertions, and the bottom image depicting the offset between the marginal and secondary insertions, (B) Marginal chordal rupture, and (C) Translocated chordae after which a slight basal movement of the coaptation is expected due to the longer length of the secondary chordae than the marginal chordae

Results from this study demonstrate that hemodynamically, chordal translocation was comparable to neochordoplasty. Leaflet coaptation length was comparable to neochordoplasty and control conditions, thus confirming the hypothesis that secondary chordal translocation to the primary/marginal position is a good technique for acute posterior leaflet prolapse. Mobility of the posterior leaflet was preserved as well, but a slight basal motion of the coaptation was observed which is to be expected. The secondary chordae are longer but stiffer than the marginal chordae, which offsets a large basal offset of coaptation. The potential for clinical translation of this procedure is

significant; however variability in the chordal pattern and insertion points between patients should be carefully assessed.

7.2.8 CLINICAL IMPLICATIONS

Chordal translocation to a large extent eliminates the challenges associated with adjustment of neochordae length, or the mismatch in the mechanical properties between artificial ePTFE sutures and native chordae tendineae. Procedural ease of translocation may prove to be an attractive option for clinical use, especially at surgical centers without expertise in heart valve repair.

7.2.9 LIMITATIONS OF THE IN VITRO PROLAPSE MODEL

The in vitro prolapse model mimics the acute setting of isolated posterior leaflet prolapse due to marginal chordal rupture. In human subjects that have fibroelastic deficiency, the prolapsing segment undergoes myxoid changes by the time of surgery resulting in significant thickening. Such thickening or distension of the prolapsing segment was not simulated in this in vitro model, which is a limitation of this study.

7.2.10 SUMMARY

In summary, chordal translocation and neochordoplasty have comparable acute hemodynamic and kinematic outcomes. With chronic clinical data already demonstrating the durability of neochordoplasty, similar results may be expected with chordal translocation as well. However, due attention must be paid to the type of chordal insertion and find appropriate methods to ensure physiological transfer of loads from the chordae to the leaflets after translocation or neochordoplasty.

7.2.11 MECHANICS OF THE CHORDAL INSERTION REGION

Studies from the previous sections clearly demonstrate superior post operative valve hemodynamics with neochordoplasty and chordal translocation. However, an important aspect of these procedures that is often ignored is the method of insertion of the chordae into the leaflet. In current practice, the chordae insert into the leaflet at one focal point or using small loops (~3mm loops) to correct local prolapse, however whether such a design would mimic physiological transfer of loads from the sub-annular components to the leaflets is currently unknown.

This study for the first time provides a detailed understanding of the mechanics of the region of insertion of the thick cylindrical strut chordae into the planar anterior leaflet. Data from this study shows a heterogeneous strain mapping over the insertion region with higher stretching of the tissue along the edges of the insertion zone than the center, as systole progressed. Temporally, as the cardiac cycle progressed from diastole to peak systole there was a gradual increase in stretch across the region, with highest stretch at the left and right edges of the insertion region and the lowest stretch at the basal end of the chordal insertion into the leaflet. The results show that the areal stretch rapidly increases at the apical segments (below horizontal line connecting marker # 15-19) and along the insertion zone edges, while minimal stretch was recorded at the central region around markers 4,10,11,12 during early systole. As systole proceeded, this pattern of stretch remained consistent but with increasingly higher stretch magnitudes at the edges of the insertion zone and a smaller region at the center that remains un-deformed. Examining the mesh deformation during systole it seems that the tissue along the axis of the strut chordae remains un-deformed, but the two edges of the insertion zone on either

sides of this axis undergo significant out of plane deformation. In such a case, if the insertion zone had a uniformly distributed collagen matrix, one would expect that the maximum deformation would be at the central axis, as it acts like a fulcrum to the two bending edges. However, the experimental results show the contrary, with maximum stretch along the edges and very little stretching at the central axis. This not-so-obvious stretch pattern, we believe, is due to the micro structural arrangement of collagen fibers wherein the collagen core from the strut chord splits into two bundles that run along the leaflet boundaries, while the collagen in the interior/central part of the zone was more circumferentially aligned. The observed areal stretch pattern correlated very well with the facts known about the physiological function of the mitral valve, wherein the A2 and A1/A3 cusps move more basally to obtain good valve closure than the region of insertion of the strut chord. This basal cusp motion stretches the tissue increasingly at either edge of the chordal insertion zone than the central region, which is more or less a part of the leaflet already.

The major and minor principal stretch maps also provide interesting insights into the transition of forces and resulting mechanics during valve closure. Initially at end diastole, the chordal insertion region seems to be in equilibrium between the tension from the leaflet and the chordae, evident from the radial orientation of the major principal vectors. At the beginning of valve closure, there were mainly radial stretches because the strut chordae pulled the leaflet relatively uniformly in radial direction as the anterior leaflet moved towards the annulus even if there is not much loading on the leaflet. As the anterior leaflet continued to move to coapt with the posterior leaflet, the ventricular pressure increased and applied load on the leaflets. The anterior leaflet built up surface

tension by stretching itself in all directions against the transvalvular pressure. At the end of valve closure, chordae insertion reached the force equilibrium from tension of leaflet and chordae tension after leaflet coaptation. Though regionally these transitional stretch patterns are sensible, they are highly dependent on the leaflet coaptation as a boundary force condition. These results show a strong coupling between the major and minor principal directions, and the complex biomechanics of the chordal insertion zone.

The results from this study extend the mechanical measurements reported by Chen et al, performed under idealized equi-biaxial loading conditions on porcine anterior mitral leaflets [133]. The novelty of the current study the mechanical behavior of the chordal insertion region is quantified under physiological anatomical and loading conditions. Though the geometric and loading conditions are different in the two studies, the results can be compared to understand the overall trend in the mechanics. Along the radial direction, Chen et al. report a maximum stretch of 35% closer to the leaflet and 20% closer to the strut chord and along the circumferential direction, a maximum stretch of 10% closer to the leaflet and ~17% closer to the strut chord. In this study, the marker array (except for marker # 31) represents the same region of interest as considered by Chen et al, and thus qualitative comparison between the results is justified. The results clearly shows that the average maximum stretch in the radial direction is ~40% near the leaflet and ~30% near the strut chord, thus agreeing with previous results. The average maximum stretch in the circumferential direction is ~45% near the leaflet and ~20% near the strut chord. The higher leaflet deformation in the circumferential direction in this study than the biaxial data could be attributed to the difference in the loading conditions between the two cases. It is worth noting that the static biaxial data does not capture the

heterogeneity in the stretch pattern nor the temporal changes in the stretch, thus limiting the extent to which a quantitative comparison can be performed.

7.2.12 CLINICAL AND BASIC SCIENCE IMPLICATIONS

This study provides detailed insights into the mechanics of the strut chordae insertion region, which are not only interesting from a scientific perspective, but also may have several clinical applications. To date several studies on the biomechanical of the mitral valve structure have been reported, but there is little understanding of the biomechanical events that develop the complex mitral valve structure from the endocardial cushions. It is speculated that the cushion tissue under increasing stretch from the papillary muscles separating from the myocardium clearly delineates the leaflet structure and the chordal structure. Though this hypothesis is yet to be verified, this study provides insights into the mechanics of the complex transition zone where the planar collagenous leaflet morphs into a cylindrical collagenous structure. In the future, this knowledge could help researchers investigate the logical sequence of events that govern the formation of different components of the mitral valve structure. From a clinical perspective, knowledge of the strut chordal insertion region may aid better surgical decision making in using techniques such as chordal cutting, where the strut chordae on the anterior leaflet are severed. Such procedures could potentially alter the local and global valve mechanics, and may have detrimental effects on the durability of the valve repairs. Even though diffusion of basic mechanics knowledge into clinical practice takes significant thrust and time, basic mechanics studies as this one may eventually aid clinical decision making and design of optimal heart valve implants.

7.2.13 LIMITATIONS

Although this study elucidates the complex biomechanics of the chordal insertion region, it has some inherent limitations. In this study we used porcine mitral valves, which may to some extent differ in their structure, function and microstructure from those in humans. However in a previous study we have shown the structural similarity between porcine and human valves, and thus expect the differences to be within reasonable limits. In addition, the ventricular model used in this study does not represent the physiological contractile muscle model in humans and thus may have not completely simulated the loading conditions in the actual human heart. A static planar annulus was used in this study, which does not represent the physiologic saddle shaped, dynamic mitral annulus. The authors acknowledge this limitation and are developing a new annular model to mimic the sphincteric motion and 3-dimensionality of the annulus. The complex collagen fiber distribution and orientation entails investigation of microstructure of the insertion region which is three dimensional. Finally, we assumed the reference image from which the anterior leaflet starts to move to annulus was a strain-free state during valve closure. It is possible that the chordae insertion region may bear some prestretch due to fluid drag forces on the chordae, even before systolic valve closure. This may cause a small error in the stretch measurements. However, given the high reproducibility of the measurements, we believe that this is a reasonable approach.

7.2.14 SUMMARY

In summary this study demonstrates the complex mechanics of the chordal insertion region of the mitral valve and elucidates new findings about the load transfer

between mitral valve components that was previously unknown. These findings may not only be relevant to the design of new repair techniques and percutaneous repair devices that seek to replace or relocate the ruptured chordae, but also have several implications towards understanding the embryonic development of the complex mitral valve structure.

7.2.15 EDGE TO EDGE REPAIR FOR POSTERIOR LEAFLET PROLAPSE

Surgical repair of posterior leaflet prolapse is the current standard of care, but in octogenarians and high surgical risk patients mitral valve repair is still a challenge. Tolerance to cardiopulmonary bypass and immune response after cardiac surgery is poor in these patients. Thus such patients are managed using medical therapy and sometimes rejected surgery [129, 134-139]. To cater to these patients, small incision surgical techniques and endoscopic methods were developed that have been quite successful. Recently with the introduction of transcatheter aortic valves, significant focus is on percutaneous mitral valve repair and valve-in-valve replacement. Established mitral valve surgical techniques, e.g. neochordoplasty, Alfieri stitch procedure etc, are now being adapted into transcatheter versions for use in these high risk patients. The Alfieri stitch or the edge-to-edge repair is one of the first mitral valve repair techniques to be adapted into a percutaneous delivery version, and is now commercially marketed (E-valve, Abbott Laboratories, Boston, MA). Though appealing for its minimally invasive nature, these techniques have demonstrated sub-optimal results in clinical trials due to several reasons. The primary reason for failure is that all mitral valve lesions are multi-dimensional problems, which require repair of the annulus, the leaflets, and sometimes chordal replacement. Mitral annuloplasty is routinely performed in all mitral valve

repairs, and is expected to stabilize the repair and restrict any post-operative annular dilatation and recurrent regurgitation. However, a major drawback of percutaneous mitral valve techniques (leaflet or chordal repair technologies) is that concomitant mitral annuloplasty cannot be performed. Thus, several patients have mild to moderate regurgitation acutely after a percutaneous repair, which gets worse in the long term. Maisano et al. reported sub optimal results in their midterm follow up studies on surgical edge-to-edge repair without annuloplasty [98]. 23% of the patients who underwent edge-to-edge repair for degenerative valve disease had moderate to severe regurgitation within 3.7 years after surgery, and often the associated risk factor was annular calcification or other annular complications. These results clearly indicate that in the absence of an annular ring, mitral valve repair is inadequate and regurgitation recurs in most patients. However, the mechanism for failure of the edge-to-edge repair with annular complications is currently unknown, and is still speculative.

The objective of the current study was to understand the impact of mitral annular dilatation on the hemodynamic outcomes of edge-to-edge repair, and delineate the mechanisms for recurrent of regurgitation. Results from this study demonstrate that at normal annular size, edge-to-edge procedure effectively repairs isolated posterior leaflet prolapse and reduces regurgitation to trace levels. However, with minimal annular dilatation of 15% or 30%, significant regurgitation recurred even though no visible damage at the region of the edge-to-edge stitch was observed. These data confirm the clinical observations reported by Maisano et al, who demonstrated that annular lesions were the primary reason for long term failure of the repair[98].

To understand the mechanisms relevant to (repair) failure, in this study the leaflet coaptation lengths at the central A2-P2 cusps, and the commissural A1-P1 and A3-P3 cusps were measured. With increasing annular dilatation, coaptation significantly decreased at the central and commissural cusps. At the A2-P2 cusps, leaflet coaptation of at least 5mm was always measured because the edge-to-edge stitch was placed at that distance above the leaflet free edge. During systole, the stitch ensured that the leaflet length below the stitch was coapting and thus a minimum coaptation was always measured. Most, clinical studies reported to date on this procedure measured this central coaptation length below the stitch and confirmed that good coaptation is preserved even with annular dilatation. These data are misleading for the aforementioned reasons, and do not explain the recurrence of mitral regurgitation with annular dilatation. Interestingly, in this study we found that commissural cusps typically have higher loss of coaptation due to annular dilatation after edge-to-edge repair. It can be speculated that with posterior displacement of the mitral annulus with annular dilatation, the edge-to-edge stitch tethers the commissural chordae, thus resulting in abnormal leaflet kinematics and regurgitant crevices in the coaptation line. The mechanisms described here are schematically depicted in Figure 7-16.

7.2.16 CLINICAL IMPLICATIONS

These data reveal that edge-to-edge repair though useful in few patient groups, may not be the most appropriate technique in patients with concomitant annular or sub annular lesions other than leaflet prolapse. Specifically, in valves without leaflet distension the impact of annular dilatation on post-repair outcomes may be magnified and

thus judicious patient selection is important. With advancements in percutaneous technologies, it may be useful to use concomitant annuloplasty techniques to perform annular stabilization while performing the edge-to-edge repair.

7.2.17 LIMITATIONS

The foremost limitation of this work is that the studies were conducted on normal mitral valves induced with leaflet prolapse due to chordal rupture. Leaflet billowing was not simulated in these studies, thus limiting the applicability of these results to non-distended fibro elastic deficient valves. Secondly, only one central stitch was studied in this thesis, but clinical practice involves placing multiple stitches laterally along the coaptation zone until regurgitation is significantly reduced. But if multiple stitches created valve stenosis, and if it is clinically advisable to relieve regurgitation but create stenosis needs to be investigated.

7.2.18 SUMMARY

In summary, this study demonstrates that leaflet techniques such as edge-to-edge repair may be effective in eliminating regurgitation only in the absence of other annular, sub annular or chordal lesions. Often patients presenting with mitral valve prolapse have a variety of lesions, and just placing a clip across the two prolapsing leaflets may not be the only solution to this problem.

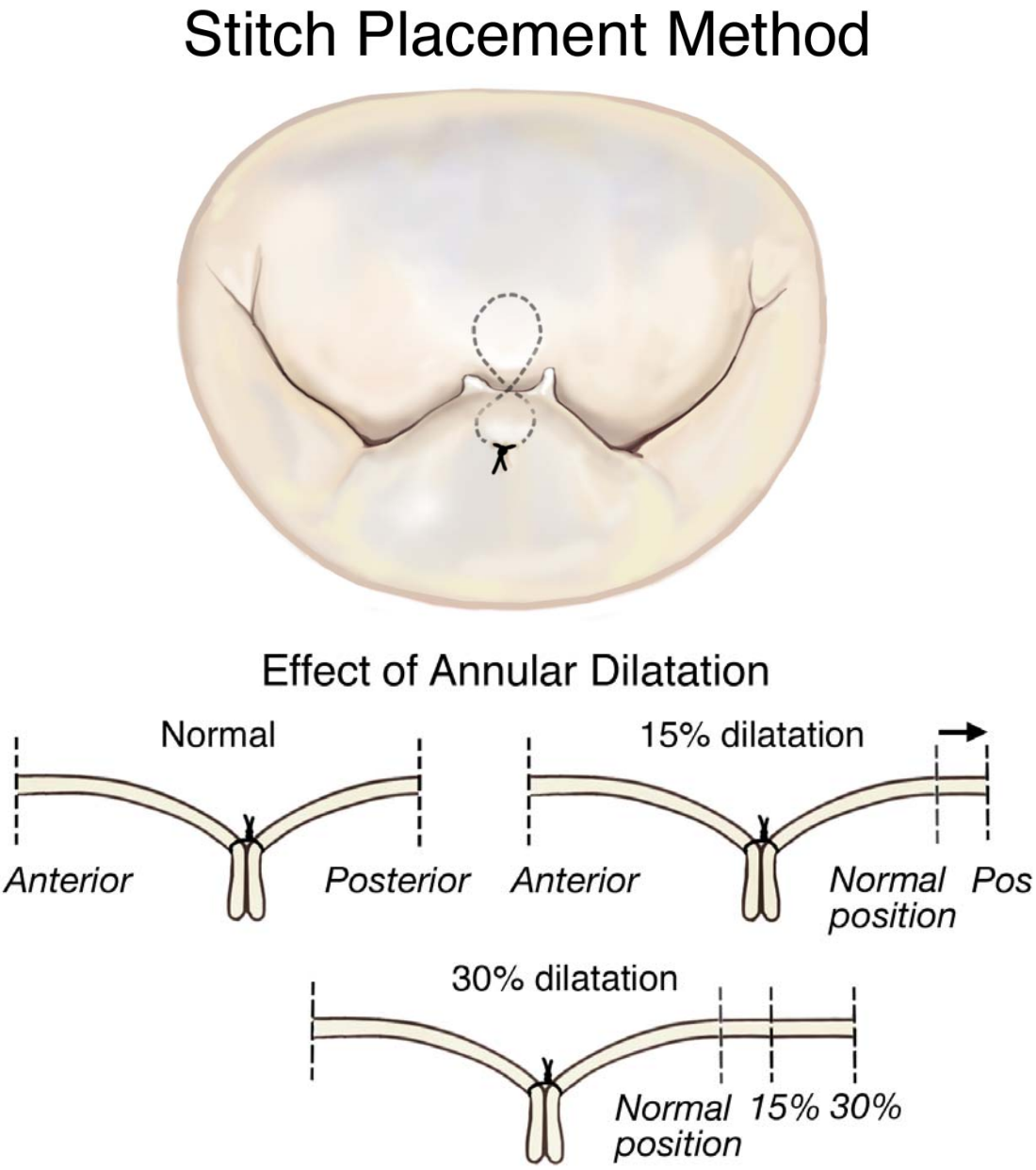

Figure 7-16 (Top) Schematic depicting the stitch placement method, with the red arrows depicting the commissural force tethering on the stitch with annular dilatation; (Below) A cross sectional view of the valve depicting the minimum coaptation length observed even with annular dilatation. Since the edge-to-edge stitch is placed 5mm above the free edge, even with annular dilatation a minimum coaptation length of 5mm is measured

7.2.19 ANNULOPLASTY RING SELECTION – IMPLICATIONS OF FLAT VS. SADDLE SHAPED RINGS ON POSTERIOR LEAFLET MECHANICS

Mitral annular motion and geometric changes have been of immense interest to cardiologists and cardiac surgeons, and repair strategies today are increasingly focusing on restoring the physiological shape of the mitral annulus. The seminal study by Levine et al. [140] has triggered great enthusiasm towards characterizing the mitral annular dynamics, which was subsequently accomplished in animal models and human subjects [17, 141]. However, clinical relevance of this knowledge has not been realized due to the lack of insights into the role of mitral annular saddle on valve function and mechanics. In the past 5 years, few studies have reported a potential impact of mitral annular saddle on leaflet curvature and mechanical strains on the anterior leaflet [50, 117, 142]. These studies laid the foundation on the importance of mitral annular saddle, and in this thesis these studies are extended to the posterior mitral leaflet, which is often the leaflet that is surgically repaired.

Data from this study demonstrate an inverse correlation between the degree of non-planarity of the mitral annulus and the systolic mechanical strain on the P2 segment of the posterior mitral leaflet. As the mitral annular non-planarity increased from 0% → 10% → 20% AHCWR, the peak areal strains reduced significantly. In comparison to the flat annulus (0% AHCWR), a 19.2% and 44.1% reduction in the peak areal strains were measured at 10% and 20% AHCWR, respectively. A similar trend was measured both in the circumferential and radial directions. In the radial direction (from annulus to free edge), the peak strains reduced from the flat annulus by 5.5% with a 10% AHCWR and by 44.4% at 20% AHCWR. Similarly in the circumferential direction (along the leaflet,

parallel to the annulus) a reduction of 20.5% with 10% saddle and 34% with 20% saddle was measured.

The results from this study demonstrate that the saddle shaped mitral annulus provides a mechanical benefit to the valve through a reduction in the leaflet strains. We speculate that the saddle shape of the annulus during systole optimizes force distribution among various mitral valve components, resulting in a minimal energy conformation of the valve. In a previous study from our group, Jimenez et.al, reported that mitral annular saddle optimizes chordal force balance by redistributing the forces between the anterior and posterior leaflets, compared to a flat annulus in which the forces are concentrated on the anterior leaflet [50]. The forces in the commissural chordae reduced by 35% from a flat to 20% saddle annulus, that may have imparted better leaflet motion and curvature during systole. Results from ongoing experiments in our laboratory demonstrate better systolic leaflet coaptation at the P1, P2 and P3 segments with improved leaflet curvature during peak systolic closure. This was also demonstrated in animal studies by Jensen et al. *(Abstract # 14824 presented at AHA Scientific Sessions 2007: Jensen et al: 'Saddle-shaped Mitral Valve Annuloplasty Rings Improve Leaflet Coaptation Geometry)*. The temporal changes in the systolic strains on the P2 segment as recorded in this study, show a distinct difference in the total time of leaflet deformation (time taken by the leaflet to deform back to the reference state) between the three annular shapes. These results lead us to speculate that the increase in mitral leaflet curvature is a visible endpoint of the annular saddle, but a subvalvular force re-distribution is the underlying driver of these changes.

7.2.20 CLINICAL IMPLICATIONS

While the complete story of the mitral annular saddle is yet to be explained, the results from this study have important implications towards current practices in mitral valve reparative therapies. Typically all degenerative mitral valve repairs involve resection of leaflet tissue, and use of sutures to reconstruct the diseased leaflet. The results from this study indicate that restoring the physiological saddle shape or restoring native mitral valve annular dynamics after the repair may reduce the forces on the suture lines and avoid suture dehiscence or tissue tearing in these regions. However, it should be noted that tissue tearing and suture dehiscence can also happen when excessive resection is utilized on fibroelastic deficient valves with only acute chordal rupture and no leaflet distension. Additionally, the spatial heterogeneity in the leaflet ultra-structure and the differences in the composition of the tissue may play an important role in suture dehiscence and thus the physiological and pathological characteristics of valve leaflets should be better understood.

From a biological perspective, reducing the leaflet strains may also decelerate the biological progression of leaflet degeneration after mitral valve surgery. Pedersen et.al recently reported that in canine mitral valves, strain magnitude correlated with over expression of endothelin-1 receptors, which are the key drivers of valve degeneration [92]. Hence, if surgically restoring the saddle shape of the mitral annulus has the ability to reduce leaflet strains; it may potentially inhibit valve degeneration. However, at this time we are unable to comment more on this topic due to lack of human data that replicate the results published in canine mitral valves.

7.2.21 LIMITATIONS

Although the in-vitro model adopted in this study simulates the physiological function, hemodynamics and mechanics of the normal mitral valve, it has some inherent limitations. Firstly, the mitral annulus has a dynamic sphincteric action that changes from a flat annulus during diastole to a saddle annulus during systole. In this study we adopt a static saddle annulus that simulates only the systolic position, which however does not impact the outcomes of this study as our focus is only on the systolic leaflet strains. Secondly, the mitral annulus also has an apical-basal motion, which was not simulated in this model. However, in a previous study from our group, we already demonstrated that such apical-basal motion does not impact the function and mechanics of the valve [48]. Finally, the rigid ventricular chamber used in this study does not mimic the ventricular motion, whose effects on mitral valve function are not studied.

7.2.22 SUMMARY

In conclusion, this study demonstrates that the non-planar saddle shape of the mitral annulus reduces mechanical strains on the clinically important P2 segment of the posterior mitral leaflet. Current strategies for mitral valve repair should acknowledge these native valve biomechanics, as it may have a potentially important role in increasing durability of degenerative mitral valve repair procedures.

7.3 MITRAL VALVE REPAIR FOR FUNCTIONAL MITRAL REGURGITATION

7.3.1 IMPACT OF 3D ANNULAR AND SUB-ANNULAR VALVE GEOMETRY ON THE HEMODYNAMIC EFFICACY OF MITRAL ANNULOPLASTY

This study provides mechanistic insight into the failure of mitral annuloplasty in alleviating IMR based on the left ventricular and sub-annular mitral geometry. Three-dimensional location of the papillary muscles is emphasized as an influential component of mitral valve repair efficacy. Specific 3-dimensional geometric alterations to the mitral valve due to the differences in the size and directionality of ventricular dilatation were modeled in the in-vitro flow simulator. These data were examined to determine which specific distortions render the valve incompetent following annuloplasty, offering an assessment tool as to the benefit of mitral annuloplasty for an individual patient.

Hemodynamic results from this study indicate that mitral annuloplasty reduces IMR effectively in the setting of apical papillary muscle displacement than apical-posterior-lateral papillary muscle displacement. In patients with apical ventricular dilatation due to non-ischemic dilated cardiomyopathy, apically directed forces on the anterior leaflet tether primarily the A2 and P2 cusps of the mitral leaflets. Their tension restricts the degree of anterior and posterior leaflet mobility during systole, thus decreasing the mitral valve coaptation. As the annulus dilates in addition to papillary muscle displacement, the mitral leaflets move further away from each other and with restricted leaflet mobility are unable to coapt. Decrease in the leaflet coaptation length and increase in leaflet tenting may exhaust the excess of leaflet tissue required for

optimal valve closure. True sized annuloplasty reduced the septal-lateral dimension and increased the leaflet area available for coaptation, and as a result the coaptation length was higher and tenting area was reduced, but not comparable to the control groups. However, since no sub-valvular procedures were performed on the valve there was persistent leaflet tethering even after annuloplasty, which manifests as remnant regurgitation in these valves after annuloplasty.

In the case of apical- posterior-lateral papillary muscle displacement due to ischemic dilated cardiomyopathy, MR was severe and annuloplasty left moderate to severe MR in these valves. While the influence of annular dilation is observed to remain comparably the same as that seen in the apically displaced PMs, the chordal tethering forces resulting from the combination of ventricular dilation directionality are distributed over a greater portion of the mitral leaflets. Unlike the apical displacement, significant tethering was measured at the central cusps (A2-P2) and the commissural cusps (A1-P1; A3-P3) as well. The commissural cusps are smaller in height and area compared to the central cusps, and have lesser leaflet area available for coaptation. Since annuloplasty restores physiological dimensions only along the septal-lateral dimension, MR still persists through the commissural cusps of the mitral valve.

In summary, this study demonstrates that sub-valvular geometry of the mitral valve has a significant impact on the outcomes of mitral annuloplasty in alleviating ischemic mitral regurgitation. This study emphasizes the need for a thorough clinical assessment of the patient's valve geometry to define the underlying mechanisms of his/her valvular regurgitation, before referring them to surgery. Improved 3D

echocardiographic imaging techniques and a better understanding of valve anatomy and function should improve surgical decision making and the choice of appropriate repair strategies for a given patient, improving the overall outcomes.

7.3.2 IMPACT OF 3D VALVE GEOMETRY ON SECONDARY CHORDAL CUTTING

Secondary chordal cutting is a surgical procedure that is believed to have the potential to relieve sub-valvular tethering in patients with functional mitral regurgitation (FMR), when used concomitantly with mitral annuloplasty. Current literature on the efficacy of this technique report conflicting outcomes, with Levine et al, championing it, and Miller et al, challenging the procedure. Though data from both the groups provides interesting evidence the reasons for contradictory outcomes still remain elusive. In this study we hypothesize that the variability in the 3D geometry of the mitral valve between patients with FMR, could determine the potential success of secondary chordal cutting. Specifically, we sought to investigate if the differences in the systolic coaptation geometry of the mitral valve, due to variations in the direction of papillary muscle displacement within the ventricle, would impact the success of secondary chordal cutting in reducing FMR.

This study was performed in an *in-vitro* left heart simulator, wherein the geometry of the mitral annulus and the spatial position of the papillary muscles can be precisely altered. Consequently, variations of cardiomyopathic etiologies can be simulated on the mitral valve, e.g. symmetric dilatation of LV in non-ischemic dilated cardiomyopathy or asymmetric dilatation of LV in a posterior-infarct ischemic cardiomyopathy patient. This

in-vitro model is unique in that it allows precise and reproducible papillary alterations which would be difficult to reliably simulate in a large animal model. Additionally control over the size of the mitral valves, hemodynamic conditions, heart rate and ability to reject valves with abnormal anatomies allows for a very well-designed and well-controlled experiment, often difficult to achieve with animal or human studies. Finally, in the *in-vitro* system the regurgitation volume, 3D echocardiographs and videoscopic images of the valve can be simultaneously obtained and the results can be used to provide mechanistic insights.

Results from this study support two main findings: (a) undersizing the mitral annulus does not eliminate FMR in valves with significant sub-annular tethering; and (b) sub-annular geometry, i.e. extent of leaflet tethering and position of papillary muscles, impact the success of sub-valvular repair techniques. Clinical literature already shows that mitral annuloplasty has limited success in patients with dilated ventricles, whether the ring is rigid, semi-rigid or flexible. This study corroborates those clinical findings, and the results clearly show persistent MR even after true-undersizing of the mitral annulus. Though reduction in FMR was observed after annuloplasty, the remnant leakage volume was significant. Extensive leaflet tethering persisted after annuloplasty, and reduction along the septal-lateral length did not enhance leaflet mobility or enable better leaflet coaptation. Failure mechanisms of annuloplasty in this model of FMR can be explained in two ways – firstly, tethering of the anterior leaflet that is not relieved by annuloplasty and thus this procedure should not have any impact on the anterior leaflet mobility or curvature. Secondly, the posterior annulus is moved anteriorly to achieve reduction in septal-lateral dimension, but at the expense of increased leaflet tethering. As

the posterior leaflet moves anteriorly, the distance between the leaflet and the papillary muscle tip (on the outwardly dilating free wall) increases and restricts leaflet motion. Thus, annuloplasty could be morphing a bi-leaflet valve into a uni-leaflet valve and potentially causing mitral stenosis. By the same principles, correction of commissural jets (Carpentier Classification Type IIIB) due to asymmetric papillary muscle tethering may be even more complex.

Secondary chordal cutting is an appealing surgical procedure due to its procedural simplicity and its potential as a percutaneous approach. Theoretically, severing the two strut chordae on the anterior leaflet would significantly relieve anterior leaflet tethering and improve valve competence. However, the results from this study demonstrate that reduction in FMR and improved valve coaptation depend largely upon the 3-dimensional geometry of the valve, i.e. the spatial location of the papillary muscles in the ventricle. When the papillary muscles were displaced apically (only), chordal cutting with concomitant annuloplasty eliminated FMR by achieving a physiological coaptation length and tenting area. Whereas when the papillary muscles were displaced apically-posteriorly-laterally, chordal cutting did not reduce the FMR volume or tenting area and the hemodynamic function of the valve did not improve compared to annuloplasty alone. This discrepancy in outcomes could be elucidated by focusing on the anatomy of the chordae tendineae in relationship to papillary muscle positions. Figure 7-17 demonstrates the chordal geometry of a porcine mitral valve, wherein the thick strut chordae inserts into the middle of the anterior leaflet and a web of marginal chordae branch out of the strut chord and insert at the rough free edge. When the papillary muscles are moved apically alone, the strut chordae experience the largest increase in the force and tether the

leaflet locally at the strut chordal insertion points without a large increase in force on the marginal chordae [49]. Thus the anterior leaflet though tethered locally, still allows the section of the leaflet between the two strut chordae to move during systole (Figure 7-17D). Cutting the two strut chordae in this case can relieve the local tethering at their insertion points and thus restore physiological levels of leaflet coaptation. On the contrary when the papillary muscles were displaced apically-posteriorly-laterally, the entire section of the anterior leaflet between the two strut chordae is tethered and stiffened. The tethering is spread out over this entire region [143], with an equal increase in tethering forces among the strut and marginal chordae. Thus cutting the two strut chordae does relieve the tethering partially, but does not restore physiological mobility or coaptation, as seen in the in vitro study.

7.3.3 CLINICAL IMPLICATIONS

The clinical implications of this study towards improving diagnosis of FMR and in appropriate patient selection for secondary chordal cutting are outlined below. Tenting area, leaflet mobility and leaflet coaptation length are three echocardiographic indices that can be used to predict the outcome of mitral annuloplasty and sub-valvular repair in cardiomyopathy patients. A recent paper on the initial clinical experience of secondary chordal cutting showed improved patient outcomes; however, the authors report that 6-8 chordae were severed until complete valve competence was obtained [144]. Even though surgically this procedure may be appealing, it is worth taking pause considering the abnormal load distribution on the mitral valve that severing several chordae may impose. In a previous study in our laboratory[49], we demonstrated that the systolic chordal

forces are evenly distributed among the chordae tendineae, and thus severing some chordae may impose non-physiological loads on the marginal chordae resulting in their subsequent rupture and potentially leading to leaflet prolapse. Thus, further studies are required to quantify the alterations in valve mechanics after chordal cutting before translation of this technique to clinical use.

7.3.4 LIMITATIONS

The *in-vitro* nature of this work, poses inherent limitations in the direct application of these results to clinical practice. To achieve precise control over the mitral valve geometry and hemodynamic conditions, the atrium and ventricles were designed to be rigid and thus the physiological or pathological ventricular geometries were not simulated in this study. However, it is worth noting that the extent of papillary muscle displacement and the directions of displacement were based on animal and human literature, and thus represent the FMR lesion in humans. A custom annuloplasty ring made of titanium wire and silicone was used in this study which does not represent any specific commercially available annuloplasty ring, but at the same time allows unbiased understanding of the failure mechanisms of annuloplasty in FMR lesions. Finally, due to the unavailability of normal human mitral valves, porcine mitral valves were used in this study, which represent the human mitral valve anatomy very well[63].

7.3.5 SUMMARY

In summary this study demonstrates the need for careful assessment of the pre-operative mitral valve geometry and relating the structure to the valve function. Such information would be essential towards developing a surgical strategy to address different

geometric perturbations of the mitral valve, and improve chronic outcomes of mitral repair for functional mitral regurgitation.

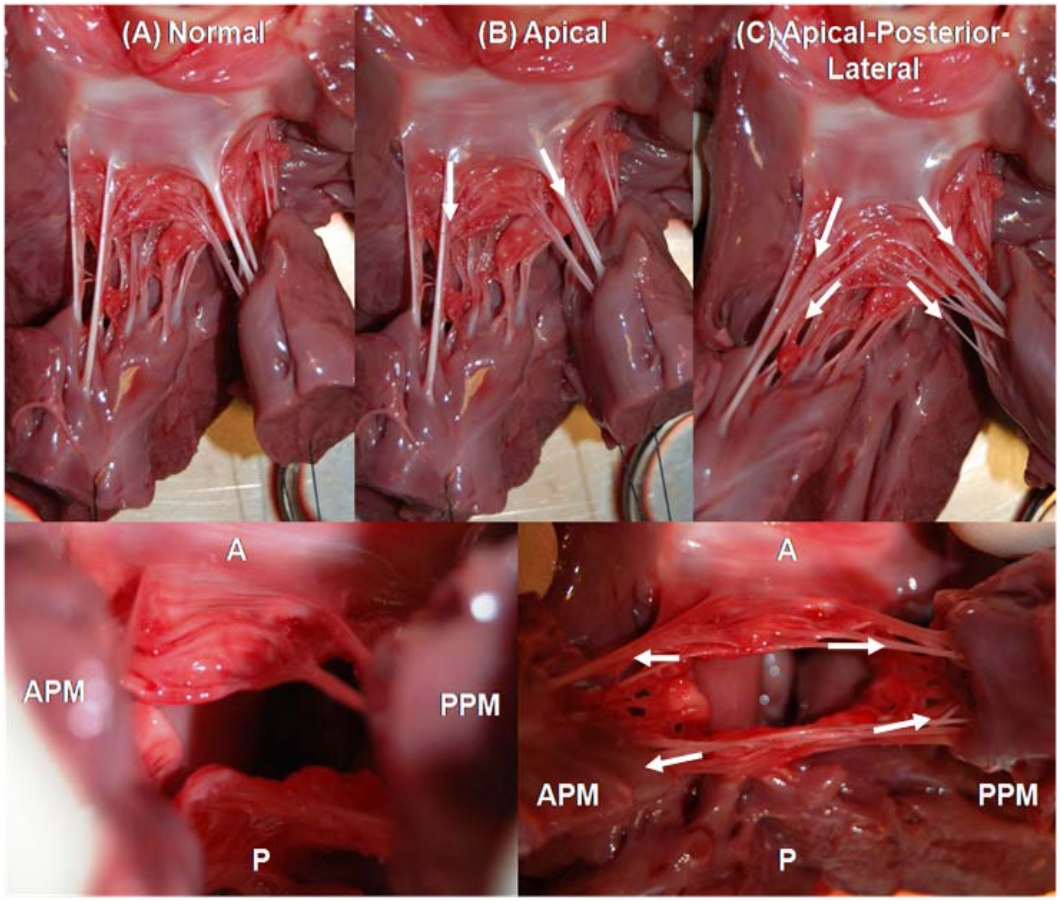

Figure 7-17 (A) Chordal distribution in a normal porcine mitral valve; (B) Localized tethering at the strut chordal insertion region due to apical displacement of the papillary muscles; (C) Increased tethering of both the base of the leaflet and the free edge due to apical, posterior and lateral displacement of the papillary muscles; (D) Short axis view of the anterior and posterior leaflet free edges after apical papillary muscle displacement, depicting minimal tethering of the free edge; (E) Significant tethering of the free edge with additional lateral and posterior displacement of the papillary muscles that would restrict free edge motion and thus reduce coaptation length.

CHAPTER 8

TRANSLATIONAL IMPACT OF CURRENT WORK

The clinical relevance of the work presented in this thesis is significant, for both the cardiac surgical community and medical device industry. In relevance to congenital mitral valve repair, this study clearly demonstrates that the growth of cardiac structures with age renders the mitral valve repair insufficient in the long term. Thus, cardiac surgeons should emphasize on this aspect and seek to develop repair techniques that evolve with the changing cardiac size, or adopt biodegradable technologies that can control the relative rate of growth between the valve and the annulus. One such type of technology that is currently being considered for clinical trials in the United States of America is the Kalangos® biodegradable ring for pediatric valve repair. Adjustable annuloplasty ring systems such as the St Jude Medical Attune® annuloplasty ring, and the Mitral Solutions® adjustable ring system may be relevant in these patients.

The data from this study also emphasizes the etiological classification of degenerative mitral valve lesions, and the importance of tailoring surgical techniques to the individual valve pathology. Focus should shift from using severity of regurgitation as the only diagnostic endpoint for referral to surgery, and move towards a thorough scientific analysis of the valve function under beating heart conditions. Developing

indices that isolate the regions of mitral valve prolapse, methods to correlate the regions of regurgitation with the leaflet kinematics, and planning the optimal surgical technique to correct the exact lesion are required. This thesis provides the hemodynamic and the biomechanics information for each surgical repair, which could be translated to clinical decision making. Additionally, the biomechanics information available from this study may be useful in optimizing annuloplasty ring shape or to develop medical device technologies that are more physiologically appropriate.

Functional mitral regurgitation remains a clinical challenge with sub optimal results in the current era of "modern" cardiac surgery. The most important message of the last specific aim of this thesis is that the pre operative geometry of the mitral valve is the key determinant of acute and chronic surgical outcomes. A proper analysis of the mitral valve geometry, which includes: relative position of the papillary muscles from the mitral annular plane and the tips of the valve leaflets; leaflet kinematics including the motion of the leaflet tips throughout the cardiac cycle; and the overall shape of the leaflets with respect to papillary muscle tip position, is extremely important before attempting surgical correction. Though several annular and sub annular surgical techniques exist in the cardiac surgeons armamentarium, the focus needs to shift from a "one shoe fits all" mitral valve repair strategy to an "individualized surgical planning" paradigm.

CHAPTER 9

CONCLUSIONS

- Morphological, hemodynamic and procedural factors contribute to poor durability of mitral repair, and a sequential investigation into the impact of each of these factors on the repair is important. This thesis for the first time provides insights into the mechanisms leading to failure of current mitral valve repair strategies, and clearly demonstrates the impact of clinical risk factors on the long term outcomes of repair.

- Congenital mitral valve repair should consider the growth of cardiac structure in the post operative period, and thus strategies to either control the growth to desirable levels should be considered, or novel materials or repair techniques that can adapt and still maintain valve competence need to be developed. These concepts also pave the path for replaceable heart valve repair devices that can be adjusted or replaced percutaneously.

- Degenerative mitral valve repair should primarily focus on etiologic classification of the valve lesions, calling for a larger role for the cardiologist to play from diagnosis till surgical decision making. Based on the data from this thesis, a quantitative method to assess leaflet distension and mobility is important to

identify the underlying causes of prolapse and choose the most appropriate surgical repair technique.

- Functional mitral regurgitation manifests with a variety of pathologies and extent of severity in individual patients, and a careful assessment of the pre operative valve geometry may be crucial to develop a surgical strategy that is most optimal for complete elimination of regurgitation in that patient and ensure durable results. A paradigm shift from “one shoe fits all” approach towards an “individualized surgical planning” is necessary for better surgical outcomes in this lesion.

CHAPTER 10

FUTURE DIRECTIONS AND RECOMMENDATIONS

10.1 DYNAMIC LEFT HEART SIMULATOR

Future pulsatile models for the left heart simulator should shift from the current static mitral annulus and papillary muscle model towards mimicking the dynamic annular and sub annular components. Mitral valve geometry and function is largely governed by the transfer of forces between its different components. Thus, an in vitro model that allows for a physiological force balance between its various components under given hemodynamic boundary conditions is necessary.

10.2 IN VITRO ACUTE STUDIES –TO- IN VIVO CHRONIC STUDIES

To translate the knowledge from well controlled bench top experimental models to clinical use, there is a need to translate the acute findings from the in vitro model to chronic durability studies in in vivo chronic disease models. Ingenious methods to develop pathological animal models are necessary, with significant emphasis on developing novel measurements techniques under chronic conditions.

10.3 SURGEON ON A CHIP APPROACH

A paradigm shift from a generic mitral valve repair towards an individualized repair approach is becoming a reality with the advancements in biomedical imaging techniques. Utilizing latest technologies, a virtual geometric modeling approach to pre plan the valve surgery and tailor it to the individual patient is necessary. As depicted in Figure 10-1, the focus should shift from a cardiac surgeon driven operating room towards a multi disciplinary team of engineers and clinicians.

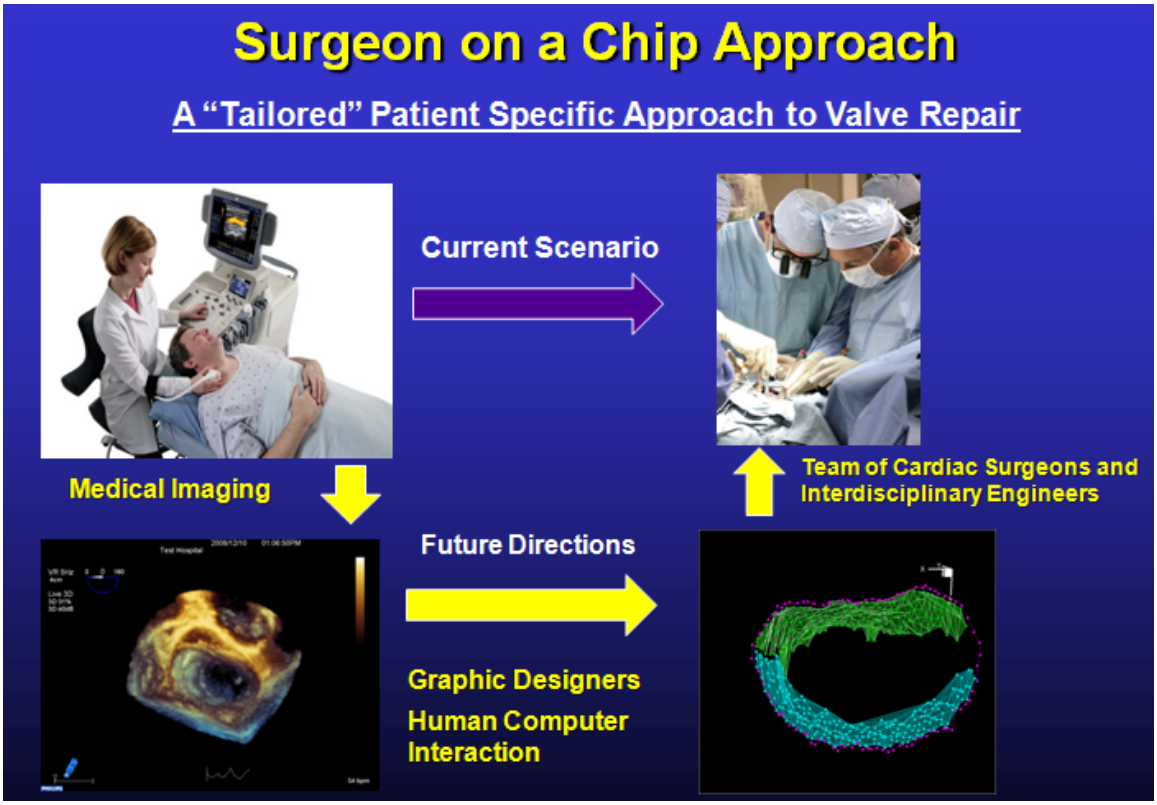

Figure 10-1 Proposed paradigm for "surgeon-on-a-chip" virtual surgical planning approach

APPENDIX # A

HEMODYNAMIC DATA

Table A1.1 – Hemodynamic data for normal and pathological papillary muscle positions

	NORMAL					PM DISP				
Expt Date	**140**	**120**	**100**	**80**	**60**	**140**	**120**	**100**	**80**	**60**
2/1/07										
MR	36.5	32.9	28.3	24.4	19.6	36.5	35.4	29.9	25.6	19.6
SV	20.8	20.9	21	21.1	20.7	20.5	20.2	21.6	19.8	20.5
Absolute	8.2	4.6	0	0	0	8.2	7.1	1.6	0	0
Fraction	28.3	18.0	0	0	0	28.6	26.0	6.9	0	0
2/8/07										
MR	37.7	32.5	28.3	23.6	18.3	35.9	33	27.8	22.5	17.6
SV	20.4	20.6	20.3	20.4	20.4	20.4	20.4	19.9	20.9	20.1
Absolute	9.4	4.2	0	0	0	7.6	4.7	0	0	0
Fraction	31.54	16.935	0	0	0	27.14	18.73	0	0	0
2/13/07										
MR	33.7	24.4	20.8	18.8	16.5	34.6	21.8	18.7	17	15.7
SV	20.9	20.9	20.9	20.9	20.9	22.4	22.5	20.3	20.4	20.6
Absolute	12.9	3.6	0	0	0	13.8	1	0	0	0
Fraction	38.17	14.694	0	0	0	38.12	4.25	0	0	0
2/26/2007										
MR	35.5	26.5	24.7	20.5	18.3	34.9	29.3	23.3	20.2	18.8
SV	20.9	20.9	20.9	20.9	20.9	22.4	22.5	20.3	20.4	20.6
Absolute	10.8	1.8	0	0	0	10.2	4.6	0	0	0
Fraction	34.07	7.9295	0	0	0	31.29	16.97	0	0	0
3/4/2007										
MR	25.5	20.3	18.1	15.2	14	31.7	24.3	19.6	17.9	15.9
SV	20.6	20.3	21	21.2	20.9	20.1	21	20.9	21	19.9
Absolute	7.4	2.2	0	0	0	13.6	6.2	1.5	0	0
Fraction	26.43	9.7778	0	0	0	40.36	22.79	6.7	0	0
3/26/2007										
MR	41.2	32.3	27.8	22.6	20.1	36.4	30	26.3	21.9	19.7
SV	21.5	21.7	20.3	20.9	20.1	22.1	19.8	21.3	19.5	20.7
Absolute	13.4	4.5	0	0	0	8.6	2.2	0	0	0
Fraction	38.4	17.176	0	0	0	28.01	10	0	0	0
3/28/2007										
MR	31.5	26.2	22.2	19.4	18.5	30.9	26.1	23.4	20.4	18.8
SV	20.7	20.2	20.2	20	20.2	20.3	21.4	20.3	19.4	21
Absolute	9.3	4	0	0	0	8.7	3.9	1.2	0	0
Fraction	31	16.529	0	0	0	30	15.42	5.58	0	0

Expt Date	NORMAL 140	120	100	80	60	PM DISP 140	120	100	80	60
3/26/2007										
MR	36.5	33.2	29.8	23.7	20.8	36.3	33.3	31	28.9	27.3
SV	20.3	21.9	21.1	19.6	20.3	19.9	20.1	21.4	21.1	20.5
Absolute	6.7	3.4	0	0	0	6.5	3.5	1.2	0	0
Fraction	24.81	13.439	0	0	0	24.62	14.83	5.31	0	0
3/26/2007										
MR	22.6	18.5	15.1	13	12.6	22.4	20	16.5	16.2	15.4
SV	20.3	20	20.4	21.2	20.7	20.9	20.1	21.1	21	20.5
Absolute	7.5	3.4	0	0	0	7.3	4.9	1.4	1.1	0.3
Fraction	26.98	14.53	0	0	0	25.89	19.6	6.22	4.98	1.44
Mean	33.41	27.422	23.9	20.13	17.63	33.29	28.13	24.1	21.2	18.76
St Dev	5.97	5.64	5.14	3.98	2.771	4.569	5.398	5.1	4.12	3.61
Absolute	9.51	3.52	0	0	0	9.39	4.23	0.77	0.12	0.03
Std Dev	2.41	0.9718	0	0	0	2.652	1.875	0.74	0.37	0.1

Table A1.2 – Hemodynamic data for a completely open cleft using the trifoliate concept

	FULL CLEFT 140	120	100	80	60
2/1/07					
MR	46.3	44.1	42.7	41.6	41
SV	20	20.5	21.4	21.6	21
Absolute	18	15.8	14.4	13.3	12
Fraction	47.368	43.5	40.223	38.1089	37
2/8/07					
MR	40.6	38.8	37.7	36.8	34
SV	19.6	20	20	20.2	20
Absolute	12.3	10.5	9.4	8.5	6
Fraction	38.558	34.4	31.973	29.6167	23
2/13/07					
MR	47.4	44.6	42.4	41.8	40
SV	26.7	18.7	20.1	19.9	20
Absolute	26.6	23.8	21.6	21	19
Fraction	49.906	56	51.799	51.3447	49
2/26/2007					
MR	37	36.6	35.6	35.2	35
SV	20.1	18.7	20.1	19.9	20
Absolute	12.3	11.9	10.9	10.5	10
Fraction	37.963	38.9	35.161	34.5395	34

	FULL CLEFT				
	140	120	100	80	60
3/4/2007					
MR	32.6	32.1	31.6	31	30
SV	19.9	19.5	20.2	20.3	20
Absolute	14.5	14	13.5	12.9	12
Fraction	42.151	41.8	40.059	38.8554	38
3/26/2007					
MR	38	39	37.4	37.3	37
SV	22.5	20.3	20.5	20.6	20
Absolute	10.2	11.2	9.6	9.5	8.7
Fraction	31.193	35.6	31.894	31.5615	30
3/28/2007					
MR	38.8	38.5	38.2	35.8	36
SV	20.5	20.5	21.1	21.1	22
Absolute	16.6	16.3	16	13.6	14
Fraction	44.744	44.3	43.127	39.1931	39
3/26/2007					
MR	37.2	36.3	33.4	32.7	33
SV	21.7	21.1	21.4	21.9	21
Absolute	7.4	6.5	3.6	2.9	3.2
Fraction	25.43	23.6	14.4	11.6935	13
3/26/2007					
MR	29.9	28.5	26.4	20.4	18
SV	20.9	20.7	20.1	19.5	19
Absolute	14.8	13.4	11.3	5.3	2.4
Fraction	41.457	39.3	35.987	21.371	11
Mean	38.644	37.6	36.156	34.7333	34
St Dev	5.6714	5.14	5.1692	6.45	6.8
Absolute	14.744	13.7	12.256	10.8333	9.8
Std Dev	5.4909	4.81	5.0045	5.27091	5.4

Table A1.3 Hemodynamic Data for Different Cleft Closure Lengths

	1/3 SUTURE					2/3 SUTURE					3/3 SUTURE				
	140	120	100	80	60	140	120	100	80	60	140	120	100	80	60
2/1/07															
MR	44.8	44.2	42.4	37.3	30.8	40.8	39.8	34.4	27.7	21.3	34.1	32.9	29.4	24.1	18.4
SV	20.4	19	20.9	21.9	20.6	19.6	21	21.5	20.2	19.8	21.1	21	21.1	20	20.5
Absolute	16.5	15.9	14.1	9	2.5	12.5	11.5	6.1	0	0	5.8	4.6	1.1	0	0
Fraction	44.7	45.56	40.29	29.1	10.8	38.9	35.38	22.101	0	0	21.6	17.97	4.95	0	0
2/8/07															
MR	38.5	37.4	35.2	34	26.8	38.1	35.7	29.8	24.7	19	37.2	34	28.8	23.2	17.9
SV	19.7	20.1	20.5	20.7	20.1	21.3	21	20.6	20.3	20.4	21.3	19.9	21.3	20.1	20.4
Absolute	10.2	9.1	6.9	5.7	0	9.8	7.4	1.5	0	0	8.9	5.7	0.5	0	0
Fraction	34.1	31.16	25.18	21.6	0	31.5	26.06	6.7873	0	0	29.5	22.27	2.29	0	0
2/13/07															
MR	42.9	42.1	40.8	39.3	37.7	42.7	40.6	35.5	28.3	22.9	34.6	32.2	28.1	20.4	17.1
SV	21	20.4	19.4	20.9	21.4	21.1	21	21.4	20.2	19.6	21.2	20.3	20.9	20.4	20.5
Absolute	22.1	21.3	20	18.5	16.9	21.9	19.8	14.7	7.5	2.1	13.8	11.4	7.3	0	0
Fraction	51.3	51.08	50.76	47	44.1	50.9	48.53	40.72	27.076	9.677	39.4	35.96	25.9	0	0
2/26/2007															
MR	37.4	33.6	29.9	27.4	25.1	36.7	29.8	23.2	19.7	17.5	33	26.6	22.6	19.9	17.8
SV	20.2	19.4	21.8	20.5	20.5	21.1	20.7	21	20.9	22	23.8	21.7	20.6	20.7	20.6
Absolute	12.7	8.9	5.2	2.7	0.4	12	5.1	0	0	0	8.3	1.9	0	0	0
Fraction	38.6	31.45	19.26	11.6	1.91	36.3	19.77	0	0	0	25.9	8.051	0	0	0
3/4/2007															
MR	35	33.7	32.8	31.6	24.9	34	28.4	25.8	20.9	17.1	30.3	23.8	20	16.6	14.2
SV	19.5	20.7	21.2	21.3	20.1	20.8	19.2	20	19.4	22.2	21.8	19.8	19.7	20.5	19.7
Absolute	16.9	15.6	14.7	13.5	6.8	15.9	10.3	7.7	2.8	0	12.2	5.7	1.9	0	0
Fraction	46.4	42.98	40.95	38.8	25.3	43.3	34.92	27.798	12.613	0	35.9	22.35	8.8	0	0

	1/3 SUTURE					2/3 SUTURE					3/3 SUTURE				
	140	120	100	80	60	140	120	100	80	60	140	120	100	80	60
3/26/2007															
MR	38.7	37.2	34.8	32.3	28.8	34.6	35.1	29	24.6	22.8	37.4	34.2	29.4	24.6	21.3
SV	19.5	19.7	19.8	20.4	19.9	21.4	20.2	20.9	21.7	23	20.8	21.3	20.7	19.2	20
Absolute	10.9	9.4	7	4.5	1	6.8	7.3	1.2	0	0	9.6	6.4	1.6	0	0
Fraction	35.9	32.3	26.12	18.1	4.78	24.1	26.55	5.4299	0	0	31.6	23.1	7.17	0	0
3/28/2007															
MR	38.8	36.2	34.3	33.1	32.5	35	32.4	32.1	29.8	26.5	32.6	24.8	21.5	19.6	18.5
SV	21.6	20.4	20.7	21.4	21.1	19	20.3	20.8	21.6	21.5	20.9	20.8	22.1	22.5	23.1
Absolute	16.6	14	12.1	10.9	10.3	12.8	10.2	9.9	7.6	4.3	10.4	2.6	0	0	0
Fraction	43.5	40.7	36.89	33.7	32.8	40.3	33.44	32.248	26.027	16.67	33.2	11.11	0	0	0
3/26/2007															
MR	36.2	33.6	31	30.7	29.8	32.2	31.2	30.5	30.4	29.7	32.4	30	30.2	28.3	26.9
SV	20	21.3	20.4	20.7	21.1	21.3	21.1	20.9	21.2	19.7	20.7	21	20.8	21.3	20.2
Absolute	6.4	3.8	1.2	0.9	0	2.4	1.4	0.7	0.6	0	2.6	0.2	0.4	0	
Fraction	24.2	15.14	5.556	4.17	0	10.1	6.222	3.2407	2.7523	0	11.2	0.943	1.89	0	0
3/26/2007															
MR	29.5	26.2	23.5	19.5	17.2	23.8	18.6	15.9	13.9	12.9	22.6	17.7	15.1	13.7	12.6
SV	19.4	19.7	20.7	21	20.3	20.3	20	21.2	21.2	21.3	21.4	21.5	20.1	20.2	19.5
Absolute	14.4	11.1	8.4	4.4	2.1	8.7	3.5	0.8	0	0	7.5	2.6	0	0	0
Fraction	42.6	36.04	28.87	17.3	9.38	30	14.89	3.6364	0	0	26	10.79	0	0	0
Mean	38	36.02	33.86	31.7	28.2	35.3	32.4	28.467	24.444	21.08	32.7	28.47	25	21.2	18.3
St Dev	4.42	5.253	5.66	5.76	5.72	5.47	6.66	6.0914	5.431	5.122	4.41	5.635	5.37	4.43	4.1
Absolute	14.1	12.12	9.956	7.79	4.44	11.4	8.5	4.7333	2.0556	0.711	8.79	4.567	1.42	0	0
Std Dev	4.62	5.14	5.755	5.68	5.83	5.55	5.39	5.1694	3.2439	1.514	3.34	3.289	2.32	0	0

Table A1.4- Effective Orifice Area (EOA) for the Valves under Different Cleft Closure Length and Annular Sizes

	2/3 Cleft Closed - 20% Undersizing	2/3 Cleft Closed- Normal	1/3 Cleft Closed - 40% Undersizing	1/3 Cleft Closed - Normal	Baseline	Full Cleft Closed - Normal
13-Feb	3.162	2.515	4.822	4.368	2.986	4.569
26-Feb	2.282	2.148	2.406	3.606	3.967	2.025
4-Mar	3.133	5.944	2.669	5.349	2.990	3.138
26-Mar	3.074	3.451	1.533	1.532	2.980	3.638
28-Mar	5.225	5.648	5.887	6.773	3.045	4.527
Average	3.375	3.941	3.463	4.326	3.231	3.580
St Dev	1.097	1.762	1.816	1.960	0.491	1.060

Table A2.1 Hemodynamic and Echocardiographic Data for Posterior Leaflet Prolapse and Different Surgical Techniques to Repair Prolapse

28 – Nov - 2008	Control	Prolapse	Neochordae	Triangular Resection	Quadrangular Resection
Regurgitation Volume	26.10	39.80	33.50	28.10	30.70
Stroke Volume	70.50	71.90	71.00	71.10	71.40
Regurgitation Fraction	37.02	55.35	47.18	39.52	43.00
Absolute Fraction	0.00	18.33	10.16	2.50	5.98
Leaflet Coaptation Length	13.00	0.00	13.00	10.10	8.00
Tenting Height	9.00	0.00	10.00	12.00	7.00
Coaptation from Anterior Annulus	19.00	0.00	22.00	21.00	25.50
Coaptation from Posterior Annulus	18.00	0.00	16.00	15.00	11.00
Anterior Angle	25.20	0.00	25.00	24.20	18.80
Posterior Angle	24.80	0.00	34.60	35.80	37.30
21 – Jan - 2008	**Control**	**Prolapse**	**Neochordae**	**Triangular Resection**	**Quadrangular Resection**
Regurgitation Volume	32.80	44.50	31.20	32.80	39.20
Stroke Volume	81.40	81.90	80.20	72.80	77.40
Regurgitation Fraction	40.29	54.33	38.90	45.05	50.65
Absolute Fraction	0.00	14.04	0.00	4.76	10.35
Leaflet Coaptation Length	13.00	0.00	14.00	9.00	8.00
Tenting Height	12.00	0.00	13.00	12.00	14.00
Coapt from Anterior Annulus	21.00	0.00	21.00	21.00	22.00
Coapt from Posterior Annulus	14.00	0.00	16.00	14.00	12.00
Anterior Angle	32.70	0.00	32.90	30.00	29.00
Posterior Angle	41.70	0.00	41.40	40.10	49.50

27-Jan-2008	Control	Prolapse	Neochordae	Triangular Resection	Quadrangular Resection
Regurgitation Volume	25.90	58.40	29.00	25.70	30.10
Stroke Volume	72.60	69.80	74.70	70.60	69.10
Regurgitation Fraction	35.67	83.67	38.82	36.40	43.56
Absolute Fraction	0.00	47.99	3.15	0.73	7.89
Leaflet Coaptation Length	12.00	0.00	13.00	11.00	8.00
Tenting Height	8.00	0.00	7.00	7.00	11.00
Coaptation from Anterior Annulus	23.00	0.00	20.00	25.00	26.00
Coaptation from Posterior Annulus	14.00	0.00	16.00	14.00	7.00
Anterior Angle	25.70	0.00	22.30	18.30	20.00
Posterior Angle	32.20	0.00	29.40	33.10	60.70
28-Jan-2008	**Control**	**Prolapse**	**Neochordae**	**Triangular Resection**	**Quadrangular Resection**
Regurgitation Volume	31.50	36.60	24.60	24.10	28.90
Stroke Volume	71.80	69.60	73.00	70.10	71.40
Regurgitation Fraction	43.87	52.59	33.70	34.38	40.48
Absolute Fraction	0.00	8.71	0.00	0.00	0.00
Leaflet Coaptation Length	13.00	0.00	13.00	11.00	8.00
Tenting Height	10.00	0.00	10.00	12.00	10.00
Coaptation from Anterior Annulus	24.00	0.00	22.00	26.00	27.00
Coaptation from Posterior Annulus	15.00	0.00	17.00	14.00	12.00
Anterior Angle	32.80	0.00	29.80	24.90	25.30
Posterior Angle	38.00	0.00	32.40	36.40	45.40

30 – Jan -2008	Control	Prolapse	Neochordae	Triangular Resection	Quadrangular Resection
Regurgitation Volume	27.9	41.2	24.2	20.7	24.3
Stroke Volume	71.4	72.2	72.1	73.2	74.4
Regurgitation Fraction	39.07563025	57.06371191	33.56449376	28.27868852	32.66129032
Absolute Fraction	0	17.98808166	0	0	0
Leaflet Coaptation Length					
Tenting Height					
Coaptation from Anterior Annulus					
Coaptation from Posterior Annulus					
Anterior Angle					
Posterior Angle					

4-Feb-2008	Control	Prolapse	Neochordae	Triangular Resection	Quadrangular Resection
Regurgitation Volume	22.8	37.4	25	28.6	30.2
Stroke Volume	72.9	73.6	71.6	72.1	74.2
Regurgitation Fraction	31.27572016	50.81521739	34.91620112	39.66712899	40.70080863
Absolute Fraction	0	19.53949723	3.640480953	8.391408823	9.425088461
Leaflet Coaptation Length	10	0	11	9	6
Tenting Height	9	0	9	10	14
Coaptation from Anterior Annulus	20	0	17	20	21
Coaptation from Posterior Annulus	12	0	15	11	10
Anterior Angle	28.8	0	32.2	29	36.5
Posterior Angle	36.8	0	33.9	38.2	53

11-Feb-2008	Control	Prolapse	Neochordae	Triangular Resection	Quadrangular Resection
Regurgitation Volume	28.9	37.4	34.3	32.7	28.3
Stroke Volume	70.3	71.6	74.3	73.1	73.8
Regurgitation Fraction	41.10953058	52.23463687	46.16419919	44.73324213	38.34688347
Absolute Fraction	0	11.12510629	5.054668609	3.623711551	0
Leaflet Coaptation Length	9	0	8	6	6
Tenting Height	9	0	9	10	11
Coaptation from Anterior Annulus	20	0	21	24	21
Coaptation from Posterior Annulus	13	0	13	12	12
Anterior Angle	27.6	0	26.3	32.5	36.1
Posterior Angle	36.9	0	34.9	35.2	43.2
18-Feb-2008	**Control**	**Prolapse**	**Neochordae**	**Triangular Resection**	**Quadrangular Resection**
Regurgitation Volume	23.9	35.6	25.2	24.5	25.3
Stroke Volume	72.3	71.4	74.2	72.9	73.3
Regurgitation Fraction	33.05670816	49.85994398	33.96226415	33.60768176	34.51568895
Absolute Fraction	0	16.80323582	0.905555991	0.550973595	1.458980789
Leaflet Coaptation Length	10	0	11	10	7
Tenting Height	9	0	9	10	11
Coaptation from Anterior Annulus	19	0	17	19	25
Coaptation from Posterior Annulus	13	0	15	12	8
Anterior Angle	34.3	0	30.8	33.9	26.7
Posterior Angle	24.6	0	33.2	43.1	69

Averaged Data	Control	Prolapse	Neochordae	Triangular Resection	Quadrangular Resection
Regurgitation Volume	27.475	41.3625	28.375	27.15	29.625
Stroke Volume	72.9	72.75	73.8875	71.9875	73.125
Regurgitation Fraction	37.67256293	56.98956905	38.40169807	37.70565137	40.48801418
Absolute Fraction	0	19.31700612	2.863693863	2.569257197	4.387034104
St Error (Absolute Fraction)	0	4.306910005	1.247735448	1.03924914	1.592536404
Leaflet Coaptation Length	11.43	0	11.85714286	9.442857143	7.285714286
St Dev (Coaptation Length)	1.488047618	0	1.762708954	1.493198867	0.823754471
Tenting Height	9.428571429	0	9.571428571	10.42857143	11.14285714
St Dev (Tenting Height)	1.272418021	0	1.812653934	1.812653934	2.410295378
Coaptation from Anterior Annulus	20.85714286	0	20	22.28571429	23.92857143
St Dev (Coaptation from Anterior)	1.951800146	0	2.160246899	2.690370837	2.523697212
Coaptation from Posterior Annulus	14.14285714	0	15.42857143	13.14285714	10.28571429
St Dev (Coaptation from Posterior)	1.951800146	0	1.272418021	1.463850109	2.058663459
Anterior Angle	29.58571429	0	28.47142857	27.54285714	27.48571429
St Dev (Anterior Angle)	3.677602739	0	3.990703483	5.427355754	7.007478998
Posterior Angle	33.57142857	0	34.25714286	37.41428571	51.15714286
St Dev (Posterior Angle)	6.664511556	0	3.647765134	3.349342508	10.83249081

Table A2.2 Areal stretch at each marker on the chordal insertion region

Time	Marker 1	Marker 2	Marker 3	Marker 4	Marker 5
0	1	1	1	1	1
0.012	1.022690969	1.012026596	1.005461997	1.003604082	1.005541328
0.024	1.048465522	1.026272234	1.012500427	1.007944172	1.011556006
0.036	1.073835377	1.040351443	1.020377061	1.012972352	1.017826821
0.048	1.094212767	1.050864064	1.027470936	1.018600908	1.024209621
0.06	1.106593337	1.056087217	1.032494273	1.024549136	1.030479973
0.072	1.110613121	1.057194056	1.035615422	1.030354444	1.03603727
0.084	1.107909603	1.056700878	1.037997932	1.035914248	1.040422758
0.096	1.102773599	1.056853608	1.040653868	1.041812287	1.044185863
0.108	1.10220691	1.059266637	1.044010775	1.048770119	1.048707306
0.12	1.112134865	1.06482843	1.048232953	1.057038308	1.055440486
0.132	1.134948355	1.073951009	1.05358403	1.066469005	1.065650226
0.144	1.170633454	1.086905862	1.0602132	1.076440052	1.079813882
0.156	1.217224075	1.103387306	1.067567113	1.085569884	1.096679377
0.168	1.269447705	1.121778619	1.074593889	1.092558893	1.113966658
0.18	1.318395978	1.139543928	1.081069015	1.097519811	1.129814331
0.192	1.3558006	1.154953873	1.088029376	1.101549688	1.142537905
0.204	1.379741259	1.168270976	1.096245587	1.104800196	1.149784081
0.216	1.394224406	1.180685682	1.104974707	1.105907709	1.149271327
0.228	1.403865831	1.192449317	1.112627005	1.103623095	1.1407094
0.24	1.413796743	1.20322926	1.118058488	1.097938829	1.126100407
0.252	1.435251951	1.213836379	1.121003808	1.089605376	1.108054627
0.264	1.478309816	1.225392334	1.121778098	1.080030015	1.089239574
0.276	1.532719485	1.235902566	1.120497903	1.071430139	1.073207646
0.288	1.576375332	1.239993977	1.116345709	1.06591233	1.064074099
0.3	1.597824651	1.234067748	1.108154754	1.064190691	1.064599253
0.312	1.599605503	1.220062603	1.096078012	1.065291503	1.074497913
0.324	1.587759265	1.203809108	1.082482039	1.067488685	1.090793124
0.336	1.566137777	1.191521892	1.071041458	1.069601101	1.109752903
0.348	1.538295002	1.186847054	1.064547932	1.071504148	1.127954435
0.36	1.507282746	1.188384812	1.063069956	1.073426413	1.141601523
0.372	1.470404292	1.18915719	1.064114168	1.074744805	1.146099333
0.384	1.417442711	1.179958684	1.064249367	1.073273981	1.137388015
0.396	1.338853906	1.15489309	1.060338268	1.065858614	1.1141117
0.408	1.2361894	1.115402048	1.050634791	1.050713008	1.079222714
0.42	1.124748101	1.07105892	1.036682344	1.029935695	1.040061657
0.432	1.027293722	1.035855196	1.023977097	1.009593383	1.006340469
0.444	0.960966578	1.018115901	1.01794103	0.996540977	0.986060623

Time	Marker 1	Marker 2	Marker 3	Marker 4	Marker 5
0.456	0.926677429	1.013652074	1.018255187	0.993332311	0.980632624
0.468	0.915399341	1.015119703	1.020952041	0.996967837	0.984844184
0.48	0.919100769	1.019433611	1.02362939	1.003240402	0.99252183

Time	Marker 6	Marker 7	Marker 8	Marker 9	Marker 10
0	1	1	1	1	1
0.012	1.00591	1.01158	0.9991	1.00824	1.00643
0.024	1.01227	1.0203	0.99719	1.01706	1.01314
0.036	1.01889	1.02536	0.99487	1.02556	1.01953
0.048	1.02552	1.027	0.99347	1.03267	1.02498
0.06	1.03158	1.02635	0.99408	1.03778	1.02918
0.072	1.03605	1.02552	0.99686	1.04103	1.03233
0.084	1.03841	1.02777	1.00123	1.04329	1.03522
0.096	1.03982	1.03613	1.00685	1.04613	1.03905
0.108	1.04276	1.05099	1.01443	1.05139	1.04504
0.12	1.04963	1.07039	1.02628	1.0605	1.05404
0.132	1.06184	1.09203	1.04643	1.07436	1.06679
0.144	1.07973	1.11459	1.07902	1.09342	1.08377
0.156	1.10276	1.13846	1.12505	1.11709	1.10457
0.168	1.13016	1.1658	1.18114	1.14368	1.12796
0.18	1.16053	1.19826	1.24087	1.17075	1.1523
0.192	1.19001	1.23522	1.29636	1.19556	1.17553
0.204	1.21275	1.27518	1.34138	1.21602	1.19555
0.216	1.22377	1.31541	1.37433	1.23107	1.21068
0.228	1.22182	1.34959	1.39679	1.24018	1.21972
0.24	1.20975	1.37227	1.4103	1.24393	1.2227
0.252	1.19184	1.38278	1.41615	1.24482	1.22101
0.264	1.17178	1.38139	1.41694	1.24561	1.21652
0.276	1.15321	1.36815	1.41446	1.2462	1.21038
0.288	1.14034	1.34719	1.40674	1.24462	1.20315
0.3	1.13642	1.32683	1.39207	1.24052	1.19586
0.312	1.14117	1.31307	1.37234	1.23526	1.18972
0.324	1.15076	1.30483	1.35121	1.22989	1.18516
0.336	1.16085	1.29572	1.33175	1.22455	1.18185
0.348	1.1684	1.27812	1.31549	1.21889	1.17897
0.36	1.17124	1.2456	1.30167	1.21153	1.17456

Time	Marker 6	Marker 7	Marker 8	Marker 9	Marker 10
0.372	1.16773	1.196	1.28368	1.19899	1.16506
0.384	1.1556	1.13757	1.2535	1.17737	1.14736
0.396	1.13266	1.09601	1.2118	1.14682	1.12281
0.408	1.10114	1.07959	1.1665	1.10992	1.09414
0.42	1.06811	1.07183	1.12592	1.07104	1.06433
0.432	1.04233	1.0693	1.09581	1.03881	1.04025
0.444	1.02927	1.0688	1.08179	1.01993	1.02731
0.456	1.02672	1.063	1.08739	1.01371	1.02459
0.468	1.028	1.04713	1.10749	1.01449	1.02687
0.48	1.02819	1.0216	1.13195	1.01746	1.02975

Time	Marker 11	Marker 12	Marker 13	Marker 14	Marker 15
0	1	1	1	1	1
0.012	1.00573	1.00577	1.00604	1.0061	1.00612
0.024	1.01149	1.01137	1.0118	1.01183	1.01177
0.036	1.01692	1.01649	1.01693	1.01682	1.01656
0.048	1.02174	1.02102	1.02133	1.02097	1.0204
0.06	1.02581	1.02498	1.02503	1.02435	1.02344
0.072	1.02922	1.02842	1.02818	1.0272	1.0261
0.084	1.03253	1.03185	1.03134	1.0302	1.02918
0.096	1.03683	1.03635	1.03567	1.0346	1.03395
0.108	1.04326	1.04317	1.04247	1.04169	1.04156
0.12	1.0527	1.05325	1.05278	1.05245	1.0528
0.132	1.06589	1.06743	1.06755	1.06779	1.06854
0.144	1.08337	1.08627	1.0875	1.08846	1.08955
0.156	1.10472	1.10936	1.11234	1.11429	1.11573
0.168	1.12873	1.1355	1.14087	1.14423	1.14599
0.18	1.15389	1.16299	1.17118	1.17635	1.17832
0.192	1.1781	1.18936	1.20033	1.20756	1.20975
0.204	1.19896	1.2118	1.22518	1.2346	1.23733
0.216	1.21443	1.22811	1.24338	1.25515	1.25907
0.228	1.22313	1.23695	1.25361	1.26772	1.27346
0.24	1.22513	1.23851	1.25609	1.27233	1.28016
0.252	1.22191	1.23452	1.25263	1.27071	1.28057
0.264	1.21541	1.22711	1.2455	1.26503	1.27669
0.276	1.20719	1.21803	1.23635	1.25675	1.26969
0.288	1.19855	1.20882	1.22669	1.24701	1.26035

Time	Marker 11	Marker 12	Marker 13	Marker 14	Marker 15
0.3	1.19108	1.20145	1.2186	1.23785	1.25053
0.312	1.18593	1.19716	1.21364	1.23104	1.24227
0.324	1.18283	1.19537	1.21135	1.22642	1.23588
0.336	1.18064	1.19434	1.20993	1.22245	1.23015
0.348	1.17799	1.19216	1.20725	1.21716	1.22325
0.36	1.17284	1.18656	1.2007	1.20809	1.21269
0.372	1.16205	1.1743	1.18674	1.19182	1.19483
0.384	1.14329	1.15317	1.16316	1.16638	1.16773
0.396	1.1188	1.12611	1.13364	1.13608	1.13651
0.408	1.09148	1.09659	1.10232	1.10521	1.10572
0.42	1.06349	1.06684	1.07145	1.07538	1.07629
0.432	1.0408	1.0429	1.04707	1.05216	1.05339
0.444	1.02845	1.02977	1.03392	1.0399	1.04123
0.456	1.02595	1.02691	1.03111	1.03742	1.03876
0.468	1.02834	1.02927	1.0333	1.03936	1.04078
0.48	1.03104	1.03197	1.03556	1.04094	1.04254

Time	Marker 16	Marker 17	Marker 18	Marker 19	Marker 20
0	1	1	1	1	1
0.012	1.00544	1.00624	1.00598	1.00593	1.00595
0.024	1.01071	1.0124	1.01181	1.01165	1.01167
0.036	1.01546	1.01804	1.01709	1.01679	1.01677
0.048	1.01957	1.02283	1.02161	1.02118	1.02111
0.06	1.02308	1.02671	1.02532	1.02484	1.02472
0.072	1.02617	1.02983	1.02843	1.02794	1.02778
0.084	1.02936	1.03287	1.03157	1.03111	1.03093
0.096	1.03368	1.03703	1.0359	1.0355	1.03533
0.108	1.04038	1.04362	1.04265	1.04235	1.04224
0.12	1.0506	1.05364	1.05278	1.05262	1.05262
0.132	1.0656	1.068	1.0672	1.06725	1.06742
0.144	1.08642	1.08734	1.08659	1.08694	1.08738
0.156	1.11289	1.11137	1.11066	1.11142	1.11226
0.168	1.14351	1.13881	1.1382	1.13948	1.14082
0.18	1.17583	1.1677	1.16732	1.1692	1.17111
0.192	1.20657	1.19535	1.19532	1.19779	1.20025
0.204	1.2326	1.21901	1.21938	1.22236	1.22528
0.216	1.25203	1.23674	1.23745	1.24079	1.24409

Time	Marker 16	Marker 17	Marker 18	Marker 19	Marker 20
0.228	1.26395	1.24734	1.24824	1.2518	1.25538
0.24	1.26864	1.25094	1.25181	1.25545	1.25924
0.252	1.26779	1.24924	1.2498	1.2534	1.25733
0.264	1.2636	1.24443	1.24429	1.24776	1.2518
0.276	1.25738	1.23775	1.23669	1.23998	1.24408
0.288	1.24949	1.22984	1.22799	1.23109	1.23516
0.3	1.24099	1.22211	1.21981	1.2228	1.22677
0.312	1.23342	1.21606	1.21365	1.21665	1.22049
0.324	1.22727	1.21177	1.20951	1.21255	1.21627
0.336	1.22196	1.20823	1.20619	1.20924	1.21281
0.348	1.2164	1.20401	1.20215	1.20505	1.20843
0.36	1.20858	1.19694	1.19512	1.19769	1.2008
0.372	1.19468	1.18356	1.18163	1.1837	1.18641
0.384	1.17149	1.16124	1.15923	1.16071	1.16289
0.396	1.14157	1.13279	1.13104	1.13207	1.13373
0.408	1.10899	1.1018	1.10078	1.10161	1.10288
0.42	1.07684	1.07071	1.07067	1.07146	1.07245
0.432	1.0514	1.04585	1.04673	1.04754	1.04838
0.444	1.03779	1.03229	1.03383	1.03465	1.03542
0.456	1.03573	1.02927	1.03122	1.03205	1.03281
0.468	1.03999	1.03155	1.03368	1.03454	1.03531
0.48	1.04515	1.0343	1.03641	1.03724	1.03801

Time	Marker 21	Marker 22	Marker 23	Marker 24	Marker 25
0	1	1	1	1	1
0.012	1.00598	1.00597	1.00595	1.00593	1.00599
0.024	1.0117	1.01169	1.01167	1.01166	1.01178
0.036	1.01681	1.01679	1.01679	1.01682	1.01699
0.048	1.02113	1.0211	1.02112	1.02121	1.02141
0.06	1.02469	1.02464	1.02468	1.02483	1.02505
0.072	1.0277	1.02765	1.0277	1.0279	1.02812
0.084	1.03082	1.03076	1.03082	1.03103	1.03124
0.096	1.03521	1.03515	1.03522	1.03538	1.03559
0.108	1.04212	1.04207	1.04212	1.04219	1.04242
0.12	1.05254	1.05251	1.05251	1.05248	1.05271
0.132	1.06742	1.0674	1.06735	1.0672	1.06741
0.144	1.08752	1.08753	1.08741	1.08714	1.08723

Time	Marker 21	Marker 22	Marker 23	Marker 24	Marker 25
0.156	1.11262	1.11266	1.11245	1.11204	1.11194
0.168	1.14149	1.14157	1.14123	1.14064	1.14028
0.18	1.17212	1.17224	1.17173	1.17091	1.17029
0.192	1.20162	1.20178	1.20105	1.19997	1.19914
0.204	1.22697	1.22719	1.22627	1.22488	1.22392
0.216	1.24609	1.24642	1.24533	1.24362	1.24257
0.228	1.25769	1.2582	1.25701	1.25495	1.25383
0.24	1.26183	1.26255	1.26133	1.25898	1.25777
0.252	1.26018	1.26113	1.25993	1.25735	1.25604
0.264	1.25489	1.25606	1.25494	1.25222	1.2508
0.276	1.24733	1.24871	1.2477	1.24495	1.2434
0.288	1.23845	1.23992	1.23904	1.23637	1.23473
0.3	1.22993	1.23135	1.23054	1.22804	1.22642
0.312	1.2234	1.22462	1.22382	1.22151	1.22003
0.324	1.21888	1.21982	1.21899	1.21688	1.21558
0.336	1.21512	1.21577	1.21493	1.21303	1.21192
0.348	1.21046	1.21086	1.21008	1.20843	1.20743
0.36	1.20258	1.20281	1.20215	1.20083	1.19987
0.372	1.18792	1.18807	1.1876	1.1867	1.1857
0.384	1.1641	1.16422	1.16395	1.16348	1.16248
0.396	1.13468	1.13481	1.13465	1.13442	1.13352
0.408	1.10366	1.10383	1.10366	1.1034	1.1027
0.42	1.07316	1.07337	1.07312	1.07272	1.07221
0.432	1.04906	1.04931	1.04896	1.0484	1.04803
0.444	1.03613	1.03641	1.03597	1.03531	1.035
0.456	1.03355	1.03385	1.0334	1.03274	1.03236
0.468	1.03607	1.03641	1.03604	1.03545	1.03488
0.48	1.03877	1.03917	1.03895	1.0385	1.03767

Time	Marker 26	Marker 27	Marker 28	Marker 29	Marker 30	Marker 31
0	1	1	1	1	1	1
0.012	1.00596	1.00596	1.00596	1.00596	1.00596	1.00596
0.024	1.0117	1.01169	1.0117	1.0117	1.0117	1.0117
0.036	1.01686	1.01683	1.01683	1.01684	1.01684	1.01685
0.048	1.02123	1.02119	1.02119	1.0212	1.0212	1.02122
0.06	1.02485	1.02479	1.02478	1.02479	1.0248	1.02482

Time	Marker 26	Marker 27	Marker 28	Marker 29	Marker 30	Marker 31
0.072	1.0279	1.02784	1.02782	1.02783	1.02785	1.02787
0.084	1.03104	1.03097	1.03095	1.03095	1.03097	1.031
0.096	1.03541	1.03535	1.03533	1.03533	1.03534	1.03537
0.108	1.04227	1.04222	1.04221	1.0422	1.04221	1.04223
0.12	1.0526	1.05257	1.05257	1.05256	1.05256	1.05257
0.132	1.06733	1.06735	1.06736	1.06735	1.06734	1.06734
0.144	1.08722	1.0873	1.08734	1.08733	1.08731	1.08728
0.156	1.11201	1.11217	1.11227	1.11227	1.11223	1.11217
0.168	1.14046	1.14075	1.14091	1.14092	1.14084	1.14075
0.18	1.17062	1.17103	1.17126	1.17127	1.17117	1.17103
0.192	1.19961	1.20015	1.20045	1.20047	1.20033	1.20015
0.204	1.22453	1.22518	1.22553	1.22556	1.22538	1.22516
0.216	1.24329	1.24402	1.24443	1.24447	1.24427	1.244
0.228	1.25464	1.25544	1.25589	1.25595	1.25574	1.25543
0.24	1.25862	1.25947	1.25997	1.26007	1.25984	1.25951
0.252	1.25689	1.25778	1.25833	1.25846	1.25824	1.25788
0.264	1.25159	1.25251	1.2531	1.25326	1.25306	1.25269
0.276	1.2441	1.24503	1.24566	1.24586	1.24568	1.2453
0.288	1.23534	1.23626	1.23691	1.23713	1.23696	1.23659
0.3	1.22696	1.22785	1.22848	1.2287	1.22854	1.22819
0.312	1.22052	1.22138	1.22197	1.22216	1.222	1.22167
0.324	1.21606	1.21688	1.21742	1.21756	1.2174	1.2171
0.336	1.21238	1.21315	1.21364	1.21374	1.21357	1.2133
0.348	1.20786	1.20857	1.20901	1.20909	1.20892	1.20867
0.36	1.20023	1.20087	1.20127	1.20133	1.20117	1.20096
0.372	1.18597	1.18651	1.18686	1.18691	1.18679	1.18663
0.384	1.16263	1.16306	1.16335	1.16341	1.16332	1.16321
0.396	1.13361	1.13394	1.13417	1.13423	1.13417	1.13409
0.408	1.10282	1.10307	1.10325	1.1033	1.10325	1.10318
0.42	1.07239	1.07261	1.07275	1.07279	1.07274	1.07267
0.432	1.0483	1.0485	1.04862	1.04865	1.0486	1.04851
0.444	1.03534	1.03553	1.03564	1.03567	1.03561	1.03551
0.456	1.03275	1.03294	1.03305	1.03308	1.03302	1.03292
0.468	1.0353	1.0355	1.03562	1.03566	1.03561	1.03551
0.48	1.03809	1.0383	1.03843	1.03849	1.03845	1.03836

Table A2.3 Hemodynamic and Echocardiographic data for Edge-to Edge Repair

Expt 1	Control	Prolapse	E2E-Norm	E2E-D1	E2E-D2	E2E-U1	E2E-U2
MR	12.7	19.5	14.9	16.4	17	12.7	12.2
SV	70.6	71.5	71.1	72.2	70.8	67.6	71.2
MRF	17.98867	27.27273	20.9564	22.71468	24.0113	18.78698	17.13483
AMRF	0	9.284059	2.967731	4.726013	6.022631	0.798314	0
LCL	11.3	0	13.5	10.5	10.7	14.3	14.1
Expt 2	**Control**	**Prolapse**	**E2E-Norm**	**E2E-D1**	**E2E-D2**	**E2E-U1**	**E2E-U2**
MR	16.7	24.8	16.8	18	20.3	16.6	14.7
SV	71.5	72.2	71.7	67.6	68.7	73.5	73.8
MRF	23.35664	34.34903	23.43096	26.62722	29.54876	22.58503	19.9187
AMRF	0	10.99239	0.074319	3.270576	6.192119	0	0
LCL	13.1	0	13.4	10.3	10.3	12.6	12.5
Expt 3	**Control**	**Prolapse**	**E2E-Norm**	**E2E-D1**	**E2E-D2**	**E2E-U1**	**E2E-U2**
MR	14.8	25.4	16.7	20.4	21.9	15.1	13.1
SV	72.3	70.5	72.5	70.2	70.5	72.2	72.4
MRF	20.47026	36.02837	23.03448	29.05983	31.06383	20.91413	18.09392
AMRF	0	15.55811	2.56422	8.589566	10.59357	0.443865	0
LCL	13.8	0	13.3	12.1	12	13.3	13.8
Expt 4	**Control**	**Prolapse**	**E2E-Norm**	**E2E-D1**	**E2E-D2**	**E2E-U1**	**E2E-U2**
MR	11.7	14.6	13.2	14.6	17.9	12.8	11.2
SV	72.5	68.8	71.6	72.2	68.5	73.1	72.1
MRF	16.13793	21.22093	18.43575	20.22161	26.13139	17.51026	15.53398
AMRF	0	5.082999	2.297823	4.083676	9.993456	1.372329	0
LCL	13	0	11.2	9.3	8.7	10.3	12.4

Expt 5	Control	Prolapse	E2E-Norm	E2E-D1	E2E-D2	E2E-U1	E2E-U2
MR	19.2	32.1	20.8	22.7	23	19.7	18.9
SV	67.8	72.5	71.6	70.7	69.9	71.8	71.6
MRF	28.3185	44.2758	29.0502	32.1075	32.9041	27.4373	26.3966
AMRF	0	15.9572	0.73169	3.78891	4.58556	0	0
LCL	11.1	0	11	10.5	9.2	11.3	11.9
Expt 6	**Control**	**Prolapse**	**E2E-Norm**	**E2E-D1**	**E2E-D2**	**E2E-U1**	**E2E-U2**
MR	14.5	28.2	14.9	25.6	25.6	11.9	3.6
SV	68.9	67.9	71.7	71.3	68.2	70.2	68.6
MRF	21.0449	41.5316	20.7810	35.9046	37.5366	16.9515	5.24781
AMRF	0	20.4866	0	14.8596	16.4916	0	0
LCL	9.6	0	8.3	7.5	6.4	9.1	9.9
Expt 7	**Control**	**Prolapse**	**E2E-Norm**	**E2E-D1**	**E2E-D2**	**E2E-U1**	**E2E-U2**
MR	21.8	27.9	23.4	25.3	25.4	23.3	22.3
SV	69.7	73.1	71.7	68.1	68	68.1	70.4
MRF	31.2769	38.1668	32.6359	37.1512	37.3529	34.2143	31.6761
AMRF	0	6.88999	1.35908	5.87434	6.07604	2.93749	0.39923
LCL	10.6	0	9.54	9.48	9.03	11.8	11.9
Average	**Control**	**Prolapse**	**E2E-Norm**	**E2E-D1**	**E2E-D2**	**E2E-U1**	**E2E-U2**
MR	15.9142	24.6428	17.2428	20.4285	21.5857	16.0142	13.7142
SV	70.4714	70.9285	71.7	70.3285	69.2285	70.9285	71.4428
MRF	22.6562	34.6922	24.0464	29.1123	31.2212	22.6285	19.1431
AMRF	0	12.0359	1.42783	6.45610	8.56500	0.79314	0.05703
LCL	11.7857	0	11.4628	9.95428	9.47571	11.8142	12.4333
STD MRF	0	5.51790	1.20965	4.11081	4.14553	1.07571	0.15089
STDE LCL	1.53560	0	2.07922	1.41571	1.89335	1.92976	1.50687

Table A2.4 Areal Stretch Data for a 0% saddle annulus

Time	27-Mar-07	30-Mar-07	3-Apr-07	10-Apr-07	21-Jun-07	28-Jun-07	26-Sep-07	19-Oct-07
0.004	1.230099	1.035085	0.998796	1.005598	0.99787	1.000661	0.999373	1.052381
0.008	1.241411	1.063456	0.999731	1.012066	1.002636	1.000645	1.00583	1.078782
0.012	1.252885	1.106985	1.003853	1.019926	1.008469	1.000839	1.012883	1.116989
0.016	1.264509	1.165814	1.012536	1.02928	1.015364	1.001284	1.020478	1.166482
0.02	1.276268	1.237801	1.026717	1.040194	1.023198	1.002	1.028842	1.225736
0.024	1.288148	1.318824	1.046652	1.052609	1.031695	1.002972	1.038512	1.292467
0.028	1.300132	1.403547	1.071834	1.066255	1.040427	1.004143	1.050282	1.363966
0.032	1.312205	1.486336	1.101094	1.080601	1.048849	1.005426	1.065057	1.437435
0.036	1.32435	1.562091	1.132832	1.094892	1.056393	1.006714	1.083669	1.510243
0.04	1.336549	1.626856	1.165292	1.108248	1.062605	1.007911	1.106691	1.580024
0.044	1.348786	1.678188	1.196825	1.119821	1.067306	1.008966	1.134345	1.644674
0.048	1.36104	1.715302	1.226094	1.128993	1.070733	1.009899	1.166495	1.702355
0.052	1.373295	1.738995	1.252212	1.135561	1.073638	1.010806	1.202738	1.751612
0.056	1.38553	1.751356	1.27479	1.139876	1.077279	1.011859	1.242501	1.791578
0.06	1.397727	1.755274	1.293919	1.142897	1.083323	1.013271	1.285104	1.822127
0.064	1.409865	1.753866	1.310065	1.146117	1.093634	1.015271	1.329753	1.843797
0.068	1.421925	1.749953	1.323921	1.151382	1.109981	1.018084	1.37552	1.857482
0.072	1.433886	1.745729	1.336239	1.160619	1.133711	1.021927	1.421353	1.864042
0.076	1.445727	1.742636	1.34768	1.175537	1.165442	1.027032	1.46614	1.864071
0.08	1.45743	1.741438	1.35872	1.19735	1.204845	1.03368	1.508825	1.857953
0.084	1.468972	1.742401	1.369603	1.226564	1.250564	1.042228	1.548492	1.846129
0.088	1.480334	1.745512	1.380361	1.262884	1.300336	1.053114	1.584412	1.829365
0.092	1.491496	1.75065	1.390854	1.305227	1.3513	1.066818	1.616038	1.80886
0.096	1.502437	1.757676	1.400836	1.351858	1.40047	1.083792	1.642997	1.786152
0.1	1.513137	1.766429	1.410004	1.400584	1.445243	1.104358	1.665116	1.762879
0.104	1.523576	1.776654	1.418046	1.448947	1.483831	1.128606	1.682478	1.740532
0.108	1.533735	1.787907	1.424671	1.494402	1.515471	1.156337	1.695464	1.720291
0.112	1.543596	1.799517	1.429622	1.53448	1.540387	1.187055	1.704741	1.702957
0.116	1.553139	1.810615	1.432701	1.566994	1.559548	1.220033	1.71116	1.688971
0.12	1.562346	1.820263	1.433777	1.590299	1.574333	1.254406	1.715618	1.678495
0.124	1.571201	1.827606	1.432807	1.603534	1.586223	1.289296	1.718912	1.671503
0.128	1.579685	1.832018	1.429853	1.606765	1.596576	1.323894	1.721659	1.667881
0.132	1.587782	1.833188	1.425085	1.600893	1.606491	1.35752	1.724274	1.667484
0.136	1.595477	1.831143	1.418776	1.587356	1.616724	1.389633	1.726997	1.670147
0.14	1.602756	1.826214	1.41128	1.567734	1.627645	1.419808	1.729934	1.675636
0.144	1.609603	1.818947	1.402992	1.54343	1.639247	1.447707	1.733071	1.683585
0.148	1.616006	1.810003	1.394306	1.515565	1.651212	1.473051	1.736265	1.693459

Time	27-Mar-07	30-Mar-07	3-Apr-07	10-Apr-07	21-Jun-07	28-Jun-07	26-Sep-07	19-Oct-07
0.156	1.627431	1.789618	1.377051	1.452883	1.674327	1.515156	1.741581	1.716224
0.16	1.63243	1.779138	1.368923	1.420117	1.684744	1.531586	1.742886	1.727765
0.164	1.636942	1.768803	1.361262	1.388089	1.694299	1.544848	1.742868	1.738817
0.168	1.640956	1.758636	1.354063	1.358213	1.70321	1.555012	1.741545	1.749324
0.172	1.644467	1.748501	1.347267	1.3318	1.711787	1.562282	1.73927	1.759535
0.176	1.647467	1.738151	1.340798	1.309857	1.720264	1.566987	1.736631	1.769893
0.18	1.649951	1.72726	1.334594	1.292943	1.728655	1.569566	1.734201	1.780837
0.184	1.651916	1.715443	1.328635	1.281128	1.736681	1.570526	1.732283	1.792604
0.188	1.653358	1.70227	1.322957	1.274032	1.743811	1.570396	1.730768	1.805101
0.192	1.654274	1.687287	1.317643	1.270936	1.749368	1.569677	1.729194	1.817907
0.196	1.654665	1.670037	1.3128	1.270917	1.75268	1.568795	1.726959	1.830396
0.2	1.654531	1.650123	1.308522	1.272984	1.753235	1.568075	1.723571	1.841957
0.204	1.653873	1.627265	1.304846	1.276199	1.750768	1.567729	1.71885	1.852226
0.208	1.652693	1.601377	1.301709	1.27976	1.74531	1.567853	1.712985	1.861225
0.212	1.650996	1.572593	1.298917	1.283056	1.737162	1.568447	1.706474	1.869339
0.216	1.648786	1.541258	1.296137	1.28568	1.726834	1.569424	1.699985	1.877096
0.22	1.64607	1.507862	1.2929	1.287425	1.714964	1.570628	1.694162	1.884795
0.224	1.642853	1.472944	1.288633	1.288273	1.702246	1.57185	1.689438	1.892049
0.228	1.639145	1.436994	1.282708	1.288378	1.689371	1.572838	1.685872	1.89741
0.232	1.634954	1.400398	1.274503	1.288064	1.67698	1.57332	1.683057	1.89821
0.236	1.63029	1.363428	1.263475	1.287791	1.665636	1.573029	1.680147	1.890743
0.24	1.625165	1.326276	1.249237	1.288123	1.655779	1.57173	1.676058	1.87082
0.244	1.619589	1.289123	1.231627	1.289668	1.647704	1.569254	1.669834	1.83464
0.248	1.613577	1.252189	1.21076	1.29301	1.641508	1.565501	1.661066	1.779747
0.252	1.60714	1.215753	1.187053	1.298646	1.637074	1.560467	1.650151	1.705821
0.256	1.600294	1.18013	1.161214	1.306927	1.634036	1.554215	1.638189	1.615061
0.26	1.593055	1.145608	1.134188	1.31801	1.631816	1.546867	1.626398	1.512005
0.264	1.585437	1.112377	1.107072	1.331833	1.629669	1.538579	1.615271	1.402831
0.268	1.577456	1.08047	1.081013	1.348126	1.626779	1.529517	1.603907	1.294327
0.272	1.569131	1.04975	1.0571	1.36647	1.622363	1.519836	1.589957	1.192809
0.276	1.560479	1.019951	1.036262	1.386388	1.615783	1.509661	1.570257	1.103271
0.28	1.551517	0.990763	1.019198	1.407443	1.606625	1.499064	1.541828	1.0289
0.284	1.542264	0.961952	1.006333	1.429295	1.594719	1.48804	1.502778	0.970993
0.288	1.532739	0.961952	0.997799	1.451683	1.580109	1.476479	1.452774	0.970993
0.292	1.522961	0.961952	0.993452	1.474326	1.562965	1.464134	1.393166	0.970993
0.296	1.512949	0.961952	0.9929	1.496773	1.54346	1.450602	1.32697	0.970993
0.3	1.502723	0.961952	0.995551	1.518239	1.521658	1.435322	1.258777	0.970993
0.304	1.492303	0.961952	1.000676	1.537486	1.497444	1.417601	1.194393	0.970993

Time	27-Mar-07	30-Mar-07	3-Apr-07	10-Apr-07	21-Jun-07	28-Jun-07	26-Sep-07	19-Oct-07
0.308	1.481708	0.961952	1.007469	1.552803	1.470522	1.39669	1.139834	0.970993
0.312	1.470959	0.961952	1.015119	1.562117	1.440515	1.371903	1.099709	0.970993
0.316	1.460074	0.961952	1.022877	1.563247	1.407125	1.34279	1.075626	0.970993
0.32	1.449074	0.961952	1.030117	1.554282	1.370342	1.309316	1.065687	0.970993
0.324	1.437979	0.961952	1.036384	1.534003	1.330607	1.272042	1.065483	0.970993
0.328	1.426807	0.961952	1.036384	1.502253	1.288888	1.232203	1.065483	0.970993
0.332	1.415578	0.961952	1.036384	1.460132	1.246623	1.191661	1.065483	0.970993
0.336	1.404311	0.961952	1.036384	1.409956	1.205527	1.152682	1.065483	0.970993
0.34	1.393024	0.961952	1.036384	1.354939	1.167322	1.117547	1.065483	0.970993
0.344	1.381736	0.961952	1.036384	1.298682	1.133465	1.088107	1.065483	0.970993
0.348	1.370465	0.961952	1.036384	1.244596	1.104948	1.065403	1.065483	0.970993
0.352	1.359227	0.961952	1.036384	1.195416	1.082224	1.049516	1.065483	0.970993
0.356	1.34804	0.961952	1.036384	1.152929	1.065238	1.039684	1.065483	0.970993
0.36	1.336921	0.961952	1.036384	1.117957	1.05354	1.034628	1.065483	0.970993
0.364	1.325884	0.961952	1.036384	1.090533	1.04641	1.03292	1.065483	0.970993

Table A2.5 Areal Stretch Data for a 10% saddle annulus

Time	27-Mar-07	30-Mar-07	3-Apr-07	10-Apr-07	21-Jun-07	28-Jun-07	26-Sep-07	19-Oct-07
0.004	1.138874	1.044533	1.007327	0.999697	0.96301	1.0022	1.002202	1.014456
0.008	1.144466	1.080488	1.006365	0.99334	0.9655	1.003713	0.995288	1.027602
0.012	1.149979	1.132532	1.005669	0.986186	0.974371	1.005694	0.987954	1.047878
0.016	1.155405	1.200705	1.005736	0.979149	0.991811	1.008031	0.980508	1.076244
0.02	1.160739	1.282632	1.007113	0.973345	1.019466	1.010501	0.973263	1.112724
0.024	1.165973	1.373716	1.010297	0.969941	1.058074	1.012776	0.966582	1.156194
0.028	1.171101	1.468008	1.015625	0.969994	1.107255	1.014463	0.960929	1.204391
0.032	1.176116	1.559392	1.023217	0.974307	1.165485	1.015155	0.95692	1.254155
0.036	1.181012	1.642654	1.032968	0.983336	1.230239	1.01451	0.955309	1.30184
0.04	1.185783	1.714125	1.044591	0.99716	1.298249	1.012318	0.95693	1.343816
0.044	1.190424	1.771874	1.057699	1.01552	1.365847	1.00856	0.962575	1.377008
0.048	1.194928	1.815559	1.071886	1.037908	1.42941	1.003435	0.972838	1.39939
0.052	1.19929	1.846081	1.08679	1.06369	1.485857	0.997357	0.98797	1.410348
0.056	1.203506	1.865195	1.102127	1.092223	1.533134	0.990915	1.007774	1.410851
0.06	1.207569	1.875114	1.117698	1.122934	1.57052	0.984817	1.03158	1.403363
0.064	1.211477	1.878176	1.133364	1.15537	1.598626	0.979813	1.05831	1.391472
0.068	1.215223	1.876606	1.149013	1.189186	1.619084	0.97664	1.086643	1.37926
0.072	1.218805	1.872375	1.164531	1.224113	1.634022	0.975969	1.115234	1.37049
0.076	1.222218	1.867136	1.179787	1.25991	1.645531	0.978383	1.142943	1.367794
0.08	1.22546	1.862205	1.194633	1.296333	1.655286	0.984363	1.169014	1.372087
0.088	1.231415	1.85676	1.222559	1.370009	1.673289	1.008368	1.215512	1.396504
0.092	1.234123	1.857093	1.235478	1.406729	1.682113	1.026721	1.236578	1.411306
0.096	1.23665	1.859469	1.247705	1.443003	1.690625	1.049232	1.257008	1.42417
0.1	1.238991	1.863556	1.259338	1.478486	1.69848	1.075581	1.277434	1.43339
0.104	1.241148	1.868837	1.270539	1.512689	1.705333	1.105218	1.298288	1.438509
0.108	1.243117	1.874677	1.28151	1.544903	1.710909	1.137391	1.319655	1.440224
0.112	1.244899	1.880424	1.29247	1.574173	1.715053	1.171206	1.341234	1.440016
0.116	1.246493	1.885484	1.303614	1.599367	1.717713	1.205717	1.362388	1.439691
0.12	1.247899	1.889416	1.315091	1.619335	1.718917	1.240029	1.382312	1.440961
0.124	1.249117	1.891992	1.326973	1.633126	1.718732	1.273377	1.400266	1.44514
0.128	1.250148	1.89322	1.339238	1.640165	1.717253	1.305185	1.415788	1.452959
0.132	1.250993	1.893311	1.351757	1.640363	1.714601	1.335082	1.428822	1.464514
0.136	1.251653	1.892616	1.364303	1.634082	1.710963	1.362876	1.43973	1.479309
0.14	1.25213	1.891552	1.376557	1.622003	1.706607	1.388507	1.44916	1.496393
0.144	1.252426	1.890506	1.38814	1.604934	1.701896	1.411985	1.457855	1.514563

Time	27-Mar-07	30-Mar-07	3-Apr-07	10-Apr-07	21-Jun-07	28-Jun-07	26-Sep-07	19-Oct-07
0.148	1.252542	1.889779	1.398649	1.583626	1.697271	1.433335	1.466416	1.53258
0.152	1.252482	1.889549	1.407692	1.558652	1.693207	1.452556	1.475125	1.549351
0.156	1.252249	1.889861	1.414938	1.530379	1.690166	1.469601	1.483832	1.564035
0.16	1.251844	1.890653	1.420139	1.499023	1.688543	1.484394	1.492015	1.576068
0.164	1.251274	1.891793	1.423156	1.464771	1.688618	1.496849	1.498941	1.585137
0.168	1.250539	1.893101	1.423957	1.427922	1.690507	1.506921	1.503929	1.59112
0.172	1.249646	1.894351	1.422604	1.38903	1.69413	1.514644	1.506579	1.59404
0.176	1.248598	1.895255	1.419221	1.348997	1.699181	1.520166	1.506898	1.594029
0.18	1.247399	1.895431	1.413961	1.309093	1.70513	1.523745	1.505278	1.59129
0.184	1.246055	1.894374	1.406969	1.270906	1.711252	1.525738	1.502349	1.586065
0.188	1.24457	1.891469	1.398361	1.236206	1.716689	1.526554	1.498803	1.578584
0.192	1.242949	1.886034	1.388222	1.206772	1.720524	1.526614	1.495222	1.56902
0.196	1.241199	1.877389	1.376616	1.184193	1.721876	1.526305	1.492001	1.55746
0.2	1.239324	1.864967	1.363623	1.169712	1.719984	1.525962	1.489352	1.543921
0.204	1.23733	1.848403	1.349382	1.164093	1.714265	1.525844	1.487352	1.528412
0.208	1.235224	1.827604	1.334118	1.167547	1.704354	1.526147	1.486014	1.511036
0.212	1.23301	1.802773	1.31817	1.179712	1.690089	1.526994	1.485329	1.492091
0.216	1.230696	1.774361	1.301966	1.199657	1.671482	1.528433	1.485285	1.472124
0.22	1.228288	1.742977	1.285996	1.225963	1.648643	1.530446	1.485856	1.451902
0.224	1.225792	1.709258	1.270737	1.256854	1.621706	1.532938	1.48697	1.432278
0.228	1.223214	1.67375	1.256595	1.290389	1.590762	1.535758	1.488487	1.413987
0.232	1.220561	1.636831	1.243847	1.324674	1.555827	1.538728	1.490167	1.397409
0.236	1.21784	1.598699	1.232622	1.358054	1.516854	1.541667	1.491676	1.382353
0.24	1.215058	1.559423	1.222905	1.389246	1.473795	1.544413	1.492615	1.367931
0.248	1.21222	1.477618	1.207424	1.442108	1.375835	1.548862	1.49116	1.334231
0.252	1.21222	1.435372	1.201222	1.4633	1.32174	1.550355	1.48813	1.310729
0.256	1.21222	1.392597	1.195688	1.481213	1.265313	1.551164	1.483316	1.280294
0.26	1.21222	1.349657	1.190498	1.496268	1.207787	1.551032	1.476638	1.242063
0.264	1.21222	1.306897	1.185263	1.508988	1.150678	1.549598	1.468015	1.19645
0.268	1.21222	1.264581	1.179518	1.51991	1.09566	1.546397	1.457272	1.145257
0.272	1.21222	1.222855	1.172727	1.529522	1.044411	1.540923	1.44406	1.091439
0.276	1.21222	1.18176	1.164321	1.538197	0.998433	1.532708	1.42784	1.038593
0.28	1.21222	1.141276	1.153757	1.546151	0.958879	1.521408	1.407933	0.990301
0.284	1.21222	1.101412	1.140598	1.553415	0.926442	1.506876	1.383665	0.949501
0.288	1.21222	1.101412	1.124596	1.55981	0.926442	1.489188	1.354547	0.949501
0.292	1.21222	1.101412	1.105769	1.56493	0.926442	1.468613	1.32047	0.949501
0.296	1.21222	1.101412	1.08444	1.568133	0.926442	1.445548	1.281874	0.949501
0.3	1.21222	1.101412	1.061231	1.568554	0.926442	1.420411	1.23982	0.949501

Time	27-Mar-07	30-Mar-07	3-Apr-07	10-Apr-07	21-Jun-07	28-Jun-07	26-Sep-07	19-Oct-07
0.304	1.21222	1.101412	1.037017	1.565143	0.926442	1.393556	1.195957	0.949501
0.308	1.21222	1.101412	1.012826	1.556761	0.926442	1.365212	1.152343	0.949501
0.312	1.21222	1.101412	0.989717	1.542301	0.926442	1.335499	1.111158	0.949501
0.316	1.21222	1.101412	0.968654	1.520858	0.926442	1.304496	1.074352	0.949501
0.32	1.21222	1.101412	0.950395	1.491889	0.926442	1.272372	1.043344	0.949501
0.324	1.21222	1.101412	0.935423	1.455343	0.926442	1.239516	1.018853	0.949501
0.328	1.21222	1.101412	0.935423	1.411735	0.926442	1.206624	1.018853	0.949501
0.332	1.21222	1.101412	0.935423	1.362142	0.926442	1.17469	1.018853	0.949501
0.336	1.21222	1.101412	0.935423	1.308121	0.926442	1.144902	1.018853	0.949501
0.34	1.21222	1.101412	0.935423	1.25156	0.926442	1.118425	1.018853	0.949501
0.344	1.21222	1.101412	0.935423	1.194495	0.926442	1.096167	1.018853	0.949501
0.348	1.21222	1.101412	0.935423	1.138921	0.926442	1.078582	1.018853	0.949501
0.352	1.21222	1.101412	0.935423	1.086629	0.926442	1.065586	1.018853	0.949501
0.356	1.21222	1.101412	0.935423	1.039105	0.926442	1.056612	1.018853	0.949501
0.36	1.21222	1.101412	0.935423	0.997497	0.926442	1.050771	1.018853	0.949501
0.364	1.21222	1.101412	0.935423	0.96264	0.926442	1.047058	1.018853	0.949501

Table A2.6 Areal stretch with 20% degree saddle annulus

Time	27-Mar-07	30-Mar-07	3-Apr-07	10-Apr-07	21-Jun-07	28-Jun-07	26-Sep-07	19-Oct-07
0.004	1.003546	1.077382	1.002276	1.016216	0.943556	1.010628	0.999874	1.031322
0.008	1.002464	1.09759	1.016277	1.018945	0.959597	1.01219	0.992718	1.057284
0.012	1.001359	1.127222	1.033263	1.025438	0.989957	1.016387	0.985132	1.088234
0.016	1.00023	1.164207	1.052926	1.036245	1.036428	1.023412	0.977856	1.122309
0.02	0.999075	1.205912	1.074689	1.051653	1.098873	1.033233	0.971784	1.157125
0.024	0.997895	1.249548	1.097751	1.071642	1.175024	1.045555	0.96789	1.190155
0.028	0.996689	1.292549	1.121186	1.095858	1.260638	1.05984	0.967152	1.21915
0.032	0.995456	1.332839	1.144071	1.123639	1.349995	1.075385	0.970484	1.242503
0.036	0.994195	1.368966	1.165614	1.154069	1.436659	1.091436	0.978675	1.259504
0.04	0.992906	1.400133	1.185256	1.186082	1.514447	1.107301	0.992355	1.270415
0.044	0.991587	1.42615	1.202703	1.218606	1.578405	1.122444	1.011951	1.276364
0.048	0.990239	1.447327	1.217915	1.250719	1.625589	1.136523	1.037637	1.279062
0.052	0.98886	1.46432	1.231031	1.281766	1.655446	1.149387	1.069251	1.28042
0.056	0.987449	1.47797	1.242282	1.311386	1.669675	1.16104	1.106193	1.282145
0.06	0.986007	1.489143	1.251908	1.33942	1.671645	1.171587	1.147335	1.285419
0.064	0.984531	1.498615	1.260109	1.36575	1.665552	1.181189	1.190993	1.29072
0.068	0.983022	1.506975	1.267022	1.390088	1.655574	1.190021	1.235011	1.297806
0.072	0.981478	1.514572	1.272733	1.41183	1.645212	1.198257	1.276965	1.305837
0.076	0.979898	1.521488	1.27731	1.430003	1.636939	1.206054	1.314463	1.313587
0.08	0.978282	1.527573	1.280827	1.44335	1.632131	1.213555	1.345494	1.319705
0.084	0.976628	1.532524	1.283387	1.45053	1.631231	1.220878	1.36873	1.322967
0.088	0.974936	1.536001	1.285124	1.450422	1.634009	1.228115	1.383746	1.322492
0.092	0.973204	1.537756	1.286187	1.442424	1.639853	1.23531	1.391091	1.31789
0.096	0.971431	1.537713	1.286726	1.426704	1.647993	1.242448	1.392195	1.309322
0.1	0.969617	1.536	1.286862	1.404307	1.65765	1.249445	1.389113	1.297449
0.104	0.967759	1.53292	1.286683	1.377084	1.668078	1.25614	1.384142	1.283313
0.108	0.965858	1.52887	1.286235	1.347457	1.678562	1.262317	1.379405	1.268149
0.112	0.963911	1.524242	1.285546	1.318075	1.688383	1.267721	1.376496	1.253191
0.116	0.961918	1.519314	1.284639	1.291432	1.696812	1.272105	1.37631	1.239501
0.12	0.959878	1.514165	1.283554	1.269543	1.703154	1.275258	1.379074	1.227856
0.124	0.957789	1.508643	1.28236	1.253729	1.706821	1.277046	1.384545	1.218688
0.128	0.95565	1.502406	1.281152	1.244548	1.707434	1.277427	1.392256	1.212084
0.132	0.95346	1.495053	1.280041	1.241865	1.704901	1.276451	1.401714	1.207826
0.136	0.951219	1.486305	1.279129	1.245021	1.69946	1.274247	1.412489	1.20545
0.14	0.948925	1.476187	1.278484	1.253065	1.691643	1.270998	1.424183	1.204329
0.144	0.946577	1.465132	1.27813	1.26498	1.682191	1.266911	1.436373	1.203765
0.148	0.944175	1.453962	1.27804	1.279863	1.671917	1.262194	1.448543	1.203076

Time	27-Mar-07	30-Mar-07	3-Apr-07	10-Apr-07	21-Jun-07	28-Jun-07	26-Sep-07	19-Oct-07
0.156	0.939205	1.435402	1.278345	1.316031	1.651724	1.251594	1.470278	1.199162
0.16	0.936636	1.429687	1.278545	1.336559	1.64271	1.246016	1.478503	1.1953
0.164	0.934011	1.426714	1.278651	1.35836	1.634623	1.240424	1.484209	1.190083
0.168	0.931331	1.426024	1.278576	1.381088	1.627378	1.23494	1.487066	1.183694
0.172	0.928595	1.426665	1.278225	1.404207	1.620787	1.229683	1.487005	1.176464
0.176	0.925803	1.427448	1.277474	1.426942	1.614654	1.22477	1.484236	1.168822
0.18	0.922957	1.427272	1.276142	1.448279	1.608842	1.220304	1.479225	1.161225
0.184	0.920058	1.425409	1.273973	1.467025	1.603301	1.216361	1.472623	1.154099
0.188	0.917107	1.42165	1.27064	1.481907	1.598052	1.212976	1.465185	1.147786
0.192	0.914106	1.416225	1.265767	1.491687	1.593152	1.21014	1.457645	1.142512
0.196	0.911057	1.409526	1.258975	1.495278	1.588636	1.207808	1.450632	1.138372
0.2	0.907962	1.401721	1.249948	1.491843	1.58448	1.205903	1.444598	1.135327
0.204	0.904825	1.392412	1.238498	1.480873	1.580574	1.204338	1.439787	1.1332
0.208	0.901649	1.380516	1.224624	1.462234	1.576712	1.203005	1.436246	1.131679
0.212	0.898439	1.364451	1.208547	1.436183	1.572576	1.20177	1.433844	1.130317
0.216	0.895199	1.342644	1.190709	1.403341	1.567712	1.200435	1.432309	1.128558
0.22	0.891933	1.314218	1.171744	1.36463	1.5615	1.198711	1.431273	1.125791
0.224	0.888648	1.279584	1.15241	1.321162	1.553117	1.196187	1.430314	1.121449
0.228	0.88535	1.240684	1.133516	1.274106	1.541538	1.192335	1.429021	1.115124
0.232	0.882046	1.200694	1.115844	1.22455	1.525577	1.18655	1.427068	1.10668
0.236	0.878743	1.163222	1.100086	1.173398	1.503996	1.178232	1.424271	1.096319
0.24	0.87545	1.131213	1.086807	1.121352	1.475682	1.166886	1.420608	1.084573
0.244	0.872177	1.105838	1.076432	1.068977	1.439869	1.152228	1.416191	1.072231
0.248	0.872177	1.085591	1.069236	1.016829	1.396364	1.134256	1.411197	1.072231
0.252	0.872177	1.065799	1.065346	0.965596	1.34572	1.113258	1.405765	1.072231
0.256	0.872177	1.038798	1.064721	0.916159	1.289287	1.08976	1.399886	1.072231
0.26	0.872177	0.995112	1.067127	0.869551	1.229132	1.06441	1.393321	1.072231
0.264	0.872177	0.92584	1.072129	0.826806	1.167808	1.037841	1.385543	1.072231
0.268	0.872177	0.825896	1.0791	0.788756	1.108033	1.010539	1.375757	1.072231
0.272	0.872177	0.696974	1.08728	0.755873	1.052348	0.982759	1.362983	1.072231
0.276	0.872177	0.548701	1.095866	0.728221	1.00282	0.954512	1.346225	1.072231
0.28	0.872177	0.396872	1.104126	0.705514	0.960844	0.925607	1.324702	1.072231
0.284	0.872177	0.258994	1.111493	0.687245	0.927072	0.895754	1.29811	1.072231
0.288	0.872177	0.258994	1.111493	0.687245	0.927072	0.864695	1.26685	1.072231
0.292	0.872177	0.258994	1.111493	0.687245	0.927072	0.832322	1.232129	1.072231
0.296	0.872177	0.258994	1.111493	0.687245	0.927072	0.798773	1.195881	1.072231
0.3	0.872177	0.258994	1.111493	0.687245	0.927072	0.764476	1.16047	1.072231
0.304	0.872177	0.258994	1.111493	0.687245	0.927072	0.730126	1.128224	1.072231

Time	27-Mar-07	30-Mar-07	3-Apr-07	10-Apr-07	21-Jun-07	28-Jun-07	26-Sep-07	19-Oct-07
0.308	0.872177	0.258994	1.111493	0.687245	0.927072	0.696617	1.100953	1.072231
0.312	0.872177	0.258994	1.111493	0.687245	0.927072	0.664919	1.0796	1.072231
0.316	0.872177	0.258994	1.111493	0.687245	0.927072	0.635952	1.06417	1.072231
0.32	0.872177	0.258994	1.111493	0.687245	0.927072	0.610449	1.053931	1.072231
0.324	0.872177	0.258994	1.111493	0.687245	0.927072	0.588865	1.047754	1.072231

Table A3.1 Hemodynamic Data under Different Pathological Conditions

8-Jul	Control	Dilated + Apical	Dilated + Apical + Lateral
MR	27.8	35.9	44.6
SV	72.3	72.6	73.2
MRF	38.450899	49.44903581	60.92896175
MRFA	0	10.99813678	22.47806272
9-Jul	**Control**	**Dilated + Apical**	**Dilated + Apical + Lateral**
MR	24.8	35	41.9
SV	74	71.2	72.8
MRF	33.513514	49.15730337	57.55494505
MRFA	0	15.64378986	24.04143154
10-Jul	**Control**	**Dilated + Apical**	**Dilated + Apical + Lateral**
MR	30.1	33.6	44.7
SV	70.7	73.1	71.7
MRF	42.574257	45.96443228	62.34309623
MRFA	0	3.390174859	19.76883881
11-Jul	**Control**	**Dilated + Apical**	**Dilated + Apical + Lateral**
MR	22.7	26.9	32.7
SV	73	72.1	69.8
MRF	31.09589	37.30929265	46.84813754
MRFA	0	6.213402238	15.75224712
14-Jul	**Control**	**Dilated + Apical**	**Dilated + Apical + Lateral**
MR	18.7	25.9	39.1
SV	72.9	73.4	70.1
MRF	25.651578	35.28610354	55.77746077
MRFA	0	9.634526039	30.12588327
16-Jul	**Control**	**Dilated + Apical**	**Dilated + Apical + Lateral**
MR	20.5	35.5	44
SV	71.8	72.2	73
MRF	28.551532	49.16897507	60.2739726
MRFA	0	20.61744304	31.72244057

17-Jul	Control	Dilated + Apical	Dilated + Apical + Lateral
MR	24.6	28.7	37
SV	72.4	69.6	72.2
MRF	33.977901	41.23563218	51.2465374
MRFA	0	7.257731631	17.26863684
21-Jul	**Control**	**Dilated + Apical**	**Dilated + Apical + Lateral**
MR	25.4	31	41
SV	73.1	71.1	73
MRF	34.746922	43.60056259	56.16438356
MRFA	0	8.853640563	21.41746154
Average	**Control**	**Disease**	**Dilated + Apical + Lateral**
MR	`	31.64	40.57
SV	72.44	72.03	71.83
MRF	33.40	43.94	56.42
MRFA	0.00	10.54	23.02
	0.00	5.50	5.69

Table A3.2 Hemodynamic Data under Annular and Sub-annular Repair

8-Jul	Undersized+Apical	Underized+Apical+Lateral	Undersized+Apical+Ctcut	Underized+Apical+Lateral+Ctcut
MR	30.9	41.4	28.9	43.2
SV	71.2	70.6	71.3	72.4
MRF	43.3988764	58.64022663	40.53295933	59.66850829
MRFA	4.947977373	20.1893276	2.082060295	21.21760926
9-Jul	**Undersized+Apical**	**Underized+Apical+Lateral**	**Undersized+Apical+Ctcut**	**Underized+Apical+Lateral+Ctcut**
MR	29.8	36.9	27.7	40.6
SV	72.1	72.8	71.5	71
MRF	41.33148405	50.68681319	38.74125874	57.18309859
MRFA	7.817970536	17.17329967	5.227745228	23.66958508
10-Jul	**Undersized+Apical**	**Underized+Apical+Lateral**	**Undersized+Apical+Ctcut**	**Underized+Apical+Lateral+Ctcut**
MR	27	35.9	27.2	39.3
SV	73.4	73.4	72.3	71.4
MRF	36.78474114	48.91008174	37.62102351	55.04201681
MRFA	0	6.335824318	0	12.46775938
11-Jul	**Undersized+Apical**	**Underized+Apical+Lateral**	**Undersized+Apical+Ctcut**	**Underized+Apical+Lateral+Ctcut**
MR	25.8	30.8	25.9	32.6
SV	69.9	73.1	74.9	74.5
MRF	36.90987124	42.13406293	34.57943925	43.75838926
MRFA	5.813980834	11.03817252	3.483548841	12.66249885

14-Jul	Undersized+Apical	Underized+Apical+Lateral	Undersized+Apical+Ctcut	Underized+Apical+Lateral+Ctcut
MR	23.7	33.6	23.3	34.6
SV	71	72.6	70.9	72.2
MRF	33.38028169	46.28099174	32.86318759	47.92243767
MRFA	7.728704187	20.62941423	7.211610085	22.27086017
16-Jul	**Undersized+Apical**	**Underized+Apical+Lateral**	**Undersized+Apical+Ctcut**	**Underized+Apical+Lateral+Ctcut**
MR	28.2	40.5	25.4	30.3
SV	70	71	70.9	62.3
MRF	40.28571429	57.04225352	35.82510578	48.63563403
MRFA	11.73418225	28.49072149	7.273573749	20.084102
17-Jul	**Undersized+Apical**	**Underized+Apical+Lateral**	**Undersized+Apical+Ctcut**	**Underized+Apical+Lateral+Ctcut**
MR	24.9	33.5	24.6	36.6
SV	70.8	71.2	73.5	71
MRF	35.16949153	47.0505618	33.46938776	51.54929577
MRFA	1.191590973	13.07266125	0	17.57139522
21-Jul	**Undersized+Apical**	**Underized+Apical+Lateral**	**Undersized+Apical+Ctcut**	**Underized+Apical+Lateral+Ctcut**
MR	30.1	30.1	27.9	36.2
SV	71.1	73.9	73.3	66.6
MRF	42.3347398	40.73071719	38.0627558	54.35435435
MRFA	7.587817778	5.983795161	3.315833773	19.60743233
Mean	**Annuloplasty**	**Underized+Apical+Lateral**	**Annuloplasty + CTcut**	**Underized+Apical+Lateral+Ctcut**
MR	27.19	36.09	26.14	36.74
SV	71.20	72.10	72.19	70.69
MRF	38.18	50.11	36.23	51.97
MRFA	5.60	16.70	3.61	18.56
STDEV	3.81	7.75	2.87	4.19

Table A3.3 Averaged Data for marginal chordal forces measured under different experimental conditions

	Control	Dil+A	Dil+AP	Dil+APL	CT+Dil+A	CT+Dil+AP	CT+Dil+APL
1	0	0	0	0	0	0	0
2	-9.5E-07	0.00049	-0.00011	2.67E-05	0.00015	0.000178	0.000168
3	-0.00031	-1.6E-05	-0.00021	-5.3E-05	-0.00073	0.000529	0.000238
4	6.48E-05	-0.00035	7.17E-05	0.000453	-0.00036	0.000599	0.00034
5	-0.00011	-0.00011	8.5E-05	0.000147	0.000139	0.00043	0.000283
6	-0.00027	8.38E-05	0.000124	0.000573	-0.00033	0.000985	0.000476
7	0.000186	8.29E-05	0.000117	0.00028	-0.00013	0.001101	0.001131
8	-9.7E-05	-0.00017	0.000122	0.000707	-6.1E-06	0.001162	0.001323
9	-8.3E-05	-0.00016	7.33E-05	0.000173	0.000155	0.001251	0.000736
10	0.000531	0.000118	0.000178	0.000453	4.44E-05	0.001089	0.00071
11	0.000426	0.000495	0.000311	0.00028	-0.00013	0.000812	0.001301
12	0.000141	0.000374	4.5E-05	0.00024	-0.00038	0.001575	0.001288
13	0.000257	0.000286	0.000218	0.000347	-7.4E-06	0.001131	0.001158
14	0.000473	0.000236	2.42E-05	0.00036	-0.00015	0.000907	0.00117
15	0.00063	0.000799	0.000178	0.00048	-0.00013	0.00117	0.001089
16	0.000603	0.000506	-1.7E-06	0.000587	0.000351	0.001407	0.001088
17	0.000646	0.000587	0.000447	0.000693	0.000206	0.001527	0.001434
18	0.00077	0.000461	0.000323	0.000667	9.83E-06	0.001766	0.001349
19	0.000781	0.000442	0.000614	0.000667	8.41E-05	0.001855	0.001141
20	0.000754	0.000661	0.000294	0.00064	1.74E-05	0.00159	0.001781
21	0.000518	0.000958	0.000377	0.001053	0.000166	0.001985	0.002021
22	0.000284	0.000616	0.000647	0.000947	0.000229	0.002078	0.001842
23	0.000579	0.000693	0.000801	0.00096	0.000251	0.002115	0.002133
24	0.000573	0.000958	0.000804	0.000867	2.85E-05	0.002093	0.002243

	Control	Dil+A	Dil+AP	Dil+APL	CT+Dil+A	CT+Dil+AP	CT+Dil+APL
25	0.000999	0.001023	0.000837	0.001067	0.000545	0.002044	0.001914
26	0.000375	0.000986	0.001041	0.001467	0.000141	0.002306	0.001845
27	0.000988	0.000938	0.000973	0.00124	0.000515	0.001996	0.002179
28	0.000741	0.000908	0.000871	0.001413	0.000537	0.00228	0.002056
29	0.00084	0.000939	0.000864	0.000973	0.000406	0.002203	0.001913
30	0.00033	0.001176	0.001203	0.00148	0.000411	0.00243	0.002275
31	0.000558	0.00113	0.001334	0.00156	0.000212	0.002564	0.002075
32	0.000978	0.000974	0.001551	0.00128	0.000451	0.002762	0.002261
33	0.001313	0.001221	0.001523	0.001733	0.000732	0.002585	0.002009
34	0.001073	0.00141	0.001713	0.0016	0.001011	0.00274	0.00285
35	0.000651	0.001023	0.001377	0.00184	0.000693	0.00249	0.002184
36	0.000764	0.001109	0.001845	0.001733	0.000904	0.002523	0.002066
37	0.000964	0.001695	0.001537	0.001907	0.001235	0.00266	0.001975
38	0.000953	0.001712	0.001687	0.001707	0.00116	0.002495	0.002172
39	0.000816	0.001448	0.001772	0.001947	0.001259	0.002716	0.002432
40	0.001	0.001477	0.001606	0.002067	0.001311	0.002703	0.002666
41	0.00117	0.001586	0.001861	0.002133	0.001132	0.003007	0.002103
42	0.001308	0.002072	0.001689	0.001627	0.001098	0.003108	0.002155
43	0.00124	0.001837	0.002086	0.001907	0.001074	0.00301	0.00276
44	0.001174	0.001811	0.001989	0.002533	0.001337	0.002931	0.002828
45	0.001387	0.001477	0.002083	0.00224	0.000892	0.003165	0.002703
46	0.00205	0.001786	0.002208	0.002053	0.001213	0.003521	0.002177
47	0.001716	0.001991	0.002394	0.00236	0.001494	0.003259	0.002784
48	0.001401	0.001642	0.002183	0.002053	0.001408	0.003457	0.002301
49	0.001454	0.00179	0.002658	0.002013	0.001696	0.003524	0.002993

	Control	Dil+A	Dil+AP	Dil+APL	CT+Dil+A	CT+Dil+AP	CT+Dil+APL
50	0.001991	0.002033	0.002756	0.00236	0.001989	0.003674	0.002756
51	0.001978	0.00257	0.002993	0.002307	0.001934	0.004075	0.003114
52	0.001895	0.002585	0.003243	0.002613	0.00202	0.003928	0.00322
53	0.00164	0.002353	0.003166	0.002933	0.002149	0.004435	0.003568
54	0.00197	0.002105	0.003278	0.003093	0.00241	0.004687	0.003442
55	0.002486	0.002312	0.003658	0.00308	0.002016	0.004447	0.002908
56	0.002042	0.00246	0.003592	0.003133	0.002259	0.00443	0.003311
57	0.002202	0.002615	0.003768	0.003227	0.002571	0.004653	0.003512
58	0.002114	0.00248	0.003768	0.003147	0.002286	0.004958	0.003683
59	0.002461	0.002804	0.004067	0.003027	0.002526	0.005033	0.003689
60	0.002693	0.002916	0.004042	0.00352	0.003016	0.005203	0.004084
61	0.002208	0.003241	0.004609	0.00352	0.002549	0.005408	0.003977
62	0.001784	0.003128	0.004663	0.0038	0.002361	0.005546	0.004213
63	0.002499	0.00331	0.005533	0.003987	0.003224	0.005727	0.004411
64	0.00253	0.003475	0.005598	0.00432	0.003646	0.00587	0.004143
65	0.002481	0.004115	0.006107	0.00436	0.003386	0.006331	0.004191
66	0.002356	0.004199	0.006401	0.004413	0.004194	0.006775	0.005006
67	0.002481	0.003849	0.006748	0.004853	0.004361	0.00728	0.005507
68	0.002831	0.004299	0.007144	0.004933	0.004051	0.007717	0.005464
69	0.003408	0.004949	0.007569	0.00508	0.004224	0.007958	0.00602
70	0.003283	0.005092	0.008135	0.006093	0.005051	0.007993	0.006616
71	0.002958	0.005125	0.008836	0.006547	0.004976	0.008601	0.006594
72	0.003288	0.005585	0.009714	0.00676	0.005109	0.009449	0.007205
73	0.00365	0.00588	0.010409	0.006933	0.005681	0.009834	0.007654
74	0.004178	0.006746	0.011103	0.007587	0.005705	0.009891	0.007298

	Control	Dil+A	Dil+AP	Dil+APL	CT+Dil+A	CT+Dil+AP	CT+Dil+APL
75	0.004004	0.006703	0.011943	0.007893	0.006137	0.010199	0.008383
76	0.004162	0.007588	0.013269	0.009027	0.006348	0.011324	0.009269
77	0.005291	0.00797	0.014464	0.009667	0.006792	0.011736	0.00929
78	0.005643	0.009164	0.015394	0.010827	0.007089	0.012362	0.009867
79	0.005906	0.009819	0.017506	0.011533	0.007667	0.013311	0.010869
80	0.006257	0.010736	0.019044	0.012547	0.008508	0.014075	0.011468
81	0.007455	0.011801	0.021456	0.01344	0.008633	0.015098	0.012586
82	0.00787	0.013203	0.024027	0.014947	0.009453	0.016536	0.01371
83	0.008468	0.014901	0.027022	0.015973	0.009718	0.017561	0.014926
84	0.009528	0.01676	0.030239	0.017147	0.01061	0.019127	0.016142
85	0.011047	0.018544	0.03357	0.018533	0.011685	0.020589	0.017682
86	0.01217	0.020722	0.037392	0.02036	0.013185	0.022317	0.019536
87	0.013245	0.02238	0.040665	0.022693	0.014354	0.023563	0.020973
88	0.014662	0.02429	0.044242	0.0256	0.015317	0.025268	0.022745
89	0.016673	0.0252	0.047952	0.02868	0.016265	0.027075	0.025632
90	0.018557	0.025969	0.051673	0.03212	0.017375	0.02948	0.028335
91	0.02015	0.027078	0.055083	0.036387	0.018717	0.031414	0.03142
92	0.02158	0.028536	0.057953	0.040373	0.019691	0.034102	0.034754
93	0.022728	0.029452	0.06051	0.044347	0.01996	0.038162	0.03917
94	0.023697	0.030123	0.062373	0.047627	0.020365	0.041951	0.043414
95	0.025245	0.031359	0.064388	0.05092	0.020904	0.045992	0.048398
96	0.026313	0.032627	0.066243	0.053667	0.021715	0.049557	0.052759
97	0.026679	0.03464	0.068243	0.055987	0.022172	0.053384	0.056618
98	0.027174	0.035603	0.070419	0.05824	0.02361	0.056804	0.060748
99	0.027604	0.037066	0.07258	0.06092	0.024926	0.060469	0.065213

	Control	Dil+A	Dil+AP	Dil+APL	CT+Dil+A	CT+Dil+AP	CT+Dil+APL
100	0.02831	0.038591	0.074466	0.064027	0.026465	0.063875	0.06904
101	0.028773	0.040187	0.07651	0.067413	0.027942	0.067237	0.073588
102	0.028626	0.041459	0.077769	0.070253	0.029327	0.070435	0.079213
103	0.028963	0.043162	0.079302	0.0734	0.031584	0.075222	0.084426
104	0.028541	0.04449	0.080104	0.0762	0.033152	0.080219	0.089482
105	0.02819	0.045379	0.080163	0.07884	0.034387	0.085935	0.093904
106	0.028057	0.04583	0.080254	0.08092	0.035615	0.092286	0.099219
107	0.028468	0.044415	0.0803	0.0824	0.037154	0.100263	0.103046
108	0.029108	0.042339	0.081042	0.084067	0.03883	0.107638	0.107458
109	0.03029	0.041011	0.081824	0.085827	0.039707	0.115095	0.112931
110	0.030116	0.040028	0.08279	0.088053	0.041205	0.120946	0.119172
111	0.029843	0.0386	0.083813	0.090773	0.043116	0.12644	0.127005
112	0.029101	0.037141	0.084538	0.094013	0.04509	0.13076	0.136339
113	0.028097	0.036317	0.084183	0.097307	0.046873	0.135277	0.144425
114	0.027099	0.036242	0.083109	0.100653	0.048738	0.13869	0.150718
115	0.026636	0.036278	0.081756	0.103373	0.050657	0.141337	0.157111
116	0.026288	0.03699	0.080589	0.105733	0.052784	0.144243	0.162577
117	0.026015	0.03706	0.079846	0.107333	0.054104	0.148071	0.168271
118	0.025938	0.037204	0.079142	0.108067	0.054999	0.152755	0.174458
119	0.0253	0.037353	0.078559	0.108907	0.055064	0.157193	0.18076
120	0.025532	0.037564	0.077705	0.10948	0.054611	0.16197	0.186621
121	0.026646	0.036971	0.077633	0.11052	0.054605	0.166341	0.192885
122	0.026532	0.03687	0.077328	0.11208	0.055497	0.169781	0.197572
123	0.026361	0.037415	0.077151	0.113813	0.055664	0.172635	0.201588
124	0.026272	0.037237	0.076812	0.116027	0.056955	0.173996	0.205512

	Control	Dil+A	Dil+AP	Dil+APL	CT+Dil+A	CT+Dil+AP	CT+Dil+APL
125	0.02594	0.036738	0.076713	0.11756	0.058086	0.175047	0.209446
126	0.025271	0.035884	0.076597	0.118787	0.058767	0.175796	0.212609
127	0.024474	0.035888	0.07636	0.119573	0.059424	0.176332	0.215301
128	0.02408	0.035726	0.076853	0.119853	0.059961	0.176689	0.217753
129	0.024364	0.035254	0.077043	0.120267	0.060356	0.17729	0.220298
130	0.02405	0.034623	0.076906	0.120027	0.060173	0.177975	0.222586
131	0.023832	0.03473	0.077497	0.120587	0.060402	0.178744	0.225083
132	0.023943	0.03463	0.077743	0.120787	0.060052	0.179406	0.226501
133	0.024107	0.035008	0.077771	0.121187	0.059312	0.180405	0.227861
134	0.024122	0.035157	0.078114	0.122053	0.058443	0.18018	0.229226
135	0.023985	0.034829	0.078108	0.122227	0.058191	0.179485	0.229788
136	0.023619	0.034728	0.078201	0.12192	0.057475	0.179133	0.230082
137	0.02302	0.034613	0.077888	0.121907	0.056277	0.178203	0.229733
138	0.023302	0.034353	0.077638	0.121813	0.05624	0.1764	0.229753
139	0.023144	0.034194	0.077703	0.121107	0.055319	0.174607	0.228589
140	0.022661	0.03403	0.077695	0.12064	0.053621	0.17373	0.227428
141	0.022116	0.033598	0.077301	0.1196	0.052858	0.172509	0.225554
142	0.021902	0.03346	0.077374	0.11812	0.051946	0.170674	0.223932
143	0.021844	0.03319	0.077298	0.116987	0.050928	0.169293	0.221198
144	0.02157	0.032945	0.077094	0.11604	0.049985	0.167915	0.218965
145	0.021362	0.0329	0.076964	0.115093	0.048839	0.166	0.216772
146	0.021049	0.032506	0.077081	0.11372	0.048105	0.164412	0.213596
147	0.021315	0.032553	0.076713	0.11268	0.046983	0.162385	0.21033
148	0.021314	0.031981	0.076528	0.11124	0.04578	0.160222	0.207712
149	0.020957	0.031497	0.076545	0.110187	0.045001	0.158019	0.203893

	Control	Dil+A	Dil+AP	Dil+APL	CT+Dil+A	CT+Dil+AP	CT+Dil+APL
150	0.020784	0.031311	0.076488	0.10908	0.04334	0.155736	0.200138
151	0.020856	0.031692	0.076841	0.107507	0.042167	0.153315	0.19654
152	0.020664	0.031647	0.076603	0.10644	0.040824	0.150923	0.192549
153	0.020225	0.03125	0.076736	0.1052	0.039354	0.148535	0.18865
154	0.020074	0.030787	0.076898	0.103853	0.038088	0.146416	0.18473
155	0.020017	0.030508	0.07703	0.102747	0.037519	0.14363	0.180396
156	0.020062	0.030785	0.07699	0.101467	0.035844	0.141008	0.175921
157	0.019775	0.030276	0.077316	0.100187	0.034995	0.138098	0.171931
158	0.01939	0.03003	0.077346	0.099413	0.034001	0.13507	0.167677
159	0.01923	0.029768	0.07738	0.09796	0.032394	0.132342	0.162898
160	0.019403	0.02959	0.07724	0.097027	0.031266	0.12881	0.157652
161	0.018883	0.029521	0.077334	0.095907	0.030121	0.125525	0.152894
162	0.018517	0.029106	0.076928	0.094827	0.028988	0.122828	0.14794
163	0.018494	0.028511	0.077179	0.09364	0.027948	0.119546	0.143293
164	0.018144	0.028592	0.076933	0.092707	0.027055	0.11666	0.138291
165	0.018286	0.028127	0.076916	0.090933	0.025884	0.113008	0.133598
166	0.017607	0.027466	0.076378	0.09	0.024947	0.109687	0.128805
167	0.017465	0.026905	0.075949	0.08908	0.023632	0.106153	0.124191
168	0.01735	0.026422	0.074938	0.087493	0.022898	0.103141	0.119238
169	0.017317	0.026131	0.074356	0.085507	0.02183	0.099852	0.114166
170	0.01686	0.025733	0.073066	0.08396	0.021073	0.096048	0.110119
171	0.016752	0.024628	0.071938	0.082213	0.020181	0.092168	0.106055
172	0.01622	0.023894	0.070772	0.08032	0.019128	0.088321	0.101569
173	0.016246	0.023383	0.0693	0.078867	0.018469	0.084668	0.097624
174	0.01601	0.023019	0.067743	0.076867	0.018061	0.08065	0.093938

	Control	Dil+A	Dil+AP	Dil+APL	CT+Dil+A	CT+Dil+AP	CT+Dil+APL
175	0.015511	0.022785	0.066423	0.075147	0.017482	0.076128	0.089815
176	0.015054	0.0221	0.064735	0.07312	0.01685	0.072244	0.086296
177	0.014983	0.02169	0.063208	0.070893	0.016333	0.068583	0.082711
178	0.014815	0.020892	0.061698	0.068933	0.016064	0.06502	0.079331
179	0.014709	0.019924	0.059514	0.06724	0.015405	0.061781	0.076028
180	0.013824	0.01944	0.058065	0.06532	0.014662	0.058675	0.073348
181	0.013397	0.01847	0.056155	0.062893	0.01433	0.055888	0.071021
182	0.01335	0.01775	0.054022	0.061307	0.014074	0.053391	0.068482
183	0.01328	0.017404	0.052228	0.059533	0.013484	0.050065	0.065498
184	0.012628	0.01688	0.050051	0.057253	0.012602	0.047504	0.063608
185	0.012013	0.015662	0.047392	0.05516	0.012092	0.044708	0.061355
186	0.011751	0.015294	0.045441	0.053333	0.011604	0.042698	0.059224
187	0.011375	0.014604	0.043548	0.050893	0.011541	0.040499	0.057565
188	0.010871	0.014029	0.041448	0.048667	0.011031	0.038012	0.055067
189	0.010255	0.013488	0.039349	0.045973	0.010581	0.03584	0.053263
190	0.009739	0.012618	0.036983	0.043733	0.009782	0.034255	0.051469
191	0.009808	0.012101	0.034935	0.04132	0.009319	0.032083	0.049376
192	0.008627	0.011773	0.032574	0.03932	0.00876	0.030507	0.046601
193	0.008524	0.01127	0.030663	0.03708	0.008653	0.028772	0.044687
194	0.007633	0.010329	0.028447	0.034747	0.008252	0.026757	0.042691
195	0.007519	0.009578	0.026281	0.032427	0.007793	0.024971	0.040378
196	0.007152	0.008981	0.024672	0.030067	0.006917	0.02363	0.03809
197	0.006557	0.008698	0.022272	0.02784	0.006491	0.021679	0.035918
198	0.006193	0.007928	0.020111	0.025453	0.006203	0.02029	0.033721
199	0.005834	0.007355	0.0184	0.023947	0.005457	0.018942	0.031623

	Control	Dil+A	Dil+AP	Dil+APL	CT+Dil+A	CT+Dil+AP	CT+Dil+APL
200	0.006005	0.007178	0.01691	0.021907	0.004871	0.017638	0.029708
201	0.005127	0.006569	0.015213	0.019627	0.004961	0.016176	0.027323
202	0.004688	0.00588	0.013812	0.018267	0.004241	0.01484	0.025362
203	0.004567	0.005282	0.011934	0.01644	0.003999	0.013501	0.023715
204	0.004308	0.004099	0.010398	0.015333	0.003461	0.012291	0.021969
205	0.004006	0.00395	0.009059	0.01344	0.003104	0.011864	0.019758
206	0.00369	0.003671	0.008145	0.012373	0.002598	0.010936	0.018268
207	0.003424	0.002517	0.007218	0.010973	0.00251	0.009557	0.016683
208	0.003232	0.001885	0.006319	0.00976	0.002345	0.00898	0.014962
209	0.003358	0.00171	0.005223	0.008333	0.002422	0.008171	0.013867
210	0.002873	0.001446	0.004763	0.007413	0.002273	0.007115	0.012702
211	0.00234	0.001252	0.003742	0.006333	0.001922	0.00615	0.01055
212	0.002259	0.00083	0.003293	0.005427	0.001853	0.00548	0.009607
213	0.002163	0.000549	0.002477	0.004693	0.00168	0.004819	0.008691
214	0.00242	0.000142	0.002238	0.004093	0.001769	0.004034	0.007468
215	0.001765	0.000193	0.001613	0.00348	0.001349	0.003267	0.006315
216	0.001478	2.57E-05	0.001463	0.002787	0.00124	0.002765	0.005324
217	0.001246	-0.0006	0.000428	0.001933	0.001268	0.002125	0.00452
218	0.001484	-0.00063	0.000593	0.001813	0.001353	0.00209	0.00369
219	0.000998	-0.00042	0.000628	0.00084	0.000861	0.001726	0.003033
220	0.000812	-0.00089	-0.00013	8E-05	0.000655	0.00184	0.002887
221	0.000808	-0.00109	1.58E-05	-0.00031	0.000762	0.001624	0.001677
222	0.00096	-0.00128	-0.00036	-0.00072	0.000917	0.001466	0.001584
223	0.000953	-0.00126	-0.0006	-0.00145	0.001015	0.001487	0.001248
224	0.000842	-0.00103	-7.6E-05	-0.00173	0.000888	0.001388	0.000903

	Control	Dil+A	Dil+AP	Dil+APL	CT+Dil+A	CT+Dil+AP	CT+Dil+APL
225	0.000406	-0.00095	-0.00014	-0.0016	0.000384	0.001405	0.000251
226	0.000694	-0.00141	-0.00047	-0.00171	0.000563	0.00158	0.000358
227	0.000943	-0.00107	-0.00034	-0.00169	0.000677	0.001578	-1.3E-05
228	0.000438	-0.00088	-0.00041	-0.002	0.000391	0.00181	-0.00048
229	0.000385	-0.0005	-0.00042	-0.00203	0.000458	0.001976	-0.00055
230	0.000656	-0.00056	-0.00079	-0.00225	0.000645	0.001684	-0.00082
231	0.00088	-0.00072	-0.00044	-0.00239	0.000255	0.001729	-0.00067
232	0.001102	-0.00077	-0.00081	-0.00219	9.68E-05	0.001738	-0.00038
233	0.000655	-0.00032	-0.00084	-0.00223	-0.0002	0.00176	-0.00018
234	0.000399	-0.00072	-0.00076	-0.00235	-0.00065	0.002006	-0.00041
235	0.000536	-0.00066	-0.00112	-0.00211	-0.00052	0.001654	-0.00023
236	0.000763	-0.00095	-0.00143	-0.00184	-0.00081	0.001224	1.67E-06
237	0.000108	-0.00071	-0.00125	-0.00163	-0.00041	0.001344	4.33E-05
238	0.00065	-0.00072	-0.0014	-0.00173	-0.00095	0.001149	-0.00061
239	0.000466	-0.00082	-0.00135	-0.0018	-0.00122	0.000906	-0.00012
240	0.00064	-0.00074	-0.00185	-0.00132	-0.00112	0.000301	0.000173
241	0.000316	-0.00082	-0.00186	-0.00153	-0.00118	-1.9E-06	-3.9E-05
242	0.000475	-0.00061	-0.00146	-0.00159	-0.0015	-0.0003	4.67E-05
243	0.000652	-0.00081	-0.00184	-0.00191	-0.00189	-0.00042	0.000307
244	0.000439	-0.001	-0.0016	-0.00183	-0.00148	-0.00139	-5.1E-05
245	0.000447	-0.00122	-0.00209	-0.00227	-0.0016	-0.00173	0.000274
246	0.000635	-0.00077	-0.00218	-0.00231	-0.00137	-0.00144	0.000374
247	0.000485	-0.00097	-0.00246	-0.00207	-0.00146	-0.0018	-0.00028
248	0.000858	-0.00127	-0.00244	-0.00215	-0.00143	-0.00171	6.5E-05
249	0.000881	-0.00112	-0.00265	-0.00215	-0.0013	-0.00196	0.000514

	Control	Dil+A	Dil+AP	Dil+APL	CT+Dil+A	CT+Dil+AP	CT+Dil+APL
250	0.000802	-0.00162	-0.00259	-0.00264	-0.00124	-0.00199	-0.00013
251	0.000763	-0.00091	-0.00235	-0.0026	-0.00127	-0.00167	-0.00028
252	0.000347	-0.00103	-0.00295	-0.00288	-0.00099	-0.00189	0.000238
253	0.000816	-0.00148	-0.00292	-0.00315	-0.00068	-0.00224	-1E-04
254	0.000374	-0.00152	-0.0031	-0.00301	-0.00077	-0.00194	0.000173
255	0.000276	-0.00108	-0.00378	-0.00303	-0.00109	-0.00183	-0.00044
256	0.000428	-0.00116	-0.00349	-0.00337	-0.00111	-0.00161	-0.00037
257	0.00029	-0.00151	-0.00343	-0.00323	-0.00075	-0.0017	-0.0008
258	0.000612	-0.00143	-0.00368	-0.00303	-0.00095	-0.00201	-0.00094
259	0.000379	-0.00128	-0.00381	-0.00307	-0.00124	-0.00218	-0.00041
260	0.000549	-0.0011	-0.00397	-0.0036	-0.00084	-0.0021	-0.00142
261	0.000697	-0.00112	-0.00408	-0.00339	-0.00073	-0.0023	-0.00189
262	0.000821	-0.00144	-0.00403	-0.0036	-0.00122	-0.00227	-0.00181
263	0.000553	-0.00175	-0.00451	-0.00324	-0.00134	-0.00244	-0.00169
264	0.00029	-0.00107	-0.00444	-0.00343	-0.00121	-0.00189	-0.00216
265	0.000205	-0.00128	-0.00436	-0.00352	-0.0013	-0.00203	-0.00223
266	0.00055	-0.00133	-0.00449	-0.00373	-0.00109	-0.00222	-0.00234
267	0.000616	-0.00147	-0.00457	-0.00333	-0.00123	-0.00239	-0.00273
268	0.000378	-0.00179	-0.00462	-0.00355	-0.00122	-0.00251	-0.00242
269	0.000216	-0.0018	-0.00469	-0.00333	-0.00113	-0.00219	-0.00265
270	0.000413	-0.00152	-0.00517	-0.00364	-0.00117	-0.00242	-0.00316
271	0.000399	-0.00183	-0.00508	-0.0034	-0.00129	-0.00258	-0.00346
272	1.43E-05	-0.00148	-0.00505	-0.00328	-0.00106	-0.00264	-0.00363
273	0.000391	-0.00167	-0.00534	-0.00355	-0.00087	-0.00273	-0.00365
274	0.000176	-0.00164	-0.00519	-0.00328	-0.00108	-0.00255	-0.00392

	Control	Dil+A	Dil+AP	Dil+APL	CT+Dil+A	CT+Dil+AP	CT+Dil+APL
275	0.00011	-0.00187	-0.0051	-0.00328	-0.00139	-0.00253	-0.00405
276	0.000193	-0.00248	-0.00515	-0.00317	-0.00131	-0.00287	-0.00392
277	0.000461	-0.00226	-0.00495	-0.00312	-0.00129	-0.0031	-0.00399
278	0.000212	-0.00176	-0.00525	-0.00333	-0.00128	-0.00361	-0.00365
279	5.71E-05	-0.00201	-0.00489	-0.00333	-0.00134	-0.00303	-0.00354
280	0.000249	-0.00201	-0.00533	-0.00315	-0.00099	-0.0032	-0.0041
281	-0.00011	-0.00216	-0.00516	-0.00297	-0.00112	-0.00316	-0.00376
282	5.24E-05	-0.00228	-0.00508	-0.0032	-0.00125	-0.00307	-0.00347
283	-8.1E-05	-0.00156	-0.00516	-0.00344	-0.00116	-0.00319	-0.00379
284	1.62E-05	-0.00204	-0.00514	-0.00311	-0.00098	-0.00302	-0.0038
285	-1.7E-05	-0.00174	-0.00529	-0.00287	-0.00152	-0.00323	-0.00344
286	-0.00025	-0.00173	-0.00517	-0.00335	-0.00136	-0.00351	-0.00349
287	-0.00027	-0.00233	-0.00533	-0.00291	-0.00159	-0.00288	-0.00368
288	-0.00047	-0.0023	-0.0055	-0.00284	-0.00144	-0.00317	-0.00367
289	-0.0001	-0.00187	-0.00516	-0.00307	-0.00165	-0.00341	-0.00368
290	0.000184	-0.002	-0.00559	-0.00283	-0.0017	-0.00322	-0.00353
291	7.05E-05	-0.00171	-0.00544	-0.00293	-0.00148	-0.00334	-0.00327
292	-8.7E-05	-0.0022	-0.00539	-0.00272	-0.00198	-0.00336	-0.00312
293	9.71E-05	-0.00222	-0.00511	-0.00253	-0.00188	-0.00302	-0.00357
294	-7.1E-05	-0.00223	-0.00514	-0.00276	-0.00225	-0.00309	-0.00333
295	-3.5E-05	-0.00198	-0.00511	-0.00251	-0.00169	-0.00317	-0.00283
296	-0.00013	-0.0018	-0.00542	-0.00241	-0.00155	-0.0031	-0.00313
297	-0.00031	-0.0019	-0.00533	-0.00225	-0.00172	-0.00244	-0.00333
298	3.81E-05	-0.00238	-0.00512	-0.00253	-0.00215	-0.00275	-0.00268
299	9.52E-06	-0.00223	-0.00538	-0.00201	-0.00156	-0.00291	-0.00341

	Control	Dil+A	Dil+AP	Dil+APL	CT+Dil+A	CT+Dil+AP	CT+Dil+APL
300	-0.00039	-0.0022	-0.00584	-0.00268	-0.00163	-0.00288	-0.00308
301	-5.5E-05	-0.00185	-0.00533	-0.00233	-0.00158	-0.00275	-0.00283
302	1.39E-18	-0.00194	-0.00531	-0.00217	-0.00157	-0.00237	-0.00302
303	-0.0003	-0.00201	-0.00524	-0.00201	-0.00173	-0.00221	-0.00295
304	-0.00026	-0.00212	-0.00495	-0.00257	-0.00183	-0.00229	-0.00242
305	-0.00013	-0.00163	-0.00488	-0.00205	-0.00167	-0.0024	-0.00216
306	6.48E-05	-0.0018	-0.00458	-0.00227	-0.00136	-0.00168	-0.00257
307	2.57E-05	-0.00196	-0.00486	-0.00212	-0.002	-0.00136	-0.00293
308	-0.00026	-0.00165	-0.00481	-0.00185	-0.002	-0.00162	-0.00271
309	2.19E-05	-0.0021	-0.00472	-0.00189	-0.00202	-0.00175	-0.00265
310	-7.3E-05	-0.00187	-0.00447	-0.0024	-0.00182	-0.0016	-0.00248
311	-8.9E-05	-0.00208	-0.00421	-0.00219	-0.00181	-0.0014	-0.00242
312	-1.6E-05	-0.00185	-0.00395	-0.00217	-0.00169	-0.00172	-0.00249
313	0.000132	-0.00182	-0.0041	-0.00232	-0.00165	-0.00161	-0.00293
314	-0.00018	-0.00184	-0.00411	-0.00239	-0.00169	-0.00141	-0.00267
315	-0.00032	-0.00167	-0.00406	-0.00213	-0.00162	-0.00171	-0.0026
316	-0.00039	-0.00201	-0.00387	-0.00227	-0.0015	-0.00156	-0.00282
317	-0.00051	-0.00182	-0.00397	-0.00203	-0.0016	-0.00168	-0.00291
318	-0.00067	-0.00178	-0.0039	-0.002	-0.00173	-0.00168	-0.00267
319	-0.00033	-0.00162	-0.004	-0.00216	-0.00121	-0.00189	-0.00323
320	-0.00057	-0.00191	-0.00361	-0.00227	-0.00147	-0.00162	-0.00315
321	-0.00062	-0.00175	-0.00379	-0.00237	-0.00142	-0.00167	-0.00301
322	-0.00069	-0.00178	-0.0039	-0.00228	-0.00121	-0.00175	-0.00296
323	-0.00079	-0.00185	-0.00357	-0.00219	-0.0015	-0.00166	-0.00305
324	-0.00068	-0.00229	-0.00371	-0.00244	-0.00147	-0.0018	-0.00252

	Control	Dil+A	Dil+AP	Dil+APL	CT+Dil+A	CT+Dil+AP	CT+Dil+APL
325	-0.00018	-0.00203	-0.00373	-0.00216	-0.00147	-0.00215	-0.00291
326	-0.00067	-0.00216	-0.00376	-0.00244	-0.00139	-0.00196	-0.00294
327	-0.00087	-0.00213	-0.00403	-0.0026	-0.0014	-0.00219	-0.00312
328	-0.00064	-0.00212	-0.00393	-0.00265	-0.00128	-0.00266	-0.00293
329	-0.0003	-0.00236	-0.0039	-0.00228	-0.00116	-0.00235	-0.00328
330	-0.00073	-0.00227	-0.00382	-0.00265	-0.00125	-0.00251	-0.00295
331	-0.0006	-0.00201	-0.00411	-0.00265	-0.00131	-0.00263	-0.003
332	-0.00072	-0.00187	-0.00432	-0.0024	-0.00103	-0.00262	-0.00327
333	-0.00087	-0.00201	-0.00418	-0.00276	-0.00125	-0.00266	-0.00324
334	-0.00103	-0.00184	-0.00407	-0.00305	-0.0013	-0.00234	-0.00304
335	-0.00077	-0.00228	-0.00447	-0.00312	-0.00135	-0.0025	-0.00327
336	-0.00045	-0.00238	-0.00468	-0.00313	-0.00156	-0.00299	-0.00311
337	-0.00068	-0.00207	-0.00494	-0.00284	-0.00168	-0.00299	-0.00289
338	-0.00053	-0.00221	-0.0049	-0.00327	-0.00172	-0.00259	-0.00336
339	-0.00069	-0.00202	-0.00482	-0.00304	-0.00117	-0.0028	-0.00357
340	-0.00103	-0.0023	-0.00521	-0.00317	-0.00147	-0.00272	-0.00332
341	-0.00059	-0.00208	-0.0055	-0.00305	-0.00123	-0.00273	-0.00332
342	-0.00076	-0.00249	-0.00551	-0.00337	-0.00148	-0.00264	-0.00377
343	-0.00101	-0.00229	-0.00505	-0.00308	-0.00131	-0.00262	-0.00351
344	-0.00098	-0.00181	-0.00497	-0.00361	-0.00157	-0.00282	-0.00358
345	-0.00092	-0.00178	-0.00567	-0.00341	-0.00156	-0.00293	-0.00418
346	-0.00061	-0.00183	-0.00502	-0.00392	-0.0019	-0.00289	-0.00375
347	-0.00092	-0.00233	-0.00499	-0.00388	-0.00157	-0.00264	-0.00346
348	-0.0008	-0.00251	-0.00474	-0.00369	-0.0013	-0.00249	-0.00361
349	-0.00054	-0.00198	-0.00472	-0.00341	-0.0016	-0.00255	-0.00346

	Control	Dil+A	Dil+AP	Dil+APL	CT+Dil+A	CT+Dil+AP	CT+Dil+APL
350	-0.00075	-0.00184	-0.00521	-0.00363	-0.00175	-0.00238	-0.00373
351	-0.0007	-0.00185	-0.00524	-0.00401	-0.00181	-0.00295	-0.00378
352	-0.00089	-0.00179	-0.00494	-0.00388	-0.00173	-0.00261	-0.0042
353	-0.00048	-0.0018	-0.00479	-0.00375	-0.00168	-0.00245	-0.00383
354	-0.00041	-0.0023	-0.00521	-0.00391	-0.00173	-0.00245	-0.00391
355	-0.00023	-0.00208	-0.0051	-0.00364	-0.00143	-0.00257	-0.00411
356	-0.00043	-0.00219	-0.00469	-0.00381	-0.00181	-0.00241	-0.00393
357	-0.0005	-0.00198	-0.0047	-0.0034	-0.00167	-0.00248	-0.00405
358	-0.00062	-0.0018	-0.00488	-0.00363	-0.00156	-0.00247	-0.00389
359	-7.7E-05	-0.00212	-0.0047	-0.00367	-0.00179	-0.00253	-0.00424
360	-0.00047	-0.00218	-0.0049	-0.00372	-0.00165	-0.00244	-0.00355
361	-0.00079	-0.00216	-0.00474	-0.00321	-0.00166	-0.0027	-0.00375
362	-0.00048	-0.00205	-0.00478	-0.00328	-0.00176	-0.00232	-0.00395
363	-0.00024	-0.00183	-0.00509	-0.00303	-0.0019	-0.00242	-0.00379
364	-1E-05	-0.0019	-0.00503	-0.00321	-0.00172	-0.00233	-0.00354
365	-0.00039	-0.00235	-0.00442	-0.00332	-0.00147	-0.00197	-0.00392
366	-0.0007	-0.00213	-0.0047	-0.00327	-0.00151	-0.00227	-0.00381
367	-0.00077	-0.0023	-0.00497	-0.00264	-0.00167	-0.00178	-0.00322
368	-0.00011	-0.0018	-0.00462	-0.00283	-0.00163	-0.00241	-0.00321
369	-0.00017	-0.00204	-0.00462	-0.00283	-0.00158	-0.00202	-0.00315
370	-0.00053	-0.00184	-0.0045	-0.00292	-0.00173	-0.00203	-0.00296
371	-0.0006	-0.00193	-0.00471	-0.00284	-0.00109	-0.00176	-0.00334
372	-0.00058	-0.0019	-0.00457	-0.00268	-0.00129	-0.00187	-0.00312
373	-0.00044	-0.0016	-0.00458	-0.00293	-0.00156	-0.00194	-0.00288
374	-0.00055	-0.00221	-0.00464	-0.00269	-0.00159	-0.00217	-0.00281

	Control	Dil+A	Dil+AP	Dil+APL	CT+Dil+A	CT+Dil+AP	CT+Dil+APL
375	-0.00093	-0.00149	-0.00458	-0.00285	-0.00142	-0.00202	-0.00306
376	-0.00057	-0.00175	-0.00416	-0.00255	-0.00158	-0.00163	-0.00259
377	-0.00012	-0.00179	-0.0042	-0.00232	-0.00157	-0.00177	-0.00255
378	-0.00077	-0.00161	-0.00379	-0.00251	-0.00127	-0.00236	-0.00288
379	-0.00077	-0.00182	-0.00401	-0.00247	-0.00163	-0.00176	-0.00267
380	-0.0003	-0.00197	-0.00374	-0.00227	-0.00126	-0.00138	-0.00269
381	-0.00022	-0.00152	-0.00384	-0.00232	-0.00111	-0.00186	-0.00282
382	8.1E-05	-0.00178	-0.00398	-0.00243	-0.00133	-0.00168	-0.00299
383	-0.0005	-0.00198	-0.00336	-0.00221	-0.00105	-0.00193	-0.00228
384	-0.00047	-0.00195	-0.00351	-0.00219	-0.00126	-0.00192	-0.00278
385	-0.00026	-0.00183	-0.0034	-0.00227	-0.00123	-0.00183	-0.00309
386	-0.00035	-0.00198	-0.00348	-0.00243	-0.00138	-0.00178	-0.00301
387	-0.00076	-0.00156	-0.00365	-0.00183	-0.00103	-0.00186	-0.00281
388	-0.00055	-0.00184	-0.00326	-0.00212	-0.00069	-0.00182	-0.00298
389	-0.00059	-0.00217	-0.00294	-0.00247	-0.00104	-0.00162	-0.00266
390	-0.00013	-0.00231	-0.00315	-0.00213	-0.00109	-0.00144	-0.0026
391	-0.0001	-0.00159	-0.00298	-0.0022	-0.00073	-0.00162	-0.00265
392	-0.00065	-0.00186	-0.00246	-0.00245	-0.00105	-0.00165	-0.00244
393	-0.00065	-0.00194	-0.0029	-0.00191	-0.00103	-0.00124	-0.00266
394	-0.00045	-0.00156	-0.0024	-0.00191	-0.00081	-0.00132	-0.00297
395	-0.00029	-0.00101	-0.00251	-0.00192	-0.00137	-0.00113	-0.0028
396	-0.00029	-0.00112	-0.00221	-0.00207	-0.00123	-0.0012	-0.00225
397	-0.00075	-0.00145	-0.0023	-0.00211	-0.00113	-0.00106	-0.0027
398	-0.00072	-0.0013	-0.00205	-0.00221	-0.00075	-0.00087	-0.00253
399	4.48E-05	-0.00127	-0.00243	-0.00196	-0.00101	-0.00082	-0.00242

	Control	Dil+A	Dil+AP	Dil+APL	CT+Dil+A	CT+Dil+AP	CT+Dil+APL
400	-0.00026	-0.00115	-0.00201	-0.00152	-0.00076	-0.00097	-0.00193
401	-0.00035	-0.00113	-0.00175	-0.00187	-0.001	-0.0009	-0.00204
402	-0.00048	-0.00145	-0.00181	-0.00184	-0.00092	-0.00061	-0.00175
403	-0.00017	-0.00166	-0.00175	-0.00167	-0.00064	-0.00081	-0.00146
404	-0.00026	-0.00117	-0.00171	-0.00153	-0.00068	-0.00043	-0.00217
405	-0.00038	-0.00121	-0.00143	-0.00133	-0.0008	-0.00057	-0.00205
406	-0.00062	-0.00135	-0.00152	-0.00151	-0.00068	-0.00068	-0.00173
407	-0.00031	-0.00146	-0.0012	-0.00127	-0.00064	-0.00038	-0.00209
408	-3.7E-05	-0.00114	-0.00124	-0.00165	-0.00053	-0.00036	-0.00172
409	-0.00028	-0.0012	-0.00117	-0.00168	-0.00073	-0.0003	-0.0017
410	-0.00056	-0.0008	-0.00082	-0.00149	-0.00073	-0.00077	-0.00176
411	-6.6E-05	-0.00088	-0.00062	-0.00177	-0.00041	-0.00066	-0.0021
412	-2.3E-05	-0.00101	-0.00111	-0.00147	-0.00046	-0.0002	-0.00172
413	-0.00012	-0.00108	-0.00064	-0.00145	-0.00062	-0.00037	-0.00167
414	-0.00028	-0.00079	-0.00077	-0.00151	-0.00018	-0.00048	-0.00147
415	-0.00041	-0.00101	-0.00065	-0.00168	-0.00045	-7.3E-05	-0.00112
416	-0.00025	-0.00074	-0.00097	-0.00141	-0.00065	0.000278	-0.00105
417	-9.5E-06	-0.00052	-0.00087	-0.00117	-0.00056	0.000242	-0.00119
418	-0.00011	-0.00074	-0.00078	-0.00119	-0.00021	-7.5E-05	-0.00087
419	-8.5E-05	-0.00054	-0.00088	-0.00159	-0.00048	-0.00015	-0.00055
420	-0.0003	-0.00082	-0.00062	-0.00128	-0.0002	-0.00026	-0.00099
421	0.00015	-0.00057	-0.00044	-0.00101	-0.00028	0.000169	-0.0009
422	-0.00012	-0.0004	-0.0004	-0.00083	-0.00011	0.000131	-0.0006
423	-0.0004	-0.00024	-0.00051	-0.00107	-0.00031	8.19E-05	-0.00048
424	-0.00024	-0.00023	-0.00056	-0.00096	3.87E-05	-4E-05	-0.00105

	Control	Dil+A	Dil+AP	Dil+APL	CT+Dil+A	CT+Dil+AP	CT+Dil+APL
425	-0.00011	-0.00045	-0.00026	-0.00067	-0.00014	-4.6E-05	-0.00036
426	0.000337	-0.00062	-2.8E-05	-0.00055	0.000167	0.000208	-0.00055
427	2.76E-05	-0.0001	-0.00012	-0.00047	-6.1E-05	0.000287	-0.00067
428	0.00011	-0.00019	-0.0003	-0.00061	-0.00014	-8.7E-05	-0.00034
429	9.14E-05	-7E-05	-0.00026	-0.00037	0.000126	0.000192	-4.9E-05
430	0.000568	3.14E-05	-0.00028	-0.0002	0.000164	0.000261	-0.00055
431	0.000257	-3.5E-05	-0.00026	-0.00024	0.000273	0.000352	-0.00064
432	0.000186	5.24E-05	-6.8E-05	-0.00037	-5.7E-06	0.000469	1E-04
433	0.000555	8.38E-05	4E-05	-0.0002	0.000201	0.000412	-9.8E-05
434	0.000536	2.48E-05	0.000133	-0.00013	0.000194	0.000534	-2.3E-05
435	0.000524	7.62E-06	0.000267	1.33E-05	0.000219	0.000763	9.08E-05
436	0.000666	5.71E-05	1.58E-05	-0.00011	0.000279	0.000395	5E-05
437	0.000283	0.000261	2.17E-05	-4E-05	0.000231	0.000545	0.000162
438	0.000202	-0.00018	3.5E-05	-0.00029	0.000151	0.000858	0.000533
439	0.000538	7.71E-05	0.000624	0.00024	-0.00015	0.000814	0.000558
440	0.000639	0.000251	0.00045	0.00012	-7.2E-05	0.000694	0.000432
441	0.000615	0.000646	0.000645	0.00032	0.000143	0.001144	0.000481
442	0.001032	0.00046	0.000666	0.00032	-0.00021	0.001144	0.001192
443	0.000966	0.000213	0.000323	0.00016	-5.5E-05	0.001232	0.000929
444	0.000924	0.00051	0.000997	0.0004	0.000346	0.001492	0.000863
445	0.000644	0.00063	0.001228	0.00028	0.000176	0.001702	0.001235
446	0.000751	0.00084	0.000803	0.00024	0.000406	0.001551	0.001246
447	0.000652	0.001014	0.000757	0.000133	0.000547	0.001308	0.001023
448	0.000822	0.000622	0.000757	0.000653	0.000279	0.001845	0.001303
449	0.000755	0.0011	0.000762	0.000453	0.000291	0.001602	0.001601

	Control	Dil+A	Dil+AP	Dil+APL	CT+Dil+A	CT+Dil+AP	CT+Dil+APL
450	0.000746	0.000512	0.000888	0.000573	0.000301	0.001515	0.00114
451	0.000597	0.000799	0.001003	0.00092	3.11E-05	0.001812	0.001911
452	0.001272	0.00125	0.001089	0.0012	0.000173	0.001978	0.001569
453	0.000769	0.001295	0.001203	0.0012	0.000268	0.00181	0.001806
454	0.00101	0.001132	0.000872	0.000987	0.000376	0.002364	0.001721
455	0.000643	0.001165	0.001125	0.00108	0.000203	0.00223	0.002223
456	0.00139	0.000796	0.001017	0.000973	0.000519	0.001969	0.001962
457	0.001389	0.000348	0.001342	0.000987	0.000818	0.001996	0.001729
458	0.00137	0.000906	0.001428	0.001293	0.000732	0.002532	0.002177
459	0.001226	0.001123	0.001185	0.001373	0.000458	0.002039	0.002014
460	0.001856	0.000976	0.001139	0.00096	0.000586	0.002226	0.00157
461	0.001593	0.001141	0.001394	0.00144	0.001089	0.002547	0.002059
462	0.00138	0.000858	0.001312	0.001613	0.000547	0.002403	0.002137
463	0.001114	0.001187	0.001386	0.001693	0.000823	0.002205	0.001429
464	0.001517	0.001874	0.001433	0.002093	0.000469	0.002675	0.002133
465	0.001618	0.001539	0.001448	0.001987	0.000777	0.002764	0.002464
466	0.001394	0.001317	0.001369	0.00216	0.001204	0.002372	0.001598
467	0.000998	0.001111	0.001632	0.001907	0.000971	0.002466	0.001963
468	0.001428	0.001213	0.001446	0.00176	0.000637	0.00282	0.002435
469	0.001804	0.001471	0.001823	0.00188	0.000829	0.002488	0.001988
470	0.001201	0.001411	0.002054	0.001613	0.001091	0.002586	0.002651
471	0.001292	0.00147	0.001918	0.001933	0.000872	0.002594	0.002852
472	0.001257	0.00153	0.001853	0.00184	0.00111	0.002994	0.002686
473	0.001861	0.001753	0.002251	0.002133	0.001439	0.003268	0.00226
474	0.001656	0.001604	0.002274	0.001933	0.001335	0.003248	0.002903

	Control	Dil+A	Dil+AP	Dil+APL	CT+Dil+A	CT+Dil+AP	CT+Dil+APL
475	0.001551	0.001811	0.002724	0.002333	0.001341	0.003243	0.002223
476	0.001419	0.001763	0.002562	0.00192	0.00172	0.003463	0.002614
477	0.001717	0.002175	0.00307	0.00208	0.002421	0.003454	0.002749
478	0.002145	0.001947	0.002448	0.00208	0.00201	0.003275	0.003048
479	0.002091	0.001968	0.002854	0.002013	0.002144	0.003179	0.003041
480	0.001735	0.001908	0.00316	0.002053	0.002386	0.003669	0.003051
481	0.001784	0.002643	0.003445	0.002267	0.002412	0.004245	0.003614
482	0.00145	0.00283	0.003442	0.0026	0.002459	0.004269	0.003241
483	0.001609	0.002568	0.00337	0.0028	0.002354	0.004224	0.003414
484	0.001286	0.002388	0.003842	0.00248	0.00208	0.00441	0.003852
485	0.001293	0.002546	0.003603	0.003027	0.002621	0.004748	0.003914
486	0.001812	0.002863	0.004629	0.00312	0.002512	0.004574	0.003474
487	0.00209	0.003456	0.004331	0.002893	0.002542	0.005132	0.003858
488	0.002003	0.00297	0.004527	0.003053	0.002799	0.005094	0.004217
489	0.001983	0.003423	0.004682	0.00316	0.003205	0.005348	0.004116
490	0.002207	0.003698	0.005376	0.003133	0.003232	0.005453	0.004443
491	0.00219	0.003563	0.005478	0.00348	0.003371	0.005929	0.005068
492	0.002209	0.00382	0.005595	0.00388	0.003491	0.005974	0.004989
493	0.002369	0.003942	0.006442	0.004093	0.003466	0.006368	0.005523
494	0.002468	0.003956	0.006668	0.004693	0.003981	0.006656	0.005742
495	0.002752	0.004308	0.006857	0.004893	0.003751	0.007084	0.005988
496	0.002685	0.004436	0.007223	0.004813	0.004603	0.007224	0.005931
497	0.002722	0.004267	0.007679	0.00528	0.00482	0.00765	0.006443
498	0.002918	0.00472	0.008278	0.00572	0.004499	0.008414	0.006998
499	0.003354	0.005154	0.00897	0.00652	0.005129	0.008703	0.007064

APPENDIX # 2

STRAIN COMPUTATION CODES

```
%PROGRAM # 1
2 %DATED - MARCH 29,2010
3 %COMMENTED BY - MURALIDHAR PADALA
4 %CODE TO CONVERT THE SELECTED SERIES OF TIFF IMAGES TO THE FORMAT SUITABLE
5 %FOR FURTHER PROCESSING USING THE MARKER CODE
6 %Eg. If an series of images for a valve in which marker analysis is desired
7 %to be performed begins from 'a010.tif' and ends at 'a100.tif', this code
8 %converts the series to start at 'new_000.tif' and end at 'new_090.tif'
9
10 % Input the string portion of the image sequence before conversion
11 % Input the first file number and the total number of files in the sequence
12 stringer=input('Please enter string portion of file name: ','s');
13 number=input('Please enter first file number: ','s');
14 number2=input('Please enter the total number of files: ','s');
15 num=str2num(number);
16 num2=str2num(number2);
17 num1=num-1;
18 tiffer=('.tif');
19
20 % A loop to change the title of the files to the new format until the last
21 % file number is reached.
22 for ind=num:num+num2,
23 newnum=int2str(ind);
24 if ind < 10
25 title1=strcat(stringer,'00',newnum,tiffer);
26 elseif ind < 100
27 title1=strcat(stringer,'0',newnum,tiffer);
28 else
29 title1=strcat(stringer,newnum,tiffer);
30 end
31 image1=imread(title1,'tiff');
32 newernum=ind-num1;
33 newtitle1=sprintf('set/new_%d.tif',newernum);
34 imwrite(image1,newtitle1,'tiff');
35 end;
```

```
1 %PROGRAM # 2
2 %DATED - MARCH 29,2010
3 %COMMENTED BY - MURALIDHAR PADALA
4 %Program to digitize the markers and obtain their [X,Y] coordinates from
5 %a sequence of images. This program loads every 10th image in a sequence of
6 %images, and the markers are manually digitized on these frames. A maximum
7 %of 32 markers can be tracked at a time on each frame.
8
9 % Input Arguments
10 fprintf(1,'Welcome to the heart valve marker tracking interface...\n');
11 fprintf(1,'\n');
12 % Enter the number of markers to be tracked on each frame
13 points=input('Please enter the number of points to be tracked (1-32): ');
14 fprintf(1,'\n');
15 % Enter the number of images on which the markers need to tracked. The
16 % number of frames are always a multiple of 10 + 1 as the index on the
17 % image sequence starts from 000.
18 last=input('Please enter the number of the last image to be processed \n(remember the
total number must be a multiple of 10 plus 1 like 51 or 131): ');
19 fprintf(1,'\n');
20 crap=input('Thank you, please press return...');
21 first=1;
22 total=last-first+1;
23 offset=first-1;
24 save set/info total points first last offset;
25 clear all;
26 load set/info;
27 %ray=zeros(16,2,2);
28
29 % Parameters that set the acceleration for the markers in the image
30 % sequence. acc1 is the acceleration parameter for the first half of the
31 % images and acc2 is the acceleration parameter for the second half of the
32 % images. The values for acc1 and acc2 fall within [-2,2] with negative
33 % indicating deceleration and + indicating acceleration.
34 acc1=1;
35 acc2=1;
36
37 %Number of first file
38 firstnum=1;
39 %Number of last file
40 secondnum=total;
41
42 % A continuous loop to select every 10th image from the total image
43 % sequence, and to track individual markers on each of these images.
44 for n1=firstnum:10:secondnum,
```

```
45 ind1=((n1-1)/10)+1;
46 small=12;
47 fact=small/2;
48
49 %Initialize number of points to be tracked
50 % set image titles
51 title1=sprintf('set/new_%d.tif',n1);
52
53 %Read images
54 image1=imread(title1,'tiff');
55
56 %Initalize point vectors
57 mag=((secondnum-firstnum)/10)+1;
58 [X1]=zeros(mag,1);
59 [Y1]=zeros(mag,1);
60
61 %Show images and input point locations
62 figure(1);
63 imshow(image1);
64 f=gcf;
65 set(f,'Position',[1 1 1200 750]);
66 [Y1,X1]=ginput(points);
67 X1=round(X1);
68 Y1=round(Y1);
69
70 ray(1:points,1,ind1)=X1;
71 ray(1:points,2,ind1)=Y1;
72
73 end;
74
75 % Loop to write the marker coordinates to a file titled 'raynew'.
76 for val1=1:2,
77 for val2=1:points,
78 int=interp(ray(val2,val1,1:mag),10,2,.1);
79 raynew(val2,val1,1:secondnum)=int(1:secondnum);
80 end;
81 end;
82
83 raynewer=raynew;
84
85 save set/raynewer raynewer;
86
87
```

```
1 %PROGRAM # 3
2 %DATED - MARCH 29,2010
3 %COMMENTED BY - MURALIDHAR PADALA
4 %Program to read the digitized 2D markers and review them to assess the
5 %accurary of marker tracking
6
7 % Input the raynewer dataset to read in the marker coordinates
8 load set/raynewer;
9 load set/info;
10
11 % Use acc1 and acc2 to either decelerate or accelerate the marker
12 % progression between images. acc1 is to be used for the first half of the
13 % images and acc2 for the second half.
14
15 acc1=0;
16 acc2=0;
17
18 %load set/raynew;
19 %raynewer=raynew;
20
21 for val1=1:2,
22 for val2=1:points,
23 for val3=1:((secondnum-1)/2),
24 raynewer(val2,val1,val3)=(raynew(val2,val1,val3+1)-raynew(val2,val1,val3))
*acc1+raynew(val2,val1,val3);
25 end;
26 end;
27 end;
28
29 for val1=1:2,
30 for val2=1:points,
31 for val3=(((secondnum-1)/2)+1):secondnum-1,
32 raynewer(val2,val1,val3)=(raynew(val2,val1,val3+1)-raynew(val2,val1,val3))
*acc2+raynew(val2,val1,val3);
33 end;
34 end;
35 end;
36
37
38
39
40 for big=1:total,
41
42 big1=big+offset;
43
```

```
% set image titles
title1=sprintf('set/new_%d.tif',big1);


%read images
image1=imread(title1,'tiff');

X=raynewer(1:points,1,big);
Y=raynewer(1:points,2,big);

figure(6);
imshow(image1);
hold on;

for np=1:points,

figure(6);
hold on;
 fill([Y(np,1)-2  Y(np,1)-2  Y(np,1)+2  Y(np,1)+2],[X(np,1)-2  X(np,1)+2  X(np,1)+2
X(np,
1)-2],'r');
end;
hold off;

P1=0;
[P1 P2]=ginput(1);
if (~isempty([P1 P2])),
[Y1,X1]=ginput(points);
raynewer(1:points,1,big)=X1;
raynewer(1:points,2,big)=Y1;
end;

end;

raynewest=raynewer;
save set/raynewest raynewest;


```

```
% PROGRAM # 4
% DATED - MARCH 29,2010
% COMMENTED BY - MURALIDHAR PADALA
% Program to transform the marker coordinates from the image coordinates
% into actual X-Y cartesian coordinates.

load set/info;
stringer=input('Please enter first frame number: ','s');
num=str2num(stringer);
num2=total+num;
fid=fopen('set/data.txt','w');
fprintf(fid,'%d\t',num);
fprintf(fid,'%d\n',num2-1);

load set/raynewest;
raynewest=round(raynewest);
for n1=1:total,
for n3=1:points,

mat=raynewest(n3,2,n1);
fprintf(fid,'%d\t',mat);
mat=raynewest(n3,1,n1);
fprintf(fid,'%d\n',1025-mat);

end;
end;


fclose(fid);

disp('finished');
```

```
%PROGRAM # 5
2 %This program computes 3D coordinates (X,Y,Z) from 2D coordinates (U,V) by
Direct
3 %Linear Transform (DLT). The program utilizes the functions dltfu.m and reconfu.m
4 %originally written by Christoph Reinschmidt from the University of Calgary ().
5 %
6 %There are 4 phases: Loading the 2D data sets, Calibrating camera coordinates,
7 %Computing 3D coordinates, and Writing output file.
8 %
9 %(1)Loading 2D data sets- The program will ask for 2 filenames. These are where
10 %the 2D coordinates are stored for each camera. Press ENTER for defaults (acoord
11 %& bcoord).
12 %
13 %(2)Calibrating camera coordinates- The program will ask for 3 filenames. These
14 %are where the 2D coordinates of cube corners (acal & bcal) and known 3D
15 %coordinates of cube (reference) are stored.
16 %
17 %(3)Computing 3D coordinates- X,Y,Z coordinates will be calculated using the
18 %least squares method.
19 %
20 %(4)Writing output file- The program will ask for a filename for the output
21 %(markers3d). The program will also ask for 2 pressure files (ventricular and
22 %transmitral). The output will be in the following format:
23 % Row 1: #frames, #markers
24 % Row n: frame#, time, LVpressure, TMpressure
25 % Row n+1: X,Y,Z
26
27                %_____END                HELP
TEXT_____
28 % 3D location calc using part of KineMat demo
29 % with addition of writing text file
30 % May 27, 2001
31 %This revision allows the operator to input filenames to be used.
32 %This revision allows the 2D marker data to be read from separate files.
33 %This revision adds frame number data to input and output marker files.
34 %This revision sets default file names.
35 %This revision reformats the output file. 7/5/01
36
37 clc
38 disp(' ')
39 disp('3D RECONSTRUCTION')
40 disp('This program executes the 3d reconstruction routine.')
41 disp('camera coefficients will be calculated and location of markers')
42 disp('can be extracted.')
43 disp(' ');
```

```
44 disp('Press ENTER for filename defaults.')
45 disp(' ')
46 disp(' ')
47
48 disp('_____(1) LOADING 2D DATA SET _____')
49 disp(' ')
50 filename2dA=input('Enter the filename of the 2D marker coordinates for camera A (e.g.
acoord.txt)> ', 's');
51 filename2dB=input('Enter the filename of the 2D marker coordinates for camera B (e.g.
bcoord.txt)> ', 's');
52 if isempty(filename2dA) filename2dA='acoord.txt'; end %default file names
53 if isempty(filename2dB) filename2dB='bcoord.txt'; end
54
55 disp(' ')
56 disp('Loading marker data...')
57 disp(' ')
58 d1=load(filename2dA); d2=load(filename2dB);
59
60 %storing the frame numbers (entered in the first row of the data sets)
61 %and removing the row from the matrix
62 frmlim=[d1(1,:); d2(1,:)]; %row1 contains frame limits
for camera1, row2 for camera2
63 d1=d1(2:size(d1,1),:); d2=d2(2:size(d2,1),:);
64
65 mkrnum=size(d2,1)/(frmlim(2,2)-frmlim(2,1)+1); %mrknum is the number of markers per
frame (i.e. 9, 16)
66
67 %cropping the larger matrix; matrices will not be the same size if a camera cannot see all markers
68 delta=(frmlim(1,:)-frmlim(2,:))*mkrnum; %delta is the difference between
rows
69
70 if delta(1) < 0 %the next 2 if statements
match frame numbers and matrix size
71 d1=d1(1-delta(1):size(d1,1),:);
72 else
73 d2=d2(1+delta(1):size(d2,1),:);
74 end
75
76 if delta(2) > 0 %this probably won't ever be
used (crops off back end)
77 d1=d1(1:size(d1,1)-delta(2),:);
```

```
78 else
79 d2=d2(1:size(d2,1)+delta(2),:);
80 end
81
82 frmlim=[max(frmlim(:,1)) min(frmlim(:,2))]; %redefine new frame limits
83 frmnum=frmlim(2)-frmlim(1)+1; %frmnum is the number of
frames
84
85 D=[d1 d2];
86 disp('done')
87 disp(' ')
88 disp(' ')
89
90 disp('_____(2) NORMALIZING CAMERA COORDINATES _____')
91 disp(' ')
92 filenameAcube=input('Enter the filename of the first calibration set (e.g. acal.txt)>
', 's');
93 filenameBcube=input('Enter the filename of the second calibration set (e.g. bcal.txt)>
', 's');
94 filenameref=input('Enter the filename of the reference coordinates (e.g. reference.
txt)> ', 's');
95 if isempty(filenameAcube) filenameAcube='acal.txt'; end
96 if isempty(filenameBcube) filenameBcube='bcal.txt'; end
97 if isempty(filenameref) filenameref='reference.txt'; end
98
99 disp(' ')
100 disp('Loading calibration data and computing DLT coefficients...')
101 acube=load (filenameAcube); bcube=load (filenameBcube);
reference=load(filenameref);
102 a1=dltfu(reference,acube);
103 a2=dltfu(reference,bcube);
104 A=[a1,a2];
105 disp(' ')
106 disp('done')
107 disp(' ')
108 disp(' ')
109
110 disp('_____(3) 3D RECONSTRUCTION _____')
111 disp(' ')
112 disp('3D reconstruction of marker coordinates using DLT coefficients...')
113 disp(' ')
114 H=[];
115
116 H=reconfu(A,D);
117
```

```
118 disp('done')
119 %disp(' ')
120 disp('Press any key to continue.')
121 pause
122 disp(' ')
123 disp(' ')
124
125 disp('_____(4) WRITING OUTPUT FILE _____');
126 disp(' ')
127 %OUTPUT filename
128 filename3d=input('Enter the filename for the OUTPUT (e.g. markers3D.txt)> ','s');
129 if isempty(filename3d) filename3d='markers3D.txt'; end
130
131 %Reading LV and TM pressure data
132  filenamePV=input('Enter the filename of the ventricular pressure data (e.g.
LVpq.txt)>
','s');
133 if isempty(filenamePV) filenamePV='LVpq.txt'; end %default filename
134 PV=load(filenamePV);
135
136  filenameTM=input('Enter the filename of the transmitral pressure data (e.g.
TMpq.txt)>
','s');
137 if isempty(filenameTM) filenameTM='TMpq.txt'; end %default filename
138 TM=load(filenameTM);
139 disp(' ');
140
141 %SYNCHRONIZE pressure
142 for h=frmlim(1):frmlim(2)
143 %P=[frame# time LVpressure TMpressure];
144 P(h-frmlim(1)+1,:)=[h PV(mod(h,250)*2+1,:) TM(mod(h,250)*2+1,2)];
145 end;
146
147 %WRITE the first row: [# of frames, # of markers];
148 [tempfile] = fopen(filename3d, 'wt');
149 count = fprintf(tempfile, '%d %d\n', frmnum, mkrnum);
150
151 %WRITE sets of data for each frame
152 [tempfile] = fopen(filename3d, 'at');
153 for f=1:frmnum
154 count = fprintf(tempfile, '\n%d %f %f %f\n', P(f,:));
155 Htemp=H((1+(f-1)*mkrnum):(f*mkrnum),1:3);
156 count = fprintf(tempfile, '%f %f %f\n', Htemp');
157 end;
158
```

```
159 fclose(tempfile);
160
161 disp(sprintf('Output is in %s.', filename3d))
162 disp('Please see help file for formatting.');
163 disp(' ')
164
165 disp('_____END OF PROGRAM _____')
166 disp(' ')
167
1 function [H] = reconfu(A,L)
2 %function [H] = reconfu(A,L)
3 % Description: Reconstruction of 3D coordinates with the use local (camera
4 % coordinates and the DLT coefficients for the n cameras).
5 % Input: - A file containing DLT coefficients of the n cameras
6 % [a1cam1,a1cam2...;a2cam1...]
7 % - L camera coordinates of points
8 % [xcam1,ycam1,xcam2,ycam2...;same at time 2]
9 % Output: - H global coordinates, residuals, cameras used
10 % [Xt1,Yt1,Zt1,residt1,cams_used@t1...; same for t2]
11 % Author: Christoph Reinschmidt, HPL, The University of Calgary
12 % Date: September, 1994
13 % Last change: November 29, 1996
14 % Version: 1.1
15
16 n=size(A,2);
17 % check whether the numbers of cameras agree for A and L
18 if 2*n~=size(L,2); disp('the # of cameras given in A and L do not agree')
19 disp('hit any key and then "try" again'); pause; break
20 end
21
22
23 H(size(L,1),5)=[0]; % initialize H
24
25 % _________Building L1, L2: L1 * G (X,Y,Z) = L2_____________________________
26
27 for k=1:size(L,1) %number of time points
28 q=[0]; L1=[]; L2=[]; % initialize L1,L2, q(counter of 'valid' cameras)
29 for i=1:n %number of cameras
30 x=L(k,2*i-1); y=L(k,2*i);
31 if ~(isnan(x) | isnan(y)) % do not construct l1,l2 if camx,y=NaN
32 q=q+1;
33 L1([q*2-1:q*2],:)=[A(1,i)-x*A(9,i), A(2,i)-x*A(10,i), A(3,i)-x*A(11,i);...
34 A(5,i)-y*A(9,i), A(6,i)-y*A(10,i), A(7,i)-y*A(11,i)];
35 L2([q*2-1:q*2],:)=[x-A(4,i);y-A(8,i)];
36 end
```

```
37 end
38
39 if (size(L2,1)/2)>1 %check whether enough cameras available (at least 2)
40 g=L1\L2; h=L1*g; DOF=(size(L2,1)-3);
41 avgres=sqrt(sum([L2-h].^2)/DOF);
42 else
43 g=[NaN;NaN;NaN]; avgres=[NaN];
44 end
45
46 %find out which cameras were used for the 3d reconstruction
47 b=fliplr(find(sum(reshape(isnan(L(k,:)),2,size(L(k,:),2)/2))==0));
48 if size(b,2)<2; camsused=[NaN];
49 else, for w=1:size(b,2), b(1,w)=b(1,w)*10^(w-1); end
50 camsused=sum(b');
51 end
52
53 H(k,:)=[g',avgres,camsused];
54 end
55
56
```

```
1
2
3 function [A,avgres] = dltfu(F,L,Cut)
4 % Description: Program to calculate DLT coefficient for one camera
5 % Note that at least 6 (valid) calibration points are needed
6 % function [A,avgres] = dltfu(F,L,Cut)
7 % Input: - F matrix containing the global coordinates (X,Y,Z)
8 % of the calibration frame
9 % e.g.: [0 0 20;0 0 50;0 0 100;0 60 20 ...]
10 % - L matrix containing 2d coordinates of calibration
11 % points seen in camera (same sequence as in F)
12 % e.g.: [1200 1040; 1200 1360; ...]
13 % - Cut points that are not visible in camera;
14 % not being used to calculate DLT coefficient
15 % e.g.: [1 7] -> calibration point 1 and 7
16 % will be discarded.
17 % This input is optional (default Cut=[])
18 % Output: - A 11 DLT coefficients
19 % - avgres average residuals (measure for fit of dlt)
20 % given in units of camera coordinates
21 %
22 % Author: Christoph Reinschmidt, HPL, The University of Calgary
23 % Date: January, 1994
24 % Last changes: November 29, 1996
```

```
25 % Version: 1.0
26 % References: Woltring and Huiskes (1990) Stereophotogrammetry. In
27 % Biomechanics of Human Movement (Edited by Berme and
28 % Cappozzo). pp. 108-127.
29
30 if nargin==2; Cut=[]; end;
31
32
33 m=size(F,1); Lt=L'; C=Lt(:);
34
35 for i=1:m
36 B(2*i-1,1) = F(i,1);
37 B(2*i-1,2) = F(i,2);
38 B(2*i-1,3) = F(i,3);
39 B(2*i-1,4) = 1;
40 B(2*i-1,9) =-F(i,1)*L(i,1);
41 B(2*i-1,10) =-F(i,2)*L(i,1);
42 B(2*i-1,11) =-F(i,3)*L(i,1);
43 B(2*i,5) = F(i,1);
44 B(2*i,6) = F(i,2);
45 B(2*i,7) = F(i,3);
46 B(2*i,8) = 1;
47 B(2*i,9) =-F(i,1)*L(i,2);
48 B(2*i,10) =-F(i,2)*L(i,2);
49 B(2*i,11) =-F(i,3)*L(i,2);
50 end
51
52 % Cut the lines out of B and C including the control points to be discarded
53 Cutlines=[Cut.*2-1, Cut.*2];
54 B([Cutlines],:)=[];
55 C([Cutlines],:)=[];
56
57 % Solution for the coefficients
58 A=B\C;
59 D=B*A;
60 R=C-D;
61 res=norm(R); avgres=res/size(R,1)^0.5;
62
```

APPENDIX # 3

COMPUTER AIDED DESIGN DRAWINGS

Figure A.1 – C-ring force transducer CAD drawing

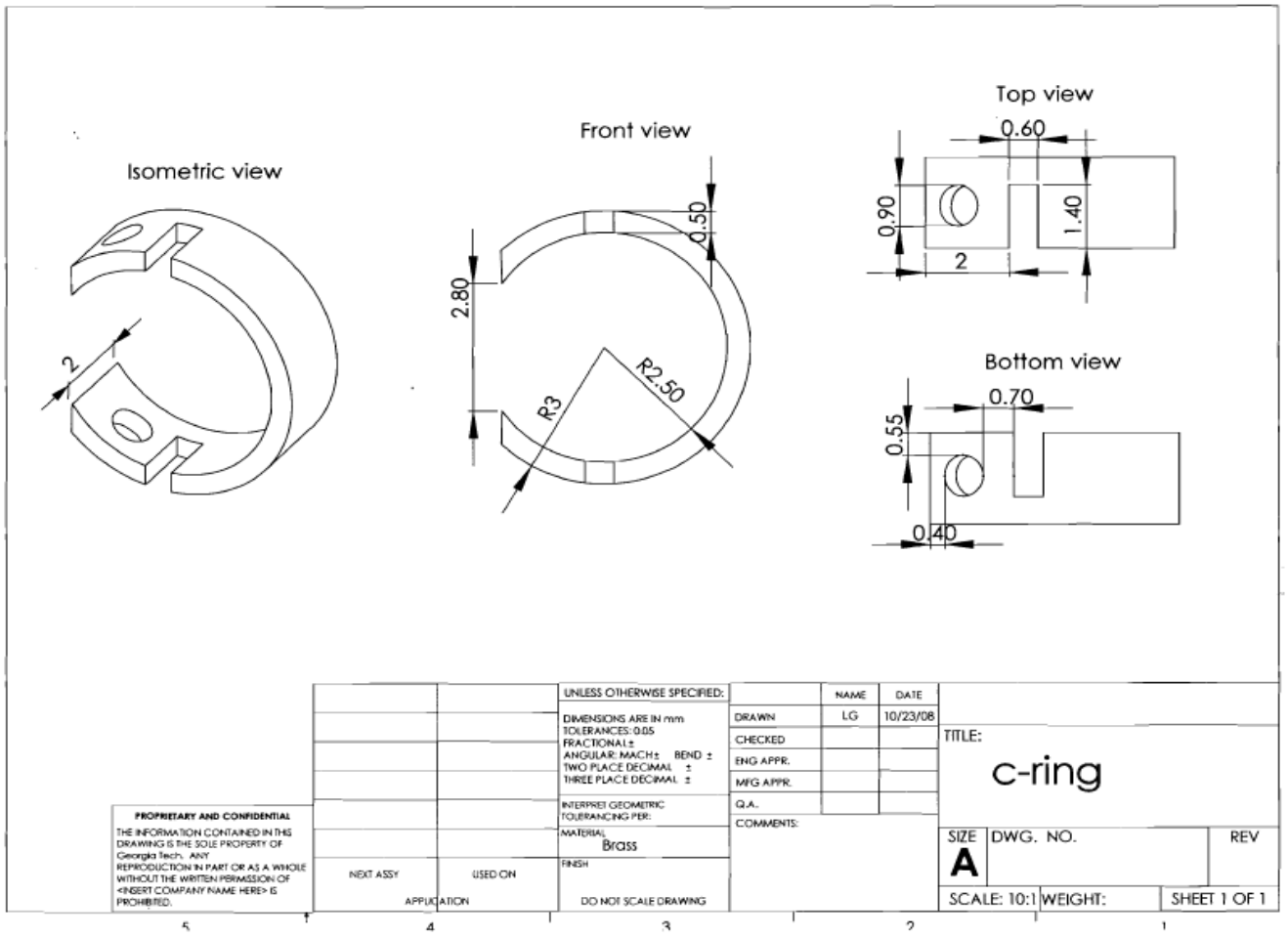

Figure A. 2 Papillary Muscle Displacement Gear System CAD Drawing

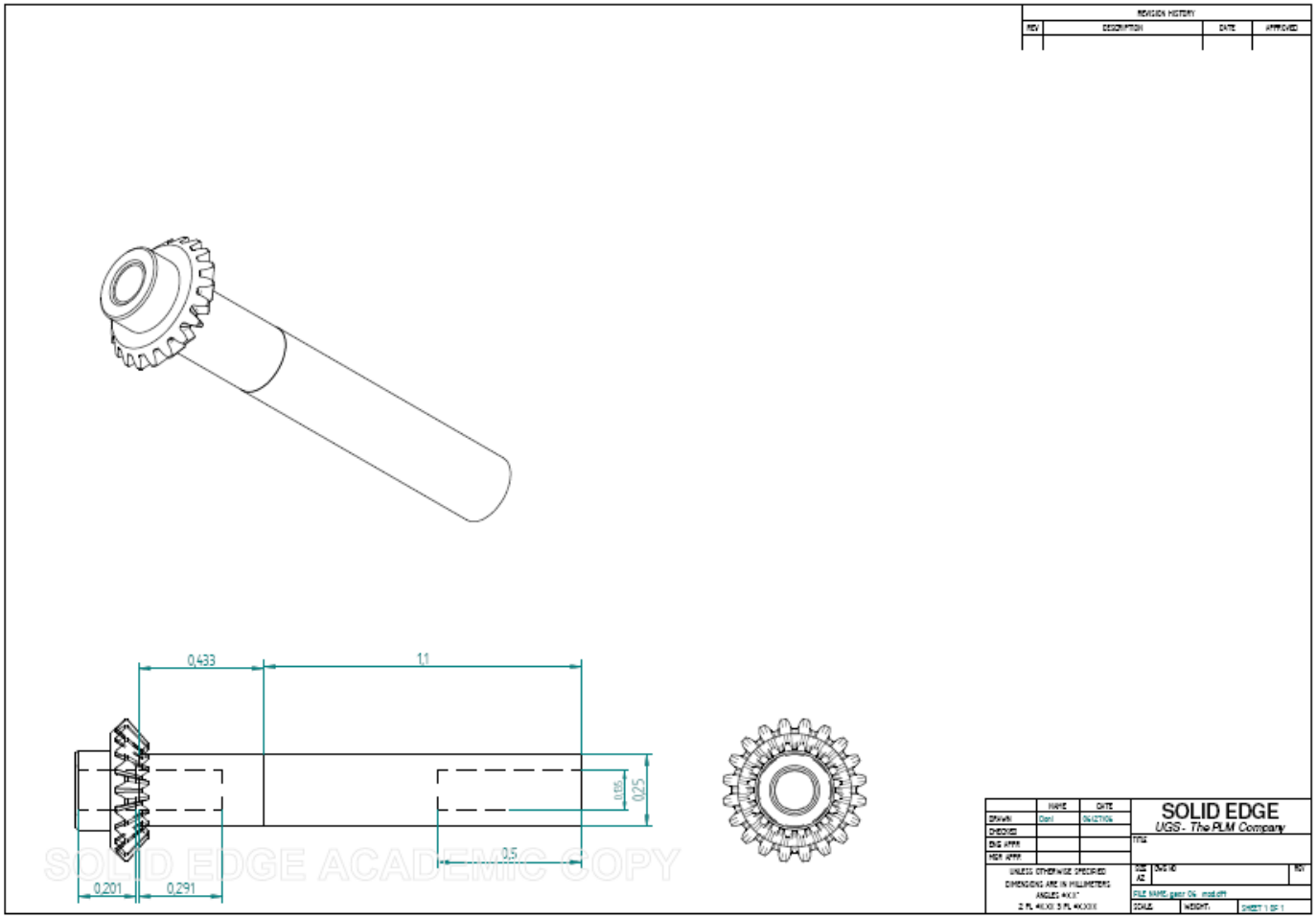

Figure A.3 Papillary Gear Movement Shaft

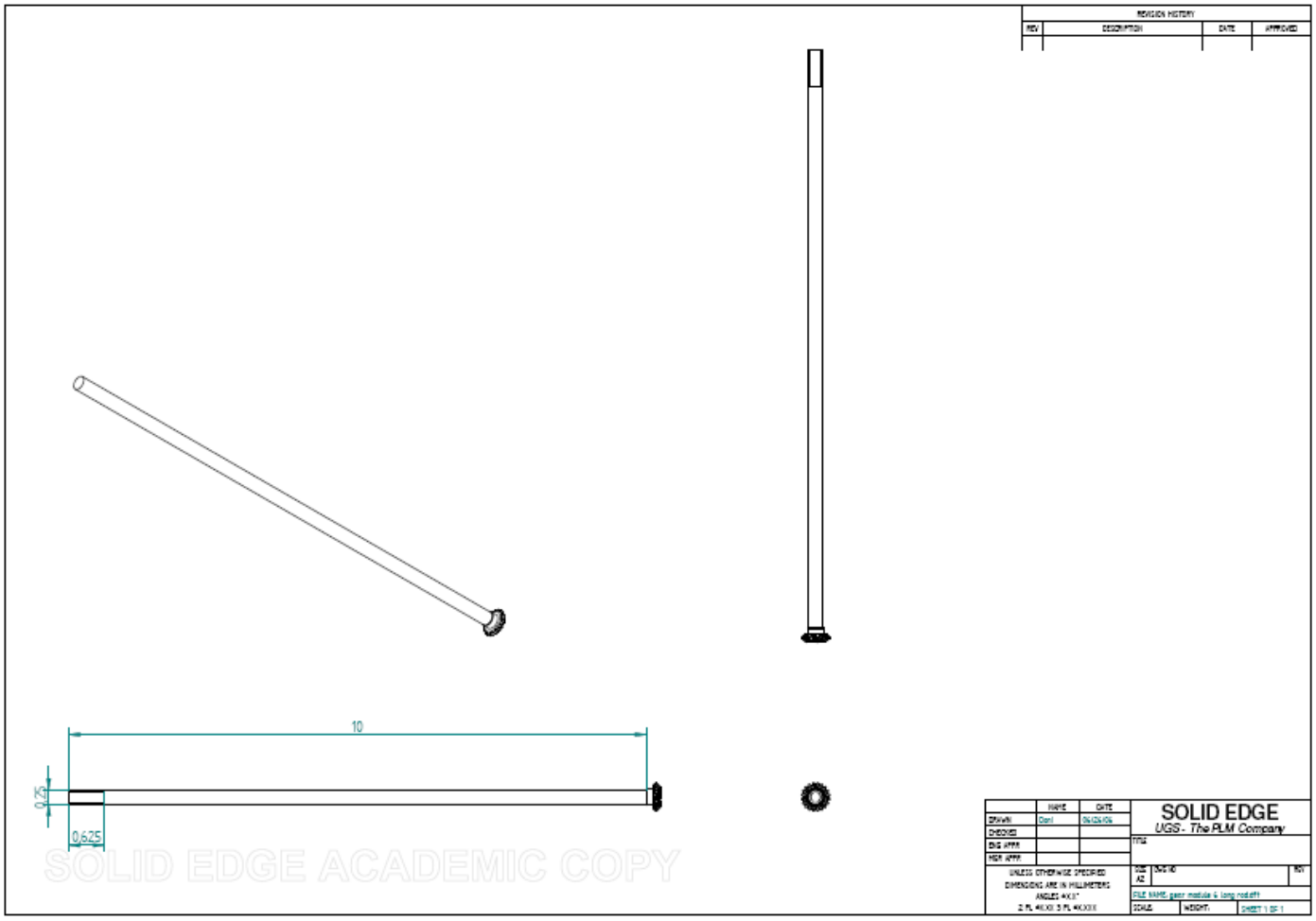

Figure A.4 Papillary Gear Outer Cylinder

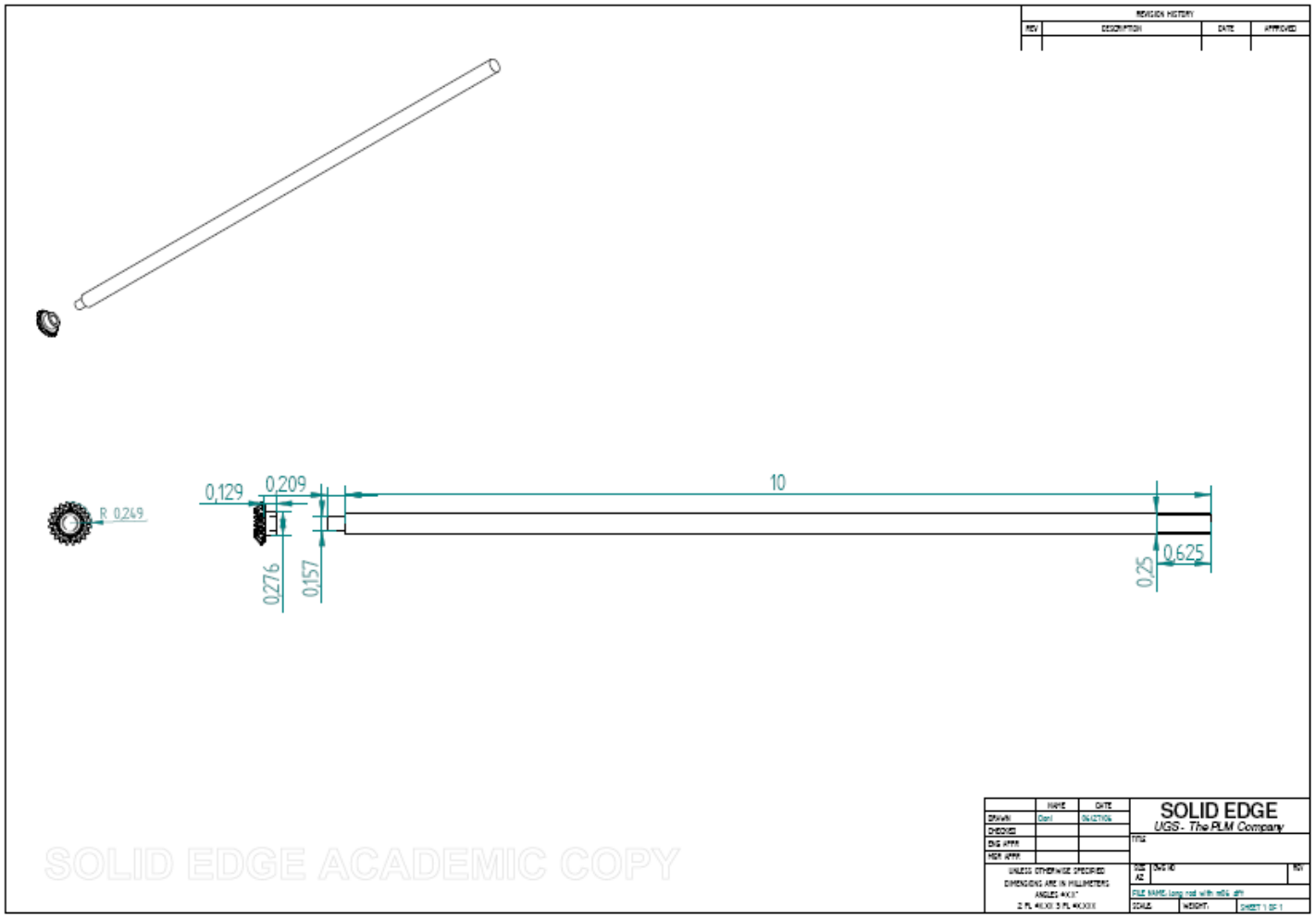

Figure A. 5 Papillary Muscle Outer Structure

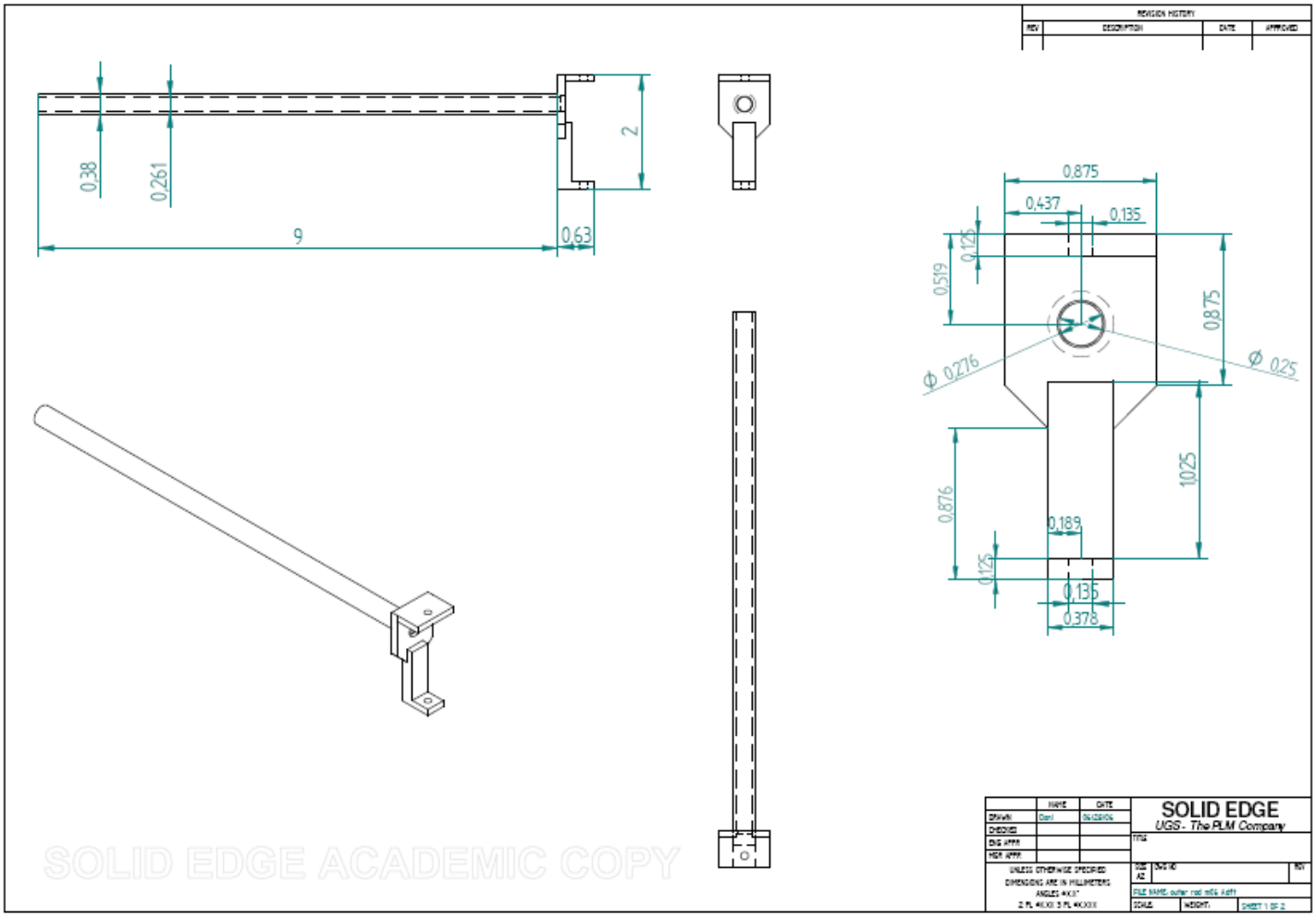

Figure A.6 Papillary Muscle Holder CAD Drawing

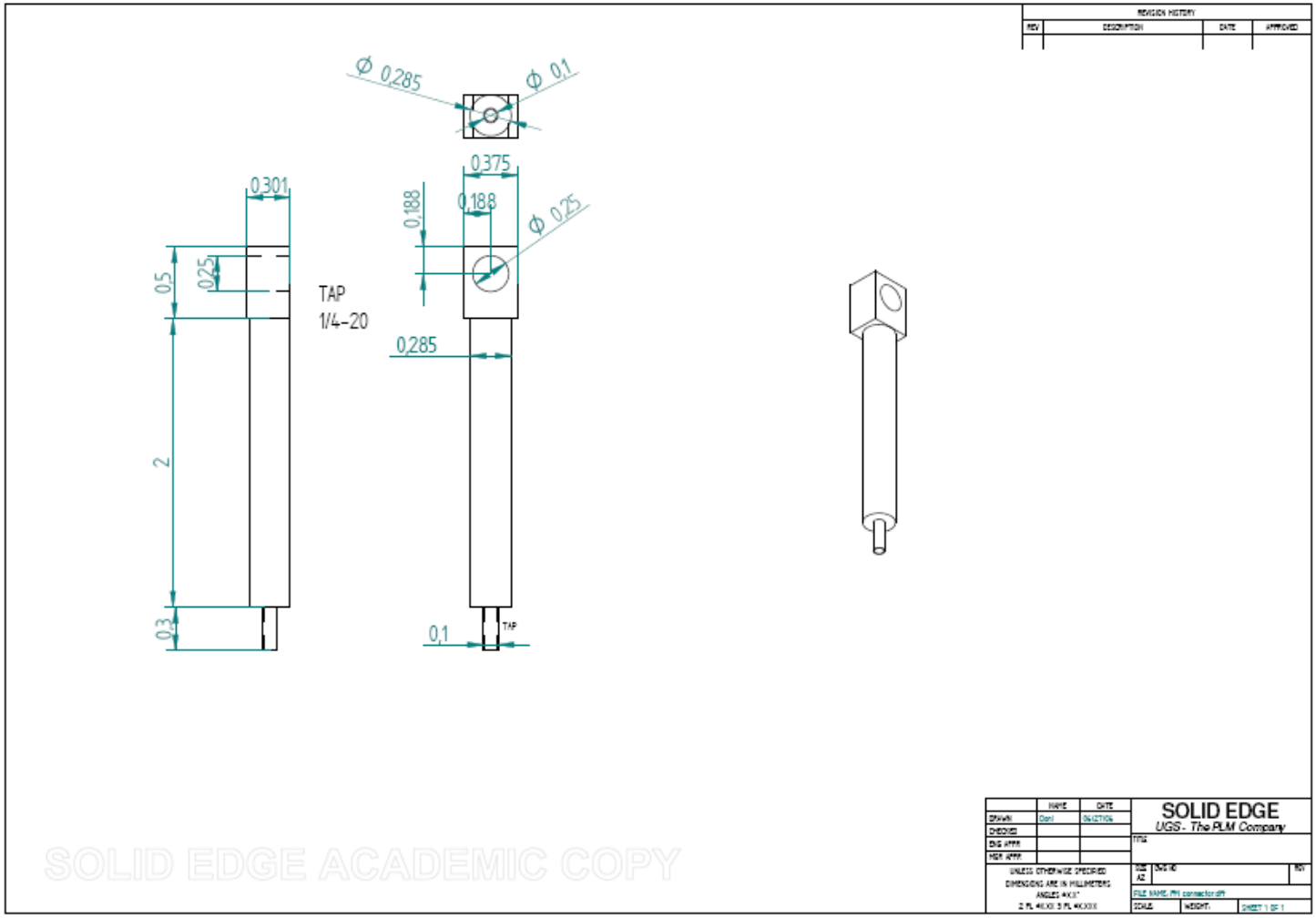

BIBLIOGRAPHY

1. Kanani, M., et al., *Late incompetence of the left atrioventricular valve after repair of atrioventricular septal defects: the morphologic perspective.* J Thorac Cardiovasc Surg, 2006. **132**(3): p. 640-6, 646 e1-3.

2. Treasure, T. and A. Hollman, *The surgery of mitral stenosis 1898-1948: why did it take 50 years to establish mitral valvotomy?* Ann R Coll Surg Engl, 1995. **77**(2): p. 145-51.

3. Warden, H.E., et al., *Controlled cross circulation for open intracardiac surgery: physiologic studies and results of creation and closure of ventricular septal defects.* J Thorac Surg, 1954. **28**(3): p. 331-41; discussion, 341-3.

4. Rose, J.C., et al., *The hemodynamic alterations produced by a plastic valvular prosthesis for severe aortic insufficiency in man.* J Clin Invest, 1954. **33**(6): p. 891-900.

5. Swanson, J.S. and A. Starr, *The ball valve experience over three decades.* Ann Thorac Surg, 1989. **48**(3 Suppl): p. S51-2.

6. Gao, G., et al., *Forty-year survival with the Starr-Edwards heart valve prosthesis.* J Heart Valve Dis, 2004. **13**(1): p. 91-6; discussion 96.

7. Carpentier, A., *Cardiac valve surgery--the "French correction".* J Thorac Cardiovasc Surg, 1983. **86**(3): p. 323-37.

8. Levowitz, B.S., et al., *Thrombus formation at the mitral annulus caused by prosthetic rings. An experimental study.* Am J Surg, 1962. **103**: p. 481-6.

9. Anyanwu, A.C. and D.H. Adams, *Etiologic classification of degenerative mitral valve disease: Barlow's disease and fibroelastic deficiency.* Semin Thorac Cardiovasc Surg, 2007. **19**(2): p. 90-6.

10. Flameng, W., et al., *Durability of mitral valve repair in Barlow disease versus fibroelastic deficiency.* J Thorac Cardiovasc Surg, 2008. **135**(2): p. 274-82.

11. Magne, J., et al., *Ischemic mitral regurgitation: a complex multifaceted disease.* Cardiology, 2009. **112**(4): p. 244-59.

12. Murashita, T., et al., *Left atrioventricular valve regurgitation after repair of incomplete atrioventricular septal defect.* Ann Thorac Surg, 2004. **77**(6): p. 2157-62.

13. Gorman, J.H., 3rd, et al., *Annuloplasty ring selection for chronic ischemic mitral regurgitation: lessons from the ovine model.* Ann Thorac Surg, 2003. **76**(5): p. 1556-63.

14. Gorman, J.H., 3rd, et al., *Distortions of the mitral valve in acute ischemic mitral regurgitation.* Ann Thorac Surg, 1997. **64**(4): p. 1026-31.

15. Gorman, J.H., 3rd, et al., *Infarct size and location determine development of mitral regurgitation in the sheep model.* J Thorac Cardiovasc Surg, 1998. **115**(3): p. 615-22.

16. Gorman, R.C., et al., *Pathogenesis of acute ischemic mitral regurgitation in three dimensions.* J Thorac Cardiovasc Surg, 1995. **109**(4): p. 684-93.

17. Tibayan, F.A., et al., *Geometric distortions of the mitral valvular-ventricular complex in chronic ischemic mitral regurgitation.* Circulation, 2003. **108 Suppl 1**: p. II116-21.

18. Timek, T.A., et al., *Ischemia in three left ventricular regions: Insights into the pathogenesis of acute ischemic mitral regurgitation.* J Thorac Cardiovasc Surg, 2003. **125**(3): p. 559-69.

19. Timek, T.A., et al., *Annular versus subvalvular approaches to acute ischemic mitral regurgitation.* Circulation, 2002. **106**(12 Suppl 1): p. I27-I32.

20. Sharma, P., *Sushruta Samhita - English Translation of Text and Dalhana's Commentary with Critical Notes*. 1983.

21. Dwivedi, G. and S. Dwivedi, *Sushruta - the Clinician - Teacher Par Excellence.* Indian Journal of Chest Diseases and Allied Science, 2007(49): p. 243-244.

22. Harvey, W., *Exercitatio Anatomica de Motu Cordis et Sanguinis in Animalibus.* 1628.

23. *The Circulatory System*. [cited; Available from: http://en.wikipedia.org/wiki/Circulatory_system.

24. *The Human Heart*. [cited; Available from: http://www.cts.usc.edu/.

25. *Trilayered Human Myocardial Structure*. [cited; Available from: http://www.jdaross.cwc.net.

26. *The Actin Myosin Structure in Human Heart.*

27. Silverthorn, D.U., *Human Physiology: an Integrated Approach*. III ed. 2003: Pearson.

28. Adams, D. *The Mitral Valve*. [cited; Available from: www.mitralvalverepair.org.

29. Anderson, R. and A. Becker, *Anatomy of the Heart*. 1982.

30. Tsakiris, A.G., et al., *Size and motion of the mitral valve annulus in anesthetized intact dogs.* J Appl Physiol, 1971. **30**(5): p. 611-8.

31. Levine, R.A., et al., *Three-dimensional echocardiographic reconstruction of the mitral valve, with implications for the diagnosis of mitral valve prolapse.* Circulation, 1989. **80**(3): p. 589-98.

32. Fenoglio, J.J., Jr., et al., *Canine mitral complex. Ultrastructure and electromechanical properties.* Circ Res, 1972. **31**(3): p. 417-30.

33. Lam, J.H., et al., *Morphology of the human mitral valve. I. Chordae tendineae: a new classification.* Circulation, 1970. **41**(3): p. 449-58.

34. Kalmanson, D., *The Mitral Valve - A Pluridisciplinary Approach*. 1976: Publishing Sciences Group.

35. Liao, J., et al., *Ultrastructure of porcine mitral valve chordae tendineae.* J Heart Valve Dis, 2009. **18**(3): p. 292-9.

36. Liao, J. and I. Vesely, *A structural basis for the size-related mechanical properties of mitral valve chordae tendineae.* J Biomech, 2003. **36**(8): p. 1125-33.

37. Liao, J. and I. Vesely, *Relationship between collagen fibrils, glycosaminoglycans, and stress relaxation in mitral valve chordae tendineae.* Ann Biomed Eng, 2004. **32**(7): p. 977-83.

38. Liao, J. and I. Vesely, *Skewness angle of interfibrillar proteoglycans increases with applied load on mitral valve chordae tendineae.* J Biomech, 2007. **40**(2): p. 390-8.

39. Kunzelman, K.S. and R.P. Cochran, *Mechanical properties of basal and marginal mitral valve chordae tendineae.* ASAIO Trans, 1990. **36**(3): p. M405-8.

40. Lim, K.O., *Mechanical properties and ultrastructure of normal human tricuspid valve chordae tendineae.* Jpn J Physiol, 1980. **30**(3): p. 455-64.

41. Lim, K.O. and D.R. Boughner, *Mechanical properties of human mitral valve chordae tendineae: variation with size and strain rate.* Can J Physiol Pharmacol, 1975. **53**(3): p. 330-9.

42. Lim, K.O. and D.R. Boughner, *Morphology and relationship to extensibility curves of human mitral valve chordae tendineae.* Circ Res, 1976. **39**(4): p. 580-5.

43. Lim, K.O. and D.R. Boughner, *Scanning electron microscopical study of human mitral valve chordae tendineae.* Arch Pathol Lab Med, 1977. **101**(5): p. 236-8.

44. Lim, K.O., D.R. Boughner, and D.G. Perkins, *Ultrastructure and mechanical properties of chordae tendineae from a myxomatous tricuspid valve.* Jpn Heart J, 1983. **24**(4): p. 539-48.

45. Sedransk, K.L., K.J. Grande-Allen, and I. Vesely, *Failure mechanics of mitral valve chordae tendineae.* J Heart Valve Dis, 2002. **11**(5): p. 644-50.

46. Ritchie, J., et al., *The material properties of the native porcine mitral valve chordae tendineae: an in vitro investigation.* J Biomech, 2006. **39**(6): p. 1129-35.

47. Ritchie, J., J.N. Warnock, and A.P. Yoganathan, *Structural characterization of the chordae tendineae in native porcine mitral valves.* Ann Thorac Surg, 2005. **80**(1): p. 189-97.

48. Jimenez, J.H., et al., *Mitral valve function and chordal force distribution using a flexible annulus model: an in vitro study.* Ann Biomed Eng, 2005. **33**(5): p. 557-66.

49. Jimenez, J.H., et al., *Effects of papillary muscle position on chordal force distribution: an in-vitro study.* J Heart Valve Dis, 2005. **14**(3): p. 295-302.

50. Jimenez, J.H., et al., *Effects of a saddle shaped annulus on mitral valve function and chordal force distribution: an in vitro study.* Ann Biomed Eng, 2003. **31**(10): p. 1171-81.

51. Yamauchi, T., et al., *Evaluation of the mitral valve leaflet morphology after mitral valve reconstruction with a concept "coaptation length index".* J Card Surg, 2005. **20**(5): p. 432-5.

52. Yamauchi, T., et al., *Evaluation of the mitral valve leaflet morphology after mitral valve reconstruction with a concept "coaptation length index".* J Card Surg, 2004. **19**(6): p. 535-8.

53. Nolan, S.P., et al., *In vivo studies of instantaneous blood flow across mitral ball-valve prostheses: effects of cardiac output and heart rate on transvalvular energy loss.* Ann Surg, 1969. **169**(4): p. 551-9.

54. Nolan, S.P., et al., *The influence of atrial contraction and mitral valve mechanics on ventricular filing. A study of instantaneous mitral valve flow in vivo.* Am Heart J, 1969. **77**(6): p. 784-91.

55. Tsakiris, A.G., et al., *Sudden interruption of leaflet opening by ventricular contractions: a mechanism of mitral regurgitation.* J Appl Physiol, 1976. **40**(2): p. 132-7.

56. Eckert, C.E., et al., *In vivo dynamic deformation of the mitral valve annulus.* Ann Biomed Eng, 2009. **37**(9): p. 1757-71.

57. Sacks, M.S., et al., *In-vivo dynamic deformation of the mitral valve anterior leaflet.* Ann Thorac Surg, 2006. **82**(4): p. 1369-77.

58. Sacks, M.S., et al., *Surface strains in the anterior leaflet of the functioning mitral valve.* Ann Biomed Eng, 2002. **30**(10): p. 1281-90.

59. He, Z., et al., *In vitro dynamic strain behavior of the mitral valve posterior leaflet.* J Biomech Eng, 2005. **127**(3): p. 504-11.

60. Salisbury, P.F., C.E. Cross, and P.A. Rieben, *Chorda Tendinea Tension.* Am J Physiol, 1963. **205**: p. 385-92.

61. Einstein, D.R., et al., *Non-linear fluid-coupled computational model of the mitral valve.* J Heart Valve Dis, 2005. **14**(3): p. 376-85.

62. Kunzelman, K.S., et al., *Finite element analysis of the mitral valve.* J Heart Valve Dis, 1993. **2**(3): p. 326-40.

63. Kunzelman, K.S., et al., *Anatomic basis for mitral valve modelling.* J Heart Valve Dis, 1994. **3**(5): p. 491-6.

64. Kunzelman, K.S., D.R. Einstein, and R.P. Cochran, *Fluid-structure interaction models of the mitral valve: function in normal and pathological states.* Philos Trans R Soc Lond B Biol Sci, 2007. **362**(1484): p. 1393-406.

65. Castaneda, A., et al., *Cardiac Surgery for the Neonate and Infant*. 1 ed. 1994: Saunders.

66. Lev, M., *The architecture of the conduction system in congenital heart disease. II. Tetralogy of Fallot.* AMA Arch Pathol, 1959. **67**(5): p. 572-87.

67. Bharati, S., et al., *The surgical anatomy of common atrioventricular orifice associated with tetralogy of Fallot, double outlet right ventricle and complete regular transposition.* Circulation, 1980. **61**(6): p. 1142-9.

68. Bharati, S. and M. Lev, *The spectrum of common atrioventricular orifice (canal).* Am Heart J, 1973. **86**(4): p. 553-61.

69. Bharati, S., et al., *Surgical anatomy of the atrioventricular valve in the intermediate type of common atrioventricular orifice.* J Thorac Cardiovasc Surg, 1980. **79**(6): p. 884-9.

70. Backer, C.L., R.D. Stewart, and C. Mavroudis, *Overview: history, anatomy, timing, and results of complete atrioventricular canal.* Semin Thorac Cardiovasc Surg Pediatr Card Surg Annu, 2007: p. 3-10.

71. Kahn, D.R., et al., *Recent results after repair of atrioventricular canal.* J Thorac Cardiovasc Surg, 1977. **73**(3): p. 413-5.

72. Midgley, F.M., et al., *Experience with repair of complete atrioventricular canal.* Ann Thorac Surg, 1980. **30**(2): p. 151-9.

73. Rastelli, G., J.W. Kirklin, and J.L. Titus, *Anatomic observations on complete form of persistent common atrioventricular canal with special reference to atrioventricular valves.* Mayo Clin Proc, 1966. **41**(5): p. 296-308.

74. Rastelli, G.C., et al., *Surgical repair of the complete form of persistent common atrioventricular canal.* J Thorac Cardiovasc Surg, 1968. **55**(3): p. 299-308.

75. Rastelli, G.C., P.A. Ongley, and D.C. McGoon, *Surgical repair of complete atrioventricular canal with anterior common leaflet undivided and unattached to ventricular septum.* Mayo Clin Proc, 1969. **44**(5): p. 335-41.

76. Rastelli, G.C., P.A. Ongley, and J.L. Titus, *Ventricular septal defect of atrioventricular canal type with straddling right atrioventricular valve and mitral valve deformity.* Circulation, 1968. **37**(5): p. 816-25.

77. Rastelli, G.C., W.H. Weidman, and J.W. Kirklin, *Surgical Repair of the Partial Form of Persistent Common Atrioventricular Canal, with Special Reference to the Problem of Mitral Valve Incompetence.* Circulation, 1965. **31**: p. SUPPL 1:31-5.

78. Barratt-Boyes, B.G. and J.M. Neutze, *Primary repair of tetralogy of Fallot in infancy using profound hypothermia with circulatory arrest and limited cardiopulmonary bypass: a comparison with conventional two stage management.* Ann Surg, 1973. **178**(4): p. 406-11.

79. Carpentier, A., *Surgical anatomy and management of the mitral components of atrioventricular canal defects.*, ed. R. Anderson and E. Shinebourne. 1978, Pediatric Cardiology: Churchill Livingstone.

80. Kohl, T. and N.H. Silverman, *Comparison of cleft and papillary muscle position in cleft mitral valve and atrioventricular septal defect.* Am J Cardiol, 1996. **77**(2): p. 164-9.

81. Gillinov, A.M., et al., *Durability of mitral valve repair for degenerative disease.* J Thorac Cardiovasc Surg, 1998. **116**(5): p. 734-43.

82. Organization, W.H., *Rheumatic Fever and Rheumatic Heart Disease - Report of a WHO Expert Cosultation*. 2001, World Health Organization.

83. Tyrrell, P.N., et al., *Rheumatic Disease and Carotid Intima-Media Thickness. A Systematic Review and Meta-Analysis.* Arterioscler Thromb Vasc Biol.

84. Barlow, J.B. and W.A. Pocock, *Mitral valve prolapse, the specific billowing mitral leaflet syndrome, or an insignificant non-ejection systolic click.* Am Heart J, 1979. **97**(3): p. 277-85.

85. Barlow, J.B. and W.A. Pocock, *The significance of aortic ejection systolic murmurs.* Am Heart J, 1962. **64**: p. 149-58.

86. Barlow, J.B. and W.A. Pocock, *The significance of late systolic murmurs and mid-late systolic clicks.* Md State Med J, 1963. **12**: p. 76-7.

87. Barlow, J.B. and W.A. Pocock, *The isolated systolic murmur.* S Afr Med J, 1965. **39**(39): p. 909-18.

88. Criley, J.M., et al., *Prolapse of the mitral valve: clinical and cine-angiocardiographic findings.* Br Heart J, 1966. **28**(4): p. 488-96.

89. Carpentier, A., et al., *Reconstructive surgery of mitral valve incompetence: ten-year appraisal.* J Thorac Cardiovasc Surg, 1980. **79**(3): p. 338-48.

90. Grau, J.B., et al., *The genetics of mitral valve prolapse.* Clin Genet, 2007. **72**(4): p. 288-95.

91. Pedersen, L.G., et al., *Transcription levels of endothelin-1 and endothelin receptors are associated with age and leaflet location in porcine mitral valves.* J Vet Med A Physiol Pathol Clin Med, 2007. **54**(3): p. 113-8.

92. Pedersen, L.G., et al., *Increased expression of endothelin B receptor in static stretch exposed porcine mitral valve leaflets.* Res Vet Sci, 2007. **82**(2): p. 232-8.

93. Gazoni, L.M., et al., *A simplified approach to degenerative disease: triangular resections of the mitral valve.* Ann Thorac Surg, 2007. **83**(5): p. 1658-64; discussion 1664-5.

94. Grossi, E.A., et al., *Early results of posterior leaflet folding plasty for mitral valve reconstruction.* Ann Thorac Surg, 1998. **65**(4): p. 1057-9.

95. Nakajima, M., et al., *Leaflet folding plasty combined with annular plication for mitral valve repair.* Ann Thorac Surg, 2004. **77**(3): p. 1103-4.

96. Falk, V., et al., *How does the use of polytetrafluoroethylene neochordae for posterior mitral valve prolapse (loop technique) compare with leaflet resection? A prospective randomized trial.* J Thorac Cardiovasc Surg, 2008. **136**(5): p. 1205; discussion 1205-6.

97. Zussa, C., et al., *Surgical technique for artificial mitral chordae implantation.* J Card Surg, 1991. **6**(4): p. 432-8.

98. Maisano, F., et al., *The edge-to-edge technique: a simplified method to correct mitral insufficiency.* Eur J Cardiothorac Surg, 1998. **13**(3): p. 240-5; discussion 245-6.

99. Krause, A.H., et al., *Early experience with mitral valve reconstruction for mitral insufficiency.* Am J Surg, 1991. **161**(5): p. 563-6.

100. Salati, M., et al., *Correction of anterior mitral prolapse. Results of chordal transposition.* J Thorac Cardiovasc Surg, 1992. **104**(5): p. 1268-73.

101. Spencer, F.C., et al., *Experiences with the Carpentier techniques of mitral valve reconstruction in 103 patients (1980-1985).* J Thorac Cardiovasc Surg, 1985. **90**(3): p. 341-50.

102. Fornes, P., et al., *Correlation between clinical and histologic patterns of degenerative mitral valve insufficiency: a histomorphometric study of 130 excised segments.* Cardiovasc Pathol, 1999. **8**(2): p. 81-92.

103. Filsoufi, F. and A. Carpentier, *Principles of reconstructive surgery in degenerative mitral valve disease.* Semin Thorac Cardiovasc Surg, 2007. **19**(2): p. 103-10.

104. Braunberger, E., et al., *Very long-term results (more than 20 years) of valve repair with carpentier's techniques in nonrheumatic mitral valve insufficiency.* Circulation, 2001. **104**(12 Suppl 1): p. I8-11.

105. Hueb, A.C., et al., *Ventricular remodeling and mitral valve modifications in dilated cardiomyopathy: new insights from anatomic study.* J Thorac Cardiovasc Surg, 2002. **124**(6): p. 1216-24.

106. Kaji, S., et al., *Annular geometry in patients with chronic ischemic mitral regurgitation: three-dimensional magnetic resonance imaging study.* Circulation, 2005. **112**(9 Suppl): p. I409-14.

107. Levine, R.A. and E. Schwammenthal, *Ischemic mitral regurgitation on the threshold of a solution: from paradoxes to unifying concepts.* Circulation, 2005. **112**(5): p. 745-58.

108. Ahmad, R.M., et al., *Annular geometry and motion in human ischemic mitral regurgitation: novel assessment with three-dimensional echocardiography and computer reconstruction.* Ann Thorac Surg, 2004. **78**(6): p. 2063-8; discussion 2068.

109. Watanabe, N., et al., *Geometric deformity of the mitral annulus in patients with ischemic mitral regurgitation: a real-time three-dimensional echocardiographic study.* J Heart Valve Dis, 2005. **14**(4): p. 447-52.

110. Watanabe, N., et al., *Quantitation of mitral valve tenting in ischemic mitral regurgitation by transthoracic real-time three-dimensional echocardiography.* J Am Coll Cardiol, 2005. **45**(5): p. 763-9.

111. Watanabe, N., et al., *Mitral annulus flattens in ischemic mitral regurgitation: geometric differences between inferior and anterior myocardial infarction: a real-time 3-dimensional echocardiographic study.* Circulation, 2005. **112**(9 Suppl): p. I458-62.

112. He, S., et al., *Integrated mechanism for functional mitral regurgitation: leaflet restriction versus coapting force: in vitro studies.* Circulation, 1997. **96**(6): p. 1826-34.

113. He, S., et al., *Mitral valve compensation for annular dilatation: in vitro study into the mechanisms of functional mitral regurgitation with an adjustable annulus model.* J Heart Valve Dis, 1999. **8**(3): p. 294-302.

114. Tahta, S.A., et al., *Outcome after mitral valve repair for functional ischemic mitral regurgitation.* J Heart Valve Dis, 2002. **11**(1): p. 11-8; discussion 18-9.

115. Agricola, E., et al., *Echocardiographic classification of chronic ischemic mitral regurgitation caused by restricted motion according to tethering pattern.* Eur J Echocardiogr, 2004. **5**(5): p. 326-34.

116. Srichai, M.B., et al., *Ischemic mitral regurgitation: impact of the left ventricle and mitral valve in patients with left ventricular systolic dysfunction.* Ann Thorac Surg, 2005. **80**(1): p. 170-8.

117. Salgo, I.S., et al., *Effect of annular shape on leaflet curvature in reducing mitral leaflet stress.* Circulation, 2002. **106**(6): p. 711-7.

118. Votta, E., et al., *The Geoform disease-specific annuloplasty system: a finite element study.* Ann Thorac Surg, 2007. **84**(1): p. 92-101.

119. Bhattacharya, S. and Z. He, *Role of annulus tension in annular dilatation.* J Heart Valve Dis, 2009. **18**(5): p. 481-7.

120. Schievano, S., et al., *Percutaneous mitral valve dilatation: single balloon versus double balloon. A finite element study.* J Heart Valve Dis, 2009. **18**(1): p. 28-34.

121. Frakes, D.H., et al., *Application of an adaptive control grid interpolation technique to morphological vascular reconstruction.* IEEE Trans Biomed Eng, 2003. **50**(2): p. 197-206.

122. Smith, D.B., et al., *Surface geometric analysis of anatomic structures using biquintic finite element interpolation.* Ann Biomed Eng, 2000. **28**(6): p. 598-611.

123. Takahashi, K., et al., *Three-dimensional echocardiography improves the understanding of the mechanisms and site of left atrioventricular valve regurgitation in atrioventricular septal defect.* J Am Soc Echocardiogr, 2006. **19**(12): p. 1502-10.

124. Wetter, J., et al., *Closure of the zone of apposition at correction of complete atrioventricular septal defect improves outcome.* Eur J Cardiothorac Surg, 2000. **17**(2): p. 146-53.

125. Acar, P., et al., *Three-dimensional echocardiographic analysis of valve anatomy as a determinant of mitral regurgitation after surgery for atrioventricular septal defects.* Am J Cardiol, 1999. **83**(5): p. 745-9.

126. Honjo, O., et al., *Midterm outcome of mitral valve repair for congenital mitral regurgitation in infants and children.* Interact Cardiovasc Thorac Surg, 2006. **5**(5): p. 589-93.

127. Barlow, J.B. and C.K. Bosman, *Aneurysmal protrusion of the posterior leaflet of the mitral valve. An auscultatory-electrocardiographic syndrome.* Am Heart J, 1966. **71**(2): p. 166-78.

128. Dreyfus, G.D., et al., *Posterior leaflet preservation in mitral valve prolapse: a new approach to mitral repair.* J Heart Valve Dis, 2006. **15**(4): p. 528-30.

129. Perier, P., et al., *Toward a new paradigm for the reconstruction of posterior leaflet prolapse: midterm results of the "respect rather than resect" approach.* Ann Thorac Surg, 2008. **86**(3): p. 718-25; discussion 718-25.

130. Cagli, K., *A simple method of making artificial chordal loops for mitral valve repair.* Ann Thorac Surg. **89**(2): p. e12-4.

131. Smith, J.M. and H. Stein, *Endoscopic placement of multiple artificial chordae with robotic assistance and nitinol clip fixation.* J Thorac Cardiovasc Surg, 2008. **135**(3): p. 610-4.

132. Seeburger, J., T. Kuntze, and F.W. Mohr, *Gore-tex chordoplasty in degenerative mitral valve repair.* Semin Thorac Cardiovasc Surg, 2007. **19**(2): p. 111-5.

133. Chen, L., F.C. Yin, and K. May-Newman, *The structure and mechanical properties of the mitral valve leaflet-strut chordae transition zone.* J Biomech Eng, 2004. **126**(2): p. 244-51.

134. Drury, N.E. and S.A. Nashef, *Outcomes of cardiac surgery in the elderly.* Expert Rev Cardiovasc Ther, 2006. **4**(4): p. 535-42.

135. Gammie, J.S., S.T. Bartlett, and B.P. Griffith, *Small-incision mitral valve repair: safe, durable, and approaching perfection.* Ann Surg, 2009. **250**(3): p. 409-15.

136. Gillinov, A.M., et al., *Valve repair versus valve replacement for degenerative mitral valve disease.* J Thorac Cardiovasc Surg, 2008. **135**(4): p. 885-93, 893 e1-2.

137. Hanania, G. and J.P. Maroni, *[Operative risk of heart valve surgery after 80 years].* Ann Cardiol Angeiol (Paris), 2005. **54**(6): p. 339-43.

138. Lee, R., et al., *Mitral valve repair in the elderly: operative risk for patients over 70 years of age is acceptable.* J Cardiovasc Surg (Torino), 2003. **44**(2): p. 157-61.

139. Maisano, F., et al., *Quality of life of elderly patients following valve surgery for chronic organic mitral regurgitation.* Eur J Cardiothorac Surg, 2009. **36**(2): p. 261-6; discussion 266.

140. Levine, R.A., et al., *The relationship of mitral annular shape to the diagnosis of mitral valve prolapse.* Circulation, 1987. **75**(4): p. 756-67.

141. Flachskampf, F.A., et al., *Analysis of shape and motion of the mitral annulus in subjects with and without cardiomyopathy by echocardiographic 3-dimensional reconstruction.* J Am Soc Echocardiogr, 2000. **13**(4): p. 277-87.

142. Jimenez, J.H., et al., *A saddle-shaped annulus reduces systolic strain on the central region of the mitral valve anterior leaflet.* J Thorac Cardiovasc Surg, 2007. **134**(6): p. 1562-8.

143. Watanabe, N., et al., *Geometric differences of the mitral valve tenting between anterior and inferior myocardial infarction with significant ischemic mitral regurgitation: quantitation by novel software system with transthoracic real-time three-dimensional echocardiography.* J Am Soc Echocardiogr, 2006. **19**(1): p. 71-5.

144. Borger, M.A., et al., *Initial results of the chordal-cutting operation for ischemic mitral regurgitation.* J Thorac Cardiovasc Surg, 2007. **133**(6): p. 1483-92.

VITA

Sai Muralidhar Padala, was born on December 23, 1982 in Hyderabad, Andhra Pradesh, INDIA. He obtained his Secondary School Certificate from Sri Satya Sai Vidya Vihar in 1998, completed Intermediate from Little Flower Junior College in 2000, a Bachelor of Engineering (B.E) degree in Mechanical Engineering from Osmania University, India in 2004 and a Master of Science (M.S) degree in Mechanical Engineering from Georgia Institute of Technology in 2008. Prior to joining Georgia Institute of Technology, Murali worked as a research intern in 2002 in the Integrated Combined Cycle Power Plant (IGCCPP) division of Bharat Heavy Electricals Limited and completed a one-year competitive internship in 2004 in the Hypersonic Propulsion Division of the Indian Defense Research and Development Organization. At Georgia Institute of Technology, he received the American Heart Association Pre-doctoral Fellowship in Cardiovascular Disease in 2008 and the Biomedical Engineering Gandy Diaz Teaching Fellowship in 2009. His hobbies include watercolor painting, photography, creative writing, travelling and outdoor activities.